frontiers | Research Topics

Animal viruses: pathogenesis, immune escape, spatio-temporal evolution, vaccines, and cross-species transmission

Edited by
Xusheng Qiu, Shen Yang, Wei Wang and
Min Zheng

Published in
Frontiers in Immunology

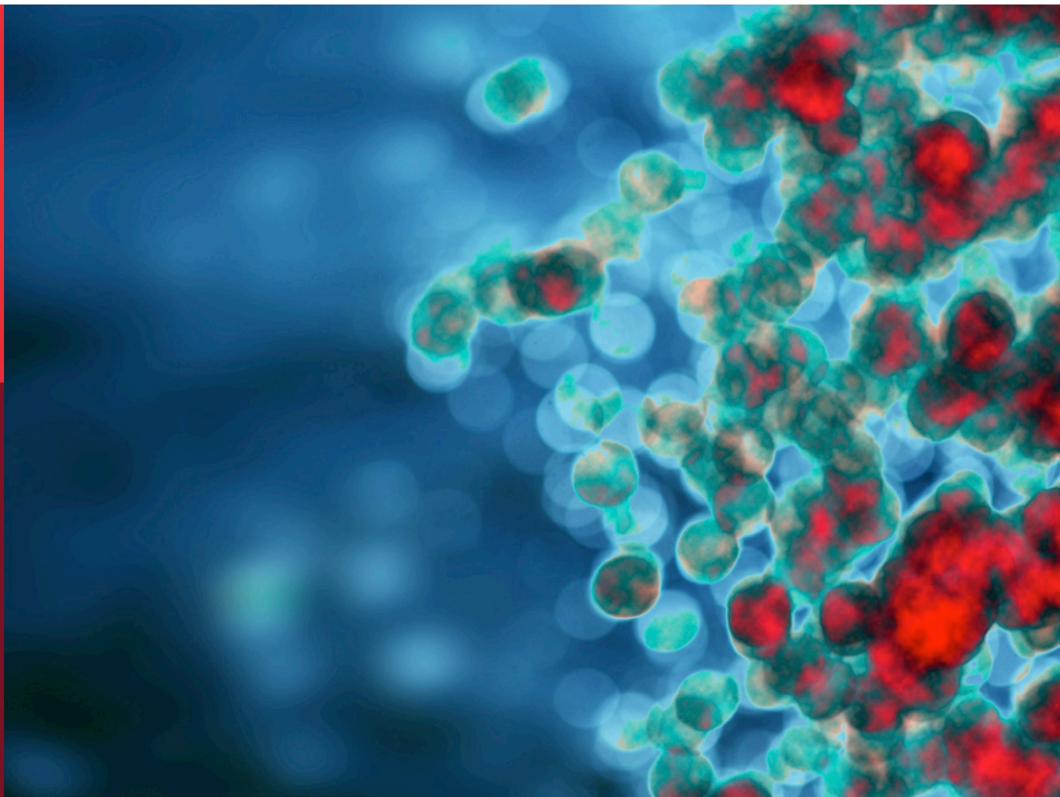

FRONTIERS EBOOK COPYRIGHT STATEMENT

The copyright in the text of individual articles in this ebook is the property of their respective authors or their respective institutions or funders. The copyright in graphics and images within each article may be subject to copyright of other parties. In both cases this is subject to a license granted to Frontiers.

The compilation of articles constituting this ebook is the property of Frontiers.

Each article within this ebook, and the ebook itself, are published under the most recent version of the Creative Commons CC-BY licence. The version current at the date of publication of this ebook is CC-BY 4.0. If the CC-BY licence is updated, the licence granted by Frontiers is automatically updated to the new version.

When exercising any right under the CC-BY licence, Frontiers must be attributed as the original publisher of the article or ebook, as applicable.

Authors have the responsibility of ensuring that any graphics or other materials which are the property of others may be included in the CC-BY licence, but this should be checked before relying on the CC-BY licence to reproduce those materials. Any copyright notices relating to those materials must be complied with.

Copyright and source acknowledgement notices may not be removed and must be displayed in any copy, derivative work or partial copy which includes the elements in question.

All copyright, and all rights therein, are protected by national and international copyright laws. The above represents a summary only. For further information please read Frontiers' Conditions for Website Use and Copyright Statement, and the applicable CC-BY licence.

ISSN 1664-8714
ISBN 978-2-8325-6111-9
DOI 10.3389/978-2-8325-6111-9

About Frontiers

Frontiers is more than just an open access publisher of scholarly articles: it is a pioneering approach to the world of academia, radically improving the way scholarly research is managed. The grand vision of Frontiers is a world where all people have an equal opportunity to seek, share and generate knowledge. Frontiers provides immediate and permanent online open access to all its publications, but this alone is not enough to realize our grand goals.

Frontiers journal series

The Frontiers journal series is a multi-tier and interdisciplinary set of open-access, online journals, promising a paradigm shift from the current review, selection and dissemination processes in academic publishing. All Frontiers journals are driven by researchers for researchers; therefore, they constitute a service to the scholarly community. At the same time, the *Frontiers journal series* operates on a revolutionary invention, the tiered publishing system, initially addressing specific communities of scholars, and gradually climbing up to broader public understanding, thus serving the interests of the lay society, too.

Dedication to quality

Each Frontiers article is a landmark of the highest quality, thanks to genuinely collaborative interactions between authors and review editors, who include some of the world's best academicians. Research must be certified by peers before entering a stream of knowledge that may eventually reach the public - and shape society; therefore, Frontiers only applies the most rigorous and unbiased reviews. Frontiers revolutionizes research publishing by freely delivering the most outstanding research, evaluated with no bias from both the academic and social point of view. By applying the most advanced information technologies, Frontiers is catapulting scholarly publishing into a new generation.

What are Frontiers Research Topics?

Frontiers Research Topics are very popular trademarks of the *Frontiers journals series*: they are collections of at least ten articles, all centered on a particular subject. With their unique mix of varied contributions from Original Research to Review Articles, Frontiers Research Topics unify the most influential researchers, the latest key findings and historical advances in a hot research area.

Find out more on how to host your own Frontiers Research Topic or contribute to one as an author by contacting the Frontiers editorial office: frontiersin.org/about/contact

Animal viruses: pathogenesis, immune escape, spatio-temporal evolution, vaccines, and cross-species transmission

Topic editors

Xusheng Qiu — Shanghai Veterinary Research Institute, Chinese Academy of Agricultural Sciences, China
Shen Yang — Cedars Sinai Medical Center, United States
Wei Wang — Wenzhou University, China
Min Zheng — Guangxi Center for Animal Disease Prevention and Control, China

Citation

Qiu, X., Yang, S., Wang, W., Zheng, M., eds. (2025). *Animal viruses: pathogenesis, immune escape, spatio-temporal evolution, vaccines, and cross-species transmission*. Lausanne: Frontiers Media SA. doi: 10.3389/978-2-8325-6111-9

Table of contents

Frontiers in Immunology

TYPE Review
PUBLISHED 25 July 2023
DOI 10.3389/fimmu.2023.1228811

Check for updates

OPEN ACCESS

EDITED BY
Wei Wang,
Wenzhou University, China

REVIEWED BY
Dai Jun,
Guangxi University, China
Liang Cao,
Jilin University, China

*CORRESPONDENCE
Hua-Ji Qiu
qiuhuaji@caas.cn
Su Li
lisu@caas.cn

†These authors have contributed equally to this work

RECEIVED 25 May 2023
ACCEPTED 07 July 2023
PUBLISHED 25 July 2023

CITATION
Li J, Wang Y, Deng H, Li S and Qiu H-J (2023) Cellular metabolism hijacked by viruses for immunoevasion: potential antiviral targets.
Front. Immunol. 14:1228811.
doi: 10.3389/fimmu.2023.1228811

COPYRIGHT
© 2023 Li, Wang, Deng, Li and Qiu. This is an open-access article distributed under the terms of the Creative Commons Attribution License (CC BY). The use, distribution or reproduction in other forums is permitted, provided the original author(s) and the copyright owner(s) are credited and that the original publication in this journal is cited, in accordance with accepted academic practice. No use, distribution or reproduction is permitted which does not comply with these terms.

Cellular metabolism hijacked by viruses for immunoevasion: potential antiviral targets

Jiaqi Li†, Yanjin Wang†, Hao Deng, Su Li* and Hua-Ji Qiu*

State Key Laboratory for Animal Disease Control and Prevention, National African Swine Fever Para-reference Laboratory, National High Containment Facilities for Animal Diseases Control and Prevention, Harbin Veterinary Research Institute, Chinese Academy of Agricultural Sciences, Harbin, China

Cellular metabolism plays a central role in the regulation of both innate and adaptive immunity. Immune cells utilize metabolic pathways to modulate the cellular differentiation or death. The intricate interplay between metabolism and immune response is critical for maintaining homeostasis and effective antiviral activities. In recent years, immunometabolism induced by viral infections has been extensively investigated, and accumulating evidence has indicated that cellular metabolism can be hijacked to facilitate viral replication. Generally, virus-induced changes in cellular metabolism lead to the reprogramming of metabolites and metabolic enzymes in different pathways (glucose, lipid, and amino acid metabolism). Metabolic reprogramming affects the function of immune cells, regulates the expression of immune molecules and determines cell fate. Therefore, it is important to explore the effector molecules with immunomodulatory properties, including metabolites, metabolic enzymes, and other immunometabolism-related molecules as the antivirals. This review summarizes the relevant advances in the field of metabolic reprogramming induced by viral infections, providing novel insights for the development of antivirals.

KEYWORDS

immunometabolism, innate immunity, adaptive immunity, immunoevasion, metabolic reprogramming

1 Introduction

Immunometabolism is involved in various disorders, including viral infections, cancers, and autoimmune diseases (1–4). Changes in the cellular microenvironment (e.g., hypoxia or pathogen invasion) result in the differences of energy requirements for cell proliferation and survival (5). Notably, viral infections usually induce the changes of cellular metabolism, which provide essential materials for the virus life cycle, including viral replication and progeny virus production (6–8). Additionally, cellular metabolic changes can alter the cellular immune responses to modulate viral replication (6).

Cellular metabolism is also indispensable for the functions of immune cells, including lymphocytes, macrophages and neutrophils. For example, glutamine is an essential nutrient for the proliferation of lymphocytes, and is also required for the immunoregulatory activities of cells (9). Interestingly, immune cells exhibit different patterns of energy metabolism in the activated and resting states (Table 1). Metabolic pathways are usually associated with signal transduction and the differentiation of immune cells, and different immune cell subpopulations utilize different metabolic programs depending on their state and environment. It is generally accepted that metabolic signaling determines the cell fate (21). Reportedly, inhibition of phosphoglyceraldehyde dehydrogenase (PHGDH)-mediated serine metabolism can enhance the antiviral activities of macrophages, which is due to the activation of the TBK1-IRF3 signaling pathway by the downregulation of the PHGDH-mediated ATP6V0d2 (22), indicating that PHGDH could act as a potential antiviral target in macrophages. Altogether, the interplay between viral infections and immune cell metabolism is a complex and rapidly evolving field of research.

Viruses depend entirely on cellular metabolism for the energy and nutrients for replication. In contrast, cellular metabolites, metabolic regulators, and metabolic enzymes involved in cellular metabolism including glucose, lipids, amino acids and nucleotide metabolism, exert antiviral activities by regulating the host immune responses (6, 23). However, these metabolic processes can be hijacked by viruses to maintain the energetic and synthetic requirements of viral progeny. Some viruses mainly activate core catabolic processes (e.g., glycolysis and the tricarboxylic acid cycle) to maintain the energy, while others mainly modulate anabolic and biosynthetic processes (e.g., nucleotide, fatty acid and amino acid synthesis) to maintain the synthetic requirements (24). More specifically, different viruses lead to multiple alterations in cellular metabolites, metabolic regulators, and metabolic enzymes in different ways, which directly or indirectly affect cellular immune responses and regulate viral infections. Previous studies have shown that infection with coronavirus (25), herpes virus (26), or African swine fever virus (27) can induce alternations in immune cell metabolism. Therefore, elucidation of the effects of viruses on cellular metabolites, metabolism-related molecules and metabolic enzymes will facilitate the development of novel antiviral strategies (28).

2 Interactions between glucose metabolism signaling and viral immunoevasion

Glucose is the most important energy source and the main nutrient involved in cellular metabolism (29). Cellular respiration is divided into three steps: the Embden-Meyerhof pathway (EMP), the tricarboxylic acid (TCA) cycle, and oxidative phosphorylation (OXPHOS). The intermediate product of EMP, 6-phosphofructose, is involved in the hexosamine biosynthetic pathway (HBP), providing uridine 5'-diphosphate *N*-acetylglucosamine (UDP-GlcNAc) for target protein modifications, and is also involved in the epidermal growth factor receptor (EGFR)-mediated glucose and glutamate metabolism (30).

Several viruses can modulate the signaling processes involved in glucose metabolism in immune cells by hijacking cellular metabolites, metabolic regulators, and metabolic enzymes, such as glucose transporter protein (GLUT1), hexokinase 2 (HK2), and lactate (Figure 1). This modulation leads to a shift in energy metabolism from OXPHOS to glycolysis, which provides a substrate for the production of several biomolecules, including TCA cycle intermediates required for fatty acid anabolism and ribose phosphate pyrophosphate (PRPP) or NADPH for a base material of nucleotide anabolism to facilitate viral replication (31). Reportedly, human cytomegalovirus (HCMV) infection can promote the biosynthesis of glycolysis, metabolic enzymes, and pyrimidine nucleotides, which facilitates viral replication (32). The changes in metabolic signaling induced by viral infections require further investigation, which may guide the development of antiviral strategies.

TABLE 1 The regulation of different cellular metabolism pathways.

Cell types	Major energy metabolic pathways	Mediators	References
M1 macrophages	Glycolysis	HIF-1α, IRF3, and IRF5	(10)
Neutrophils	Glycolysis and glutaminolysis	HIF-1α	(11)
M2 macrophages	Oxidative phosphorylation and fatty acid oxidation	PPARγ	(12)
Näive T cells	Oxidative phosphorylation	HIF-1α	(13)
Memory T cells	Oxidative phosphorylation and fatty acid oxidation	AMPK	(14–16)
Effector T cells	Oxidative phosphorylation, glycolysis, and amino acid metabolism (arginine, tryptophan, serine, leucine, glutamine, and cysteine)	c-Myc and PI3K/Akt/mTORC	(17)
Effector B cells	Oxidative phosphorylation and glycolysis	HIF-1α	(18)
NK cells	Glycolysis	SREBP and c-Myc	(19, 20)

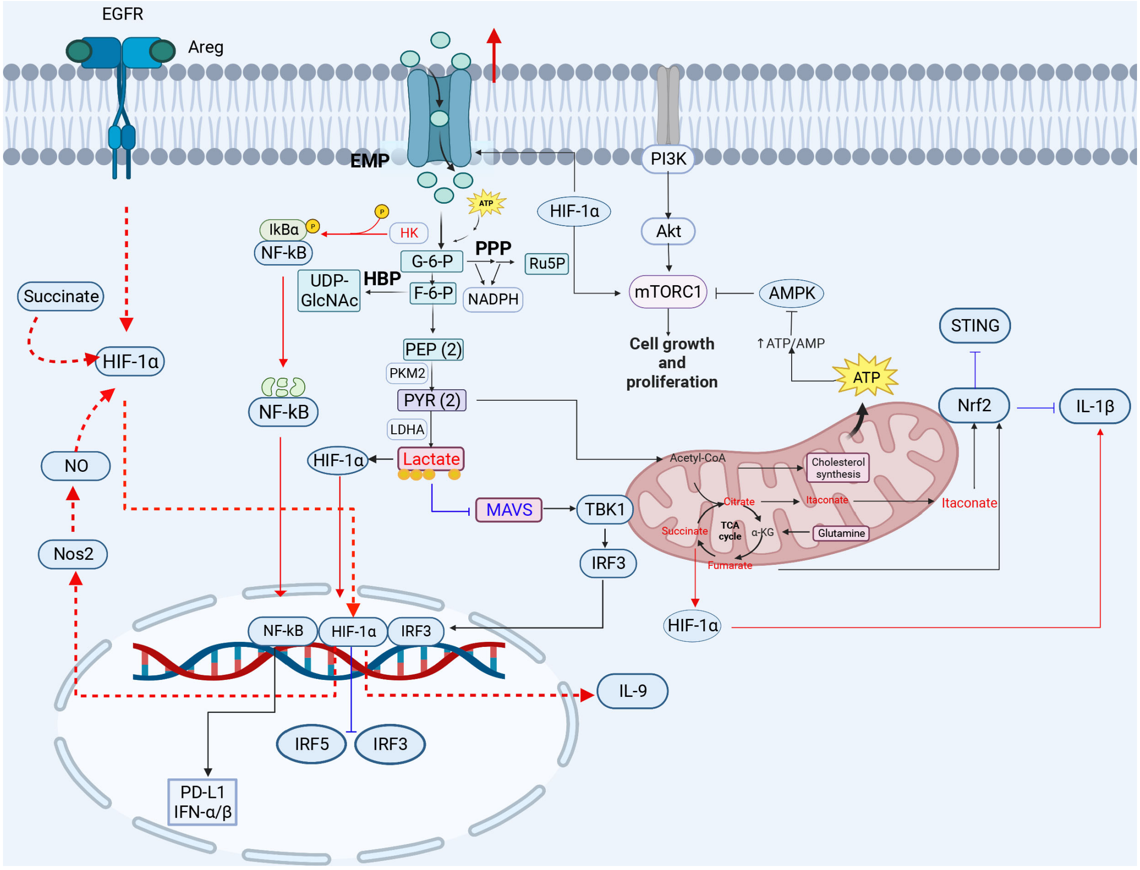

FIGURE 1
The crosstalk between glucose metabolism and innate immunity pathways. Glucose enters the cell and produces pyruvate, which is converted to lactate under hypoxic conditions. When high concentrations of fructose 6-phosphate are produced, the remaining fructose 6-phosphate enters the HBP pathway to produce UDP-GlcNAC. Acetyl-CoA enters the tricarboxylic acid cycle in the presence of sufficient oxygen, and is oxidized to produce citrate, eventually generating carbon dioxide and water, and releasing a large amount of energy. Glucose metabolism-related GLUT1, HK, LADH, OGT, HIF-1*α*, lactate, citrate, and succinate play important roles in inflammation, viral infection, and immunity (red lines indicate activation, blue lines indicate inhibition). 3-PG, 3-phosphoglycerate; 1,3-BPG, 1,3-bisphosphoglycerate; 2-PG, 2-phosphoglycerate; PEP, phosphoenolpyruvate; PYR, pyruvate; G3P, glyceraldehyde 3-phosphate; HK, hexokinase; LDH, lactate dehydrogenase; HBP, hexosamine pathway; PPP, pentose phosphate pathway. The red circle represents increased glucose intake. The figure was created by the BioRender software.

2.1 The involvement of the metabolic reprogramming of enzymes in the glucose metabolism pathway and viral immunoevasion

Upregulation of glycolysis-associated GLUT and enzyme expression drives the proliferation and activation of T cells and the secretion of cytokines such as IL-2. GLUT and HK2 are vital enzymes in the glycolytic process (33). Glycolytic reprogramming involves increased expression of glucose transporter proteins, particularly GLUT1, which increases glucose uptake and allows immune cells to compete for glucose in a nutrient-restricted environment, and increased glucose uptake usually promotes viral replication (34, 35). The CD4$^+$ T cells infected with human immunodeficiency virus type 1 (HIV-1) show increased glucose and glutamine metabolism due to the high-level GLUT1, which enhances HIV-1 infection (36, 37). Importantly, blockade of GLUT1 signaling or siRNA-mediated GLUT1 downregulation significantly impairs the HIV-1 infection in human T cells (38). Dengue virus (DENV) also induces the expression of GLUT1 and HK2 to promote glucose uptake and the downstream glycolytic processes to favor viral replication (39). In the rhinovirus (RV)-infected cells, viral replication is dependent on the availability of glucose and glutamine, which is affected by increasing glycogenolysis and upregulating GLUT1 expression (17). The envelope protein of white spot syndrome virus (WSSV) hijacks GLUT1 to promote viral infection (40). Furthermore, the Epstein-Barr virus (EBV) LMP1 protein can enhance transcription of GLUT1, which promotes aerobic glycolysis and the tumorigenic growth of NPC cells through the mTORC1/NF-κB signaling (41). The elucidation of interplay between GLUT1 and viruses will provide a direction for the development of effective antiviral strategies.

HK2 is an important enzyme in the glycolytic pathway and a kinase that modifies the phosphorylation of proteins to regulate immune signaling pathways. HK2 can activate the NF-κB signaling pathway by phosphorylating and degrading IκB. It has been demonstrated that aberrantly activated aerobic glycolysis in tumor cells promotes the segregation and binding of HK2 from mitochondria to cytoplasmic IκB, where HK2 acts as a protein kinase to phosphorylate IκB, leading to IκB degradation and NF-κB activation-dependent PD-L1 expression to escape tumor immunity (42) (Figure 1). Notably, the NF-κB p65 plays a key role in the HBx-induced spontaneous hepatocellular carcinoma. The hepatitis B virus (HBV) x protein can activate the NF-κB signaling via the p65 phosphorylation by HK2 to promote immunoevasion of the virus and enhance glycolysis, further activating PI3K/Akt signaling to increase hepatocyte proliferation (43). HK2 and lactate can suppress the activation of the retinoic acid-inducible gene I (RIG-I)-mitochondrial antiviral signaling protein (MAVS) pathway by inhibiting MAVS. HK2 and glycolysis-derived lactate also play important roles in the immunoevasion of HBV and the regulation of energy metabolism in innate immunity during HBV infection. A previous study showed that HBV isolates MAVS from RIG-I by forming a ternary complex including hexokinase (HK), which inhibits the RLR signaling pathway through LDHA-dependent lactate production (44). Influenza A virus (H1N1) utilizes HK2 and the pyruvate kinase M2 (PKM2) to enhance glycolysis and further promote viral replication (45). These studies highlight the importance of the HK enzyme in regulating viral infection through the regulation of innate immune signals, revealing the possibility of a potential antiviral target.

Lactate dehydrogenase (LDH) is a crucial enzyme in glycolysis in inflammatory macrophages (M1 phenotype). Lactate dehydrogenase B (LDHB) can regulate the NF-κB signaling pathway through the mitochondrial autophagy pathway to facilitate viral replication. LDHB negatively regulates classical swine fever virus (CSFV) growth, whereas CSFV infection inhibits LDHB production and reconstructs the glycolytic metabolic pathway in immune cells by the NS3 protein (46, 47). Interestingly, LDHA expression restricts viral protein synthesis in the ARV-infected cells, whereas the avian reovirus (ARV) σA protein inhibits LDHA expression and upregulates HIF-1α and glycolytic enzymes to promote glycolysis level, thereby favoring viral replication (48). Furthermore, LDH can increase interferon gamma (IFN-γ) expression by promoting histone acetylation (49). Reportedly, glucose consumption is restricted by the inhibition of LDH in CD4$^+$ T cells, thus reducing the production of acetyl-CoA, which leads to insufficient histone acetylation modification and reduced IFN-γ production (49). However, the effect of LDH on histone acetylation during virus replication remains largely unknown, and requires further investigation.

Hexosamine, a key metabolite linking glucose metabolism and immunity, activates inflammasomes, innate immune signaling pathways and autophagy. *N*-acetylglucosamine transferase (OGT) is a critical enzyme in the hexosamine pathway that mediates the glycosylation of target proteins with UDP-GlcNAc to regulate host antiviral immunity and influence viral infections. Hexosamine can induce activation of the inflammatory response and inflammatory cytokine expression through crosstalk between the hexosamine biosynthetic pathway and *O*-GlcNAc protein modification (50). OGT overexpression promotes *O*-GlcNAc modification of thioredoxin interacting protein (TxNIP) to facilitate the interaction between TxNIP and NLRP3, which promotes IL-1β production in HEK293T or INS1 832/13 cells (51). OGT is important for NLRP3 activation; however, its activation during viral infections remain largely unknown and requires further investigation. Alternatively, innate immunity can be activated by *O*-GlcNAc protein modification to regulate viral infection, such as influenza A virus (IAV) and Vesicular stomatitis virus (VSV) (52). A previous study showed that supplementation with D-glucosamine increases *O*-GlcNAc modification of MAVS to inhibit viral replication, which protects mice against IAV or vesicular stomatitis virus (VSV) challenge (52). During IAV infection, OGT mediates the *O*-GlcNAcylation of IFN regulatory factor 5 (IRF5) on serine-430, and IAV utilizes the hexosamine pathway to increase the expression of proinflammatory cytokines by stimulating IRF5 leading to in tissue injury (50). VSV infection can enhance HBP activity and *O*-GlcNAcylation of the downstream protein MAVS at S366, which leads to ubiquitination of the K63 link of MAVS to activate downstream antiviral signals in macrophages (53). Hexosamine can also activate the autophagy pathway to regulate viral infections, a catabolic process that is essential for maintaining cellular homeostasis. It has been shown that low-levels glucose cause decreases in UDP-GlcNAc levels and induce autophagy via the AMPK-Akt/mTOR signaling in the HBV-infected cells (54). Low-level hexosamine can promote HBV replication by inducing autophagosome formation and inhibiting autophagic degradation *in vitro* and *in vivo* (54, 55). In addition, low-dose glucosamine treatment promotes the replication of IAV, enterovirus 71 (EV 71), and VSV *in vitro* (55). *O*-GlcNAc modification can regulate iron death through iron autophagy and mitochondrial autophagy (56). SNAP-29 is one of the components of the soluble *N*-ethylmaleimide-sensitive factor attachment protein receptor (SNARE) complex that promotes autophagic vesicle maturation. A recent study revealed that OGT-mediated SNAP-29 *O*-GlcNAc modification in nematode-infected mammalian cells facilities the activation of autophagy, suggesting that OGT could indirectly promote the maturation of autophagic vesicles in cells (57) (Table 2).

2.2 The interplay of activation of metabolism-related molecules in the glucose metabolic pathway and viral immunoevasion

HIF-1α regulates the gene transcription of key enzymes (GLUT1, PKM2, LDHA etc.) (Figure 1) in the glycolytic pathway, which is involved in the modulation of immune responses. Due to its major role in the regulation of glycolysis, HIF-1α can be targeted and hijacked by viruses for viral infections. A recent study has shown that Newcastle disease virus (NDV) infection results in the inhibition of TCA cycle flux and an increase in EMP flux through stable expression of HIF-1α, indicating a shift in energy metabolism from OXPHOS to EMP, which promotes the viral replication, indicating that NDV infection induces mitochondrial damage and hijacks cellular metabolism to promote a shift toward glycolysis to favor viral replication (58). Additionally, under hypoxic conditions, the Kaposi's sarcoma-associated herpesvirus (KSHV) vGPCR

TABLE 2 The relationship between OGT and immunometabolism.

Pathways involving OGT	Regulated proteins	Mechanisms	Responses to *O*-GlcNAcylation	Pathogens	References
Innate immune signaling pathways	IRF5	OGT mediates the *O*-GlcNAcylation of IRF5 on serine 430 to promote IRF5 activation	Promoting anti-viral response	IAV	(50, 52)
	MAVS	OGT-mediated *O*-GlcNAcylation of MAVS on S366 promotes its K63-linked ubiquitination to activate antiviral signals	Promoting anti-viral response	VSV	(52, 53)
Inflammatory response	NLRP3, TxNIP	TxNIP *O*-GlcNAcylation in INS1832/13 cells is modulated by OGT or OGA activity to activate NLRP3	Promoting IL-1β production	Unknown	(51)
Autophagy	SNAP-29	OGT-mediated *O*-GlcNAcylation of SNAP-29 is on Ser 2, Ser 61, Thr 130, and Ser 153	Autophagy inhibition	*C. elegans*	(57)
	Akt and mTOR	Akt and mTOR undergo *O*-GlcNAcylation	antagonizing autophagosome-lysosome fusion and inhibiting viral replication	HBV	(55)

protein induces stable expression of the HIF-1α protein, which leads to metabolic Warburg phenotypic changes associated with KSHV and promotes viral replication in the KSHV-infected PBMCs (18). SARS-CoV-2 infection triggers mitochondrial reactive oxygen species (ROS) production, which stabilizes HIF-1α and promotes glycolysis, thereby contributing to SARS-CoV-2 infection and cytokine production in SARS-CoV-2-infected monocytes and macrophages (59, 60). Therefore, this broad-spectrum effect of HIF-1α on viruses reveals its importance. Moreover, HIF-1α regulates Th9 cell differentiation and exerts antitumor functions. TGF-β1 and IL-4 promote naive CD4$^+$ T cells to differentiate into immunoregulatory IL-9-producing helper T (Th9) cells and induce EGFR expression in the EGFR-HIF-1α pathway. EGFR is activated upon binding to the ligand double-regulated protein (AREG), which triggers downstream signaling via HIF-1α and activates the IL-9 and NOS2 promoters, facilitating IL-9 production (61). Notably, HIF-1α is a transcriptional repressor of IRF5 and IRF3 (62), which inhibits the production of type I IFNs. For example, SARS-CoV-2 infection triggers an inflammatory cascade, leading to elevated HMGB1 levels that inhibit IRF5-mediated type I IFN production under hypoxic conditions, only through the NF-κB signaling pathway to trigger monocytes to produce inflammatory cytokines. High mobility group box 1 (HMGB1) can activate NF-κB, IRF3 and IRF5 to release proinflammatory cytokines and I-IFN under normoxia, but SARS-CoV-2 infection can enhance HIF-1α expression, which inhibits IRF3 and IRF5 activity, leading to severe disease in COVID-19 patients (62). HIF-1α is a key activator of inflammatory responses in the SARS-CoV-2-infected PBMCs. HIF-1α expression is correlated with immune-inflammatory cytokine production. SARS-CoV-2-encoded ORF3a induces mitochondrial damage and mitochondrial-ROS production, thus promoting the stable expression of HIF-1α and resulting in cytokine production to enhance the inflammatory response, which is also observed in the VSV or SV-1 infection (58). In particular, HIF-1α is regulated by glycolytic metabolites and further stabilized by succinate and nitric oxide (NO) (61). α-Ketoglutarate (α-KG), a TCA cycle metabolite, is regulated by HIF-1α in Th9 cells. α-KG negatively regulates the stability of HIF-1α. Succinate increases the stability of HIF-1α by impairing prolyl hydroxylase 2 (PHD2) activity, thereby enhancing the antitumor activities of Th9 cells and macrophages (61, 63). HIF-1α can also promote programmed death ligand 1 (PD-L1) expression (64) to inhibit T-cell activation and promote immunoevasion in tumor cells. The high-risk human papilloma virus (HR-HPV) E1/E6 increases HIF-1α levels in cervical cell lines, thereby enhancing the Warburg effect (65–67).

2.3 The crosstalk of the metabolic reprogramming of metabolites in the glucose metabolic pathway and viral immunoevasion

Lactate is an end product of the glycolytic pathway. Lactate can promote the conversion of macrophages to M2 macrophages by modifying histones and regulating polarization-related genes (68), lactate promotes the formation of immunosuppressive M2 macrophages via the induction of arginase differentiation after lactate uptake by macrophages. In addition to modifying histones, lactate regulates viral immunoevasion through innate immune signaling pathways. MAVS is the protein downstream of RIG-I and is involved in crosstalk between the antiviral immune signaling pathways and glycolytic metabolic pathways. Basically, MAVS links energy metabolism and innate immunity through the recognition of lactate (69). Inactivation of glycolysis is essential for the promotion of RLR-mediated type I IFN production. Upon activation of RLR signaling, activated RIG-I “traps” MAVS through the CARD domain to activate downstream molecules and produce IFNs. Then, the oligomerized MAVS dissociates from HK2, which results in a reduction of HK activity, which in turn leads to the inhibition of glycolysis (33). Remarkably, viral infections promote glycolysis, and excess lactate inhibits MAVS and type I IFN production by binding to the transmembrane (TM) domain of MAVS directly and preventing its aggregation. The increased lactate levels in the ASFV-infected porcine alveolar macrophages (PAMs) can inhibit IFN-β production via the RIG-I-MAVS signaling pathway, which can contribute to viral immunoevasion (70). HBV inhibits RLR signaling via the LDHA-dependent lactate production (44). Similarly, LDHA-dependent lactate promotes IAV replication by inhibiting the MAVS-dependent type I IFN response (71). However, LDHA-dependent lactate inhibits SARS-CoV-2 replication (71). There exists interplay between lactate and innate immune responses, indicating that lactate could act as an antiviral target.

Itaconate, a derivative of the TCA cycle citrate, exhibits anti-inflammatory effects and is closely associated with the cGAS-STING signaling pathway (9). A recent study showed that the cell-permeable derivative of itaconate (4-octyl-itaconate, 4-OI) inhibits IL-1β transcription by activating the transcription factor Nrf2, which acts as a transcriptional repressor of IL-1β (72). Inhibition of STING expression is observed during metabolic reprogramming of TLR signaling, and it can also be induced by the TCA cycle via the activation of Nrf2. 4-OI, a cell-permeable derivative of the metabolite oxalic acid, can activate Nrf2 to induce an IFN-independent antiviral program, thereby inhibiting viral replication and suppressing inflammatory responses induced by SARS-CoV-2 infection (72). Furthermore, it has been reported that treatment with Nrf2-inducing agents, such as 4-OI, can sufficiently reduce the STING-dependent type I IFN release in the SAVI-derived fibroblasts, reducing the STING-associated inflammatory disease (9).

Succinate is a TCA cycle intermediate that contributes to the inflammatory response or apoptosis through stabilization of HIF-1α expression or succinylation of proteins (73). It has been shown that succinate can stabilize HIF-1α expression and then induce the expression of IL-1β (Figure 1). Succinate is an endogenous danger signal that stabilizes HIF-1α, which specifically regulates the expression of IL-1β and other HIF-1α-dependent genes, leading to protein succinylation and playing an important role in cell apoptosis or tumor proliferation (63, 74). Succinate promotes HIF-1α stabilization by inhibiting PHD2 activity in macrophages. Succinate can induce the expression of IL-9, HIF-1α and Th9-related genes in Th9 cells, and the induction of Th9 cell differentiation by succinate may occur via inhibiting PHD2 and promoting HIF-1α activity; therefore, succinate treatment enhances the antitumor activity of Th9 cells (61). Succinate is oxidized by succinate dehydrogenase to produce fumarate. Fumarate and its derivatives monomethyl fumarate (MMF) and dimethyl fumarate (DMF) are potent immunomodulators and antioxidants that can activate Nrf2 and modulate oxidative stress in cells, which can suppress HIV replication (75). The Nrf2 agonist DMF significantly inhibits SARS-CoV-2 replication and the expression of inflammatory genes (72). This inhibitory effect has also been observed in infection with viruses, such as herpes simplex virus 1 and 2 (HSV-1 and -2), vaccinia virus (VACV), or Zika virus (ZIKV), indicating that Nrf2 exhibits the extensive antiviral activities (72).

3 Interactions between lipid metabolism signaling and viral immunoevasion

Lipid is the general term for fats and lipids, such as triacylglycerols or triglycerides, but lipids also include phospholipids, glycolipids, cholesterol and its esters.

Fatty acid biosynthesis provides sufficient substrates for viral replication. There are two key metabolic enzymes involved in fatty acid biosynthesis, acetyl-CoA carboxylase (ACC) and fatty acid synthase (FASN). Notably, the expression of both FASN and ACC, is regulated by the sterol regulatory element binding protein 1 (SREBP1) family members 1a and 1c, which can regulate fatty acid synthesis (76, 77) (Figure 2).

Cholesterol is mainly localized in the cell membrane and also involved in the immunoevasion of viruses. In metabolically reprogrammed cells, cholesterol is thought to be a substance with several different biological functions, such as immunosuppression, viral replication (78), attachment (79), and entry (80).

The metabolism of cholesterol and fatty acids can be reprogrammed during viral infections, which regulates the host immune responses as well as viral replication. Therefore, understanding the potential mechanisms underlying metabolic reprogramming of cellular metabolites, metabolic regulators, and metabolic enzymes in the cholesterol and fatty acid metabolic pathways during viral infections can provide new insights into the development of therapeutic strategies for combating viral infections, such as ACC and SREBP.

3.1 The association of the fatty acid metabolic pathway and viral immunoevasion

The enzymes associated with the fatty acid biosynthesis pathway not only meet the requirements of the viral life cycle but also participate in the antiviral response. Reportedly, deletion of the fatty acid synthesis-related genes *SCD2* and *ACC* results in reduced production of monounsaturated fatty acids (MUFAs), leading to the activation of the cGAS-STING pathway-mediated interferon-stimulated gene (ISG) expression due to the spontaneous production of IFN-α by CD4^{+} T cells, thereby increasing the antiviral activities of IAV (81). Furthermore, a negative feedback regulatory pathway between STING and FADS2/SCD1 fine-tunes the generation of polyunsaturated fatty acids (PUFAs) associated with inflammatory response, which in turn suppresses the STING-related inflammatory response (82).

The members of the SREBP family modulate the T-cell metabolism and the gene transcription of immune-associated molecules. CD8^{+} T cells with deficient SREBP activity are unable

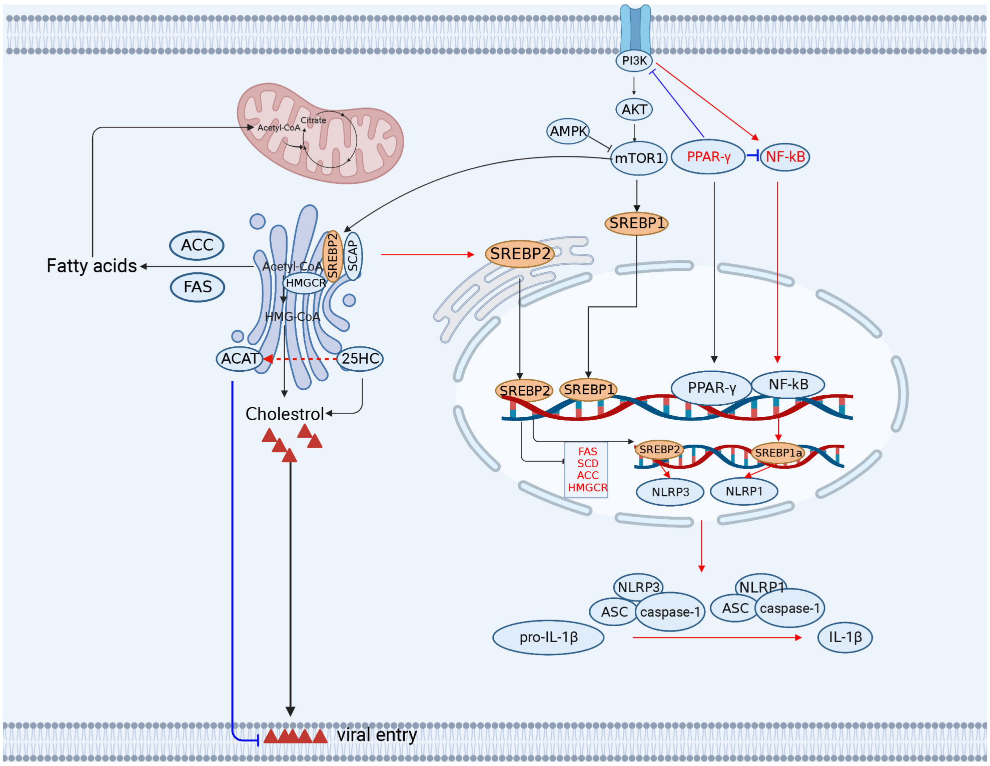

FIGURE 2
The engagement of fatty acid and cholesterol metabolism in innate immunity. The TCA cycle provides the precursor (citrate) for fatty acid synthesis (FAS). Acetyl-CoA synthesizes a variety of acetyl-CoA-based fatty acids *de novo* through the further activity of ACC and FASN using fatty acids. Lipid metabolism-related SREBP, 25HC, FANS, SCD2/ACC, and PPAR-γ play important roles in antiviral immunity (red lines indicate activation, blue lines indicate inhibition). ACC, (acetyl-CoA carboxylase); FANS, (fatty acid synthase); SREBP, sterol regulatory element binding protein; CH25H, cholesterol 25-hydroxylase. The figure was created by the BioRender software.

to undergo metabolic reprogramming and blastogenesis, which results in the inability to generate a functional T-cell response (83). Furthermore, the SREBP1c isoform is involved in Th17 cell differentiation and binds directly to the IL-17 promoter to suppress the AhR-induced IL-17 expression in CD4$^+$ T cells (84). In addition, the SREBP1a isoform is required for myeloid cells to exert proinflammatory effects, including the secretion of IL-1β, which promotes the expression of NLRP1, a key component of the inflammasome (85). Notably, SREBP1a is required for macrophages to exert proinflammatory effects, including secretion of IL-1β and the expression of NLRP1 (a key component of the inflammasome) (85) (Figure 2).

NF-κB inhibition induced by the peroxisome proliferator-activated receptor gamma (PPAR-γ) activation is the major reason for virus hijacking of fatty acid metabolism to trigger immunoevasion (86). PPAR-γ activation inhibits HIV genomic LTR promoter activity and suppresses the NF-κB response, thereby reducing NF-κB occupancy of the LTR promoter in the infected cells and ultimately impairing HIV replication in macrophages (87). Although both the HIV and HCMV genomes contain elements responsive to NF-κB, the major immediate early promoter (MIEP) contains two PPAR response elements (PPRE) in the HCMV-infected cells. In fact, PPAR-γ promotes viral replication through transactivation of the HCMV promoter MIEP by two PPREs in the HCMV-infected cells (88). The increased activity of PPAR-γ may promote both viral replication and host cell survival. Overexpression of PPAR-γ promotes IAV replication by inhibiting IFN signaling in alveolar macrophages (89).

3.2 The correlation of the cholesterol metabolic pathway and viral immunoevasion

Apolipoprotein E (ApoE) is linked to a variety of immune responses, including the suppression of T-cell proliferation, the modulation of macrophage function, lipid antigen transport to natural killer T cells, and the regulation of inflammation or oxidation. Proinflammatory cytokines induce the downregulation of ApoE in monocytes. However, TGF-β promotes the expression of ApoE. In addition, ApoE is required for lipoprotein transport. ApoE is known to promote the entry, assembly, and transmission of hepatitis C virus (HCV) (90–92). ApoE has been shown to modulate IAV infection *in vitro* and *in vivo*, and ApoE knockout markedly increases the susceptibility of mice to IAV. Notably, when cells are unable to synthesize ApoE, cell cholesterol homeostasis is disrupted to promote IAV attachment (93).

Cholesterol 25-hydroxylase (CH25H) is the key enzyme that regulates cholesterol metabolism and catalyzes the conversion of cholesterol to a soluble, broad-spectrum antiviral effector (25-hydroxycholesterol (25HC)) by adding a second hydroxyl group at position 25 (94). Interestingly, CH25H as an antiviral ISG, forms a part of the sterol metabolic network through interferon signaling (95, 96). It has been shown that CH25H activity is induced by the STAT1-dependent proinflammatory factor IL-1β/TNF-α/IL-6 in the ZIKV-infected cells (96). In addition, 25HC can inhibit virus-induced intercellular membrane fusion and viral infections. ZIKV infection can markedly increase the expression levels of CH25H in cells, thus augmenting the production of 25HC to prevent the virus entry by blocking virus-mediated membrane fusion between cells (97). Interestingly, 25HC can activate an acyl coenzyme A-cholesterol acyltransferase (ACAT) in the endoplasmic reticulum (ER) of cells, which subsequently eliminates accessible cholesterol from the cell membrane, thereby inhibiting viral entry. SARS-CoV-2 initially binds to human lung cells via the ACE2 receptor, and cholesterol in the cellular membrane is required for the membrane fusion of the virus (94). CSFV infection same as well (98) Therefore, 25HC can inhibit the virus entry. Notably, 25HC and 27HC not only inhibit viral entry but also induce the production of proinflammatory cytokines and suppress viral immune evasion. It has been demonstrated that the stimulation of oxysterols enhances HSV-1-induced IL-6 production, indicating that IL-6 exerts antiviral effects during HSV-1 infection, which is an additional antiviral mechanism of action for 25HC and 27HC (99).

Cholesterol is involved in the immunoevasion of viruses. High-levels cholesterol can weaken the host's antiviral immunity. The PRRSV Nsp4 protein upregulates protein phosphatase 2 (PP2) activity, which activates the rate-limiting enzyme 3-hydroxy-3-methylglutaryl coenzyme A reductase HMGCR in the cholesterol synthesis pathway and increases cellular cholesterol levels, thereby inhibiting virus-induced IFN-β production and promoting PRRSV replication (100). CSFV infection modulates the cholesterol biosynthesis pathway to favor the virus entry and disrupt the type I IFN response (101, 102). On the contrary, low-levels cholesterol may enhance antiviral immunity in host cells. However, a reduction in cholesterol biosynthesis also enhances host antiviral immunity. When cholesterol synthesis is decreased, STING, a critical antiviral signaling protein, is stimulated to generate antiviral responses. STING appears to require a cholesterol-deficient ER membrane to promote type I IFN production (103) (Figure 2). In summary, CH25H is a molecule with broad spectrum antiviral activity.

SREBP2 is involved in cholesterol metabolism. The maturation of SREBP2, a master transcription factor for cholesterol metabolism, regulates NLRP3 inflammasome activation through the translocation of the SCAP-SREBP2 complex from the ER into the Golgi, thus promoting the activation of the NLRP3 inflammasome. NLRP3 has been reported to form ternary complexes with the SREBP cleavage-activating proteins SCAP and SREBP2, which in turn translocate proximally to the Golgi apparatus to form mitochondrial clusters for efficient assembly of the inflammasome (104).

4 Interactions between amino acid metabolism signaling and viral immunoevasion

Amino acid metabolism also known as one carbon metabolism, plays important roles in viral replication and immune regulation (105).

Generally, viral infections can affect the host's immune response by inducing changes in host cell glutamine metabolism and tryptophan metabolism. Therefore, metabolic reprogramming of glutamine and tryptophan plays a crucial role in viral immunoevasion, and exploring the mechanisms will help provide an in-depth understanding of viral infections and immunoevasion (Figure 3).

4.1 Metabolic reprogramming of glutamine regulates the viral immunoevasion

Glutamine is critical for viral replication, and viral infection regulates the metabolism of glutamine depending on glucose levels. Several viruses transfer carbon to biosynthetic reactions via aerobic glycolysis, using glutamine to replenish intermediates of the TCA cycle, and then reprogramming cellular metabolism to provide the energy required for viral replication and the molecular material for the production of progeny virus. For example, in the VACV-infected HeLa or 2FTGH cells, HIF-1α mediates the shift from glucose to glutamine metabolism via the viral C16 protein, and stimulation of the viral protein contributes to glutamine metabolism to produce α-ketoglutarate and some of the macromolecular precursors of TCA cycle metabolism, which is dependent on glutamine, and asparagine, in the absence of glutamine to promote the production of VACV proteins (39, 106). In the HIV-infected CD4$^+$ T cells, the carbon generated from glutamine catabolism enters the TCA cycle to facilitate HIV infection, which is also necessary for maintaining the balance between the TCA cycle and oxidative phosphorylation (107). It has also been shown that glutaminase: kidney-type glutaminase (KGA), glutaminase C (GAC), phosphoribosyl pyrophosphate aminotransferase (PPAT) (key enzymes for *de novo* purine nucleotide synthesis) and glutamine-fructose-6-phosphate transaminase 1 (a key enzyme in the hexosamine pathway) are significantly differentially expressed after glucose deprivation in the HIV-infected CD4$^+$ T cells (35), indicating that the utilization of the glutamine metabolic pathway significantly promotes HIV replication. Glutamine is essential for RGNNV replication as it is converted to α-KG by the enzyme glutaminase (GLS), which is involved in the TCA cycle, and the process promotes RGNNV replication through the TCA cycle (108). HCMV infection increases the glutamine catabolism, which produces α-KG to replenish the TCA cycle and promote HCMV replication (109). In addition,

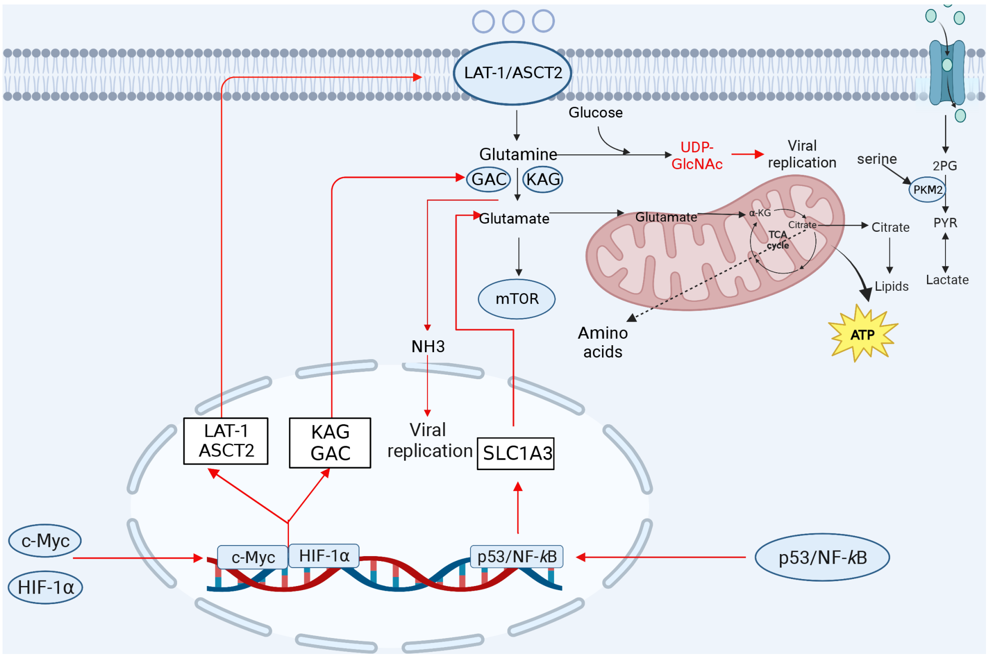

FIGURE 3
The involvement of amino acid metabolism in innate immunity. Glutamine is transformed into glutamate after entering the cell to facilitate the TCA cycle repair. Glutamate is transformed to α-KG, which is integrated into the TCA cycle and oxidized to generate ATP for energy. Glutamine can produce a variety of amino acids. Serine is linked to several glycolytic enzymes. Serine aids aerobic glycolysis and lactate production by activating PKM2. Amino acid metabolism-related ASCT2, citrate, NH3, glutamine, and α-KG play important roles in viral replication. After viral infection, some transcription factors can induce a reprogramming of glutamine metabolism, leading to increased expression of the genes involved in glutamine uptake and metabolism, which promotes viral replication (red lines indicate activation, blue lines indicate inhibition). KGA, kidney-type glutaminase; GAC, glutaminase C. The figure was created by the BioRender software.

ASFV infection dramatically induces the activation of intracellular glutamine metabolism and facilitates the viral replication in alveolar mononuclear macrophages (27). Furthermore, EV 71 infection can be promoted by increasing glutamine catabolism, while pharmacological inhibition of pyrimidine metabolizing enzymes can inhibit viral replication in Vero cells (110).

Glutamine produces glutamate and glutathione, an antioxidant compound that plays an important role in the prevention of oxidative stress. Similarly, HCV infection increases the utilization and dependence on glutamine, whereas inhibition of glutamine metabolism attenuates the viral infection and the cellular oxidative stress (111). The expression of Myc, two transporter proteins (SLC1A5 and SLC7A5) and two GLSs (KGA and GAC) was increased in the HCV-infected Huh7.5 cells (Figure 3). Myc is a transcription factor that induces the transcription of transporter proteins, thereby driving increased cellular glutamine utilization and thus metabolic reprogramming of cells. Inhibition of glutamine metabolism reduces viral replication and oxidative stress induced by HCV infection, suggesting that the inhibition of glutamine utilization is a novel strategy for the treatment or prevention of viral infection (111).

Glutamine metabolism plays a crucial role in regulating antiviral immunity, as evidenced by the inhibition of the viral infections through glutamine degradation. For example, the proliferation of HSV-infected T cells requires the metabolic breakdown of glutamine. Interestingly, glutamine supplementation has been shown to inhibit the reactivation of latent HSV through a mechanism involving enhancement of the IFN-γ-related immune response, which in turn inhibits the activation of the latent virus (112).

SLC1A3 (aspartic acid transporter, GLAST) is a member of the solute family and is significantly upregulated through the P53 and NF-κB pathways in the NDV-infected DF-1 or A549 cells, and SLC1A3 hijacked by NDV promotes glutamate catabolism and viral replication in host cells (113).

Glutamine has been shown to produce glucosamine, which in turn allows the modification of key proteins through acetylation. This modification helps to regulate cytokine production downstream, which can affect the antiviral immune response in host cells. The process of producing glucosamine involves the catalysis of glutamine and fructose-6-phosphate by glutamine fructose-6-phosphate amidotransferase (GFAT), generating glucosamine-6-phosphate. Finally, UDP-GlcNAc induces modification of the *O*-GlcNAc protein.

4.2 Tryptophan metabolism and viral immunoevasion

The kynurenine pathway is a complex network of enzymatic reactions that metabolizes tryptophan into various downstream metabolites, including kynurenine, quinolinic acid, and picolinic acid. These metabolites are involved in the modulation of immune responses, oxidative stress, and neurotransmitter synthesis.

Tryptophan degradation is primarily mediated by the conversion of tryptophan to kynurenine by two different dioxygenases: indoleamine-2,3-dioxygenase (IDO1) and tryptophan-2,3-dioxygenase (TDO2); the rate-limiting step in the tryptophan-kynurenine pathway is performed by IDO1. IDO1 is a multifunctional enzyme that typically acts as a negative regulator of inflammatory and immune responses (114, 115). IDO is a critical regulator of acute pulmonary inflammation. IDO deficiency severely exacerbates lung inflammation in mice. Therefore, IFN signaling in the lung parenchyma inhibits idiopathic pneumonia syndrome by promoting IDO expression (116). It has been demonstrated that changes in tryptophan metabolism are associated with IL-6 levels. In the context of viral infection, IFNs can enhance tryptophan metabolism by inducing IDO1 production subsequently leading to alterations in metabolism and inflammation, which ultimately affect viral replication (117, 118). SARS-CoV-2 infection induces metabolic reprogramming of tryptophan toward the kynurenine pathway, which regulates host inflammation and immunity (119). Furthermore, IFN-γ-induced antiviral activity against measles virus can be counteracted by the addition of excess tryptophan (120). In the context of SARS-CoV-2 infection, dysregulation of the kynurenine pathway has been associated with severe disease outcomes, including cytokine storm and respiratory failure.

5 Other potential targets of immunometabolism

Methylenetetrahydrofolate dehydrogenase 2 (MTHFD2) reductase is an important enzyme in folate metabolism. Folate plays an indirect or direct role in cell proliferation and differentiation. Reportedly, EBV infection remodels B-cell metabolism and hijacks serine metabolism by upregulating MTHFD2 to promote rapid B-cell growth, which leads to B-cell lymphoma (121). MTHFD2 is a metabolic checkpoint controlling effector and regulatory T-cell fate and function. The MTHFD2 regulates purine synthesis and signal transduction in activated T-cells to promote the cell proliferation and inflammatory cytokine production (122). NDV hijacks MTHFD2 of the nucleotide pathway to maintain nucleotide availability required for viral replication, revealing the dependence of NDV on the cellular oxidative pentose phosphate pathway (PPP) and folate-mediated one-carbon metabolism (123). Thus, MTHFD2 is a metabolic checkpoint, which is combined purine metabolism with the pathogenic effector cell signaling pathway, indicating that MTHFD2 is a potential therapeutic target in the one-carbon metabolic pathway.

Isocitrate dehydrogenase (IDH) is a key rate-limiting enzyme in the TCA cycle and plays an important role in energy metabolism, which is a noteworthy potential therapeutic target. On one hand, IDH mutation can generate high levels of 2-hydroxyglutaric acid (2-HG), which inhibits glioma stem cell differentiation (124). On the other hand, IDH mutation can also induce high levels of HIF-1α to promote glioma invasion (125). Reportedly, the ARV σA protein can promote viral replication by upregulating IDH3B and glutamate dehydrogenase (GDH) to promote glutaminolysis (48). Importantly, IDH has been clinically useful as a therapeutic target for acute myeloid leukemia (126).

6 The metabolic enzymes as potential antiviral targets

Metabolic reprogramming is an important characteristic of viral infections. To date, abnormal glucose metabolism has been extensively studied. In the presence of sufficient oxygen, glycolysis is the principal glucose metabolic pathway in several virus-infected cells. In addition, metabolic enzymes are attractive potential therapeutic targets. To date, few drugs targeting metabolism are available. We summarize recent progress in the virus-induced metabolic changes and the drugs (Table 3) to provide novel strategies for targeting metabolism to inhibit viral replication *in vivo* or *in vitro*. Generally, the identified antiviral targets are associated with the enzymes in cellular metabolism, it is not clear whether targeted metabolic enzymes will induce cytotoxicity, thus the future clinical use of metabolic drugs requires multifaceted evaluation.

Ongoing antiviral research will focus on the metabolic enzymes involved in abnormal processes, such as glycolysis (34, 37, 63). Although virus infections induce aerobic glycolysis, several viruses utilize cellular mitochondrial function for replication. Therefore, targeting the glycolytic pathway is not the only therapeutic approach, and alternative antimetabolic approaches, such as targeting mitochondrial metabolism, including the pentose phosphate pathway, fatty acid synthesis, and amino acid metabolism, may be potential antiviral targets in the future. In summary, a more in-depth understanding of the regulatory mechanisms of metabolic alterations and viral replication will facilitate the development of antiviral drugs.

Currently, the precise mechanisms of metabolic reprogramming induced by viral infections remain largely unknown. In-depth exploration of these questions will enhance our understanding of virus-cell interactions, increase the possibility of future drug development targeting metabolism, and expand the library of drugs available for the treatment of viral infections.

7 Conclusions and perspectives

In this review, we have outlined the impact of cellular metabolism on viral infection and immunoevasion. The relationship between cell metabolism and viruses is very intricate. Viral infections can induce the changes in cellular metabolic pathways (Table 4), thereby providing the essential nutrients and energy for viral replication. When discussing the mechanisms of viral immunoevasion, we focus on key intermediate metabolic substances involved in several metabolic pathways hijacked by viruses, including glycolysis, the hexosamine pathway, the TCA cycle, the fatty acid synthesis pathway, the cholesterol metabolic

TABLE 3 Intervention strategies targeting metabolic enzymes.

Targets of metabolism	Compounds	Pathways	References
Phosphoglucose-isomerase	2-DG	Glycolysis	(127)
PKM2	TT-232 Shikonin/alkannin	Glycolysis	(128, 129)
LDH	Oxamic acid Galloflavin	Glycolysis	(130, 131)
LDHA	FX11 Quinoline 3-sulfonamides	Glycolysis	(132, 133)
HK II	3-Bromopyruvate (3BP) Combination of 3-BrOP and rapamycin Combination of MGCD265 and erlotinib	Glycolysis	(134–137)
GLUT1	Phloretin Quercetin STF31 WZB117 Oxime-based GLUT1 inhibitors	Glycolysis	(138–142)
ACC	TOFA	Fatty acid metabolism	(143, 144)
Succinate dehydrogenase	Sodium malonate	TCA cycle	(145)
Fumarase	Fumaric acid esters	TCA cycle	(146)
Aconitase	Fluoroacetate	TCA cycle	(147)
FASN	C75	Fatty acid metabolism	(148)
SREBP	AM580	Fatty acid metabolism	(149)
HMG-CoA	Statins	Cholesterol metabolism	(150)
Glutaminase	BPTES	Amino acid metabolism	(108)

TABLE 4 Cellular metabolism changes in viral infections.

Viruses	Up-regulated	Down-regulated	References
HIV-1	GLUT1, glutamine and PPAR-γ		(36, 37, 87, 107)
DENV	GLUT1 and HK2		(39)
RV	GLUT1 and glutamine		(17)
HBV	Lactate and HK2		(43, 44)
WSSV	GLUT1		(40)
EBV	GLUT1		(41)
HPV	HIF-1α		(65–67)
ARV	Glutamine and IDH3	LDHA	(48, 125)
IAV	Lactate, OGT, HK2, ACC and PPAR-γ	ApoE	(45, 50, 71, 81, 89, 93)
VSV	OGT and HIF-1A		(52, 53, 58)
KSHV	HIF-1α		(18)
SARA-CoV-2	Succinate, HIF-1α and IDO1		(59, 60, 62, 72, 119)
CSFV		LDHB	(46, 47)
ASFV	Lactate and glutamine		(27)
HCMV	PPAR-γ and glutamine		(88, 109)

(Continued)

TABLE 4 Continued

Viruses	Up-regulated	Down-regulated	References
HCV	ApoE		(90–92)
HSV-1	Succinate and glutamine		(72, 112)
ZIKV	Succinate		(72)
VACV	Succinate and glutamine		(39, 72, 106)
NDV	HIF-1α, SLC1A3 and MTHFD2		(58, 113, 123)
RGNNV	Glutamine		(108)
EV-71	Glutamine		(110)

pathway, the glutamine metabolic pathway, and the tryptophan metabolic pathway. These pathways not only provide nutrients and metabolites for the viral replication, but also participate in the regulation of immune responses.

Viruses cause reprogramming of glucose metabolism, which affects their immune evasion ability (151). More specifically, SARS-CoV-2 reprograms glucose metabolism and glycolysis can be hijacked by various viruses for favoring the viral infections (36, 37, 44, 45, 56, 152). The reprogramming promotes metabolic pathways and stabilizes genes involved in glucose transport and glycolysis, such as GLUT, LDH-A, and LDHB. HIF-1α activates the expression of a variety of glycolytic enzymes, including GLUT1, GLUT3, HK1, HK2, GAPDH, PGK1, PKM2, LDHA, and PDK1 (153–156). Importantly, HIF-1α not only increases glucose uptake and lactate production, but also blocks the TCA cycle and oxidative phosphorylation in mitochondria (156). Moreover, glycolytic flux and TCA cycle activity increase significantly with glucose uptake and lactate release (58). LDHA can enhance IFN-γ expression by upregulating histone acetylation (49, 157). Aerobic glycolysis can also promote IFN-γproduction by binding GAPDH to the 3'UTR of IFN-γ mRNA (158). In addition, many intermediate metabolites, such as succinate, fumarate, itaconate, and α-ketoglutarate, are involved in immune activation or regulation. UDP-GlcNAc, the end product of the HBP, plays an important role in the process of viral inflammation through OGT (159). OGT mediates the transfer of UDP-GlcNAc to serine or threonine residues of target proteins to modify immune-related proteins (160) and coordinates glucose and glutamine metabolism induced by growth factors (32).

Viruses can utilize lipid-related factors for immunoevasion. For example, the deletion of *ACC* and *SCD2* can indirectly activate the cGAS-STING signaling pathway and enhance the host's antiviral activities (81). Moreover, some viruses can antagonize the NF-κB or IFN-β signaling through regulating the lipid metabolism (87, 100). Amino acids are the key nutrients that can be converted into α-ketoglutaric acid to participate in the TCA cycle (108). Amino acid metabolism also plays an important role in the immunoevasion of viruses. Previous studies have shown that viruses can hijack glutamine and SLC1A3 (the amino acid transporter) to facilitate the viral latency and infection (112, 113).

In summary, there is a potential role for metabolism-related molecules in the development of antiviral drugs and diagnostic reagents by inducing host metabolic reprogramming to regulate viral replication (161). However, the application of immunotherapy in the treatment of viruses has not yet been extensively developed. Therefore, targeting immune cell function through metabolic modulation is a promising avenue for immunotherapy in the future (9, 72, 162).

Author contributions

JL wrote the manuscript. YW, HD, SL and H-JQ revised this manuscript. All authors contributed to the article and approved the submitted version.

Funding

This work was supported by the Heilongjiang Provincial Natural Science Foundation of China (JQ2020C002) and the National Natural Science Foundation of China (32072866).

Conflict of interest

The authors declare that the research was conducted in the absence of any commercial or financial relationships that could be construed as a potential conflict of interest.

Publisher's note

All claims expressed in this article are solely those of the authors and do not necessarily represent those of their affiliated organizations, or those of the publisher, the editors and the reviewers. Any product that may be evaluated in this article, or claim that may be made by its manufacturer, is not guaranteed or endorsed by the publisher.

References

1. Makowski L, Chaib M, Rathmell JC. Immunometabolism: From basic mechanisms to translation. *Immunol Rev* (2020) 295(1):5–14. doi: 10.1111/imr.12858

2. Mirzaei R, Sholeh M, Jalalifar S, Zafari E, Kazemi S, Rasouli-Saravani A, et al. Immunometabolism in human brucellosis: An emerging field of investigation. *Microb Pathog* (2021) 158:105–15. doi: 10.1016/j.micpath.2021.105115

3. Mirzaei R, Zamani F, Hajibaba M, Rasouli-Saravani A, Noroozbeygi M, Gorgani M, et al. The pathogenic, therapeutic, and diagnostic role of exosomal microRNA in the autoimmune diseases. *J Neuroimmunol* (2021) 358:577640. doi: 10.1016/j.jneuroim.2021.577640

4. Rodríguez C, Puente-Moncada N, Reiter RJ, Sánchez-Sánchez AM, Herrera F, Rodríguez-Blanco J, et al. Regulation of cancer cell glucose metabolism is determinant for cancer cell fate after melatonin administration. *J Cell Physiol* (2021) 236(1):27–40. doi: 10.1002/jcp.29886

5. Pei J, Yuan Y, Tian D, Huang F, Zhang C, Wang C, et al. Comprehensive analysis of protein acetylation and glucose metabolism in mouse brains infected with rabies virus. *J Virol* (2022) 96(4):194–221. doi: 10.1128/JVI.01942-21

6. Moreno-Altamirano MB, Kolstoe SE, Sánchez-García FJ. Virus control of cell metabolism for replication and evasion of host immune responses. *Front Cell Infect Microbiol* (2019) 9:95. doi: 10.3389/fcimb.2019.00095

7. Sanchez EL, Lagunoff M. Viral activation of cellular metabolism. *Virology* (2015) 479–480:609–18. doi: 10.1016/j.virol.2015.02.038

8. Mayer KA, Stöckl J, Zlabinger GJ, Gualdoni GA. Hijacking the supplies: Metabolism as a novel facet of virus-host interaction. *Front Immunol* (2019) 10:1533. doi: 10.3389/fimmu.2019.01533

9. Cruzat V, Macedo Rogero M, Noel Keane K, Curi R, Newsholme P. Glutamine: metabolism and immune function, supplementation and clinical translation. *Nutrients* (2018) 10:1564. doi: 10.3390/nu10111564

10. Peyssonnaux C, Datta V, Cramer T, Doedens A, Theodorakis EA, Gallo RL. HIF-1alpha expression regulates the bactericidal capacity of phagocytes. *J Clin Invest* (2005) 115:1806–15. doi: 10.1172/JCI23865

11. Cramer T, Yamanishi Y, Clausen B, Förster I, Pawlinski R, Mackman N, et al. HIF-1alpha is essential for myeloid cell-mediated inflammation. *Cell* (2003) 112:645–57. doi: 10.1016/s0092-8674(03)00154-5

12. Michelet X, Dyck L, Hogan A, Loftus RM, Duquette D, Wei K, et al. Metabolic reprogramming of natural killer cells in obesity limits antitumor responses. *Nat Immunol* (2018) 19:1330–40. doi: 10.1038/s41590-018-0251-7

13. Blagih J, Coulombe F, Vincent E, Dupuy F, Galicia-Vázquez G, Yurchenko E, et al. The energy sensor AMPK regulates T cell metabolic adaptation and effector responses in *vivo*. *Immunity* (2015) 42:41–54. doi: 10.1016/j.immuni.2014.12.030

14. Assmann JC, Farthing DE, Saito K, Maglakelidze N, Oliver B, Warrick KA, et al. Glycolytic metabolism of pathogenic T cells enables early detection of GvHD by 13C-MRI. *Blood* (2021) 137(1):126–37. doi: 10.1182/blood.2020005770

15. Balmer ML, Ma EH, Thompson AJ, Epple R, Unterstab G, Lötscher J, et al. Memory CD8$^+$ T cells balance pro- and anti-inflammatory activity by reprogramming cellular acetate handling at sites of infection. *Cell Metab* (2020) 32(3):457–467.e5. doi: 10.1016/j.cmet.2020.07.004

16. Pearce E, Walsh M, Cejas P, Harms GM, Shen H, Wang LS, et al. Enhancing CD8 T-cell memory by modulating fatty acid metabolism. *Nature* (2009) 460:103–7. doi: 10.1038/nature08097

17. Gualdoni GA, Mayer KA, Kapsch AM, Kreuzberg K, Puck A, Kienzl P, et al. Rhinovirus induces an anabolic reprogramming in host cell metabolism essential for viral replication. *Proc Natl Acad Sci U.S.A.* (2018) 115:E7158–65. doi: 10.1073/pnas.1800525115

18. Singh RK, Lang F, Pei Y, Jha HC, Robertson ES. Metabolic reprogramming of Kaposi's sarcoma associated herpes virus infected B-cells in hypoxia. *PloS Pathog* (2018) 14(5):e1007062. doi: 10.1371/journal.ppat.1007062

19. Assmann N, O'Brien K, Donnelly R, Dyck L, Zaiatz-Bittencourt V, Loftus RM, et al. SREBP-controlled glucose metabolism is essential for NK cell functional responses. *Nat Immunol* (2017) 18:1197–206. doi: 10.1038/ni.3838

20. Dong H, Adams N, Xu Y, Cao J, Allan DSJ, Carlyle JR, et al. The IRE1 endoplasmic reticulum stress sensor activates natural killer cell immunity in part by regulating c-Myc. *Nat Immunol* (2019) 20:865–78. doi: 10.1038/s41590-019-0388-z

21. Ganapathy-Kanniappan S. Linking tumor glycolysis and immune evasion in cancer: Emerging concepts and therapeutic opportunities. *Biochim Biophys Acta Rev Cancer* (2017) 1868(1):212–20. doi: 10.1016/j.bbcan.2017.04.002

22. Shen L, Hu P, Zhang Y, Ji Z, Shan X, Ni L, et al. Serine metabolism antagonizes antiviral innate immunity by preventing ATP6V0d2-mediated YAP lysosomal degradation. *Cell Metab* (2021) 33(5):971–87. doi: 10.1016/j.cmet.2021.03.006

23. Mirzaei R, Sabokroo N, Ahmadyousefi Y, Motamedi H, Karampoor S. Immunometabolism in biofilm infection: lessons from cancer. *Mol Med* (2022) 28 (1):1–42. doi: 10.1186/s10020-022-00435-2

24. Thaker SK, Ch'ng J, Christofk HR. Viral hijacking of cellular metabolism. *BMC Biol* (2019) 17(1):59. doi: 10.1186/s12915-019-0678-9

25. Rudiansyah M, Jasim SA, Mohammad Pour ZG, Athar SS, Jeda AS, Doewes RI, et al. Coronavirus disease 2019 (COVID-19) update: From metabolic reprogramming to immunometabolism. *J Med Virol* (2022) 94(10):4611–27. doi: 10.1002/jmv.27929

26. Gou H, Bian Z, Li Y, Cai R, Jiang Z, Song S, et al. Metabolomics exploration of pseudorabies virus reprogramming metabolic profiles of PK-15 cells to enhance viral replication. *Front Cell Infect Microbiol* (2021) 10:599087. doi: 10.3389/fcimb.2020.599087

27. Xue Q, Liu H, Zhu Z, Yang F, Song Y, Li Z, et al. African swine fever virus regulates host energy and amino acid metabolism to promote viral replication. *J Virol* (2022) 96(4):e0191921. doi: 10.1128/JVI.01919-21

28. Boodhoo N, Kamble N, Sharif S, Behboudi S. Glutaminolysis and glycolysis are essential for optimal replication of Marek's disease virus. *J Virol* (2020) 94(4):e01680–19. doi: 10.1128/JVI.01680-19

29. DeBerardinis RJ, Thompson CB. Cellular metabolism and disease: what do metabolic outliers teach us? *Cell* (2012) 148(6):1132–44. doi: 10.1016/j.cell.2012.02.032

30. Wellen KE, Lu C, Mancuso A, Lemons JM, Ryczko M, Dennis JW, et al. The hexosamine biosynthetic pathway couples growth factor-induced glutamine uptake to glucose metabolism. *Genes Dev* (2010) 24(24):2784–99. doi: 10.1101/gad.1985910

31. Hui EK, Nayak DP. Role of ATP in influenza virus budding. *Virology* (2001) 290 (2):329–41. doi: 10.1006/viro.2001.1181

32. Munger J, Bajad SU, Coller HA, Shenk T, Rabinowitz JD. Dynamics of the cellular metabolome during human cytomegalovirus infection. *PloS Pathog* (2006) 2: e132. doi: 10.1371/journal.ppat.0020132

33. Ren Z, Yu Y, Chen C, Yang D, Ding T, Zhu L, et al. The triangle relationship between long noncoding RNA, RIG-I-like receptor signaling pathway, and glycolysis. *Front Microbiol* (2021) 12:807737. doi: 10.3389/fmicb.2021.807737

34. Macintyre AN, Gerriets VA, Nichols AG, Michalek RD, Rudolph MC, Deoliveira D, et al. The glucose transporter Glut1 is selectively essential for CD4 T cell activation and effector function. *Cell Metab* (2014) 20(1):61–156. doi: 10.1016/j.cmet.2014.05.004

35. Hegedus A, Kavanagh Williamson M, Khan MB, Dias Zeidler J, Da Poian AT, El-Bacha T, et al. Evidence for altered glutamine metabolism in human immunodeficiency virus type 1 infected primary human CD4$^+$ T cells. *AIDS Res Hum Retroviruses* (2017) 33(12):1236–47. doi: 10.1089/AID.2017.0165

36. Kavanagh Williamson M, Coombes N, Juszczak F, Athanasopoulos M, Khan MB, Eykyn TR, et al. Upregulation of glucose uptake and hexokinase activity of primary human CD4$^+$ T cells in response to infection with HIV-1. *Viruses* (2018) 10(3):114. doi: 10.3390/v10030114

37. Palmer CS, Duette GA, Wagner MC, Henstridge DC, Saleh S, Pereira C, et al. Metabolically active CD4$^+$ T cells expressing Glut1 and OX40 preferentially harbor HIV during in *vitro* infection. *FEBS Lett* (2017) 591:3319–32. doi: 10.1002/1873-3468.12843

38. Loisel-Meyer S, Swainson L, Craveiro M, Oburoglu L, Mongellaz C, Costa C, et al. Glut1-mediated glucose transport regulates HIV infection. *Proc Natl Acad Sci U.S.A.* (2012) 109(7):2549–54. doi: 10.1073/pnas.1121427109

39. Fontaine KA, Sanchez EL, Camarda R, Lagunoff M. Dengue virus induces and requires glycolysis for optimal replication. *J Virol* (2015) 89(4):2358–66. doi: 10.1128/JVI.02309-14

40. Huang HT, Chan HL, Shih TY, Chen LL. A study of the role of glucose transporter 1 (Glut1) in white spot syndrome virus (WSSV) infection. *Fish Shellfish Immunol* (2015) 46(2):305–14. doi: 10.1016/j.fsi.2015.06.034

41. Zhang J, Jia L, Lin W, Yip YL, Lo KW, Lau VMY, et al. Epstein-Barr Virus-Encoded latent membrane protein 1 upregulates Glucose Transporter 1 Transcription via the mTORC1/NF-κB signaling pathways. *J Virol* (2017) 91(6):e02168–16. doi: 10.1128/JVI.02168-16

42. Guo D, Tong Y, Jiang X, Meng Y, Jiang H, Du L, et al. Aerobic glycolysis promotes tumor immune evasion by hexokinase2-mediated phosphorylation of IκBα. *Cell Metab* (2022) 34(9):1312–1324.e6. doi: 10.1016/j.cmet.2022.08.002

43. Chen L, Lin X, Lei Y, Xu X, Zhou Q, Chen Y, et al. Aerobic glycolysis enhances HBx-initiated hepatocellular carcinogenesis via NF-κBp65/HK2 signalling. *J Exp Clin Cancer Res* (2022) 41(1):329. doi: 10.1186/s13046-022-02531-x

44. Zhou L, He R, Fang P, Li M, Yu H, Wang Q, et al. Hepatitis B virus rigs the cellular metabolome to avoid innate immune recognition. *Nat Commun* (2021) 12 (1):98. doi: 10.1038/s41467-020-20316-8

45. Ren L, Zhang W, Zhang J, Zhang J, Zhang H, Zhu Y, et al. Influenza A virus (H1N1) infection induces glycolysis to facilitate viral replication. *Virol Sin* (2021) 36 (6):1532–42. doi: 10.1007/s12250-021-00433-4

46. Fan S, Wu K, Zhao M, Yuan J, Ma S, Zhu E, et al. LDHB inhibition induces mitophagy and facilitates the progression of CSFV infection. *Autophagy* (2021) 17 (9):2305–24. doi: 10.1080/15548627.2020.1823123

47. Gou H, Zhao M, Xu H, Yuan J, He W, Zhu M, et al. CSFV induced mitochondrial fission and mitophagy to inhibit apoptosis. *Oncotarget* (2017) 8 (24):39382–400. doi: 10.18632/oncotarget.17030

48. Chi PI, Huang WR, Chiu HC, Li JY, Nielsen BL, Liu HJ. Avian reovirus σA-modulated suppression of lactate dehydrogenase and upregulation of glutaminolysis and the mTOC1/eIF4E/HIF-1α pathway to enhance glycolysis and the TCA cycle for virus replication. *Cell Microbiol* (2018) 20(12):e12946. doi: 10.1111/cmi.12946

49. Peng M, Yin N, Chhangawala S, Xu K, Leslie CS, Li MO. Aerobic glycolysis promotes T helper 1 cell differentiation through an epigenetic mechanism. *Science* (2016) 354(6311):481–4. doi: 10.1126/science.aaf6284

50. Wang Q, Fang P, He R, Li M, Yu H, Zhou L, et al. *O*-GlcNAc transferase promotes influenza A virus-induced cytokine storm by targeting interferon regulatory factor-5. *Sci Adv* (2020) 6(16):70–86. doi: 10.1126/sciadv.aaz7086

51. Filhoulaud G, Benhamed F, Pagesy P, Bonner C, Fardini Y, Ilias A, et al. *O*-GlcNacylation links TxNIP to inflammasome activation in pancreatic β cells. *Front Endocrinol* (2019) 10:291. doi: 10.3389/fendo.2019.00291

52. Song N, Qi Q, Cao R, Qin B, Wang B, Wang Y, et al. MAVS *O*-GlcNAcylation is essential for host antiviral immunity against lethal RNA viruses. *Cell Rep* (2019) 28:2386. doi: 10.1016/j.celrep.2019.07.085

53. Li T, Li X, Attri KS, Liu C, Li L, Herring LE, et al. *O*-GlcNAc transferase links glucose metabolism to MAVS-mediated antiviral innate immunity. *Cell Host Microbe* (2018) 24(6):791–803.e6. doi: 10.1016/j.chom.2018.11.001

54. Wang X, Lin Y, Liu S, Zhu Y, Lu K, Broering R, et al. *O*-GlcNAcylation modulates HBV replication through regulating cellular autophagy at multiple levels. *FASEB J* (2020) 34(11):14473–89. doi: 10.1096/fj.202001168RR

55. Lin Y, Wu C, Wang X, Liu S, Zhao K, Kemper T, et al. Glucosamine promotes hepatitis B virus replication through its dual effects in suppressing autophagic degradation and inhibiting MTORC1 signaling. *Autophagy* (2020) 16(3):548–61. doi: 10.1080/15548627.2019.1632104

56. Yu F, Zhang Q, Liu H, Liu J, Yang S, Luo X, et al. Dynamic O-GlcNAcylation coordinates ferritinophagy and mitophagy to activate ferroptosis. *Cell Discovery* (2022) 8(1):40. doi: 10.1038/s41421-022-00390-6

57. Guo B, Liang Q, Li L, Hu Z, Wu F, Zhang P, et al. *O*-GlcNAc-modification of SNAP-29 regulates autophagosome maturation. *Nat Cell Biol* (2014) 16:1215–26. doi: 10.1038/ncb3066

58. Tian M, Liu W, Li X, Zhao P, Shereen MA, Zhu C, et al. HIF-1α promotes SARS-CoV-2 infection and aggravates inflammatory responses to COVID-19. *Signal Transduct Target Ther* (2021) 6(1):308. doi: 10.1038/s41392-021-00726-w

59. Codo AC, Davanzo GG, Monteiro LB, de Souza GF, Muraro SP, Virgilio-da-Silva JV, et al. Elevated glucose levels favor SARS-CoV-2 infection and monocyte response through a HIF-1α/glycolysis-dependent axis. *Cell Metab* (2020) 32(3):437–446.e5. doi: 10.1016/j.cmet.2020.07.007

60. Gong Y, Tang N, Liu P, Sun Y, Lu S, Liu W, et al. Newcastle disease virus degrades SIRT3 via PINK1-PRKN-dependent mitophagy to reprogram energy metabolism in infected cells. *Autophagy* (2022) 18(7):1503–21. doi: 10.1080/15548627.2021.1990515

61. Tong Y R, Guo D, Lin SH, Liang J, Yang D, Ma C, et al. SUCLA2-coupled regulation of GLS succinylation and activity counteracts oxidative stress in tumor cells. *Mol Cell* (2021) 81(11):2303–16. doi: 10.1016/j.molcel.2021.04.002

62. Cross S, Cook DR, Chi AW, Vance PJ, Kolson LL, Wong BJ, et al. Dimethyl fumarate, an immune modulator and inducer of the antioxidant response, suppresses HIV replication and macrophage-mediated neurotoxicity: a novel candidate for HIV neuroprotection. *J Immunol* (2011) 187:5015–25. doi: 10.4049/jimmunol.1101868

63. Roy S, Rizvi ZA, Clarke AJ, Macdonald F, Pandey A, Zaiss DMW, et al. EGFR-HIF-1α signaling positively regulates the differentiation of IL-9 producing T helper cells. *Nat Commun* (2021) 12(1):3182. doi: 10.1038/s41467-021-23042-x

64. Peng T, Du SY, Son M, Diamond B. HIF-1α is a negative regulator of interferon regulatory factors: Implications for interferon production by hypoxic monocytes. *Proc Natl Acad Sci U.S.A.* (2021) 118(26):e2106017118. doi: 10.1073/pnas.2106017118

65. Tannahill GM, Curtis AM, Adamik J, Palsson-McDermott EM, McGettrick AF, Goel G, et al. Succinate is an inflammatory signal that induces IL-1β through HIF-1α. *Nature* (2013) 496:238–42. doi: 10.1038/nature11986

66. Noman MZ, Desantis G, Janji B, Hasmim M, Karray S, Dessen P, et al. PD-L1 is a novel direct target of HIF-1α, and its blockade under hypoxia enhanced MDSC-mediated T cell activation. *J Exp Med* (2014) 211(5):781–90. doi: 10.1084/jem.20131916

67. Bodily JM, Mehta KP, Laimins LA. Human papillomavirus E7 enhances hypoxia-inducible factor 1-mediated transcription by inhibiting binding of histone deacetylases. *Cancer Res* (2011) 71(3):1187–95. doi: 10.1158/0008-5472.CAN-10-2626

68. Nakamura M, Bodily JM, Beglin M, Kyo S, Inoue M, Laimins LA. Hypoxia-specific stabilization of HIF-1alpha by human papillomaviruses. *Virology* (2009) 387 (2):442–8. doi: 10.1016/j.virol.2009.02.036

69. Knuth J, Sharma SJ, Würdemann N, Holler C, Garvalov BK, Acker T, et al. Hypoxia-inducible factor-1α activation in HPV-positive head and neck squamous cell carcinoma cell lines. *Oncotarget* (2017) 8(52):89681–91. doi: 10.18632/oncotarget.20813

70. Zhang D, Tang Z, Huang H, Zhou G, Cui C, Weng Y, et al. Metabolic regulation of gene expression by histone lactylation. *Nature* (2019) 574(7779):575–80. doi: 10.1038/s41586-019-1678-1

71. Zhang W, Wang G, Xu ZG, Tu H, Hu F, Dai J, et al. Lactate is a natural suppressor of RLR signaling by targeting MAVS. *Cell* (2019) 178(1):176–89. doi: 10.1016/j.cell.2019.05.003

72. Thyrsted J, Storgaard J, Blay-Cadanet J, Heinz A, Thielke AL, Crotta S, et al. Influenza A induces lactate formation to inhibit type I IFN in primary human airway epithelium. *iScience* (2021) 24(11):103300. doi: 10.1016/j.isci.2021.103300

73. Olagnier D, Brandtoft AM, Gunderstofte C, Villadsen NL, Krapp C, Thielke AL, et al. Nrf2 negatively regulates STING indicating a link between antiviral sensing and metabolic reprogramming. *Nat Commun* (2018) 9(1):3506. doi: 10.1038/s41467-018-05861-7

74. Olagnier D, Farahani E, Thyrsted J, Blay-Cadanet J, Herengt A, Idorn M, et al. SARS-CoV2-mediated suppression of NRF2-signaling reveals potent antiviral and anti-inflammatory activity of 4-octyl-itaconate and dimethyl fumarate. *Nat Commun* (2020) 11(1):4938. doi: 10.1038/s41467-020-18764-3

75. Elia I, Rowe JH, Johnson S, Joshi S, Notarangelo G, Kurmi K, et al. Tumor cells dictate anti-tumor immune responses by altering pyruvate utilization and succinate signaling in $CD8^+$ T cells. *Cell Metab* (2022) 34(8):1137–50. doi: 10.1016/j.cmet.2022.06.008

76. Horton JD. Sterol regulatory element-binding proteins: transcriptional activators of lipid synthesis. *Biochem Soc Trans* (2002) 30(6):1091–5. doi: 10.1042/bst0301091

77. Xue L, Qi H, Zhang H, Ding L, Huang Q, Zhao D, et al. Targeting SREBP-2-Regulated mevalonate metabolism for cancer therapy. *Front Oncol* (2020) 10:1510. doi: 10.3389/fonc.2020.01510

78. Shawli GT, Adeyemi OO, Stonehouse NJ, Herod MR. The oxysterol 25-hydroxycholesterol inhibits replication of murine norovirus. *Viruses* (2019) 11(2):97. doi: 10.3390/v11020097

79. Yin J, Glende J, Schwegmann-Wessels C, Enjuanes L, Herrler G, Ren X. Cholesterol is important for a post-adsorption step in the entry process of transmissible gastroenteritis virus. *Antiviral Res* (2010) 88(3):311–6. doi: 10.1016/j.antiviral.2010.10.002

80. Liu SY, Aliyari R, Chikere K, Li G, Marsden MD, Smith JK, et al. Interferon-inducible cholesterol-25-hydroxylase broadly inhibits viral entry by production of 25-hydroxycholesterol. *Immunity* (2013) 38(1):92–105. doi: 10.1016/j.immuni.2012.11.005

81. Kanno T, Nakajima T, Yokoyama S, Asou HK, Sasamoto S, Kamii Y, et al. SCD2-mediated monounsaturated fatty acid metabolism regulates cGAS-STING-dependent type I IFN responses in $CD4^+$ T cells. *Commun Biol* (2021) 4(1):820. doi: 10.1038/s42003-021-02310-y

82. Vila IK, Chamma H, Steer A, Saccas M, Taffoni C, Turtoi E, et al. STING orchestrates the crosstalk between polyunsaturated fatty acid metabolism and inflammatory responses. *Cell Metab* (2022) 34(1):125–139.e8. doi: 10.1016/j.cmet.2021.12.007

83. Kidani Y, Elsaesser H, Hock MB, Vergnes L, Williams KJ, Argus JP, et al. Sterol regulatory element-binding proteins are essential for the metabolic programming of effector T cells and adaptive immunity. *Nat Immunol* (2013) 14(5):489–99. doi: 10.1038/ni.2570

84. Cui G, Qin X, Wu L, Zhang Y, Sheng X, Yu Q, et al. Liver X receptor (LXR) mediates negative regulation of mouse and human Th17 differentiation. *J Clin Invest* (2011) 121(2):658–70. doi: 10.1172/JCI42974

85. Im SS, Yousef L, Blaschitz C, Liu JZ, Edwards RA, Young SG, et al. Linking lipid metabolism to the innate immune response in macrophages through sterol regulatory element binding protein-1a. *Cell Metab* (2011) 13(5):540–9. doi: 10.1016/j.cmet.2011.04.001

86. Layrolle P, Payoux P, Chavanas S. PPAR gamma and viral infections of the brain. *Int J Mol Sci* (2021) 22(16):8876. doi: 10.3390/ijms22168876

87. Potula R, Ramirez SH, Knipe B, Leibhart J, Schall K, Heilman D, et al. Peroxisome proliferator-activated receptor-gamma activation suppresses HIV-1 replication in an animal model of encephalitis. *AIDS* (2008) 22(13):1539–49. doi: 10.1097/QAD.0b013e3283081e08

88. Rauwel B, Mariamé B, Martin H, Nielsen R, Allart S, Pipy B, et al. Activation of peroxisome proliferator-activated receptor gamma by human cytomegalovirus for *de novo* replication impairs migration and invasiveness of cytotrophoblasts from early placentas. *J Virol* (2010) 84:2946–54. doi: 10.1128/JVI.01779-09

89. Huang S, Zhu B, Cheon IS, Goplen NP, Jiang L, Zhang R, et al. PPAR-γ in Macrophages limits pulmonary inflammation and promotes host recovery following respiratory viral Infection. *J Virol* (2019) 93(9):e00030–19. doi: 10.1128/JVI.00030-19

90. Cun W, Jiang J, Luo G. The C-terminal alpha-helix domain of apolipoprotein E is required for interaction with nonstructural protein 5A and assembly of hepatitis C virus. *J Virol* (2010) 84(21):11532–41. doi: 10.1128/JVI.01021-10

91. Rosch K, Kwiatkowski M, Hofmann S, Schöbel A, Grüttner C, Wurlitzer M, et al. Quantitative lipid droplet proteome analysis identifies annexin A3 as a cofactor for HCV particle production. *Cell Rep* (2016) 16(12):3219–31. doi: 10.1016/j.celrep.2016.08.052

92. Wrensch F, Crouchet E, Ligat G, Zeisel MB, Keck ZY, Foung SKH, et al. Hepatitis C virus (HCV)-apolipoprotein interactions and immune evasion and their impact on HCV vaccine design. *Front Immunol* (2018) 9:1436. doi: 10.3389/fimmu.2018.01436

93. Gao P, Ji M, Liu X, Chen X, Liu H, Li S, et al. Apolipoprotein E mediates cell resistance to influenza virus infection. *Sci Adv* (2022) 8(38):eabm6668. doi: 10.1126/sciadv.abm6668

94. Wang S, Li W, Hui H, Tiwari SK, Zhang Q, Croker BA, et al. Cholesterol 25-Hydroxylase inhibits SARS-CoV-2 and other coronaviruses by depleting membrane cholesterol. *EMBO J* (2020) 39(21):e106057. doi: 10.15252/embj.2020106057

95. Blanc M, Hsieh WY, Robertson KA, Kropp KA, Forster T, Shui G, et al. The transcription factor STAT-1 couples macrophage synthesis of 25-hydroxycholesterol to the interferon antiviral response. *Immunity* (2013) 38(1):106–18. doi: 10.1016/j.immuni.2012.11.004

96. Magoro T, Dandekar A, Jennelle LT, Bajaj R, Lipkowitz G, Angelucci AR, et al. IL-1β/TNF-α/IL-6 inflammatory cytokines promote STAT1-dependent induction of CH25H in Zika virus-infected human macrophages. *J Biol Chem* (2019) 94(40):14591–602. doi: 10.1074/jbc.RA119.007555

97. Li C, Deng YQ, Wang S, Ma F, Aliyari R, Huang XY, et al. 25-hydroxycholesterol protects host against Zika virus infection and its associated microcephaly in a mouse model. *Immunity* (2017) 46(3):446–56. doi: 10.1016/j.immuni.2017.02.012

98. Zhang L, Yi Y, Wang T, Song M, Guo K, Zhang Y. 25-hydroxycholesterol inhibits classical swine fever virus entry into porcine alveolar macrophages by depleting plasma membrane cholesterol. *Vet Microbiol* (2023) 278:109668. doi: 10.1016/j.vetmic

99. Cagno V, Civra A, Rossin D, Calfapietra S, Caccia C, Leoni V, et al. Inhibition of herpes simplex-1 virus replication by 25-hydroxycholesterol and 2-hydroxycholesterol. *Redox Biol* (2017) 12:522–7. doi: 10.1016/j.redox.2017.03.016

100. Ke W, Zhou Y, Lai Y, Long S, Fang L, Xiao S. Porcine reproductive and respiratory syndrome virus nsp4 positively regulates cellular cholesterol to inhibit type I interferon production. *Redox Biol* (2022) 49:102207. doi: 10.1016/j.redox.2021.102207

101. Zou X, Lin F, Yang Y, Chen J, Zhang H, Li L, et al. Cholesterol biosynthesis modulates CSFV replication. *Viruses* (2022) 14(7):1450. doi: 10.3390/v14071450

102. Liang XD, Zhang YN, Liu CC, Chen J, Chen XN, Sattar Baloch A, et al. U18666A inhibits classical swine fever virus replication through interference with intracellular cholesterol trafficking. *Vet Microbiol* (2019) 238:108436. doi: 10.1016/j.vetmic.2019.108436

103. O'Neill LA. How low cholesterol is good for anti-viral immunity. *Cell* (2015) 163(7):1572–4. doi: 10.1016/j.cell.2015.12.004

104. Guo C, Chi Z, Jiang D, Xu T, Yu W, Wang Z, et al. Cholesterol Homeostatic Regulator SCAP-SREBP2 integrates NLRP3 inflammasome activation and cholesterol biosynthetic signaling in macrophages. *Immunity* (2018) 49(5):842–56. doi: 10.1016/j.immuni.2018.08.021

105. Grohmann U, Bronte V. Control of immune response by amino acid metabolism. *Immunol Rev* (2010) 236:243–64. doi: 10.1111/j.1600-065X.2010.00915.x

106. Pant A, Cao S, Yang Z. Asparagine is a critical limiting metabolite for vaccinia virus protein synthesis during glutamine deprivation. *J Virol* (2019) 93:e01834–18. doi: 10.1128/JVI.01834-18

107. Clerc I, Moussa DA, Vahlas Z, Tardito S, Oburoglu L, Hope TJ, et al. Entry of glucose- and glutamine-derived carbons into the citric acid cycle supports early steps of HIV-1 infection in CD4 T cells. *Nat Metab* (2019) 1(7):717–30. doi: 10.1038/s42255-019-0084-1

108. Asim M, Jiang S, Yi L, Chen W, Sun L, Zhao L, et al. Glutamine is required for red-spotted grouper nervous necrosis virus replication via replenishing the tricarboxylic acid cycle. *Virus Res* (2017) 227:245–8. doi: 10.1016/j.virusres.2016.11.007

109. Hirabara SM, Gorjao R, Levada-Pires AC, Masi LN, Hatanaka E, Cury-Boaventura MF, et al. Host cell glutamine metabolism as a potential antiviral target. *Clin Sci (Lond)* (2021) 135(2):305–25. doi: 10.1042/CS20201042

110. Cheng ML, Chien KY, Lai CH, Li GJ, Lin JF, Ho HY. Metabolic reprogramming of host cells in response to enteroviral infection. *Cells* (2020) 9(2):473. doi: 10.3390/cells9020473

111. Lévy PL, Duponchel S, Eischeid H, Molle J, Michelet M, Diserens G, et al. Hepatitis C virus infection triggers a tumor-like glutamine metabolism. *Hepatology* (2017) 65(3):789–803. doi: 10.1002/hep.28949

112. Wang K, Hoshino Y, Dowdell K, Bosch-Marce M, Myers TG, Sarmiento M, et al. Glutamine supplementation suppresses herpes simplex virus reactivation. *J Clin Invest* (2017) 127(7):2626–30. doi: 10.1172/JCI88990

113. Liu P, Tang N, Meng C, Yin Y, Qiu X, Tan L, et al. SLC1A3 facilitates Newcastle disease virus replication by regulating glutamine catabolism. *Virulence* (2022) 13 (1):1407–22. doi: 10.1080/21505594.2022.2112821

114. Powers RK, Culp-Hill R, Ludwig MP, Smith KP, Waugh KA, Minter R, et al. Trisomy 21 activates the kynurenine pathway via increased dosage of interferon receptors. *Nat Commun* (2019) 10(1):4766. doi: 10.1038/s41467-019-12739-9

115. Wu H, Gong J, Liu Y. Indoleamine 2, 3-dioxygenase regulation of immune response (Review). *Mol Med Rep* (2018) 17(4):4867–73. doi: 10.3892/mmr.2018.8537

116. Lee SM, Park HY, Suh YS, Yoon EH, Kim J, Jang WH, et al. Inhibition of acute lethal pulmonary inflammation by the IDO-AhR pathway. *Proc Natl Acad Sci U.S.A.* (2017) 114(29):E5881–90. doi: 10.1073/pnas.1615280114

117. Li L, Huang L, Lemos HP, Mautino M, Mellor AL. Altered tryptophan metabolism as a paradigm for good and bad aspects of immune privilege in chronic inflammatory diseases. *Front Immunol* (2012) 3:109. doi: 10.3389/fimmu.2012.00109

118. Fritsch SD, Weichhart T. Effects of interferons and viruses on metabolism. *Front Immunol* (2016) 7:630. doi: 10.3389/fimmu.2016.00630

119. Xiao N, Nie M, Pang H, Wang B, Hu J, Meng X, et al. Integrated cytokine and metabolite analysis reveals immunometabolic reprogramming in COVID-19 patients with therapeutic implications. *Nat Commun* (2021) 12(1):1618. doi: 10.1038/s41467-021-21907-9

120. Obojes K, Andres O, Kim, Däubener W, Schneider-Schaulies J. Indoleamine 2,3-dioxygenase mediates cell type-specific anti-measles virus activity of gamma interferon. *J Virol* (2005) 79(12):7768–76. doi: 10.1128/JVI.79.12

121. Wang LW, Shen H, Nobre L, Ersing I, Paulo JA, Trudeau S, et al. Epstein-Barr-virus-induced one-carbon metabolism drives B cell transformation. *Cell Metab* (2019) 30(3):539–555.e11. doi: 10.1016/j.cmet.2019.06.003

122. Sugiura A, Andrejeva G, Voss K, Heintzman DR, Xu X, Madden MZ, et al. MTHFD2 is a metabolic checkpoint controlling effector and regulatory T cell fate and function. *Immunity* (2022) 55(1):65–81.e9. doi: 10.1016/j.immuni.2021.10.011

123. Tang N, Chen P, Zhao C, Liu P, Tan L, Song C, et al. Newcastle disease virus manipulates mitochondrial MTHFD2-Mediated nucleotide metabolism for virus replication. *J Virol* (2023) 97(3):e0001623. doi: 10.1128/jvi.00016-23

124. Khurshed M, Molenaar RJ, Lenting K, Leenders WP, van Noorden CJF. *In silico* gene expression analysis reveals glycolysis and acetate anaplerosis in IDH1 wild-type glioma and lactate and glutamate anaplerosis in IDH1-mutated glioma. *Oncotarget* (2017) 8(30):49165–77. doi: 10.18632/oncotarget.17106

125. Semukunzi H, Roy D, Li H, Khan GJ, Lyu X, Yuan S, et al. IDH mutations associated impact on related cancer epidemiology and subsequent effect toward HIF-1α. *BioMed Pharmacother* (2017) 89:805–11. doi: 10.1016/j.biopha.2017.02.083

126. Stein EM, DiNardo CD, Pollyea DA, Fathi AT, Roboz GJ, Altman JK, et al. Enasidenib in mutant IDH2 relapsed or refractory acute myeloid leukemia. *Blood* (2017) 130:722–31. doi: 10.1182/blood-2017-04-779405

127. Courtney RJ, Steiner SM, Benyesh-Melnick M. Effects of 2-deoxy-D-glucose on herpes simplex virus replication. *Virology* (1973) 52(2):447–55. doi: 10.1016/0042-6822(73)90340-1

128. Yuce M, Sarica Z, Ates B, Kurkcuoglu O. Exploring species-specific inhibitors with multiple target sites on *S. aureus* pyruvate kinase using a computational workflow. *J Biomol Struct Dyn* (2023) 8):3496–510. doi: 10.1080/07391102.2022.2051743

129. Chen J, Xie J, Jiang Z, Wang B, Wang Y, Hu X. Shikonin and its analogs inhibit cancer cell glycolysis by targeting tumor pyruvate kinase-M2. *Oncogene* (2011) 30 (42):4297–306. doi: 10.1038/onc.2011.137

130. Kebriaei R, Bayer AS, Lapitan CK, Rybak MJ, Somerville GA, Mishra NN. Activity of the lactate dehydrogenase inhibitor oxamic acid against the fermentative bacterium *Streptococcus mitis/oralis*: Bactericidal effects and prevention of daptomycin resistance in *vitro* and in an *ex vivo* model. *Antibiotics (Basel)* (2022) 11(10):1409. doi: 10.3390/antibiotics11101409

131. Farabegoli F, Vettraino M, Manerba M, Fiume L, Roberti M, Di Stefano G. Galloflavin, a new lactate dehydrogenase inhibitor, induces the death of human breast cancer cells with different glycolytic attitude by affecting distinct signaling pathways. *Eur J Pharm Sci* (2012) 47(4):729–38. doi: 10.1016/j.ejps

132. Le A, Cooper CR, Gouw AM, Dinavahi R, Maitra A, Deck LM, et al. Inhibition of lactate dehydrogenase a induces oxidative stress and inhibits tumor progression. *Proc Natl Acad Sci U.S.A.* (2010) 107(5):2037–42. doi: 10.1073/pnas.0914433107

133. Billiard J, Dennison JB, Briand J, Annan RS, Chai D, Colón M, et al. Quinoline 3-sulfonamides inhibit lactate dehydrogenase A and reverse aerobic glycolysis in cancer cells. *Cancer Metab* (2013) 1(1):19. doi: 10.1186/2049-3002-1-19

134. Vital PDS, Bonatelli M, Dias MP, de Salis LVV, Pinto MT, Baltazar F, et al. 3-Bromopyruvate suppresses the malignant phenotype of vemurafenib-resistant melanoma cells. *Int J Mol Sci* (2022) 23(24):15650. doi: 10.3390/ijms232415650

135. Levy AG, Zage PE, Akers LJ, Ghisoli ML, Chen Z, Fang W, et al. The combination of the novel glycolysis inhibitor 3-BrOP and rapamycin is effective against neuroblastoma. *Invest New Drugs* (2012) 30(1):191–9. doi: 10.1007/s10637-010-9551-y

136. Jiao L, Zhang HL, Li DD, Yang KL, Tang J, Li X, et al. Regulation of glycolytic metabolism by autophagy in liver cancer involves selective autophagic degradation of HK2 (hexokinase 2). *Autophagy* (2018) 14(4):671–84. doi: 10.1080/15548627

137. Claire B, Normand B, Marielle F, Helene SC, Jeffrey MB, Christiane RM. The combination of MGCD265, a Met/VEGFR inhibitor in clinical development, and erlotinib potently inhibits tumor growth by altering multiple pathways including glycolysis. *Cancer Res* (2012) 72(8):1790. doi: 10.1158/1538-7445

138. Song Y, Li W, Li W, Yang J, Song T. The inhibition of GLUT1-induced glycolysis in macrophage by phloretin participates in the protection during acute lung injury. *Int Immunopharmacol* (2022) 110:109049. doi: 10.1016/j.intimp.2022.109049

139. Jia L, Huang S, Yin X, Zan Y, Guo Y, Han L. Quercetin suppresses the mobility of breast cancer by suppressing glycolysis through Akt-mTOR pathway mediated autophagy induction. *Life Sci* (2018) 208:123–30. doi: 10.1016/j.lfs.2018.07.027

140. Wang L, Pavlou S, Du X, Bhuckory M, Xu H, Chen M. Glucose transporter 1 critically controls microglial activation through facilitating glycolysis. *Mol Neurodegener* (2019) 14(1):2. doi: 10.1186/s13024-019-0305-9

141. Ojelabi OA, Lloyd KP, Simon AH, De Zutter JK, Carruthers A. WZB117 [2-Fluoro-6-(m-hydroxybenzoyloxy) phenyl m-hdroxybenzoate] inhibits glut1-mediated sugar transport by binding reversibly at the exofacial sugar binding site. *J Biol Chem* (2016) 291(52):26762–72. doi: 10.1074/jbc.M116.759175

142. Tuccinardi T, Granchi C, Legre J, Paterni I, Bertini S, Macchia M, et al. Oxime-based inhibitors of glucose transporter 1 displaying antiproliferative effects in cancer cells. *Bioorg Med Chem Lett* (2013) 23(24):6923–7. doi: 10.1016/j.bmcl.2013.09.037

143. Sanchez EL, Pulliam TH, Dimaio TA, Thalhofer AB, Delgado T, Lagunoff M. Glycolysis, glutaminolysis, and fatty acid synthesis are required for distinct stages of Kaposi's sarcoma-associated herpesvirus lytic replication. *J Virol* (2017) 91:e02237–16. doi: 10.1128/JVI.02237-16

144. Delgado T, Sanchez EL, Camarda R, Lagunoff M. Global metabolic profiling of infection by an oncogenic virus: KSHV induces and requires lipogenesis for survival of latent infection. *PloS Pathog* (2012) 8:e1002866. doi: 10.1371/journal.ppat.1002866

145. Consegal M, Núñez N, Barba I, Benito B, Ruiz-Meana M, Inserte J, et al. Citric Acid cycle metabolites predict infarct size in pigs submitted to transient coronary artery occlusion and treated with succinate dehydrogenase inhibitors or remote ischemic perconditioning. *Int J Mol Sci* (2021) 22(8):4151. doi: 10.3390/ijms22084151

146. Moharregh-Khiabani D, Linker RA, Gold R, Stangel M. Fumaric acid and its esters: an emerging treatment for multiple sclerosis. *Curr Neuropharmacol* (2009) 7 (1):60–4. doi: 10.2174/157015909787602788

147. Ackermann WW. The relation of the Krebs cycle to viral synthesis. II. The effect of sodium fluoroacetate on the propagation of influenza virus in mice. *J Exp Med* (1951) 93(6):635–42. doi: 10.1084/jem.93.6.635

148. Yang W, Hood BL, Chadwick SL, Liu S, Watkins SC, Luo G, et al. Fatty acid synthase is up-regulated during hepatitis C virus infection and regulates hepatitis C virus entry and production. *Hepatology* (2008) 48(5):1396–403. doi: 10.1002/hep.22508

149. Yuan S, Chu H, Chan JF, Ye ZW, Wen L, Yan B, et al. SREBP-dependent lipidomic reprogramming as a broad-spectrum antiviral target. *Nat Commun* (2019) 10 (1):120. doi: 10.1038/s41467-018-08015-x

150. Cohen JI. HMG CoA reductase inhibitors (statins) to treat Epstein-Barr virus-driven lymphoma. *Br J Cancer* (2005) 92(9):1593–8. doi: 10.1038/sj.bjc.6602561

151. Ganesh GV, Mohanram RK. Metabolic reprogramming and immune regulation in viral diseases. *Rev Med Virol* (2022) 32(2):e2268. doi: 10.1002/rmv.2268

152. Bojkova D, Klann K, Koch B, Widera M, Krause D, Ciesek S, et al. Proteomics of SARS-CoV-2-infected host cells reveals therapy targets. *Nature* (2020) 583 (7816):469–72. doi: 10.1038/s41586-020-2332-7

153. Zhou F, Yu T, Du R, Fan G, Liu Y, Liu Z, et al. Clinical course and risk factors for mortality of adult inpatients with COVID-19 in Wuhan, China: a retrospective cohort study. *Lancet* (2020) 395(10229):1054–62. doi: 10.1016/S0140-6736(20)30566-3

154. Graven KK, Yu Q, Pan D, Roncarati JS, Farber HW. Identification of an oxygen responsive enhancer element in the glyceraldehyde-3-phosphate dehydrogenase gene. *Biochim Biophys Acta* (1999) 1447(2–3):208–18. doi: 10.1016/s0167-4781(99)00118-9

155. Kress S, Stein A, Maurer P, Weber B, Reichert J, Buchmann A. Expression of hypoxia-inducible genes in tumor cells. *J Cancer Res Clin Oncol* (1998) 124(6):315–20. doi: 10.1007/s004320050175

156. Infantino V, Santarsiero A, Convertini P, Todisco S, Iacobazzi V. Cancer cell metabolism in hypoxia: Role of HIF-1 as key regulator and therapeutic target. *Int J Mol Sci* (2021) 22(11):5703. doi: 10.3390/ijms22115703

157. Cham CM, Gajewski TF. Glucose availability regulates IFN-gamma production and p70S6 kinase activation in $CD8^+$ effector T cells. *J Immunol* (2005) 174(8):4670–7. doi: 10.4049/jimmunol.174.8.4670

158. Chang CH, Curtis JD, Maggi LBJr, Faubert B, Villarino AV, O'Sullivan D, et al. Posttranscriptional control of T cell effector function by aerobic glycolysis. *Cell* (2013) 153(6):1239–51. doi: 10.1016/j.cell.2013.05.016

159. Hardivillé S, Hart GW. Nutrient regulation of signaling, transcription, and cell physiology by *O*-GlcNAcylation. *Cell Metab* (2014) 20(2):208–13. doi: 10.1016/j.cmet.2014.07.014

160. Levine ZG, Walker S. The biochemistry of O-GlcNAc transferase: Which functions make it essential in mammalian cells? *Annu Rev Biochem* (2016) 85:631–57. doi: 10.1146/annurev-biochem-060713-035344

161. Cheng K, Martin-Sancho L, Pal LR, Pu Y, Riva L, Yin X, et al. Genome-scale metabolic modeling reveals SARS-CoV-2-induced metabolic changes and antiviral targets. *Mol Syst Biol* (2021) 17(11):e10260. doi: 10.15252/msb.202110260

162. Grimes JM, Khan S, Badeaux M, Rao RM, Rowlinson SW, Carvajal RD. Arginine depletion as a therapeutic approach for patients with COVID-19. *Int J Infect Dis* (2021) 102:566–70. doi: 10.1016/j.ijid.2020.10.100

frontiers | Frontiers in Immunology

TYPE Original Research
PUBLISHED 17 August 2023
DOI 10.3389/fimmu.2023.1237630

Characterization of a fatal feline panleukopenia virus derived from giant panda with broad cell tropism and zoonotic potential

Shan Zhao[1,2†], Huanyuan Hu[1,2†], Jingchao Lan[3†], Zhisong Yang[4†], Qianling Peng[1,2], Liheng Yan[1,2], Li Luo[3], Lin Wu[4], Yifei Lang[1,2*] and Qigui Yan[1,2*]

[1]College of Veterinary Medicine, Sichuan Agricultural University, Chengdu, China, [2]Key Laboratory of Animal Disease and Human Health of Sichuan Province, Sichuan Agricultural University, Chengdu, China, [3]Chengdu Research Base of Giant Panda Breeding, Chengdu, China, [4]Sichuan Academy of Giant Panda, Chengdu, China

Check for updates

OPEN ACCESS

EDITED BY
Wei Wang,
Wenzhou University, China

REVIEWED BY
Keith Chappell,
The University of Queensland, Australia
Dai Jun,
Guangxi University, China
Liang Cao,
Jilin University, China

*CORRESPONDENCE
Yifei Lang
✉ y_langviro@163.com
Qigui Yan
✉ yanqigui@126.com

†These authors have contributed equally to this work

RECEIVED 09 June 2023
ACCEPTED 02 August 2023
PUBLISHED 17 August 2023

CITATION
Zhao S, Hu H, Lan J, Yang Z, Peng Q, Yan L, Luo L, Wu L, Lang Y and Yan Q (2023) Characterization of a fatal feline panleukopenia virus derived from giant panda with broad cell tropism and zoonotic potential.
Front. Immunol. 14:1237630.
doi: 10.3389/fimmu.2023.1237630

COPYRIGHT
© 2023 Zhao, Hu, Lan, Yang, Peng, Yan, Luo, Wu, Lang and Yan. This is an open-access article distributed under the terms of the Creative Commons Attribution License (CC BY). The use, distribution or reproduction in other forums is permitted, provided the original author(s) and the copyright owner(s) are credited and that the original publication in this journal is cited, in accordance with accepted academic practice. No use, distribution or reproduction is permitted which does not comply with these terms.

Represented by feline panleukopenia virus (FPV) and canine parvovirus (CPV), the species *carnivore protoparvovirus 1* has a worldwide distribution through continuous ci13rculation in companion animals such as cats and dogs. Subsequently, both FPV and CPV had engaged in host-to-host transfer to other wild animal hosts of the order *Carnivora*. In the present study, we emphasized the significance of cross-species transmission of parvoviruses with the isolation and characterization of an FPV from giant panda displaying severe and fatal symptoms. The isolated virus, designated pFPV-sc, displayed similar morphology as FPV, while phylogenetic analysis indicated that the nucleotide sequence of pFPV-sc clades with Chinese FPV isolates. Despite pFPV-sc is seemingly an outcome of a spillover infection event from domestic cats to giant pandas, our study also provided serological evidence that FPV or other parvoviruses closely related to FPV could be already prevalent in giant pandas in 2011. Initiation of host transfer of pFPV-sc is likely with association to giant panda transferrin receptor (TfR), as TfR of giant panda shares high homology with feline TfR. Strikingly, our data also indicate that pFPV-sc can infect cell lines of other mammal species, including humans. To sum up, observations from this study shall promote future research of cross-host transmission and antiviral intervention of *Carnivore protoparvovirus 1*, and necessitate surveillance studies in thus far unacknowledged potential reservoirs.

KEYWORDS

feline panleukopenia virus, giant panda, cross-species transmission, TfR, fatal

Introduction

Parvoviruses (family *Parvoviridae*) are a group of small, non-enveloped, single-stranded DNA viruses. They have a linear DNA genome that are about 4.5–5.5 kb in length, with hairpin structures composed of inverted terminal repeat (ITR) folds at both ends of the viral genome (1). The rest of the viral genome contains two major open reading frames which encode two non-structural proteins (NS1, NS2) and two structural proteins (VP1, VP2) in the same mRNA through variable splicing (2, 3). Parvoviruses are currently endemic worldwide and can naturally infect a wide range of hosts (4–9). Due to its characteristics of rapid evolution and transmission, the host spectrum of parvovirus is still expanding, posing a threat on a variety of endangered wild animal species.

Carnivore protoparvovirus 1 is a distinctive species under the *Protoparvovirus* genus of family *Parvoviridae* (1). Members of this species include feline panleukopenia virus (FPV), canine parvovirus (CPV), mink enteritis virus (MEV) and raccoon dog parvovirus (RaPV) (4, 10–12). Both FPV and CPV have a worldwide distribution in companion animals, causing symptoms such as vomiting, severe diarrhea and leukopenia (13, 14). Importantly, FPV and CPV do not limit themselves in cats and dogs. In recent years, infection with both virus were recurrently reported in wild animals such as giant panda, raccoon, African lion, leopard and white tiger (15–20).

Host range is a key distinctive of viruses, which determines the host specificity and also reflects the diversity of natural host tropism. Virus host range expansion often provides a certain basis for the emergence of new diseases. In the case of carnivore protoparvovirus 1, studies showed that transferrin receptor (TfR) is the main host receptor that mediates virus binding and cellular entry (21–23). TfR is a dimeric membrane-associated protein located on the cell surface, which functions through binding and importing iron particles of transferrin-mediated cell intake of iron ions (21). As the parvoviral receptor, TfR interacts with the virus capsid through a compartment that appears to center around residue 300 of the viral VP2 protein, but other rather distanced VP2 residues are also involved, suggesting a broad interaction with the viral capsid (24–26). Consequently, such machnism shall allow viruses to bind TfRs of other carnivores, hence initiate cross-species virus transmission (27).

In the present study, we confirmed the multi-host nature of carnivore protoparvovirus 1 with isolation and characterization of an FPV in giant pandas from Chengdu Research Base of Giant Panda Breeding. Genetic and biological features of this virus were studied, and the findings revealed the zoonotic threats of this virus and *carnivore protoparvovirus 1* in general.

Materials and methods

Fecal and serum samples from giant panda

Giant panda fecal samples were collected from captive giant pandas at Chengdu Research Base of Giant Panda Breeding in 2020. All of the sampled giant pandas (n=15) displayed severe symptoms such as diarrhea, vomiting and anorexia, while two juvenile pandas were dead before effective treatment. Serum samples (n=14) were retrieved from the serum bank of our lab, which were sera from 14 different healthy captive giant pandas between 2010 and 2018. All samples were stored at -80°C before usage.

Cells

Feline kidney cells (F81), Crandell-Rees Feline Kidney (CRFK), African green monkey kidney cells (Vero-CCL81), African Green monkey foetal kidney (MA-104), porcine kidney epithelial cells (LLC-PK1), porcine endothelial cells (PIEC), human hepatoma cells (Huh7), human rectal Adenocarcinoma cells (HRT-18), Hela and human embryonic kidney 293 cells stably expressing the SV40 large T antigen (HEK-293T) were maintained in Dulbecco modified Eagle medium (DMEM, Gibco) supplemented with 10% fetal bovine serum (FCS), penicillin (100 IU/mL) and streptomycin (100 μg/mL).

Detection of parvovirus infection and virus isolation

Total DNA of giant panda fecal samples were extracted using the RoomTempTM sample lysis kit (Vazyme, P073) or Stool DNA Isolation Kit (Foregene, DE-05713) per the instructions of the manufacturer. Two primer pairs targeting the conserved ORF1 region of parvovirus genomes, namely P1F 5'-AACAAGCAACTGGTAAATGGCT-3', P1R 5'-CACAGCTTGTGCTATGGCTTGA-3', P2F 5'-TCACGCTATAGCATGTGTTTTA-3' and P2R 5'-ACTAACACACCCTTACCTCTCC-3', were used to detect traces of parvovirus infection. Polymerase chain reaction (PCR) was carried out by GoTaq® DNA Polymerase (Promega, M3001). The PCR procedure was as follows: 95°C for 3 min, followed by 34 cycles of 95°C for 15 s, 51°C (P1) or 47°C (P2) for 15s, and 72°C for 15s, with a final extension at 72°C for 5 min. For virus isolation, PCR-positive samples were homogenized in phosphate buffered saline (PBS), filtrated through 0.22μm filters and inoculated onto monolayers of F81 cells. Four hours post inoculation, the inoculum was replaced with virus growth medium (DMEM supplemented with 2% FCS and 10mM HEPES) and incubated at 37°C, 5% CO_2. Supernatants from inoculated cells were then blind passaged in F81 cells until cytopathic effect (CPE) started to appear. Viruses were then titrated and purified by end-point dilution on F81 cells with CPE as read-out. Titer of the propagated clonal virus, designated as pFPV-SC, was calculated by the Spearman–Kaerber formula. Morphology of the virus particles was observed via transmission electron microscopy post ultracentrifugation and negative staining with 0.5% phosphotungstic acid.

Genetic and growth characterization of the isolated virus

To obtain complete genetic information of the isolated virus, multiple overlapped PCRs were performed using a set of primers designed in the present study after analysis of different parvoviral genomes (detailed in Table 1). PCR products were cloned with CloneJET PCR Cloning Kit (Thermo Fisher, K1231) followed by

TABLE 1 Primers used to amplify the genome sequences of the isolated parvovirus.

Primer pair	Sequence (5′-3′)	Position	Target (nt)
1	F: ATCATTCTTTAGAACCAACT R: GGTGTTAAGTTTACCGAACA	1-20 778-759	759
2	F: GTACGTATGACGTGATGACGC R: ATTCACTATCTTCTGCAATTT	33-53 822-802	770
3	F:CACACGTCATACGTACGCTCCT R: GTACGTATGACGTGATGACGC	80-101 856-835	756
4	F:TAAAGAATGATAGGCGGTTTGTGT R: TTTGTCTGTCTTGATACTTCATAA	116-139 1014-991	876
5	F:AACAAGCAACTGGTAAATGGCT R: CACAGCTTGTGCTATGGCTTGA	691-712 1523-1502	812
6	F:TCACGCTATAGCATGTGTTTTA R: ACTAACACACCCTTACCTCTCC	1409-1430 2332-2311	793
7	F:GAAGATTTTCGAGACGACTTGGAT R:TACTATCTAATGCAACCATCAATG	2253-2276 3301-3324	1049
8	F: GAGATTGGCAACTAATTGTTAA R:TTATTTAATGCAGTTAAAGGAC	3157-3178 4162-4141	985
9	F:CAGGAAGATATCCAGAAGGAGA R:CAACCACCCACACCATAACAAC	4003-4024 4800-4821	780
10	F:TATCAACTAGCACCTAGAAAATTA R: AAGTATCAATCTGTCTTTAAGGGG	4572-4595 5100-5123	528
11	F:TATTAATGTATGTTGTTATGGTGT R:AGATACACAACATCAGTAGACTGA	4789-4812 5087-5064	276

Nucleotide positions were marked based on the reference strain HH-1/86.

conventional bidirectional sanger sequencing. Deduced viral sequences were assembled via DNASTAR Lasergene software package to acquire the full viral genome. To determine viral growth kinetics, F81 cells were infected with the isolated parvovirus at a multiplicity of infection (MOI) of 0.01. Cell culture medium supernatants were harvested every 12 hours from 0 to 72 hours post-infection (hpi). Viral titers ($TCID_{50}$/mL) were determined by end-point dilution with F81 cells as described above. Experiments were performed in independent triplicates, and the calculated values are expressed as the mean ± standard deviation.

Animal studies with the isolated parvovirus

To facilitate research described in this study, hyperimmune serum was collected from an inoculated rabbit. Briefly, a 4-week-old gnotobiotic rabbit was subcutaneously injected with two consecutive doses of heat-inactivated virus (14 days interval; 10^4 $TCID_{50}$/dose), and hyperimmune serum was collected 14 days post the second injection. The animal use protocols commissioned in this study were reviewed and approved by the Animal Ethics Committee of Sichuan Agricultural University.

Phylogenetic analysis

Sequence containing the complete viral genome, assembled by the DNASTAR Lasergene software package, were further processed by the online tool Clustal Omega (https://www.ebi.ac.uk/Tools/msa/clustalo/). Multiple alignments of the full-length genomes and VP2 genes with representative parvovirus sequences and phylogenetic analyses were then conducted using the neighbor-joining method in MEGA X, respectively.

Virus neutralization assay

Neutralization assays were performed with pFPV-sc to examine the seropositivity of giant panda serum samples. Different samples were two-fold serially diluted in virus growth medium, and mixed 1:1 with pFPV-sc (2000 $TCID_{50}$/mL). The mixtures were incubated at 37°C for one hour, and 100 μL of each mixture was used for inoculation onto F81 cells. At 3–5 days post infection, CPE was observed by microscopy. Virus neutralization titers (VNT) were expressed as the highest serum dilution resulting in 90% reduction of CPE. Experiments were performed in independent triplicate.

Hemagglutination and hemagglutination inhibition assay

Hemagglutination (HA) assay was performed with giant panda, human, rat, pig and rabbit erythrocytes (0.5% suspension in PBS). Two-fold serial dilutions of viruses, starting at 10^4 $TCID_{50}$ per well, were mixed 1:1 with the erythrocytes in a V-shape plate (Corning$^{\text{TM}}$, 3894). Hemagglutination was assessed after 2-hour incubation on ice, and hemagglutinating units (HAU) were inspected for erythrocytes of each species. For desialylation, erythrocytes were treated with *Arthrobacter ureafaciens* neuraminidase (Roche, 10mU/mL) for 3 hours at 37°C, and washed 5 times with cold PBS prior to the HA assay.

Hemagglutination inhibition (HI) assays were carried out to study the HA inhibition ability of different serum samples. Different samples were two-fold serially diluted, and mixed 1:1 with PBS containing 8 HAU of pFPV-sc. The mixtures were incubated at room temperature for one hour, and then mixed 1:1 with human erythrocytes (0.5% in PBS). Hemagglutination inhibition was documented after 2-hour incubation on ice. The HI titer of one serum sample is conveyed as the reciprocal of the highest serum dilution that still shows hemagglutination inhibition.

Immunofluorescence assay

An immunofluorescence assay (IFA) was carried out to examine the susceptibility of different cell lines to pFPV-sc. Briefly, cells on 24-well plates were infected with the virus at a MOI of 0.1, then incubated at 37°C, 5% CO_2 prior to washing with PBS and fixation with 4% Paraformaldehyde. Cells were then blocked with PBS containing 2% bovine serum albumin (Sigma), and incubated with 200 µl rabbit hyperimmune serum at a 1:150 dilution. One hour later, cells were washed three times with PBS, followed by another incubation step with 200 µl FITC-conjugated goat anti-rabbit IgG antibody (Thermo Fisher Scientific) at 1:400 dilution mixed with 4′, 6-diamidino-2-phenylindole (DAPI) at 1:1000 dilution. Lastly, cells were washed, mounted on glass slides and visualized under a fluorescence microscope.

Modelling of the giant panda transferrin receptor

Structure homology-modeling of transferrin receptors (TfRs) of giant panda (NCBI reference sequence: XM_011221715.3) and cat (GenBank accession number: AF276984.1) was performed by the SWISS-MODEL server (https://www.swissmodel.expasy.org/) using the deciphered structure of human TfR (PDB accession number: 7ZQS) as a search model.

Results

Isolation and characterization of a feline panleukopenia virus from captive giant panda

In 2020, captive giant pandas from Chengdu Research Base of Giant Panda Breeding were reported to display fatal symptoms such as diarrhea and vomiting, and two giant panda cubs did not survive the infection. Fecal samples from those pandas were tested pan-parvovirus positive by conventional PCR. To further validate the infection status, fecal samples were inoculated on F81 cells for probable virus isolation. As shown in Figure 1A, after five blind passages in F81 cells, typical

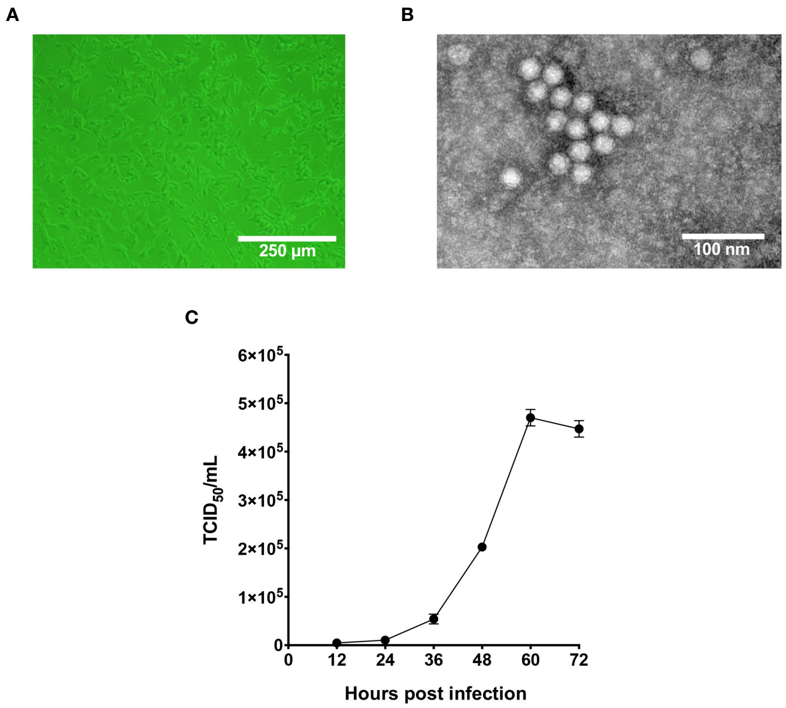

FIGURE 1
Characterization of the infectivity and morphology of pFPV-sc. **(A)** Cytopathic effect induced by pFPV-sc (clonal virus population) in F81 cells. **(B)** Morphology of pFPV-sc particles exhibited with negative-stained transmission electron microscopy. **(C)** Growth curve of pFPV-sc as measured by end-point dilution. Each datapoint shows averages of three independent replicates, and standard deviations are indicated as error bars.

parvovirus-induced CPE was formed, indicated by cell rounding, pyknosis, disturbance of cell monolayers and eventually full necrosis. At passage 10, the titer of the nonclonal virus population had reached 1x10^6 $TCID_{50}$/mL measured by end-point dilution assay. TEM analysis of negative stained, purified cell supernatant showed spherical particles with an average diameter around 20 nm, which falls to the typical parvovirus morphology (Figure 1B). To study the cellular infectivity of the isolated parvovirus in detail, the mixed viral population was further purified and propagated, and growth kinetics was analyzed of the clonal virus, designated pFPV-sc. The results indicated that the viral growth took a steady start, and peaked at 60 hours post infection (Figure 1C).

pFPV-sc is genetically closely related to FPV than CPV

To acquire the complete genetic information of this isolated virus, the viral genome was amplified in several fragments via PCR followed by Sanger sequencing (Table 1). Noticeably, sequences of the long inverted terminal repeats (ITR) at both the 5' and 3' end of the viral genome were obtained with two overlapping PCRs, of which primers were designed based on the conserved regions of different parvovirus genomes. After validation of sequencing results, it is confirmed that the full-length genome of the isolate pFPV-sc was amplified and sequenced. The genome is of 5,119 nucleotides in length, which encompasses the two ITRs and encoding regions for the nonstructural protein (NS) and two capsid proteins (VP1 and VP2). The full genome information is deposited to Genbank (OR264206). The 5' and 3' ITR form two imperfect palindromes typical for parvoviruses, and their sequences are identical with reference FPV strain HH-1/86 (28). In the meantime, the NS gene of this isolate exhibited similar identities to FPV, CPV and mink enteritic virus (99.1%–100%). To gain further insight into the antigenicity of this isolate, multiple sequences alignment analysis was performed on the nucleotide and translated amino acid sequences of the VP2 gene. The results indicated that the VP2 gene shared higher identities with FPV (98.8%-99.4%) than CPV (96.4%-98.5%). Noticeably, the VP2 sequence of pFPV-sc presents a unique amino acid substitution $His^{234}Tyr$, which is not found in cat FPVs but in a FPV strain isolated from leopard. The phylogenetic tree based on the VP2 nucleotide sequences showed that pFPV-sc is located in clade A, which is composed by representative FPV strains recently isolated from China and other countries (Figure 2).

pFPV-sc exhibits hemagglutination activity against selected erythrocytes

Next, the ability of the isolated pFPV-sc to cause hemagglutination was examined. Erythrocytes from different species, including giant panda, human, rabbit, pig and rat, were included in the analysis. Strong hemagglutination against pig erythrocytes was observed, but not with erythrocytes of other species (Figure 3A). At 1x10^5 $TCID_{50}$/mL, the virus exhibited

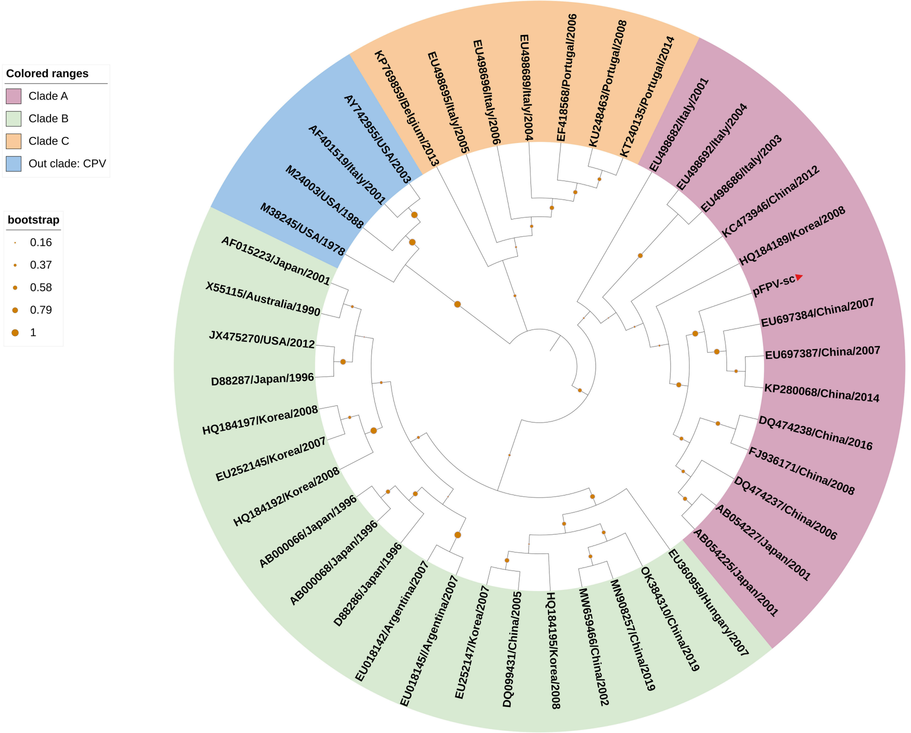

FIGURE 2
VP2-based phylogenetic analysis indicates pFPV-sc clades with recent FPV strains. The tree was generated based on full-length VP2 sequence of different FPVs using the neighbor-joining method with the Jukes-Cantor algorithm of distance correction, with bootstrapping up to 1000 replicates. GenBank accession numbers are specified for each reference strain. The three FPV clades, namely clade A, B and C, were highlighted with different colors, with the branch of pFPV-sc highlighted in red. CPV was used as out group.

more than 128 hemagglutination units. Noticeably, treatment of the erythrocytes with *A.ureafaciens* neuraminidase did not hamper hemagglutination (Figure 3B), suggesting that the hemagglutination is likely not mediated by virus binding to 5-N-aceylated-sialic acids. To allow confirmation of the specificity of virus-erythrocytes interaction, we embarked on an hemagglutination inhibition (HI) assay with hyperimmune serum collected from an immunized rabbit. As shown in Figure 3C, the hyperimmune serum displays prominent HI titer against the virus, while mock immunized serum did not show inhibition. Therefore, the results confirmed that the interaction between the virus and erythrocytes is specific.

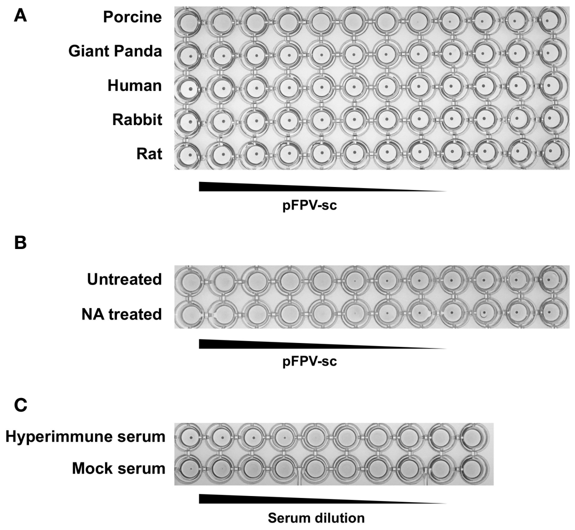

FIGURE 3
pFPV-sc has specific hemagglutination ability towards porcine erythrocytes. **(A)** Hemagglutination assay (HAA) of pFPV-sc performed with giant panda, human, rat, pig and rabbit erythrocytes. Twofold serial dilutions of pFPV-sc, starting at 10^4 $TCID_{50}$ per well, were mixed 1:1 with 0.5% erythrocytes diluted in PBS. Hemagglutination was assessed after 2 hour incubation on ice. HAAs were repeated at least three times and representative experiments are shown. **(B)** Hemagglutination of pFPV-sc is not sensitive to neuraminidase (NA) treatment. Untreated and NA (from *Arthrobacter ureafaciens*) treated porcine erythrocytes were compared via HAA as in **(A)**, and NA treatment does not affect the outcome. **(C)** Inhibition of pFPV-sc hemagglutination with hyperimmune serum. Hemagglutination inhibition assay was twofold serial dilutions of unimmunized serum and immunized hyperimmune serum mixed with 8 hemagglutination units of pFPV-sc.

Serologic evidence of early prevalence of parvoviruses in giant panda

Here in the present study, the pathogenetic virus pFPV-sc is newly isolated, however the possibility remains that FPV is already present in the giant panda population through continuous circulation. To this end, a series of giant panda serum samples collected at various time points were tested via different serological methods, with the earliest sample collected in 2011. The virus neutralization titer (VNT) and HI titer of positive samples varied from 8 to 64 and 4 to 16, respectively (Figure 4). Within the total 14 serum samples, one particular sample collected in 2011 displayed the highest VNT and HI titer. Despite no clear pattern was observed, our data provided evidence for early prevalence of parvoviruses in the giant panda population in early 2010's.

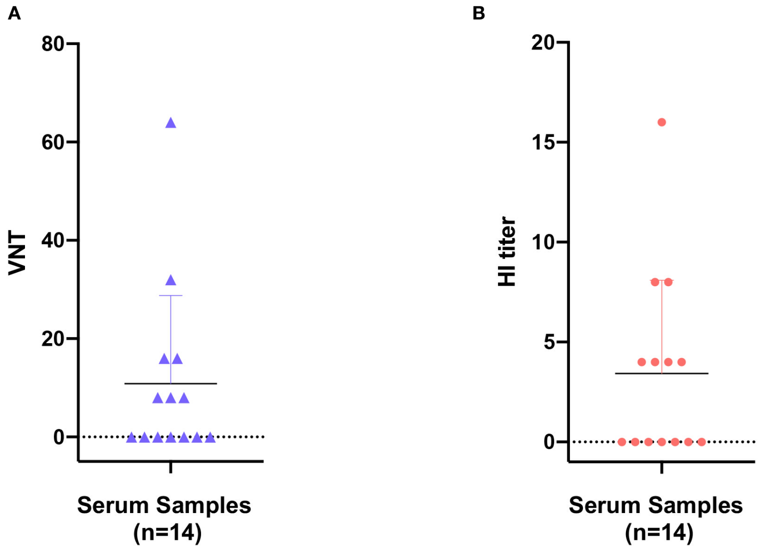

FIGURE 4
Seroprevalence of parvovirus antibodies in giant panda samples from 2010 to 2018. Reactivity of giant panda serum samples (n=14) against pFPV-sc were measured by virus neutralization assay **(A)** and hemagglutination inhibition (HI) assay **(B)**. Reactivity profiles of all serum samples are displayed as distribution dot plots, with each data point represents the virus neutralization titer (VNT) or HI titer of a particular sample.

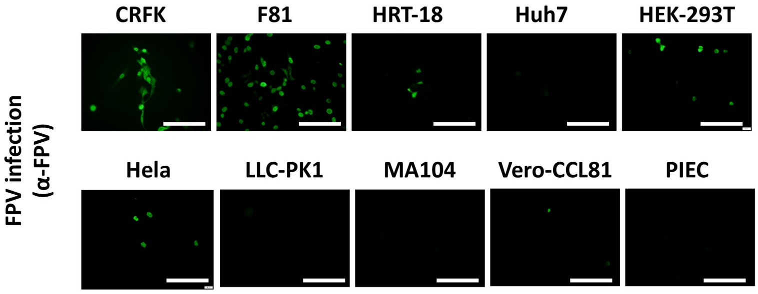

FIGURE 5
pFPV-sc can infect cells other than feline origin. Immunofluorescent staining was performed with hyperimmune serum upon pFPV-sc infected human, feline, porcine and African green monkey cell lines. Green fluorescence indicates infection; scale bars, 250 µm. Note that three out of four human cell lines tested (HRT-18, HEK-293T and Hela) are susceptible to pFPV-sc. This panel shows representative micrographs from at least three repeats.

pFPV-sc can infect Cells other than feline origin

The family parvovirus has a relatively wide host spectrum and colonizes a lot of species. To inspect on the cross-species transmission potential of pFPV-sc, we investigated the susceptibility of cell lines from species other than cat (as there is no giant panda cell lines available). Several human, feline, porcine and monkey cell lines were inoculated with viruses at a MOI = 0.1 for 1 h, and infection levels were assessed by immunostaining with the hyperimmune serum (Figure 5). Strong fluorescence was noticed in infected CRFK cells, indicated that pFPV-sc can replicate to similar levels in CRFK as in F81 cells (Figure 5). Strikingly, Vero-CCL81 and three out of four human cell lines tested (HRT-18, HEK-293T and Hela) also showed susceptibility of PFPV-SC to a particular level (Figure 5).

Giant panda transferrin receptor as a putative receptor for pFPV-sc

Carnivore protoparvovirus 1 utilizes transferrin receptor (TfR) as their main receptor for cellular entry, and attachment to TfR of a different species is the starting point of parvovirus cross-species transmission (27). To this end, we evaluated the molecular properties of the predicted giant panda TfR ortholog in comparison with feline TfR. Alignment of the primary sequences shows that the two TfRs share 87.7% identity, while the amino acid residues involved in virus binding are mainly conserved (Figure 6A). Next, using homology modeling, we showed that the topology of giant panda TfR is similar to feline TfR and human TfR, where the residues that likely induce virus binding are conserved and exposed on the edge of TfR molecule (Figure 6B). Such topology shall allow attachment of the virus, henceforth mediate viral entry.

Discussion

Carnivore protoparvovirus 1 can infect a wide range of domestic and wild carnivores, making it a worldwide endemic virus with a broad host range (9, 18). Researchers had identified feline panleukopenia virus (FPV) and canine parvovirus (CPV) infection in different species such as raccoon, African lion, leopard and white tiger, but infection in giant pandas had only received limited attention (15–20). We here isolated an FPV (pFPV-sc) from giant panda displaying severe and even lethal symptoms, and provided the full genome information for a giant panda derived parvovirus for the first time. The damage of this virus caused to giant panda, together with its unique features and the ability of this isolate to infect cells of different mammalian species warrant further investigation into the virus' characteristics and transmissibility across host spectrums.

Transmission of Carnivore protoparvovirus 1 to other (wild) animal species largely occurs through indirect contact with fomites like feces or saliva from domestic animals. Over the past decades, acute or persistent infections of FPV were reported in wild animals such as lion, leopard and white tiger, leading to symptoms from mild to lethal (16, 18, 19). Domestic or stray cats were proven to be the source of infection in most cases. Here we demonstrate that the isolated giant panda derived pFPV-sc virus shares high identities with Chinese FPV strains, as shown by phylogenetic analysis with the complete genome and the VP2 encoding region. Observations as such indicate that cats were the probable cause of infection, where the workers involved in giant panda breeding might have direct or indirect contact with FPV-infected cats. The isolated pFPV-sc is most likely the result of a spillover infection, as no sign of adaptive mutations were detected. However, our observations do not completely rule out the possibility of FPV persistent infection in giant panda. Serological evidence indicates that giant panda serum samples collected from 2011 are FPV seropositive, suggesting that continuous circulation or repeated infection might occur. Therefore, recurrent epidemiological surveillance is important to monitor possible sustained transmission of Carnivore protoparvovirus 1 infection in giant panda and a wider range of other wild animal species, which could serve as an early cautioning system for imminent threats.

Receptor interaction is the very first and essential step in virus infection of host cells. Therefore, receptor specificity has a direct impact on virus host tropism, and effective virus cross-species

A

	βI-1/βII-1 loop	βII-1 loop			βII-1/βII-2 loop							
Residue	207	209	211	213	214	215	216	217	218	219	220	221
Feline TfR	S	S	T	V	G	T	N	S	G	M	V	Y
Giant panda TfR	Q	S	T	V	G	T	D	S	G	V	V	Y

	βII-2 loop				βII-3 loop	βI-6/βII-7 loop	βII-8 loop	
Residue	222	224	225	227	239	304	382	384
Feline TfR	L	E	S	E	T	E	N	K
Giant panda TfR	L	E	S	E	T	E	N	K

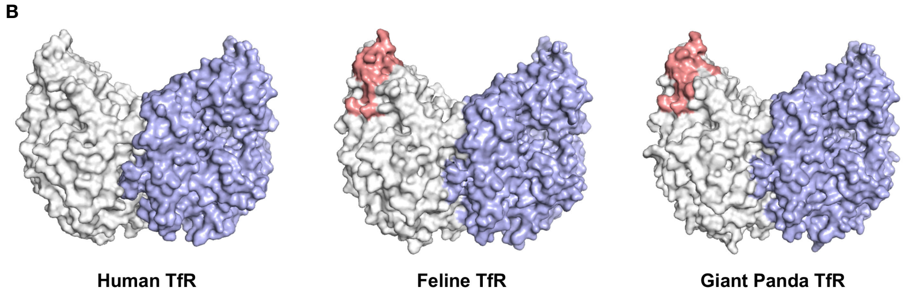

FIGURE 6
Bioinformatical and structural analysis indicates giant panda transferrin receptor (TfR) as a putative receptor for pFPV-sc. **(A)** Giant panda TfR is akin to the feline TfR at the virus-binding motif. Multiple sequence alignment indicated that the majorities of the crucial amino acid residues that forms the virus binding motif (βI-1, βII-1, βII-2, βII-3, βI-6, βII-7 and βII-8 loops) are conserved between feline and giant panda TfRs. Differences between giant panda TfR and feline TfR are marked red. **(B)** TfR topology are relatively conserved between different host species, with the virus binding motif well exposed. Side view of the dimeric human TfR (PDB accession number: 7ZQS), feline TfR and giant panda TfR (modelled using homology modelling) are shown in surface representation and colored by one monomer gray, and another monomer blue. Virus binding motifs of feline and giant panda TfRs, specified in **(A)**, were depicted in red in the gray-colored monomer.

transmission depends on the ability of functional utilization of a receptor of an alternative host. In the case of *Carnivore protoparvovirus 1*, transferrin receptor (TfR) serves as its receptor and affinity of TfR association determines both the antigenicity and host range (22, 24, 27). In our analysis, we showed that giant panda TfR shares high similarity with feline TfR, especially the virus interacting motif (26) is highly conserved. This resembles the classic pathway of virus host switching and virus speciation, where binding to giant panda TfR by FPV could initiate infection. Direct studies on the interaction mechanism *in vitro* between FPV and giant panda TfR may reveal the molecular basis for this particular receptor usage.

Besides presumed utilization of giant panda TfR, the isolate pFPV-sc is also shown to be able to agglutinate erythrocytes of certain species. For most viruses, ability of inducing hemagglutination means preferential binding to sialic acids, a group of nine carbon sugars that commonly forms the terminal residues of glycoconjugates (29). Due to its unique topology, binding to sialic acids will allow enhanced adhesion of the virus to the cell surface, hence in closer proximity to the main receptor (29–31). Noticeably, the hemagglutination activity of the isolate pFPV-sc is resistant to neuraminidase treatment, indicating that it might bind to N-glycolylneuraminic acid (Neu5Gc), which correlates with previous findings (32). To this point, the exact machnism and the evolutional advantage in virus fitness upon Carnivore protoparvovirus 1-sialic acid association is still remains to be appreciated.

Despite a successful host jump from domestic cats to giant panda, one of our most striking observations is that pFPV-sc can also infect different cell lines from other mammal species, including humans. Whether susceptibility of those cell lines is due to virus binding to their TfR orthologues or a yet unidentified (co-) receptor, is still unclear. Meanwhile, this finding is currently limited to the level of tissue cultured cells, while infection models build upon organoids or genetically engineered lab animals might collectively reveal the proneness of pFPV-sc to other potential hosts.

Taken together, our observations emphasized the damage of pFPV-sc to the giant panda population, and also underscored the multi-host potential of *Carnivore protoparvovirus 1* in general. Future studies shall focus on the infection machnism and antiviral intervention of *Carnivore protoparvovirus 1*, as its global distribution in domestic and wild animals with cross-species potential is alarming from an epidemiological perspective.

Data availability statement

The original contributions presented in the study are included in the article/supplementary material, further inquiries can be directed to the corresponding authors.

Ethics statement

The animal study was approved by Animal Ethics Committee of Sichuan Agricultural University. The study was conducted in accordance with the local legislation and institutional requirements.

Author contributions

SZ, JL, HH and ZY carried out the experiments. YL and QY supervised the study. YL and SZ contributed to the conception of this article. SZ, JL, HH, ZY, LY, QP, LL, LW, YL and QY analysed data. SZ and YL wrote the manuscript with input from all authors. All authors contributed to the article and approved the submitted version.

Funding

This work was supported by the Chengdu Giant Panda Breeding Research Foundation, China (Grant No. CPF2017-35), the Self-supporting Project of Chengdu Giant Panda Breeding Research Base, China (Grant No. 2021CPB-C13), the Self-supporting Project of Sichuan Academy of Giant Panda and the Natural Science Foundation of Sichuan Province (Grant No. 2022NSFSC1692 and Grant No. 2022NSFSC1625).

Conflict of interest

The authors declare that the research was conducted in the absence of any commercial or financial relationships that could be construed as a potential conflict of interest.

Publisher's note

All claims expressed in this article are solely those of the authors and do not necessarily represent those of their affiliated organizations, or those of the publisher, the editors and the reviewers. Any product that may be evaluated in this article, or claim that may be made by its manufacturer, is not guaranteed or endorsed by the publisher.

References

1. Cotmore SF, Agbandje-McKenna M, Canuti M, Chiorini JA, Eis-Hubinger AM, Hughes J, et al. ICTV virus taxonomy profile: parvoviridae. *J Gen Virol* (2019) 100:367. doi: 10.1099/jgv.0.001212

2. Reed AP, Jones EV, Miller TJ. Nucleotide sequence and genome organization of canine parvovirus. *J Virol* (1988) 62:266. doi: 10.1128/jvi.62.1.266-276.1988

3. Chung HC, Kim SJ, Nguyen VG, Shin S, Kim JY, Lim SK, et al. New genotype classification and molecular characterization of canine and feline parvoviruses. *J Vet Sci* (2020) 21. doi: 10.4142/jvs.2020.21.e43

4. Parrish CR. Emergence, natural history, and variation of canine, mink, and feline parvoviruses. *Adv Virus Res* (1990) 38:403. doi: 10.1016/S0065-3527(08)60867-2

5. Parrish CR, Have P, Foreyt WJ, Evermann JF, Senda M, Carmichael LE. The global spread and replacement of canine parvovirus strains. *J Gen Virol* (1988) 69:1111–6. doi: 10.1099/0022-1317-69-5-1111

6. Stucker KM, Pagan I, Cifuente JO, Kaelber JT, Lillie TD, Hafenstein S, et al. The role of evolutionary intermediates in the host adaptation of canine parvovirus. *J Virol* (2012) 86:1514–21. doi: 10.1128/JVI.06222-11

7. Jager MC, Tomlinson JE, Lopez-Astacio RA, Parrish CR, Van de Walle GR. Small but mighty: old and new parvoviruses of veterinary significance. *Virol J* (2021) 18:210. doi: 10.1186/s12985-021-01677-y

8. François S, Filloux D, Roumagnac P, Bigot D, Gayral P, Martin DP, et al. Discovery of parvovirus-related sequences in an unexpected broad range of animals. *Sci Rep* (2016) 6. doi: 10.1038/srep30880

9. Calatayud O, Esperón F, Cleaveland S, Biek R, Keyyu J, Eblate E, et al. Carnivore parvovirus ecology in the serengeti ecosystem: vaccine strains circulating and new host species identified. *J Virol* (2019) 93. doi: 10.1128/JVI.02220-18

10. Stuetzer B, Hartmann K. Feline parvovirus infection and associated diseases. *Vet J* (2014) 201:150–5. doi: 10.1016/j.tvjl.2014.05.027

11. Clinical Signs I, Csiza CK, Scott FW, Lahunta A DE, Gillespie JH. Pathogenesis of feline panleukopenia virus in susceptible newborn kittens I. Clinical signs, hematology, serology, and virology. *Infect Immun* (1971) 3:833–7. doi: 10.1128/iai.3.6.833-837.1971

12. Parrish CR, Aquadro CF, Carmichael LE. Canine host range and a specific epitope map along with variant sequences in the capsid protein gene of canine parvovirus and related feline, mink, and raccoon parvoviruses. *Virology* (1988) 166:293–307. doi: 10.1016/0042-6822(88)90500-4

13. MIranda C, Thompson G. Canine parvovirus: the worldwide occurrence of antigenic variants. *J Gen Virol* (2016) 97:2043–57. doi: 10.1099/jgv.0.000540

14. Barrs VR. Feline panleukopenia: A re-emergent disease. *Vet Clin North Am Small Anim Pract* (2019) 49:651–70. doi: 10.1016/j.cvsm.2019.02.006

15. Guo L, Yang SL, Chen SJ, Zhang Z, Wang C, Hou R, et al. Identification of canine parvovirus with the Q370R point mutation in the VP2 gene from a giant panda (Ailuropoda melanoleuca). *Virol J* (2013) 10. doi: 10.1186/1743-422X-10-163

16. Huang S, Li X, Xie W, Guo L, You D, Xu H, et al. Molecular detection of parvovirus in captive siberian tigers and lions in northeastern China from 2019 to 2021. *Front Microbiol* (2022) 13. doi: 10.3389/fmicb.2022.898184

17. Zhao J, Zhang H, Zhang L, Zhang Q, Zhou N, Du T, et al. Isolation and genetic characterization of parvoviruses from dogs, cats, minks, and raccoon dogs in the eastern region of shandong province, China. *Front Microbiol* (2022) 13. doi: 10.3389/fmicb.2022.862352

18. Guerrero-Sánchez S, Wilson A, González-Abarzúa M, Kunde M, Goossens B, Sipangkui R, et al. Serological evidence of exposure of Bornean wild carnivores to feline-related viruses at the domestic animal-wildlife interface. *Transbound Emerg Dis* (2022) 69:e3250–4. doi: 10.1111/tbed.14549

19. Chen CC, Chang AM, Wada T, Chen MT, Tu YS. Distribution of Carnivore protoparvovirus 1 in free-living leopard cats (Prionailurus bengalensis chinensis) and its association with domestic carnivores in Taiwan. *PloS One* (2019) 14. doi: 10.1371/journal.pone.0221990

20. Kim YJ, Yoon SW, Jang JH, Jeong DG, Lee BJ, Kim HK. Genetic characterization of feline parvovirus isolate fe-P2 in korean cat and serological evidence on its infection in wild leopard cat and asian badger. *Front Vet Sci* (2021) 8. doi: 10.3389/fvets.2021.650866

21. Wessling-Resnick M. Crossing the iron gate: why and how transferrin receptors mediate viral entry. *Annu Rev Nutr* (2018) 38:431. doi: 10.1146/annurev-nutr-082117-051749

22. Parker JSL, Murphy WJ, Wang D, O'Brien SJ, Parrish CR. Canine and feline parvoviruses can use human or feline transferrin receptors to bind, enter, and infect cells. *J Virol* (2001) 75:3896–902. doi: 10.1128/JVI.75.8.3896-3902.2001

23. Hueffer K, Parker JSL, Weichert WS, Geisel RE, Sgro J-Y, Parrish CR. The natural host range shift and subsequent evolution of canine parvovirus resulted from virus-specific binding to the canine transferrin receptor. *J Virol* (2003) 77:1718–26. doi: 10.1128/JVI.77.3.1718-1726.2003

24. Hueffer K, Govindasamy L, Agbandje-McKenna M, Parrish CR. Combinations of two capsid regions controlling canine host range determine canine transferrin receptor binding by canine and feline parvoviruses. *J Virol* (2003) 77:10099–105. doi: 10.1128/JVI.77.18.10099-10105.2003

25. Hafenstein S, Palermo LM, Kostyuchenko VA, Xiao C, Morais MC, Nelson CDS, et al. Asymmetric binding of transferrin receptor to parvovirus capsids. *Proc Natl Acad Sci USA* (2007) 104:6585–9. doi: 10.1073/pnas.0701574104

26. Lee H, Callaway HM, Cifuente JO, Bator CM, Parrish CR, Hafenstein SL. Transferrin receptor binds virus capsid with dynamic motion. *Proc Natl Acad Sci U.S.A.* (2019) 116:20462–71. doi: 10.1073/pnas.1904918116

27. Callaway HM, Welsch K, Weichert W, Allison AB, Hafenstein SL, Huang K, et al. Complex and dynamic interactions between parvovirus capsids, transferrin receptors, and antibodies control cell infection and host range. *J Virol* (2018) 92:460–78. doi: 10.1128/JVI.00460-18

28. Cheng N, Zhao Y, Han Q, Zhang W, Xi J, Yu Y, et al. Development of a reverse genetics system for a feline panleukopenia virus. *Virus Genes* (2019) 55:95–103. doi: 10.1007/s11262-018-1621-9

29. Thompson AJ, de Vries RP, Paulson JC. Virus recognition of glycan receptors. *Curr Opin Virol* (2019) 34:117–29. doi: 10.1016/j.coviro.2019.01.004

30. Neu U, Bauer J, Stehle T. Viruses and sialic acids: Rules of engagement. *Curr Opin Struct Biol* (2011) 21:610–18. doi: 10.1016/j.sbi.2011.08.009

31. Ströh LJ, Stehle T. Glycan engagement by viruses: receptor switches and specificity. *Annu Rev Virol* (2014) 1:285–306. doi: 10.1146/annurev-virology-031413-085417

32. Löfling J, Michael Lyi S, Parrish CR, Varki A. Canine and feline parvoviruses preferentially recognize the non-human cell surface sialic acid N-glycolylneuraminic acid. *Virology* (2013) 440:89–96. doi: 10.1016/j.virol.2013.02.009

Frontiers in Immunology

TYPE Original Research
PUBLISHED 24 October 2023
DOI 10.3389/fimmu.2023.1251001

OPEN ACCESS

EDITED BY
Xusheng Qiu,
Chinese Academy of Agricultural Sciences, China

REVIEWED BY
Shanhui Ren,
Chinese Academy of Agricultural Sciences, China
Changlong Liu,
Chinese Academy of Agricultural Sciences, China
Bin Zhou,
Nanjing Agricultural University, China

*CORRESPONDENCE
Jinding Chen
jdchen@scau.edu.cn

RECEIVED 30 June 2023
ACCEPTED 05 October 2023
PUBLISHED 24 October 2023

CITATION
Du P, Yan Q, Zhang X-A, Zeng W, Xie K, Yuan Z, Liu X, Liu X, Zhang L, Wu K, Li X, Fan S, Zhao M and Chen J (2023) Virus-like particle vaccines with epitopes from porcine epidemic virus and transmissible gastroenteritis virus incorporated into self-assembling ADDomer platform provide clinical immune responses in piglets. *Front. Immunol.* 14:1251001.
doi: 10.3389/fimmu.2023.1251001

COPYRIGHT
© 2023 Du, Yan, Zhang, Zeng, Xie, Yuan, Liu, Liu, Zhang, Wu, Li, Fan, Zhao and Chen. This is an open-access article distributed under the terms of the Creative Commons Attribution License (CC BY). The use, distribution or reproduction in other forums is permitted, provided the original author(s) and the copyright owner(s) are credited and that the original publication in this journal is cited, in accordance with accepted academic practice. No use, distribution or reproduction is permitted which does not comply with these terms.

Virus-like particle vaccines with epitopes from porcine epidemic virus and transmissible gastroenteritis virus incorporated into self-assembling ADDomer platform provide clinical immune responses in piglets

Pengfei Du[1], Quanhui Yan[1], Xiao-Ai Zhang[2], Weijun Zeng[1], Kaiyuan Xie[1], Zhongmao Yuan[1], Xiaodi Liu[1], Xueyi Liu[1], Lihong Zhang[1], Keke Wu[1], Xiaowen Li[1], Shuangqi Fan[1], Mingqiu Zhao[1] and Jinding Chen[1]*

[1]Department of Preventive Veterinary Medicine, College of Veterinary Medicine, South China Agricultural University, Guangzhou, Guangdong, China, [2]Agro-Biological Gene Research Center, Guangdong Academy of Agricultural Sciences, State Key Laboratory of Livestock and Poultry Breeding, Guangzhou, China

Introduction: Porcine epidemic diarrhea virus (PEDV) and transmissible gastroenteritis virus (TGEV) are major intestinal coronaviruses that cause vomiting, diarrhea, dehydration, and mortality in piglets. These viruses coexist and lead to significant economic losses in the swine industry. Virus-like particles (VLPs) have emerged as promising alternatives to conventional inactivated vaccines due to their exceptional safety, efficacy, and ability to provide multi-disease protection with a single dose.

Methods: Our study focused on specific antigenic epitopes from the PEDV S protein (SS2 and 2C10 regions) and the TGEV S protein (A and D sites) as target candidates. These epitopes were integrated into the ADDomer framework, and we successfully generated recombinant proteins AD, AD-P, AD-T, and AD-PT using the baculovirus expression vector system (BEVS). By meticulously optimizing conditions in High Five cells, we successfully expressed and purified the recombinant proteins. Subsequently, we developed the recombinant ADDomer-VLP vaccine and conducted a comprehensive evaluation of its efficacy in piglets.

Results: Following ultrafiltration concentration and sucrose gradient centrifugation purification, the recombinant proteins self-assembled into VLPs as observed by transmission electron microscopy (TEM). Administration of the vaccine did not result in any adverse reactions in the immunized piglets. Additionally, no significant instances of fever were detected in any of the experimental groups, and there were no notable changes in average daily weight gain compared to the control group that received PBS. The recombinant ADDomer-VLP vaccines demonstrated strong immunogenicity, effectively stimulating the production of neutralizing antibodies against both PEDV and TGEV. Moreover, the recombinant ADDomer-VLP vaccine induced elevated levels of IFN-γ, IL-2, and IL-4, and enhanced cytotoxic T lymphocyte (CTL) activity in the peripheral blood of piglets.

Discussion: These recombinant VLPs have demonstrated the ability to induce strong cellular and humoral immune responses in piglets, making them an incredibly promising platform for the rapid and simplified development of epitope vaccines.

KEYWORDS

porcine epidemic diarrhea virus, transmissible gastroenteritis virus, virus-like particles, ADDomer, insect baculovirus expression system, epitope

1 Introduction

Porcine epidemic diarrhea virus (PEDV) and Transmissible gastroenteritis virus (TGEV), which belong to the family of Swine enteric coronaviruses (SeCoV) are responsible for causing Porcine epidemic diarrhea (PED) and Transmissible gastroenteritis (TGE) in pigs (1). Pigs of all age groups are susceptible to infection by PEDV and TGEV, with pregnant sows capable of transmitting the viruses to newborn piglets through vertical transmission. In cases of infection among lactating piglets, the mortality rate can reach alarming levels of up to 100% (2). The primary mode of transmission for PEDV is through the fecal-oral route. However, recent studies have indicated the potential for airborne transmission of PEDV as an additional route of spread (3). The PEDV strain has rapidly spread to various countries across Asia, North America, and Europe (4–12). Particularly noteworthy is the significant prevalence of GII PEDV in China since 2010, resulting in a surge in morbidity and mortality rates among afflicted piglets (8). In 1946, the initial documentation of TGEV occurred in the United States (13), followed by subsequent identifications in Europe, Asia, Africa, and South America (5, 14–16). This widespread distribution of TGEV has resulted in substantial economic losses within the global pig industry. The primary modes of TGEV transmission include fecal-oral transmission, respiratory transmission, and breastfeeding transmission (17, 18). TGEV and PEDV often present clinically mixed infections with indistinguishable symptoms and similar pathological changes. However, cross-protection between the two viruses is limited (19).

The widely used PEDV/TGEV dual vaccines are mainly inactivated and weakly virulent vaccines prepared from isolated strains. In March 2015, a trivalent vaccine developed from attenuated TEGV (strain H), PEDV (strain CV777, subgroup GI-a) and porcine rotavirus (strain NX) was approved in China. Sows vaccinated with inactivated or attenuated vaccines will produce sIgA and IgG antibodies in colostrum, which will allow piglets to establish passive immunity to PEDV and TGEV. Existing commercial vaccines still have several drawbacks. Weak vaccines carry the risk of reverting to strong virulence, and there is also the possibility of antigenic mutation in the virulent strain. Inactivated vaccines can experience changes in immunogenicity during the inactivation process, often necessitating multiple doses and booster injections. Additionally, piglets often do not receive sufficient protective antibodies through the maternal route from immunized sows (20, 21).

VLPs are empty structures formed by assembling viral proteins without any nucleic acids present inside. However, they maintain numerous essential characteristics of the viral capsid, such as precise structural and size uniformity, biocompatibility, stability, immunogenicity, and affinity for cells (22). The formation of VLP shells occurs through a spontaneous process, wherein the interactions among protein monomers contribute to the highly organized structure. These unique properties of VLPs make them appealing nanoplatforms for various applications, as they can effectively showcase and accommodate functional biomolecules.

ADDomer is an adenovirus-derived self-assembling nanoparticle scaffold based on multimeric proteins. It enables plug-and-play access to multiple immunogenic epitopes of pathogens (23). Every ADDomer VLP particle is formed through the assembly of 12 pentameric protein complexes, each measuring 300 kDa in size. These particles offer up to 360 insertion regions for the display of antigenic epitopes. Remarkably, they demonstrate outstanding thermal stability comparable to that of conventional VLPs. This breakthrough in the field of traditional vaccines overcomes significant obstacles, simplifying the vaccine design and production process to a great extent. In previous preclinical trials, a vaccine utilizing ADDomer to showcase the chikungunya virus E2 protein demonstrated promising immunogenicity (23). In the context of the SARS-CoV-2 pandemic, one study targeted modifications to the ADDomer platform and constructed an ADDomer VLP that expresses the RBD of the SARS-CoV-2 S-protein. Immunization of mice showed that the VLP triggered a significant humoral immune response in the body, and neutralization assays with a SARS-CoV-2 S-protein pseudovirus demonstrated a very high serum neutralization potency after immunization (24). ADDomer, with its BEVS-based plug-and-play antigen display platform, holds great promise as an innovative VLP vaccine vector against emerging pathogens.

PEDV and TEGV S proteins can induce the body to produce neutralizing antibodies (25). In the PEDV S protein, four B-cell epitopes have been identified. These include the core neutralizing epitope (COE) located in the S1 region (aa 499-638), SS2 (aa 748-755), SS6 (aa 764-771), and 2C10 (aa 1368-1374) in the S2 region (26). The SS2 epitope (aa 748-755) and epitope 2C10 (aa 1368-1374) have demonstrated the ability to induce neutralizing antibodies against PEDV. Importantly, these epitopes have been found to be conserved in all wild strains of PEDV isolated from China (27, 28). However, it is worth noting that the COE epitope region and the SS6 epitope exhibit significant diversity among the majority of wild PEDV strains, serving as high-frequency mutation regions within the epitope region (29). Particularly in the CT-P120 and PT-P96 strains, epitope region mutations may impair neutralizing antibody recognition, and the F636R and F636S mutations in the COE epitope region may lessen the responsiveness of viral neutralizing antibodies (30). Studies have demonstrated that both the SS2 and 2C10 epitopes are capable of inducing PEDV-specific neutralizing antibodies in mice (31, 32). Consequently, the SS2 and 2C10 epitope regions serve as valuable references for the development of antigenic epitope vaccines against PEDV.

Based on the protease hydrolysis sites, TGEV S proteins can be split into the S1 region (aa 1-790) and the S2 region (aa 790-1383) (33). The S1 region is distinguished as S1-NTD and S1-CTD and contains RBD (aa 560-655). The epitopes crucial for stimulating neutralizing antibodies in the TGEV S protein are situated in the NTD of the S1 protein. Earlier studies have identified four antigenic sites within the anterior portion of the S1 region, namely C (aa 49-52), B (aa 75-142), D (aa 385-386), and A (aa 540-592) (34, 35). The A and D sites, with the potential presence of multiple RBDs on their surface, play a vital role in the production of neutralizing antibodies (36). The A site, located on the surface of the TGEV virus particle, is characterized by the presence of crucial amino acids 538, 543, and 591. These amino acids are essential for maintaining the proper conformation of the site. The D site, a highly conserved linear antigenic site, shares similarities with the A site in its ability to stimulate the production of neutralizing antibodies within the body (37, 38). Consequently, the A and D sites of the S protein serve as crucial target antigenic regions for the prevention and control of TGEV through the utilization of novel vectors.

Therefore, the SS2 and 2C10 regions of PEDV S protein and the A and D sites of TGEV S protein were selected as candidate antigenic epitopes in this study. These epitopes were inserted into the adomer framework and the recombinant proteins AD, AD-P, AD-T, and AD-PT were expressed by BEVS.Subsequently, the self-assembled recombinant ADDomer-VLPs were prepared into a vaccine, and the immune efficacy of the recombinant ADDomer-VLPs vaccine was evaluated by immunization experiments in piglets.

2 Materials and methods

2.1 Cells culture

Vero cells, ST cells, DH10Multibac receptor cells, and transfer plasmid pFBDM were obtained from the Department of Veterinary Microbiology and Immunology, South China Agricultural University. sf9 cells and High Five cells were purchased from Beijing Yiqiao Shenzhou Technology Co. Vero cells and ST cells were cultured using Dulbecco's modified Eagle's medium (Gibco, USA) containing 10% fetal bovine serum (Gibco, USA) in a 37°C, 5% -CO2 incubator. sf9 cells and High Five cells were cultured using SIM SF medium and SIM High Five medium purchased from Beijing Yiqiao Shenzhou Technology Co., Ltd. at 27°C and 110 rpm in a shaker.

2.2 Protein design

The PEDV AJ1102 strain (GenBank Accession: JX188454.1) and the TGEV SHXB strain (GenBank Accession: KP202848.1) available in GenBank were used as references. From these strains, the SS2 and 2C10 antigenic regions of the PEDV S protein and the A and D antigenic sites of the TGEV S protein were selected as exogenous antigens for further investigation (Table 1). The ADDomer recombinant protein AD, as well as the recombinant proteins AD-P, AD-T, and AD-PT, were generated by incorporating different tandem forms of exogenous antigens into specific regions of the ADDomer structure. Specifically, the PEDV antigen epitope was inserted into the VL region, RGD1 region, and RGD2 region of ADDomer. The sequences provided in Patent No. US2020325179A1 were utilized as references for the design and construction of these recombinant proteins (39). For the spatial structure simulation of the recombinant VLP, the crystal structure file with the PDB number 6hcr was chosen. The simulation was conducted using UCSF Chimera X, a software tool commonly used for visualizing and analyzing molecular structures. The designed exogenous gene sequences were subjected to optimization for insect cell-preferred codons.

TABLE 1 Selected S protein antigen sites.

Virus	Name	Amino acid sites	Amino acid sequence
PEDV	SS2	aa 748～755	YSNIGVCK
	2C10	aa 1368～1374	GPRLQPY
TGEV	SA	aa 538～591	KRSGYGQPIASTLSNITLPMQDHNTDVYCIRSDQFSVYVHSTCKSALWDNIFKR
	SD	aa 373～398	CYTVSDSSFFSYGEIPFGVTDGPRYC

2.3 Virus acquisition

Subsequently, the optimized gene sequences were synthesized and directly inserted into the pFBDM plasmid by Sangon (Sangon, China). This process resulted in the generation of recombinant transfer plasmids, namely pFBDM-AD, pFBDM-AD-P, pFBDM-AD-T, and pFBDM-AD-P & TGEV.

The recombinant transfer plasmids were subjected to agarose gel electrophoresis for identification, followed by submission to Sangon (Sangon, China) for sequencing analysis. The constructed recombinant transfer plasmid was transformed into DH10Multibac receptor cells, and then the monoclonal colonies were picked and incubated on shaker at 37°C for 6 h. 150 μL of bacterial solution was aspirated and spread on LB agar medium containing Gen, Kan, Amp, IPTG, and X-Gal, and the blue and white spots of the colonies were observed in an incubator after the dishes were placed upside down in the incubator for 48 h. The colonies were then placed in the incubator for 48 h to observe the blue and white spots. White monoclonal colonies were picked and cultured for 24 h at 37°C on a shaker, followed by extraction of recombinant baculovirus plasmids The recombinant baculovirus plasmid successfully identified by PCR was transfected into sf9 cells, which were subsequently incubated at 27°C for 96 h in an incubator (40). The recombinant baculoviruses obtained by centrifugation of the culture medium and aspiration of the supernatant. They were named Ac-AD, Ac-AD-P, Ac-AD-T and Ac-AD-PT, respectively.

The titer of P1 generation viruses is relatively low, so P1 generation recombinant baculoviruses can be passaged in suspension culture of sf9 cells to increase the titer. We inoculated the recombinant baculovirus into sf9 cells in a shaker at 27°C and cultured at 140 r/min for 96 h, and passaged to the P3 generation of recombinant baculovirus.

2.4 Virus titer determination

The AceQ Universal SYBR qPCR Master Mix (Vazyme, USA) was utilized for absolute quantitative RT-qPCR analysis. Multiple dilutions of known concentrations of plasmid pMD18-T-Ac were performed and a standard curve was plotted based on the copy number and Cq value of the plasmid. Recombinant baculovirus DNA was extracted using the Omega Viral DNA Kit (Omega Bio-Tek, USA) following the provided instructions, and this DNA served as the template for the RT-qPCR assay. The Cq value obtained from each sample well was then used to determine the recombinant baculovirus nucleic acid copy number by interpolating it into the standard curve. Finally, the virus titer was calculated using the formula specified in the user manual of the Bac-to-Bac® Baculovirus Expression System from Invitrogen.

2.5 Protein identification

Cell precipitates from the P1 to P3 generations were collected separately for protein expression verification through Western blot analysis. The recombinant proteins were detected using specific primary antibodies. The mouse-derived anti-ADDomer polyclonal antibody, mouse-derived anti-PEDV S1 protein monoclonal antibody (Guangzhou Qianxun Biological Co., Ltd., China), and rabbit-derived anti-TGEV S1 protein polyclonal antibody (Alpha Diagnostic International, USA) were used as primary antibodies for detection. Subsequently, secondary antibodies such as goat anti-mouse IgG-HRP antibody or goat anti-rabbit IgG-HRP antibody (Shanghai Biyuntian Biotechnology Co., Ltd., China) were employed. Primary antibodies were incubated overnight at 4°C and secondary antibodies at room temperature for 1h.The displayed images were obtained using an ECL chemiluminescent solution (Shanghai Yase Biotechnology Co., Ltd., China) on PVDF membranes.

The recombinant proteins were detected using an Indirect Immunofluorescence assay (IFA). Initially, the sf9 cells were fixed with 4% paraformaldehyde fixative, and subsequently, cells infected with the P3 generation recombinant baculovirus were introduced. To ensure permeability, the cell membranes were treated with TritonX-100. Primary antibodies, specifically a mouse-derived anti-PEDV S1 protein monoclonal antibody (Qianxun Biological, China) and a rabbit-derived anti-TGEV S1 protein polyclonal antibody (Alpha Diagnostic International, USA), were employed. Following this, secondary antibodies were used, including a goat anti-mouse IgG-FITC antibody or a goat anti-rabbit IgG-FITC antibody (Beyotime, China).The resulting images were captured and observed utilizing an inverted fluorescence microscope known as Eclipse Ti-S (Nikon, Japan). These images were then saved for further analysis (41).

2.6 Expression time phase analysis

High Five cells can express exogenous proteins more efficiently, so in this study, we analyzed the expression time phase of recombinant proteins in terms of harvesting time and inoculation dose to find out the optimal expression conditions. The steps were as follows: adjust the density of suspended High Five cells to 2×106 cells/mL, inoculate the cells with each recombinant baculovirus at MOI=1, 5, 10, and incubate the cells in suspension at 140 r/min at 27°C, and then take the suspension at 48 h, 72 h, 96 h and 120 h after inoculation to prepare protein samples. The levels of recombinant protein expression were assessed using Western Blot analysis. The grayscale values of the protein bands were quantitatively analyzed with the assistance of ImageJ software. Subsequently, the data obtained from the temporal phase of recombinant protein expression were plotted to visualize the results effectively.

2.7 Protein purification and morphology detection

A recombinant baculovirus was introduced into High Five cells to produce a large amount of protein. The cell cultures were harvested and sonicated, and the resulting mixture was centrifuged at 5000 r/min for 50 minutes. The supernatant was then transferred to Millipore ultrafiltration tubes and subjected to further centrifugation. To concentrate the protein samples, ultracentrifugation was performed using sucrose solutions with concentrations of 70%, 50%, and 30%. Finally, the proteins from different protein loops were collected using a syringe. The proteins collected were subsequently filtered through a 0.22 μm membrane to remove impurities. The resulting filtrate underwent SDS-PAGE electrophoresis and was stained with BeyoBlue™ Komas Brilliant Blue Ultrafast Staining Solution to assess VLP purification. The concentration of recombinant proteins was quantified using the Thermo Scientific Pierce™ BCA Protein Assay Kit (Thermo Fisher Scientific, USA) as per the manufacturer's instructions. The percentage of target proteins was determined by analyzing grayscale values using Image J software.

TEM is a highly effective experimental technique for investigating internal swelling structures in materials. To confirm the self-assembly phenomenon of ADDomer, four proteins were examined using a Talos F200S transmission electron microscope (FEI, USA). The samples were applied onto a carbon-coated grid and negatively stained with a 2% phosphotungstic acid solution for 1 minute. Subsequently, the grid was air-dried for 6 hours and subjected to TEM analysis for observation of the samples' internal structures.

2.8 Vaccine preparation and piglet immunization experiments

Each purified ADDomer-VLP was adjusted to a concentration of 50 μg/mL using sterile PBS. Subsequently, it was emulsified with ISA 201VG adjuvant (Seppic, France) at a 1:1 ratio. This emulsification process was carried out in a biosafety cabinet using a magnetic stirrer to ensure safety. The resulting mixture was prepared and analyzed to assess the physicochemical properties of the vaccine.

Four-week-old castrated male Large White × Duroc binary cross piglets, sourced from a pig farm in Guangdong Province, were selected for the study. Before the experiment, the piglets were subjected to antigen and antibody tests to confirm their negative status for PEDV/TGEV. The experimental animal procedures were approved by the Experimental Animal Ethics Committee of South China Agricultural University (No. 2021F503).

The piglets were randomly divided into 6 groups of 3 piglets each. Groups 1-6 were vaccinated with AD vaccine, AD-P vaccine, AD-T vaccine, AD-PT vaccine, PEDV/TGEV weakly virulent vaccine, and PBS immunized control group, respectively. The vaccine formulations used in this study were all W/O/W emulsions, administered via intramuscular injection (Table 2). Peripheral blood samples were collected from the piglets to isolate serum, and on day 35, peripheral blood was also used to isolate lymphocytes. The piglets' body temperature was monitored twice daily at fixed intervals throughout the immunization trial, and their clinical signs were observed. The piglets' weights were recorded on days 0, 14, and 35 after immunization to calculate the average daily weight gain (Figure 1A).

TABLE 2 Piglet immunization program design.

Group	Antigens	Type and composition	Immunization dose and method
1	AD (Negative control)	W/O/W, ISA 201 VG	2 mL (50 μg)/pig;im
2	AD-P	W/O/W, ISA 201 VG	2 mL (50 μg)/pig;im
3	AD-T	W/O/W, ISA 201 VG	2 mL (50 μg)/pig;im
4	AD-PT	W/O/W, ISA 201 VG	2 mL (50 μg)/pig;im
5	PEDV/TGEV diphasic attenuated vaccine	SCJY-1+SCSZ-1	1 mL/pig;im
6	PBS (Non-immune control)	PBS	2 mL/pig;im

2.9 The determination of antibody level

The levels of piglet anti-PEDV/TGEV specific antibodies were determined using the porcine PEDV IgG indirect ELISA kit (Ruixin Biotech, China) and the porcine TGEV IgG indirect ELISA kit (Ruixin Biotech, China), following the provided instructions. Peripheral blood samples were collected from piglets on days 7, 14, 21, 28, and 35. The PEDV/TGEV-specific antibody levels were measured in these samples using the respective ELISA kits.

2.10 The determination of VNT

VNT(Virus Neutralization Test) assays were conducted to measure the peripheral serum antibody neutralization titers on day 0 and day 35. Vero and ST cells were cultivated in 96-well cell culture plates until a monolayer was formed, ensuring their optimal condition for experimentation. The serum samples collected on day 0 and day 35 were inactivated by exposing them to a 56°C water bath for 30 minutes, and then diluted at an initial ratio of 1:10. Subsequently, the serum was further diluted to a 1:640 ratio at a 1:2 ratio, followed by a 2-hour pre-reaction with 100 $TCID_{50}$ of PEDV/TGEV. After that, the virus/serum mixture was added to the cell wells and incubated for 1 hour. The supernatant was discarded, and serum-free DMEM medium was added to the wells. Eight replicate wells were set up for each group. The cytopathic effects of the cells in each well were observed and recorded. The neutralizing antibody potency (ND_{50}) of the peripheral blood from piglets was calculated using the Reed-Muench method.

2.11 Cytokine assay

Peripheral blood cytokines in piglets at day 0 and day 35 were analyzed using ELISA kits (MEIMIAN, China). Specifically, the pig IFN-γ ELISA kit, pig IL-2 ELISA kit, and pig IL-4 ELISA kit were employed for this purpose. The levels of IFN-γ, IL-2, and IL-4 in the

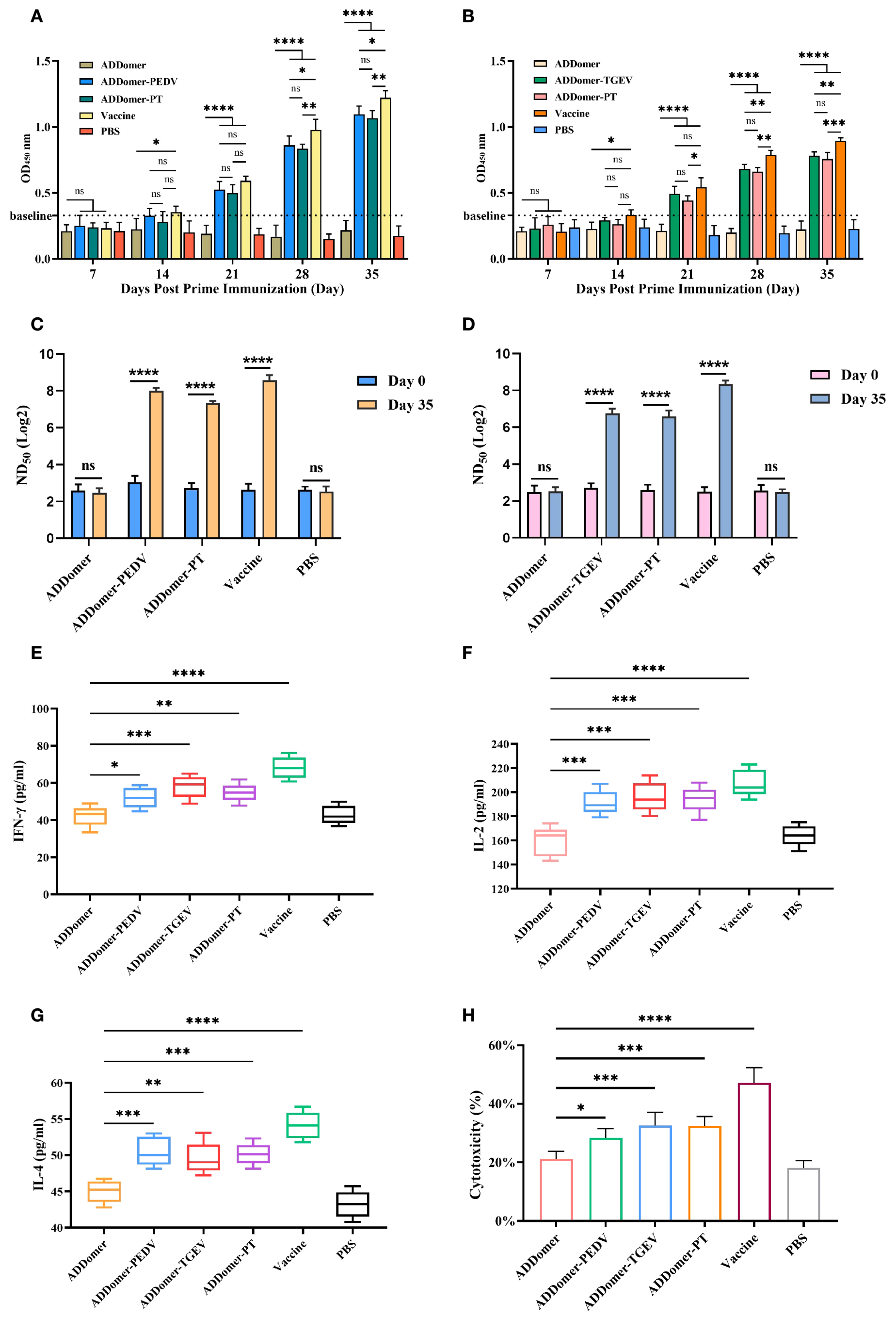

FIGURE 1
Evaluation of immunization effect in piglets. **(A, B)** Detection of PEDV-specific and TGEV-specific antibodies in the peripheral blood of piglets with commercial kits. **(C, D)** Detection of anti-PEDV and anti-TGEV neutralizing antibodies ND$_{50}$ in peripheral blood of piglets. **(E–H)** Detection of IFN-γ, IL-2, IL-4, and CTL in peripheral blood of piglets at d 35 with commercial kits. **P*<0.05, ***P*<0.01, ****P*<0.01, *****P*<0.0001, ns >0.05.

peripheral blood of each group of piglets were measured following the instructions provided by the respective ELISA kits.

2.12 CTL activity detection

To evaluate the CTL activity in peripheral blood, peripheral blood lymphocytes were isolated at day 35. The isolation process was performed using the porcine peripheral blood lymphocyte isolation kit (TBD, China). Subsequently, the CTL activity in piglet serum was determined using the Lactate dehydrogenase (LDH) assay. The LDH cytotoxicity assay kit (Beyotime, China) was employed for this purpose, following the provided instructions.

2.13 Statistical analysis

Statistical analysis between groups was performed using GraphPad Prism 9 software. One-way ANOVA and two-way

ANOVA were utilized for this purpose. Statistical significance was considered at the following levels: * for $P<0.05$, ** for $P<0.01$, *** for $P<0.001$, and **** for $P<0.0001$.

3 Results

3.1 Design and structure prediction of recombinant proteins

To generate recombinant proteins AD-P, AD-T, and AD-PT, the ADDomer framework was utilized, allowing the insertion of different tandem forms of exogenous antigens (Figure 2A). Using UCSF Chimera X, the spatial structure of ADDomer-VLP was simulated, revealing that the VL region, RGD1 region, and RGD2 region of the ADDomer framework are located on the surface of the ADDomer subunit monomer, enabling the carrying of exogenous antigens (Figure 2B). The assembled VLP formed a spherical particle consisting of 60 aggregates, facilitating the presentation and delivery of antigens (Figure 2C). Through sequence synthesis according to the designed sequences, and subsequent ligation to the transfer vector pFBDM, four recombinant pFBDM plasmids were obtained (Figures 2D–H).

3.2 Identification and titer determination of baculovirus

The recombinant baculovirus plasmid was successfully constructed and transfected into sf9 cells during their logarithmic growth phase. After 72 hours of transfection, the cells were observed under an inverted microscope. Diseased cells exhibited typical cytopathic effects (CPE), characterized by larger size, swollen nucleus, and significant shedding and cell death. In contrast, normal cells displayed a clear outline, regular morphology, and no shedding or floating phenomenon (Figure 3A). The cell culture fluid supernatant was collected to obtain the P1 generation of recombinant baculoviruses, including Ac-AD, Ac-AD-P, Ac-AD-T, and Ac-AD-PT.

The P3 generation of recombinant baculoviruses was assessed for virus titer using absolute quantitative RT-qPCR. The results demonstrated that the constructed baculovirus standard curve exhibited good linearity (Figure 3B). By substituting the corresponding Cq values into the standard curve, the copy numbers of P3 generation recombinant baculoviruses were determined. The calculated copy numbers were as follows: Ac-AD (7.31×106 copies/μL), Ac-AD-P (6.46×106 copies/μL), Ac-AD-T (7.64×106 copies/μL), and Ac-AD-PT (2.38×106 copies/μL). The viral titers were subsequently calculated using the formula, resulting in the following values: Ac-AD (1.38×108 pfu/mL), Ac-AD-P (1.25×108 pfu/mL), Ac-AD-T (1.44×10^{8} pfu/mL), and Ac-AD-PT (4.49×10^{7} pfu/mL).

3.3 Expression and identification of recombinant proteins

The expression of recombinant proteins (AD, AD-P, AD-T, and AD-PT) was confirmed through Western Blot analysis (Figure 4A). The results revealed the presence of specific bands at approximately 60 kDa, 64 kDa, 70 kDa, and 69 kDa, respectively, corresponding to the recombinant proteins. However, it is worth noting that there were additional heterobands observed near the target bands, which could be attributed to the depolymerization of multimeric proteins by SDS and the nonspecific binding of other heteroproteins to the primary antibody in the samples.

Additionally, the expression of recombinant proteins from the P3 generation of recombinant baculoviruses was assessed using IFA (Figure 4B). The sf9 cells infected with the recombinant baculovirus exhibited specific green fluorescence, indicating the successful construction of the recombinant baculovirus and the expression of the recombinant proteins in sf9 cells with good reactogenicity.

The expression of recombinant proteins was enhanced through optimization of time and MOI (Figures 4C–F). Among the different variants, namely AD protein, AD-P protein, AD-T protein, and AD-PT protein, the highest protein expression was observed when the MOI was set to 1 and the infection duration was 96 hours. Consequently, an MOI of 1 was chosen as the optimal infection dose, and an infection duration of 96 hours was deemed optimal for viral amplification and collection of the recombinant protein solution.

3.4 Purification of recombinant protein and TEM observation

The recombinant protein was added to the ultracentrifuge tube and floated above the sucrose (Figure 5A). Following the centrifugation of the recombinant proteins using a sucrose density gradient, distinct “protein loops” were observed in the centrifuge tube (Figure 5B). These protein loops were most prominent within the sucrose concentration range of 30%-50%. Subsequently, the protein ring samples were subjected to SDS-PAGE analysis. The purified products of each recombinant protein exhibited specific bands at their expected positions, with fewer peripheral bands indicating reduced heterogeneity (Figures 5C–F). This observation suggested that the majority of the purified recombinant proteins were concentrated within the 30%-50% sucrose concentration range. The final concentrations of the purified recombinant proteins, AD, AD-P, AD-T, and AD-PT, were determined as 202 μg/mL, 110 μg/mL, 83 μg/mL, and 87 μg/mL, respectively. These concentrations were calculated using the BCA assay and grayscale value analysis.

The purified VLPs, as observed by TEM, exhibited diameters ranging approximately from 20 to 40 nm. However, the overall field of view exhibited high impurities, including many sucrose crystals remaining (Figures 5G–J). These findings confirm the successful purification of the respective recombinant proteins, which demonstrated their ability to self-assemble *in vitro* and form VLPs utilizing ADDomer as the structural framework. These VLPs can now be employed as immunogens for the upcoming piglet immunization study.

3.5 Clinical manifestations

The piglets underwent immunization according to the designated plan (Figure 6A). Following a 35-day immunization period, all piglets survived. Additionally, they displayed a positive demeanor and showed

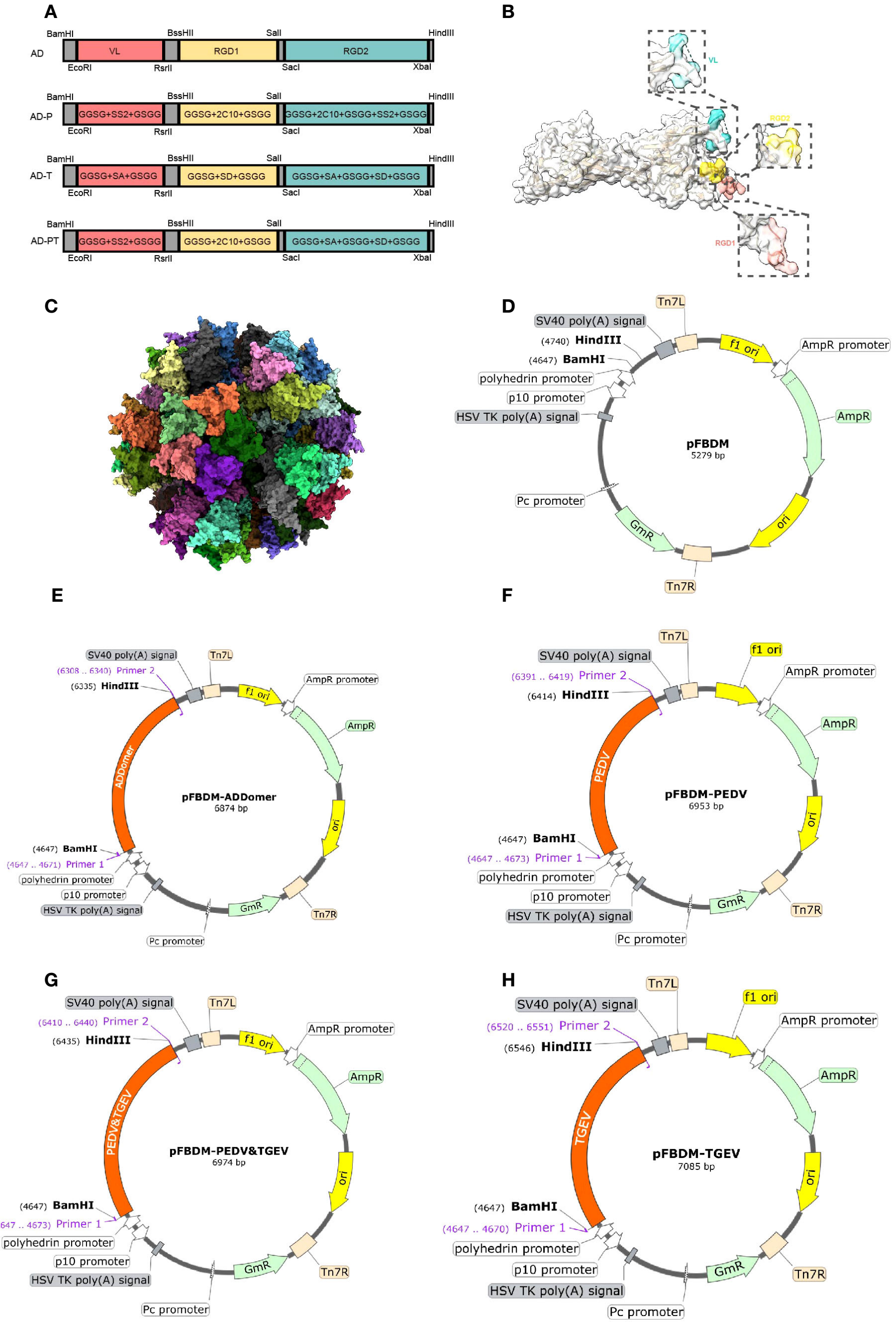

FIGURE 2
Recombinant protein sequence design. **(A)** The designed sites of recombinant protein on ADDomer, the red region is the VL region in the ADDomer sequence, the yellow region is the RGD1 region, and the green region is the RGD2 region. **(B)** Simulation of the spatial structure of ADDomer protein in the monomeric state, with the VL region in blue, the RGD1 region in red, and the RGD2 region in yellow; **(C)** The synthetic self-assembling ADDomer particle formed by 60 identical protomers. The protomers assemble into 12 pentons, forming a dodecahedron characterized by remarkable thermostability. **(D–H)** Schematic diagram of the recombinant transfer vector, with the designed sequence inserted into the pFBDM vector.

no signs of inflammation or swelling at the immunization site. However, piglets in the AD-P group experienced a temporary loss of appetite on the 7th day post-immunization. This symptom swiftly improved upon administering a combination of multivitamin powder and Astragalus polysaccharide powder in their drinking water. In contrast, the piglets in the remaining experimental groups did not manifest any discernible clinical symptoms.

3.6 Body temperature change

Rectal temperatures of the piglets were monitored in all experimental groups (Figure 6B). Except for the AD-T and AD-PT immunized groups, no notable instances of fever (body temperature ≥40°C) were detected at any time point. The AD-T group experienced a slight elevation in body temperature on the 3rd

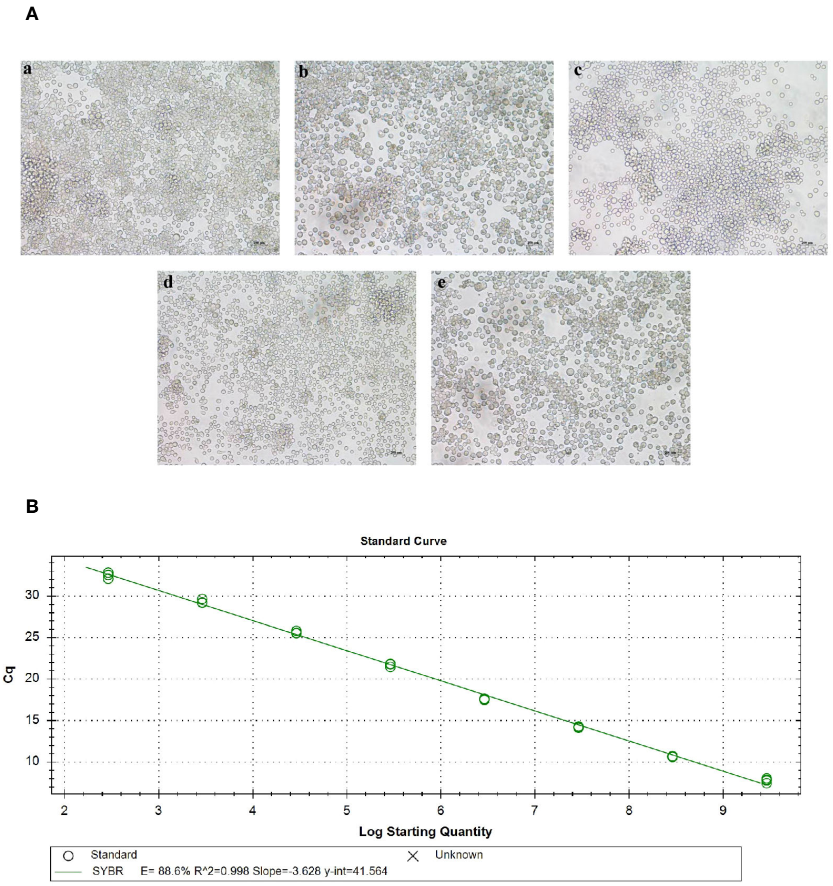

FIGURE 3
Acquisition of baculovirus. **(A)** Picture of lesions in sf9 cells after baculovirus plasmid transfection. a, b, c, and d represent sf9 cells transfected with rMultibac-ADDomer, rMultibac-ADDomer-PEDV, rMultibac-ADDomer-TGEV, and rMultibac-ADDomer-PT, respectively. e represents normal sf9 cells. **(B)** Mycobacteriophage plasmid copy number standard curve.

day after immunization, while the AD-PT group exhibited a similar increase on the 2nd day post-immunization.

3.7 Weight change

Each piglet's weight was measured before vaccination as well as on days 14 and 35 afterward. The piglets' average daily weight gain was computed and statistically examined (Figure 6C). The findings showed that there were no differences in the mean daily weight gain between any of the immunized groups and the PBS-treated non-immunized control group ($P>0.05$). It is crucial to recognize that variations in piglet body weight can be influenced by a variety of elements, including the feeding environment and feed palatability. Therefore, the observed differences in body weight across the various groups may have been caused by these causes.

3.8 Specific antibody testing in peripheral blood

We measured the levels of PEDV and TGEV antibodies in piglets' peripheral blood at days 7, 14, 21, 28, and 35 using an indirect ELISA kit. The statistical results were expressed as OD values measured at 450 nm. Samples were considered positive for PEDV and TGEV when the OD values exceeded baseline values of 0.33 and 0.34, respectively (Figures 1A, B).

Comparison of PEDV-specific antibody levels at day 35 revealed the following: The AD-P vaccine immunization group and the AD-PT vaccine immunization group did not show a significant difference ($P>0.05$). However, there was a significant difference between the commercialized attenuated vaccine immunization group and the AD-P vaccine immunization group ($P<0.05$) and compared to the AD-PT vaccine immunization group ($P<0.01$). There was also a significant difference between the AD vaccine-immunized group and the other vaccine-immunized groups ($P<0.0001$). These results indicate that both AD-P and AD-PT based on baculovirus expression system have good immunogenicity and can induce the body to generate humoral immune response against PEDV.

Comparison of TGEV-specific antibody levels at day 35 revealed the following: There was a significant difference ($P<0.01$) between the group immunized with the commercial weakened vaccine and the group immunized with the AD-T vaccine and a significant difference ($P<0.001$) compared to the group immunized

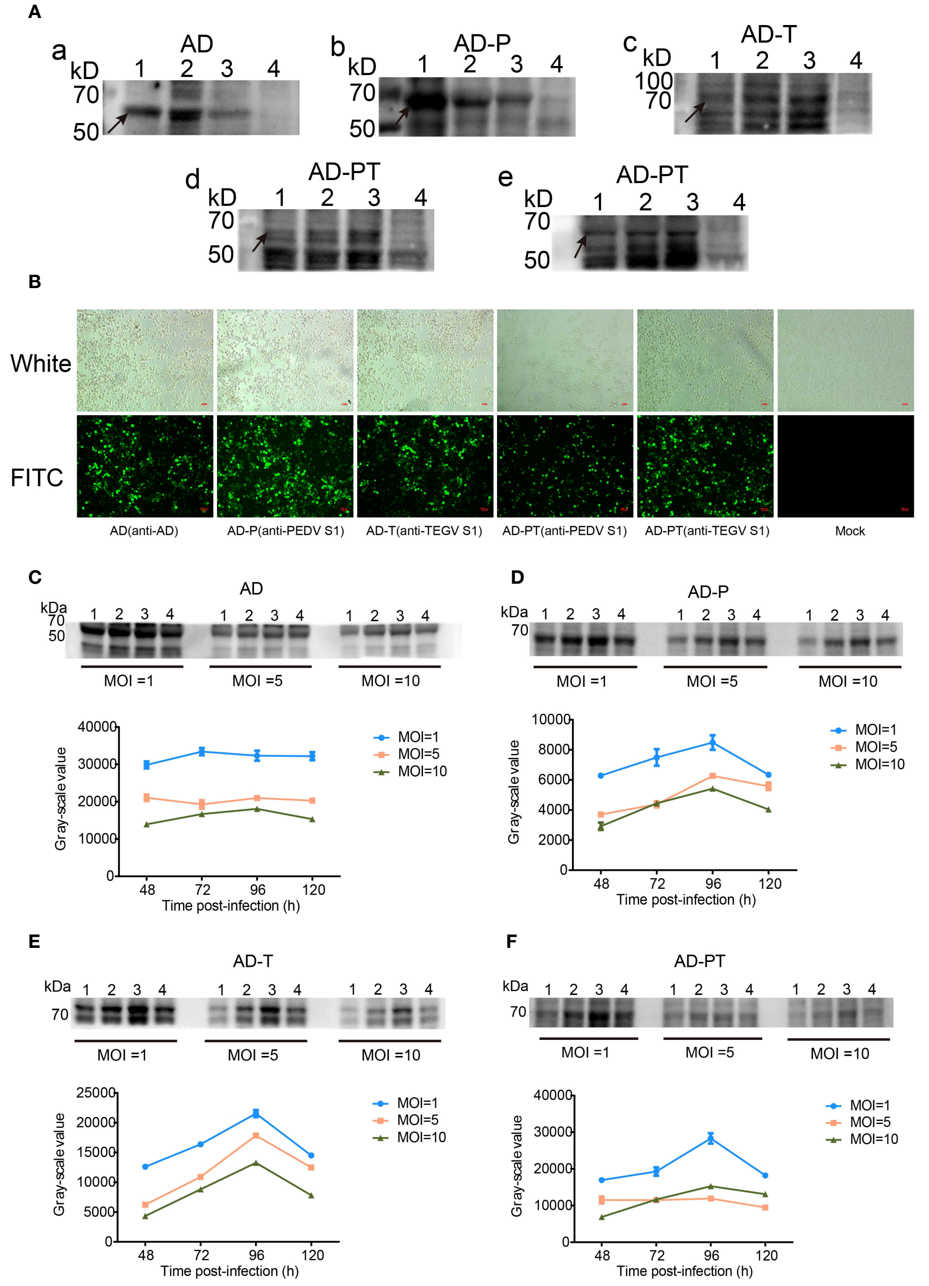

FIGURE 4
Expression and characterization of target proteins. **(A)** a-e are Western Blot analyses of recombinant proteins. d Primary antibody is mouse-derived anti-PEDV S1 protein monoclonal antibody, e Primary antibody is rabbit-derived anti-TGEV S1 protein polyclonal antibody. 1-3 Lane: P1-P3 generation of recombinant proteins, 4 Lane: negative control. **(B)** Indirect immunofluorescence identification plots of recombinant proteins under white light and fluorescence. **(C-F)** Upper panel shows Western Blot analysis of the changes in expression of recombinant proteins AD, AD-P, AD-T, and AD-PT. 1-4 Lane: Western Blot identification plots of recombinant proteins at 48 h, 72 h, 96 h, and 120 h after recombinant baculovirus infection. The corresponding gray value-time folding plots are shown below.

with the AD-PT vaccine. There was no significant difference between the AD-T and AD-PT vaccine immunization groups (*P*>0.05). There was a significant difference between the AD vaccine-immunized group and the other vaccine-immunized groups (*P*<0.0001). These results indicate that both AD-P and AD-PT based on baculovirus expression system have good immunogenicity and can induce the body to generate humoral immune response against TEGV.

3.9 Peripheral blood-neutralizing antibody test

To verify the protective effect induced by recombinant ADDomer-VLP in piglets, serum micro-neutralization experiments were performed *in vitro*. We determined the changes in ND50 of serum against PEDV and TGEV in piglets at day 0 and day 35 after immunization, respectively (Figures 1C, D).

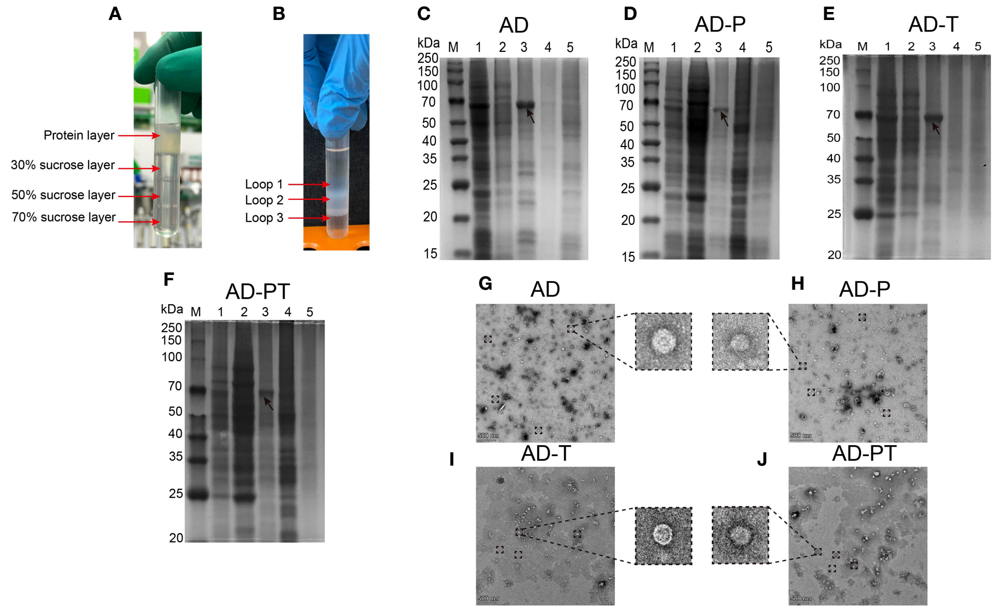

FIGURE 5
Purification of recombinant proteins and TEM table evidence **(A)** Protein samples before purification by sucrose gradient. **(B)** Distribution of each recombinant protein sample in the ultrafiltration tube after sucrose gradient centrifugation. **(C–F)** The results of the recombinant protein staining with Thomas Brilliant Blue, Lane M: Protein Marker; Lane 1: Protein sample before sucrose gradient purification; Lane 2: Mezzanine 1 protein sample; Lane 3: Mezzanine 2 protein sample; Lane 4: Mezzanine 3 protein sample; Lane 5: Negative control; **(G-J)** Recombinant ADDomer-VLP under transmission electron microscope 14000x field of view, the zoom field of view of individual VLPs is shown in the large dashed box.

There was no significant difference in the changes of anti-PEDV neutralizing antibodies between piglets in the AD vaccine-immunized and PBS groups before and after immunization (*P*>0.05). However, the ND50 of the sera of piglets in the AD-P, AD-PT and commercial weak vaccine immunized groups on the 35th d were elevated and significantly different (*P*<0.0001) from those before immunization. Their neutralizing antibody titers reached 258, 157 and 445, respectively. The above results indicate that AD-P and AD-PT vaccines induced different degrees of protection against PEDV in the organism.

There was no significant difference in the changes of anti-TGEV neutralizing antibodies between the AD vaccine-immunized and PBS groups of piglets before and after immunization (*P*>0.05). However, the ND50 of serum of piglets in the AD-T, AD-PT and commercial weak vaccine immunized groups on the 35th d were all elevated and significantly different from those before immunization (*P*<0.0001). Their neutralizing antibody titers reached 119, 97and 315, respectively. The above results indicate that AD-T and AD-PT vaccines induced different degrees of protection against TGEV in the organism.

3.10 Peripheral blood IFN-γ, IL-2, and IL-4 assays

We employed an indirect ELISA kit to measure IFN-γ and IL-2 concentrations in peripheral blood samples from piglets on day 35 to assess the Th1-type immune response level (Figures 1E, F).

There were significant differences in serum IFN-γ concentrations in piglets from AD-P and AD-PT vaccine-immunized groups compared with AD vaccine-immunized groups (*P*<0.05). Among them, IFN-γ concentration was higher in the AD-T vaccine-immunized group than in the AD-P and AD-PT vaccine-immunized groups. However, all of them had lower IFN-γ concentrations than the immunized group with commercial weak vaccine. The above results indicate that all the recombinant ADDomer-VLP vaccines prepared in this study were able to induce an increase in the concentration of IFN-γ in the organism, generate a Th1-type immune response, and trigger cellular immunity. There were significant differences in piglet serum IL-2 concentrations from the AD-P, AD-T, and AD-PT vaccine-immunized groups compared with the AD vaccine-immunized group (*P*<0.001). The above results indicated that all recombinant ADDomer-VLP vaccines prepared in this study were able to induce an increase in the concentration of IL-2 in the organism, generate a Th1-type immune response, and trigger cellular immunity.

To assess the level of Th2 immune response in the peripheral blood of piglets after immunization, the concentration of IL-4 in the peripheral blood at day 35 was measured using an indirect ELISA assay kit (Figure 1G). There were significant differences in IL-4 concentration in serum of piglets in the AD-P, AD-T and AD-PT vaccine-immunized groups compared with the PBS group (*P*<0.01). Among them, IL-4 concentrations were higher in the AD-P and AD-PT vaccine-immunized groups than in the AD-T vaccine-immunized group. The above results indicate that all recombinant ADDomer-VLP vaccines prepared in this study are capable of inducing an increase in the concentration of IL-4 in the organism, generating a Th2-type immune response and triggering a high level of humoral immunity.

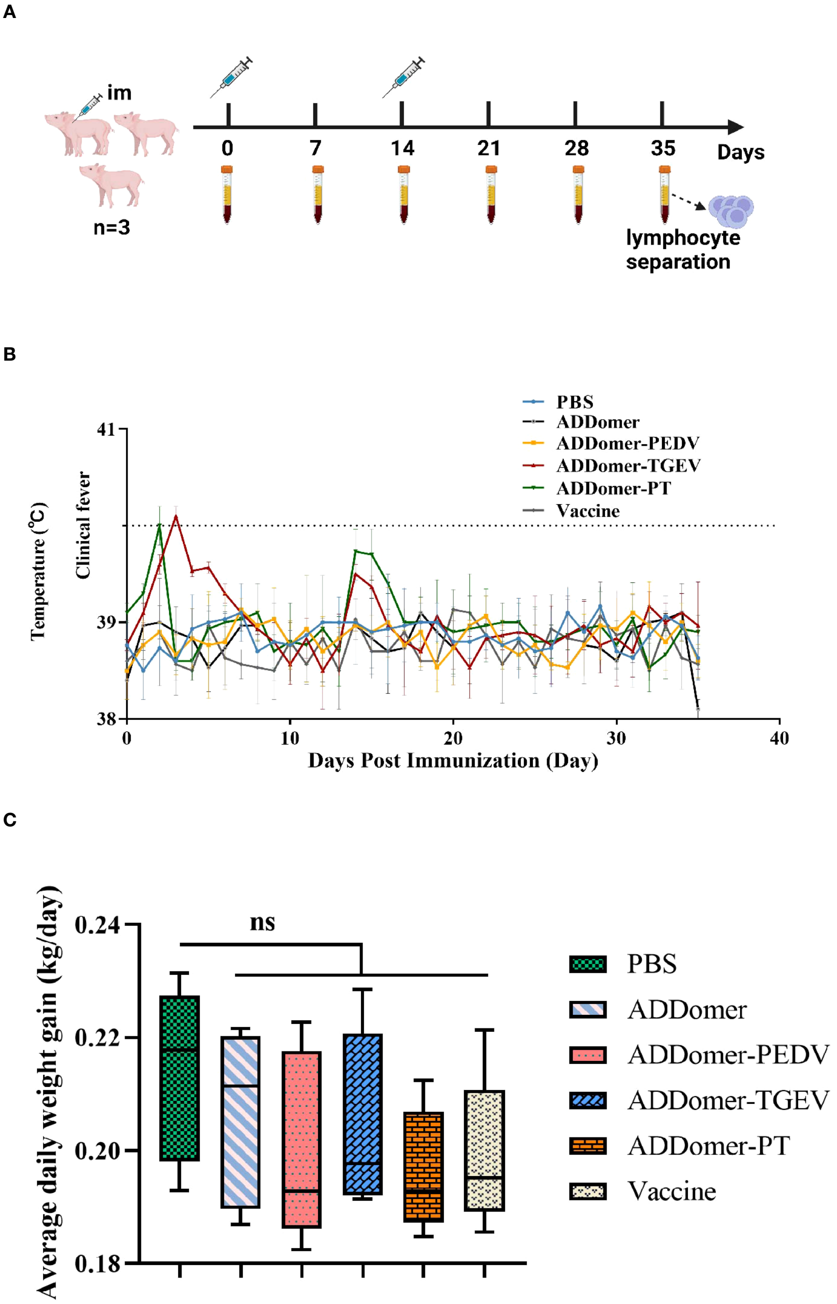

FIGURE 6
Immunization schedule and body temperature and weight changes in piglets **(A)** Immunization trial design for piglets with intramuscular injections and prior blood collection at weeks 0 and 2, respectively. The negative control group was piglets injected with PBS. **(B)** Body temperature changes of piglets during the immunization trial. **(C)** Statistical results of average daily weight gain of piglets. Note: ns represents no statistically significant difference between the current experimental group and the PBS group ($P>0.05$).

3.11 Peripheral blood CTL activity test

LDH can be used as an indicator of cytotoxicity because it is steadily released from the cytoplasm when cellular structures are damaged. Therefore, we measured CTL activity in the peripheral blood of piglets on the 35th day by the LDH method to evaluate the level of cellular immunity in the body (Figure 1H). There were significant differences in CTL activity in the other immunized groups compared to the AD vaccine-immunized group ($P<0.05$). Among them, the peripheral blood CTL activities of piglets in the AD-P, AD-T and AD-PT vaccine-immunized groups were about 30%, 35% and 33%, respectively. Moreover, the peripheral blood CTL activity of piglets in the commercial vaccine group reached 47%. The above results indicate that all recombinant VLPs based on baculovirus expression system induced higher CTL activity in piglets.

4 Discussion

Since 2019, COVID-19 has exerted significant global pressure on public health, leading to increasing demand for coronavirus prevention and control measures (42). Within the pig breeding industry in China, SeCoVs such as PEDV and TGEV have inflicted substantial losses and persist as ongoing challenges. The emergence of PDCoV, another SeCoV, with potential transmission to humans, has raised concerns and alerted us to the potential dangers of SeCoVs (43). These two viruses commonly manifest as mixed infections clinically and exhibit synergistic effects with other enterovirus infections (44). Vaccination is the primary method for the prevention and control of PEDV and TGEV. However, due to the rapid mutation and frequent recombination of both strains, traditional vaccines derived from specific strains are insufficient in providing effective protection. Traditional attenuated vaccines carry the potential risk of viral spread, whereas inactivated vaccines are less effective and necessitate multiple immunizations with large doses (45). Hence, there is a pressing need to explore novel genetically engineered vaccines that offer improved safety and efficacy for the prevention and control of PEDV and TGEV.

A study reported that expression of a conserved epitope of influenza virus in Salmonella flagellin produced effective protection in mice (46). Most of the studies were conducted through immunoinformatics analyses, which involved studying dominant epitopes, designing epitope vaccines, establishing structural models, and conducting immune simulation analysis. These investigations served as preliminary studies on epitope vaccines, but their findings still require validation through experimental methods (47–51). We selected four neutralizing antigenic epitope regions in the S proteins of PEDV and TGEV, respectively, based on the results obtained experimentally by our predecessors. SS2 and 2C10 induce PEDV-specific neutralizing antibodies in mice (32, 33). The A and D sites induce the body to produce neutralizing antibodies against TGEV (52, 53). In our study, we selected the highly conserved SS2 and 2C10 as the target antigen epitope region for the PEDV S protein. Similarly, for the TGEV S protein, we chose site A and site D as the target antigen epitope region. These selections were made to prepare the PEDV/TGEV VLP vaccine.

ADDomer has been used in the development of vaccines for human and animal diseases (23, 24, 40, 54, 55). BEVS, known for its low cost and ability to facilitate post-translational protein modifications, is the preferred method for preparing VLP vaccines in actual production. The combination of ADDomer and BEVS in producing VLP vaccines not only exhibited superior epitopes but also demonstrated excellent immunogenicity (40).

We utilized BEVS to obtain recombinant proteins AD, AD-P, AD-T, and AD-PT. After sucrose gradient centrifugation purification, we used TEM to observe the assembly morphology of the recombinant VLPs. The results revealed that the VLPs exhibited similar morphologies to natural viral particles, indicating the successful preparation of recombinant VLPs carrying PEDV and TGEV antigenic epitopes. Following immunization in piglets, specific antibodies, neutralizing antibodies, IFN-γ, IL-2, and IL-4 levels were elevated in the piglets' bodies. Moreover, the immunization induced higher CTL activity, triggering both PEDV/TGEV-specific humoral and cell-mediated immune responses.

To preliminarily investigate the immunogenicity of the recombinant ADDomer-VLP, this study prepared the purified recombinant ADDomer-VLP and ISA 201VG adjuvant in a 1:1 emulsion to formulate the vaccine. The immune response of the ADDomer-VLP vaccine was evaluated by immunizing 4-week-old piglets. Following immunization, no significant adverse reactions were observed in any of the vaccinated groups, and the vaccine did not adversely affect the growth status of the piglets, demonstrating that the prepared ADDomer-VLP vaccine exhibits excellent safety.

IgG is the primary antibody produced by the body and serves as a key antibody in serological diagnosis and post-immunization detection. During the immune response, IgG plays a role in complement activation and neutralization of various toxins. IgG antibodies not only have a long duration of action but are also the only antibodies that can cross the placenta to protect the fetus. IgG can be transferred to newborns through colostrum, which is crucial for their protection against infections. The AD-P vaccine induces a slightly lower level of anti-PEDV antibodies in the body compared to commercial attenuated vaccines but slightly higher than the AD-PT vaccine. The AD-T vaccine stimulates the production of TGEV-specific antibodies at a level slightly lower than commercial attenuated vaccines but slightly higher than the AD-PT vaccine. The AD-PT vaccine can simultaneously stimulate the production of specific antibodies against both PEDV and TGEV. It is speculated that the results may be attributed to the higher density and specificity of the PEDV/TGEV neutralizing antigenic epitopes displayed on the surface of AD-P and AD-T compared to AD-PT. All vaccines induce piglets to produce high levels of specific antibodies against PEDV and TGEV, triggering a robust humoral immune response.

One of the most crucial indicators for evaluating vaccine effectiveness is the titer of neutralizing antibodies in the body. Neutralizing antibodies can block viral infections by binding to the virus and causing spatial hindrance effects. Thus, the titer of neutralizing antibodies in the blood is essential as it directly reflects the immune protective effect. In this study, piglet peripheral blood serum samples were collected on day 0 and day 35, and the changes in neutralizing antibody levels against 100 $TCID_{50}$ of PEDV and TGEV were examined before and after immunization. The results showed that the serum from the AD-P vaccine group had an ND_{50} of 258 against PEDV, which was superior to the AD-PT vaccine group ($ND_{50} = 157$). Additionally, the serum from the AD-T vaccine group had an ND_{50} of 119 against TGEV, outperforming the AD-PT vaccine group ($ND_{50} = 97$). Except for the AD vaccine group, the serum from all the recombinant ADDomer-VLP vaccine groups exhibited extremely significant differences ($P<0.0001$) in ND50 on day 35 compared to day 0. While both AD-T and AD-PT vaccines demonstrated good immune effects, their neutralizing antibody titers were slightly lower. This could be attributed to the relatively complex conformation of the TGEV S protein antigen sites after translation, resulting in suboptimal exposure levels and spatial configurations of sites A and D. Consequently, this may have affected their ability to stimulate the host's immune response. The serum from the AD-P vaccine group displayed a stronger neutralizing antibody titer, although it did not reach the level of commercial bivalent attenuated vaccines. In conclusion, the SS2 and 2C10 epitopes can still serve as potential candidate antigenic sites for novel PEDV vaccines.

After vaccination, the levels of IFN-γ and IL-4 in the body reflect Th1 and Th2 cell responses, respectively. Typically, Th1 immune responses are pro-inflammatory and can trigger cell-mediated immune reactions, while Th2 immune responses are anti-inflammatory and lead to humoral immune responses. IL-2 is mainly synthesized by CD4+ T cells upon antigen stimulation, promoting T cell proliferation and inducing CTL responses by acting on CD8+ T cells. Therefore, IFN-γ/IL-2 and IL-4 are representative indicators used to assess the degree of cell-mediated and humoral immune responses triggered by vaccines. In this study, cytokine analysis was performed on the peripheral blood serum of piglets on day 35. The results showed that AD-T and AD-PT vaccines had a more significant effect on elevating IFN-γ levels in piglets compared to the AD-P vaccine. Conversely, the AD-P vaccine showed a more pronounced increase in IL-4 levels compared to the AD-T and AD-PT vaccines. This suggests that the SS2 and 2C10 epitopes of PEDV tend to induce humoral immune responses, while the A and D epitopes of TGEV lean towards inducing cell-mediated immune responses. Moreover, the AD-PT vaccine, which carries all four epitopes mentioned above, can simultaneously stimulate the production of both humoral and cell-mediated immune responses in the host.

CTL is the primary effector cells in cell-mediated immune responses. It exerts their immune functions by secreting various cytokines and plays a crucial role in clearing viral infections within the body. The results of the CTL activity assay conducted on day 35 in the peripheral blood of piglets revealed significant differences ($P<0.05$) in CTL activity between all the groups immunized with ADDomer-VLP vaccines carrying exogenous antigenic epitopes and the AD vaccine group. This indicates that each recombinant ADDomer-VLP vaccine can induce a cellular immune response in the body. Among them, the AD-T vaccine induced higher CTL activity compared to the AD-P and AD-PT vaccines, which carry the SS2 and 2C10 antigenic epitopes, respectively.

After sucrose gradient centrifugation for the purification of recombinant VLPs, the SDS-PAGE results showed a significant reduction in impurities in the lanes corresponding to 30% to 50% sucrose concentration, indicating the relatively high purity of ADDomer-VLPs at this concentration. However, when observing the structural morphology of ADDomer-VLPs under TEM electron microscopy, there were still many impurities within the field of view, including a large amount of residual sucrose crystallization. This suggests that the purification process of VLPs needs further optimization and improvement. In the actual production process, the preparation of VLPs, especially downstream processing, faces significant challenges such as low yield, lack of platform-based processes, and rapid analytical techniques (56). Ultracentrifugation is commonly used for purification at the laboratory scale, but it can lead to issues such as variability in results between different batches. Therefore, the optimization of VLP purification processes remains a focal point in the research and development of VLP vaccines.

For chimeric VLP vaccines, the antigenic epitope display density and insertion method are crucial factors that influence their immunogenicity. The differences in immunization efficacy observed between AD-P, AD-T, and AD-PT groups are attributed to variations in the insertion positions and linkage methods of the antigenic epitopes within the recombinant ADDomer-VLPs. Therefore, future research can explore different insertion positions and concatenation strategies for VLP groups to screen for more effective vaccine design strategies. PEDV and TGEV are intestinal coronaviruses, and mucosal immunity serves as the first line of defense, representing a more direct and efficient form of immune response. Therefore, the detection priority for antibodies should be given to IgA over IgG. The neutralizing titer of peripheral blood serum antibodies in piglets partially reflects the humoral immune level in the body. However, the primary evaluation parameter after vaccination is the vaccine's protective efficacy against challenge infections. Therefore, future studies should focus on investigating the recombinant ADDomer-VLP vaccine's protective ability against PEDV/TGEV of different genotypes to assess its broad-spectrum protection. The recombinant ADDomer-VLP vaccine prepared in this study can induce specific humoral and cellular immune responses against PEDV/TGEV. Since newborn piglets primarily rely on maternal antibodies for protection against infection, it is essential to consider applying the research findings to firstborn sows and sows in reserve to evaluate the vaccine's immunogenicity and protective efficacy in newborn piglets.

In addition, compared to commercialized vaccines, the immune efficacy of the recombinant ADDomer-VLP vaccine we constructed is not as good. Traditional live attenuated vaccines and inactivated vaccines have complete viral particles, which confer good immunogenicity and can activate the body to produce a robust immune response. Our recombinant vaccine expresses dominant antigenic epitopes of the virus, but its immunogenicity is relatively low. Recombinant vaccines require adjuvants or fusion with immune enhancers to improve their immunogenicity. Therefore, we chose the ISA 201VG adjuvant to enhance immunogenicity, but the immune response is still not as effective as that of traditional live attenuated and inactivated vaccines. As we further explore and research dominant antigenic epitopes and adjuvants, epitope-based vaccines hold the potential to replace traditional live attenuated and inactivated vaccines.

In summary, our team has successfully developed an ADDomer-VLP delivery system that carries antigenic epitopes of PEDV/TGEV, resulting in an effective vaccine capable of stimulating both Th1-type and Th2-type immune responses in piglets against PEDV and TGEV infections. This research highlights the potential of ADDomer-VLP as a highly efficient delivery system for PEDV and TGEV epitopes, emphasizing the promising role of the recombinant ADDomer-VLP vaccine in combating PEDV and TGEV infections.

Data availability statement

The original contributions presented in the study are included in the article/supplementary material, further inquiries can be directed to the corresponding author.

Ethics statement

The animal study was approved by The Experimental Animal Ethics Committee of South China Agricultural University (No. 2021F503). The study was conducted in accordance with the local legislation and institutional requirements.

Author contributions

SF, MZ, and JC conceived and designed the research. PD, QY, and WZ carried out the experiment. PD wrote the main manuscript text. KX, ZY, XDL, XYL, LZ, KW, and XWL prepared Figures 2–6. All authors contributed to the article and approved the submitted version.

Funding

This work was supported by the Science and Technology Program of Guangzhou, China (No. 202206010161), the Major Project of Basic and Applied Basic Research of Guangdong Province (2020B0301030007) and the Quality and Efficiency Improvement Project of South China Agricul-tural University (No. C18).

Acknowledgments

We thank the authors and laboratories who submitted sequences to the GenBank Database. We thank Gen Li of the College of Veterinary Medicine, South China Agricultural University.

Conflict of interest

The authors declare that the research was conducted in the absence of any commercial or financial relationships that could be construed as a potential conflict of interest.

Publisher's note

All claims expressed in this article are solely those of the authors and do not necessarily represent those of their affiliated organizations, or those of the publisher, the editors and the reviewers. Any product that may be evaluated in this article, or claim that may be made by its manufacturer, is not guaranteed or endorsed by the publisher.

References

1. Song L, Chen J, Hao P, Jiang Y, Xu W, Li L, et al. Differential transcriptomics analysis of IPEC-J2 cells single or coinfected with porcine epidemic diarrhea virus and transmissible gastroenteritis virus. *Front Immunol* (2022) 13:844657. doi: 10.3389/fimmu.2022.844657

2. Jung K, Annamalai T, Lu Z, Saif LJ. Comparative pathogenesis of US porcine epidemic diarrhea virus (PEDV) strain PC21A in conventional 9-day-old nursing piglets vs. 26-day-old weaned pigs. *Vet Microbiol* (2015) 178:31–40. doi: 10.1016/j.vetmic.2015.04.022

3. Alonso C, Goede DP, Morrison RB, Davies PR, Rovira A, Marthaler DG, et al. Evidence of infectivity of airborne porcine epidemic diarrhea virus and detection of airborne viral RNA at long distances from infected herds. *Vet Res* (2014) 45:73. doi: 10.1186/s13567-014-0073-z

4. Ojkic D, Hazlett M, Fairles J, Marom A, Slavic D, Maxie G, et al. The first case of porcine epidemic diarrhea in Canada. *Can Vet J* (2015) 56:149–52.

5. Takahashi K, Okada K, Ohshima K. An outbreak of swine diarrhea of a new-type associated with coronavirus-like particles in Japan. *Nihon Juigaku Zasshi* (1983) 45:829–32. doi: 10.1292/jvms1939.45.829

6. Vlasova AN, Marthaler D, Wang Q, Culhane MR, Rossow KD, Rovira A, et al. Distinct characteristics and complex evolution of PEDV strains, North America, May 2013-February 2014. *Emerg Infect Dis* (2014) 20:1620–8. doi: 10.3201/eid2010.140491

7. Wood EN. An apparently new syndrome of porcine epidemic diarrhoea. *Vet Rec* (1977) 100:243–4. doi: 10.1136/vr.100.12.243

8. Chen F, Pan Y, Zhang X, Tian X, Wang D, Zhou Q, et al. Complete genome sequence of a variant porcine epidemic diarrhea virus strain isolated in China. *J Virol* (2012) 86:12448. doi: 10.1128/JVI.02228-12

9. Wang D, Fang L, Xiao S. Porcine epidemic diarrhea in China. *Virus Res* (2016) 226:7–13. doi: 10.1016/j.virusres.2016.05.026

10. Debouck P, Pensaert M. Experimental infection of pigs with a new porcine enteric coronavirus, CV 777. *Am J Vet Res* (1980) 41:219–23.

11. Sun R-Q, Cai R-J, Chen Y-Q, Liang P-S, Chen D-K, Song C-X. Outbreak of porcine epidemic diarrhea in suckling piglets, China. *Emerg Infect Dis* (2012) 18:161–3. doi: 10.3201/eid1801.111259

12. Stevenson GW, Hoang H, Schwartz KJ, Burrough ER, Sun D, Madson D, et al. Emergence of Porcine epidemic diarrhea virus in the United States: clinical signs, lesions, and viral genomic sequences. *J Vet Diagn Invest* (2013) 25:649–54. doi: 10.1177/1040638713501675

13. Lee KM, Moro M, Baker JA. Transmissible gastroenteritis in pigs. *J Am Vet Med Assoc* (1954) 124:294.

14. Paton D, Ibata G, Sands J, McGoldrick A. Detection of transmissible gastroenteritis virus by RT-PCR and differentiation from porcine respiratory coronavirus. *J Virol Methods* (1997) 66:303–9. doi: 10.1016/s0166-0934(97)00055-4

15. Cubero MJ, León L, Contreras A, Astorga R, Lanza I, Garcia A. Transmissible gastroenteritis in pigs in south east Spain: prevalence and factors associated with infection. *Vet Rec* (1993) 132:238–41. doi: 10.1136/vr.132.10.238

16. Hess RG, Bollwahn W, Pospischil A, Heinritzi K, Bachmann PA. Current aspects in the etiology of viral diarrheas of swine: occurrence of infections with the epizootic viral diarrhea (EVD) virus. *Berl Munch Tierarztl Wochenschr* (1980) 93:445–9.

17. Casanova L, Rutala WA, Weber DJ, Sobsey MD. Survival of surrogate coronaviruses in water. *Water Res* (2009) 43:1893–8. doi: 10.1016/j.watres.2009.02.002

18. Kemeny LJ, Woods RD. Quantitative transmissible gastroenteritis virus shedding patterns in lactating sows. *Am J Vet Res* (1977) 38:307–10.

19. Lin C-M, Gao X, Oka T, Vlasova AN, Esseili MA, Wang Q, et al. Antigenic relationships among porcine epidemic diarrhea virus and transmissible gastroenteritis virus strains. *J Virol* (2015) 89:3332–42. doi: 10.1128/JVI.03196-14

20. Wesley RD, Lager KM. Increased litter survival rates, reduced clinical illness and better lactogenic immunity against TGEV in gilts that were primed as neonates with porcine respiratory coronavirus (PRCV). *Vet Microbiol* (2003) 95:175–86. doi: 10.1016/s0378-1135(03)00150-0

21. DeZure AD, Berkowitz NM, Graham BS, Ledgerwood JE. Whole-inactivated and virus-like particle vaccine strategies for chikungunya virus. *J Infect Dis* (2016) 214:S497–9. doi: 10.1093/infdis/jiw352

22. Charlton Hume HK, Vidigal J, Carrondo MJT, Middelberg APJ, Roldão A, Lua LHL. Synthetic biology for bioengineering virus-like particle vaccines. *Biotechnol Bioeng* (2019) 116:919–35. doi: 10.1002/bit.26890

23. Vragniau C, Bufton JC, Garzoni F, Stermann E, Rabi F, Terrat C, et al. Synthetic self-assembling ADDomer platform for highly efficient vaccination by genetically encoded multiepitope display. *Sci Adv* (2019) 5:eaaw2853. doi: 10.1126/sciadv.aaw2853

24. Chevillard C, Amen A, Besson S, Hannani D, Bally I, Dettling V, et al. Elicitation of potent SARS-CoV-2 neutralizing antibody responses through immunization with a versatile adenovirus-inspired multimerization platform. *Mol Ther* (2022) 30:1913–25. doi: 10.1016/j.ymthe.2022.02.011

25. Chang S-H, Bae J-L, Kang T-J, Kim J, Chung G-H, Lim C-W. Identification of the epitope region capable of inducing neutralizing antibodies against the porcine epidemic diarrhea virus. *Molecules Cells* (2002) 14:295–9.

26. Sun D, Feng L, Shi H, Chen J, Cui X, Chen H, et al. Identification of two novel B cell epitopes on porcine epidemic diarrhea virus spike protein. *Vet Microbiol* (2008) 131:73–81. doi: 10.1016/j.vetmic.2008.02.022

27. Yu J, Chai X, Cheng Y, Xing G, Liao A, Du L, et al. Molecular characteristics of the spike gene of porcine epidemic diarrhoea virus strains in Eastern China in 2016. *Virus Res* (2018) 247:47–54. doi: 10.1016/j.virusres.2018.01.013

28. Zhang F, Luo S, Gu J, Li Z, Li K, Yuan W, et al. Prevalence and phylogenetic analysis of porcine diarrhea associated viruses in southern China from 2012 to 2018. *BMC Veterinary Res* (2019) 15:470. doi: 10.1186/s12917-019-2212-2

29. Tian Y, Yang X, Li H, Ma B, Guan R, Yang J, et al. Molecular characterization of porcine epidemic diarrhea virus associated with outbreaks in southwest China during 2014-2018. *Transbound Emerg Dis* (2021) 68:3482–97. doi: 10.1111/tbed.13953

30. Li C, Li W, Lucio de Esesarte E, Guo H, van den Elzen P, Aarts E, et al. Cell attachment domains of the porcine epidemic diarrhea virus spike protein are key targets of neutralizing antibodies. *J Virol* (2017) 91:e00273–17. doi: 10.1128/JVI.00273-17

31. Cruz DJM, Kim C-J, Shin H-J. Phage-displayed peptides having antigenic similarities with porcine epidemic diarrhea virus (PEDV) neutralizing epitopes. *Virology* (2006) 354:28–34. doi: 10.1016/j.virol.2006.04.027

32. Cruz DJM, Kim C-J, Shin H-J. The GPRLQPY motif located at the carboxy-terminal of the spike protein induces antibodies that neutralize Porcine epidemic diarrhea virus. *Virus Res* (2008) 132:192–6. doi: 10.1016/j.virusres.2007.10.015

33. *Evaluation on the efficacy and immunogenicity of recombinant DNA plasmids expressing spike genes from porcine transmissible gastroenteritis virus and porcine epidemic diarrhea virus.*(Accessed July 17, 2023).

34. Correa I, Gebauer F, Bullido MJ, Suñé C, Baay MF, Zwaagstra KA, et al. . doi: 10.1099/0022-1317-71-2-271

35. Laviada MD, Videgain SP, Moreno L, Alonso F, Enjuanes L, Escribano JM. Expression of swine transmissible gastroenteritis virus envelope antigens on the surface of infected cells: epitopes externally exposed. *Virus Res* (1990) 16:247–54. doi: 10.1016/0168-1702(90)90051-c

36. Sánchez CM, Gebauer F, Suñé C, Mendez A, Dopazo J, Enjuanes L. Genetic evolution and tropism of transmissible gastroenteritis coronaviruses. *Virology* (1992) 190:92–105. doi: 10.1016/0042-6822(92)91195-z

37. Simkins RA, Weilnau PA, Bias J, Saif LJ. Antigenic variation among transmissible gastroenteritis virus (TGEV) and porcine respiratory coronavirus strains detected with monoclonal antibodies to the S protein of TGEV. *Am J Vet Res* (1992) 53:1253–8.

38. Kim L, Hayes J, Lewis P, Parwani AV, Chang KO, Saif LJ. Molecular characterization and pathogenesis of transmissible gastroenteritis coronavirus (TGEV) and porcine respiratory coronavirus (PRCV) field isolates co-circulating in a swine herd. *Arch Virol* (2000) 145:1133–47. doi: 10.1007/s007050070114

39. Berger I, Garzoni F, Fender P. Adenoviral coat protein derived delivery vehicles. *European Patent Office US 2020325179A1* (2020).

40. Luo C, Yan Q, Huang J, Liu J, Li Y, Wu K, et al. Using self-assembling ADDomer platform to display B and T epitopes of type O foot-and-mouth disease virus. *Viruses* (2022) 14:1810. doi: 10.3390/v14081810

41. Gai W, Zheng W, Zhao Z, Wong G, Sun P, Yan L, et al. Assembly of pigeon circovirus-like particles using baculovirus expression system. *Microbial Pathogenesis* (2020) 139:103905. doi: 10.1016/j.micpath.2019.103905

42. Lu R, Zhao X, Li J, Niu P, Yang B, Wu H, et al. Genomic characterisation and epidemiology of 2019 novel coronavirus: implications for virus origins and receptor binding. *Lancet* (2020) 395:565–74. doi: 10.1016/S0140-6736(20)30251-8

43. Ji W, Peng Q, Fang X, Li Z, Li Y, Xu C, et al. Structures of a deltacoronavirus spike protein bound to porcine and human receptors. *Nat Commun* (2022) 13:1467. doi: 10.1038/s41467-022-29062-5

44. Zhang Y, Chen Y, Zhou J, Wang X, Ma L, Li J, et al. Porcine epidemic diarrhea virus: an updated overview of virus epidemiology, virulence variation patterns and virus-host interactions. *Viruses* (2022) 14:2434. doi: 10.3390/v14112434

45. Gerdts V, Zakhartchouk A. Vaccines for porcine epidemic diarrhea virus and other swine coronaviruses. *Vet Microbiol* (2017) 206:45–51. doi: 10.1016/j.vetmic.2016.11.029

46. Ben-Yedidia T, Marcus H, Reisner Y, Arnon R. Intranasal administration of peptide vaccine protects human/mouse radiation chimera from influenza infection. *Int Immunol* (1999) 11:1043–51. doi: 10.1093/intimm/11.7.1043

47. Dar HA, Almajhdi FN, Aziz S, Waheed Y. Immunoinformatics-aided analysis of RSV fusion and attachment glycoproteins to design a potent multi-epitope vaccine. *Vaccines (Basel)* (2022) 10:1381. doi: 10.3390/vaccines10091381

48. Aziz S, Almajhdi FN, Waqas M, Ullah I, Salim MA, Khan NA, et al. Contriving multi-epitope vaccine ensemble for monkeypox disease using an immunoinformatics approach. *Front Immunol* (2022) 13:1004804. doi: 10.3389/fimmu.2022.1004804

49. Naqvi STQ, Yasmeen M, Ismail M, Muhammad SA, Nawazish-I-Husain S, Ali A, et al. Designing of potential polyvalent vaccine model for respiratory syncytial virus by system level immunoinformatics approaches. *BioMed Res Int* (2021) 2021:9940010. doi: 10.1155/2021/9940010

50. *Exploring whole proteome to contrive multi-epitope-based vaccine for NeoCoV: An immunoinformtics and in-silico approach.*(Accessed July 24, 2023).

51. De Groot AS, Moise L, Terry F, Gutierrez AH, Hindocha P, Richard G, et al. Better epitope discovery, precision immune engineering, and accelerated vaccine design using immunoinformatics tools. *Front Immunol* (2020) 11:442. doi: 10.3389/fimmu.2020.00442

52. Simkins RA, Weilnau PA, Bias J, Saif LJ. Antigenic variation among transmissible gastroenteritis virus (TGEV) and porcine respiratory coronavirus strains detected with monoclonal antibodies to the S protein of TGEV. *Am J Vet Res* (1992) 53:1253–8.

53. Kim L, Chang KO, Sestak K, Parwani A, Saif LJ. Development of a reverse transcription-nested polymerase chain reaction assay for differential diagnosis of transmissible gastroenteritis virus and porcine respiratory coronavirus from feces and nasal swabs of infected pigs. *J Vet Diagn Invest* (2000) 12:385–8. doi: 10.1177/104063870001200418

54. Sari-Ak D, Bufton J, Gupta K, Garzoni F, Fitzgerald D, Schaffitzel C, et al. VLP-factory^{TM} and ADDomer$^{©}$: self-assembling virus-like particle (VLP) technologies for multiple protein and peptide epitope display. *Curr Protoc* (2021) 1:e55. doi: 10.1002/cpz1.55

55. Naz SS, Munir I. An outline of contributing vaccine technologies for SARS coV2 advancing in clinical and preclinical phase-trials. *Recent Pat Biotechnol* (2022) 16:122–43. doi: 10.2174/1872208316666220118094344

56. Hillebrandt N, Vormittag P, Bluthardt N, Dietrich A, Hubbuch J. Integrated process for capture and purification of virus-like particles: enhancing process performance by cross-flow filtration. *Front Bioeng Biotechnol* (2020) 8:489. doi: 10.3389/fbioe.2020.00489

Frontiers in Immunology

TYPE Original Research
PUBLISHED 14 March 2024
DOI 10.3389/fimmu.2024.1328266

OPEN ACCESS

EDITED BY
Wei Wang,
Wenzhou University, China

REVIEWED BY
Huapeng Feng,
Zhejiang Sci-Tech University, China
Lunguang Yao,
Nanyang Normal University, China

*CORRESPONDENCE
Lingxue Yu
✉ yulingxue@shvri.ac.cn
Guoxin Li
✉ guoxinli@shvri.ac.cn

[†] These authors have contributed equally to this work and share first authorship

RECEIVED 26 October 2023
ACCEPTED 28 February 2024
PUBLISHED 14 March 2024

CITATION
Wang Y, Song J, Deng X, Wang J, Zhang M, Liu Y, Tang P, Liu H, Zhou Y, Tong G, Li G and Yu L (2024) Nanoparticle vaccines based on the receptor binding domain of porcine deltacoronavirus elicit robust protective immune responses in mice.
Front. Immunol. 15:1328266.
doi: 10.3389/fimmu.2024.1328266

COPYRIGHT
© 2024 Wang, Song, Deng, Wang, Zhang, Liu, Tang, Liu, Zhou, Tong, Li and Yu. This is an open-access article distributed under the terms of the Creative Commons Attribution License (CC BY). The use, distribution or reproduction in other forums is permitted, provided the original author(s) and the copyright owner(s) are credited and that the original publication in this journal is cited, in accordance with accepted academic practice. No use, distribution or reproduction is permitted which does not comply with these terms.

Nanoparticle vaccines based on the receptor binding domain of porcine deltacoronavirus elicit robust protective immune responses in mice

Yuanhong Wang[1†], Junhan Song[1†], Xiaoying Deng[1], Junna Wang[1], Miao Zhang[1], Yun Liu[1], Pan Tang[2], Huili Liu[2], Yanjun Zhou[1], Guangzhi Tong[1], Guoxin Li[1,3*] and Lingxue Yu[1,3*]

[1]Shanghai Veterinary Research Institute, Chinese Academy of Agricultural Sciences, Shanghai, China, [2]Institute of Animal Husbandry and Veterinary Science, Shanghai Academy of Agricultural Sciences, Shanghai, China, [3]Jiangsu Co-innovation Center for Prevention and Control of Important Animal Infectious Diseases and Zoonoses, Yangzhou University, Yangzhou, China

Background: Porcine deltacoronavirus (PDCoV), a novel swine enteropathogenic coronavirus, challenges the global swine industry. Currently, there are no approaches preventing swine from PDCoV infection.

Methods: A new PDCoV strain named JS2211 was isolated. Next, the dimer receptor binding domain of PDCoV spike protein (RBD-dimer) was expressed using the prokaryotic expression system, and a novel nanoparticle containing RBD-dimer and ferritin (SC-Fe) was constructed using the SpyTag/SpyCatcher system. Finally, the immunoprotection of RBD-Fe nanoparticles was evaluated in mice.

Results: The novel PDCoV strain was located in the clade of the late Chinese isolate strains and close to the United States strains. The RBD-Fe nanoparticles were successfully established. Immune responses of the homologous prime-boost regime showed that RBD-Fe nanoparticles efficiently elicited specific humoral and cellular immune responses in mice. Notably, high level PDCoV RBD-specific IgG and neutralizing antibody (NA) could be detected, and the histopathological results showed that PDCoV infection was dramatically reduced in mice immunized with RBD-Fe nanoparticles.

Conclusion: This study effectively developed a candidate nanoparticle with receptor binding domain of PDCoV spike protein that offers protection against PDCoV infection in mice.

KEYWORDS

porcine deltacoronavirus, nanoparticle vaccine, ferritin, SpyTag/SpyCatcher, RBD

1 Introduction

Porcine deltacoronavirus (PDCoV) is a novel enteropathogenic coronavirus. It leads to any age of pigs especially newborn piglets developed gastrointestinal symptoms such as diarrhea and vomiting. Newborn piglets are highly susceptible to PDCoV infection, resulting in mortality rates ranging from 30% to 40% (1). Since PDCoV was first reported in 2012, the newly emerged PDCoV have spread worldwide, causing a high number of pig deaths and significant economic impacts (1–7).

PDCoV has a broad host range, including mammals and avains (8, 9). Moreover, a case report in 2021 has identified PDCoV in plasma samples of three Haitian children with acute undifferentiated febrile illness (10). The rapid transmission and potential for interspecies transmission of PDCoV pose significant threats to both human and animal health. Nonetheless, there are presently no commercially available vaccines for the prevention and control of PDCoV. This underscores the pressing need for PDCoV vaccine development (11).

Among various vaccine platforms, subunit vaccines typically offer excellent safety profiles, rapid production, and ease of scalability. PDCoV enters the cell via the RBD region of spike protein binding the aminopeptidase N (APN) (12, 13). Currently, comprehensive understanding of the structures and biological function of the PDCoV spike protein has motivated the RBD as the vaccine immunogen. And the recombinant RBD proteins derived from other coronaviruses such as SARS-CoV, SARS-CoV-2, and MERS-CoV have previously demonstrated their immunogenicity, effectively eliciting protective neutralizing antibodies in animal models (14, 15).

However, the application of RBD-based subunit vaccines as candidate vaccines is hindered by low immunogenicity (16). To enhance immunogenicity multimerization modified strategy has been used for vaccine development. And the modified vaccines have induced significantly immune responses to target pathogens (17, 18). In recent years, there has been notable advancement in protein covalent linkage strategies, simplifying protein modification and multimerization. Since the inception of the bacterially derived self-assembling SpyTag/SpyCatcher system in 2012, this linkage system has undergone refinement to enhance its efficiency and stability (19). This approach allows for rapid protein purification and macromolecular assembly, making it suitable for vaccine development (20). Previous works with HBV and HIV vaccines using SpyTag/SpyCatcher to present antigens on nanoparticle scaffolds has shown improved immunogenicity compared to unattached monomers (21, 22). In addition, ferritin nanoparticles, composed of 24 copies of the same ferritin subunits, self-assemble to form a highly symmetrical octahedral cage-like structure, showing significant thermal and chemical stability, making them suitable carriers for drug delivery and scaffolds for displaying exogenous peptides or protein (23–25). In this study, we constructed RBD-Fe nanoparticles by covalentially coupling PDCoV RBD-dimer and SC-Fe using the SpyTag/SpyCatcher system and evaluated the immunoprotection in mice. These data showed that we have developed a low-cost and effective candidate vaccine against PDCoV.

2 Materials and methods

2.1 Cells, and animals

LLC-PK1 cells (porcine kidney cells) were maintained in our laboratory, and grow in Dulbecco's modified Eagle's medium (DMEM) (Hyclone, USA) supplemented with trypsin (Gibico, Australia) in 5% CO_2 at 37°C. Animal experiments were conducted following the guidelines approved by the Experimental Animal Care and Use Committee of the Shanghai Veterinary Research Institute, Chinese Academy of Agricultural Sciences (No. SV-20230512-02).

2.2 Sample collection

Fecal samples were collected from piglets with diarrhea on a piggery in Jiangsu, China. RT-PCR was performed to identify the PDCoV and excluded the Porcine epidemic diarrhea virus (PEDV), TGEV and porcine rotavirus (PRoV) infection using cDNA templates synthesized from the RNA extracted from fecal samples and specific primer pairs (Table 1).

TABLE 1 Specific primer pairs to identify PDCoV.

Primers	Sequences (5′-3′)	Annealing temperature (°C)	GenBank ID	Amplification size
PDCoV	CTTAAGTATGGTGAACTCCCTCCTAATG	60	MN942260.2	245 bp
PDCoV	GATTGAGATCTTGGGCCACTTCCACGC			
PEDV-F	GTAATTCACAGAATCTTGGAAATAAC	58	OP784565.1	241 bp
PEDV-R	GACCTTTCCTGTTTGGGCTTCTGCTG			
TGEV-F	GACACAGAAAAACAACAGCAACGCTC	58	DQ811785.1	486 bp
TGEV-R	GTAATTTTCTATTAATGCATCAGGTAC			
PRoV-F	GATTATTCATGCGCTTTAAATGCACC	56	KT820772.1	462 bp
PRoV-R	CGTTACATTTGCCAATAAAGTTTCTG			

2.3 Isolation of PDCoV JS2211 strain

To isolate PDCoV, the fecal sample was aseptically treated and inoculated it into a monolayer LLC-PK1 cells with trypsin. When approximately 80-90% of the cells exhibited cytopathic effect (CPE), repeated freezing and thawing was performed, and then cell debris was removed by centrifugation at 1500×g for 5 minutes at room temperature. Viral titer was measured using 50% tissue culture infectious dose ($TCID_{50}$) assays on LLC-PK1 cells in a 96-well plate.

2.4 Immunofluorescence assays and Western blot

LLC-PK1 cells in 6-well plates were infected with the PDCoV at a 0.1 multiplicity of infection (MOI) and fixed with 4% paraformaldehyde after 24 hpi. Subsequently, PDCoV N-protein polyclonal antibody which were produced from PDCoV N-immunized BALB/c mice was used as the primary antibody (1:100), followed by fluorescent isothiocyanate (FITC)-labeled goat anti-mouse immunoglobulin-G (IgG) secondary antibody (1:10000) (Invitrogen, 31569), after counterstained with 4',6-diamidino-2-phenylindole (DAPI) at room temperature for 5min, the fluorescence were detected by microscope (Nikon,Japan). Mock infected LLC-PK1 cells served as a negative control.

In addition, when >80% CPE was evident in the inoculated cell monolayers (around post inoculate day 2), the plates were frozen at −80°C and thawed twice. the cell lysates were prepared for 12% sodium dodecyl sulfate-polyacrylamide gel electrophoresis (SDS-PAGE), and proteins were electroblotted onto a polyvinylidene difluoride membrane (Bio-Rad, USA). The primary antibody PDCoV N-protein polyclonal antibody and the secondary antibody horseradish peroxidase (HRP) conjugated goat anti-mouse IgG (ZSBio, ZB2305) (1:5000) were subjected to the Western blot analysis.

2.5 Phylogenetic analysis

The complete genome of novel isolated PDCoV strain named PDCoV JS2211 was obtained by using next-generation sequencing (tpbio Co., LTd). For comparing and sorting the spike gene, ModelFinder software was used to select best model which is TN+F+93. The Maximum Likelihood (ML) tree obtained after 10,000 calculations, and the final ML tree was optimized using the iTOL website.

2.6 Plasmid construction and protein expression

6x His-tagged *Helicobacter pylori* nonheme iron-containing ferritin (GenBank accession no. NP223316) and PDCoV spike RBD-dimer (GenBank accession no. MW349841.1) were synthesized by Sangon Biotech. Additionally, Spy Tag (ST) (13 amino acids) was fused to the N-terminus of RBD-dimer (ST-RBD), and Spy Catcher (SC) (113 amino acids) was fused to the N-terminus of ferritin (SC-Fe). SC-Fe and ST-RBD were separately cloned into the pET32a vector and sequenced by Sangon Biological Co., LTD. The verified vectors were transformed into BL21 competent cells (Takara) to introduce the protein expression. Single clone was amplified in LB with ampicillin at 37°C to an OD600 of 0.4-0.6. Bacteria solution was added with 0.1mM/L isopropyl β-D-1thiogalactopyranoside (IPTG) to induce protein expression. After 4h post induction, protein-expressing bacteria were harvested by centrifugation and pellets washed twice were suspended in sterile PBS. After lysed by sonication, the supernatants were incubated with Ni-NTA agarose to enrich His-tagged SC-Fe and ST-RBD. Following purification, the concentrated proteins were quantified using the BCA assay (26).

2.7 Protein extracellular self-assembly *in vitro*

ST-RBD and SC-Fe were mixed in a 1:1 molar ratio at 4°C overnight to produce the assembly RBD-Fe nanoparticle. Western blotting was performed to verify the self-assembly of the RBD-Fe using mouse anti-His-Tag antibody. Furthermore, the endotoxin levels in SC-Fe, ST-RBD, and assembled protein RBD-Fe were assessed using tachypleus amebocyte lysate test (less than 10 EU/dose).

2.8 Transmission electron microscopy

5 μL of SC-Fe and RBD-Fe nanoparticles were stained with 2% phosphotungstic acid and imaged using a Tecnai G2 Spirit BIOTWIN electron microscope (ThermoFisher) operated at an accelerating voltage of 80 kV.

2.9 Immunofluorescence identification

5 μL of SC-Fe and RBD-Fe nanoparticles were subjected to centrifugation to collect the precipitate. The precipitate was then washed with PBS, followed by fixation and blocking with 5% BSA-PBS. After centrifugation and removing the supernatant, 100 μL of mouse anti-PDCoV RBD polyclonal antibody prepared by our laboratory (1:400) and 100 μL of rabbit anti-ferritin monoclonal antibody (Abcam, ab75973) (1:1000) were added and incubated overnight at 4°C. After three times washing with PBS, 100 μL of Alexa Fluor 594 goat anti-rabbit IgG (Invitrogen, A-11012)(1:500) and Alexa Fluor 488 goat anti-mouse IgG (Invitrogen, A-10680) (1:500) were added and incubated at 37°C for 1 hour protected from light. After three times washing with PBS, the samples were resuspended in 100 μL of PBS. The particles were transferred to slides, coverslipped and sealed with neutral resin. Finally, the fluorescence was confirmed by Zeiss fluorescence microscope.

2.10 Mouse challenge and protection efficacy evaluation

Six-week-old Kunming mice (n=40) were randomly divided into four groups (n=10; SC-Fe, RBD-Fe, challenge, and control groups). Antigens were mixed with ISA 201VG adjuvant (Seppic, France) in a 50:50 w/w ratio. In the SC-Fe and RBD-Fe group, mice received subcutaneous injection of 100 μg mixtures, respectively. The Challenge and Control groups received an equivalent volume of PBS. A booster immunization was administered two weeks later. Blood samples were collected on 0, 2, 4 and 6 weeks post-immunization through retro-orbital bleeding. Serum was isolated and heat-inactivated at 56°C for 30 minutes and stored at -80°C.

At week 4, mice in the SC-Fe, RBD-Fe, and challenge groups were orally administered 200 μL and intramuscularly injected with 100 μL of PDCoV strain JS2211 ($TCID_{50} = 10^{7.6}$/mL), respectively (27). Control group mice were received an equivalent volume of physiological saline via the same route. Then, mice were observed daily for clinical symptoms. Mice were euthanized at week 6, and tissues (lungs, stomach, small intestine) were collected for PDCoV detection and histopathological observation.

2.11 Serological analysis

PDCoV-RBD specific IgG was evaluated from the serum collected on 0, 2, 4 and 6 weeks post-immunization by ELISA assay. Briefly, Recombinant ST-RBD was coated on high-binding 96-well plates at 100 ng per well and incubated overnight at 4°C. After washing three times with PBST, plates were blocked with 5% skim milk at 37°C for 2 hours. Following another three washes with PBST, immunized animal serum were serially diluted and added into each well in duplicate followed by incubating at 37°C for 1 hour. After three washes with PBST, HRP-conjugated goat anti-mouse IgG (1:5000 diluted in PBST) was added and incubated at 37°C for 1 hour. The reaction was terminated with 2M-H_2SO_4 after incubation with 3,3′,5,5′-tetramethylbenzidine (TMB) for 15 minutes at room temperature. The OD value was measured at 450 nm using a microplate reader.

2.12 Neutralizing antibody detection

Virus neutralizing antibody test was performed using PDCoV JS2211 to determine the neutralizing antibodies (NA) in mouse serum collected at week 4. 100 μL of serum at two-fold serial dilutions were mixed with 100 μL of DMEM containing 200 $TCID_{50}$ PDCoV with trypsin and incubated at 37°C for 1 hour to inoculate LLC-PK1 cells. The highest dilution of serum that showed at least 50% CPE compared to the negative control was determined as the NA titer.

2.13 PDCoV detection

Approximately 1g of lung, stomach, colon, and duodenum tissues collected from mice in each group were homogenized using a 3D cryogenic grinder (servicebio), respectively. RNA was extracted using a DNA/RNA Extraction Kit FT (vazyme). Subsequently, cDNA was synthesized from 2 μg of total RNA using 5× PrimeScript RT Master Mix (Takara, RR036Q). Primers N-F (5′- TGCTACCTCTCCGATTCCCAACC -3′), N-R (5′- GCT GATTGCCTGTGCCTCTGG –3′), β-actin-F (5′- TATGCTCTCC CTCACGCCATCC -3′), and β-actin-R (5′- GTCACGCACG ATTTCCCTCTCAG –3′) were designed and synthesized for qRT-PCR to determine the relative levels of mRNA in different tissues. The reaction conditions were as follows: 95°C initial denaturation for 60 s; 94°C denaturation for 5 s, 60°C annealing for 30 s; 40 cycles of amplification; melting curve analysis at 95°C for 10 s, 65°C for 60 s, and 97°C for 1 s. Viral infection in various organ tissues was analyzed using the $2^{-\Delta\Delta Ct}$ method.

2.14 Histopathological analysis

The duodenum from each group of mice was fixed in 4% paraformaldehyde for 48 hours and subsequently embedded in paraffin. Sections (3-4 μM) were stained with hematoxylin and eosin (H&E). For immunohistochemistry, sections were incubated overnight at 4°C with rabbit anti-PDCoV N polyclonal antibody at a dilution of 1:200. Subsequently, sections were incubated with goat anti-rabbit IgG secondary antibody (HRP) for 2 hours at room temperature, followed by staining with 3,3'-diaminobenzidine (DAB). For IFA staining, sections were incubated overnight at 4°C with rabbit anti-PDCoV N polyclonal antibody at a dilution of 1:200. Subsequently, sections were incubated with Alexa Fluor® 680-conjugated donkey anti-rabbit IgG (Servicebio) for 60 minutes and counterstained with DAPI for nuclear staining. Microscopic observations and photography were performed.

2.15 Flow cytometry analysis

At week 6, spleens from each group were collected in RPMI medium containing 2% FBS (Hyclone) and single-cell suspensions were prepared as previously described (28). For staining of T and B cell surface markers, live cells were stained with fluorescently conjugated monoclonal antibodies in PBS containing 0.5% BSA at 4°C for 30 min protected from light. The following antibodies were used: anti-CD3 (Invitrogen, 12-0031-82), anti-CD4 (Invitrogen, 11-0041-82), anti-CD8 (Invitrogen, 25-0081-82), and anti-CD19 (Invitrogen, 48-0193-82). Data acquisition and analysis were performed using an ACEN flow cytometer.

2.16 Statistical analysis

Values are shown as the mean ± standard error (s.e.m.) and the collected experimental data were analyzed using GraphPad Prism 7.0. Independent sample t-tests were used for comparisons between two groups, and one-way ANOVA followed by *post hoc* tests were used for comparisons among multiple groups. *P* value of less than

0.05 was considered statistically significant. Homology modeling of PDCoV's RBD-dimer and ferritin structures was performed using Alphafold2, and model images generated by Alphafold2 were further optimized using PyMOL (29).

3 Results

3.1 Isolation and biological characteristics of the PDCoV JS2211 strain

The RT-PCR results showed that the sample were positive for PDCoV with the negative-PEDV,TGEV and PRoV (Figure 1A). The feacal sample was passed through 0.22-µm filters and used to inoculate LLC-PK1 cells. After 24 h, LLC-PK1 cells exhibited CPE, including shrinking, rounding, lighting, and disruptive morphological characteristics, and the cells were subjected to Western blot and IFA staining. As shown in Figure 1B, PDCoV JS2211 was used to infect LLC-PK1 cells, and N-specific fluorescence was observed by IFA (Figure 1C). Moreover, multistep replication curves revealed that mean virus titer of JS2211 was reached $10^{7.6}$ $TCID_{50}$ at 36 hpi (Figure 1D).

The results of the ML tree showed that the JS2211 strains located in the clade of the late Chinese isolate strains and close to the United States strains, indicating that JS2211 is a relatively new strain, and probably came from the United States through international trade and became popular in China (Figure 1E). Furthermore, the JS2211 was closed with the Haiti strains which could infect child. The spread of PDCoV is relatively fast, suggests that development a PDCoV vaccines is necessary for both the livestock industry and human health.

3.2 Characterization of the recombinant protein

The SpyTag (ST) (13 aa) was genetically fused at the N terminus of RBD and SpyCatcher (SC) (113 aa) was genetically fused at the N-terminus of ferritin at the downstream of 6xHis-tag (Figure 2A). AlphaFold2 simulations demonstrated that the RBD-dimer arranged into an axisymmetric-like structure with its external structural domains extensively exposed (Figure 2B). Ferritin proteins spontaneously formed octahedral spherical particles (Figure 2C). To construct RBD-Fe nanoparticle vaccine, ST-RBD was incubated with equal mole of SC-Fe (Figure 2D).

To identify the nanoparticles, purified ST-RBD, SC-Fe, and assembled RBD-Fe were subjected to Western blotting using mouse anti-His antibodies and approximately 27 kDa ST-RBD dimer protein, 35 kDa SC-Fe protein, and 62 kDa RBD-Fe protein were observed. The results confirmed that RBD-Fe assembled successfully (Figure 2E). Moreover, SC-Fe and the assembled RBD-Fe nanoparticles were negatively stained, and TEM showed that SC-Fe and RBD-Fe could form spherical nanoparticles (Figure 2F). To further confirm the formation of nanoparticles, the colocalization of Alexa Fluor 488-labeled ST-RBD proteins and Alexa Fluor 594-labeled SC-Fe proteins were determined by confocal microscopy. The results showed that SC-Fe and RBD-Fe nanoparticles overlapped with orange-yellow fluorescence

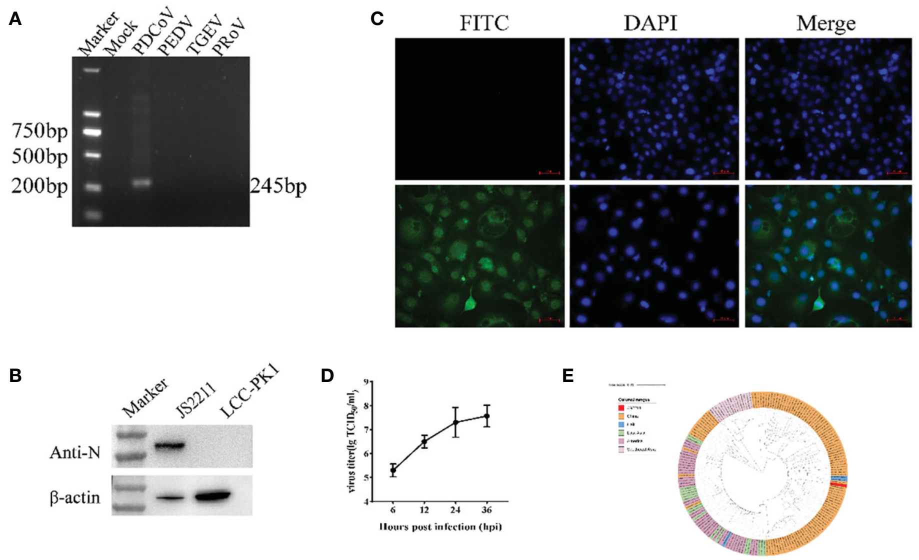

FIGURE 1
Characteristics of isolated PDCoV. **(A)** RT-PCR assay to identify PDCoV infection. **(B)** Immunofluorescence assay of JS2211 in LLC-PK1 cells. **(C)** Western blot analysis of JS2211 proliferation in LLC-PK1 cells. N protein was detected by anti-PDCoV N polyclonal antibody (top) and β-actin served as loading control (bottom); **(D)** Multistep replication curves of JS2211 in LLC-PK1 cells at 6, 12, 24 and 36 hpi. **(E)** The ML tree of PDCoV was deduced using the Spike gene of the different PDCoV. The different coronaviruses are expressed by different RGB colors as indicated. JS2211 is labeled in red.

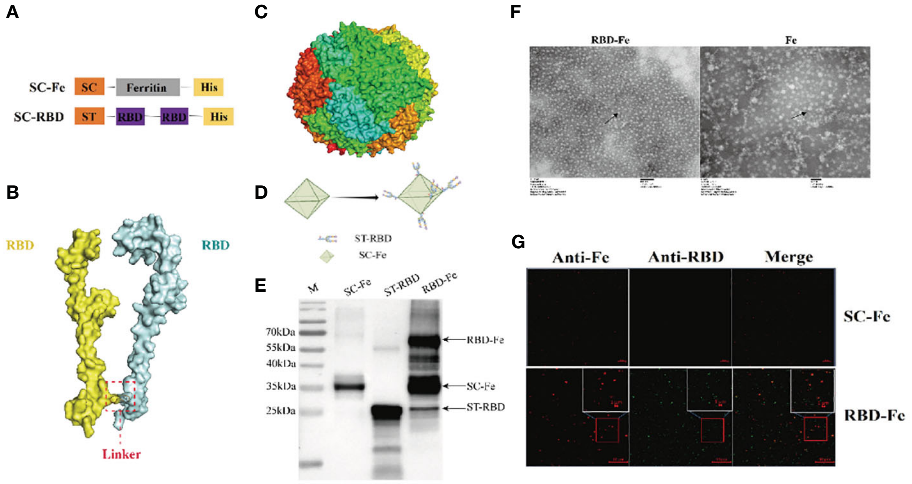

FIGURE 2
Construction and identification of RBD-Fe Nanoparticle Vaccine. **(A)** Schematic of vaccine components which were 6 × His-tagged SC-Ferritin and ST-RBD. SC: SpyCatcher. ST: SpyTag. **(B)** A schematic diagram of the structure simulation of the RBD-dimer using AlphaFold2. **(C)** Schematic diagram of the structure simulation of the Fe protein using AlphaFold2. **(D)** Schematic illustration of RBD-Fe nanoparticles. **(E)** Western blot analysis of the ST-RBD, SC-Fe and RBD-Fe. **(F)** Negative-staining EMs of unlinked nanoparticles SC-Fe and RBD-Fe NPs. **(G)** Confocal microscopy imaging of Fe and RBD-Fe nanoparticles.

(Figure 2G). These results suggest that the nanoparticles were assembled through the SpyTag/SpyCatcher presentation strategy.

3.3 Protective antibodies induced by RBD-Fe nanoparticle in mice

Since the RBD-Fe nanoparticles were constructed, mice were subcutaneously immunized to assess the immunogenicity of the nanoparticles (Figure 3A). First, the RBD-specific IgG antibody titers reach over $1:10^6$ at week 4, significantly higher than the other groups (Figure 3B). Furthermore, serum NA assay was performed and revealed that the neutralizing capability against PDCoV induced by the RBD-Fe nanoparticle vaccine was also dramatically increased at week 4 with a NA titer between $1:2^7$-$1:2^8$, whereas the NA titers in the other groups remained below 1:2 (Figure 3C).

In order to address the adaptive immune responses in the immunized mice, immune cell populations were analyzed from splenocytes of the mice by flow cytometry. The results showed that the RBD-Fe group exhibited an increase in $CD3^+CD4^+CD8^-$ and $CD3^+CD4^-CD8^+$ T cell populations in the spleen compared to the SC-Fe groups on week 6. Also, $CD3^-CD19^+$ B cell populations increased in the RBD-Fe group compared to the other groups, suggesting that the RBD-Fe group generated a specific humoral immune response (Figure 3D).

3.4 RBD-Fe nanoparticle provides significant protection against PDCoV JS2211 challenge in mice

Necropsy was performed at week 6. In the RBD-Fe group, only one mouse (1/10) showed mild intestinal distension, while other organ examinations were normal. The Control group remained normal. In contrast, mice in the SC-Fe and Challenge groups displayed typical symptoms such as intestinal wall thinning, mesenteric and intestinal bleeding, and intestinal distension.

Histopathological observations showed that the Control and RBD-Fe group exhibited a high density of villi, organized villi arrangement, thicker intestinal walls, and deeper crypts. In contrast, the Challenge group and SC-Fe group exhibited villus atrophy, fusion, shallow villus contraction, vacuolar degeneration, necrosis, and sloughing of villous tip epithelial cells, and degenerated intestinal epithelial cells detached into the lumen. Infiltration of a few lymphocytes and neutrophils in the lamina propria was observed, and the small intestine walls became thinner, and crypts shortened or disappeared (Figure 4A). Immunohistochemistry (IHC) and IFA using rabbit anti-PDCoV-N polyclonal antibodies revealed that, compared to the Control group, the RBD-Fe group exhibited minimal PDCoV antigen detection. In contrast, the SC-Fe group and Challenge group showed abundant PDCoV viral N protein, primarily localized to epithelial cells, consistent with previous research findings (30, 31). To further determine the distribution of the virus in different tissues of mice following PDCoV infection, qRT-PCR was used to assess the PDCoV mRNA in the lungs, stomach, duodenum, and rectum of mice. The results revealed that the RBD-Fe group exhibited significantly lower relative PDCoV mRNA in the lungs, stomach, rectum, and duodenum compared to the Challenge and SC-Fe groups (Figure 4B).

4 Discussion

It is reported that frequent recombination between different lineages may result in the emergence of PDCoV strains with divergent pathogenicity and host tropism (1, 32). PDCoV as a

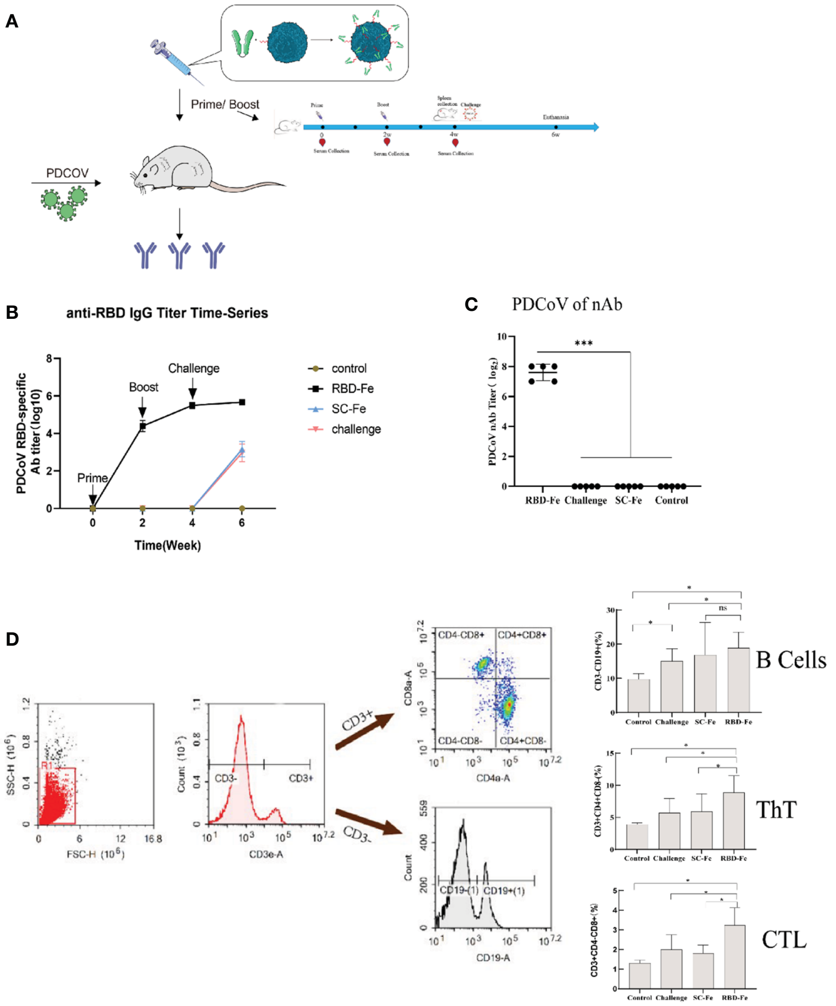

FIGURE 3

Immunogenicity of RBD-Fe nanoparticles. **(A)** Schematic flow diagram of the animal immunization procedure. Mice from each group were prime and boost-vaccinated at week 0 and week 2. Serum was collected every two week. The spleens were collected at week 6. Mice in SC-Fe, challenge and RBD-Fe groups were challenged orally with PDCoV at week 4 while control group treated with physical saline. **(B)** PDCoV-specific RBD-IgG titers of immunized mice at 0, 2, 4 and 6 week were detected by ELISA, and the IgG titers in each week were calculated and plotted as time-course curve. Bars represent the mean (standard deviation) of three replicates per treatment in one experiment. **(C)** The levels of neutralizing antibodies. The levels of neutralizing antibodies in mice serum at week 4 were determined using PDCoV strain JS2011 with a virus neutralization test. Bars represent the mean (standard deviation) of three replicates per treatment in one experiment. Statistical significance was indicated by $*P < 0.05$ (significant) compared with Control group. **(D)** Flow cytometry of splenocytes. At week 6, spleen cells were immunolabeled with antibody-fluorophore coupled antibodies to CD3e-PE, CD4-FITC, CD8a-PE-Cyanine7 and CD19-eFluorTM 450. B cells defined CD3$^-$CD19$^+$, ThT cells (CD3$^+$CD4$^+$CD8$^-$) and CTL cells (CD3$^+$CD4$^-$CD8$^+$). The numbers in the gates refer to the percentage of positive cells for each marker. Statistical significance was assessed using a one-way ANOVA followed by a Dunnett's test (ns, non significance; *, $p < 0.05$; **, $p < 0.01$; ***, $p < 0.001$).

novel coronavirus has been reported to infect humans, suggesting that PDCoV has potential to proceed interspecies transmission or evolute as a new human strain (10). In this study, we isolated a newly PDCoV strain, JS2211. In order to analyze the genetic evolution of the PDCoV, we constructed a ML tree and found that the JS2211 strain was in latest China lineage. Kong et al. demonstrated that multiple PDCoV lineages, including US lineage, early Chinese lineage, Chinese lineage, and Vietnam/Laos/Thailand lineage, coexist in mainland China (33). Compared with the early Chinese lineage, the PDCoV JS2211 was closely related to the USA lineage, suggesting that the newly emerged PDCoV was spreading rapidly in the worldwide. Therefore, it is urgent to develop an effective vaccine to control the spread of PDCoV.

The efficacy of inactivated vaccine and subunit vaccine-based S protein or RBD have been investigated in several studies (34–36). Zhang et al. evaluated the protective efficacy of inactivated PDCoV vaccines in pregnant sows, with results showing an 87.1% protection rate in piglets (34). And the inactive PDCoV vaccine showed good immune effects in mice after injected in a third-boost manner (37). However, aluminum adjuvants commonly used in inactivated vaccines can lead to animal inflammation (31). Subunit vaccines based on synthetic peptides or recombinant proteins have the characteristics of high safety and strong immune targeting, and are currently a very promising vaccine in the world. In this study, we chose an E. coli expression system to express RBD protein, which can induce efficient immune response, as this is a

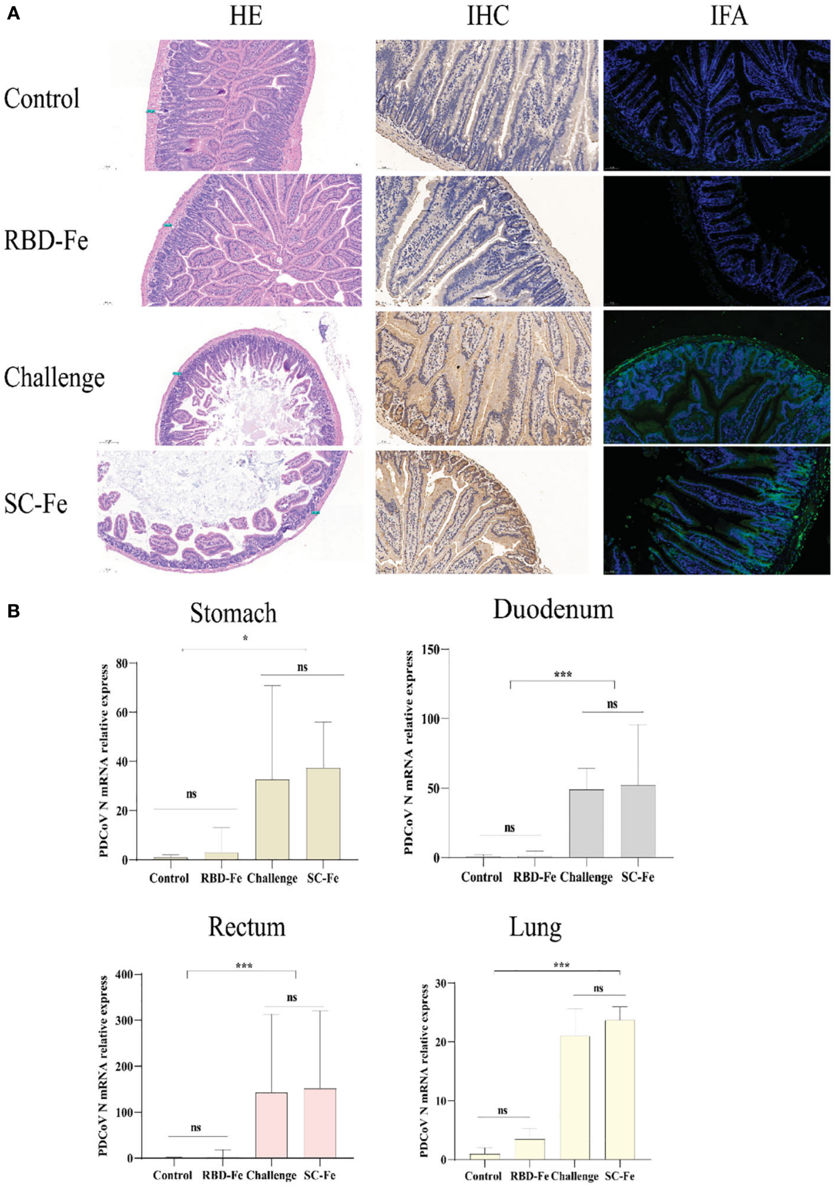

FIGURE 4
Histology and Viral RNA changes post-challenge. **(A)** HE, IHC and IFA staining. HE results showed that SC-Fe and challenge mice exhibited mild villus atrophy in the duodenum post-challenge. No obvious lesions were observed in the control and RBD-Fe mice post-challenge. IHC and IFA analysis showed viral antigens were detected in the SC-Fe and challenge mice, no PDCoV N antigens were detected in the control and RBD-Fe group mice. **(B)** Detection of PDCoV N mRNA with RT-qPCR in stomach, duodenum, rectum and lung. Statistical significance was assessed using a one-way ANOVA followed by a Dunnett's test (ns, non significance; *, $p < 0.05$; **, $p < 0.01$; ***, $p < 0.001$).

commercially feasible system and can manufacture the candidate vaccine. Full-length trimeric S proteins often exhibit high immunogenicity, as they not only contain the receptor-binding domain (RBD) which is the primary target of neutralizing antibodies, but also non-RBD regions (residues 50-286 and 278-616 in the S1 subunit and residues 601-1087 in the S2 subunit) that can induce protective antibodies (30, 31, 38). However, it has been reported that various coronaviruses exhibit antibody-dependent enhancement (ADE) (39–41). Hence, seeking the minimal effective immunogen is a crucial strategy to enhance vaccine safety. But the small molecular size mono-RBD may face serious challenges in vaccine development, primarily due to their relatively low immunogenicity. Wang et al. evaluated the immunogenic efficacy of RBD region expressed by a baculovirus combined with different adjuvants through a prime-boost-second immunization regimen in mice (36). The results indicated that mice only exhibited an effective specific immune response after the third immunization, suggesting that mono-RBD has low immunogenicity, even though combined with adjuvants. Therefore, RBD should be optimized with appropriate adjuvants or multimerization modification. In this study, we employed a multimerization modification approach, creating an RBD-dimer that increases the antigen's molecular weight to reach 27 kDa, which might make contribution to enhance immunoprotection in mice.

It was known that structure-guided antigen design is a key tool for rapid and precise subunit vaccine development (42, 43). Non-hemoglobin ferritin nanoparticles from Helicobacter pylori (H. pylori) have been successfully applied in influenza and COVID-19 nanoparticle vaccines, eliciting broad-spectrum neutralizing antibodies (26, 44). A previous study targeting HBV indicated that covalently coupled ferritin nanoparticles had higher expression levels than fusion expression (45). Furthermore, H. pylori ferritin differs significantly from mammal ferritin, making it less likely to induce autoantibodies. Therefore, we selected H. pylori ferritin as the scaffold of the PDCoV nanoparticle vaccine. We introduced the SpyTag/SpyCatcher system derived from Streptococcus pyogenes to covalently couple the ferritin nanoparticles instead of direct fusion expression, which is easily synthesized in large-scale and pure form, and greatly increased immunogenicity.

A Kunming mouse challenge model has been developed previously to investigate the pathogenicity of PDCoV JS2211 (27), and were used in this study to evaluate the immunoprotective effect of nanoparticle vaccines (RBD-Fe). The RBD-Fe elicited high level IgG and NA antibody titers (NA titer between 1:27-1:28, Figure 3C), which may play an important role in the protection against virulent PDCoV challenge in mice. In addition, T cell responses are also important for virus clearance, decreasing severe illness, and prognostic recovery (35, 46, 47). In this study, the nanoparticle vaccine (RBD-Fe) elicited not only high-level antibodies titers but also high percentage of CD3+CD4+CD8- and CD3+CD4-CD8+ T lymphocytes in Kunming mice (Figure 3D). The strong T cell immune responses activated by RBD-Fe may help to eliminate the infected cells, thereby contributing to the protection for mice against PDCoV. The challenge assay showed that the mice in the RBD-Fe group were detected the lower viral RNA copies in the lung, stomach, and intestinal tissues compared with those in other groups. Moreover, only one mouse in RBD-Fe group displayed mild pathological changes of intestinal tissues, whereas all mice in other control groups displayed serious pathological damage of intestinal tissues. Li et al.'s study showed that S-based subunit vaccine induced high level NAbs (about between $1:2^6$-$1:2^8$) and cellular immune responses post two immunizations in mice, similar to that did by RBD-Fe in this study, and provided significant protection for newborn piglets in the following passive immunity (35). These results suggested the nanoparticle vaccine (RBD-Fe) may provide significant protection for newborn piglets in the passive immunity experiment, which will be performed in the future.

In conclusion, we constructed RBD-Fe nanoparticles, which could induce high level cellular and humoral immune responses, and provide almost full protection against virulent PDCoV challenge in mice. Therefore, RBD-Fe nanoparticle is a promising vaccine candidate against PDCoV.

Data availability statement

The datasets presented in this study can be found in online repositories. The names of the repository/repositories and accession number(s) can be found below: https://www.ncbi.nlm.nih.gov/genbank/, MW349841.1.

Ethics statement

The animal study was approved by the Experimental Animal Care and Use Committee of the Shanghai Veterinary Research Institute, Chinese Academy of Agricultural Sciences(No. SV-20230512-02). The study was conducted in accordance with the local legislation and institutional requirements.

Author contributions

YW: Writing – original draft. JS: Methodology, Writing – original draft. XD: Methodology, Writing – original draft. JW: Methodology, Writing – original draft. MZ: Software, Writing – original draft. LuY: Data curation, Writing – original draft. PT: Formal Analysis, Writing – original draft. HL: Investigation, Writing – original draft. YZ: Resources, Writing – original draft. GT: Funding acquisition, Writing – original draft. GL: Writing – review & editing. LxY: Writing – review & editing.

Funding

The author(s) declare financial support was received for the research, authorship, and/or publication of this article. This study was supported by the foundation from Shanghai Agriculture Applied Technology Development Program, China (NO.X2023-02-08-00-12-F04612), the Key Laboratory of Veterinary Biotechnology (No. BB1500010), Shanghai, P.R. China, and the Agricultural-Science and Technology InnovationProgram (CAAS-ASTIP-2021-SHVRI).

Conflict of interest

The authors declare that the research was conducted in the absence of any commercial or financial relationships that could be construed as a potential conflict of interest.

Publisher's note

All claims expressed in this article are solely those of the authors and do not necessarily represent those of their affiliated organizations, or those of the publisher, the editors and the reviewers. Any product that may be evaluated in this article, or claim that may be made by its manufacturer, is not guaranteed or endorsed by the publisher.

Supplementary material

The Supplementary Material for this article can be found online at: https://www.frontiersin.org/articles/10.3389/fimmu.2024.1328266/full#supplementary-material

References

1. He WT, Ji X, He W, Dellicour S, Wang S, Li G, et al. Genomic epidemiology, evolution, and transmission dynamics of porcine Deltacoronavirus. *Mol Biol Evol.* (2020) 37:2641–54. doi: 10.1093/molbev/msaa117

2. Woo PC, Lau SK, Lam CS, Lau CC, Tsang AK, Lau JH, et al. Discovery of seven novel Mammalian and avian coronaviruses in the genus deltacoronavirus supports bat coronaviruses as the gene source of alphacoronavirus and betacoronavirus and avian coronaviruses as the gene source of gammacoronavirus and deltacoronavirus. *J Virol.* (2012) 86:3995–4008. doi: 10.1128/JVI.06540-11

3. Wang L, Byrum B, Zhang Y. Porcine coronavirus HKU15 detected in 9 US state. *Emerg Infect Dis.* (2014) 20:1594–5. doi: 10.3201/eid2009.140756

4. Jang G, Lee KK, Kim SH, Lee C. Prevalence, complete genome sequencing and phylogenetic analysis of porcine deltacoronavirus in South Korea 2014-2016. *Transbound Emerg Dis.* (2017) 64:1364–70. doi: 10.1111/tbed.2017.64.issue-5

5. Ajayi T, Dara R, Misener M, Pasma T, Moser L, Poljak Z. Herd-level prevalence and incidence of porcine epidemic diarrhoea virus (PEDV) and porcine deltacoronavirus (PDCoV) in swine herds in Ontario, Canada. *Transbound Emerg Dis.* (2018) 65:1197–207. doi: 10.1111/tbed.2018.65.issue-5

6. Suzuki T, Shibahara T, Imai N, Yamamoto T, Ohashi S. Genetic characterization and pathogenicity of Japanese porcine deltacoronavirus. *Infect Genet Evol.* (2018) 61:176–82. doi: 10.1016/j.meegid.2018.03.030

7. Stott CJ, Sawattrakool K, Saeng-Chuto K, Tantituvanont A, Nilubol D. The phylodynamics of emerging porcine deltacoronavirus in Southeast Asia. *Transbound Emerg Dis.* (2022) 69:2816–27. doi: 10.1111/tbed.14434

8. Boley PA, Alhamo MA, Lossie G, Yadav KK, Vasquez-Lee M, Saif LJ, et al. Porcine deltacoronavirus infection and transmission in poultry, United States(1). *Emerg Infect Dis.* (2020) 26:255–65. doi: 10.3201/eid2602.190346

9. Li HY, Zhang HL, Zhao FJ, Wang SQ, Wang ZX, Wei ZY. Modulation of gut microbiota, short-chain fatty acid production, and inflammatory cytokine expression in the cecum of porcine deltacoronavirus-infected chicks. *Front Microbiol.* (2020) 11:897. doi: 10.3389/fmicb.2020.00897

10. Lednicky JA, Tagliamonte MS, White SK, Elbadry MA, Alam MM, Stephenson CJ, et al. Independent infections of porcine deltacoronavirus among Haitian children. *Nature.* (2021) 600:133–7. doi: 10.1038/s41586-021-04111-z

11. Zhai K, Zhang Z, Liu X, Lv J, Zhang L, Li J, et al. Mucosal immune responses induced by oral administration of recombinant Lactococcus lactis expressing the S1 protein of PDCoV. *Virology.* (2023) 578:180–9. doi: 10.1016/j.virol.2022.12.010

12. Yang YL, Liu J, Wang TY, Chen M, Wang G, Yang YB, et al. Aminopeptidase N is an entry co-factor triggering porcine deltacoronavirus entry via an endocytotic pathway. *J Virol.* (2021) 95:e0094421. doi: 10.1128/JVI.00944-21

13. Ji W, Peng Q, Fang X, Li Z, Li Y, Xu C, et al. Structures of a deltacoronavirus spike protein bound to porcine and human receptors. *Nat Commun.* (2022) 13:1467. doi: 10.1038/s41467-022-29062-5

14. Dai L, Zheng T, Xu K, Han Y, Xu L, Huang E, et al. A universal design of betacoronavirus vaccines against COVID-19, MERS, and SARS. *Cell.* (2020) 182:722–33.e11. doi: 10.1016/j.cell.2020.06.035

15. Yang J, Wang W, Chen Z, Lu S, Yang F, Bi Z, et al. Publisher Correction: A vaccine targeting the RBD of the S protein of SARS-CoV-2 induces protective immunity. *Nature.* (2021) 590:E23. doi: 10.1038/s41586-020-03108-4

16. Xu K, Gao P, Liu S, Lu S, Lei W, Zheng T, et al. Protective prototype-Beta and Delta-Omicron chimeric RBD-dimer vaccines against SARS-CoV-2. *Cell.* (2022) 185:2265–78 e14. doi: 10.1016/j.cell.2022.04.029

17. Liang Q, Wang Y, Zhang S, Sun J, Sun W, Li J, et al. RBD trimer mRNA vaccine elicits broad and protective immune responses against SARS-CoV-2 variants. *iScience.* (2022) 25:104043. doi: 10.1016/j.isci.2022.104043

18. Shi R, Zeng J, Xu L, Wang F, Duan X, Wang Y, et al. A combination vaccine against SARS-CoV-2 and H1N1 influenza based on receptor binding domain trimerized by six-helix bundle fusion core. *EBioMedicine.* (2022) 85:104297. doi: 10.1016/j.ebiom.2022.104297

19. Sun XB, Cao JW, Wang JK, Lin HZ, Gao DY, Qian GY, et al. SpyTag/SpyCatcher molecular cyclization confers protein stability and resilience to aggregation. *N Biotechnol.* (2019) 49:28–36. doi: 10.1016/j.nbt.2018.12.003

20. Tan TK, Rijal P, Rahikainen R, Keeble AH, Schimanski L, Hussain S, et al. A COVID-19 vaccine candidate using SpyCatcher multimerization of the SARS-CoV-2 spike protein receptor-binding domain induces potent neutralising antibody responses. *Nat Commun.* (2021) 12:542. doi: 10.1038/s41467-020-20654-7

21. Peyret H, Ponndorf D, Meshcheriakova Y, Richardson J, Lomonossoff GP. Covalent protein display on Hepatitis B core-like particles in plants through the in *vivo* use of the SpyTag/SpyCatcher system. *Sci Rep.* (2020) 10:17095. doi: 10.1038/s41598-020-74105-w

22. Ximba P, Chapman R, Meyers A, Margolin E, van Diepen MT, Sander AF, et al. Development of a synthetic nanoparticle vaccine presenting the HIV-1 envelope glycoprotein. *Nanotechnology.* (2022) 33:48–63. doi: 10.1088/1361-6528/ac842c

23. Wang W, Liu Z, Zhou X, Guo Z, Zhang J, Zhu P, et al. Ferritin nanoparticle-based SpyTag/SpyCatcher-enabled click vaccine for tumor immunotherapy. *Nanomedicine.* (2019) 16:69–78. doi: 10.1016/j.nano.2018.11.009

24. Mu Z, Wiehe K, Saunders KO, Henderson R, Cain DW, Parks R, et al. mRNA-encoded HIV-1 Env trimer ferritin nanoparticles induce monoclonal antibodies that neutralize heterologous HIV-1 isolates in mice. *Cell Rep.* (2022) 38:110514. doi: 10.1016/j.celrep.2022.110514

25. Wu X, Sheng H, Zhao L, Jiang M, Lou H, Miao Y, et al. Co-loaded lapatinib/PAB by ferritin nanoparticles eliminated ECM-detached cluster cells via modulating EGFR in triple-negative breast cancer. *Cell Death Dis.* (2022) 13:557. doi: 10.1038/s41419-022-05007-0

26. Ma X, Zou F, Yu F, Li R, Yuan Y, Zhang Y, et al. Nanoparticle vaccines based on the receptor binding domain (RBD) and heptad repeat (HR) of SARS-CoV-2 elicit robust protective immune responses. *Immunity.* (2020) 53:1315–30.e9. doi: 10.1016/j.immuni.2020.11.015

27. Song J, Wang Y, Deng X, Wang J, Yu L, Wang B, et al. Establishment of Kunming mouse model infected with Porcine Deltacoronavirus. *Chin J Anim Infect Dis.* (2023). doi: 10.19958/j.cnki.cn31-2031/s.20230303.001

28. Jeong H, Choi YM, Seo H, Kim BJ. A novel DNA vaccine against SARS-CoV-2 encoding a chimeric protein of its receptor-binding domain (RBD) fused to the amino-terminal region of hepatitis B virus preS1 with a W4P mutation. *Front Immunol.* (2021) 12:637654. doi: 10.3389/fimmu.2021.637654

29. Cramer P. AlphaFold2 and the future of structural biology. *Nat Struct Mol Biol.* (2021) 28:704–5. doi: 10.1038/s41594-021-00650-1

30. Chen Q, Gauger P, Stafne M, Thomas J, Arruda P, Burrough E, et al. Pathogenicity and pathogenesis of a United States porcine deltacoronavirus cell culture isolate in 5-day-old neonatal piglets. *Virology.* (2015) 482:51–9. doi: 10.1016/j.virol.2015.03.024

31. Deng X, Buckley AC, Pillatzki A, Lager KM, Baker SC, Faaberg KS. Development and utilization of an infectious clone for porcine deltacoronavirus strain USA/IL/2014/026. *Virology.* (2021) 553:35–45. doi: 10.1016/j.virol.2020.11.002

32. Li G, Zhai SL, Zhou X, Chen TB, Niu JW, Xie YS, et al. Phylogeography and evolutionary dynamics analysis of porcine delta-coronavirus with host expansion to humans. *Transbound Emerg Dis.* (2022) 69:e1670–81. doi: 10.1111/tbed.14503

33. Kong F, Wang Q, Kenney S, Jung K, Vlasova A, Saif L. Porcine deltacoronaviruses: origin, evolution, cross-species transmission and zoonotic potential. *Pathogens.* (2022) 11:79. doi: 10.3390/pathogens11010079

34. Zhang J, Chen J, Liu Y, Da S, Shi H, Zhang X, et al. Pathogenicity of porcine deltacoronavirus (PDCoV) strain NH and immunization of pregnant sows with an inactivated PDCoV vaccine protects 5-day-old neonatal piglets from virulent challenge. *Transbound Emerg Dis.* (2020) 67:572–83. doi: 10.1111/tbed.13369

35. Li J, Zhao S, Zhang B, Huang J, Peng Q, Xiao L, et al. A novel recombinant S-based subunit vaccine induces protective immunity against porcine deltacoronavirus challenge in piglets. *J Virol.* (2023) 97(11):e0095823. doi: 10.1128/jvi.00958-23

36. Wang N, Wang Z, Ma M, Jia X, Liu H, Qian M, et al. Expression of codon-optimized PDCoV-RBD protein in baculovirus expression system and immunogenicity evaluation in mice. *Int J Biol Macromol.* (2023) 252:126113. doi: 10.1016/j.ijbiomac.2023.126113

37. Zhao F, Liu L, Wang Z, Wang N, Ma M, Jia X, et al. Development and immunogenicity evaluation of porcine deltacoronavirus inactivated vaccine with different adjuvants in mice. *Vaccine.* (2022) 40:4211–9. doi: 10.1016/j.vaccine.2022.05.085

38. Chen R, Fu J, Hu J, Li C, Zhao Y, Qu H, et al. Identification of the immunodominant neutralizing regions in the spike glycoprotein of porcine deltacoronavirus. *Virus Res.* (2020) 276:197834. doi: 10.1016/j.virusres.2019.197834

39. Hohdatsu T, Yamada M, Tominaga R, Makino K, Kida K, Koyama H. Antibody-dependent enhancement of feline infectious peritonitis virus infection in feline alveolar macrophages and human monocyte cell line U937 by serum of cats experimentally or naturally infected with feline coronavirus. *J Vet Med Sci.* (1998) 60:49–55. doi: 10.1292/jvms.60.49

40. Bournazos S, Gupta A, Ravetch JV. The role of IgG Fc receptors in antibody-dependent enhancement. *Nat Rev Immunol.* (2020) 20:633–43. doi: 10.1038/s41577-020-00410-0

41. Wang Z, Deng T, Zhang Y, Niu W, Nie Q, Yang S, et al. ACE2 can act as the secondary receptor in the FcgammaR-dependent ADE of SARS-CoV-2 infection. *iScience.* (2022) 25:103720. doi: 10.1016/j.isci.2021.103720

42. Graham BS. Rapid COVID-19 vaccine development. *Science.* (2020) 368:945–6. doi: 10.1126/science.abb8923

43. Pallesen J, Wang NS, Corbett KS, Wrapp D, Kirchdoerfer RN, Turner HL, et al. Immunogenicity and structures of a rationally designed prefusion MERS-CoV spike antigen. *Proc Natl Acad Sci U S A.* (2017) 114:E7348–57. doi: 10.1073/pnas.1707304114

44. Nelson SA, Richards KA, Glover MA, Chaves FA, Crank MC, Graham BS, et al. CD4 T cell epitope abundance in ferritin core potentiates responses to hemagglutinin nanoparticle vaccines. *NPJ Vaccines*. (2022) 7:124. doi: 10.1038/s41541-022-00547-0

45. Wang W, Zhou X, Bian Y, Wang S, Chai Q, Guo Z, et al. Dual-targeting nanoparticle vaccine elicits a therapeutic antibody response against chronic hepatitis B. *Nat Nanotechnol*. (2020) 15:406–16. doi: 10.1038/s41565-020-0648-y

46. Alter G, Yu J, Liu J, Chandrashekar A, Borducchi E, Tostanoski L, et al. Immunogenicity of Ad26.COV2.S vaccine against SARS-CoV-2 variants in humans. *Nature*. (2021) 596:268–72. doi: 10.1038/s41586-021-03681-2

47. Liu J, Chandrashekar A, Sellers D, Barrett J, Jacob-Dolan C, Lifton M, et al. Vaccines elicit highly conserved cellular immunity to SARS-CoV-2 Omicron. *Nature*. (2022) 603:493–6. doi: 10.1038/s41586-022-04465-y

frontiers | Frontiers in Immunology

TYPE Original Research
PUBLISHED 16 April 2024
DOI 10.3389/fimmu.2024.1358036

Critical role of G3BP1 in bovine parainfluenza virus type 3 (BPIV3)-inhibition of stress granules formation and viral replication

Nian Liu[1], Wei Yang[1,2], Lingzhi Luo[1], Mingshuang Ma[1], Jin Cui[1,2], Xiumei Dong[1,2]* and Yijing Li[1,2]*

[1]College of Veterinary Medicine, Northeast Agricultural University, Harbin, China, [2]Heilongjiang Key Laboratory for Animal Disease Control and Pharmaceutical Development, Harbin, China

Check for updates

OPEN ACCESS

EDITED BY
Wei Wang,
Wenzhou University, China

REVIEWED BY
David Jesse Sanchez,
Western University of Health Sciences, United States
Priya Ranjan,
Centers for Disease Control and Prevention (CDC), United States

*CORRESPONDENCE
Yijing Li
yijingli@163.com
Xiumei Dong
neaudxm@163.com

RECEIVED 19 December 2023
ACCEPTED 05 April 2024
PUBLISHED 16 April 2024

CITATION
Liu N, Yang W, Luo L, Ma M, Cui J, Dong X and Li Y (2024) Critical role of G3BP1 in bovine parainfluenza virus type 3 (BPIV3)-inhibition of stress granules formation and viral replication.
Front. Immunol. 15:1358036.
doi: 10.3389/fimmu.2024.1358036

COPYRIGHT
© 2024 Liu, Yang, Luo, Ma, Cui, Dong and Li. This is an open-access article distributed under the terms of the Creative Commons Attribution License (CC BY). The use, distribution or reproduction in other forums is permitted, provided the original author(s) and the copyright owner(s) are credited and that the original publication in this journal is cited, in accordance with accepted academic practice. No use, distribution or reproduction is permitted which does not comply with these terms.

Background: It remains unclear whether BPIV3 infection leads to stress granules formation and whether G3BP1 plays a role in this process and in viral replication. This study aims to clarify the association between BPIV3 and stress granules, explore the effect of G3BP1 on BPIV3 replication, and provide significant insights into the mechanisms by which BPIV3 evades the host's antiviral immunity to support its own survival.

Methods: Here, we use Immunofluorescence staining to observe the effect of BPIV3 infection on the assembly of stress granules. Meanwhile, the expression changes of eIF2α and G3BP1 were determined. Overexpression or siRNA silencing of intracellular G3BP1 levels was examined for its regulatory control of BPIV3 replication.

Results: We identify that the BPIV3 infection elicited phosphorylation of the eIF2α protein. However, it did not induce the assembly of stress granules; rather, it inhibited the formation of stress granules and downregulated the expression of G3BP1. G3BP1 overexpression facilitated the formation of stress granules within cells and hindered viral replication, while G3BP1 knockdown enhanced BPIV3 expression.

Conclusion: This study suggest that G3BP1 plays a crucial role in BPIV3 suppressing stress granule formation and viral replication.

KEYWORDS
BPIV3, G3BP1, inhibition, stress granules, viral replication

Abbreviations: BPIV3, Bovine parainfluenza virus type 3; eIF2α, Eukaryotic translation initiation factor; FBS, Fetal bovine serum; MDBK, Madin-Darby bovine kidney; MOI, Multiplicity of infection; DMEM, Dulbecco's Modified Eagle Medium; qRT-PCR, Quantitative real-time PCR; RNAi, RNA interference; SA, Sodium arsenite.

1 Introduction

Bovine parainfluenza is an acute contact infectious disease caused by a bovine parainfluenza virus type 3 (BPIV3) infection. BPIV3 can affect either local or systemic immunity and favor the establishment of secondary bacterial infections, which are common causes of respiratory disease in calves. BPIV3 infection is now a major cause of morbidity and economic losses in cattle worldwide (1–3). The mechanisms underlying the pathogenicity of and immunosuppression by BPIV3 remain unclear, and there is currently no targeted treatment available for BPIV3 infection. A better understanding of the mechanisms underlying BPIV3 pathogenesis and the interactions between BPIV3 and its host will facilitate the development of more effective control strategies.

Various external stress stimuli, such as heat shock, oxidative stress, nutritional deficiencies, and the viral infections can lead to the formation of stress granules (SGs) (4). In response to stress, eukaryotic protein translation is disrupted, eukaryotic translation initiation factor (eIF2α) is phosphorylated, and untranslated mRNAs and untranslated messenger ribonucleoproteins (mRNPs) accumulate in the cytoplasm to form SGs with G3BP1 as the nucleus, thus improving the cell's ability to respond to external stimuli (5). Viral infection is a powerful external pressure, and host cells need to mobilize multiple pathways to resist viral attacks. SGs can recruit various signal transduction pathway proteins, such as PKR, RIG-I, and MDA-5 to participate in multiple antiviral pathways and play a role in clearing infections (6–8). To evade host antiviral immunity, many viruses have evolved methods to hinder SG assembly. For example, human parainfluenza virus type 3 forms inclusion bodies from auxiliary proteins to segregate newly synthesized viral RNA and inhibit SG formation (9). Middle East respiratory coronavirus auxiliary protein 4a exerts its antagonistic effects by hindering SG formation (10). Short-term infection with porcine epidemic diarrhea virus stimulates the assembly of stress granules, followed by viral activation of caspase 8 that cleaves G3BP1 and depolymerizes SGs (11). The virus targets G3BP1 because G3BP1 is essential for SG formation, and depletion of G3BP1 inhibits SG assembly (12). Typically, SGs are antiviral structures produced by host cells. However, many viruses inhibit or modify SGs to facilitate their replication.

The Ras GTPase-activated (SH3 structural domain) RNA- and protein-binding protein G3BP1 contains several structural domains. These structural domains allow G3BP1 to be actively involved in the regulation of RNA metabolism and multiple signaling pathways, such as regulating mRNA stability and translation, binding to specific transcripts under stress conditions, and activating interferon (IFN)-stimulated gene (ISG) expression (13, 14). G3BP1 has known antiviral functions (15). G3BP1 enhances immune responses against viral invasion by inducing IFN expression and ISG translation. In virus-infected cells, G3BP1 binds to dsRNA produced by viral replication intermediates through the RGG structural domain and enhances RIG-I-induced IFN-β mRNA expression (8); G3BP1, G3BP2, and caprin1 interact to promote ISG translation to synthesize antiviral factors (16). Most importantly, G3BP1 promotes SG assembly to restrict viral protein synthesis. Recent studies have shown that G3BP1 is a central node in protein-protein interaction networks within SGs and that G3BP1 makes an important contribution to SG assembly (12). In addition, G3BP1 interacts with various SG components, including caprin 1 to form a complex that promotes the formation of SGs and USP10 to inhibit the formation of SGs. Even G3BP1 mutants lacking the RGG interaction region can bind caprin 1 and USP10 to affect SG formation (17, 18). However, it remains unclear whether BPIV3 infection leads to SG formation and whether G3BP1 plays a role in this process and in viral replication.

In this study, we found that BPIV3 infection activated phosphorylation of eIF2α but did not induce the SG assembly. It could, however, inhibit the formation of sodium arsenite (SA)-induced SGs at a late stage of infection. Overexpression of G3BP1 inhibited BPIV3 replication, while reducing G3BP1 expression promoted BPIV3 replication, suggesting that G3BP1 plays an important role in BPIV3 infection.

2 Materials and methods

2.1 Cells and virus

Madin-Darby bovine kidney (MDBK) and HeLa cells were obtained from the American Type Culture Collection, Manassas, USA. All cells were cultured in Dulbecco's Modified Eagle Medium (DMEM) supplemented with 10% fetal bovine serum (FBS) in a 5% CO_2 37°C incubator. BPIV3 (GenBank: HQ530153.1) is a virulent strain that was isolated and adapted to cell culture in the laboratory.

2.2 Immunofluorescence antibody assay

MDBK or HeLa cells were inoculated into 96-well plates and cultured overnight at 37°C with 5% CO_2. Cells were infected with BPIV3 at a multiplicity of infection (MOI) of 2.0. After 1 h of virus adsorption incubation, the medium was replaced with DMEM maintenance medium containing 2% FBS for a period ranging from 3 to 24 h. At different infection time points, cells were fixed using a pre-cooled methanol-acetone mixture, followed by the application of G3BP1 rabbit monoclonal antibody (CST, #45656) at room temperature for 2 h. Subsequently, goat anti-mouse antibody coupled with Alex Fluor 488 antibody and goat anti-rabbit antibody coupled with Alexa Fluor 594 antibody (Proteintech, Rosemont, IL, USA) was applied at room temperature for 1 h. The cells were then incubated for 1 h in 2% DMEM containing 2% FBS (Rosemont). Finally, cell nuclei were stained with DAPI. Cell samples were visualized using a fully automated smart imaging system (BioTek, Vermont, USA).

2.3 G3BP1 overexpression plasmid construction

The reference sequence of G3BP1 (GenBank accession number NM_005754.3) was used to design the homologous recombination primers listed in Table 1 and synthesized by Shanghai Biotech. The

G3BP1 gene fragment was amplified from HeLa cells using PCR, and the gene was inserted into the VR-3×FLAG plasmid via homologous recombination with a FLAG-tag at the C-terminus of G3BP1.

2.4 Knockdown of G3BP1 by RNA interference

The siRNA reference sequence used for the G3BP1 knockdown (GenBank accession number NM_005754.3), was designed and synthesized by Shanghai Sangon Biotechnology Co. The sequences are listed in Table 1. HeLa cells were seeded in 24-well plates in advance and allowed to grow until they reached 50% confluence (approximately 24 h). Using RAN Transfer (Sangong, Shanghai, China), the RNA transfection mixture was prepared according to the ratio indicated in the instruction manual and added to the culture medium after it was left to stand at room temperature for 10 min. The culture medium was replaced 12 h after transfection, and the cells were collected after 48 h of maintenance.

2.5 Quantitative real-time PCR analysis

Total RNA from MDBK or HeLa cells was isolated using a Total RNA Extraction Kit (Tengen, China) according to the manufacturer's instructions. cDNA was synthesized using a Novozymes HiScript III 1st Strand cDNA Synthesis Kit (Novozymes, Beijing, China). quantitative real-time PCR (qRT-PCR) was performed on a Roche LightCycler 480 II with 2× SYBR Green qPCR Master Mix (Selleck, Beijing, China) according to the manufacturer's instructions. All qRT-PCR experiments were performed in triplicate. Relative gene levels were determined using the $2^{-\Delta\Delta}Ct$ method with GAPDH as an internal control. The primers used for qRT-PCR are listed in Table 1.

2.6 Western blot analysis

Cellular proteins were extracted using RIPA lysis buffer (Proteintech,Rosemont, IL, USA). Proteins were subjected to sodium dodecyl sulfate-polyacrylamide gel electrophoresis and transferred onto nitrocellulose membranes (Millipore, USA). After blocking with 5% skimmed milk in TBST for 1 h, membranes were incubated with primary antibodies, including phospho-EIF2S1 (Ser51) Polyclonal antibody (Proteintech, Rosemont, IL, USA), EIF2S1 polyclonal antibody (Proteintech, Rosemont, IL, USA), alpha tubulin monoclonal antibody (Proteintech, Rosemont, IL, USA)/G3bp1 (E8N8F) rabbit mAb, then HRP-conjugated affinipure goat anti-mouse IgG or HRP-conjugated affinipure goat anti-rabbit IgG (Proteintech, Rosemont) were labeled for color development. The blots were visualized using an ECL kit.

2.7 Assessment of BPIV3 growth in HeLa cells

HeLa cells were inoculated into 24-well plates and cultured overnight at 37°C with 5% CO_2. Untreated cells were used as a control, and G3BP1 overexpressing cells and G3BP1 knockdown cells were infected with BPIV3 at an MOI of 2.0. Cell cultures were harvested at different time points and inoculated with 10-fold dilutions of the viral solution. Cells were cultured at 37°C with 5% CO_2 for 3 days. The number of wells and dilutions showing cytopathic effects were recorded, and the $TCID_{50}$ was calculated according to Reed and Muench's two-component method.

2.8 Quantification of SGs

SG formation was determined under a fluorescence microscope, with 3–5 sets of randomly photographed fields of view captured under a high-magnification microscope at 20× magnification,

TABLE 1 Primer and siRNA sequences.

Name		Sequence (5′-3′)
qPCR primer	G3BP1 Forward primer	GGATGTTATTTGACGCCAACAA
	G3BP1 Reverse primer	TCCCTCTATCGAGTGGAAGACACT
	GAPDH Forward primer	GCATCGGAGGGACTTATGA
	GAPDH Reverse primer	GGGCCATCCACAGTCTTCTG
plasmid construction primer	Forward primer	AGTCACCGTCGTCGAGCCACCATGGTTATGGAGAAGCC
	Reverse primer	CTTTGTAGTCTCTAGGCTGCCTTGGAGCAATGC
siRNA	RNAi#1	AUGAAUCUCCUCAAAGCCUGGTT
	RNAi#2	UACUUUAACAACAUGAGGUGGTT
	RNAi#3	UUUCCCACCACUGUUAAUGCGTT
	RNAi#NC	ACGUGACACGUUCGGAGAATT

ensuring that the total number of cells was greater than 300. Significant G3BP1 aggregation was used as a marker of SGs. The total number of cells was quantified by counting DAPI-stained nuclei. Cells containing multiple SG marker sites were identified as SG-positive. The percentage of cells containing SGs was calculated as follows: (SG-positive cells/total cells)*100%.

2.9 Statistical analysis

Differences between groups of data was assessed using the Student's t-test, or analysis of variance (ANOVA). Statistical analyses were performed in GraphPad prism software, and results were expressed as the mean ± standard deviation (SD) of at least three independent experiments, with P values < 0.05 considered statistically significant (*P < 0.05; **P < 0.01).

3 Results

3.1 BPIV3 infection induces phosphorylation of eIF2α but not the formation of SGs

Phosphorylation of eIF2α is an initiating condition for SG formation, and regulates SG assembly during viral infection. To determine whether BPIV3 infection induces the formation of SGs, the phosphorylation level of eIF2α was first determined in cells at different infection durations. The experimental results showed that BPIV3 infection led to phosphorylation of eIF2α, and this phosphorylation level was downregulated after 24 h of virus infection (Figure 1A). To further investigate the formation of intracellular SGs during BPIV3 infection, MDBK cells were first infected (inoculated with) with BPIV3 (MOI = 2.0), treated with sodium arsenite (SA, 0.5 mM) as a positive control, and the aggregation of G3BP1 in the cells was examined using indirect immunofluorescence. As shown in Figure 1B, infection lasted for 3–24 h. There was significant formation of SGs in SA-treated cells, whereas the infected group did not show aggregation of SGs at any time during infection. Further, there was no significant difference in the rates of SG formation between the infected and uninfected groups throughout the BPIV3 infection (Figure 1C). The results suggest that BPIV3 infection of host cells stimulates eIF2α phosphorylation but does not induce SG aggregation.

3.2 BPIV3 infection inhibits the formation of SGs induced by SA and downregulates G3BP1 protein expression

BPIV3 infection stimulated the phosphorylation of the eIF2α protein but did not induce the formation of SGs, preventing the aggregation and assembly of SG components during viral infection. To determine whether BPIV3 infection inhibited SG assembly, BPIV3-infected or uninfected cells were treated with SA. The rate of SG formation in the uninfected MDBK cell group was consistently > 70% in all cases (Figure 2A), which was different from that observed in the BPIV3-infected cells. As BPIV3 viral replication increased, SA-induced SG formation gradually decreased, with almost no SGs formed in the MDBK cells infected for 24 h (Figure 2B). Further, the number of the infected cells forming SGs gradually decreased with the duration of viral infection (Figure 2C). This suggests that BPIV3 infection hindered the formation of SGs induced by SA.

To determine whether BPIV3 infection affected the SG-nucleating protein G3BP1, intracellular G3BP1 mRNA levels were examined by quantitative reverse transcriptase PCR (qRT-PCR)at differen.t infection times, and protein expression was examined using a G3BP1-specific antibody to label the BPIV3-N protein as an indicator of viral replication. As shown in Figures 2D, E, the G3BP1 mRNA transcript level initially increased and then decreased with the progression of viral infection time (Figure 2D), while the total amount of protein gradually decreased (Figure 2E). This suggested that BPIV3 infection decreased intracellular G3BP1 protein expression and that BPIV3 infection simultaneously inhibited SG assembly and downregulated G3BP1 expression.

3.3 Overexpression of G3BP1 enhances SG assembly and inhibits BPIV3 replication

SG and its related protein, G3BP1, play an important role in viral replication. Pre-laboratory findings showed that MDBK cells had poor transfection efficiency compared to HeLa cells, whereas BPIV3 could replicate and grow normally in HeLa cells. Therefore, we transfected HeLa cells with VR-G3BP1-3×FLAG to increase the total amount of G3BP1 in the cells and observed whether overexpression of G3BP1 affected BPIV3 replication. Overexpression of G3BP1 stimulated the formation of SGs in HeLa cells, as determined by immunofluorescence (Figure 3A). BPIV3-infected G3BP1-overexpressing cells were assessed for viral titers and intracellular viral loads. Viral titers increased more slowly in G3BP1-overexpressing cells than in non-overexpressing G3BP1 cells. At 12, 24, and 36 h after infection, viral titers were more than 10-fold lower in the G3BP1 overexpression group than in the non-overexpression group (Figure 3B). The viral load in HeLa cells infected with BPIV3 for 24 h was significantly lower in the G3BP1-overexpression group than in the non-overexpression group (Figure 3C). Overexpression of G3BP1 also suppressed the expression of the viral N protein (Figure 3D). These data suggest that overexpression of G3BP1 induces the formation of SGs and reduces BPIV3 proliferation efficiency.

3.4 Knockdown of G3BP1 promotes BPIV3 replication

To confirm that G3BP1 plays a role in inhibiting BPIV3 replication, HeLa cells were transfected with three siRNAs. The

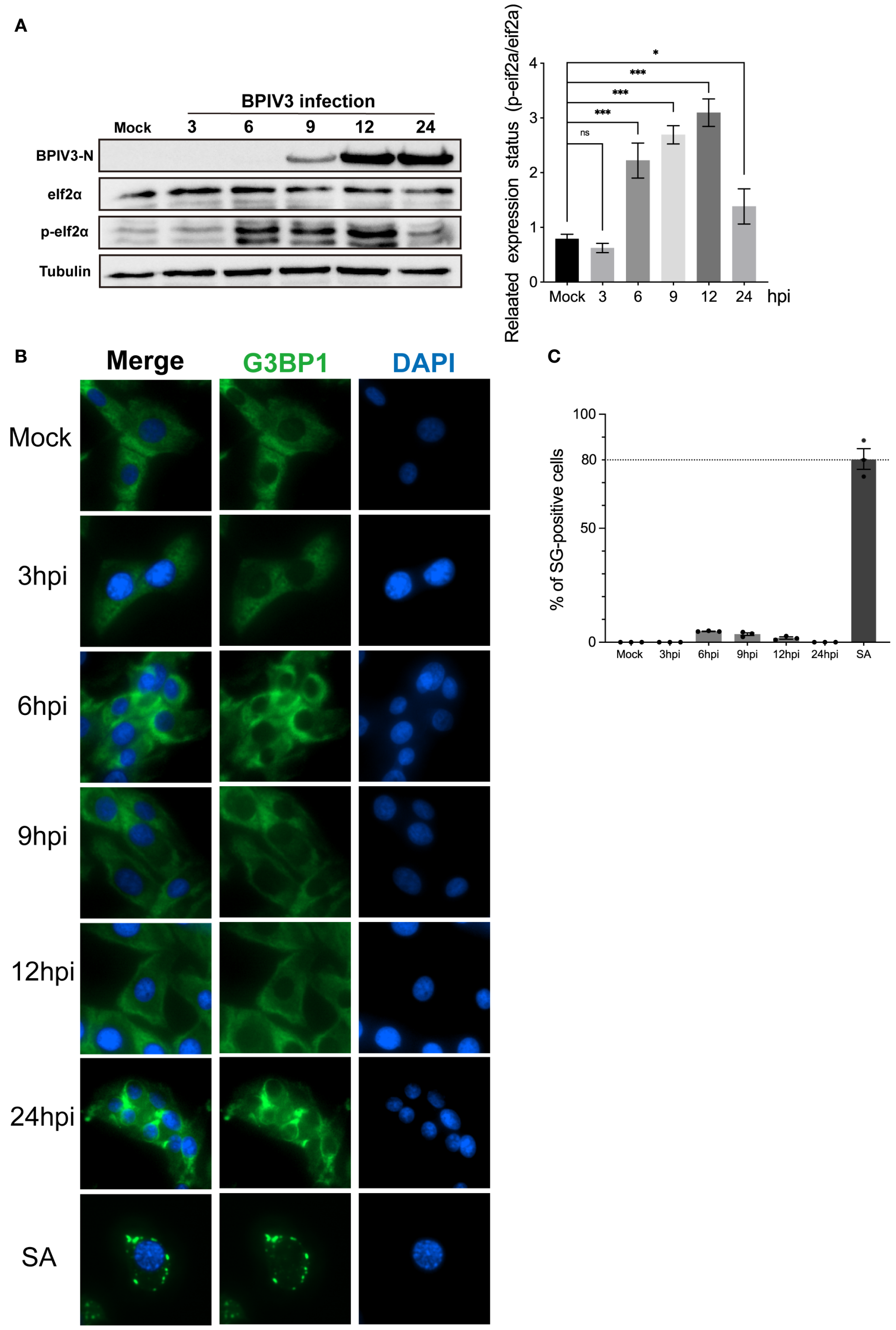

FIGURE 1
BPIV3 infection induces phosphorylation of eIF2α but not the formation of SGs. **(A)** BPIV3 infection induces eIF2α phosphorylation. MDBK cells were either mock-infected or uninfected with BPIV3 (MOI = 2.0). Cell samples were collected at the indicated time points after infection, and total cellular proteins were extracted and examined for P-eIF2α and eIF2α expression using protein immunoblotting with anti-P-eIF2α, anti-eIF2α, and anti-BPIV3-N antibodies. Tubulin was used as an endogenous control. **(B)** SGs do not form during BPIV3 infections. MDBK cells were inoculated into 96-well plates and cultured for 24 h. AS (0.5 mM) treatment for 45 min served as a positive control, and BPIV3 (MOI = 2.0) infected or uninfected cells were fixed at the indicated time points (3, 6, 9, 12, and 24 h). The cells were detected with rabbit anti-G3BP1 antibody and then probed with goat anti-rabbit-coupled Alexa Fluor 488 antibody. Cell nuclei were restained by DAPI. **(C)** Percentages of cells with SG formation relative to the total number of cells were determined by counting three randomly selected groups in different microscopic fields of view. The calculated percentage represented the proportion of cells with SGs in the total number of cells. Data are expressed as mean ± SD, n = 3. The significance of difference between the groups was performed by ANOVA (* stands for $p < 0.05$; *** stands for $p < 0.001$; ns stands for $p > 0.05$).

effects of the constructs on endogenous G3BP1 expression were examined using immunoblotting and immunofluorescence. As shown in Figures 4A, B, the RNAi #3 construct effectively reduced endogenous G3BP1 levels compared to the control. This construct was used to knock down G3BP1 expression in HeLa cells in subsequent experiments. Further, G3BP1 knockdown reduced the total amount of intracellular viral N protein in HeLa cells (Figure 4C). Subsequently, viral titers and mRNA levels in HeLa

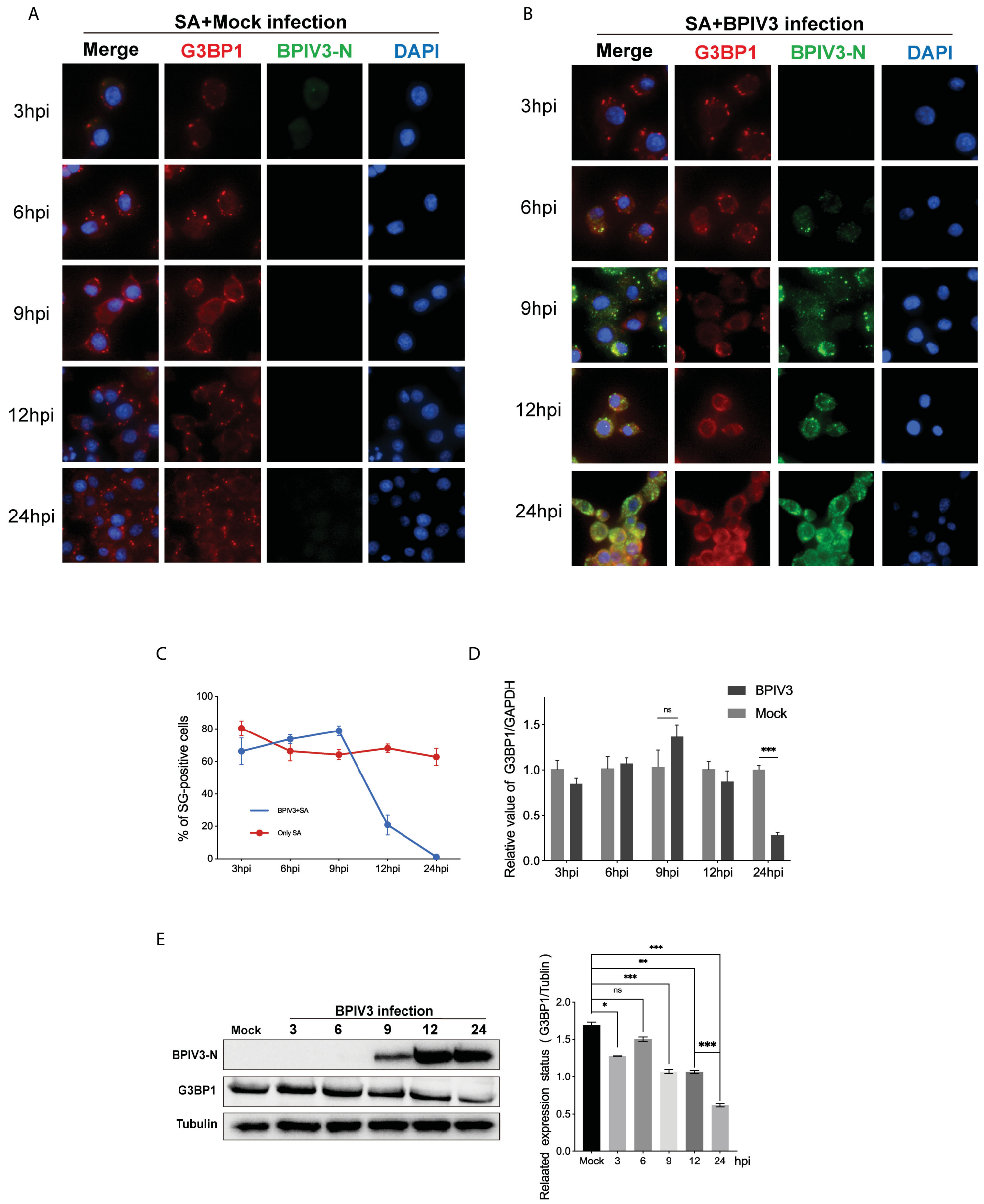

FIGURE 2
BPIV3 infection inhibits the formation of SGs induced by SA and downregulates G3BP1 protein expression. **(A, B)** Cells were either mock-infected or uninfected with BPIV3 (MOI = 2.0) after treatment with AS (0.5 mM) for 45 min at the indicated infection time points prior to fixation. Cells were stained with rabbit anti-G3BP1 antibody and mouse anti-BPIV3-N antibody, and then labeled with goat anti-rabbit coupled Alexa Fluor 594 antibody and goat anti-mouse coupled Alexa Fluor 488 antibody. Cell nuclei were restained with DAPI. **(C)** BPIV3 infection resulted in a decrease in the percentage of cells forming SGs. The number of cells forming SGs and the total number of cells were counted for AS-treated cells to determine the percentage of cells containing stress granules. **(D)** BPIV3 infection downregulates G3BP1 mRNA levels in MDBK cells. G3BP1 mRNA expression was measured using qRT-PCR at different time points of infection (3, 6, 9, 12, and 24 h) using primers specific for the BPIV3-M gene. GAPDH mRNA expression was used as an internal control to calculate relative levels of gene expression. **(E)** BPIV3 infection downregulates G3BP1 protein levels in MDBK cells. Cell lysates were prepared from the same cell culture samples as those used to perform the qRT-PCR assay. G3BP1 expression was examined using protein blotting with anti-G3BP1 and anti-BPIV3-N antibodies. Tubulin was used as an endogenous control. Data are expressed as mean ± SD, n = 3. The significance of difference between the groups was performed by ANOVA (* stands for $p < 0.05$; ** stands for $p < 0.01$; *** stands for $p < 0.001$; ns stands for $p > 0.05$).

cells after knockdown were examined, and an increase in viral titers was accelerated (Figure 4D) and the viral load was higher (Figure 4E) after knockdown compared to that of the non-knockdown G3BP1 group. These results suggest that a reduction in intracellular G3BP1 promotes BPIV3 replication.

4 Discussion

When eukaryotic host organisms are exposed to external stimuli such as oxidative stress and viral infections, specific protein translation "intermediates" are sequestered within the cytoplasm. This

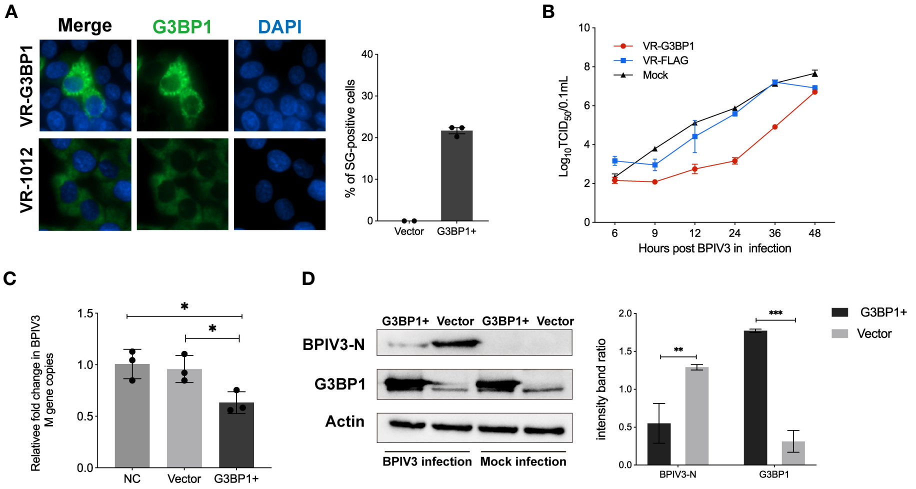

FIGURE 3
Overexpression of G3BP1 enhances SG assembly and inhibits BPIV3 replication. **(A)** G3BP1 overexpression promotes the formation of SGs in cells. HeLa cells were transfected with VR-G3BP1-3×FLAG or VR-3×FLAG plasmids (100 ng, 96-well plates) for 36 h and detected with rabbit anti-G3BP1 antibody, which was followed by probing with goat anti-rabbit-coupled Alexa Fluor 488 antibody. Cell nuclei were restained with DAPI. The rate of SG formation was calculated after counting the cells with SG formation and the total number of cells. **(B)** Overexpression of G3BP1 inhibits the growth of BPIV3. HeLa cells were transfected with VR-G3BP1-3×FLAG or VR-3×FLAG plasmids; controls were not transfected. After infection with BPIV3 (MOI = 2.0), viral titers in cell culture at different time points were determined using the $TCID_{50}$ method. **(C)** G3BP1 overexpression reduces the BPIV3 viral copy number. HeLa cells were transfected with VR-G3BP1-3×FLAG or VR-3×FLAG plasmid (500 ng, 24-well plate) for 36 h. The controls were not transfected with the plasmid. Simulated infection with BPIV3 (MOI = 2.0) for 24 h was used to detect intracellular viral mRNA levels using qRT-PCR. GAPDH mRNA expression was used as an internal control. **(D)** Overexpression of G3BP1 reduces BPIV3-N protein expression. Cells were infected or not infected with BPIV3 after transfection (MOI = 2.0). Proteins were examined using an anti-G3BP1 antibody against cell lysates and an anti-BPIV3-N antibody. Actin was used as an endogenous cellular reference. Data are expressed as mean ± SD, n = 3. The significance of difference between the groups was performed by ANOVA (* stands for $p < 0.05$; ** stands for $p < 0.01$; *** stands for $p < 0.001$).

phenomenon leads to the development of compact and continuously changing granular formations referred to as SGs. Phosphorylation of eIF2α has been identified as a crucial protein in the signaling pathway for SG formation (19). Phosphorylation of eIF2α, induced by external stimuli, results in inhibition of the translation initiation complex and impedes mRNA translation. Subsequently, core proteins of SGs, including G3BP1, TIAR, and TIA-1, facilitate the formation of messenger ribonucleoprotein complexes (20). After aggregation is complete, mature SGs are formed through protein-protein interactions with multiple proteins involved in signal transduction pathways that are recruited to the core aggregates. Viral infections commonly lead to SG formation. However, our findings indicated that no SGs were formed in the host cells 24 h after infection with BPIV3. Interestingly, our examination of eIF2α phosphorylation in cells that did not form SGs revealed a biphasic pattern, with an initial increase followed by a subsequent decrease as the viral infection progressed. As a crucial mechanism in the formation of SGs, phosphorylation of eIF2α is typically followed by the intracellular assembly of SGs. In the present study, no SGs were identified in cells infected with BPIV3. This suggested that BPIV3 may hinder SG formation, thereby facilitating replication.

To investigate the inhibitory effects of BPIV3 on SG assembly, SG formation was promoted in BPIV3-infected cells using SA. SA is a widely employed potent inducer of SGs, and SA triggers the formation of eIF2α-G3BP1-mediated SGs primarily through activation of the kinase heme-regulated inhibitor, which distinguishes it from the mechanisms employed by most viruses to stimulate SG formation, such as activation of PKR or PERK (21). In this study, we used SA to treat MDBK cells either infected with BPIV3 or not. The rate of SG formation in the cells following SA treatment decreased as the duration of the BPIV3 infection increased. When BPIV3 was cultured onto MDBK cells for 24 h, SA failed to induce SG formation. This suggests that BPIV3 hinders SA-induced SG formation. Furthermore, BPIV3 can impede the aggregation and assembly of SG, similar to the effects of other viral infections. For instance, rotavirus NSP9 protein inhibits SG assembly within host cells during infection (22). Similarly, foot-and-mouth disease virus impedes SG assembly through its leader proteins, which cleave G3BP1 and G3BP2 (23). Additionally, SGs do not form during infection with severe acute respiratory syndrome coronavirus 2 (SARS-CoV-2) because the nuclear capsid protein (NP) of SARS-CoV-2 targets G3BP1 to prevent SG formation (24). SARS-CoV-2 NP interacts with the SG-nucleating protein G3BP1 to inhibit the assembly of SGs. Therefore, it was worth investigating whether BPIV3 targets G3BP1 to inhibit SG formation. During BPIV3 infection, downregulation of G3BP1 transcription and translation was a notable finding. This suggests that BPIV3 significantly impacts the expression of G3BP1. However, further comprehensive investigations are required to elucidate the precise mechanisms by which BPIV3 diminishes G3BP1 expression.

Studies have provided evidence that G3BP1 functions as a pivotal effector molecule, facilitating the formation of SGs and

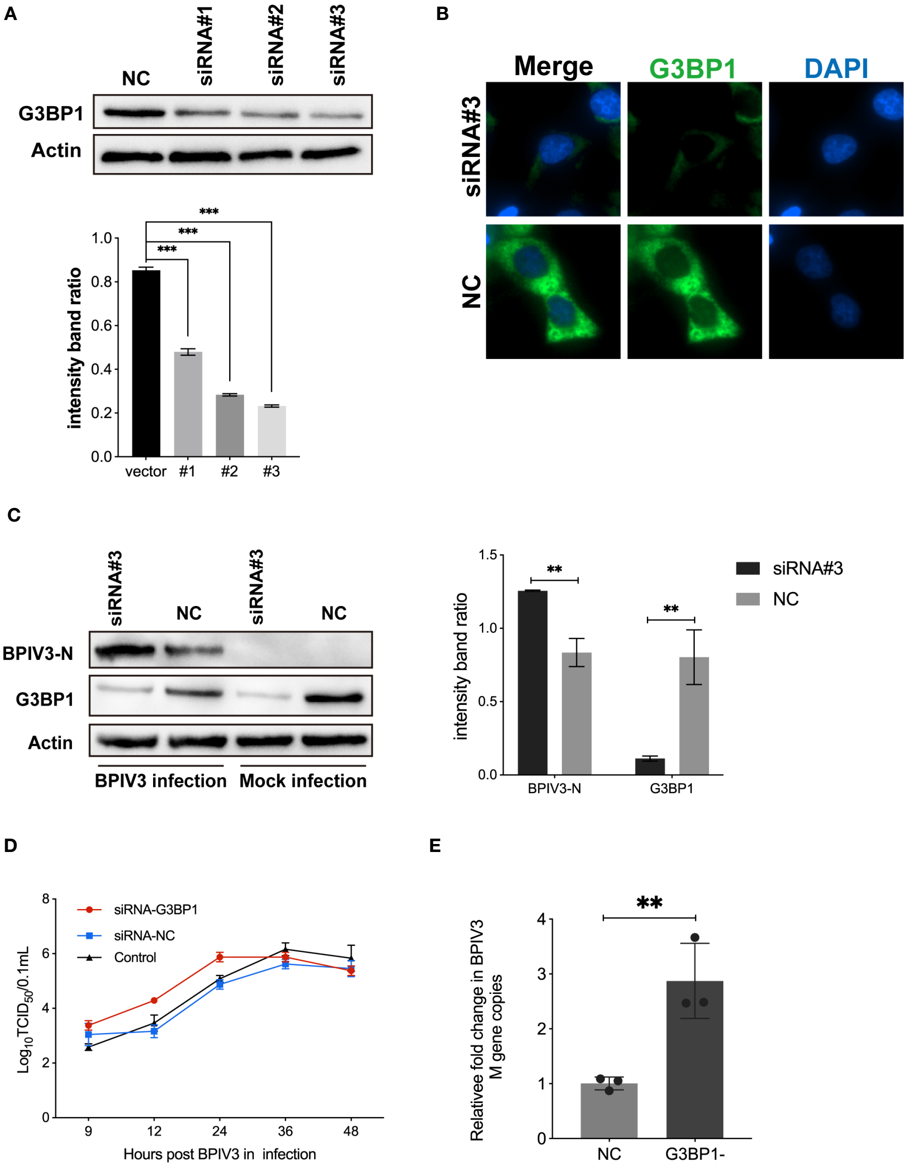

FIGURE 4

Knockdown of G3BP1 promotes BPIV3 replication. **(A)** siRNA #3 effectively interfered with endogenous expression of G3BP1. HeLa cells were inoculated in 24-well plates for overnight culture and transfected with siRNA #1–3 and siRNA-NC interfering RNA (50 nM), respectively, and cell lysates were prepared 36 h after transfection, and the protein level was determined using an anti-G3BP1 antibody. Actin was used as a reference for endogenous expression. **(B)** HeLa cells were inoculated in 96-well plates and cultured overnight. After 36 h of transfection with siRNA #3 to interfere with G3BP1 expression, the cells were fixed. The cells were detected with rabbit anti-G3BP1 antibody and then probed with goat anti-rabbit coupled Alexa Fluor 488 antibody. Cell nuclei were restained with DAPI. **(C)** Knockdown of G3BP1 resulted in increased BPIV3-N expression. Cells were either infected or not infected with BPIV3 after transfection (MOI = 2.0). After lysing the cells, protein blots were examined using an anti-G3BP1 antibody and an anti-BPIV3-N antibody. Actin was used as an endogenous cellular reference. **(D)** Knockdown of G3BP1 expression promotes growth of BPIV3 titres. HeLa cells were transfected with siRNA #3 or siRNA-NC (50 nM) for 24 h. Controls were not transfected. After infection with BPIV3 (MOI = 2.0), viral titers in cell culture at different time points were determined using the $TCID_{50}$ method. **(E)** Knockdown of G3BP1 increases mRNA levels of BPIV3. HeLa cells were grown to 50% confluence in 24-well plates and transfected with siRNA #3 and siRNA-NC 50 nM, respectively. At 24 h after transfection, mock infection with BPIV3 (MOI = 2.0) was performed for 24 h, and intracellular viral mRNA levels were detected using qRT-PCR. GAPDH mRNA expression was used as an internal control. Data are expressed as mean ± SD, n = 3. The significance of difference between the groups was performed by ANOVA (** stands for $p < 0.01$; *** stands for $p < 0.001$).

playing a substantial role in antiviral defense mechanisms (25). For instance, the PXXP structural domain of G3BP1 plays a crucial role in facilitating recruitment of the classical antiviral protein PKR to SGs (6). Additionally, it is believed that G3BP1 possesses certain antiviral functions (8). In the present study, overexpression of G3BP1 in HeLa cells facilitated SG formation within host cells. We also observed that G3BP1 inhibited BPIV3 replication. Following overexpression of G3BP1, replication of BPIV3 was diminished, leading to a reduction in viral mRNA levels and viral protein expression. In contrast, G3BP1 downregulation resulted in elevated BPIV3 titers, viral mRNA levels, and viral protein expression levels. Prior research has indicated that G3BP1 can impede replication of porcine epidemic diarrheal virus, SARS-CoV-2, and enteroviruses (6, 26, 27). These previous results align with the outcomes of the current study, suggesting that G3BP1 plays a role in inhibiting viral replication and exerts an antiviral function during BPIV3 infection. A limitation of this study was the use of HeLa cells, which are not natural host cells for BPIV3 infection. This choice was made because of the low transfection efficiency of MDBK cells. Previous studies have also used HeLa cells to investigate bovine-derived viruses (28, 29). The next step in our investigation will involve examining how G3BP1 disrupts BPIV3 replication in host cells.

5 Conclusion

In conclusion, the findings of our study indicate that infection with BPIV3 impedes the formation of SGs and can potentially affect the expression of host G3BP1. Overexpression of G3BP1 enhances SG formation in cells, thereby inhibiting replication of BPIV3. Conversely, G3BP1 knockdown promotes BPIV3 replication. Therefore, G3BP1 plays a crucial role in suppressing SG formation induced by BPIV3. These data suggested that BPIV3 infection did not induce the formation of SGs, and that the critical SG regulator, G3BP1, inhibits BPIV3 replication.

Data availability statement

The original contributions presented in the study are included in the article/supplementary materials, further inquiries can be directed to the corresponding author/s.

Ethics statement

Ethical approval was not required for the studies on animals in accordance with the local legislation and institutional requirements because only commercially available established cell lines were used.

Author contributions

NL: Methodology, Writing – original draft. WY: Writing – review & editing, Supervision. LL: Data curation, Writing – review & editing. MM: Formal analysis, Writing – review & editing. JC: Supervision, Writing – review & editing. XD: Conceptualization, Supervision, Writing – review & editing. YL: Supervision, Writing – review & editing.

Funding

The author(s) declare financial support was received for the research, authorship, and/or publication of this article. Financial support for this study was provided by grants from the National Science and Technology Support Project (2012BAD12B03-3, 2012BAD12B05-2), Natural Science Foundation of Heilongjiang Province (LH2022C037, LH2023C023) and the Science and Technology Planning Project of Heilongjiang Province (GC12B303). The funders had no role in study design, data collection and analysis, decision to publish, or preparation of the manuscript.

Conflict of interest

The authors declare that the research was conducted in the absence of any commercial or financial relationships that could be construed as a potential conflict of interest.

Publisher's note

All claims expressed in this article are solely those of the authors and do not necessarily represent those of their affiliated organizations, or those of the publisher, the editors and the reviewers. Any product that may be evaluated in this article, or claim that may be made by its manufacturer, is not guaranteed or endorsed by the publisher.

References

1. Nuijten P, Cleton N, van der Loop J, Makoschey B, Pulskens W, Vertenten G. Early activation of the innate immunity and specific cellular immune pathways after vaccination with a live intranasal viral vaccine and challenge with bovine parainfluenza type 3 virus. *Vaccines*. (2022) 10:104. doi: 10.3390/vaccines10010104

2. Bryson DG. Calf pneumonia. *Veterinary Clinics North America: Food Anim Pract*. (1985) 1:237–57. doi: 10.1016/S0749-0720(15)31326-8

3. Makoschey B, Berge AC. Review on bovine respiratory syncytial virus and bovine parainfluenza – usual suspects in bovine respiratory disease – a narrative review. *BMC Veterinary Res*. (2021) 17:261. doi: 10.1186/s12917-021-02935-5

4. Anderson P, Kedersha N. Stress granules. *Curr Biol*. (2009) 19:R397–8. doi: 10.1016/j.cub.2009.03.013

5. Onomoto K, Yoneyama M, Fung G, Kato H, Fujita T. Antiviral innate immunity and stress granule responses. *Trends Immunol*. (2014) 35:420–8. doi: 10.1016/j.it.2014.07.006

6. Reineke LC, Lloyd RE. The stress granule protein G3BP1 recruits protein kinase R to promote multiple innate immune antiviral responses. *J Virol*. (2015) 89:2575–89. doi: 10.1128/JVI.02791-14

7. Burke JM, Lester ET, Tauber D, Parker R. RNase L promotes the formation of unique ribonucleoprotein granules distinct from stress granules. *J Biol Chem*. (2020) 295:1426–38. doi: 10.1074/jbc.RA119.011638

8. Kim SS-Y, Sze L, Lam K-P. The stress granule protein G3BP1 binds viral dsRNA and RIG-I to enhance interferon-β response. *J Biol Chem*. (2019) 294:6430–8. doi: 10.1074/jbc.RA118.005868

9. Wang Y, Tang Q, Yang X, Qin Y, Chen M. Inclusion bodies of human parainfluenza virus type 3 inhibit antiviral stress granule formation by shielding viral RNAs. *PloS Pathog.* (2018) 14:e1006948. doi: 10.1371/journal.ppat.1006948

10. Rabouw HH, Langereis MA, Knaap RCM, Dalebout TJ, Canton J, Sola I, et al. Middle east respiratory coronavirus accessory protein 4a inhibits PKR-mediated antiviral stress responses. *PloS Pathog.* (2016) 12:e1005982. doi: 10.1371/journal.ppat.1005982

11. Sun L, Chen H, Ming X, Bo Z, Shin H-J, Jung Y-S, et al. Porcine epidemic diarrhea virus infection induces caspase-8-mediated G3BP1 cleavage and subverts stress granules to promote viral replication. *J Virol.* (2021) 95:e02344–20. doi: 10.1128/JVI.02344-20

12. Yang P, Mathieu C, Kolaitis RM, Zhang P, Messing J, Yurtsever U, et al. G3BP1 is a tunable switch that triggers phase separation to assemble stress granules. *Cell.* (2020) 181:325–345.e28. doi: 10.1016/j.cell.2020.03.046

13. Somasekharan SP, Zhang F, Saxena N, Huang JN, Kuo I-C, Low C, et al. G3BP1-linked mRNA partitioning supports selective protein synthesis in response to oxidative stress. *Nucleic Acids Res.* (2020) 48:6855–73. doi: 10.1093/nar/gkaa376

14. He X, Yuan J, Wang Y. G3BP1 binds to guanine quadruplexes in mRNAs to modulate their stabilities. *Nucleic Acids Res.* (2021) 49:11323–36. doi: 10.1093/nar/gkab873

15. Yang W, Ru Y, Ren J, Bai J, Wei J, Fu S, et al. G3BP1 inhibits RNA virus replication by positively regulating RIG-I-mediated cellular antiviral response. *Cell Death Dis.* (2019) 10:946. doi: 10.1038/s41419-019-2178-9

16. Bidet K, Dadlani D, Garcia-Blanco MA. G3BP1, G3BP2 and CAPRIN1 are required for translation of interferon stimulated mRNAs and are targeted by a dengue virus non-coding RNA. *PloS Pathog.* (2014) 10:e1004242. doi: 10.1371/journal.ppat.1004242

17. Kedersha N, Panas MD, Achorn CA, Lyons S, Tisdale S, Hickman T, et al. G3BP-Caprin1-USP10 complexes mediate stress granule condensation and associate with 40S subunits. *J Cell Biol.* (2016) 212:845–60. doi: 10.1083/jcb.201508028

18. Solomon S, Xu Y, Wang B, David MD, Schubert P, Kennedy D, et al. Distinct Structural Features ofCaprin-1 Mediate Its Interaction with G3BP-1 and Its Induction of Phosphorylation of Eukaryotic Translation Initiation Factor 2α, Entry to Cytoplasmic Stress Granules, and Selective Interaction with a Subset of mRNAs. *Mol Cell Biol.* (2007) 27:2324–42. doi: 10.1128/MCB.02300-06

19. McInerney GM, Kedersha NL, Kaufman RJ, Anderson P, Liljeström P. Importance of eIF2α Phosphorylation and stress granule assembly in alphavirus translation regulation. *Mol Biol Cell.* (2005) 16:3753–63. doi: 10.1091/mbc.e05-02-0124

20. Mazroui R, Sukarieh R, Bordeleau M-E, Kaufman RJ, Northcote P, Tanaka J, et al. Inhibition of ribosome recruitment induces stress granule formation independently of eukaryotic initiation factor 2alpha phosphorylation. *Mol Biol Cell.* (2006) 17:4212–9. doi: 10.1091/mbc.e06-04-0318

21. McEwen E, Kedersha N, Song B, Scheuner D, Gilks N, Han A, et al. Heme-regulated inhibitor kinase-mediated phosphorylation of eukaryotic translation initiation factor 2 inhibits translation, induces stress granule formation, and mediates survival upon arsenite exposure. *J Biol Chem.* (2005) 280:16925–33. doi: 10.1074/jbc.M412882200

22. Montero H, Rojas M, Arias CF, López S. Rotavirus Infection Induces the Phosphorylation of eIF2α but Prevents the Formation of Stress Granules. *J Virol.* (2008) 82:1496–504. doi: 10.1128/JVI.01779-07

23. Visser LJ, Medina GN, Rabouw HH, de Groot RJ, Langereis MA, de Los Santos T, et al. Foot-and-mouth disease virus leader protease cleaves G3BP1 and G3BP2 and inhibits stress granule formation. *J Virol.* (2019) 93:e00922–18. doi: 10.1128/JVI.00922-18

24. Zheng Z-Q, Wang S-Y, Xu Z-S, Fu Y-Z, Wang Y-Y. SARS-CoV-2 nucleocapsid protein impairs stress granule formation to promote viral replication. *Cell Discovery.* (2021) 7:38. doi: 10.1038/s41421-021-00275-0

25. Tourrière H, Chebli K, Zekri L, Courselaud B, Blanchard JM, Bertrand E, et al. The RasGAP-associated endoribonuclease G3BP mediates stress granule assembly. *J Cell Biol.* (2023) 222:e200212128072023new. doi: 10.1083/jcb.200212128072023new

26. Pandey K, Zhong S, Diel DG, Hou Y, Wang Q, Nelson E, et al. GTPase-activating protein-binding protein 1 (G3BP1) plays an antiviral role against porcine epidemic diarrhea virus. *Vet Microbiol.* (2019) 236:108392. doi: 10.1016/j.vetmic.2019.108392

27. Liu H, Bai Y, Zhang X, Gao T, Liu Y, Li E, et al. SARS-coV-2 N protein antagonizes stress granule assembly and IFN production by interacting with G3BPs to facilitate viral replication. *J Virol.* (2022) 96:e00412–22. doi: 10.1128/jvi.00412-22

28. Lv L, Zhao G, Wang H, He H. Cholesterol 25-Hydroxylase inhibits bovine parainfluenza virus type 3 replication through enzyme activity-dependent and -independent ways. *Veterinary Microbiol.* (2019) 239:108456. doi: 10.1016/j.vetmic.2019.108456

29. Pan W, Nie H, Wang H, He H. Bovine parainfluenza virus type 3 (BPIV3) enters heLa cells via clathrin-mediated endocytosis in a cholesterol- and dynamin-dependent manner. *Viruses.* (2021) 13:1035. doi: 10.3390/v13061035

frontiers | Frontiers in Immunology

TYPE Original Research
PUBLISHED 18 April 2024
DOI 10.3389/fimmu.2024.1361531

Check for updates

OPEN ACCESS

EDITED BY
Wei Wang,
Wenzhou University, China

REVIEWED BY
Junjun Shao,
Chinese Academy of Agricultural Sciences, China
Cesar Pedroza-Roldan,
Universidad de Guadalajara, Mexico
Nan Wenlong,
China Animal Health and Epidemiology Center, China

*CORRESPONDENCE
Xingqi Zou
✉ zouxingqi@163.com
Haidong Wang
✉ wanghaidong@sxau.edu.cn

†These authors have contributed equally to this work and share first authorship

RECEIVED 26 December 2023
ACCEPTED 02 April 2024
PUBLISHED 18 April 2024

CITATION
Zuo X, Peng G, Zhao J, Zhao Q, Zhu Y, Xu Y, Xu L, Li F, Xia Y, Liu Y, Wang C, Wang Z, Wang H and Zou X (2024) Infection of domestic pigs with a genotype II potent strain of ASFV causes cytokine storm and lymphocyte mass reduction. *Front. Immunol.* 15:1361531. doi: 10.3389/fimmu.2024.1361531

COPYRIGHT
© 2024 Zuo, Peng, Zhao, Zhao, Zhu, Xu, Xu, Li, Xia, Liu, Wang, Wang, Wang and Zou. This is an open-access article distributed under the terms of the Creative Commons Attribution License (CC BY). The use, distribution or reproduction in other forums is permitted, provided the original author(s) and the copyright owner(s) are credited and that the original publication in this journal is cited, in accordance with accepted academic practice. No use, distribution or reproduction is permitted which does not comply with these terms.

Infection of domestic pigs with a genotype II potent strain of ASFV causes cytokine storm and lymphocyte mass reduction

Xuezhi Zuo[1,2†], Guorui Peng[1†], Junjie Zhao[1], Qizu Zhao[1], Yuanyuan Zhu[1], Yuan Xu[1], Lu Xu[1], Fangtao Li[1], Yingju Xia[1], Yebing Liu[1], Cheng Wang[1,2], Zhen Wang[1], Haidong Wang[2*] and Xingqi Zou[1*]

[1]China/WOAH Reference Laboratory for Classical Swine Fever, China Institute of Veterinary Drug Control, Beijing, China, [2]College of Veterinary Medicine, Shanxi Agricultural University, Jinzhong, Shanxi, China

The whole-genome sequence of an African swine fever virus (ASFV) strain (HuB/HH/2019) isolated from Hubei, China, was highly similar to that of the Georgia 2007/1 strain ASFV. After infection with strong strains, domestic pigs show typical symptoms of infection, including fever, depression, reddening of the skin, hemorrhagic swelling of various tissues, and dysfunction. The earliest detoxification occurred in pharyngeal swabs at 4 days post-infection. The viral load in the blood was extremely high, and ASFV was detected in multiple tissues, with the highest viral loads in the spleen and lungs. An imbalance between pro- and anti-inflammatory factors in the serum leads to an excessive inflammatory response in the body. Immune factor expression is suppressed without effectively eliciting an immune defense. Antibodies against p30 were not detected in acutely dead domestic pigs. Sequencing of the peripheral blood mononuclear cell transcriptome revealed elevated transcription of genes associated with immunity, defense, and stress. The massive reduction in lymphocyte counts in the blood collapses the body's immune system. An excessive inflammatory response with a massive reduction in the lymphocyte count may be an important cause of mortality in domestic pigs. These two reasons have inspired researchers to reduce excessive inflammatory responses and stimulate effective immune responses for future vaccine development.

KEYWORDS

ASFV, inflammatory, pigs, immune, vaccine

1 Introduction

African swine fever virus (ASFV) has a large and complex genome. It is the only member of the genus ASFV in the family ASFV and is the only known arbovirus (1). Its genome size is 170–190 kb, including 151–167 open reading frames (ORFs) (2). It can be classified into 24 genotypes based on the B646L gene (3, 4).

ASFV predominantly infects the monocyte-macrophage system, including circulating monocytes, intra-tissue macrophages, and dendritic cells, providing a favorable environment for ASFV replication and infection. These cells play an important role in host innate and adaptive immunity; therefore, ASFV can inhibit host immunity and evade innate and adaptive immune responses (5). It can evade host immunity through multiple pathways, which mainly include the inhibition of IFN secretion through signaling pathways such as cGAS-STING and JAK-STAT (6–10); moreover, it inhibits IFN secretion through signaling pathways such as NF-κB to impede the host inflammatory response (11, 12) and the apoptosis of infected cells (13–15).

ASFV-infected hosts lacking certain genes can develop immune protection and defend against their original strains, such as ASFV/CN/GS/2018-Δ9L/Δ7R, ASFV-G-ΔA137R, and ASFV-G-ΔA151R, although the virus can still be detected in the blood (16–18). The absence of these genes provides effective protection; however, their safety is a major concern. Neutralizing antibodies produced by ASFV-stimulated hosts are effective against weak strains but are insufficient to produce robust protection against strong strains (19). It is important to understand the effects of the original strain on the host immune system to develop effective vaccines.

This study used HuB/HH/2019 genotype II ASFV-infected domestic pigs and collected pharyngeal swabs, anal swabs, tissues, blood, serum, and peripheral blood mononuclear cells (PBMCs) to analyze the dynamic changes in carriage and detoxification, blood viral load, cytokines, PBMCs transcripts, and immune cells in domestic pigs with the infection.

2 Materials and methods

2.1 Viral virulence determination and whole-genome sequencing

Each dilution of HuB/HH/2019 ASFV and the negative and positive controls were sequentially added to PAM 96-well cell plates, and 20 µL of fresh 1% porcine erythrocytes were added to each well and incubated in a 37°C, 5% CO_2 incubator. The plates were observed every day to see whether the erythrocyte adsorption phenomenon (HAD) occurred until the positive control showed HAD. The results were calculated as HAD_{50} using the method proposed by Reed and Muench (20).

Nucleic acids were extracted from HuB/HH/2019 strain ASFV according to the instructions of the QIAamp DNA Mini Kit (Qiagen, Germany). 200µl of the sample was mixed with 20µl of QIAGEN protease from the kit and 200µl of buffer AL with sufficient shaking and then incubated for 10 min at 56°C to allow for sufficient cleavage of the sample. Subsequently, 200µl of anhydrous ethanol was added, mixed thoroughly and then added to the QIAamp Mini rotary column (into a 2ml collection tube) and centrifuged at 6000g (8000rpm) for 1 min and the liquid was discarded. Then, 500µl Buffer AW1 was added and it was centrifuged at 6000g (8000rpm) for 1 min and the liquid was discarded liquid. We then added500µl of Buffer AW2 and centrifuged at 20,000g (14,000rpm) for 3 min, discarding the liquid and the collection tube. The QIAamp Mini Spin Column was placed into a new 2 ml collection tube and centrifuged at full speed for 1 min to help eliminate residual Buffer AW2. The QIAamp Mini Spin Column was placed into a new 1.5 ml centrifuge tube with 50 µl of Buffer AE, incubated for 1 min at room temperature (15-25°C), and centrifuged at 6,000g (8,000 rpm) for 1 min to elute the DNA. The DNA was eluted by centrifugation at 6000 g (8000 rpm) for 1 min. To improve the recovery rate, the eluted DNA was added to the QIAamp Mini rotary column again and centrifuged by incubation at room temperature. The extracted nucleic acids were subjected to whole genome sequencing.

The strain used in the present experiment was isolated during an outbreak in Hubei Province, China, in July 2019. The strain has been reported in the Veterinary Bulletin of the Ministry of Agriculture and Rural Affairs of China, Volume 21, Issue 8, 2019, in addition to the World Organization for Animal Health, Reference Laboratory for Classical Swine Fever, China Institute of Veterinary Drug Control, Beijing, China.

2.2 Animal experiments

All animal experiments were approved by the Animal Welfare and Ethics Committee of the China Veterinary Drug Inspection Institute (IVDC), and animal experiments and virus sampling were conducted in a biosafety level III laboratory of the IVDC, approved by the Ministry of Agriculture and Rural Affairs of the People's Republic of China.

Nine 60-day-old Dugongs (ternary pigs) were divided into two groups: six in the inoculation group and three in the negative control group. Before inoculation, their blood was tested for ASFV, PEDV, TGEV, CSFV, PPV, PCV II, PRV, and PRRSV antigens. All results were negative. The inoculation group was intramuscularly injected with the $10HAD_{50}$ HuB/HH/2019 strain of ASFV in the neck (no. 2#, 3#, 5#, 7#, 8#, and 9#).

Their temperature was recorded daily to observe clinical signs and scored, expressed as a quantitative clinical score (CS) obtained by summing the values of the eight clinical signs recorded daily, namely, temperature, anorexia, flatus, skin hemorrhage or cyanosis, joint swelling, respiratory distress, ocular discharge, and the digestive system. The findings were scored on a severity scale of 0–3 (most severe), and the sum of these points was recorded as CS, which was also used to define human endpoints (21). Pigs with a clinical score greater than 15 were culled under anesthesia using 1 ml of Zoletil 50, indicating that five or more of the eight clinical signs recorded reached the most severe stage and that three pigs with a score greater than 15 died naturally in the subsequent experiment. The period after the onset of typical signs and natural death or culling was defined as the near-death period, during which the disease progressively deteriorated less than 3 days before natural death and culling. Blood and swabs were collected 0, 2, 4, 6, and 8 days post-inoculation (dpi) in the inoculated group. PBMCs were isolated for transcriptome sequencing and analysis of changes in immune cell subsets. Their serum was isolated for cytokine expression assays. The pigs that survived were observed until day 21 of the necropsy, and tissues were collected for ASFV nucleic acid testing.

2.3 Carrying and detoxification pattern after infection with HuB/HH/2019 strain of ASFV

Blood was diluted 10-fold with PBS before nucleic acid extraction, with pharyngeal swabs and anal swabs centrifuged to obtain supernatants. Small tissue samples were taken (soybean-sized) and ground with 1 mL of PBS, and the resulting mixture was centrifuged to obtain supernatants. All samples were processed, and nucleic acids were extracted using the Tecan nucleic acid workstation and magnetic bead method viral DNA/RNA extraction kit (Beijing, China). The primer probe sequences are shown in Table 1 (22). A 25-μl system was prepared, including HyperProbe Mixture 12.5 μl, upstream primer (20 μM) 0.2 μl, downstream primer (20 μM) 0.2 μl, probe (10 μM) 0.1 μl, nucleic acid 3 μl, and ddH2O 9 μl. The amplification program was pre-denaturation at 95°C for 30s, denaturation at 95°for C 10s, annealing/extension at 58°C for 20s for 45 cycles.

2.4 Dynamic changes in serum antibodies with different days of infection

Changing levels of p30 antibody in serum with days of infection were measured using an indirect ELISA (JNT, China), and all components were removed from the kit and returned to room temperature. To the wells of the antigen-coated plate, 100 μl of extracted samples diluted in a dilution plate were added (samples were diluted 50-fold using sample diluent). Next, 100 μl of undiluted negative control serum (NC) and positive control serum (PC) were added to the indicated wells. The plate sealing membrane was covered and incubated for 30 min (± 2 min) at room temperature (25 ± 3°C). The plate was washed with a micropipette, the liquid in the wells was discarded, and 300 μl of 1x washing solution was added to each well, and washed three times. After the last washing, the plate was gently patted dry on absorbent paper, and the drying of the plate between steps was strictly prohibited. Next, 100μl ASFV HPR labeled antibody was added to each well. The plate sealing membrane was covered and incubated for 30min (± 2min) at room temperature (25 ± 3°C). The plate was washed with a micropipette, the liquid was discarded in the wells, and 300 μl of 1x washing solution was added to each well, and washed three times. After the last washing, the plate was gently patted dry on absorbent paper, and drying of the plate between steps was strictly prohibited. At this point, 100μl TMB substrate solution was added to each well. The plate was covered with a sealing membrane and incubated for 15min (± 1min) at room temperature (25 ± 3°C). The enzymatic reaction was terminated by adding 50 μl of termination solution to each well. Absorbance values were measured using a wavelength of 450 nm. Results were determined and calculated.

TABLE 1 p72 primer/probe sequences.

p72	Sequences
Upstream Primer	5’-GAACGTGAACCTTGCTA-3’
Downstream Primer	5’-GGAAATTCATTCACCAAATCC-3’
Probe	5’-6-FAM-TAAAGCTTGCATCGCA-MGB-3’

The conditions for the establishment of the experiment were positive control OD450 > 0.8 and negative control OD450 < 0.2. The formula for calculating the S/P of the samples was (OD value of the samples - mean value of the OD of the negative control)/(mean value of the OD of the positive control - mean value of the OD of the negative control). The criteria for determining the S/P of positive samples were positive S/P ≥ 0.4, suspicious 0.4 > S/P > 0.3, and negative S/P ≤ 0.3, and the suspicious samples were tested again to confirm these results.

2.5 Changes in serum cytokine dynamics under different days of infection

Serum was collected and assayed using Luminex for changes in the concentrations of IFN-α, IFN-γ, IL-1β, IL-4, IL-6, IL-8, IL-10, IL-12p40, and TNF-α with different days of infection. The standards were dissolved and the components diluted according to the instructions of the kit (Thermo, USA, EPX090-60829-901). Next, 50 μl of pre-mixed microspheres was added to a 96-well plate and the plate was washed with a magnetic separator. The 96-well plate was taken out and 25 μl of Universal Assay Buffer was added to each well. Next, 25 μl of standards or samples was added; 25 μl of Universal Assay Buffer was then added to the blank control; and the plate was sealed with a membrane and incubated for 30 min at 500 rpm at room temperature with shaking. Afterward, 25μl of Universal Assay Buffer was added to the blank control; the membrane of the well plate was sealed, incubated for 30min at 500rpm with shaking at room temperature, and left at 4°C overnight. The plate was removed the next day and incubated with shaking at 500 rpm for 30 min at room temperature. The 96-well plate was placed in a magnetic separator plate, 150 μl of 1×wash buffer was added to each well, and it was allowed to stand for 30 s. The liquid from the well plate was removed by inverting it. The steps were repeated for a total of 3 washes; at the end of the last wash, the residual liquid was adsorbed with a paper towel. Next, 25 μl of 1× detection antibody mixture was added to each well; the plate was sealed with a new sealing film; the 96-well plate was removed from the magnetic separator plate and placed in a plate shaker at 500 rpm for 30 min at room temperature; the washing procedure was repeated. Then, 50μl of SA-PE was added to each well; the plate was sealed with a new sealing membrane; the 96-well plate was removed from the magnetic separator plate and placed in a well plate shaker at 500rpm for 30min at room temperature. the plate-washing step was repeated. Next, 120 μl of Reading Buffer was added to each well; the plate was sealed with a new sealing membrane; the 96-well plate was removed from the magnetic separator plate and placed in a well plate shaker at 500 rpm for 5 min; the sealing membrane was gently removed and placed in a Luminex 200 instrument for reading. The standard curve was fitted by five-parameter nonlinear regression and the concentration values were calculated.

2.6 RNA-sequencing and quantitative polymerase chain reaction analysis of PBMCs transcriptional differences in different days of infection

PBMCs were isolated using Porcine Peripheral Blood Single Nucleated Cell Isolation Kit (IPHASE, China). 10 ml of blood was taken from the jugular vein and added to the EDTA anticoagulation tube, 10 ml of 1× dilution solution pre-diluted with ultrapure water was added to a 50 ml centrifuge tube and 10 ml of blood was added. The 20 ml of diluted blood was spread into a 50 ml centrifuge tube containing 10 ml of separating solution, while ensuring that the liquid level was stratified. After centrifugation at 800 g for 20 min, a flocculent white membrane layer was visible. The white membrane layer was aspirated with a pasteurized pipette and added to the centrifuge tube containing 10 ml of diluent solution by centrifugation at 400 g for 10 min and the supernatant was discarded. The white membrane layer was removed from the vein and added to the EDTA anticoagulant tube. The precipitate was suspended with 10 ml of erythrocyte lysate and then centrifuged at 400 g for 10 min. The precipitate was suspended in cryopreservation solution, part of which was frozen and the other part was added to RNAiso Plus (Invitrogen, USA) for RNA-seq sequencing.

A total of five groups were set up for RNA-seq sequencing, including the negative control (0 dpi), P0521 (2 dpi), P0523 (4 dpi), P0525 (6 dpi), and P0527 (8 dpi) groups. The Illumina II high-throughput sequencing platform was utilized with the PE150 sequencing strategy. Comparison and transcript splicing analyses were completed using star and Cufflinks software, respectively, and then all genes were quantitatively analyzed to identify the differential genes, which were subsequently subjected to functional enrichment analyses to mine their functions.

Based on the RNA-seq results, six chemokines (Table 2) were selected for qPCR validation. PMBCs with RNAiso Plus were thawed, chloroform was added and shaken gently, and allowed to stand on ice for 7 min, and delamination could be observed. Centrifugation was performed at 12,000 rpm for 15 min, and the supernatant was aspirated into a new 1.5 mL centrifuge tube, isopropanol was added and shaken gently, and allowed to stand on ice for 15 min. Centrifugation was performed at 12,000 rpm for 15 min, and the supernatant was poured off. The precipitate was washed by adding pre-cooled 75% ethanol (anhydrous ethanol configured with depc water) at 4°C. It was then centrifuged at 8000rpm for 8min, after which the supernatant was poured off, and the wells left to air-dry to add depc water to solubilize the RNA.

The extracted RNA was tested for purity and quality using a NanoDrop 1000 (Thermo, USA), and qualified RNA was mixed with PrimeScript^{TM} RT Master Mix (Takara,Japan) at a ratio of 1:4, and reverse transcribed into cDNA at 37°C for 15 min and 85°C for 5 s. The cDNAs were extracted from the RNAs using a NanoDrop 1000 (Thermo, USA).

The internal reference gene for qPCR validation was β-actin. 10 µl of MonAmp^{TM} SYBR$^{®}$ Green qPCR Mix (Monad, China), 0.4 µl each of F/R, 2 µl of cDNA, 7.2 µl of ddH2O, and 20 µl of the total system were used to set up the reaction system. In the LightCycler 480II fluorescent qPCR instrument (Roche Holding AG, Switzerland), the program was set to pre-denaturation at 95°C for 30s, amplification at 95°C for 10s, 57°C for 15s, 72°C for 15s for a total of 45 cycles, and the lysis curve at 95°C for 10s, 65°C for 1min, 95°C for Continuous, and 40°C for None. The results were analyzed using the $2^{-\Delta\Delta Ct}$ method.

2.7 Immune cell dynamics in PBMCs at different days of infection

The collected PBMCs were centrifuged at 350 g for 5 min, and the supernatant was discarded. The precipitate was suspended in 300 µL FBS Buffer (BD, USA) and centrifuged; this step was repeated once. Next, 4% paraformaldehyde was fixed and washed 3 times. Subsequently, cells were suspended with 100 µl FBS Buffer containing 2 µl CD3-FITC (Abcam, UK,ab34722), 10 µl CD4-Percp/cy5.5 (BD, USA,561474), and 10 µl CD8-PE (Abcam, UK, ab22548). Next, the cells were incubated at room temperature and protected from the light for 15 min, washed twice, and then, suspended with 100 µL FBS buffer for on-board testing. Flow cytometry was performed using the CytoFLEX SRT system (Beckman Coulter, USA).

TABLE 2 Sequences of chemokine primers.

Chemokine Name	Forward (5,)	Reverse (3,)
CXCL14	ACCCAGCACTTTTACCGAGG	TGTCTGGAGCGCAAGAGAAG
CXCL11	AATACCACTGCCCAGAGTAGC	ATACCCAGTTGGGAACCAGC
CXCL9	CTCAGCTTTTCCCGCAGAGT	TTGGTGGCCTTCTTGTCAGG
CXCL10	ACTGATAAGGATGGGCCGGA	TTACTGCTCAACAGCTCGGG
CCL2	GATCTTCAAGACCATCGCGG	GGTTTTTCTTGTCCAGGTGGC
CCL21	GCTATGTGCAGACCCCCAAA	ATTTGGAGGCCCTCTTGTCC

2.8 Statistical analyses

All data are presented as individual or mean+SEM, plotted using Prism 9 (GraphPad, San Diego, CA, USA), with statistically significant differences determined using one-way ANOVA and Bonferroni's correction. P < 0.05 (*), P < 0.01 (**), P < 0.001 (***), and P < 0.0001 (****).

3 Results

3.1 Whole-genome sequence of the HuB/HH/2019 strain

Whole-genome sequence comparison between the HuB/HH/2019 strain ASFV and Georgia 2007/1 strain ASFV (NCBI GenBank: FR682468.2) revealed that the two strains were highly homologous, with seven base mismatches. The positions of the mismatches were 7059, 26425, 44576, 134514, 167062, 170862, and 183902 in Georgia 2007/1 ASFV (Figure 1).

3.2 Clinical scoring and necropsy observations

The body temperatures of the five pigs started to rise at 5 dpi, and all reached above 40°C at 6 dpi (Figure 2A). Three pigs died naturally at 8 dpi. Two had typical symptoms at 8 and 9 dpi and were dissected when they entered the near-death stage. Pig 3# remained alive till 21 dpi without elevated body temperature and obvious clinical symptoms (Figures 2B, C). All morbid pigs showed signs of generalized redness, huddling, decreased appetite, depression, recumbency, and shortness of breath (Figures 2B, C). The control group did not show a significant increase in body temperature, and no abnormal clinical signs were observed.

An autopsy of the affected pigs revealed inflamed submandibular, gastrohepatic, inguinal, and pulmonary hilar lymph nodes, hemorrhagic swelling of the tonsils, solid changes in the lungs, hemorrhages in the intestinal tract, and obvious enlargement of the spleen. Among them, five pigs had jelly-like liver sludge in their liver capsules (Figure 2D). Pig 3# did not develop any disease during the 21-day observation period. Slight hemorrhagic swelling of the spleen and lungs was observed through autopsy.

3.3 The pattern of virus excretion and virus tissue distribution

Pharyngeal swabs, anal swabs, and blood were collected on different days after infection to detect the pattern of virus exocytosis and viremia over time, and the tissues were collected by dissection to detect the distribution of the virus; viral nucleic acids began to be detected in pharyngeal swabs at 4 dpi

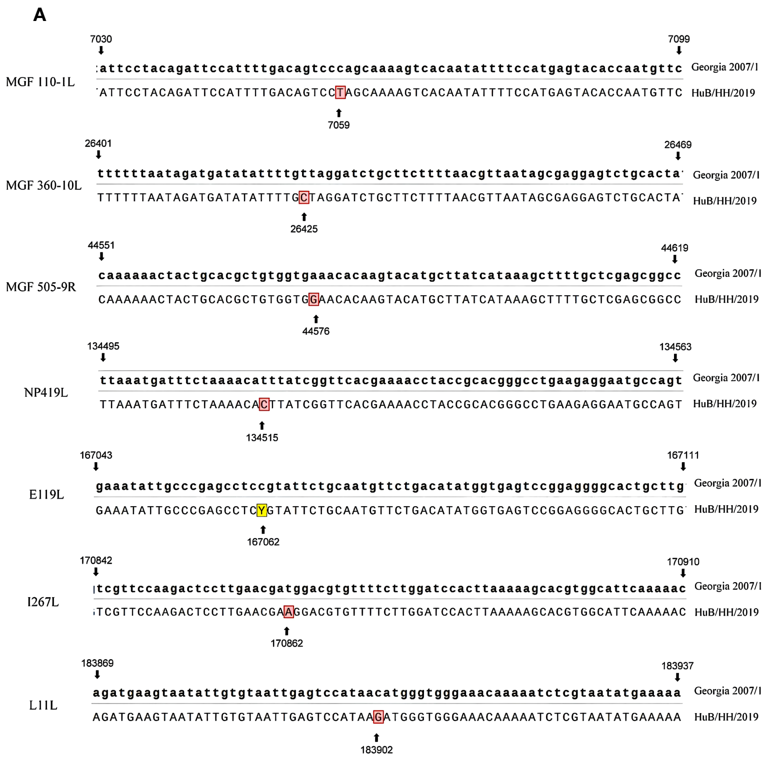

FIGURE 1
Sequence comparison of Georgia 2007/1 with HuB/HH/2019, with Georgia 2007/1 at the top and HuB/HH/2019 at the bottom.

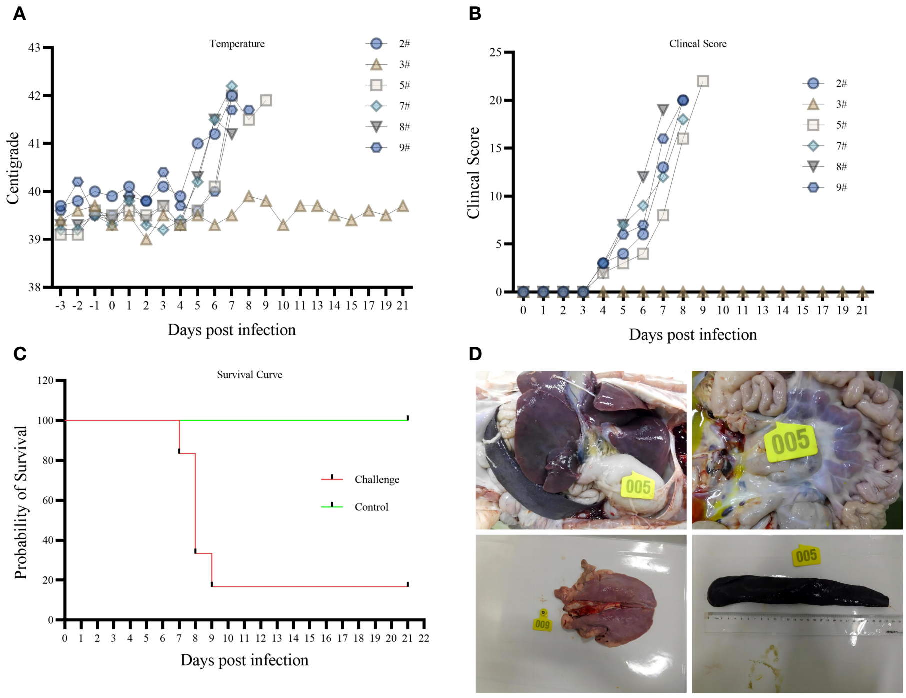

FIGURE 2
(A) body temperature variation. **(B)** Clinical Score. **(C)** survival curve. **(D)** Histopathology.

(Figure 3A), blood at 4 dpi (Figure 3B), and anal swabs at 6 dpi (Figure 3C). The amount of detoxification carryover gradually increased with the number of days of infection, and the amount of nucleic acids in the blood was higher than that in the swabs collected on the same day. Viral nucleic acids were detected in all 13 tissues collected (heart, liver, spleen, lungs, kidneys, brain, tonsils, duodenum, ileocecal valve, hilar lymph nodes, gastrohepatic lymph nodes, mesenteric lymph nodes, and inguinal lymph nodes) (Figure 3D). The lungs and spleen had the highest viral loads, and the ileocecal valve had the lowest viral load. Nucleic acids were only detected at very low levels in the spleen and lungs of Pig #3 (results not shown).

3.4 Serum antibody levels

The ASFV p30 protein is an early expressing protein, detected in one of the six swine serum samples starting at 19 dpi (Figure 4). Although pig #3 did not show symptoms throughout the observation period, the presence of antibodies in the body indicated a low level of infection. In contrast, nucleic acid testing of swabs, blood, and tissues showed a lower level of carryover detoxification than in the rest of the pigs. This indicates the presence of infection in #3, but it was in good condition throughout the observation period. In a related study, p72 antibodies were detected in the serum of only one pig that survived for 12 days after infection of 16 domestic pigs with the Georgia 2007/1 strain of ASFV, whereas p72 antibodies were not detected in the remaining pigs that survived for 9 days (23).

3.5 Cytokine storm caused by ASFV infection

To better demonstrate the cytokine changes in domestic pigs, we categorized and analyzed them according to different life processes.

No significant changes were found in the expression of pro-inflammatory factors IL-1β (Figures 5A, B) and IL-6 (Figures 5C, D) during the incubation period, but the expression increased significantly during the near-death period. The expression of pro-inflammatory factor TNF-α (Figures 5E, F) gradually increased after the attack. The expression of the anti-inflammatory factor IL-4 (Figures 5G, H) was not significantly different in domestic pigs with a life cycle of 6 days. In contrast, it was significantly elevated during the near-death period in domestic pigs with a life cycle of 8 dpi. The expression of the anti-inflammatory factor IL-10 (Figures 5I, J) was significantly elevated during the near-death period. An imbalance between anti-inflammatory and proinflammatory factors results in a cytokine storm that induces acute inflammation. The expression of the innate immune factor IFN-α (Figures 5K, L) was significantly increased during the dying phase. The levels of the granulocyte chemokine IL-8 (Figures 5M, N) significantly rose at 6 dpi and declined to pre-attack levels at 8 dpi. The activating T and NK cytokine IL-12p40 (Figures 5O, P) did not show significant changes in domestic pigs with a life cycle of 8 days. In contrast, it was significantly elevated in pigs in the near-death period with a life cycle of 6 days. All these cytokines involved in innate immunity were suppressed, and the organism failed to produce adequate innate immune protection. The low level of IL-4 expression with

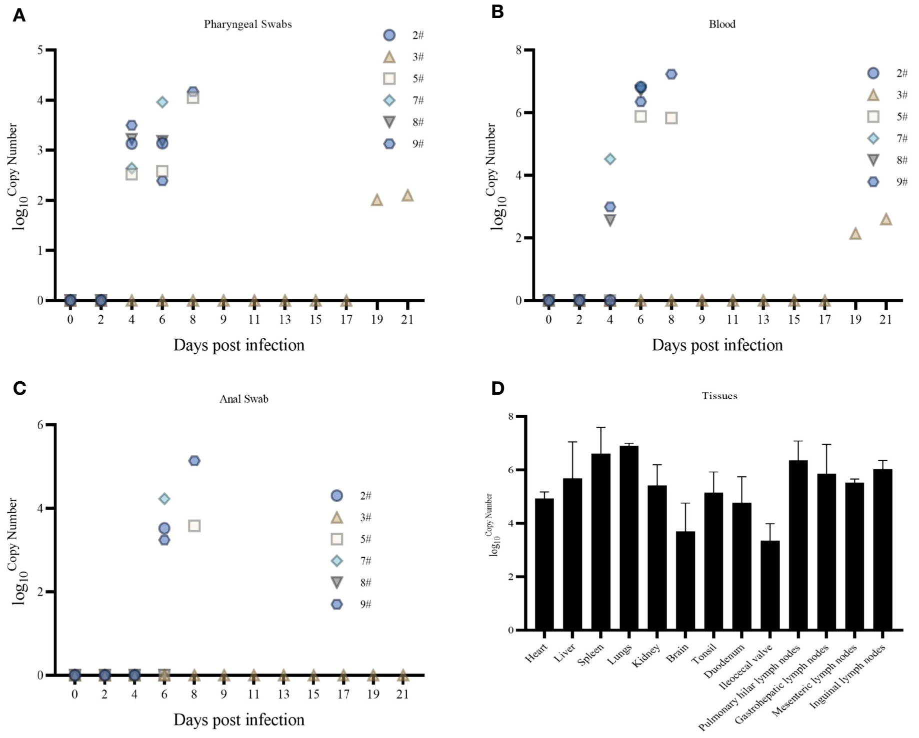

FIGURE 3
(A) Pharyngeal swab viral nucleic acid load. **(B)** Blood Viral Nucleic Acid Volume. **(C)** Anal swab viral nucleic acid load. **(D)** Tissue viral nucleic acid load.

undetectable IFN-γ levels (results not shown) suggested that the level of adaptive immunity in the organism was not high.

No abnormalities were found in pig No. 3 throughout the observation period. IL-1β (Figure 5Q) expression was significantly down-regulated after infection. IL-6 (Figure 5R) was significantly up-regulated at 4 dpi and then down-regulated, and there was no significant change in TNF-α (Figure 5S). IL-4 (Figure 5T) expression was also significantly down-regulated after infection, and IL-10 was not detected (results are for display). In terms of clinical signs and autopsy observations, there were no typical symptoms and tissue lesions were mild. In terms of inflammatory factors, there was no serious imbalance between pro-inflammatory and anti-inflammatory factors, and the inflammatory response was mild. It has been reported that significantly elevated levels of IL-10 in pigs infected with African swine fever predicted a lethal outcome (24, 25), whereas the remaining five pigs in this study showed a significant increase in levels during the near-death period. IFN-α (Figure 5U) was significantly down-regulated after infection and failed to cause a significant up-regulation in subsequent infections, a result that was opposite to that of the remaining five pigs that died. The expression of chemokine IL-8 (Figure 5V) and activator IL-12p40 (Figure 5W) was significantly up-regulated after infection, and the body was actively mobilizing immune cells to mature and activate, thus exerting an immune effect to antagonize the virus.

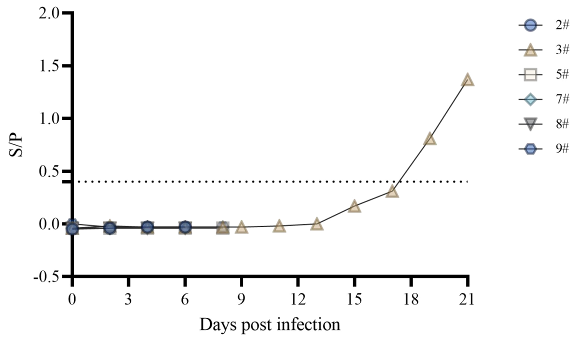

FIGURE 4
Expression of serum p30 antibody.

3.6 Transcriptional changes in PBMCs induced by ASFV infection of hosts

Changes in genes at the transcriptional level were analyzed for different days of infection relative to those in the negative controls, with 289 differential genes at 2 dpi (Figure 6A), 615 differential genes at 4 dpi (Figure 6B), 717 differential genes at 6 dpi (Figure 6C), and 602 differential genes at 8 dpi (Figure 6D). We screened the cytokine genes measured by serum (absolute value of Log2FoldChange ≥ 1, pval < 0.05) for consistency in transcription and translation levels. Both IFN-α8 and IFN-α15 tended to be downregulated (no significant difference), whereas the serum results showed significant upregulation of IFN-α at 6 and 8 dpi. IFN-γ appeared to be upregulated (no significant difference), with very low or even undetectable amounts in the serum. IL-4 insignificantly changed but was significantly upregulated in the serum at 8 dpi. IL-6 was

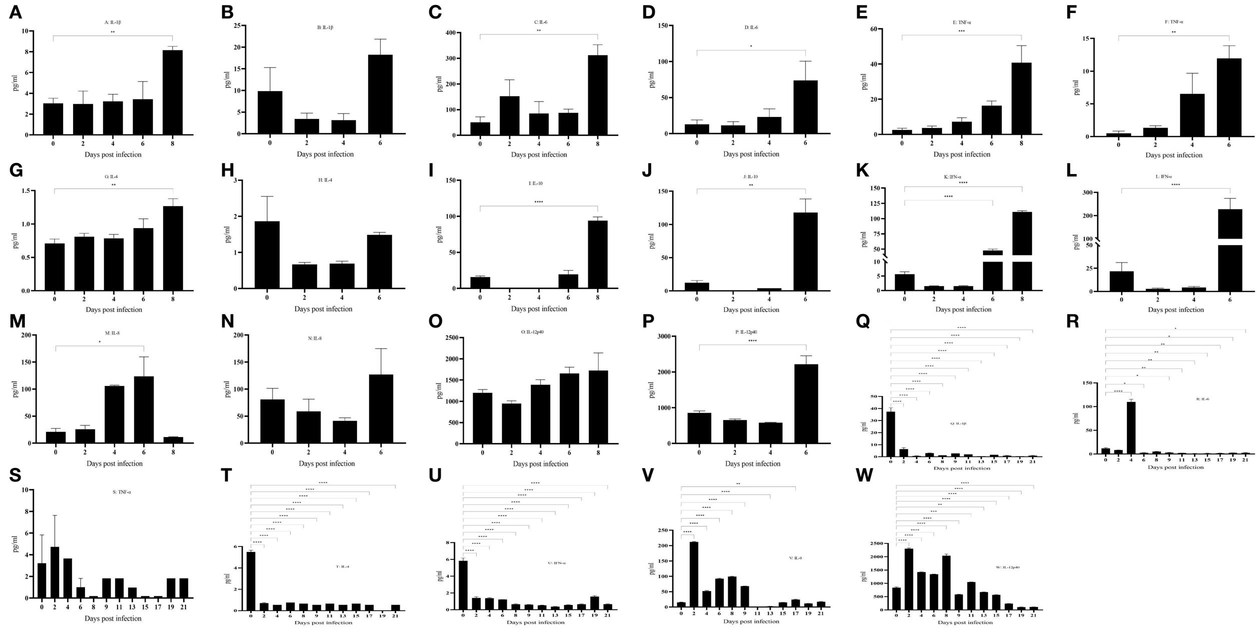

FIGURE 5
(A–W) Cytokine changes in different life processes. P < 0.05 (*), P < 0.01 (**), P < 0.001 (***), and P < 0.0001 (****).

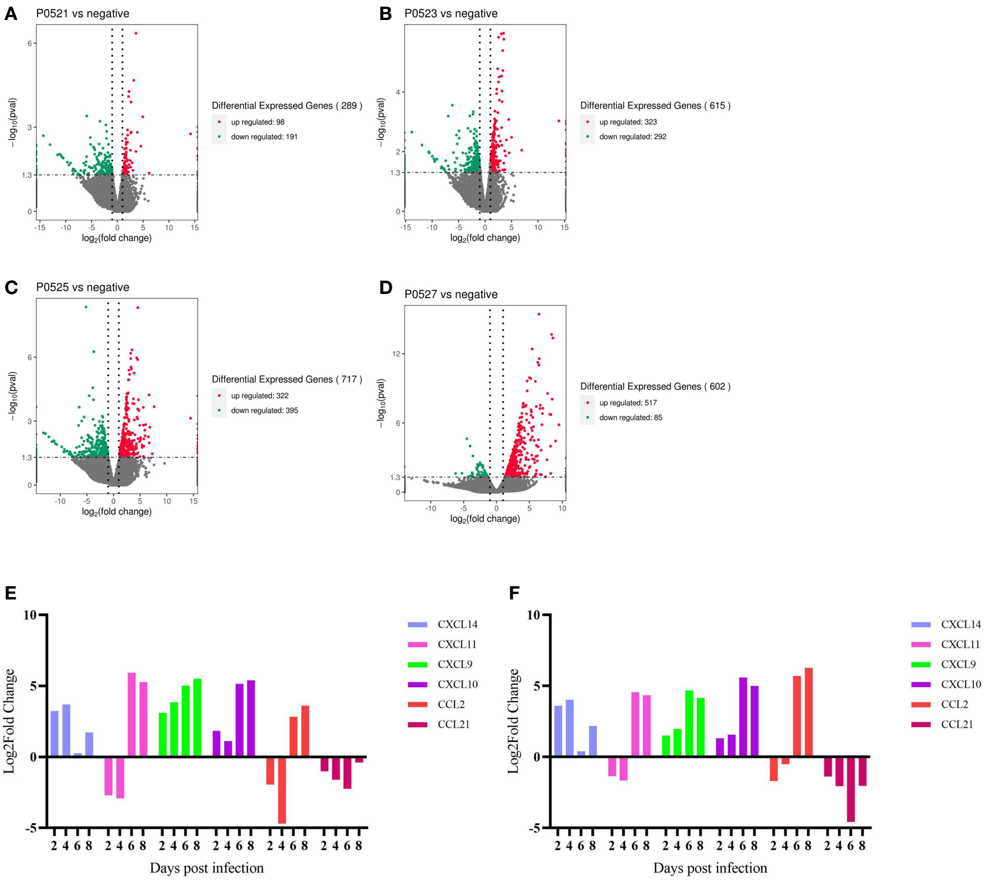

FIGURE 6
(A-D) Number of differential genes in PBMCs at different days of infection. **(E)** qpcr gene validation. **(F)** RNA-Seq gene changes.

upregulated (no significant difference), with serum IL-8 upregulated at 6 dpi vs. 8 dpi (no significant difference) and significantly upregulated at 6 dpi but downregulated at 8 dpi in the serum (no significant difference). IL-10 transcriptional and translational levels were consistent and significantly upregulated at 6 and 8 dpi. IL12p40 was downregulated and then upregulated (no significant difference) but was significantly upregulated at 6 dpi in the serum. TNFAIP2 was significantly upregulated at 4 dpi versus 6 dpi, and TNFAIP3 was significantly upregulated at 4 dpi, Serum TNFα was significantly upregulated in the dying phase (Supplementary File 1).

The top 30 genes enriched to the most genes per term were analyzed, with the most genes enriched to biological process, with more genes enriched to immune system processes and protein targeting at 2 dpi (Supplementary File 2A), more genes enriched to positive–negative feedback regulation as well as other stimulus-feedback regulation at 4 dpi (Supplementary File 2B), and more genes enriched to stress response, external stimulus-response, immune response at 6 dpi, defense responses, and inter-tissue interactions (Supplementary File 2C) according to Gene Ontology (GO). The results at 8 dpi were similar to those at 6 dpi, except that more extracellular genes were enriched (Supplementary File 2D), and the remaining changes were similar to those at 6 dpi.

The top 20 most significant pathways enriched in each pathway were analyzed, and the enrichment of immune inflammation-related pathways was more significant at 2, 4, 6, and 8 dpi (Supplementary Files 3A-D). The immunoinflammation-related genes of the enriched pathways were screened (absolute value of Log2FoldChange ≥ 1, pval < 0.05). C1QA, C1QB, TCRα, and TCRβ on 2 dpi; C1QA, C1QB, TCRα, TCRβ, CD28, IL-1A, CCL4, TNFAIP3, and TRF9 on 4 dpi; C1QA, C1QB, C1QC, CD86, IL-10, CCL2, CCL4, CXCL9, CXCL10, CXCL11, CSF1, SLA-DOA, SLA-DMA, SLA-DMB, IgG, IRF7, and BCR on 6 dpi; C1QA, C1QB, C1QC, C4BP, C5aR, IL-1R2, IL-10, CCL2, CXCL10, CCL4, CCL3L1, CXCL11 XCL1, CXCR2, CCR10, CXCR1, CCR1, XCR1, TNFSF13, CSF1, IgA, IgG, IRF4, IRF7, CD14, and CD209 on 8 dpi were involved in two and above pathways (Supplementary File 1).

Comparing the changes in transcript levels of the six chemokines analyzed using qPCR with the results of RNA-seq (Figures 6E, F), CXCL14, CXCL9, and CXCL10 were upregulated from post infection to end of life, CXCL11 and CXCL2 were first downregulated at 2 and 4 dpi and then upregulated, and CCL21 was downregulated in all cases after infection.

3.7 Massive reduction in lymphocyte counts after ASFV infection

PBMCs were isolated from domestic pigs infected with HuB/HH/2019 ASFV (Supplementary File 4), and a clear trend of lymphocytes decreasing with days of infection was found by FSC-A and SSC-A set gates (Figures 7A, B). CD3+ T cells also gradually decreased in PBMCs (Figures 7C, D), and a transient rise in the latency period of CD4+ T cells was followed by the onset of a decline (Figures 7E, F), CD8+ T, CD4+CD8+ double-positive T cells all gradually decreased in PBMC (Figures 7G, H).

4 Discussion

African swine fever is a class I animal disease that needs to be reported to the World Organization for Animal Health (WOAH) once detected. Its widespread global epidemic has caused serious losses to the global pig farming industry, particularly since its introduction in China in 2018 (26). The virulent strain in this study was isolated in Hubei in 2019, and whole-genome sequencing revealed that the sequence was extremely similar to that of Georgia 2007/1 strain ASFV. HuB/HH/2019 strain ASFV-infected domestic pigs with typical symptoms of a strong genotype II strain (23).

Data on the patterns of virus carriage and detoxification in infected hosts can provide guidance for early diagnosis on farms. Our study found that infection with the Hub/2019 strain ASFV was detectable in oral saliva as early as 4 dpi, in blood at 4 dpi, and in feces at 6 dpi. Multiple tissues and lymph nodes were virulent after ASFV infection, with the highest viral loads in the spleen and lungs.

Only one pig secreted antibody while the rest of the pigs that died of acute morbidity did not secrete antibodies. From the RNA-seq results of this study (Supplementary File 1), antigen-presenting genes such as SLA were down-regulated in the PBMCs of the five

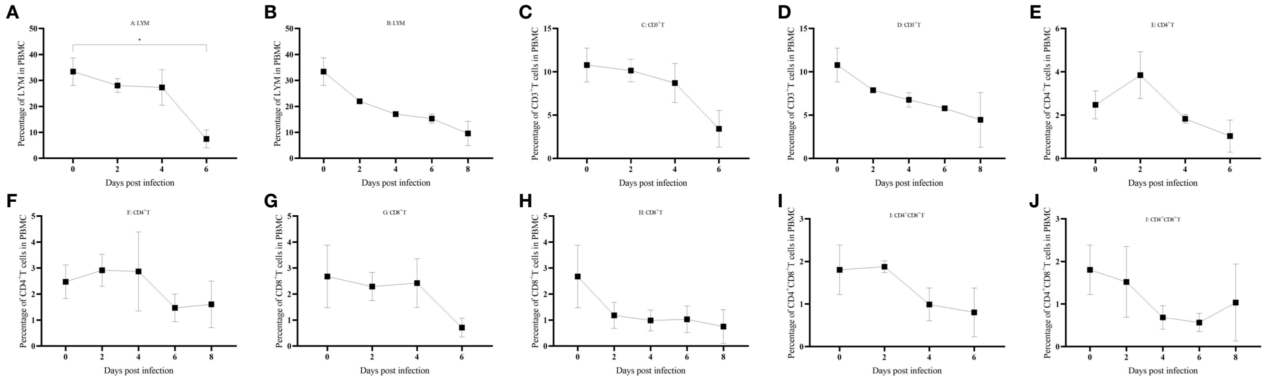

FIGURE 7
(A–J) Immune cell changes in different life processes. P < 0.05 (*), P < 0.01 (**), P < 0.001(***), and P < 0.0001 (****).

pigs, and BCR was also down-regulated, resulting in a weakening of the ability of the B cells to recognize bound antigens and failing to differentiate into plasma cells to secrete antibodies. In addition, some antigen-presenting cells cause apoptosis (27) after infection with a strong virulent strain of the African swine fever virus, resulting in immune cells that cannot effectively recognize antigens to generate a humoral immune response. The final point is that B cells also cause apoptosis (28) after infection.

Cytokines, as a kind of protein secreted by a variety of cells, play important roles in immunity, inflammation, and tumor (29–31). And cytokine storm leads to an imbalance between pro-inflammatory and anti-inflammatory factors in the body, triggering an excessive inflammatory response, which can cause damage or even death to the body (32). The three criteria reported to measure cytokine storm are elevated circulating cytokine levels, acute systemic inflammation, and secondary organ dysfunction (usually kidney, liver, and lungs) caused by inflammation (33). Measured by these three criteria our study found that an imbalance between pro-inflammatory factors such as IL-1β, IL-6, and TNF-α and anti-inflammatory factors such as IL-4 and IL-10 triggers a systemic multiorgan inflammatory response, leading to fever, hemorrhagic swelling of various organs, and dysfunction in the body. Exogenous pyrogens (viruses, bacteria, parasites, steroids, antigen-antibody complexes, etc.) stimulate the organism and activate endogenous pyrogenic cells to release endogenous pyrogens, leading to an increase in body temperature (34). The rapid increase in body temperature after ASFV infection in domestic pigs may be caused by the increase in the release of endogenous pyrogens, such as IL-1β, IL-6, TNF-α, etc. (35, 36). Th1 and Th2 cells are a kind of helper T cells, the former is involved in cellular immunity and mainly secretes IFN- γ (37), while the latter is mainly involved in humoral immunity and secretes cytokines such as IL-4 (38). In this study, IFN- γ was not detected or was detected at very low levels throughout the pig's life cycle, suggesting that NK cells and T cells that may secrete IFN-γ fail to activate effectively. IFN- γ plays an important role in defense against ASFV infection but is not the only indicator of the rate of protection generated. In immunization with certain deletion strains, IFN- γ levels were not elevated, but they were able to resist attack by their original strong strains (39–42). Certain weak strains infecting domestic pigs failed to protect against strong strains when IFN- γ levels were elevated (39, 42, 43). Although P30 antibody was not detected in the morbid pigs of this study, IL-4 levels were elevated significantly at 8 dpi in domestic pigs with a life cycle of 8 days, which is no longer able to promote antibody secretion in domestic pigs, and no significant increase in IL-4 levels was observed in domestic pigs with a life cycle of 6 days. In a study of ASFV and IL-10, a negative correlation was found between survival and IL-10 levels in domestic pigs (44). IL-10 levels remained stable in surviving pigs, while IL-10 levels increased significantly in dead pigs (24, 32, 42, 45–47). ASFV has evolved several strategies to inhibit IFN-α secretion, such as the pH240R protein that inhibits IFN-α production by disrupting STING oligomerization (48), pF778R that attenuates the I type interferon response (49). In this study, the IFN-α in the serum did not change in the early stage of infection, but the level of IFN-α increased significantly after the fever in domestic pigs. IFN-α is mainly involved in the innate immune response, and the inhibition of IFN-α secretion in the early stage of ASFV replication (50), which led to the avoidance of the innate immune response of ASFV, and then a large number of replications to infringe on the organism, and the level of IFN-α did not rise significantly until the end of life, but it was too late. IL-12 is a heterodimeric cytokine composed of two subunits, p35 and p40 (51, 52). It is mainly produced by antigen-presenting cells (APCs), especially monocytes and macrophages, in response to microbial pathogens (51, 52). There are fewer studies on the level of IL-12 changes in serum after ASFV infection. No changes in IL-12 levels were observed after ASFV-GΔ9GL/ΔUK, Netherland'86, HLJ/18-7GD, and HLJ/18 infections in domestic pigs (41, 44, 47). After SY18 infection, IL-12 levels increased rapidly (32). In this study, no significant changes in IL-12 were seen in domestic pigs with a life cycle of 8 days, whereas domestic pigs with a life cycle of 6 days showed a significant increase at 6 dpi.IL-8 is also known as CXCL8. CXCL8 is widely regarded as a potent neutrophil chemotactic agent that promotes the aggregation of neutrophils and other granulocytes to the site of infection (53). In addition, this chemokine triggers neutrophil degranulation and enhances their phagocytosis (51, 54). IL-8, similarly to IL-12, is found in varying serum levels in hosts infected with different strains. Benin97/1, OURT88/3, Pret4Δ9GL, ASFV-G-Δ9GL/ΔUK, Netherland '86 and other strains did not show significant changes in IL-8 levels after infection of the host (40, 41, 44, 55). In contrast, strains such as Armenia07, Armenia08, and SY18 showed elevated IL-8 levels after host infection (32, 56, 57). In the present study, domestic pigs with a life cycle of 6 and 8 days had the highest levels at 6 dpi. However, domestic pigs with a life cycle of 8 days had rapidly decreasing levels at 8 dpi.

Infection with the HuB/HH/2019 strain of ASFV results in an imbalance between pro- and anti-inflammatory factors, leading to a cytokine storm manifested as fever, multiple tissue swelling and hemorrhage, and organ dysfunction. Factors involved in the innate immune response were suppressed and failed to protect the pig. IL-4 was elevated in the dying phase, and IFN-γ was not detected, suggesting that humoral and cellular immunity were not effectively activated. The lack of detection of the p30 antibody and the massive reduction in lymphocytes in PBMCs seems to provide more evidence of the suppression of adaptive immunity. The combination of acute inflammation and immunosuppression results in the inability of the organism to resist ASFV, leading to a lethal outcome.

Transcriptome RNA-seq is a recently developed technology that can elucidate the pathogenic and immune mechanisms of pathogens by revealing dynamic changes in the genomes of pathogens and systematic changes in host genes during pathogen infection (58). The complement level was significantly increased at 2, 4, 6, and 8 dpi. The complement system is an important component of innate immunity, which plays an important role in antimicrobial activity and inflammation, and C1 participates in the classical activation pathway (59). The chemokine family showed a significant increase after infection. Chemokines are important mediators of acute inflammation and components in generating primary and secondary adaptive cellular and humoral immune responses. Chemokine receptors (CCR1, CCR10, CXCR1, CXCR10, and XCR1) were significantly upregulated in this study, and these receptors are expressed on the cell surface of granulocytes, T cells, plasma cells, monocytes, and macrophages, and perform functions such as lymphangiogenesis, immune cell transport, and innate and adaptive immunity (60). Chemokines (CCL2, CCL3L1, CCL4, CXCL9, CXCL10, CXCL11, and XCL1) were also significantly upregulated after infection. These chemokines mainly play a role in the migration of monocytes, Th1 cells, NK cells, macrophages, and other cells (60). Therefore, we hypothesized that genes such as complement, interleukins, chemokines, interferon modulators, T-cell receptors, B-cell receptors, SLA-like molecules, CD molecules, and immunoglobulins play important roles in resisting viral infection after HuB/HH/2019 ASFV infection in domestic pigs.

African swine fever has evolved multiple immune escape mechanisms to ensure its replication. When the viral infection is in the latent phase, innate immunity fails to effectively detect the invasion of the virus, providing a safe and effective environment for virus replication (61). When the virus is released in large quantities, on the one hand, the increase of apoptotic factors leads to a large reduction of lymphocytes (62), and on the other hand, the cells involved in antigen presentation (B-cells, DC-cells, etc.) are reduced so that lymphocytes do not recognize the antigen effectively, and the immune system is not able to defend against the virus, which ultimately leads to lethal results (27). African swine fever mainly infects the monocyte/macrophage system (63) and does not infect lymphocytes, but lymphocytes in infected pigs die in large numbers (28), suggesting that lymphocyte apoptosis is indirectly rather than directly affected by African swine fever. TNF-α has an apoptotic effect, and some articles report that the apoptosis of lymphocytes is affected by TNF-α (62). Therefore, the dramatic increase in inflammatory and pro-apoptotic factors secreted by macrophages infected with African swine fever virus is an important cause of the cytokine storm and lymphocytopenia.

Data availability statement

The datasets presented in this study can be found in online repositories. The names of the repository/repositories and accession number(s) can be found below: PRJNA1054340 (SRA).

Ethics statement

The animal studies were approved by Animal Welfare Ethics Committee of the China Institute of Veterinary Drug Control, China Institute of Veterinary Drug Control. The studies were conducted in accordance with the local legislation and institutional requirements. Written informed consent was obtained from the owners for the participation of their animals in this study.

Author contributions

XZZ: Writing – original draft, Writing – review & editing. GP: Writing – original draft, Writing – review & editing. JZ: Writing – original draft, Writing – review & editing. QZ: Writing – original draft, Writing – review & editing. YZ: Writing – original draft, Writing – review & editing. YX: Writing – original draft, Writing – review & editing. LX: Writing – original draft, Writing – review & editing. FL: Writing – original draft, Writing – review & editing. YJX: Writing – original draft, Writing – review & editing. YL: Writing – original draft, Writing – review & editing. CW: Writing – original draft, Writing – review & editing. ZW: Writing – original draft. HW: Writing – original draft, Writing – review & editing. XQZ: Writing – original draft, Writing – review & editing.

Funding

The author(s) declare financial support was received for the research, authorship, and/or publication of this article. This work was funded by the National Key Research and Development Program of China (2021YFD1800105), the Earmarked Fund for Modern Agro-industry Technology Research System (No. 2023CYJSTX12-05), the "SixNew" Project of Agriculture and Rural Department of Shanxi Province, and the Fund for Shanxi "1331 Project" Key Innovative Research Team (No. 20211331-12, 20211331-16), the Fund for Shanxi Provincial Key Research and Development Program (No. 202102140601020).

Acknowledgments

We thank Shanxi Agricultural University and the Biosafety Level III Laboratory of China Veterinary Drug Inspection Institute for their support toward the completion of this study.

Conflict of interest

The authors declare that the research was conducted in the absence of any commercial or financial relationships that could be construed as a potential conflict of interest.

Publisher's note

All claims expressed in this article are solely those of the authors and do not necessarily represent those of their affiliated organizations, or those of the publisher, the editors and the reviewers. Any product that may be evaluated in this article, or claim that may be made by its manufacturer, is not guaranteed or endorsed by the publisher.

Supplementary material

The Supplementary Material for this article can be found online at: https://www.frontiersin.org/articles/10.3389/fimmu.2024.1361531/full#supplementary-material

References

1. Wang N, Zhao D, Wang J, Zhang Y, Wang M, Gao Y, et al. Architecture of African swine fever virus and implications for viral assembly. *Science.* (2019) 366:640–4. doi: 10.1126/science.aaz1439

2. Alejo A, Matamoros T, Guerra M, Andrés G. A proteomic atlas of the African swine fever virus particle. *J Virol.* (2018) 92:10.1128/jvi.01293-18. doi: 10.1128/JVI.01293-18

3. Bastos AD, Penrith ML, Crucière C, Edrich JL, Hutchings G, Roger F, et al. Genotyping field strains of African swine fever virus by partial p72 gene characterisation. *Arch Virol.* (2003) 148:693–706. doi: 10.1007/s00705-002-0946-8

4. Quembo CJ, Jori F, Vosloo W, Heath L. Genetic characterization of African swine fever virus isolates from soft ticks at the wildlife/domestic interface in Mozambique and identification of a novel genotype. *Transbound Emerg Dis.* (2018) 65:420–31. doi: 10.1111/tbed.12700

5. Yu L, Zhu Z, Deng J, Tian K, Li X. Antagonisms of ASFV towards host defense mechanisms: knowledge gaps in viral immune evasion and pathogenesis. *Viruses.* (2023) 15(2):574. doi: 10.3390/v15020574

6. Yang K, Xue Y, Niu H, Shi C, Cheng M, Wang J, et al. African swine fever virus MGF360-11L negatively regulates cGAS-STING-mediated inhibition of Type I interferon production. *Vet Res.* (2022) 53:7. doi: 10.1186/s13567-022-01025-0

7. Wang Y, Cui S, Xin T, Wang X, Yu H, Chen S, et al. African swine fever virus MGF360-14L negatively regulates Type I interferon signaling by targeting IRF3. *Front Cell Infect Microbiol.* (2021) 11:818969. doi: 10.3389/fcimb.2021.818969

8. Huang L, Xu W, Liu H, Xue M, Liu X, Zhang K, et al. African swine fever virus pI215L negatively regulates cGAS-STING signaling pathway through recruiting RNF138 to inhibit K63-linked ubiquitination of TBK1. *J Immunol.* (2021) 207:2754–69. doi: 10.4049/jimmunol.2100320

9. Riera E, Pérez-Núñez D, García-Belmonte R, Miorin L, García-Sastre A, Revilla Y. African swine fever virus induces STAT1 and STAT2 degradation to counteract IFN-I signaling. *Front Microbiol.* (2021) 12:722952. doi: 10.3389/fmicb.2021.722952

10. Zhang K, Yang B, Shen C, Zhang T, Hao Y, Zhang D, et al. MGF360-9L is a major virulence factor associated with the African swine fever virus by antagonizing the JAK/STAT signaling pathway. *mBio.* (2022) 13:e0233021. doi: 10.1128/mbio.02330-21

11. Liu X, Ao D, Jiang S, Xia N, Xu Y, Shao Q, et al. African swine fever virus A528R inhibits TLR8 mediated NF-κB activity by targeting p65 activation and nuclear translocation. *Viruses.* (2021) 13(10):2046. doi: 10.3390/v13102046

12. Zhuo Y, Guo Z, Ba T, Zhang C, He L, Zeng C, et al. African swine fever virus MGF360-12L inhibits Type I interferon production by blocking the interaction of importin α and NF-κB signaling pathway. *Virol Sin.* (2021) 36:176–86. doi: 10.1007/s12250-020-00304-4

13. Barber C, Netherton C, Goatley L, Moon A, Goodbourn S, Dixon L. Identification of residues within the African swine fever virus DP71L protein required for dephosphorylation of translation initiation factor eIF2α and inhibiting activation of pro-apoptotic CHOP. *Virology.* (2017) 504:107–13. doi: 10.1016/j.virol.2017.02.002

14. Powell PP, Dixon LK, Parkhouse RM. An IkappaB homolog encoded by African swine fever virus provides a novel mechanism for downregulation of proinflammatory cytokine responses in host macrophages. *J Virol.* (1996) 70:8527–33. doi: 10.1128/JVI.70.12.8527-8533.1996

15. Miskin JE, Abrams CC, Dixon LK. African swine fever virus protein A238L interacts with the cellular phosphatase calcineurin via a binding domain similar to that of NFAT. *J Virol.* (2000) 74:9412–20. doi: 10.1128/jvi.74.20.9412-9420.2000

16. Ding M, Dang W, Liu H, Xu F, Huang H, Sunkang Y, et al. Combinational deletions of MGF360-9L and MGF505-7R attenuated highly virulent African swine fever virus and conferred protection against homologous challenge. *J Virol.* (2022) 96: e0032922. doi: 10.1128/jvi.00329-22

17. Gladue DP, Ramirez-Medina E, Vuono E, Silva E, Rai A, Pruitt S, et al. Deletion of the A137R gene from the pandemic strain of African swine fever virus attenuates the strain and offers protection against the virulent pandemic virus. *J Virol.* (2021) 95: e0113921. doi: 10.1128/JVI.01139-21

18. Ramirez-Medina E, Vuono E, Pruitt S, Rai A, Espinoza N, Valladares A, et al. ASFV gene A151R is involved in the process of virulence in domestic swine. *Viruses.* (2022) 14(8):1834. doi: 10.3390/v14081834

19. Takamatsu HH, Denyer MS, Lacasta A, Stirling CM, Argilaguet JM, Netherton CL, et al. Cellular immunity in ASFV responses. *Virus Res.* (2013) 173:110–21. doi: 10.1016/j.virusres.2012.11.009

20. Reed LJ, Muench H. A simple method of estimating fifty per cent endpoints. *Am J Epidemiol.* (1938) 27:493–7. doi: 10.1093/oxfordjournals.aje.a118408

21. Gallardo C, Soler A, Nurmoja I, Cano-Gómez C, Cvetkova S, Frant M, et al. Dynamics of African swine fever virus (ASFV) infection in domestic pigs infected with virulent, moderate virulent and attenuated genotype II ASFV European isolates. *Transbound Emerg Dis.* (2021) 68:2826–41. doi: 10.1111/tbed.14222

22. Zuo X, Peng G, Xia Y, Xu L, Zhao Q, Zhu Y, et al. A quadruple fluorescence quantitative PCR method for the identification of wild strains of african swine fever and gene-deficient strains. *Virol J.* (2023) 20:150. doi: 10.1186/s12985-023-02111-1

23. Guinat C, Reis AL, Netherton CL, Goatley L, Pfeiffer DU, Dixon L. Dynamics of African swine fever virus shedding and excretion in domestic pigs infected by intramuscular inoculation and contact transmission. *Vet Res.* (2014) 45:93. doi: 10.1186/s13567-014-0093-8

24. Reis AL, Abrams CC, Goatley LC, Netherton C, Chapman DG, Sanchez-Cordon P, et al. Deletion of African swine fever virus interferon inhibitors from the genome of a virulent isolate reduces virulence in domestic pigs and induces a protective response. *Vaccine.* (2016) 34:4698–705. doi: 10.1016/j.vaccine.2016.08.011

25. Sánchez-Cordón PJ, Jabbar T, Chapman D, Dixon LK, Montoya M. Absence of long-term protection in domestic pigs immunized with attenuated african swine fever virus isolate OURT88/3 or BeninΔMGF correlates with increased levels of regulatory T cells and interleukin-10. *J Virol.* (2020) 94:10.1128/jvi.00350-20. doi: 10.1128/JVI.00350-20

26. Ge S, Li J, Fan X, Liu F, Li L, Wang Q, et al. Molecular characterization of African swine fever virus, China, 2018. *Emerg Infect Dis.* (2018) 24:2131–3. doi: 10.3201/eid2411.181274

27. Franzoni G, Dei Giudici S, Oggiano A. Infection, modulation and responses of antigen-presenting cells to African swine fever viruses. *Virus Res.* (2018) 258:73–80. doi: 10.1016/j.virusres.2018.10.007

28. Oura CA, Powell PP, Parkhouse RM. African swine fever: a disease characterized by apoptosis. *J Gen Virol.* (1998) 79:1427–38. doi: 10.1099/0022-1317-79-6-1427

29. Becher B, Spath S, Goverman J. Cytokine networks in neuroinflammation. *Nat Rev Immunol.* (2017) 17:49–59. doi: 10.1038/nri.2016.123

30. Altan-Bonnet G, Mukherjee R. Cytokine-mediated communication: a quantitative appraisal of immune complexity. *Nat Rev Immunol.* (2019) 19:205–17. doi: 10.1038/s41577-019-0131-x

31. Garber K. Cytokine resurrection: engineered IL-2 ramps up immuno-oncology responses. *Nat Biotechnol.* (2018) 36:378–9. doi: 10.1038/nbt0518-378

32. Wang S, Zhang J, Zhang Y, Yang J, Wang L, Qi Y, et al. Cytokine storm in domestic pigs induced by infection of virulent african swine fever virus. *Front Vet Sci.* (2020) 7:601641. doi: 10.3389/fvets.2020.601641

33. Fajgenbaum DC, June CH. Cytokine storm. *N Engl J Med.* (2020) 383:601641. doi: 10.3389/fvets.2020.601641

34. Lai J, Wu H, Qin A. Cytokines in febrile diseases. *J Interferon Cytokine Res.* (2021) 41:1–11. doi: 10.1089/jir.2020.0213

35. Bennett IL, Beeson PB. The properties and biologic effects of bacterial pyrogens. *Medicine.* (1950) 29:365–400. doi: 10.1097/00005792-195012000-00003

36. Beeson PB. Temperature-elevating effect of a substance obtained from polymorphonuclear leucocytes. *J Clin Invest.* (1948) 27:524. doi: 10.1084/jem.103.5.589

37. Kalinski P, Wieckowski E, Muthuswamy R, de Jong E. Generation of stable Th1/CTL-, Th2-, and Th17-inducing human dendritic cells. *Methods Mol Biol.* (2010) 595:117–33. doi: 10.1007/978-1-60761-421-0_7

38. Moschovakis GL, Bubke A, Dittrich-Breiholz O, Braun A, Prinz I, Kremmer E, et al. Deficient CCR7 signaling promotes TH2 polarization and B-cell activation in vivo. *Eur J Immunol.* (2012) 42:48–57. doi: 10.1002/eji.201141753

39. Sánchez-Cordón PJ, Jabbar T, Berrezaie M, Chapman D, Reis A, Sastre P, et al. Evaluation of protection induced by immunisation of domestic pigs with deletion mutant African swine fever virus BeninΔMGF by different doses and routes. *Vaccine.* (2018) 36:707–15. doi: 10.1016/j.vaccine.2017.12.030

40. Carlson J, O'Donnell V, Alfano M, Velazquez Salinas L, Holinka LG, Krug PW, et al. Association of the host immune response with protection using a live attenuated african swine fever virus model. *Viruses.* (2016) 8(10):291. doi: 10.3390/v8100291

41. O'Donnell V, Risatti GR, Holinka LG, Krug PW, Carlson J, Velazquez-Salinas L, et al. Simultaneous deletion of the 9GL and UK genes from the african swine fever virus Georgia 2007 isolate offers increased safety and protection against homologous challenge. *J Virol.* (2017) 91:10.1128/jvi.01760-16. doi: 10.1128/JVI.01760-16

42. Sánchez-Cordón PJ, Chapman D, Jabbar T, Reis AL, Goatley L, Netherton CL, et al. Different routes and doses influence protection in pigs immunised with the naturally attenuated African swine fever virus isolate OURT88/3. *Antiviral Res.* (2017) 138:1–8. doi: 10.1016/j.antiviral.2016.11.021

43. Karalyan Z, Zakaryan H, Sargsyan K, Voskanyan H, Arzumanyan H, Avagyan H, et al. Interferon status and white blood cells during infection with African swine fever virus in vivo. *Veterinary Immunol immunopathology.* (2012) 145:551–5. doi: 10.1016/j.vetimm.2011.12.013

44. Post J, Weesendorp E, Montoya M, Loeffen WL. Influence of age and dose of african swine fever virus infections on clinical outcome and blood parameters in pigs. *Viral Immunol.* (2017) 30:58–69. doi: 10.1089/vim.2016.0121

45. Reis AL, Goatley LC, Jabbar T, Sanchez-Cordon PJ, Netherton CL, Chapman DAG, et al. Deletion of the African Swine Fever Virus Gene DP148R Does Not Reduce Virus Replication in Culture but Reduces Virus Virulence in Pigs and Induces High Levels of Protection against Challenge. *J Virol.* (2017) 91:10.1128/jvi.01428-17. doi: 10.1128/JVI.01428-17

46. Reis AL, Goatley LC, Jabbar T, Lopez E, Rathakrishnan A, Dixon LK. Deletion of the gene for the type I interferon inhibitor I329L from the attenuated african swine fever virus OURT88/3 strain reduces protection induced in pigs. *Vaccines.* (2020) 8 (2):262. doi: 10.3390/vaccines8020262

47. Fan Y, Chen W, Jiang C, Zhang X, Sun Y, Liu R, et al. Host responses to live-attenuated ASFV (HLJ/18-7GD). *Viruses*. (2022) 14(9):2003. doi: 10.3390/v14092003

48. Ye G, Liu H, Liu X, Chen W, Li J, Zhao D, et al. African swine fever virus H240R protein inhibits the production of type I interferon through disrupting the oligomerization of STING. *J Virol*. (2023) 97:e0057723. doi: 10.1128/jvi.00577-23

49. Chen Q, Li L, Liu L, Liu Z, Guo S, Tan C, et al. African swine fever virus pF778R attenuates type I interferon response by impeding STAT1 nuclear translocation. *Virus Res*. (2023) 335:199190. doi: 10.1016/j.virusres.2023.199190

50. Fan W, Jiao P, Zhang H, Chen T, Zhou X, Qi Y, et al. Inhibition of african swine fever virus replication by porcine type I and type II interferons. *Front Microbiol*. (2020) 11:1203. doi: 10.3389/fmicb.2020.01203

51. Arango Duque G, Descoteaux A. Macrophage cytokines: involvement in immunity and infectious diseases. *Front Immunol*. (2014) 5:491. doi: 10.3389/fimmu.2014.00491

52. Vignali DA, Kuchroo VK. IL-12 family cytokines: immunological playmakers. *Nat Immunol*. (2012) 13:722–8. doi: 10.1038/ni.2366

53. Comerford I, McColl SR. Mini-review series: focus on chemokines. *Cell Immunol*. (2011) 89:183–4. doi: 10.1038/icb.2010.164

54. Beste MT, Lomakina EB, Hammer DA, Waugh RE. Immobilized IL-8 triggers phagocytosis and dynamic changes in membrane microtopology in human neutrophils. *Ann Biomed Eng*. (2015) 43:2207–19. doi: 10.1007/s10439-014-1242-y

55. Fishbourne E, Hutet E, Abrams C, Cariolet R, Le Potier MF, Takamatsu HH, et al. Increase in chemokines CXCL10 and CCL2 in blood from pigs infected with high compared to low virulence African swine fever virus isolates. *Vet Res*. (2013) 44:87. doi: 10.1186/1297-9716-44-87

56. Zakaryan H, Cholakyans V, Simonyan L, Misakyan A, Karalova E, Chavushyan A, et al. A study of lymphoid organs and serum proinflammatory cytokines in pigs infected with African swine fever virus genotype II. *Arch Virol*. (2015) 160:1407–14. doi: 10.1007/s00705-015-2401-7

57. Radulovic E, Mehinagic K, Wüthrich T, Hilty M, Posthaus H, Summerfield A, et al. The baseline immunological and hygienic status of pigs impact disease severity of African swine fever. *PloS Pathog*. (2022) 18:e1010522. doi: 10.1371/journal.ppat.1010522

58. Yang B, Shen C, Zhang D, Zhang T, Shi X, Yang J, et al. Mechanism of interaction between virus and host is inferred from the changes of gene expression in macrophages infected with African swine fever virus CN/GS/2018 strain. *Virol J*. (2021) 18:170. doi: 10.1186/s12985-021-01637-6

59. Mortensen SA, Sander B, Jensen RK, Pedersen JS, Golas MM, Jensenius JC, et al. Structure and activation of C1, the complex initiating the classical pathway of the complement cascade. *Proc Natl Acad Sci U.S.A*. (2017) 114:986–91. doi: 10.1073/pnas.1616998114

60. Griffith JW, Sokol CL, Luster AD. Chemokines and chemokine receptors: Positioning cells for host defense and immunity. *Annu Rev Immunol*. (2014) 32:659–702. doi: 10.1146/annurev-immunol-032713-120145

61. He WR, Yuan J, Ma YH, Zhao CY, Yang ZY, Zhang Y, et al. Modulation of host antiviral innate immunity by african swine fever virus: A review. *Anim (Basel)*. (2022) 12:21. doi: 10.3390/ani12212935

62. Gómez del Moral M, Ortuño E, Fernández-Zapatero P, Alonso F, Alonso C, Ezquerra A, et al. African swine fever virus infection induces tumor necrosis factor alpha production: implications in pathogenesis. *J Virol*. (1999) 73:2173–80. doi: 10.1128/JVI.73.3.2173-2180.1999

63. Carrillo C, Borca MV, Afonso CL, Onisk DV, Rock DL. Long-term persistent infection of swine monocytes/macrophages with African swine fever virus. *J Virol*. (1994) 68:580–3. doi: 10.1128/JVI.68.1.580-583.1994

Frontiers in Immunology

TYPE Original Research
PUBLISHED 23 May 2024
DOI 10.3389/fimmu.2024.1352404

Check for updates

OPEN ACCESS

EDITED BY
Wei Wang,
Wenzhou University, China

REVIEWED BY
Matthew G. Brewer,
University of Rochester Medical Center,
United States
Tao Lin,
Elpiscience, China

*CORRESPONDENCE
Jing Wang
jingw_biomed@163.com
Yaojiang Huang
yaojiang@muc.edu.cn
Yuanqiang Zheng
zhengyq688@163.com

†These authors have contributed equally to this work and share first authorship

RECEIVED 08 December 2023
ACCEPTED 06 May 2024
PUBLISHED 23 May 2024

CITATION
Fan R, Wei Z, Zhang M, Jia S, Jiang Z, Wang Y, Cai J, Chen G, Xiao H, Wei Y, Shi Y, Feng J, Shen B, Zheng Y, Huang Y and Wang J (2024) Development of novel monoclonal antibodies for blocking NF-κB activation induced by CD2v protein in African swine fever virus. *Front. Immunol.* 15:1352404. doi: 10.3389/fimmu.2024.1352404

COPYRIGHT
© 2024 Fan, Wei, Zhang, Jia, Jiang, Wang, Cai, Chen, Xiao, Wei, Shi, Feng, Shen, Zheng, Huang and Wang. This is an open-access article distributed under the terms of the Creative Commons Attribution License (CC BY). The use, distribution or reproduction in other forums is permitted, provided the original author(s) and the copyright owner(s) are credited and that the original publication in this journal is cited, in accordance with accepted academic practice. No use, distribution or reproduction is permitted which does not comply with these terms.

Development of novel monoclonal antibodies for blocking NF-κB activation induced by CD2v protein in African swine fever virus

Rongrong Fan[1,2†], Zeliang Wei[1,3,4†], Mengmeng Zhang[5†], Shanshan Jia[1†], Zhiyang Jiang[1], Yao Wang[3], Junyu Cai[1,4], Guojiang Chen[1], He Xiao[1], Yinxiang Wei[4], Yanchun Shi[3], Jiannan Feng[1], Beifen Shen[1], Yuanqiang Zheng[3*], Yaojiang Huang[2*] and Jing Wang[1*]

[1]Laboratory for Genetic Engineering of Antibodies and Functional Proteins, Beijing Institute of Pharmacology and Toxicology, Beijing, China, [2]Beijing Engineering Research Center of Food Environment and Public Health, Minzu University of China, Beijing, China, [3]Inner Mongolia Key Laboratory of Molecular Biology, Inner Mongolia Medical University, Hohhot, China, [4]Joint National Laboratory for Antibody Drug Engineering, The First Affiliated Hospital of Henan University, Henan University, Kaifeng, China, [5]BCA Bio-Breeding Center, Beijing Capital Agribusiness Co., Ltd., Beijing, China

Background: CD2v, a critical outer envelope glycoprotein of the African swine fever virus (ASFV), plays a central role in the hemadsorption phenomenon during ASFV infection and is recognized as an essential immunoprotective protein. Monoclonal antibodies (mAbs) targeting CD2v have demonstrated promise in both diagnosing and combating African swine fever (ASF). The objective of this study was to develop specific monoclonal antibodies against CD2v.

Methods: In this investigation, Recombinant CD2v was expressed in eukaryotic cells, and murine mAbs were generated through meticulous screening and hybridoma cloning. Various techniques, including indirect enzyme-linked immunosorbent assay (ELISA), western blotting, immunofluorescence assay (IFA), and bio-layer interferometry (BLI), were employed to characterize the mAbs. Epitope mapping was conducted using truncation mutants and epitope peptide mapping.

Results: An optimal antibody pair for a highly sensitive sandwich ELISA was identified, and the antigenic structures recognized by the mAbs were elucidated. Two linear epitopes highly conserved in ASFV genotype II strains, particularly in Chinese endemic strains, were identified, along with a unique glycosylated epitope. Three mAbs, 2B25, 3G25, and 8G1, effectively blocked CD2v-induced NF-κB activation.

Conclusions: This study provides valuable insights into the antigenic structure of ASFV CD2v. The mAbs obtained in this study hold great potential for use in the development of ASF diagnostic strategies, and the identified epitopes may contribute to vaccine development against ASFV.

KEYWORDS

ASFV-CD2v, eukaryotic expression, monoclonal antibodies, glycosylation, NF-κB, epitope

1 Introduction

Both wild and domestic pigs are susceptible to African swine fever (ASF), a highly contagious and fatal disease caused by the African swine fever virus (ASFV) (1, 2). ASFV causes acute hemorrhagic fever in these hosts, with a mortality rate of up to 100% (3). Despite extensive research efforts, there is no effective vaccine against the disease. ASFV was first reported in Kenya in the 1920s (4), and genotype II then emerged in Georgia in 2007, spreading to the Russian Federation and Eastern Europe (5–7). In 2018, ASFV spread to China, world's largest producer of pigs, and subsequently to other Asian countries, resulting in economic losses of approximately USD 111.2 billion in 2019 (8, 9). ASF has become widespread globally, inflicting significant economic losses on the global swine industry (10).

ASFV belongs to the ASFV genus, which consists of a single species. Its genome ranges between 170 and 193 kilobase pairs (11–14) and encodes 68 structural proteins and over 100 non-structural proteins (15, 16). The virions have an icosahedral shape with a multilayer structure, including an internal core, internal lipid

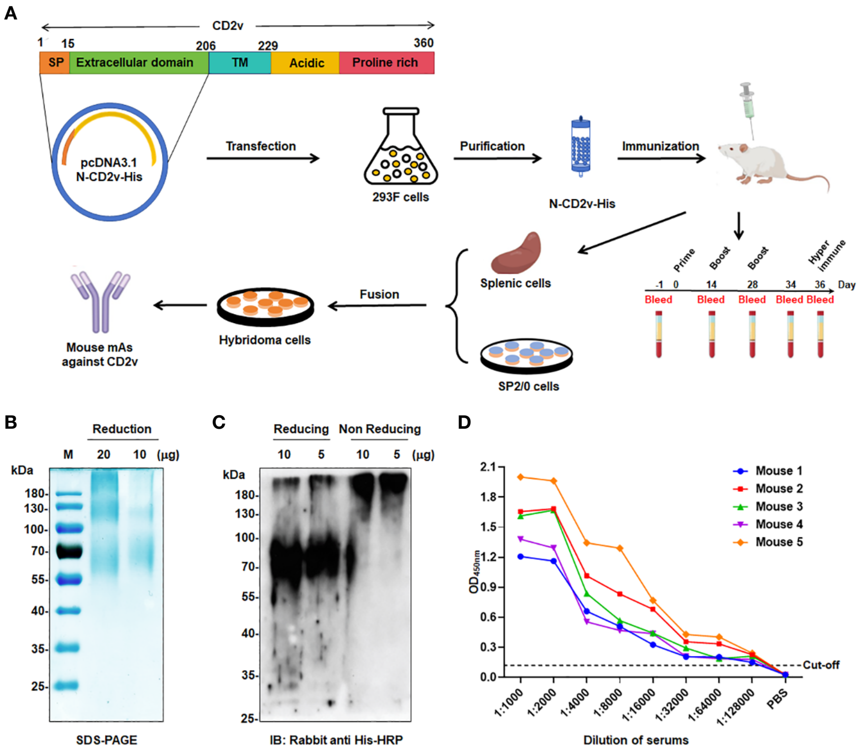

FIGURE 1
Generation of mAbs against ASFV-CD2v protein. **(A)** Schematic representation of the generation process for anti-CD2v mAbs. **(B)** SDS-PAGE analysis of purified recombinant N-CD2v-His protein in a 12% gel. **(C)** Western blotting of N-CD2v-His protein using anti-6×His tag antibody, under reducing or non-reducing conditions. **(D)** Indirect ELISA of the serum titers of five mice immunized with N-CD2v-His, with the serum of unimmunized mice serving as the negative control. The cut-off values were calculated based on the mean+3 SD of the optical density (OD) value of the negative control.

membrane, icosahedral capsid, and outer lipid envelope (10). In harsh environments and under protein-rich conditions, it is sufficient for long-term survival (17). However, the limited understanding of the functions of most of the ASFV proteins has hindered vaccine development. Due to the absence of available vaccines or treatments, the current control measures primarily involve strict quarantine and biosecurity practices, which heavily restrict animal movement and require the slaughter of affected animals.

EP402R encodes the CD2v protein, which is similar to the CD2 protein in the host (18). CD2v is composed of a signal peptide, a transmembrane region, two immunoglobulin-like domains, and a variable number of proline-rich repeats in the cytoplasmic domain (Figure 1A). As a glycoprotein (gp110–140), CD2v is inserted into the outer lipid envelope and it is the only viral protein that can be detected on the surface of extracellular virions. During the late stage of infection, CD2v is highly expressed and its extracellular domain acts as a key mediator in the hemadsorption process, thereby facilitating viral transport and evasion of the immune system (19–21). CD2v interacts with two adaptor proteins, clathrin adaptor protein 1 (AP-1) (22) and actin-binding adaptor protein (DBNL, also known as SH3P7) (23). Through these interactions, cellular transport mechanisms can be modified, contributing to Golgi reorganization. Additionally, CD2v hinders the translocation of STING from the endoplasmic reticulum to the Golgi body, thereby preventing STING activation (24). CD2v establishes interactions with surrounding lymphocytes and macrophages via lymphocyte function-associated antigen-3 (LFA-3/CD58), promoting the activation of nuclear factor (NF)-κB. This activation subsequently upregulates interferon (IFN)-β and IFN-stimulated genes (ISGs), such as 2'5'-oligoadenylate synthetase (OAS) proteins, while also potentially activating other intrinsic or extrinsic apoptotic pathways, ultimately leading to the apoptosis of lymphocytes and macrophages (25).

CD2v is an immunoprotective antigen that has been identified as crucial in the context of ASFV. It plays a significant role in inducing serotype-specific cross-protective immunity and contributes to the mediation of serological specificity through hemagglutination inhibition (21, 26, 27). Research using various virus models has provided valuable insights into the role of CD2v in virulence and immunoprotection (28, 29). Notably, some ASFV strains possess truncated or interrupted *EP402R* genes, resulting in the loss of their hemadsorption ability, and they often exhibit an attenuated phenotypic profile and have been utilized as a promising model for vaccine research (30). Despite the induction of specific antibodies and cellular immunity by viral vaccines, achieving optimal immunoprotection in pigs remains an unresolved challenge (31–33).

In recent years, the development of monoclonal antibodies (mAbs) targeting linear epitopes of CD2v has made progress, though their bioactivity has not been evaluated extensively (Table 1) (34–38). Hence, we opted for the Expi293F eukaryotic expression system to express the recombinant N-CD2v-His protein (extracellular region of CD2v), as it offers superior post-translational modifications, particularly glycosylation, ensuring that the antigens expressed closely resemble the *in vivo* structure of CD2v (Figure 1A). As a result, we successfully generated three specific mAbs with a high affinity, as indicated in Table 2. These mAbs displayed strong reactivity towards glycosylated and/or deglycosylated CD2v. Additionally, we established a highly sensitive sandwich ELISA configuration. Furthermore, our study identified two conserved

TABLE 1 Identification of B-cell epitopes on ASFV-CD2v protein.

ASFV strain	Antigen structure	Expression system	B-cell epitopes	Experiment	Ref.
China/2018/Anhui XCGQ strain (GenBank: MK128995.1)	CD2v dimeric protein with His tag	Baculovirus expression system in Sf21 cells	^{147}FVKYT^{151} ^{157}EYNWN^{161} ^{195}SSNY^{198}	I-ELISA, Dot-ELISA	(34)
ASFV-SY18 strain (GenBank: MH766894)	CD2v fused with Norovirus P particle assembled into nanoparticle	HEK293F cells	^{28}LDSNITNDNNDINGVSWNFFNNSF^{51}	IFA	(35)
China/2018/Anhui XCGQ strain (GenBank: MK128995.1)	CD2v extracellular domain with C-terminal His tag	CHO-S cells	^{128}TCKKNNGTNT^{137} ^{148}VKYTNESILE^{157}	I-ELISA, Dot-ELISA	(36)
China/2018/Anhui XCGQ strain (GenBank: MK128995.1)	CD2v extracellular domain with C-terminal 6×His tag	Eukaryotic expression system	^{38}DINGVSWN^{45} ^{134}GTNTNIY^{140}	I-ELISA, Dot-ELISA	(37)
ASFV-SY18 strain (GenBank accession MH766894)	CD2v extracellular domain	HEK293F cells	^{154}SILEYNW^{160} ^{154}SILE^{157}	Dot-blot; Peptide-based ELISA	(38)
ASFV Georgia 2007/1 strain (GenBank: NC044959)	NA	NA	^{160}WNNSNINNFT^{169}	Bioinformatics prediction, Dot-ELISA	(39)
ASFV Pig/HLJ/2018 strain (GenBank ID MK333180.1)	CD2v intracellular region with N-terminal 6×His tag	Prokaryotic expression system	^{264}EPSPREP^{270}	ELISA, Dot-blot	(40)

NA, not applicable.

TABLE 2 Summary of anti-CD2v mAbs generated in this study.

mAb	Western blotting		IFA	ELISA	Epitope region	K_D (nM)	NF-κB blocking activity
	Glyco	deGlyco					
2B25	+	–	+	+	AA16–48*	15.4	+
3J25	+	+	+	+	^{25}TIILDSNITNDNN^{37}	9.94	+
8G1	+	+	+	+	^{141}LNINDTFVKYTNE^{153}	23.5	+

Glyco, glycosylation; deGlyco, deglycosylation; AA, amino acid; +, positive; –, negative.
*, glycosylated epitope.

linear B-cell epitopes, along with a unique glycosylated epitope. Most importantly, our findings demonstrated that the identified mAbs effectively blocked CD2v-induced NF-κB activation.

Taken together, our results demonstrate that mAbs have significant potential as valuable tools for conducting ASFV CD2v structure–function studies, and other applications. Moreover, our results provide a foundation for the development of novel ASFV diagnostic reagents and therapeutic strategies.

2 Materials and methods

2.1 Cell lines, plasmids, and animals

Human embryonic kidney 293T (HEK293T) cells, porcine kidney cells (PK15), and Sp2/0 myeloma cells were obtained from the American Type Culture Collection (ATCC, USA). The HEK293T cells were incubated in Dulbecco's modified eagle medium (DMEM), supplemented with 10% fetal bovine serum (FBS) (Gibco, USA). The HEK293T and PK15 cells were maintained at 37°C with 5% CO_2. The eukaryotic expression plasmid pcDNA3.1-CD2v-HA containing a hemagglutinin (HA)-tagged full-length coding sequence of the *EP402R* gene (encoding CD2v) from the ASFV SY-1 strain (GenBank: OM161110.1; Chinese strain; genotype II ASFV) was obtained from GenScript Biotech Co, Ltd. (Nanjing, China). The pEGFP-N1-CD2v-GFP plasmid containing a green fluorescent protein (GFP)-tagged full-length coding sequence of the *EP402R* gene was constructed by our laboratory based on pcDNA3.1-CD2v-HA. From Beijing Vital River Laboratory Animal Technology Co., Ltd (Beijing, China), we purchased female specific-pathogen-free BALB/c mice. The animal experiments were conducted in accordance with national guidelines and were approved by the Ethics Committee of the Academy of Beijing Institute of Pharmacology and Toxicology (IACUC-DWZX-2021–621).

2.2 Main reagents

We purchased restriction endonucleases *Xba*I and *Not*I from New England Biolabs Inc. (USA). Roswell Park Memorial Institute (RPMI) 1640 medium, DMEM, MEM, hypoxanthine–aminopterin–thymidine (HAT) selective medium, An Expi293 expression system kit (including Expi293F cells, Expi293 expression medium, ExpiFectamine 293 transfection kit, and Opti-MEM I antiserum medium), Alexa 594-labeled Goat anti-mouse IgG, and mouse IgG (mIgG) as the isotype control, etc. were purchased from Thermo Fisher Scientific (USA). Freund's complete adjuvant, Freund's incomplete adjuvant, tunicamycin, and Triton X-100 were purchased from Sigma-Aldrich (USA). Enhanced chemiluminescence (ECL) solution was purchased from Cytiva Co., Ltd. (USA). Radioimmunoprecipitation assay (RIPA) cell lysis buffer was purchased from Solarbio technology Co., Ltd, (Beijing, China). Human and mouse CD2 with His tag (hCD2-His and mCD2-His) were purchased from ACROBiosystems (USA). Recombinant ASFV-P30, P72 and pp62 protein with His tag were sourced from East-Mab Bio Technology (Suzhou, China). Rabbit anti-6×HA tag antibody was purchased from R&D Systems (USA). Rabbit anti-His tag antibody was purchased from Abcam (USA). Horseradish peroxidase (HRP)-labeled goat anti-mouse and anti-rabbit IgG secondary antibodies and 4′,6diamidino2′phenylindole (DAPI) were purchased from ZSGB Biotechnology Co., Ltd. (Beijing, China). Rabbit antibodies against phosphorylated NF-κB p65 (p-NF-κB p65), NF-κB p65, glyceraldehyde 3-phosphate dehydrogenase (GAPDH), and β-actin were purchased from Cell Signaling Technology Inc. (USA).

2.3 Construction of eukaryotic expression plasmid expressing the CD2v extracellular domain

To construct the eukaryotic expression plasmid expressing the CD2v extracellular domain (amino acids 16–206), we amplified the target fragment using the pcDNA3.1-CD2v-HA plasmid as a template. To enhance the expression and secretion efficiency, we replaced the original signal peptide (amino acids 1–15) with a signal peptide sequence derived from IL-10 (MHSSALLCCLVLLTGVRA). Additionally, to enable convenient downstream purification, we introduced a C-terminal 6×His tag. After digestion with the *Not*I and *Xba*I restriction enzymes, the gene fragment corresponding to the CD2v extracellular domain was directly cloned into the pcDNA3.1(+) eukaryotic expression plasmid, which was designated pcDNA3.1-N-CD2v-His. The recombinant expression plasmid was verified by double enzyme digestion and sequencing.

2.4 Expression and purification of the CD2v extracellular domain fusion protein

Expression of the CD2v extracellular domain fusion protein (N-CD2v-His) was conducted following the guidelines provided in the Expi293 expression system kit (Thermo Fisher Scientific, USA). Briefly, a 50-mL cell culture was prepared in a 125-mL cell shake flask. Expi293F cells were added to the flask and diluted to a concentration of 3×10^6 cells/mL. The expression plasmid (pcDNA3.1-N-CD2v-His) and ExpiFectamine 293 transfection reagents were diluted with Opti-MEM. The transfection reagents were mixed with the diluted plasmid and added to the flask. After incubation for 18–22 h, ExpiFectamine 293 transfection enhancers were added. The cells were then cultured for an additional 5–7 days. The culture supernatant, which contained N-CD2v-His, was filtered using a 0.45-μm filter membrane. Purification of the protein was carried out using a Ni-NTA His Bind protein purification kit (GenScript Biotech Co, Ltd., Nanjing, China). Following elution, the protein was concentrated by ultrafiltration, and its concentration was determined using a bicinchoninic acid (BCA) protein concentration determination kit (Thermo Fisher Scientific, USA). Finally, the purified protein was analyzed using sodium dodecyl sulfate-polyacrylamide gel electrophoresis (SDS-PAGE), followed by detection using western blotting with a rabbit anti-His tag antibody.

2.5 Preparation of and screening for anti-CD2v mAbs

Anti-CD2v mAbs were generated following a previously described method (41). Anti-CD2v mAbs were generated as described (15). Female BALB/c mice were subcutaneously immunized with 100 μg purified N-CD2v-His protein per mouse in combination with Freund's adjuvant, followed by two biweekly booster immunizations using the same dose and incomplete adjuvant. Antibody titer in serum were measured by ELISA. Mice received a final hyperimmunization dose with 100 μg/mouse intraperitoneally, and were euthanized 3 days later. Splenocytes were fused with Sp2/0 myeloma cells using PEG 1500. Positive hybridomas were subcloned and high-producing lines were injected into mice to induce ascites. Purification was achieved using a HiTrap Protein G HP column (GE Healthcare, Cytiva, USA).

2.6 Identification of anti-CD2v mAb subclasses and isotypes

To perform mAb subclass analysis, a mouse antibody isotype detection ELISA kit (Thermo Fisher Scientific, USA) was used following the manufacturer's instructions. Hybridoma cell total RNA was isolated using an RNeasy Plus Micro Kit (QIAGEN, Germany) as instructed by the manufacturer. The isolated RNA was then reverse transcribed into cDNA using SMARTScribe Reverse Transcriptase (TaKaRa, Japan) according to the manufacturer's instructions. Heavy and light chain antibody fragments were amplified using a previously reported protocol (42) and sent to GenScript Biotech Co., Ltd. (Nanjing, China) for sequencing. The complementarity-determining region 3 (CDR3) sequences were verified using the IMGT online software (https://imgt.org/IMGT_vquest/input).

2.7 Detection of binding titers of anti-CD2v mAbs by indirect ELISA

ELISA plates were coated with 0.2 μg/well of N-CD2v-His and incubated overnight at 4°C. The plates were then blocked with 4% skim milk in PBST (PBS with 0.1% Tween-20) at 37°C for 1 hour. Gradient dilutions of purified mAbs and a negative control mouse IgG isotype were added to the wells and incubated at 37°C for 2 hours. After washing with PBST, HRP-labeled goat anti-mouse IgG secondary antibody (1:3000 dilution) was added and incubated at 37°C for 45 minutes. Tetramethylbenzidine (TMB) solution (Kangwei Century Biotechnology Co., Ltd., Beijing, China) was then added for visualization. The optical density (OD) at 450 nm was measured using an ELISA microplate reader.

2.8 Detection of mAb affinity by bio-layer interferometry

To determine the affinity of anti-CD2v mAbs, we utilized a ForteBio-Octet molecular interaction analyzer with the BLI technique. First, N-CD2v-His was immobilized onto Ni-NTA biosensors. Then, the mAbs were diluted and added to the biosensors to bind to N-CD2v-His. The binding and dissociation times were 200 and 400 s respectively. To regenerate the biosensor surfaces, a pH 1.7 solution of 10 mM Gly-HCl was applied in 5-s pulses, repeated three times. The data obtained were analyzed using a 1:1 binding model to calculate the equilibrium dissociation constant (K_D).

2.9 Detection of mAb specificity by western blotting

HEK293T cells were transfected with pcDNA3.1-CD2v-HA or empty plasmid pcDNA3.1 (control), using jetPRIME transfection reagent (Polyplus, France) for 12 h. The cells were then incubated with or without 10 μg/ml tunicamycin for 24 h (22, 43). To extract the cellular proteins, RIPA buffer containing a protease inhibitor cocktail (R&D, USA) was used for cell lysis. The protein lysates were separated by SDS-PAGE on 12% gels and transferred onto polyvinylidene fluoride (PVDF) membranes. Subsequently, the membranes were submerged in blocking buffer (5% skim milk in PBST) for 1h at 37°C, incubated with mAbs or a rabbit anti-HA tag primary antibody (positive control) at 4°C overnight, washed with PBST, and then incubated for 1 h at room temperature with HRP-labeled goat anti-rabbit IgG secondary antibody (diluted in blocking buffer). After washing with PBST again, the bound antibodies were detected using an ECL western blotting detection system.

2.10 Detection of CD2v and mAb localization by IFA

HEK293T cells were inoculated in 35mm confocal dishes (1×10^5 cells/dish). When the cells grew to about 70%

confluence, a pEGFP-N1-CD2v-GFP plasmid or an empty pEGFP-N1 plasmid (negative control) were transfected into the cells. After 36 h, 4% paraformaldehyde was added for fixation for 24 h at 4°C. Next, absorbed paraformaldehyde and dialysate (1% bovine serum albumin [BSA]+0.1% Triton X-100/PBS buffer) were added for permeabilization for 20 min at room temperature. Dialysate containing 5% goat serum was then added and incubated for 1 h at 37°C. Thereafter, 1 mg/mL of each of the selected mAbs was separately added and incubated overnight at 4°C. Alexa 594-labeled goat anti-mouse IgG secondary antibody was added and incubated at room temperature in the dark for 1 h. Next, 1 drop of DAPI was added and the fluorescence localization in cells was observed by confocal microscopy.

2.11 Competitive ELISA and sandwich ELISA

To evaluate the overlapping epitopes recognized by different anti-CD2v mAbs, competitive ELISA was conducted. The selected mAbs (2B25, 3J25, and 8G1) were biotinylated using an EZ-Link™ Sulfo-NHS-Biotinylation kit (ThermoFisher, USA). N-CD2v-His protein (0.2 µg/well) was coated onto 96-well ELISA plates overnight at 4°C. The plates were then blocked with 4% skim milk in PBST at 37°C for 1 hour. Varying concentrations (35.2 ng/mL to 36 µg/mL) of a competitor mAb (2B25, 3J25, or 8G1) and 1 µg/mL of a biotinylated detection mAb (2B25-biotin, 3J25-biotin, or 8G1-biotin) were added to each well and incubated at 37°C for 1 hour. After washing, streptavidin–HRP conjugate (1:4000 dilution, Thermo Fisher, USA) was added and incubated at 37°C for 45 minutes. TMB solution was added, and the reaction was stopped by adding H2SO4. The OD at 450 nm was measured as before.

To develop a sensitive sandwich ELISA for CD2v detection, the reactivity of the anti-CD2v mAbs as capture and detection antibodies was evaluated. Each mAb (1 µg/mL) was coated separately onto an ELISA plate. Serially diluted N-CD2v-His protein (1.9 ng/mL to 2 µg/mL) was added to the plate. After washing, each biotinylated mAb (1 µg/mL) was added to the appropriate wells. After washing again, streptavidin–HRP conjugate (1:8000 dilution in blocking buffer) was added and incubated at 37°C for 45 minutes. TMB solution was added, and the reaction was stopped using 1N H_2SO_4. The OD at 450 nm was measured.

2.12 Identification of ASFV CD2v B-cell epitopes

Based on the sequence characteristics of the CD2v extracellular region, obtained from the Swiss Model database (https://swissmodel.expasy.org), we utilized secondary structure discrimination and potential epitope prediction analysis to design, express, and purify five truncation mutants (CD2v D1–D5) of the CD2v extracellular domain. To identify the CD2v regions recognized by mAbs, we initially conducted an indirect ELISA. Based on these results, we designed 11 overlapping peptides that spanned the CD2v extracellular domain (specifically, D1 and D4). To facilitate better coupling, cysteine residues were added at the C-terminus of the shorter peptides. These peptides were synthesized and conjugated to Bovine Serum Albumin (BSA) by Chinese Peptide (Hangzhou, China), ensuring their purity was confirmed to be ≥95%. To further investigate the binding sites, a peptide-based ELISA was performed. The 96-well plates were coated with the peptides (0.1 µg/well) at 4°C overnight and then blocked with 4% skim milk at 37°C for 1 h. Each mAb (0.1 µg/well) was added separately and incubated for 37°C for 1 h. Next, an HRP-labeled goat anti-mouse IgG secondary antibody (1:3000 dilution) was added and incubated at 37°C for 45 min. Subsequently, the plates were processed following the same steps as described above for indirect ELISA. To construct the theoretical 3D structure of the CD2v extracellular domain, we used the model with the highest sequence similarity (PDB code: 2dru). The optimized model was visualized using PyMol software.

2.13 Conserved analysis of epitopes among different ASFV strains

To evaluate the conserved nature of epitope sequences among different ASFV strains, 15 Chinese epidemic strains and 27 representative globally circulating strains (comprising 5 genotypes) were selected, with strain information presented in Supplementary Table S1. The conservation of mAb-binding CD2v epitope amino acid sequences in different ASFV strains was assessed by multiple sequence alignment in Jalview v2.11.3.2 (44). A maximum likelihood phylogenetic tree was constructed based on the CD2v amino acid sequence of the 42 representative ASFV strains in MEGA v11.0 (45) and visualized utilizing ggtree v3.10.0 (46).

2.14 Impact of mAbs on the CD2v-induced activation of the NF-κB signaling pathway

In a time course experiment, PK-15 cells were incubated with 500 ng of N-CD2v-His and PBS (negative control) for 15–120 minutes to study CD2v-induced NF-κB activation. Cell lysis was performed using RIPA buffer containing a protease and phosphatase inhibitor cocktail (R&D, USA), followed by western blotting using specific rabbit primary antibodies to detect phosphorylated NF-κB p65 (p-NF-κB p65), total NF-κB p65, and the reference protein GAPDH. To assess the inhibitory activity of mAbs on CD2V-induced NF-κB signaling activation, different concentrations of each mAb (2–16 µg) were preincubated with 500 ng of N-CD2v-His protein for 30 min at 37°C. The mAb and CD2v mixture were then added to PK-15 cells and incubated for 90 min at 37°C. After cell lysis, western blotting was performed to detect phosphorylated NF-κB p65, total NF-κB p65, and the reference protein β-actin using specific rabbit primary antibodies.

2.15 Statistical analyses

Statistical analyses were conducted using Prism v8.0 (GraphPad, San Diego, CA, USA). The experimental data are presented as mean ± standard deviation (SD). Unpaired *t*-tests were used for statistical analyses, and differences were considered significant at $p < 0.05$.

3 Results

3.1 Preparation of CD2v protein and generation of four anti-CD2v mAbs

Anti-CD2v mAbs were generated using the hybridoma technique through a series of selection and cloning processes (Figure 1A; Supplementary Figure S1). Initially, the recombinant CD2v extracellular domain was purified, and then SDS-PAGE and western blotting confirmed that it was highly glycosylated, with an approximate molecular weight of 55–80 kDa, with the main band at around 70 kDa (Figures 1B, C). This is consistent with previous findings (22, 23, 43). Subsequently, five BALB/c mice were immunized with the purified protein, and serum samples were collected for antibody titer detection using indirect ELISA. The serum from all five mice exhibited high titers against the N-CD2v-His glycosylated protein, indicating strong immunogenicity (Figure 1D). Hybridoma cell lines were generated by fusing mouse splenocytes from the three mice with the highest titers with Sp2/0 cells. Initially, a total 158 hybridoma cell lines that showed affinity to CD2v were obtained. Following two rounds of subcloning, sequencing analysis, and the exclusion of clones with repetitive sequences, we carefully selected four hybridoma cell lines (2B25, 3J25, 7B1, and 8G1) based on their superior binding affinity for further investigation. The purified antibodies were identified using SDS-PAGE (Supplementary Figure S2). The isotypes of mAbs were determined to be IgG2b for 2B25 and IgG1 for the other three mAbs. Moreover, all antibodies had kappa light chains (Table 3; Supplementary Figure S3). The V gene subclasses and the CDR3 sequence for each mAb are presented in Table 3.

3.2 Preliminary analysis of binding activity of anti-CD2v mAbs and specificity to CD2v using indirect ELISA

Using indirect ELISA, the N-CD2v-His binding activity of the mAbs was confirmed. All four mAbs (2B25, 3J25, 8G1, and 7B1) showed dose-dependent binding, with half maximal effective concentration (EC_{50}) values of 33.71, 56.32, 59.23, and 539.10 ng/mL, respectively. The mouse IgG isotype control antibody exhibited no binding (Figure 2A). To assess the specificity of the four mAbs for CD2v, known for its high similarity to CD2 found in T cells (18), their binding to hCD2 and mCD2 was evaluated using ELISA. The results clearly revealed that all four mAbs specifically bound to N-CD2v-His but no binding to hCD2-His or mCD2-His (Figure 2B). Furthermore, we investigated the binding interactions of the four mAbs with ASFV structural proteins P30, P72, and pp62,

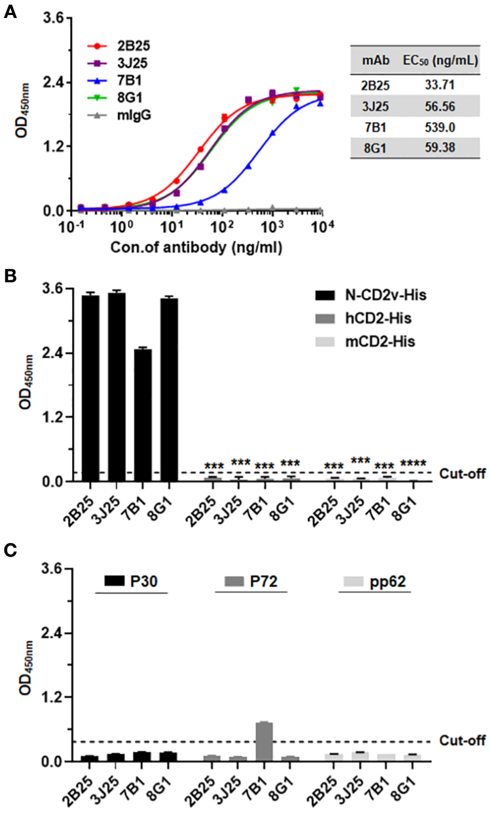

FIGURE 2
Analysis of antibody–antigen binding and specificity. **(A)** Determination of four mAbs (2B25, 3J25, 7B1, and 8G1) binding titer to N-CD2v-His by indirect ELISA. The results are presented as the mean ± SD of experiments performed in triplicate. **(B)** Preliminary analysis of mAbs specificity for N-CD2v-His compared to hCD2-His and mCD2-His using indirect ELISA. ***: $p < 0.001$, ****: $p < 0.0001$. **(C)** Analysis of the binding interactions of the four mAbs with ASFV structural proteins P30, P72, and pp62 through indirect ELISA.

TABLE 3 Identification of anti-CD2v mAb subclasses.

mAb	Chain	Isotype	V gene	CDR3	Germline V gene identity
2B25	H	IgG2b	IGHV3–1	ARLGGVDY	97.92%
	L	κ	IGKV4–68	QQWTSNPFT	95.29%
3J25	H	IgG1	IGHV5-6-5	VRGYRYYSMDY	91.93%
	L	κ	IGKV4–57-1	QRYSGNPPIT	96.81%
7B1	H	IgG1	IGHV1–74	ATAFFDY	91.32%
	L	κ	IGKV1–135	WQGTHFPQT	98.64%
8G1	H	IgG1	IGHV5–9-1	ARSNPYYFDY	98.26%
	L	κ	IGKV1–135	WQGTHFPT	97.96%

respectively. The results revealed that 2B25, 3J25, and 8G1 did not exhibit significant binding to any of the three ASFV structural proteins. Conversely, antibody 7B1 showed no binding to P30 and pp62, but displayed partial cross-reactivity with P72 (Figure 2C). These findings indicate that the screened mAbs, 2B25, 3J25, and 8G1, are specifically targeted towards the CD2v antigen.

3.3 Analysis of anti-CD2v mAb affinity using BLI

The affinity of the four mAbs was evaluated using BLI (47, 48). The results demonstrated favorable association and dissociation curves for all four mAbs with the CD2v antigen at the nanomolar level (Figure 3). The results demonstrated that 3J25 exhibited the lowest K_D value (9.94 nM), indicating the highest affinity among the four mAbs, while 7B1 exhibited the highest K_D value (32.7 nM), indicating the lowest affinity. In the subsequent experiments, we primarily focused on the three mAbs with higher affinity to the CD2v antigen (2B25, 3J25, and 8G1).

3.4 Characterization of anti-CD2v mAbs using western blotting assay and IFA

In the western blotting assay of the binding of the three mAbs (2B25, 3J25, and 8G1) to exogenous CD2v-HA, HEK293T cells were transfected with a pcDNA3.1-CD2v-HA plasmid encoding the full-length CD2v protein fused with a C-terminal HA tag (Figure 4A). The results revealed that all three mAbs effectively recognized the glycosylated CD2v-HA full-length protein (about 100 kDa), but only 3J25 and 8G1 recognized the deglycosylated CD2v protein (about 43 kDa). Notably, none of the mAbs recognized the intracellular C-terminal region of CD2v (26 kDa) (Figure 4A). These findings highlight the dependence of the recognition of CD2v by 2B25 on the presence of the glycosylated epitope on the surface of CD2v. Furthermore, the findings suggest that the three of mAbs could target linear epitopes on CD2v.

In the IFA of the cellular localization of CD2v, we transfected HEK293T cells with a pEGFP-N1-CD2v-GFP plasmid expressing full-length CD2v with a C-terminal GFP tag. The results showed that CD2v-GFP exhibited green fluorescence and predominantly localized to the cytoplasmic and perinuclear regions, as well as the cytomembranes (Figure 4B). This localization pattern confirms previous findings (22, 23, 25, 43). Simultaneously, the mAbs, employed as primary antibodies, displayed red fluorescence upon detection using Alexa 594-labeled secondary antibody. Notably, there was significant colocalization between the red signal from the mAbs and the green signal from CD2v-GFP in the merged image (Figure 4B). These results provide evidence that all three mAbs specifically recognize the naturally spatially structured CD2v-GFP protein expressed in HEK293T cells.

3.5 Competitive ELISA assessing the epitope overlap of anti-CD2v mAbs and the development of sandwich ELISA

Competitive ELISA was employed to elucidate the relationships of the epitopes recognized by the three mAbs. N-CD2v-His was immobilized on ELISA plates, followed by adding an mAb (2B25, 3J25, or 8G1; competitor antibody) at varying concentrations and

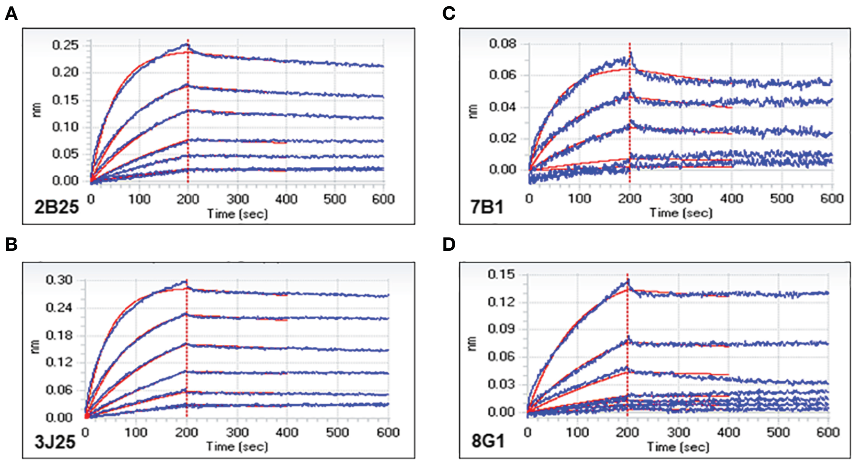

E

mAb	K_{on} ($M^{-1}S^{-1}$)	K_{off} (S^{-1})	K_D (nM)
2B25	2.58E+04	3.96E-04	15.4
3J25	2.75E+04	2.73E-04	9.94
7B1	2.40E+04	7.84E-04	32.7
8G1	1.26E+04	2.97E-04	23.5

FIGURE 3
Bio-layer interferometry (BLI) analysis of anti-CD2v mAb affinity. **(A–D)** Association and dissociation curves for 2B25, 3J25, 7B1, and 8G1, respectively. **(E)** Summary of kinetic constants (K_{on}, $K_{off,}$ and K_D) of the four mAbs.

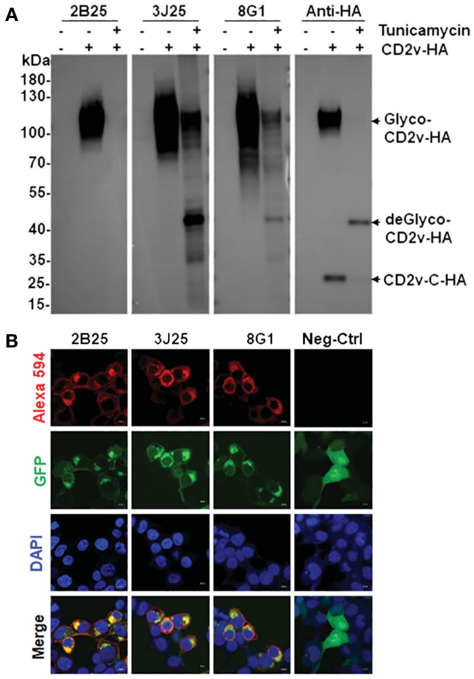

FIGURE 4
Characterization and identification of mAbs by western blotting and immunofluorescence assay (IFA). **(A)** Western blotting assay of the binding of the four mAbs to exogenous full-length CD2v-HA protein. After transfection with pcDNA3.1-CD2v-HA plasmid, HEK293T cells were treated with or without 10 µg/mL tunicamycin for 24 (h) Glyco: glycosylated, deGlyco-: deglycosylated, CD2v-C-HA: intracellular C-terminal region of CD2v. **(B)** IFA of the cellular localization of exogenous full-length CD2v-GFP protein and mAbs. The empty pEGFP-N1 plasmid served as the negative control (Neg-Ctrl). Scale bar, 10 µm.

then a biotinylated mAb (2B25-biotin, 3J25-biotin, or 8G1-biotin; detection antibody), allowing for competition for binding to CD2v. As the concentration of 2B25 increased, the binding of 2B25-biotin to CD2v gradually decreased but minimal changes were observed regarding the binding of 3J25-biotin and 8G1-biotin (Figure 5A). This indicates that the epitopes recognized by 2B25 do not overlap with those recognized by 3J25 and 8G1. Similar results were obtained when using 3J25 or 8G1 as the competitor antibody (Figures 5B, C). Therefore, it can be concluded that 2B25, 3J25, and 8G1 do not exhibit epitope overlap. To establish a sandwich ELISA, an orthogonal experiment was conducted with these mAbs (Figures 5D, E). By utilizing 3J25 as the capture antibody and 2B25-biotin as the detection antibody, successful detection of viral ASFV-CD2v antigen at ng/mL levels was achieved.

3.6 Analysis of CD2v epitopes bound by anti-CD2v mAbs

Based on the sequence characteristics of the CD2v extracellular region (Figures 6A, B) and using secondary structure discrimination and potential epitope prediction analysis, we designed, expressed, and purified five CD2v extracellular domain truncation mutants (CD2v D1–D5; Figure 6C; Supplementary Figure S4). Indirect ELISA (Figures 6D-F) showed that 2B25 and 3J25 mainly recognized the D1 region. However, at high CD2v concentrations (1 µg/mL), there was a slight binding of 3J25 to the D1 region compare the negative control; at low CD2v concentrations (0.008 µg/ml), there was a slight lower recognition of the D1 region by 3J25 than 2B25. This indicates that 2B25 and 3J25 have subtle differences regarding their recognition of the fine epitopes within the N-terminal D1 region of CD2v. Additionally, 8G1 predominantly recognized the D4 region, which is different from the other two mAbs.

To distinguish the epitopes recognized by these three mAbs, we designed 11 overlapping polypeptides spanning the D1 and D4 regions (Figure 7). The results revealed that 3J25 primarily recognized the P2 region, while 8G1 recognized the P14 region. Intriguingly, 2B25 did not exhibit binding affinity towards any of the peptides tested, indicating its potential recognition of glycosylated epitopes due to the absence of glycosylation modifications in the peptides. Thus, through epitope analysis, we have identified two novel linear B-cell epitopes (^{25}TIILDSNITNDNN^{37} and ^{141}LNINDTFVKYTNE^{153}). Furthermore, when analyzing the conservation of these epitopes among 42 epidemic strains of ASFV (Supplementary Table S1), we observed high conservation within Chinese epidemic strains and Georgia 2008/1 strains, but differences compared to Benin97/1, Nu1979, E75, BA71V, K-49 strains, among others (Figure 8). Overall, our results underscore distinct epitope recognition patterns exhibited by the three mAbs.

3.7 Anti-CD2v mAbs inhibit CD2v-induced NF-κB signaling activation

CD2v has been shown to induce activation and nuclear translocation of NF-κB p65 in swine peripheral blood mononuclear cells and macrophages (25). To assess the effects of the mAbs on the NF-κB signaling pathway, we conducted a time course experiment to determine the duration regarding CD2v-induced NF-κB activation. Treatment with purified N-CD2v-His protein resulted in the phosphorylation of NF-κB p65 (70 kDa), which exhibited a continuous increase from 15 to 120 min (Figure 9A). Based on these findings, we selected a 90-minute incubation period for PK-15 cells with purified N-CD2v-His protein, either alone or in combination with the anti-CD2v mAbs (2B25, 3J25, or 8G1). All three mAbs exhibited significantly and dose-dependently inhibition of CD2v-mediated NF-κB phosphorylation in PK-15 cells (Figures 9B-D). Furthermore, when used individually, neither the three mAbs nor the mIgG isotype control were capable of stimulating NF-κB activation (Supplementary Figure S5). These findings indicate that the anti-CD2v mAbs specifically interfered with the ability of soluble CD2v to induce NF-κB p65 activation in PK-15 cells.

4 Discussion

Associated with severe economic losses, ASF is a devastating and highly contagious hemorrhagic disease that threatens the swine

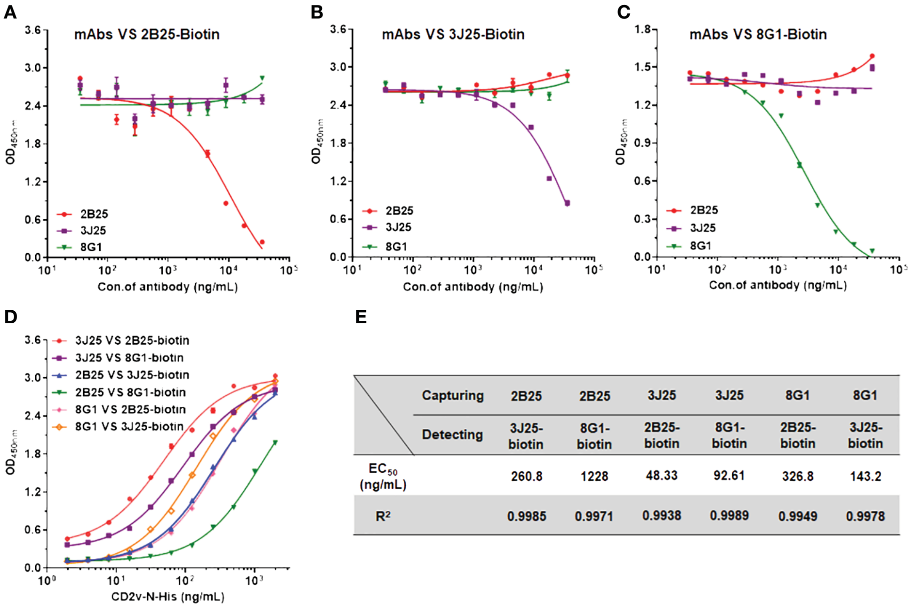

Capturing	2B25	2B25	3J25	3J25	8G1	8G1
Detecting	3J25-biotin	8G1-biotin	2B25-biotin	8G1-biotin	2B25-biotin	3J25-biotin
EC_{50} (ng/mL)	260.8	1228	48.33	92.61	326.8	143.2
R^2	0.9985	0.9971	0.9938	0.9989	0.9949	0.9978

FIGURE 5

Identification of potential epitope overlaps using competitive ELISA and development of sandwich ELISA. **(A–C)** Competitive ELISA was performed to assess the potential overlap of epitopes recognized by different anti-CD2v mAbs. Varying concentrations (35.2 ng/mL to 36 µg/mL) of an unconjugated mAb (2B25, 3J25, or 8G1; competitor antibody) and 1 µg/mL of a biotinylated mAb (2B25, 3J25, or 8G1; detection antibody) were added to wells precoated with N-CD2v-His protein and allowed to compete for antigen binding. **(D)** Sandwich ELISA was conducted using various concentrations (1.9 ng/mL to 2 µg/mL) of N-CD2v-His as the antigen and various combinations of capture and detection antibodies. **(E)** Summary of EC_{50} values for the various combinations of capture and detection antibodies.

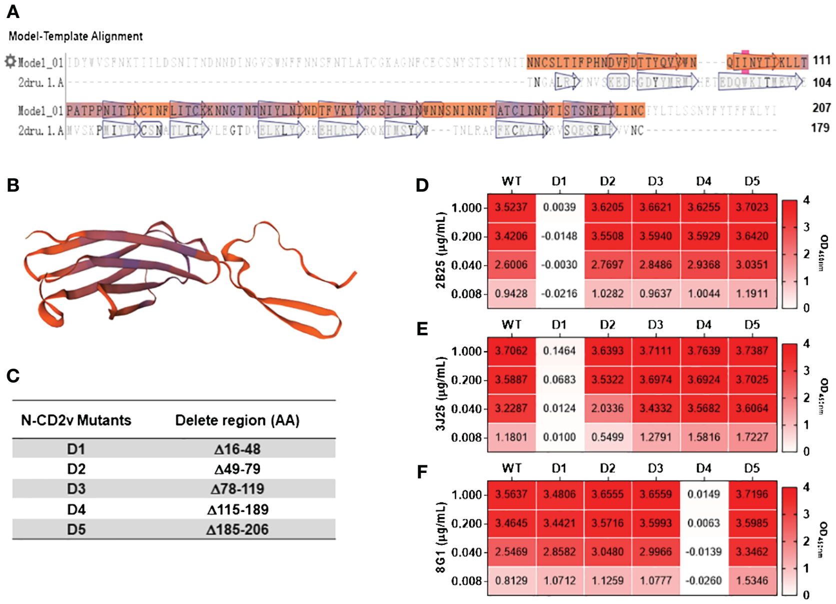

N-CD2v Mutants	Delete region (AA)
D1	Δ16-48
D2	Δ49-79
D3	Δ78-119
D4	Δ115-189
D5	Δ185-206

2B25 (µg/mL)	WT	D1	D2	D3	D4	D5
1.000	3.5237	0.0039	3.6205	3.6621	3.6255	3.7023
0.200	3.4206	-0.0148	3.5508	3.5940	3.5929	3.6420
0.040	2.6006	-0.0030	2.7697	2.8486	2.9368	3.0351
0.008	0.9428	-0.0216	1.0282	0.9637	1.0044	1.1911

3J25 (µg/mL)	WT	D1	D2	D3	D4	D5
1.000	3.7062	0.1464	3.6393	3.7111	3.7639	3.7387
0.200	3.5887	0.0683	3.5322	3.6974	3.6924	3.7025
0.040	3.2287	0.0124	2.0336	3.4332	3.5682	3.6064
0.008	1.1801	0.0100	0.5499	1.2791	1.5816	1.7227

8G1 (µg/mL)	WT	D1	D2	D3	D4	D5
1.000	3.5637	3.4806	3.6555	3.6559	0.0149	3.7196
0.200	3.4645	3.4421	3.5716	3.5993	0.0063	3.5985
0.040	2.5469	2.8582	3.0480	2.9966	-0.0139	3.3462
0.008	0.8129	1.0712	1.1259	1.0777	-0.0260	1.5346

FIGURE 6

Preliminary analysis of the CD2v extracellular domain regions recognized by mAbs. **(A)** Sequence analysis of the CD2v extracellular domain was performed using the SwissModel server (https://swissmodel.expasy.org). **(B)** Homology modeling of the CD2v extracellular domain was conducted using PyMol software based on the model with the highest sequence similarity (PDB code: 2dru). **(C)** Design of five CD2v extracellular domain truncation mutants (D1–D5). **(D–F)** Indirect ELISA of mAbs 2B25, 3J25, and 8G1, respectively, recognizing D1–D5 using different concentrations of D1–D5.

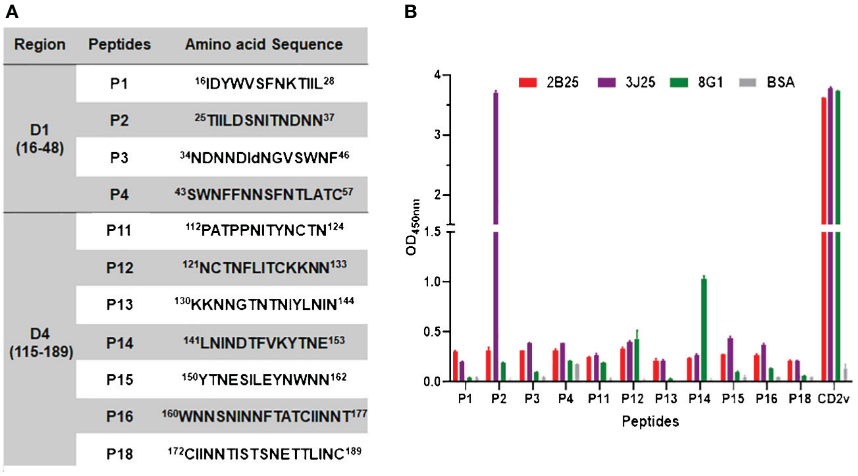

A

Region	Peptides	Amino acid Sequence
D1 (16-48)	P1	^{16}IDYWVSFNKTIIL^{28}
	P2	^{25}TIILDSNITNDNN^{37}
	P3	^{34}NDNNDIdNGVSWNF^{46}
	P4	^{43}SWNFFNNSFNTLATC^{57}
D4 (115-189)	P11	^{112}PATPPNITYNCTN^{124}
	P12	^{121}NCTNFLITCKKNN^{133}
	P13	^{130}KKNNGTNTNIYLNIN^{144}
	P14	^{141}LNINDTFVKYTNE^{153}
	P15	^{150}YTNESILEYNWNN^{162}
	P16	^{160}WNNSNINNFTATCIINNT^{177}
	P18	^{172}CIINNTISTSNETTLINC^{189}

FIGURE 7
Epitope peptide mapping for mAbs recognizing CD2v. **(A)** Design of overlapping polypeptides with their corresponding amino acid sequences. **(B)** Indirect ELISA of three mAbs (2B25, 3J25, and 8G1) binding to peptides conjugated with BSA. ELISA plates were coated with 0.1 µg/well of the respective peptides, followed by adding each of the three mAbs separately. N-CD2v-His served as a positive control, while BSA served as a negative control. The experiment was performed in triplicate.

industry worldwide. The identification of antigenic target proteins is key for mitigating the risks associated with ASFV (38). The outer envelope, which forms during ASFV budding from the host cytoplasm, plays a pivotal role in the virus's pathogenicity (49). Deletion of the *EP402R* gene, which encodes outer envelope protein CD2v, in various ASFV strains reduces their pathogenicity (50–52). Furthermore, CD2v has been identified as a critical antigen in the immunoprotective response against ASFV, as indicated by numerous studies (22, 28–30). Immunization with recombinant baculovirus carrying the ASFV *EP402R* gene effectively protects pigs from subsequent challenges with virulent strains, suggesting the potential of the CD2v protein to activate cytotoxic T lymphocytes (53).

This study aimed to develop a highly specific and sensitive mAb targeting the ASFV outer envelope protein CD2v. CD2v, with a molecular weight of 105–110 kDa after glycosylation, presents a challenge due to its numerous glycosylation sites, making complete glycosylation using prokaryotic expression systems difficult (43, 54). As the immunogenicity of CD2v is pivotal for obtaining high-titer mAbs, we opted for the Expi293F eukaryotic expression system to express the recombinant N-CD2v-His protein (extracellular region of CD2v). This system offers superior post-translational modifications, particularly glycosylation, ensuring that the antigens expressed closely resemble the *in vivo* structure of CD2v. SDS-PAGE revealed that our recombinant protein had a molecular weight of approximately 70–100 kDa (Figures 1B, C), significantly larger than the predicted molecular weight of 23 kDa. This finding indicates significant glycosylation of the recombinant N-CD2v-His protein, consistent with previous findings (22, 23, 43, 55). It should be noted that higher molecular weight bands (120 kDa and >180 kDa) in the SDS-PAGE gel but not detect in the western blotting analysis. These bands could potentially be contaminants from the purification process. Another possibility is that they may arise from the oligomerization of CD2v, which could hinder accessibility to the His epitope. While there is currently no conclusive evidence for the oligomerization of the CD2v protein, we plan to conduct further experiments to confirm this in future research.

Next, the recombinant N-CD2v-His protein was utilized to immunize BALB/c mice. These mice had high-titer antibodies that specifically bound to CD2v, indicating the excellent immunogenicity of N-CD2v-His (Figure 1D). Subsequently, using hybridoma technology, we obtained four mAbs (2B25, 3J25, 7B1, and 8G1) with robust binding activity (Figure 2A). Importantly, all four mAbs exhibited specifically recognition of CD2v, while showing no binding to hCD2 or mCD2, despite the high similarity between hCD2/mCD2 and CD2v (18) (Figure 2B). Furthermore, it was observed that mAbs 2B25, 3J25, and 8G1 did not display significant binding to the ASFV structural proteins P30, P72, and pp62 (Figure 2C). These findings indicate that the screened mAbs, particularly 2B25, 3J25, and 8G1, are specifically targeted towards the CD2v antigen.

BLI showed that all four mAbs exhibited a high-affinity K_D to the CD2v antigen at the nanomolar level (Figure 3); 3J25 demonstrated the strongest binding affinity, while 7B1 exhibited the weakest. Notably, the order of binding strength according to BLI (3J25, 2B25, 8G1, 7B1) slightly differed from that according to indirect ELISA (2B25, 3J25, 8G1, 7B1). This variance may be attributable to the direct fixation of the antigen onto the ELISA plate (potentially changing the antigen conformation), while the antigen was immobilized onto the Ni-TNA biosensor in the BLI experiments (closely resembling the actual *in vivo* conditions). Following this, we selected the three mAbs with the highest affinity (3J25, 2B25, and 8G1) for further experiments.

Western blotting of the three mAbs indicated that they reacted with the denatured full-length CD2v protein (containing linear B-cell epitopes) (Figure 4A). Interestingly, all three mAbs were able to bind to glycosylated CD2v, while only 3J25 and 8G1 (not 2B25) recognized deglycosylated CD2v. This suggested that the binding of

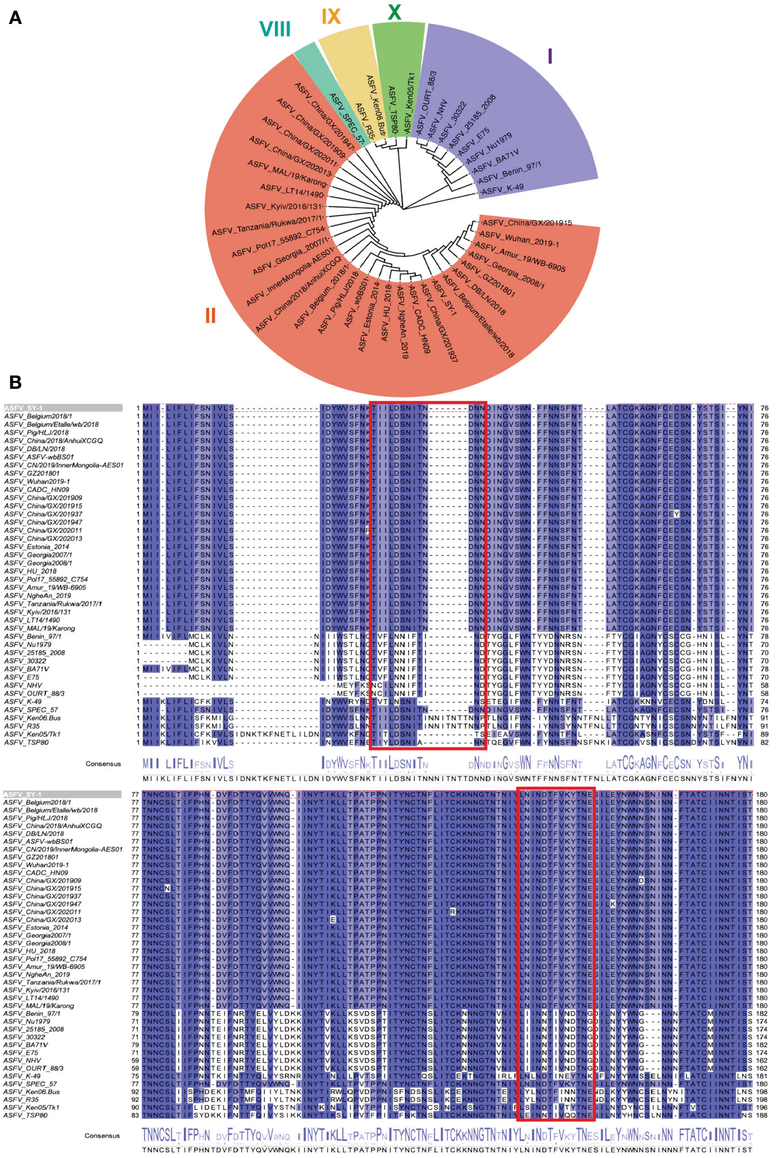

FIGURE 8

Conservation analysis of CD2v extracellular domains and epitopes across representative ASFV strains. **(A)** Maximum likelihood phylogenetic tree was built in MEGA v11.0 based on the CD2v protein sequences of the 42 representative strains. **(B)** Conservation of epitopes based on multiple sequence alignment of CD2v protein sequences in Jalview v2.11.1.4. The red box indicates the antigenic region, including ^{25}TIILDSNITNDNN^{37} and ^{141}LNINDTFVKYTNE^{153} epitopes.

2B25 depended on the glycosylation status of the CD2v surface. Furthermore, IFA demonstrated that all three mAbs recognized the full-length CD2v-GFP fusion protein and co-localized with green fluorescence (Figure 4B), confirming their ability to recognize naturally glycosylated epitopes of CD2v.

To develop a sandwich ELISA detection kit, we first assessed epitope overlap among the three mAbs using competitive ELISA. 2B25, 3J25, and 8G1 did not exhibit competition with each other in binding to CD2v (Figures 5A-C), indicating no epitope overlap. Based on these results, pairwise sandwich ELISAs were performed, which revealed that using 3J25 as the capture antibody and 2B25-biotin as the detection antibody led to the successful detection of CD2v at ng/mL levels. (Figures 5D, E).

Although multiple linear B-cell epitopes of CD2v have recently been identified (34–40), their functions remain unknown (Table 1). To analyze the antigenic epitopes recognized by our anti-CD2v mAbs, we designed and constructed five CD2v extracellular domain truncation mutants (D1–D5) (Figures 6A-C). Our results indicated that mAbs 2B25 and 3J25 primarily target the D1 region, while 8G1 primarily targets the D4 region. Moreover, the fine epitope recognition by 2B25 and 3J25 differed. To further differentiate the epitopes recognized by these three mAbs, we designed 11 overlapping polypeptides spanning the D1 and D4 regions (Figure 7). Through peptide-based ELISA, we identified two novel epitopes. The first epitope, recognized by mAb 3J25, was identified as ^{25}TIILDSNITNDNN^{37}. It overlapped with the linear epitope of

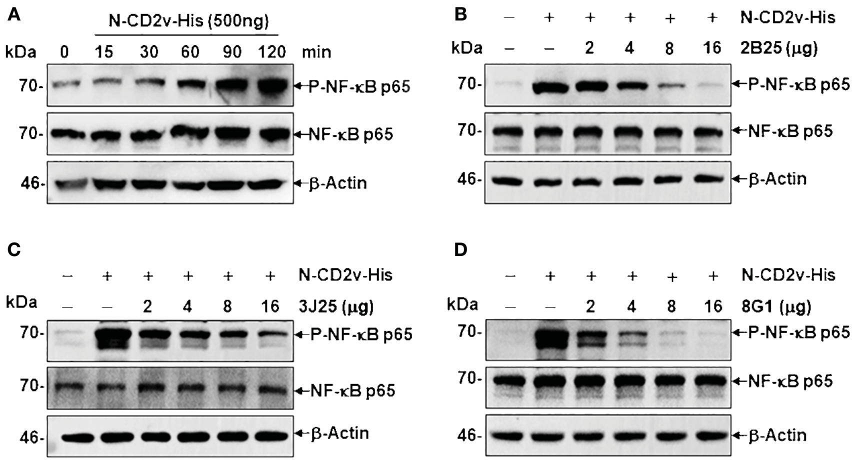

FIGURE 9
Anti-CD2v mAbs inhibit CD2v-induced NF-κB activation. **(A)** Time course experiment of CD2v-induced NF-κB activation. PK-15 cells were incubated with 500 ng of N-CD2v-His protein for various durations (0, 15, 30, 60, 90, and 120 min). Whole-cell lysates were separated by western blotting and probed with antibodies against p-NF-κB p65, NF-κB p65, and β-actin. **(B–D)** Effect of mAbs (2B25, 3J25, and 8G1) on CD2v-induced NF-κB activation. Purified N-CD2v-His (500 ng) was preincubated with each of the three mAbs (at doses of 2–16 μg) separately for 30 min at 37°C. The mixture was then co-cultured with PK-15 cells for 90 min at 37°C, and p-NF-κB p65, NF-κB p65, and β-actin were detected.

amino acids 28–51 in the CD2v extracellular domain, which was identified by Zhang's group (35). The other epitope, recognized by mAb 8G1, was identified as ^{141}LNINDTFVKYTNE^{153}. It contained the epitope ^{147}FVKYT^{151}, which was identified by Wang's group (34), and partially overlapped with the epitope ^{148}VKYTNESILE^{157}, which was identified by the same group in a separate study (36). Interestingly, we could not identify the B-cell linear epitopes of mAb 2B25, which may recognize glycosylated epitopes in the D1 region. This is likely because directly synthesized peptides lack glycosylation modifications. Furthermore, multiple sequence alignment revealed that the two identified epitopes (^{25}TIILDSNITNDNN^{37} and ^{141}LNINDTFVKYTNE^{153}) are conserved in ASFV genotype II strains, particularly in Chinese strains. This indicates that the two epitopes are an important feature of this branch of ASFV and could be used for the differential diagnosis of different strains (Figure 8). These findings may have implications for novel ASFV vaccine design.

During *in vivo* infection, pigs infected with highly virulent strains of ASFV exhibit elevated systemic production of IFN, TNF-α, IL-1α, IL-1β, and IL-6, mainly facilitated by NF-κB or alternative transcription factors (56–58). Notably, recent research has shown that ASFV CD2v induces NF-κB-dependent IFN-β and ISGs transcription in swine PK15 cells (25). when purified N-CD2v-His was preincubated with an anti-CD2v mAb (2B25, 3J25, or 8G1) before incubation for 90 min with PK-15 cells (Figures 9B-D), the mAbs significantly and dose-dependently inhibited CD2v-dependent NF-κB activation. This implies that anti-CD2v antibodies might be an important immune mechanism for neutralizing CD2v. These findings underscore the potential significance of targeting CD2v in the development of immunotherapeutic strategies against ASFV infection.

In summary, we successfully expressed recombinant CD2v protein in eukaryotic cells and generated mAbs (Table 2) that recognize two novel linear CD2v epitopes and one glycosylated epitope. By utilizing the mAbs 2B25 and 3G25, we established a highly sensitive sandwich ELISA to detect the CD2v antigen. These mAbs and their target epitopes are likely to be valuable for studying the structure and function of CD2v, differentiating between virus strains, and other applications. Additionally, the identified B cell epitopes may serve as candidate vaccine antigens for preventing infections by prevalent ASFV strains in China. Nonetheless, our study does have certain limitations that need to be addressed in future research. Specifically, further refinement of the epitope information, determination of the specific amino acids within the glycosylated epitope of CD2v, and additional evaluation of the specificity and sensitivity of the sandwich ELISA (using ASFV reference strains and infected pig samples) are required. Additionally, the identified mAbs need further validation to confirm their specificity in blocking ASFV infection in relevant animal models or *in vitro* systems. These areas will be the primary focus of our future research endeavors.

Data availability statement

The original contributions presented in the study are included in the article/Supplementary Material. Further inquiries can be directed to the corresponding authors.

Ethics statement

The animal study was approved by Ethics Committee of the Academy of Beijing Institute of Pharmacology and Toxicology. The study was conducted in accordance with the local legislation and institutional requirements.

Author contributions

RF: Data curation, Formal Analysis, Investigation, Methodology, Writing – original draft. ZW: Data curation, Investigation, Methodology, Writing – review & editing. MZ: Data curation, Investigation, Methodology, Software, Writing – review & editing, Validation. SJ: Data curation, Investigation, Methodology, Writing – review & editing. ZJ: Data curation, Investigation, Methodology, Writing – review & editing. YW: Investigation, Methodology, Writing – review & editing. JC: Data curation, Investigation, Methodology, Writing – review & editing. GC: Investigation, Writing – review & editing, Formal Analysis, Methodology. HX: Investigation, Writing – review & editing, Data curation, Methodology. YXW: Funding acquisition, Investigation, Writing – review & editing, Formal Analysis, Methodology. YS: Investigation, Writing – review & editing. JF: Investigation, Supervision, Writing – review & editing, Data curation, Software. BS: Supervision, Writing – review & editing, Conceptualization, Investigation, Methodology. YZ: Investigation, Supervision, Writing – review & editing, Conceptualization, Methodology. YH: Investigation, Supervision, Writing – review & editing, Conceptualization, Methodology. JW: Conceptualization, Funding acquisition, Methodology, Project administration, Supervision, Visualization, Writing – original draft, Writing – review & editing, Investigation.

Funding

The author(s) declare financial support was received for the research, authorship, and/or publication of this article. This work was supported by the Natural Science Foundation of Beijing (No. 7222262), the National Key Research and Development Program of China (No. 2023YFC2605002), and the National Natural Science Foundation of China (Nos. 81672368, 83101913).

Acknowledgments

We thank Ms. Xinying Li and Ms. Ming Yu for hybridoma technical assistance.

Conflict of interest

Author MZ was employed by (BCA) Bio-Breeding Center, Beijing Capital Agribusiness Co., Ltd.

The remaining authors declare that the research was conducted in the absence of any commercial or financial relationships that could be construed as a potential conflict of interest.

Publisher's note

All claims expressed in this article are solely those of the authors and do not necessarily represent those of their affiliated organizations, or those of the publisher, the editors and the reviewers. Any product that may be evaluated in this article, or claim that may be made by its manufacturer, is not guaranteed or endorsed by the publisher.

Supplementary material

The Supplementary Material for this article can be found online at: https://www.frontiersin.org/articles/10.3389/fimmu.2024.1352404/full#supplementary-material

References

1. Tesfagaber W, Wang L, Tsegay G, Hagoss YT, Zhang Z, Zhang J, et al. Characterization of anti-p54 monoclonal antibodies and their potential use for African swine fever virus diagnosis. *Pathogens*. (2021) 10:178. doi: 10.3390/pathogens10020178

2. Wu K, Liu J, Wang L, Fan S, Li Z, Li Y, et al. Current state of global African swine fever vaccine development under the prevalence and transmission of ASF in China. *Vaccines (Basel)*. (2020) 8:531. doi: 10.3390/vaccines8030531

3. Sereda AD, Kazakova AS, Namsrayn SG, Vlasov ME, Sindryakova IP, Kolbasov DV. Subsequent immunization of pigs with African swine fever virus (ASFV) seroimmunotype IV vaccine strain fk-32/135 and by recombinant plasmid DNA containing the cd2v derived from mk-200 ASFV seroimmunotype iii strain does not protect from challenge with ASFV seroimmunotype III. *Vaccines (Basel)*. (2023) 11:1007. doi: 10.3390/vaccines11051007

4. Hakizimana JN, Yona C, Kamana O, Nauwynck H, Misinzo G. African swine fever virus circulation between Tanzania and neighboring countries: A systematic review and meta-analysis. *Viruses*. (2021) 13:306. doi: 10.3390/v13020306

5. Cwynar P, Stojkov J, Wlazlak K. African swine fever status in Europe. *Viruses*. (2019) 11:310. doi: 10.3390/v11040310

6. Woźniakowski G, Kozak E, Kowalczyk A, Łyjak M, Pomorska-Mól M, Niemczuk K, et al. Current status of African swine fever virus in a population of wild boar in eastern Poland (2014–2015). *Arch Virol*. (2016) 161:189–95. doi: 10.1007/s00705-015-2650–5

7. Pejsak Z, Truszczyński M, Niemczuk K, Kozak E, Markowska-Daniel I. Epidemiology of African swine fever in Poland since the detection of the first case. *Pol J Vet Sci*. (2014) 17:665–72. doi: 10.2478/pjvs-2014–0097

8. Juszkiewicz M, Walczak M, Wozniakowski G, Podgorska K. African swine fever: Transmission, spread, and control through biosecurity and disinfection, including polish trends. *Viruses*. (2023) 15:2275. doi: 10.3390/v15112275

9. Pakotiprapha D, Kuhaudomlarp S, Tinikul R, Chanarat S. Bridging the gap: Can covid-19 research help combat African swine fever? *Viruses*. (2023) 15:1925. doi: 10.3390/v15091925

10. Sánchez-Cordón PJ, Montoya M, Reis AL, Dixon LK. African swine fever: A re-emerging viral disease threatening the global pig industry. *Vet J*. (2018) 233:41–8. doi: 10.1016/j.tvjl.2017.12.025

11. Wardley RC, de MAC, Black DN, de Castro Portugal FL, Enjuanes L, Hess WR, et al. African swine fever virus. *Brief review Arch Virol*. (1983) 76:73–90. doi: 10.1007/bf01311692

12. Dixon LK, Chapman DA, Netherton CL, Upton C. African swine fever virus replication and genomics. *Virus Res*. (2013) 173:3–14. doi: 10.1016/j.virusres.2012.10.020

13. Zhou JH, Gao ZL, Sun DJ, Ding YZ, Zhang J, Stipkovits L, et al. A comparative analysis on the synonymous codon usage pattern in viral functional genes and their translational initiation region of ASFV. *Virus Genes*. (2013) 46:271–9. doi: 10.1007/s11262-012-0847–1

14. Galindo I, Alonso C. African swine fever virus: A review. *Viruses*. (2017) 9:103. doi: 10.3390/v9050103

15. Gallardo C, Fernández-Pinero J, Pelayo V, Gazaev I, Markowska-Daniel I, Pridotkas G, et al. Genetic variation among African swine fever genotype ii viruses, eastern and central Europe. *Emerg Infect Dis*. (2014) 20:1544–7. doi: 10.3201/eid2009.140554

16. Wang G, Xie M, Wu W, Chen Z. Structures and functional diversities of ASFV proteins. *Viruses*. (2021) 13:2124. doi: 10.3390/v13112124

17. Alonso C, Borca M, Dixon L, Revilla Y, Rodriguez F, Escribano JM, et al. Ictv virus taxonomy profile: Asfarviridae. *J Gen Virol*. (2018) 99:613–4. doi: 10.1099/jgv.0.001049

18. Rodriguez JM, Yanez RJ, Almazan F, Vinuela E, Rodriguez JF. African swine fever virus encodes a cd2 homolog responsible for the adhesion of erythrocytes to infected cells. *J Virol*. (1993) 67:5312–20. doi: 10.1128/JVI.67.9.5312–5320.1993

19. Borca MV, Kutish GF, Afonso CL, Irusta P, Carrillo C, Brun A, et al. An African swine fever virus gene with similarity to the t-lymphocyte surface antigen cd2 mediates hemadsorption. *Virology*. (1994) 199:463–8. doi: 10.1006/viro.1994.1146

20. Dixon LK, Abrams CC, Bowick G, Goatley LC, Kay-Jackson PC, Chapman D, et al. African swine fever virus proteins involved in evading host defence systems. *Vet Immunol Immunopathol*. (2004) 100:117–34. doi: 10.1016/j.vetimm.2004.04.002

21. Rowlands RJ, Duarte MM, Boinas F, Hutchings G, Dixon LK. The cd2v protein enhances African swine fever virus replication in the tick vector, ornithodoros erraticus. *Virology*. (2009) 393:319–28. doi: 10.1016/j.virol.2009.07.040

22. Perez-Nunez D, Garcia-Urdiales E, Martinez-Bonet M, Nogal ML, Barroso S, Revilla Y, et al. Cd2v interacts with adaptor protein ap-1 during African swine fever infection. *PloS One*. (2015) 10:e0123714. doi: 10.1371/journal.pone.0123714

23. Kay-Jackson PC, Goatley LC, Cox L, Miskin JE, Parkhouse RM, Wienands J, et al. The cd2v protein of African swine fever virus interacts with the actin-binding adaptor protein sh3p7. *J Gen Virol*. (2004) 85:119–30. doi: 10.1099/vir.0.19435–0

24. Huang L, Chen W, Liu H, Xue M, Dong S, Liu X, et al. African swine fever virus hlj/18 cd2v suppresses type i ifn production and ifn-stimulated genes expression through negatively regulating cgmp-amp synthase-sting and ifn signaling pathways. *J Immunol*. (2023) 210:1338–50. doi: 10.4049/jimmunol.2200813

25. Chaulagain S, Delhon GA, Khatiwada S, Rock DL. African swine fever virus cd2v protein induces beta-interferon expression and apoptosis in swine peripheral blood mononuclear cells. *Viruses*. (2021) 13:1480. doi: 10.3390/v13081480

26. Perez-Nunez D, Garcia-Belmonte R, Riera E, Fernandez-Sesma MH, Vigara-Astillero G, Revilla Y. Signal peptide and n-glycosylation of n-terminal-cd2v determine the hemadsorption of African swine fever virus. *J Virol*. (2023) 97:e0103023. doi: 10.1128/jvi.01030–23

27. Malogolovkin A, Sereda A. African swine fever virus hemadsorption inhibition assay. *Methods Mol Biol*. (2022) 2503:159–67. doi: 10.1007/978–1-0716–2333-6_11

28. Burmakina G, Malogolovkin A, Tulman ER, Zsak L, Delhon G, Diel DG, et al. African swine fever virus serotype-specific proteins are significant protective antigens for African swine fever. *J Gen Virol*. (2016) 97:1670–5. doi: 10.1099/jgv.0.000490

29. Hemmink JD, Khazalwa EM, Abkallo HM, Oduor B, Khayumbi J, Svitek N, et al. Deletion of the cd2v gene from the genome of ASFV-Kenya-ix-1033 partially reduces virulence and induces protection in pigs. *Viruses*. (2022) 14:1917. doi: 10.3390/v14091917

30. King K, Chapman D, Argilaguet JM, Fishbourne E, Hutet E, Cariolet R, et al. Protection of European domestic pigs from virulent African isolates of African swine fever virus by experimental immunisation. *Vaccine*. (2011) 29:4593–600. doi: 10.1016/j.vaccine.2011.04.052

31. Feng Z, Chen J, Liang W, Chen W, Li Z, Chen Q, et al. The recombinant pseudorabies virus expressing African swine fever virus cd2v protein is safe and effective in mice. *Virol J*. (2020) 17:180. doi: 10.1186/s12985–020-01450–7

32. Lopera-Madrid J, Osorio JE, He Y, Xiang Z, Adams LG, Laughlin RC, et al. Safety and immunogenicity of mammalian cell derived and modified vaccinia ankara vectored African swine fever subunit antigens in swine. *Vet Immunol Immunopathol*. (2017) 185:20–33. doi: 10.1016/j.vetimm.2017.01.004

33. Sunwoo SY, Perez-Nunez D, Morozov I, Sanchez EG, Gaudreault NN, Trujillo JD, et al. DNA-protein vaccination strategy does not protect from challenge with African swine fever virus Armenia 2007 strain. *Vaccines (Basel)*. (2019) 7:12. doi: 10.3390/vaccines7010012

34. Jia R, Zhang G, Bai Y, Liu H, Chen Y, Ding P, et al. Identification of linear b cell epitopes on cd2v protein of African swine fever virus by monoclonal antibodies. *Microbiol Spectr*. (2022) 10:e0105221. doi: 10.1128/spectrum.01052–21

35. Ren D, Ding P, Liu S, Zhang N, Chen Y, Li Q, et al. Development and characterization of recombinant ASFV cd2v protein nanoparticle-induced monoclonal antibody. *Int J Biol Macromol*. (2022) 209:533–41. doi: 10.1016/j.ijbiomac.2022.03.069

36. Liu H, Wang A, Yang W, Liang C, Zhou J, Chen Y, et al. Expression of extracellular domain of ASFV cd2v protein in mammalian cells and identification of b cell epitopes. *Virus Res*. (2023) 323:199000. doi: 10.1016/j.virusres.2022.199000

37. Jiang W, Jiang D, Li L, Wang J, Wang P, Shi X, et al. Identification of two novel linear b cell epitopes on the cd2v protein of African swine fever virus using monoclonal antibodies. *Viruses*. (2022) 15:131. doi: 10.3390/v15010131

38. Liu S, Ding P, Du Y, Ren D, Chen Y, Li M, et al. Development and characterization of monoclonal antibodies against the extracellular domain of African swine fever virus structural protein, cd2v. *Front Microbiol*. (2022) 13:1056117. doi: 10.3389/fmicb.2022.1056117

39. Song J, Wang M, Du Y, Wan B, Zhang A, Zhang Y, et al. Identification of a linear b-cell epitope on the African swine fever virus cd2v protein. *Int J Biol Macromol*. (2023) 232:123264. doi: 10.1016/j.ijbiomac.2023.123264

40. Lu W, Bai Y, Zhang S, Zhao X, Jin J, Zhu X, et al. An intracellular epitope of ASFV cd2v protein elicits humoral and cellular immune responses. *Anim (Basel)*. (2023) 13:1967. doi: 10.3390/ani13121967

41. Muhsin A, Rangel R, Vien L, Bover L. Monoclonal antibodies generation: Updates and protocols on hybridoma technology. *Methods Mol Biol*. (2022) 2435:73–93. doi: 10.1007/978–1-0716–2014-4_6

42. Meyer L, Lopez T, Espinosa R, Arias CF, Vollmers C, DuBois RM. A simplified workflow for monoclonal antibody sequencing. *PloS One*. (2019) 14:e0218717. doi: 10.1371/journal.pone.0218717

43. Goatley LC, Dixon LK. Processing and localization of the African swine fever virus cd2v transmembrane protein. *J Virol*. (2011) 85:3294–305. doi: 10.1128/JVI.01994–10

44. Waterhouse AM, Procter JB, Martin DM, Clamp M, Barton GJ. Jalview version 2–a multiple sequence alignment editor and analysis workbench. *Bioinformatics*. (2009) 25:1189–91. doi: 10.1093/bioinformatics/btp033

45. Tamura K, Stecher G, Kumar S. Mega11: Molecular evolutionary genetics analysis version 11. *Mol Biol Evol*. (2021) 38:3022–7. doi: 10.1093/molbev/msab120

46. Yu G, Smith DK, Zhu H, Guan Y, Lam TT-Y. Ggtree: An r package for visualization and annotation of phylogenetic trees with their covariates and other associated data. *Methods Ecol Evol*. (2017) 8:28–36. doi: 10.1111/2041–210X.12628

47. Nagashima K, Mousa JJ. Epitope binning of monoclonal and polyclonal antibodies by biolayer interferometry. *Methods Mol Biol*. (2023) 2673:17–32. doi: 10.1007/978–1-0716–3239-0_2

48. Petersen RL. Strategies using bio-layer interferometry biosensor technology for vaccine research and development. *Biosensors (Basel)*. (2017) 7:49. doi: 10.3390/bios7040049

49. Salas ML, Andres G. African swine fever virus morphogenesis. *Virus Res*. (2013) 173:29–41. doi: 10.1016/j.virusres.2012.09.016

50. Monteagudo PL, Lacasta A, Lopez E, Bosch L, Collado J, Pina-Pedrero S, et al. Ba71deltacd2: A new recombinant live attenuated African swine fever virus with cross-protective capabilities. *J Virol*. (2017) 91:e01058-17. doi: 10.1128/JVI.01058–17

51. Chen W, Zhao D, He X, Liu R, Wang Z, Zhang X, et al. A seven-gene-deleted African swine fever virus is safe and effective as a live attenuated vaccine in pigs. *Sci China Life Sci*. (2020) 63:623–34. doi: 10.1007/s11427–020-1657–9

52. Teklue T, Wang T, Luo Y, Hu R, Sun Y, Qiu HJ. Generation and evaluation of an African swine fever virus mutant with deletion of the cd2v and uk genes. *Vaccines (Basel)*. (2020) 8:763. doi: 10.3390/vaccines8040763

53. Argilaguet JM, Perez-Martin E, Lopez S, Goethe M, Escribano JM, Giesow K, et al. Bacmam immunization partially protects pigs against sublethal challenge with African swine fever virus. *Antiviral Res*. (2013) 98:61–5. doi: 10.1016/j.antiviral.2013.02.005

54. Portolano N, Watson PJ, Fairall L, Millard CJ, Milano CP, Song Y, et al. Recombinant protein expression for structural biology in hek 293f suspension cells: A novel and accessible approach. *J Vis Exp*. (2014) 92):e51897. doi: 10.3791/51897

55. Jia N, Ou Y, Pejsak Z, Zhang Y, Zhang J. Roles of African swine fever virus structural proteins in viral infection. *J Vet Res*. (2017) 61:135–43. doi: 10.1515/jvetres-2017–0017

56. Tait SW, Reid EB, Greaves DR, Wileman TE, Powell PP. Mechanism of inactivation of nf-kappa b by a viral homologue of i kappa b alpha. Signal-induced release of i kappa b alpha results in binding of the viral homologue to nf-kappa b. *J Biol Chem*. (2000) 275:34656–64. doi: 10.1074/jbc.M000320200

57. Salguero FJ, Sanchez-Cordon PJ, Nunez A, Fernandez de Marco M, Gomez-Villamandos JC. Proinflammatory cytokines induce lymphocyte apoptosis in acute African swine fever infection. *J Comp Pathol*. (2005) 132:289–302. doi: 10.1016/j.jcpa.2004.11.004

58. Powell PP, Dixon LK, Parkhouse RM. An ikappab homolog encoded by African swine fever virus provides a novel mechanism for downregulation of proinflammatory cytokine responses in host macrophages. *J Virol*. (1996) 70:8527–33. doi: 10.1128/JVI.70.12.8527–8533.1996

frontiers | Frontiers in Immunology

TYPE Original Research
PUBLISHED 28 May 2024
DOI 10.3389/fimmu.2024.1392804

Check for updates

OPEN ACCESS

EDITED BY
Shen Yang,
Cedars Sinai Medical Center, United States

REVIEWED BY
Mixia Cao,
Anhui Science and Technology University, China
Nan Wenlong,
China Animal Health and Epidemiology Center, China

*CORRESPONDENCE
Xiaoning Li
✉ xiaoningli@gxu.edu.cn
Ting Rong Luo
✉ tingrongluo@gxu.edu.cn

RECEIVED 28 February 2024
ACCEPTED 02 May 2024
PUBLISHED 28 May 2024

CITATION
Zhang H, Liang X, Li D, Zhang C, Wang W, Tang R, Zhang H, Kiflu AB, Liu C, Liang J, Li X and Luo TR (2024) Apolipoprotein D facilitates rabies virus propagation by interacting with G protein and upregulating cholesterol.
Front. Immunol. 15:1392804.
doi: 10.3389/fimmu.2024.1392804

COPYRIGHT
© 2024 Zhang, Liang, Li, Zhang, Wang, Tang, Zhang, Kiflu, Liu, Liang, Li and Luo. This is an open-access article distributed under the terms of the Creative Commons Attribution License (CC BY). The use, distribution or reproduction in other forums is permitted, provided the original author(s) and the copyright owner(s) are credited and that the original publication in this journal is cited, in accordance with accepted academic practice. No use, distribution or reproduction is permitted which does not comply with these terms.

Apolipoprotein D facilitates rabies virus propagation by interacting with G protein and upregulating cholesterol

Hongyan Zhang[1,2], Xingxue Liang[1,2], Duoduo Li[1,2], Chuanliang Zhang[1,2], Wenfeng Wang[1,2], Rongze Tang[1,2], Hongyun Zhang[1,2], Abraha Bahlbi Kiflu[1,2], Cheng Liu[1,2,3,4], Jingjing Liang[1,2,3,4], Xiaoning Li[1,2,3,4]* and Ting Rong Luo[1,2,3,4]*

[1]State Key Laboratory for Conservation and Utilization of Subtropical Agro-Bioresources, Guangxi University, Nanning, China, [2]College of Animal Sciences and Veterinary Medicine, Guangxi University, Nanning, China, [3]Guangxi Key Laboratory of Animal Breeding, Disease Control and Prevention, Guangxi University, Nanning, China, [4]Guangxi Zhuang Autonomous Region Engineering Research Center of Veterinary Biologics, Guangxi University, Nanning, China

Rabies virus (RABV) causes a fatal neurological disease, consisting of unsegmented negative-strand RNA, which encodes five structural proteins (3′-N-P-M-G-L-5′). Apolipoprotein D (ApoD), a lipocalin, is upregulated in the nervous system after injury or pathological changes. Few studies have focused on the role of ApoD during virus infection so far. This study demonstrated that ApoD is upregulated in the mouse brain (*in vivo*) and C8-D1A cells (*in vitro*) after RABV infection. By upregulating ApoD expression in C8-D1A cells, we found that ApoD facilitated RABV replication. Additionally, Co-immunoprecipitation demonstrated that ApoD interacted with RABV glycoprotein (G protein). The interaction could promote RABV replication by upregulating the cholesterol level. These findings revealed a novel role of ApoD in promoting RABV replication and provided a potential therapeutic target for rabies.

KEYWORDS

rabies virus, apolipoprotein D, glycoprotein, cholesterol, viral replication

Introduction

Rabies virus (RABV), a typical neurotropic virus, causes a fatal zoonosis with an almost 100% mortality rate (1). RABV infects the central nervous system (CNS) that causes approximately 60,000 deaths each year worldwide (2). Vaccination and immunoglobulin are effective in mitigating and preventing the development of rabies post-virus exposure. However, specific drugs are not available to treat rabies (3, 4).

RABV is a single-stranded, negative-sense RNA virus and belongs to the genus *Lyssavirus* and the family *Rhabdoviridae* (5). The genome of RABV encodes the following five structural proteins: nucleoprotein (N), phosphoprotein (P), matrix protein (M), glycoprotein (G), and a large polymerase (L) (6). The viral RNA is encapsulated by N to form a helical nucleocapsid. The nucleocapsid along with P and L forms the ribonucleoprotein that constitutes the core of the bullet-shaped virion and the active viral unit for viral replication (6, 7). RABV G protein, which is the sole virion surface protein, plays a crucial role in viral attachment and fusion with target cell membranes. Viral budding is a complex process. Previous studies have demonstrated that the RABV M lattice is involved in inducing membrane bending for budding site formation. G protein supports this process by facilitating the formation of the M lattice, promoting viral budding (8, 9). However, the role of other cellular molecules in RABV budding has not been elucidated.

Apolipoprotein D (ApoD), a highly conserved glycoprotein, is a member of the transporter superfamily. Previous studies have reported that ApoD, a lipocalin, is involved in lipid metabolism and neuroprotective functions (10). ApoD was first detected in 1963 as a distinct component of the human plasma lipoprotein system (11) and is bound to plasma high-density lipoprotein (12). Additionally, ApoD is composed of 169 residues, including a 20–amino acid secretion signal peptide with two glycosylation sites (asparagine residues 45 and 78). The molecular weight of the mature protein varies from 20 kDa to 32 kDa (13, 14). Several potential ligands exhibiting diverse structures and functions have been identified in ApoD. ApoD is considered a multi-ligand, multi-function protein owing to the apparent heterogeneity and widespread tissue distribution of the ligands and is involved in lipid trafficking, food intake, inflammation, antioxidative response, and development (15). Several studies have confirmed that ApoD exerts neuroprotective effects against different neurodegeneration-inducing factors, such as oxidative stress, inflammatory stress, and excitotoxicity (16, 17). The neuroprotective effect of ApoD is associated with its anti-inflammatory properties and regulatory effects on neuronal cholesterol distribution and the levels of excitotoxicity-related proteins.

The upregulation of ApoD in the aging brain (18), as well as in multiple neurological conditions, suggests that ApoD is critical for neuronal maintenance and protection against injury. Rabies is an acute CNS disease with an almost 100% mortality rate. This study aimed to examine the neuroprotective mechanisms of ApoD during RABV infection. Here, we attempt to explore the interaction between ApoD and RABV. The findings of this study will improve our understanding of the functional properties of ApoD and highlight its potential as a novel therapeutic target for rabies. Based on these findings, novel therapeutic strategies may be developed for rabies, a fatal disease.

Materials and methods

Viruses and animals

Four RABV strains (rRC-HL, GX074, CVS-24, and CVS-11) were used in this study. The rRC-HL strain was rescued from an infectious complementary DNA (cDNA) clone pRC-HL (kindly provided by Professor Minamoto, Gifu University, Japan) based on the fixed strain RC-HL used as a vaccine for animals in Japan (19, 20). GX074 is a street RABV strain isolated from a healthy-looking dog brain in Debao County, Baise City, Guangxi Province of southern China (21, 22). CVS-24 is a mouse-adapted challenge standard RABV strain, whereas CVS-11 is a laboratory-fixed RABV strain.

All animal experiments in this study were performed in the P3 biosafety laboratory and conducted according to the ethical review of laboratory animal welfare of the People's Republic of China (National Standard GB/T35892–2018). The animal experiments were approved by the Animal Experiment Committee of Guangxi University (approval number GXU2019–021). Male and female Kunming mice (purchased from Guangxi Medical University, Nanning, China) aged 4 weeks were intracerebrally inoculated with 30 μl of Dulbecco's Modified Eagle Medium (DMEM) (mock) or 30 μL of DMEM containing 1,000 fluorescent focus units (FFU) of RABV. On 4 and 7 days post-infection (dpi), the mice were euthanized. The mouse brains were collected to examine the mRNA and protein levels using quantitative real-time polymerase chain reaction (qRT-PCR) and Western blotting analyses, respectively.

Cells and plasmids

The HEK (human embryonic kidney)–293T, BSR/T7-9 (cloned from BHK-21 cells, derived from baby hamster kidney), N2A (mouse neuroblastoma), and C8-D1A cells (mouse astrocytes) were cultured in DMEM supplemented with 10% fetal bovine serum (Biological Industries) at 37°C in a humidified 5% CO_2 incubator. The FLAG-tagged RABV G protein–encoding genes (G^{-FLAG} genes) derived from rRC-HL, GX074, and CVS-11 strains were cloned into the PCAGGS vector (pC-rRC-HL-G^{-FLAG}, pC-GX074-G^{-FLAG}, and pC-CVS-11-G^{-FLAG}, respectively) for expression in eukaryotic cells. The FLAG-tagged RABV N protein-encoding genes (N^{-FLAG} genes), P protein-encoding genes (P^{-FLAG} genes), and M protein-encoding genes (M^{-FLAG} genes) derived from rRC-HL, GX074, and CVS-11 strains were cloned into the pcDNA3.0 vector (pcDNA3.0-N^{-FLAG}, pcDNA3.0-P^{-FLAG}, and pcDNA3.0-M^{-FLAG}, respectively) for expression in eukaryotic cells. Additionally, the MYC-tagged ApoD (ApoD^{-MYC}) (*Mus musculus*) was cloned into the pcDNA3.0 vector (pcDNA3.0-ApoD^{-MYC}).

Co-immunoprecipitation assay

HEK-293T cells were co-transfected with the mammalian expression vector pcDNA3.0-ApoD^{-MYC} (for ApoD expression) and/or PCAGGS-G^{-FLAG} (pC-rRC-HL-G^{-FLAG} and pC-GX074-G^{-FLAG}) (for RABV G protein expression). At 24 h post-transfection (hpt), the cells were washed with cold phosphate-buffered saline (PBS) and lysed with NP-40 lysis buffer containing an anti-protease cocktail (100× protease inhibitor cocktail) for 40 min at 4°C. The cell lysates were centrifuged at 12,000 *g* and 4°C for 10 min. The supernatant was transferred to a new tube and incubated with mouse anti-FLAG (Abmart, Shanghai, China, M20008, 1:100) or rabbit anti-MYC (ABclonal, Wuhan, China, AE070, 1:500) monoclonal antibodies for 8 h. Next, the samples were incubated with the protein A/G agarose (Beyotime, Shanghai, China, P2055) for 8 h at 4°C with rotation. The agarose beads were washed five times with cold PBS, and the bound proteins were examined using Western blotting analysis.

Glutathione S transferase pulldown assay

Glutathione S transferase (GST) or GST-tagged ApoD (ApoD^{-GST})–fused proteins were expressed in BL-21 cells and subsequently purified and conjugated into glutathione (GSH) beads (Solarbio, Beijing, China, P2020) at 4°C for 12 h with continuous rotation. The HEK-293T cell extracts were incubated with the GSH beads at 4°C for 12 h with continuous rotation. The protein complexes were pulled down with GSH beads and subjected to Western blotting analysis with the mouse anti-FLAG (Abmart, Shanghai, China, M20008, 1:5,000) and anti-GST monoclonal antibodies (Abmart, Shanghai, China, M20007, 1:5,000).

Confocal microscopy

HEK-293T cells were seeded on coverslips and transfected with pC-GX074-G^{-FLAG} and pcDNA-ApoD^{-MYC} plasmids. At 24 hpt, the cells were fixed with methanol and acetone in a 1:1 ratio, probed with anti-FLAG tag and anti-MYC tag antibodies, and stained with 4′,6-diamidino-2-phenylindole. Protein localization was evaluated using a confocal microscope.

Total RNA extraction and qRT-PCR analysis

Total RNA was extracted using the RNA isolation kit (Vazyme, Nanjing, China, RC112–01), following the manufacturer's instructions. The quality and quantity of total RNA were evaluated using a Nanodrop 1000 spectrophotometer (Thermo, USA). qRT-PCR analysis was performed using the SYBR Green method as previously described (20). Briefly, 1 μg of total RNA (template) was subjected to first-strand cDNA synthesis using the Hiscript II Q RT SuperMix for qRT-PCR (+gDNA wiper), following the manufacturer's instructions. A LightCycler 96 PCR detection system (Roche Diagnostics Ltd.) was used for quantitative assessment of the mRNA levels of genes encoding ApoD and RABV N, P, M, and G under the standard cycling conditions. The β-actin–encoding gene was used as a control in all reactions. The primer sequences used in qRT-PCR analysis are provided in Supplementary Table 1.

Western blotting analysis

Western blotting analysis was performed as previously described (20). C8-D1A, BSR/T7-9, and N2A cells were lysed using radioimmunoprecipitation assay (RIPA) lysis buffer containing protease inhibitors. The lysate was subjected to sodium dodecyl sulfate-polyacrylamide gel electrophoresis using a 12% gel. The resolved proteins were transferred onto a polyvinylidene difluoride (PVDF) membrane (Millipore, Billerica, MA). The PVDF membrane was blocked with 5% skim milk powder in 1× Tris-buffered saline containing Tween-20 (TBST) for 2 h at room temperature. Next, the membrane was incubated with primary antibodies at 4°C overnight. After washing five times with 1× TBST, the membrane was incubated with the corresponding secondary antibody for 2 h at 37°C. The membrane was washed five times with 1× TBST, and the immunoreactive signals were visualized using a 5-bromo-4-chloro-3-indolyl-phosphate/nitro blue tetrazolium kit (Beyotime Ltd, China). Immunoreactivity was quantified using densitometric analysis with an Odyssey scanner (Li-Cor, Lincoln, NE, USA).

Antibodies

Specific antibodies were used for the Western blotting analysis. Mouse anti-ApoD monoclonal antibody was purchased from Santa Cruz Biotechnology Co., Ltd. (CA, USA, sc-166612, 1:1,000); mouse anti-RABVM protein monoclonal antibody was obtained from CUSABIO™Co., Ltd. (WuHan, China, 1–202AA, 1:2,000); and mouse anti-RABV N protein monoclonal antibody was purchased from Hangzhou Dayao Biotechology™ Co., Ltd. (Hangzhou, China, Ab-0056, 1:20,000). Mouse anti–β-actin monoclonal antibody was purchased from Beijing ComWin Biotech™ Co., Ltd. (Beijing, China, cw0096A, 1:1,000). Mouse anti-RABV P and G protein monoclonal antibodies were kindly provided by Dr. Minamoto Nobuyuki (Gifu University, Japan).

Virus infection and titration

C8-D1A cells and N2A cells were infected with rRC-HL at an indicated multiplicity of infection (MOI) for 2 h at 37°C. The cell culture supernatants and cells were collected at 12, 24, and 48 h post-infection (hpi) for virus titration. Viral titers were determined using the indirect immunofluorescence assay (IFA) as previously described (23).

Cell viability assay

Cell viability was analyzed using the cell counting kit–8 (CCK-8) method, following the manufacturer's instructions. Briefly, the C8-D1A cells were seeded in 96-well microplates with six replicates and pre-treated with or without cholesterol (Sigma, USA) at 5% CO_2 and 37°C for 24 h. Next, the cells were incubated with the CCK-8 reagent at 37°C for 1 h. Finally, the absorbance of the reaction mixture was determined using a Microplate Reader (Tecan Infinite 200Pro, Switzerland). The data were analyzed using GraphPad software.

Cellular cholesterol assay

To quantify the total cellular cholesterol level, C8-D1A cells were seeded in 12-well plates and transfected with empty vector, pcDNA-ApoD^{-MYC}, and pC-GX074-G^{-FLAG} plasmids and co-transfected with pcDNA-ApoD^{-MYC} and pC-GX074-G^{-FLAG} plasmids, separately. After washing thrice with PBS, the cells were harvested and lysed. The cholesterol level was quantified using a cholesterol quantification kit (Catalog; 40006; AAT Bioquest, USA), following the manufacturer's instructions.

Statistical analysis

Data were expressed as the mean ± SD (standard deviation). Significances were calculated from at least three independent experiments using GraphPad Prism (8.0.0, MA, USA) by the Student's t-test for unpaired data or the one/two-way analysis of variance, as indicated in the figure legend. Asterisks indicate statistical significance (*$P < 0.05$, **$P < 0.01$, ***$P < 0.001$, and ****$P < 0.0001$).

Results

RABV infection upregulates ApoD expression

Proteomic analysis using iTRAQ revealed that ApoD expression was significantly altered at 7 dpi. In particular, the ApoD levels in rRC-HL–infected and GX074-infected mice were 1.8-fold and 1.9-fold higher, respectively, than those in mock-infected mice at 7 dpi (Figure 1A). The RABV-infected mouse brain was harvested at 4 and 7 dpi and homogenized. The mRNA and protein levels of ApoD were examined using qRT-PCR and Western blotting analyses, respectively. Compared with those in mock-infected mice, the brain ApoD mRNA level was five-fold higher in CVS-24–infected mice and was slightly upregulated in rRC-HL–infected and GX074-infected mice at 4 dpi. At 7 dpi, the brain ApoD mRNA level in rRC-HL–infected, GX074-infected, and CVS-24–infected mice was 2.3-fold, 4.8-fold, and 8.2-fold higher, respectively, than that in mock-infected mice (Figure 1B). Consistently, Western blotting analysis revealed that the brain protein level of ApoD in RABV-infected mice was markedly higher than that in mock-infected mice (Figure 1C). Compared with that in mock-infected mice, the brain ApoD intensity was 2.2-fold and 2.9-fold higher in rRC-HL–infected and CVS-24–infected mice, respectively, at 4 dpi and was 2.4-fold, 2.7-fold, and 3.2-fold higher in rRC-HL–infected, GX074-infected, and CVS-24–infected mice, respectively, at 7 dpi (Figure 1D).

To further confirm these results *in vitro*, C8-D1A cells were infected with rRC-HL, GX074, or CVS-11 strains at an MOI of 0.1. The mRNA level of ApoD was measured using qRT-PCR analysis. Compared with those in mock-infected cells, the ApoD mRNA levels were 1.3-fold and 2.4-fold higher in rRC-HL–infected and GX074-infected C8-D1A cells, respectively, at 12 hpi. However, the ApoD mRNA levels were not significantly different between CVS-11-infected at 12 hpi. The ApoD mRNA levels in rRC-HL–infected, GX074-infected, and CVS-24–infected cells were 5.0-fold, 3.5-fold, and 3.2-fold higher, respectively, than those in mock-infected cells at 24 hpi. At 48 hpi, only the ApoD mRNA level in rRC-HL–infected cells was significantly upregulated (by 4.4-fold) when compared with that in mock-infected cells (Figure 1E). These findings suggested that RABV infection significantly upregulates ApoD expression both *in vitro* and *in vivo*.

ApoD overexpression promotes RABV replication in C8-D1A cells

Based on above experimental results, RABV infection could upregulate ApoD expression *in vitro* and *in vivo*. Next, the role of ApoD in RABV infection was examined. C8-D1A cells were transiently transfected with a pcDNA-ApoD^{-MYC} plasmid to overexpress ApoD. ApoD-overexpressing C8-D1A cells were infected with the rRC-HL strain. The mRNA and protein levels of N, P, M, and G genes were evaluated using qRT-PCR and Western blotting analyses, respectively. Additionally, the titer of rRC-HL strains was examined. The mRNA levels of viral genes in ApoD-overexpressing cells were significantly higher than those in empty vector–transfected cells at 12, 24, and 48 hpi. In particular, the N mRNA levels in pcDNA-ApoD^{-MYC}–transfected cells were 1.5-fold, 2.0-fold, and 3.4-fold higher than those in empty vector–transfected cells at 12, 24, and 48 hpi, respectively. The P mRNA levels in pcDNA-ApoD^{-MYC}–transfected cells were 1.7-fold, 2.14-fold, and 4.1-fold higher than those in empty vector–transfected cells at 12, 24, and 48 hpi, respectively. The M mRNA levels in pcDNA-ApoD^{-MYC}–transfected cells were 2.3-fold and 4.9-fold higher than those in empty vector–transfected cells at 24 and 48 hpi, respectively. The G mRNA levels in pcDNA-ApoD^{-MYC}–transfected cells were 2.2-fold and 4.2-fold higher than those in empty vector–transfected cells at 24 and 48 hpi, respectively (Figure 2A). The rRC-HL titers in the culture supernatant of C8-D1A cells transfected with pcDNA-ApoD^{-MYC} plasmid were 4.69×10^2 FFU/mL, 1.11×10^4 FFU/mL, and 2.13×10^4 FFU/mL at 12, 24, and 48 hpi, respectively, which were significantly higher than those in empty vector–transfected cells (2.57×10^2 FFU/mL, 4.25×10^3 FFU/mL, and 6.17×10^3 FFU/mL, respectively) (Figure 2B). In contrast, the intracellular rRC-HL titers in pcDNA-ApoD^{-MYC}–transfected C8-D1A cells were 2.87×10^1, 1.79×10^2, and 1.42×10^3 FFU/mL at 12, 24, and 48 hpi, respectively, which were significantly lower than those in empty vector–transfected C8-D1A cells (6.6×10^1 FFU/mL, 8.12×10^2 FFU/mL, and 9.16×10^3 FFU/mL, respectively) (Figure 2C). The protein levels of rRC-HL N, P, M, and G were measured using Western blotting. The rRC-HL N protein levels in pcDNA-ApoD^{-MYC}–transfected cells were 1.33-fold and 2.16-fold higher than those in empty vector–transfected cells at 24 and 48 hpi, respectively. Meanwhile, the P protein levels in pcDNA-ApoD^{-MYC}–transfected cells were 1.4-fold, 1.3-fold, and 1.1-fold higher than those in empty vector–transfected cells at 12, 24, and 48 hpi, respectively. The M protein levels in pcDNA-ApoD^{-MYC}–

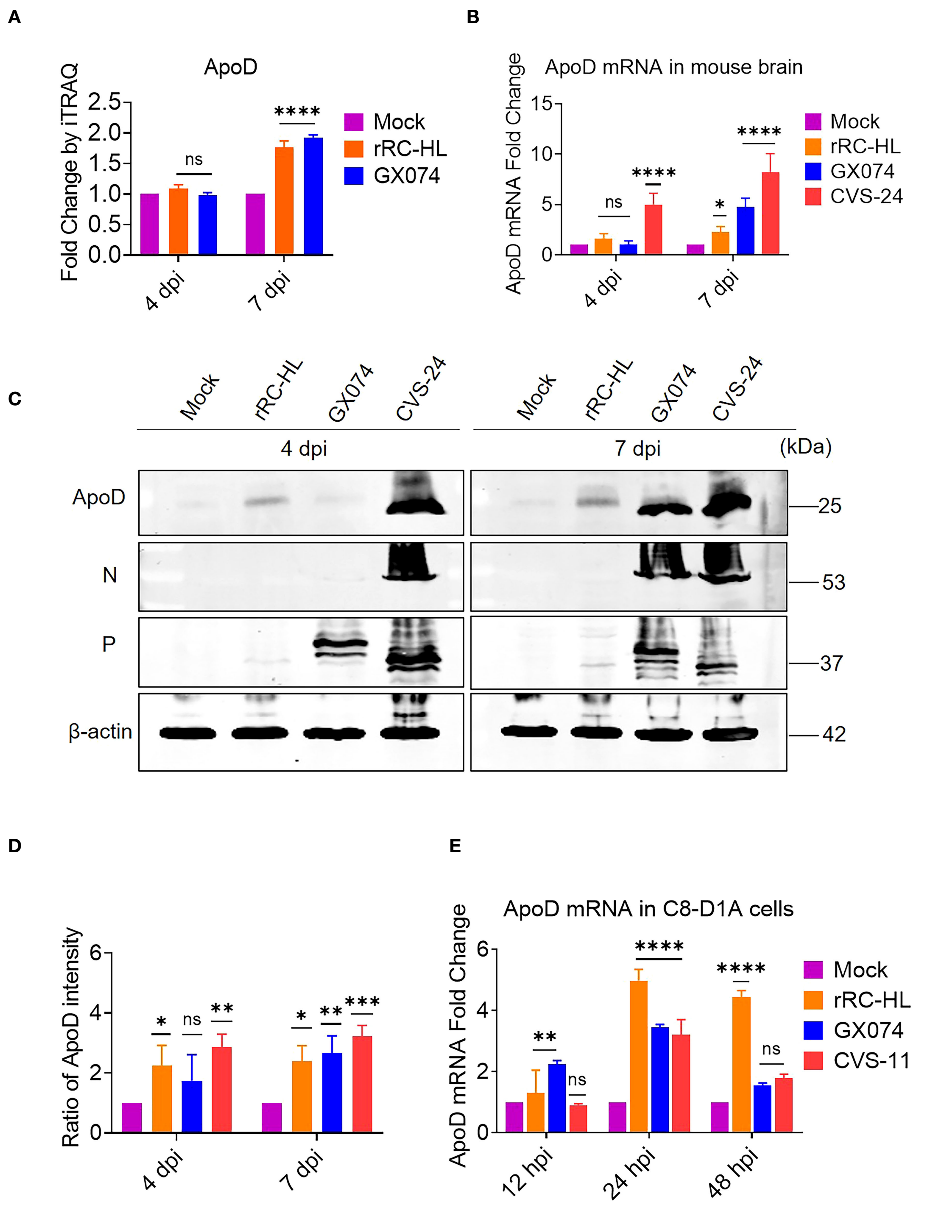

FIGURE 1
Rabies virus (RABV) infection upregulates apolipoprotein D (ApoD) expression. Kunming mice were intracerebrally inoculated with 30 μL of Dulbecco's Modified Eagle Medium (DMEM) containing 1,000 fluorescent focus units (FFU) of three different RABV strains (rRC-HL, GX074, and CVS-24) or mock-infected with 30 μL of DMEM. At 4 and 7 days post-infection (dpi), the mouse brain was harvested for further analysis. **(A)** The ApoD protein level in the mouse brain after infection with rRC-HL and GX074 strains was quantified using iTRAQ analysis. **(B)** Total RNA of the brain tissue was extracted and subjected to quantitative real-time polymerase chain reaction (qRT-PCR) analysis to examine the mRNA level of ApoD. **(C)** The protein levels of ApoD and RABV N and P in the brain tissue of RABV-infected and mock-infected mice were examined at 4 and 7 dpi using Western blotting analysis. β-actin was used as a reference protein. **(D)** The ApoD protein level was quantified using ImageJ software. The levels of ApoD protein were standardized to those of β-actin and normalized to those in the mock-infected mouse brain. **(E)** C8-D1A cells were infected with rRC-HL at a multiplicity of infection (MOI) of 0.1 or mock-infected. At 12, 24, and 48 h post-infection (hpi), cells were collected and subjected to qRT-PCR analysis to examine the mRNA level of ApoD. Data are represented as mean ± standard deviation. Statistical differences were analyzed using two-way analysis of variance (ns, non-significant; *$P < 0.05$, **$P < 0.01$, ***$P < 0.001$, and ****$P < 0.0001$).

transfected cells were 1.80-fold and 1.44-fold higher than those in empty vector–transfected cells at 24 and 48 hpi, respectively. The G protein levels in pcDNA-ApoD^{-MYC}–transfected cells were 2.1-fold and 2.3-fold higher than those in empty vector–transfected cells at 24 and 48 hpi, respectively (Figures 2D, E). Analysis of viral mRNA, proteins, and titers suggested that ApoD promotes RABV replication in C8-D1A cells.

ApoD upregulates RABV G protein expression

Previous experiments have suggested that ApoD could promote RABV replication. To further investigate how the ApoD impact RABV replication. The ApoD plays a role on viral mRNA or viral protein levels. BSR/T7-9 cells were transfected with 1 μg of pcDNA-

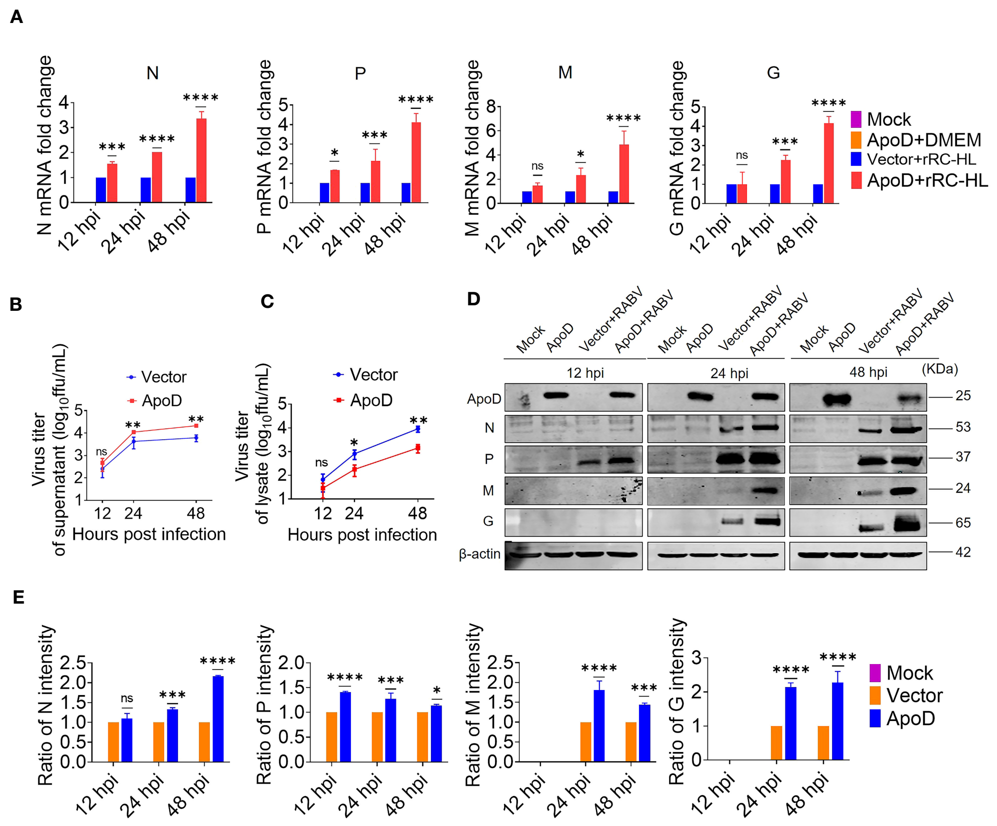

FIGURE 2
Apolipoprotein D (ApoD) overexpression promotes rabies virus (RABV) replication in C8-D1A cells. ApoD overexpression upregulated the mRNA level of RABV genes, the viral titer in the cell supernatant, and the viral protein expression level in cells. C8-D1A cells were transfected with 1 μg of the empty vector or pcDNA-ApoD^{-MYC} plasmid. At 12 h post-transfection (hpt), the cells were infected with rRC-HL at a multiplicity of infection (MOI) of 0.1. **(A)** At 12, 24, and 48 h post-infection (hpi), C8-D1A cells were lysed with buffer RL, and the mRNA levels of RABV N, P, M, and G genes were examined using quantitative real-time polymerase chain reaction (qRT-PCR) analysis. **(B, C)** At 12, 24, and 48 hpi, the culture supernatant and the lysate of C8-D1A cells were collected, and the viral titers were tested with BSR/T7-9 cells. **(D)** At 12, 24, and 48 hpi, C8-D1A cells were lysed with radioimmunoprecipitation assay buffer, and the protein expression levels of RABV N, P, M, and G were examined using Western blotting analysis. **(E)** Statistical analysis of the protein expression levels of RABV N, P, M, and G proteins was performed using ImageJ software. The expression levels of RABV N, P, M, and G proteins were standardized to those of β-actin and normalized to those of empty vector–transfected cells. Data are represented as mean ± standard deviation. Two-way analysis of variance for **(A, E)**; Student's t-test for **(B, C)** (ns, non-significant; *$P < 0.05$, **$P < 0.01$, ***$P < 0.001$, and ****$P < 0.0001$).

ApoD^{-MYC} plasmid for 12 h, followed by transfection with 1 μg of pC-rRC-HL-G^{-FLAG}, pC-GX074-G^{-FLAG}, or pC-CVS-11-G^{-FLAG} plasmid. The cell lysates were prepared at 12, 24, and 48 hpt using RIPA buffer. The G protein expression level was examined using Western blotting analysis. The rRC-HL G, GX074 G, and CVS-11 G levels in pcDNA-ApoD^{-MYC}–transfected cells were significantly higher than those in mock-transfected cells at 12, 24, and 48 hpt. The expression levels of rRC-HL G protein in pcDNA-ApoD^{-MYC}–transfected cells were 2.81-fold, 1.95-fold, and 1.33-fold higher than those in mock-transfected cells at 12, 24, and 48 hpt, respectively (Figure 3A). The GX074 G expression levels in pcDNA-ApoD^{-MYC}–transfected cells were 1.3-fold, 1.5-fold, and 2.1-fold higher than those in mock-transfected cells at 12, 24, and 48 hpt, respectively (Figure 3B). The CVS-11 G levels in pcDNA-ApoD^{-MYC}–transfected cells were 1.6-fold, 2.51-fold, and 1.91-fold higher than those in mock-transfected cells at 12, 24, and 48 hpt, respectively (Figure 3C). Next, the effect of ApoD on the expression of other RABV proteins (N, P, and M) was examined. The experimental procedure used to evaluate RABV N, P, and M protein levels was similar to that used to evaluate RABV G protein levels. ApoD did not significantly affect the expression of RABV N, P, and M proteins (Supplementary Figure 1). These results suggest that ApoD regulated the expression of RABV G protein but not that of N, P, and M proteins.

ApoD interacts with RABV G protein

Previous experiments have showed that ApoD upregulates RABV G protein expression. To further investigate the mechanism how the ApoD promotes RABV replication and to explore whether ApoD interacts with RABV G protein, ApoD and RABV G protein were subjected to co-immunoprecipitation (Co-IP) assay. HEK-293T cells were co-transfected with the pC-GX074-G^{-FLAG} and pcDNA-ApoD^{-MYC} plasmids and harvested at 24 hpt. The Co-IP assay was performed with anti-MYC or anti-FLAG antibodies. ApoD could interact with GX074 G protein (Figure 4A). Parallel experiments for analyzing the interaction

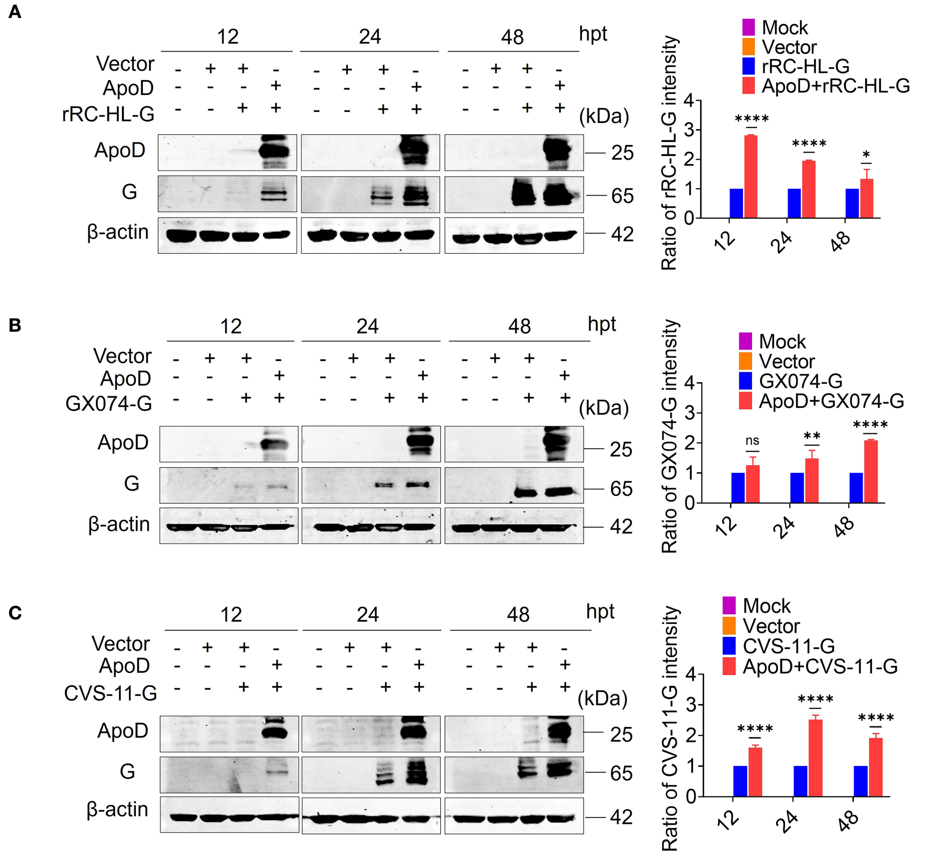

FIGURE 3
Apolipoprotein D (ApoD) upregulates rabies virus (RABV) G protein expression. **(A–C)** BSR/T7-9 cells were transfected with 1 μg of pcDNA-ApoD$^{\text{-MYC}}$ plasmid. At 12 h post-transfection (hpt), cells were transfected with 1 μg pC-rRC-HL-G$^{\text{-FLAG}}$, pC-GX074-G$^{\text{-FLAG}}$, or pC-CVS-11-G$^{\text{-FLAG}}$ plasmid. At 12, 24, and 48 h, the G genes of rRC-HL, GX074, and CVS-11 were expressed in BSR/T7-9 cells. The cell lysates were prepared using radioimmunoprecipitation assay lysis buffer. The protein expression levels of rRC-HL G **(A)**, GX074 G **(B)**, and CVS-11 G **(C)** were examined using Western blotting analysis. ImageJ software was used to quantify the G protein level. The expression levels of G protein were standardized to those of β-actin and normalized to those in cells not transfected with pcDNA-ApoD$^{\text{-MYC}}$. Data are represented as mean ± standard deviation. Statistical differences were analyzed using two-way analysis of variance (ns, non-significant; **P* < 0.05, ***P* < 0.01, and *****P* < 0.0001).

between ApoD and rRC-HL G protein were performed. ApoD could interact with rRC-HL G protein (Figure 4B). To further explore the interaction of ApoD with GX074 N, P, and M proteins, pcDNA-GX074-N$^{\text{-FLAG}}$, pcDNA-GX074-P$^{\text{-FLAG}}$, and pcDNA-GX074-M$^{\text{-FLAG}}$ plasmids were constructed. HEK-293T cells were co-transfected with pcDNA-GX074-N$^{\text{-FLAG}}$/pcDNA-ApoD$^{\text{-MYC}}$, pcDNA-GX074-P$^{\text{-FLAG}}$/pcDNA-ApoD$^{\text{-MYC}}$, or pcDNA-GX074-M$^{\text{-FLAG}}$/pcDNA-ApoD$^{\text{-MYC}}$. ApoD did not interact with N, P, and M proteins of the street strain GX074 (Figure 4C). In short, the results revealed that ApoD could interact with the G protein from the street strain GX074 and attenuate strain rRC-HL.

To further identify the interaction between ApoD and GX074 G protein, a protein–protein colocalization test was performed. HEK-293T cells were co-transfected with pC-GX074-G$^{\text{-FLAG}}$ and pcDNA-ApoD$^{\text{-MYC}}$ plasmids for 24 h. The HEK-293T cells expressing GX074-G$^{\text{-FLAG}}$ and ApoD$^{\text{-MYC}}$ proteins were fixed and subjected to IFA using anti-FLAG tag and anti-MYC tag antibodies. GX074-G$^{\text{-FLAG}}$ co-localized with ApoD$^{\text{-MYC}}$ proteins in the cytoplasm of HEK-293T cells (Figure 4D), further confirming the interaction between ApoD and G protein.

The GST pulldown assay was performed to verify the ApoD–G protein interaction. GST-fused ApoD (ApoD$^{\text{-GST}}$) was expressed and purified. ApoD$^{\text{-GST}}$ was used to fish the GX074 G protein expressed in the HEK-293T cells (transfected with pC-GX074-G$^{\text{-FLAG}}$) using the GST pulldown assay. The result revealed that the ApoD$^{\text{-GST}}$ could directly interact with GX074 G protein *in vitro* (Figure 4E).

ApoD–G protein interaction facilitates RABV replication

Next, to investigate how the ApoD–G protein interaction facilitates RABV replication or the ApoD–G protein interaction influences which step of the viral cycle. N2A cells were co-transfected with pcDNA-ApoD$^{\text{-MYC}}$ and pC-GX074-G$^{\text{-FLAG}}$ plasmids. The control group was transfected with pcDNA-ApoD$^{\text{-MYC}}$ plasmid alone. At 24 hpt, the N2A cells were infected with RABV rRC-HL strain at an MOI of 0.1. The N2A cells were collected and used to detect the mRNA and protein expression

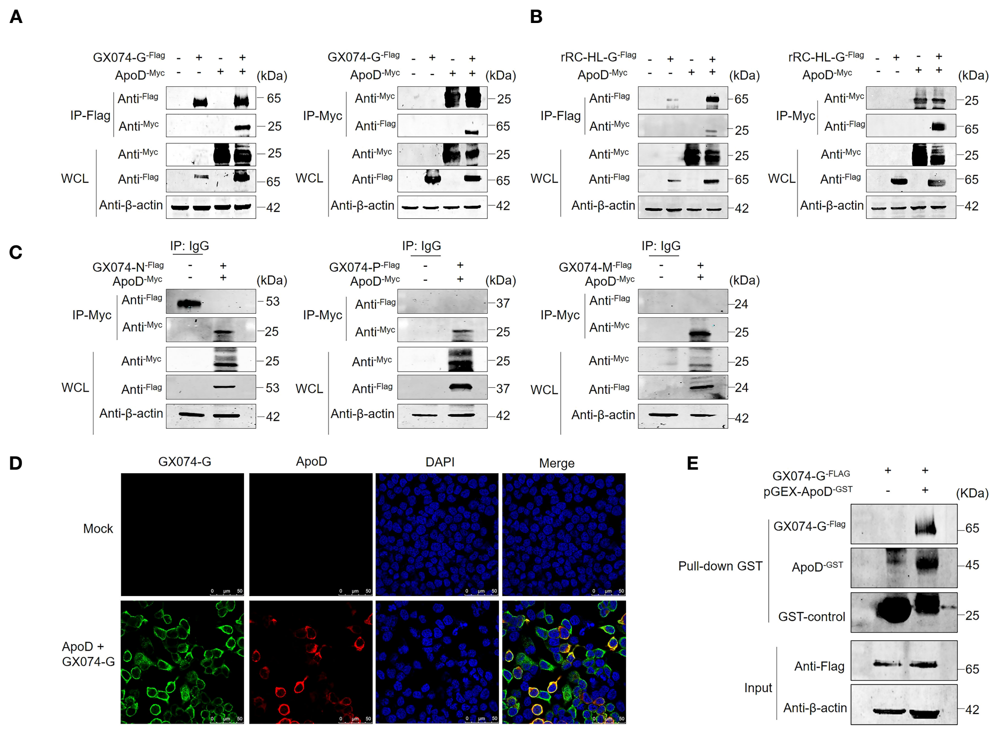

FIGURE 4
Apolipoprotein D (ApoD) interacts with rabies virus (RABV) G protein. **(A, B)** HEK-293T cells were co-transfected with pC-GX074-G^{-FLAG} and pcDNA-ApoD^{-MYC} plasmids **(A)** or pC-rRC-HL-G^{-FLAG} and pcDNA-ApoD^{-MYC} plasmids **(B)**. Cells transfected with individual plasmids served as a control. The cells were lysed with NP-40 lysis buffer and subjected to co-immunoprecipitation (Co-IP) using a monoclonal antibody (Mab) against the FLAG/MYC tag. Western blotting analysis was performed to detect the products from the immunoprecipitation and the whole-cell lysate with the relevant antibodies. **(C)** HEK-293T cells were co-transfected with pcDNA-GX074-N^{-FLAG}, pcDNA-GX074-P^{-FLAG}, or pcDNA-GX074-M^{-FLAG} plasmids and pcDNA-ApoD^{-MYC} plasmid. Cell extracts were used to perform immunoprecipitation with IgG or anti-MYC antibody. The products of immunoprecipitation and the whole-cell lysate were examined using Western blotting analysis with the relevant antibodies. **(D)** HEK-293T cells were co-transfected with pC-GX074-G^{-FLAG} and pcDNA-ApoD^{-MYC} plasmids or mock-transfected for 24 h, fixed with methanol and acetone at a 1:1 ratio, and stained with anti-MYC and anti-FLAG Mabs and 4′,6-diamidino-2-phenylindole (DAPI). The cells were observed under a confocal fluorescence microscope. Scale bar, 50 µm. **(E)** Glutathione S transferase (GST) pulldown assay of ApoD and GX074 G protein. The GST-ApoD–fused protein (ApoD^{-GST}) and GST were purified and incubated with HEK-293T whole-cell lysate. ApoD, GX074 G protein, and GST control in the pulldown samples were detected using Western blotting analysis with specific antibodies.

levels of rRC-HL genes. The mRNA levels of rRC-HL N, P, and M genes in pcDNA-ApoD^{-MYC}/pcDNA-GX074-G^{-FLAG}–co-transfected cells were not significantly higher than those in pcDNA-ApoD^{-MYC}–transfected cells at 12, 24, and 48 hpi. Compared with those in pcDNA-ApoD^{-MYC}–transfected cells, the mRNA levels of rRC-HL G gene were 1.7-fold higher at 12 hpi and 1.3-fold and 1.2-fold higher at 24 and 48 hpi, respectively, in pcDNA-ApoD^{-MYC}/pcDNA-GX074-G^{-FLAG}–co-transfected cells (Figure 5A). The expression levels of rRC-HL N, P, M, and G proteins in pcDNA-ApoD^{-MYC}/pcDNA-GX074-G^{-FLAG}–co-transfected cells were higher than those in pcDNA-ApoD^{-MYC}–transfected cells at 12, 24, and 48 hpi. In particular, the expression levels of rRC-HL N protein in pcDNA-ApoD^{-MYC}/pcDNA-GX074-G^{-FLAG}–co-transfected cells were 1.18-fold higher than those in pcDNA-ApoD^{-MYC}–transfected cells at 48 hpi. Meanwhile, the rRC-HL P protein expression levels in pcDNA-ApoD^{-MYC}/pcDNA-GX074-G^{-FLAG}–co-transfected cells were 1.13-fold higher than those in pcDNA-ApoD^{-MYC}–transfected cells at 48 hpi. The rRC-HL M protein expression levels in pcDNA-ApoD^{-MYC}/pcDNA-GX074-G^{-FLAG}–co-transfected cells were 1.05-fold and 1.04-fold higher than those in pcDNA-ApoD^{-MYC}–transfected cells at 24 and 48 hpi, respectively. The rRC-HL G protein expression levels in pcDNA-ApoD^{-MYC}/pcDNA-GX074-G^{-FLAG}–co-transfected cells were 2.1-fold, 1.03-fold, and 1.03-fold higher than those in pcDNA-ApoD^{-MYC}–transfected cells at 12, 24, and 48 hpi, respectively (Figures 5B, C). Next, the rRC-HL virus titer in the culture supernatant was measured. The rRC-HL virus titers in the supernatant of N2A cells co-transfected pcDNA-ApoD^{-MYC} and pC-GX074-G^{-FLAG} plasmids were 1.24 × 10^3 FFU/mL, 1.0 × 10^5 FFU/mL, and 6.28 × 10^7 FFU/mL at 12, 24, and 48 hpt, respectively, which were significantly higher than those in the supernatant of cells transfected with pcDNA-ApoD^{-MYC} plasmid (6.18 × 10^2 FFU/mL, 3.72 × 10^4 FFU/mL, and 1.25 × 10^6 FFU/mL, respectively) (Figure 5D). Taken together, these results confirmed that ApoD–G protein interaction facilitates RABV replication.

ApoD–G protein interaction upregulates the cholesterol level

Based on the above experimental results, we hypothesized that ApoD–G protein interaction is correlated with cholesterol. Thus,

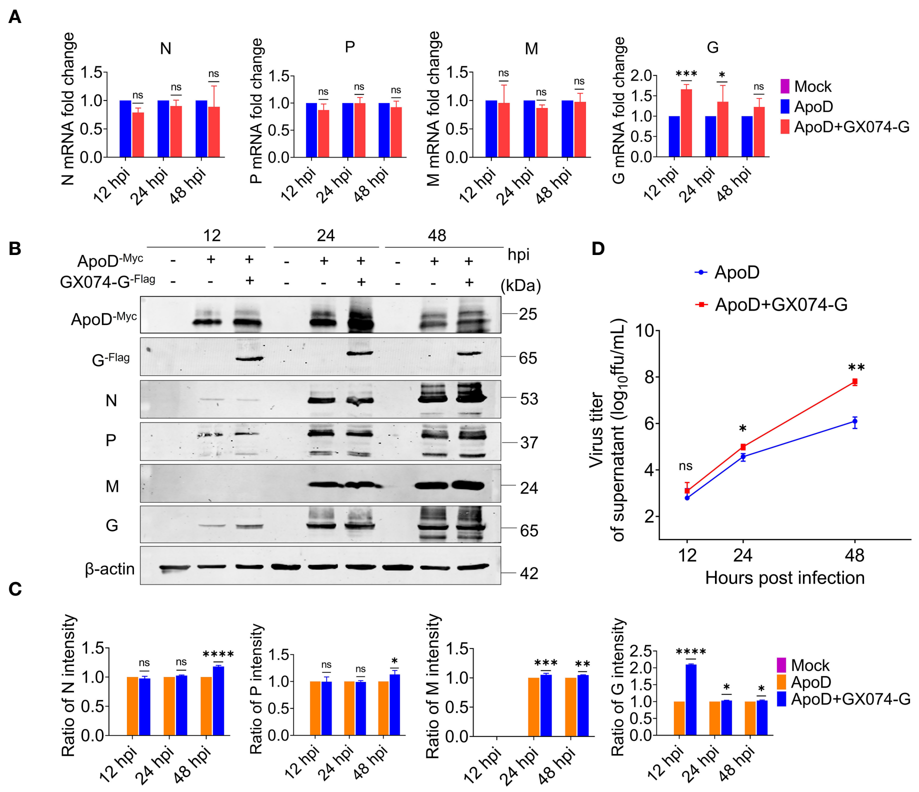

FIGURE 5
Apolipoprotein D (ApoD)–G protein interaction facilitates rabies virus (RABV) replication. N2A cells were co-transfected with pcDNA-ApoD^{-MYC} and pC-GX074-G^{-FLAG} plasmids. The control group was transfected with pcDNA-ApoD^{-MYC} plasmid alone. Next, the cells were infected with rRC-HL at a multiplicity of infection (MOI) of 0.1 at 24 h post-transfection (hpt). **(A)** At 12, 24, and 48 h post-infection (hpi), N2A cells were lysed with buffer RL. The mRNA levels of RABV N, P, M, and G genes were measured using quantitative real-time polymerase chain reaction (qRT-PCR) analysis. **(B)** At 12, 24, and 48 hpi, N2A cells were lysed with radioimmunoprecipitation assay lysis buffer. The protein expression levels of RABV N, P, M, and G were examined using Western blotting analysis. **(C)** Statistical analysis of the N, P, M, and G protein levels in the cells was performed using ImageJ software. The expression levels of N, P, M, and G proteins were standardized to those of β-actin and normalized to those in pcDNA-ApoD^{-MYC}–transfected cells. **(D)** At 12, 24, and 48 hpi, the culture supernatant of N2A cells was collected. The viral titer was tested using BSR/T7-9 cells. Data are represented as mean ± standard deviation. Two-way analysis of variance for **(A, C)**; Student's t-test for **(D)**. (ns, non-significant; **P* < 0.05; ***P* < 0.01; ****P* < 0.001; *****P* < 0.0001).

the cholesterol level in C8-D1A cells was measured using the Amplex Red cholesterol assay. As shown in Figure 6, the cholesterol level in pcDNA-ApoD^{-MYC}–transfected cells were significantly higher (36% higher) than those in empty vector–transfected cells. Transfection with GX074-G^{-FLAG} plasmid increased the cholesterol level by 28%, whereas co-transfection with pcDNA-ApoD^{-MYC} and pC-GX074-G^{-FLAG} increased the cholesterol level by 44%. This indicated that ApoD–G protein interaction could further upregulate the cholesterol level and that cholesterol upregulation might promote virus replication.

Cholesterol promotes RABV replication

Cholesterol is the main component of cell membrane lipid rafts, which are the specific membrane microdomains required for the entry, biosynthesis, assembly, and budding of various viruses. Viperin was reported to inhibit RABV budding by downregulating the levels of cholesterol and sphingomyelin (20). To further determine the role of cholesterol in RABV replication, a type of water-soluble cholesterol was used to examine the effect of cholesterol on RABV replication. The effect of cholesterol on cell viability was examined using the CCK-8 assay to determine the toxic concentration of cholesterol for C8-D1A cells. Cholesterol exerted toxic effects on C8-D1A cells at concentrations of ≥ 300 ng/mL (Figure 7A).

To confirm the effect of cholesterol on RABV rRC-HL replication, C8-D1A cells were treated with a fresh medium containing water-soluble cholesterol (200 ng/mL) at 37°C for 4 h, followed by infection with rRC-HL at an MOI of 0.1. The RABV rRC-HL titers in the culture supernatant of water-soluble cholesterol-treated cells were 4.12×10^2 FFU/mL, 5.5×10^3 FFU/mL, and 1.35×10^4 FFU/mL at 12, 24, and 48 hpi respectively, which were significantly higher than those in untreated cells (2.75×10^2 FFU/mL, 2.89×10^3 FFU/mL, and 5.63×10^3 FFU/mL, respectively) (Figure 7B). This confirmed that cholesterol promotes RABV replication.

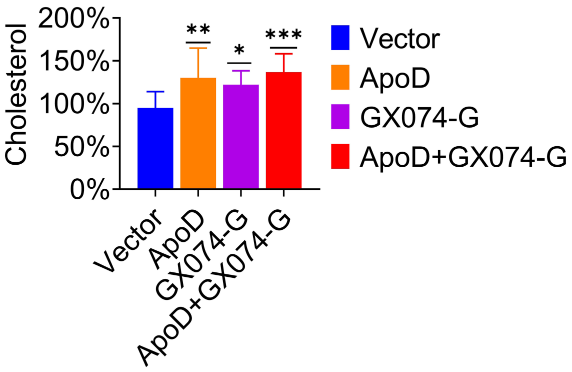

FIGURE 6
Apolipoprotein D (ApoD)–G protein interaction upregulates cholesterol level. C8-D1A cells were transfected with empty vector, pcDNA-ApoD^{-MYC}, pC-GX074-G^{-FLAG} plasmid, and co-transfected with pcDNA-ApoD^{-MYC} and pC-GX074-G^{-FLAG} plasmids, separately. These transfected cells were harvested at 48 h post-transfection (hpt) to detect the cholesterol level using a cholesterol kit (n = 6). Statistical differences were analyzed using one-way analysis of variance (ns, non-significant; *P < 0.05, **P < 0.01, and ***P < 0.001).

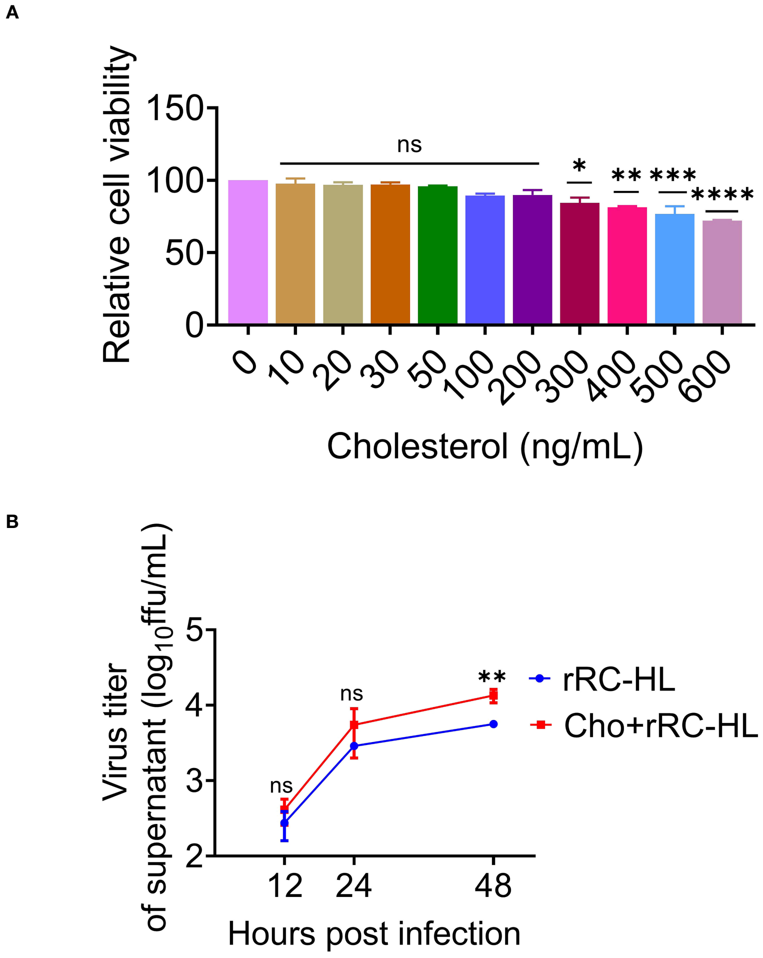

FIGURE 7
Cholesterol promotes rabies virus (RABV) replication. **(A)** C8-D1A cells were treated with different concentrations of cholesterol for 24 h. The effect of cholesterol on cell viability was determined using the cell counting kit–8 (CCK-8) assay. **(B)** C8-D1A cells were treated with a fresh medium containing water-soluble cholesterol at 37°C for 4 h. The control group was treated with fresh medium alone. The cells were then infected with rRC-HL at a multiplicity of infection (MOI) of 0.1. At 12, 24, and 48 h post-infection (hpi), the culture supernatant of C8-D1A cells was collected to examine the viral titer using BSR/T7-9 cells. Data are represented as mean ± standard deviation. One-way analysis of variance for **(A)**; Student's t-test for **(B)** (ns, non-significant; *P < 0.05, **P < 0.01, ***P <0.001 and ****P < 0.0001).

Discussion

RABV, a highly neurotropic pathogen, causes fatal encephalitis in warm-blooded mammals, including humans. RABV transmitted to humans and animals by biting or scratching from the wound site to the CNS. At the CNS, RABV establishes a productive infection and replication without interference by the peripheral immune system (4, 24). The replication of RABV in the nervous system, especially in the CNS, can be attributed to a complex process involving receptor-mediated absorption, membrane fusion, entry, transcription, synthesis, and assembly of proteins and budding. The G protein mediates the absorption and membrane fusion process of RABV. Viral replication is initiated after RABV is internalized into host cells via clathrin-mediated endocytosis (4, 25).

Apolipoprotein is a key regulator of lipid transport and lipoprotein metabolism. ApoD occurs in the macromolecular complex with lecithin-cholesterol acetyltransferase and mediates the transport and binding of bilin (12). ApoD is involved in a lot of biological processes and also closely associated with many neurological diseases. Limited studies have reported the effect of ApoD on viral replication, especially neurotropic viral replication. ApoD gene was previously reported to be upregulated in the CNS of mice infected with encephalitis-associated viruses, such as Japanese encephalitis virus (26), herpes simplex type-1 virus (27), and RABV (28).

Lipid rafts, which are an important membrane lipid domain, have been considered an active region for host-virus interactions and play an important role during the viral lifecycle (29–31). Several enveloped viruses use cholesterol in lipid rafts for infection (32, 33). Cholesterol, an important component of the cell membrane, is critical for maintaining cell viability, signaling, and physiology (34). Previous studies have demonstrated that various viruses, such as human immunodeficiency virus (35), influenza virus (36), and herpes simplex virus (37), enter the host cells through cholesterol. Additionally, mammalian ApoD is reported to be involved in cholesterol transport (38).

The functional upregulation of ApoD during virus infection was previously unclear. ApoD exerts neuroprotective effects against various neurodegeneration-inducing factors, such as oxidative stress, inflammatory stress, and excitotoxicity, as well as against aging (16, 17, 39, 40). Previously, we reported that ApoD is upregulated in the RABV-infected mouse brain using iTRAQ (Figure 1A). Based on this previous iTRAQ data, this study demonstrated that ApoD is upregulated in the mouse brain during RABV infection, as well as in RABV-infected cells *in vitro* (Figure 1E). Therefore, this study aimed to examine the role of ApoD during RABV infection and the correlation between ApoD and RABV proteins.

In this study, ApoD overexpression promoted RABV replication in C8-D1A cells. However, this finding is in contrast to the previously reported neuroprotective effects of ApoD. Further analysis revealed that ApoD facilitates RABV replication, which was consistent with the results of a previous study demonstrating that ApoD facilitates the proliferation of *Bombyx mori* nuclear polyhedrosis virus (41).

The G protein forms spikes outside the lipid envelope, recognizes cell receptors through direct interaction, and mediates cell membrane fusion with the M protein to allow RABV to enter the cells. This study investigated the correlation between ApoD and RABV proteins. ApoD could interact with RABV G protein. Additionally, ApoD interacted with G protein from the attenuated strain rRC-HL and the street strain GX074. This indicated that ApoD is a conserved target for RABV G protein, revealing novel biological characteristics (Figure 4).

The disruption of cholesterol/sphingomyelin biosynthesis can impair RABV budding (20). This study examined which step of the RABV lifecycle was affected by the interaction. N2A cells were co-transfected with pcDNA-ApoD$^{\text{-MYC}}$ and pC-GX074-G$^{\text{-FLAG}}$, followed by infection with rRC-HL. The viral titer in the culture supernatant of pcDNA-ApoD$^{\text{-MYC}}$/pC-GX074-G$^{\text{-FLAG}}$–transfected cells was 2.7-fold and 50-fold higher than that in pcDNA-ApoD$^{\text{-MYC}}$–transfected cells at 24 and 48 hpi, respectively (Figure 5). Additionally, ApoD–G protein interaction promoted cholesterol synthesis, so we speculate that the ApoD–G protein interaction may probably promote RABV budding. However, further studies are needed to confirm this speculation.

In summary, ApoD was upregulated in the mouse brain (*in vivo*) and C8-D1A cells (*in vitro*) after RABV infection. ApoD overexpression promoted RABV replication in C8-D1A cells. Meanwhile, ApoD–G protein interaction promoted RABV replication by upregulating the cholesterol level. These findings are important to reveal a novel role of ApoD in promoting typical neurotropic virus replication and may provide a potential therapeutic target for rabies.

Data availability statement

The original contributions presented in the study are included in the article/Supplementary Material. Further inquiries can be directed to the corresponding authors.

Ethics statement

The animal study protocol was approved by the Animal Experiment Committee of Guangxi University with the approval number GXU2019-021. The studies were conducted in accordance with the local legislation and institutional requirements. Written informed consent was obtained from the owners for the participation of their animals in this study.

Author contributions

HYanZ: Conceptualization, Data curation, Formal analysis, Methodology, Software, Writing – original draft, Investigation, Writing – review & editing. XL: Data curation, Formal analysis, Writing – review & editing. DL: Data curation, Formal analysis, Writing – review & editing. CZ: Software, Writing – review & editing. WW: Software, Writing – review & editing. RT: Data curation, Writing – review & editing. HYunZ: Methodology,

Writing – review & editing. ABK: Software, Writing – review & editing. CL: Writing – review & editing, Software. JL: Writing – review & editing, Software. XNL: Conceptualization, Methodology, Supervision, Writing – review & editing. TRL: Conceptualization, Funding acquisition, Methodology, Project administration, Resources, Supervision, Validation, Visualization, Writing – review & editing.

Funding

The author(s) declare financial support was received for the research, authorship, and/or publication of this article. This work was supported by the National Key Research and Development Program of China (No. 2022YFD1800100), the National Natural Science Foundation of China (No. 32070161), and the Natural Science Foundation of Guangxi Province, China (No. 2020GXNSFAA297212).

Acknowledgments

We appreciate the brothers and sisters of the Luo Team for their help with the collection of materials, as well as the friends who assisted with research work.

Conflict of interest

The authors declare that the research was conducted in the absence of any commercial or financial relationships that could be construed as a potential conflict of interest.

Publisher's note

All claims expressed in this article are solely those of the authors and do not necessarily represent those of their affiliated organizations, or those of the publisher, the editors and the reviewers. Any product that may be evaluated in this article, or claim that may be made by its manufacturer, is not guaranteed or endorsed by the publisher.

Supplementary material

The Supplementary Material for this article can be found online at: https://www.frontiersin.org/articles/10.3389/fimmu.2024.1392804/full#supplementary-material

SUPPLEMENTARY TABLE 1

Primers used for quantitative real-time polymerase chain reaction (qRT-PCR) analysis.

SUPPLEMENTARY FIGURE 1

Apolipoprotein D (ApoD) does not significantly influence the expression of rabies virus (RABV) N, P, and M proteins. **(A–F)** BSR/T7-9 cells were transfected with 1 μg of pcDNA-ApoD$^{\text{-MYC}}$ plasmid. At 12 h post-transfection (hpt), 1 μg of pcDNA-rRC-HL-N$^{\text{-FLAG}}$, pcDNA-GX074-N$^{\text{-FLAG}}$, or pcDNA-CVS-11-N$^{\text{-FLAG}}$ was transfected. The cell lysates were collected at 12, 24, and 48 hpt to determine the protein expression levels of rRC-HL N **(A)**, GX074 N **(C)**, and CVS-11 N **(E)** using Western blotting analysis. ImageJ software was used to quantify the rRC-HL N **(B)**, GX074 N **(D)**, and CVS-11 N **(F)** protein levels. The expression levels of N protein were standardized to those of β-actin and normalized to those in cells not transfected with pcDNA-ApoD$^{\text{-MYC}}$. **(G–L)** BSR/T7-9 cells were transfected with 1 μg of pcDNA-ApoD$^{\text{-MYC}}$ plasmid. At 12 hpt, 1 μg of pcDNA-rRC-HL-P$^{\text{-FLAG}}$, pcDNA-GX074-P$^{\text{-FLAG}}$, or pcDNA-CVS-11-P$^{\text{-FLAG}}$ was transfected. The cell lysates were collected at 12, 24, and 48 hpt to determine the protein expression levels of rRC-HL P **(G)**, GX074 P **(I)**, and CVS-11 P **(K)** using Western blotting analysis. ImageJ software was used to quantify rRC-HL P **(H),** GX074 P **(J)**, and CVS-11 P **(L)** protein levels. The expression levels of P protein were standardized to those of β-actin and normalized to those in cells not transfected with pcDNA-ApoD$^{\text{-MYC}}$. **(M–R)** BSR/T7-9 cells were transfected with 1 μg of pcDNA-ApoD$^{\text{-MYC}}$ plasmid. At 12 hpt, 1 μg of pcDNA-rRC-HL-M$^{\text{-FLAG}}$, pcDNA-GX074-M$^{\text{-FLAG}}$, or pcDNA-CVS-11-M$^{\text{-FLAG}}$ was transfected. The cell lysates were collected at 12, 24, and 48 hpt to determine the protein expression levels of rRC-HL M **(M)**, GX074 M **(O)**, and CVS-11 M **(Q)** using Western blotting analysis. ImageJ software was used to quantify the rRC-HL M **(N)**, GX074 M **(P)**, and CVS-11 M **(R)** protein levels. The expression levels of M protein were standardized to those of β-actin and normalized to those in cells not transfected with pcDNA-ApoD$^{\text{-MYC}}$. Data are represented as mean ± standard deviation. Statistical differences were analyzed using two-way analysis of variance (ns, non-significant).

References

1. Fooks AR, Cliquet F, Finke S, Freuling C, Hemachudha T, Mani RS, et al. Rabies. *Nat Rev Dis Primers.* (2017) 3:17091. doi: 10.1038/nrdp.2017.91

2. Zan J, Liu S, Sun D-N, Mo K-K, Yan Y, Liu J, et al. Rabies virus infection induces microtubule depolymerization to facilitate viral RNA synthesis by upregulating HDAC6. *Front Cell Infect Microbiol.* (2017) 7:146. doi: 10.3389/fcimb.2017.00146

3. O'Brien KL, Nolan T. The WHO position on rabies immunization – 2018 updates. *Vaccine.* (2019) 37:A85–7. doi: 10.1016/j.vaccine.2018.10.014

4. Fisher CR, Streicker DG, Schnell MJ. The spread and evolution of rabies virus: conquering new frontiers. *Nat Rev Microbiol.* (2018) 16:241–55. doi: 10.1038/nrmicro.2018.11

5. Hidaka Y, Lim C-K, Takayama-Ito M, Park C-H, Kimitsuki K, Shiwa N, et al. Segmentation of the rabies virus genome. *Virus Res.* (2018) 252:68–75. doi: 10.1016/j.virusres.2018.05.017

6. Wunner WH, Larson JK, Dietzschold B, Smith CL. The molecular biology of rabies viruses. *Rev Infect Dis.* (1988) 10 Suppl 4:S771–784. doi: 10.1093/clinids/10.supplement_4.s771

7. Emerson SU, Yu Y. Both NS and L proteins are required for in *vitro* RNA synthesis by vesicular stomatitis virus. *J Virol.* (1975) 15:1348–56. doi: 10.1128/jvi.15.6.1348-1356.1975

8. Schnell MJ. Requirement for a non-specific glycoprotein cytoplasmic domain sequence to drive efficient budding of vesicular stomatitis virus. *EMBO J.* (1998) 17:1289–96. doi: 10.1093/emboj/17.5.1289

9. Garoff H, Hewson R, Opstelten D-JE. Virus maturation by budding. *Microbiol Mol Biol Rev.* (1998) 62:1171–90. doi: 10.1128/mmbr.62.4.1171–1190.1998

10. He X, Jittiwat J, Kim J-H, Jenner AM, Farooqui AA, Patel SC, et al. Apolipoprotein D modulates F2-isoprostane and 7-ketocholesterol formation and has a neuroprotective effect on organotypic hippocampal cultures after kainate-induced excitotoxic injury. *Neurosci Lett.* (2009) 455:183–6. doi: 10.1016/j.neulet.2009.03.038

11. Ayrault Jarrier M, Levy G, Polonovski J. Study of humanserum alpha-lipoproteins by immunoelectrophoresis. *Bull Soc Chim Biol* (Paris). (1963) 45:703–713.

12. McConathy WJ, Alaupovic P. Isolation and partial characterization of apolipoprotein D: A new protein moiety of the human plasma lipoprotein system. *FEBS Lett.* (1973) 37:178–82. doi: 10.1016/0014–5793(73)80453–3

13. Schindler PA, Settineri CA, Collet X, Fielding CJ, Burlingame AL. Site-specific detection and structural characterization of the glycosylation of human plasma proteins lecithin:cholesterol acyltransferase and apolipoprotein D using HPLC/electrospray mass spectrometry and sequential glycosidase digestion. *Protein Sci.* (1995) 4:791–803. doi: 10.1002/pro.5560040419

14. Yang CY, Gu ZW, Blanco-Vaca F, Gaskell SJ, Yang M, Massey JB, et al. Structure of human apolipoprotein D: locations of the intermolecular and intramolecular disulfide links. *Biochemistry*. (1994) 33:12451–5. doi: 10.1021/bi00207a011

15. Rassart E, Desmarais F, Najyb O, Bergeron K-F, Mounier C. Apolipoprotein D. *Gene*. (2020) 756:144874. doi: 10.1016/j.gene.2020.144874

16. Ganfornina MD, Do Carmo S, Lora JM, Torres-Schumann S, Vogel M, Allhorn M, et al. Apolipoprotein D is involved in the mechanisms regulating protection from oxidative stress. *Aging Cell*. (2008) 7:506–15. doi: 10.1111/j.1474-9726.2008.00395.x

17. Najyb O, Do Carmo S, Alikashani A, Rassart E. Apolipoprotein D overexpression protects against kainate-induced neurotoxicity in mice. *Mol Neurobiol*. (2017) 54:3948–63. doi: 10.1007/s12035–016-9920–4

18. Kalman K, McConathy W, Araoz C, Kasa P, Lacko AG. Apolipoprotein D in the aging brain and in Alzheimer's dementia. *Neurol Res*. (2000) 22:330–6. doi: 10.1080/01616412.2000.11740678

19. Ishikawa Y, Samejima T, Nunoya T, Motohashi T, Nomura Y. Biological properties of the cell culture-adapted RC·EHL strain of rabies virus as a candidate strain for an inactivated vaccine. *J Japan Vet Med Assoc*. (1989) 42:637–43. doi: 10.12935/jvma1951.42.637

20. Tang H-B, Lu Z-L, Wei X-K, Zhong T-Z, Zhong Y-Z, Ouyang L-X, et al. Viperin inhibits rabies virus replication via reduced cholesterol and sphingomyelin and is regulated upstream by TLR4. *Sci Rep*. (2016) 6:30529. doi: 10.1038/srep30529

21. Tang H-B, Pan Y, Wei X-K, Lu Z-L, Lu W, Yang J, et al. Re-emergence of rabies in the Guangxi province of Southern China. *PloS Negl Trop Dis*. (2014) 8:e3114. doi: 10.1371/journal.pntd.0003114

22. Liu Q, Xiong Y, Luo TR, Wei YC, Nan SJ, Liu F, et al. Molecular epidemiology of rabies in Guangxi Province, south of China. *J Clin Virol*. (2007) 39:295-303. doi: 10.1016/j.jcv.2007.04.021

23. Zhang W, Liu Y, Li M, Zhu J, Li X, Luo TR, et al. Host desmin interacts with RABV matrix protein and facilitates virus propagation. *Viruses*. (2023) 15:434. doi: 10.3390/v15020434

24. Schnell MJ, McGettigan JP, Wirblich C, Papaneri A. The cell biology of rabies virus: using stealth to reach the brain. *Nat Rev Microbiol*. (2010) 8:51–61. doi: 10.1038/nrmicro2260

25. Guo Y, Duan M, Wang X, Gao J, Guan Z, Zhang M. Early events in rabies virus infection—Attachment, entry, and intracellular trafficking. *Virus Res*. (2019) 263:217–25. doi: 10.1016/j.virusres.2019.02.006

26. Saha S, Rangarajan PN. Common host genes are activated in mouse brain by Japanese encephalitis and rabies viruses. *J Gen Virol*. (2003) 84:1729–35. doi: 10.1099/vir.0.18826–0

27. Kang S, Seo S, Hill J, Kwon B, Lee H, Cho H, et al. Changes in gene expression in latent HSV-1-infected rabbit trigeminal ganglia following epinephrine iontophoresis. *Curr Eye Res*. (2003) 26:225–9. doi: 10.1076/ceyr.26.3.225.14894

28. Prosniak M, Hooper DC, Dietzschold B, Koprowski H. Effect of rabies virus infection on gene expression in mouse brain. *Proc Natl Acad Sci USA*. (2001) 98:2758–63. doi: 10.1073/pnas.051630298

29. Bender FC, Whitbeck JC, Ponce de Leon M, Lou H, Eisenberg RJ, Cohen GH. Specific association of glycoprotein B with lipid rafts during herpes simplex virus entry. *J Virol*. (2003) 77:9542–52. doi: 10.1128/jvi.77.17.9542–9552.2003

30. Blaising J, Pécheur E-I. Lipids: a key for hepatitis C virus entry and a potential target for antiviral strategies. *Biochimie*. (2013) 95:96–102. doi: 10.1016/j.biochi.2012.07.016

31. Mañes S, del Real G, Martínez-A C. Pathogens: raft hijackers. *Nat Rev Immunol*. (2003) 3:557–68. doi: 10.1038/nri1129

32. Chazal N, Gerlier D. Virus entry, assembly, budding, and membrane rafts. *Microbiol Mol Biol Rev*. (2003) 67:226–37. doi: 10.1128/MMBR.67.2.226–237.2003

33. Waheed AA, Freed EO. The role of lipids in retrovirus replication. *Viruses*. (2010) 2:1146–80. doi: 10.3390/v2051146

34. Incardona JP, Eaton S. Cholesterol in signal transduction. *Curr Opin Cell Biol*. (2000) 12:193–203. doi: 10.1016/s0955–0674(99)00076–9

35. Yang S-T, Kiessling V, Simmons JA, White JM, Tamm LK. HIV gp41-mediated membrane fusion occurs at edges of cholesterol-rich lipid domains. *Nat Chem Biol*. (2015) 11:424–31. doi: 10.1038/nchembio.1800

36. Biswas S, Yin S-R, Blank PS, Zimmerberg J. Cholesterol promotes hemifusion and pore widening in membrane fusion induced by influenza hemagglutinin. *J Gen Physiol*. (2008) 131:503–13. doi: 10.1085/jgp.200709932

37. Wudiri GA, Schneider SM, Nicola AV. Herpes simplex virus 1 envelope cholesterol facilitates membrane fusion. *Front Microbiol*. (2017) 8:2383. doi: 10.3389/fmicb.2017.02383

38. Flores R, Jin X, Chang J, Zhang C, Cogan DG, Schaefer EJ, et al. LCAT, ApoD, and ApoA1 expression and review of cholesterol deposition in the cornea. *Biomolecules*. (2019) 9:785. doi: 10.3390/biom9120785

39. Dassati S, Waldner A, Schweigreiter R. Apolipoprotein D takes center stage in the stress response of the aging and degenerative brain. *Neurobiol Aging*. (2014) 35:1632–42. doi: 10.1016/j.neurobiolaging.2014.01.148

40. Do Carmo S, Jacomy H, Talbot PJ, Rassart E. Neuroprotective effect of apolipoprotein D against human coronavirus OC43-induced encephalitis in mice. *J Neurosci*. (2008) 28:10330–8. doi: 10.1523/JNEUROSCI.2644–08.2008

41. Fei S, Xia J, Ma G, Zhang M, Sun J, Feng M, et al. Apolipoprotein D facilitate the proliferation of BmNPV. *Int J Biol Macromol*. (2022) 223:830–6. doi: 10.1016/j.ijbiomac.2022.11.032

frontiers | Frontiers in Immunology

TYPE Original Research
PUBLISHED 11 June 2024
DOI 10.3389/fimmu.2024.1381026

Check for updates

OPEN ACCESS

EDITED BY
Shen Yang,
Cedars Sinai Medical Center, United States

REVIEWED BY
Kai Li,
Chinese Academy of Agricultural Sciences, China
Madhu Chhanda Mohanty,
National Institute of Virology (ICMR), India

*CORRESPONDENCE
Maopeng Wang
wangmaopenga@126.com
Chang Li
lichang78@163.com
Ningyi Jin
ningyik@126.com

RECEIVED 02 February 2024
ACCEPTED 27 May 2024
PUBLISHED 11 June 2024

CITATION
Jiang Y, Zhang G, Li L, Chen J, Hao P, Gao Z, Hao J, Xu Z, Wang M, Li C and Jin N (2024) A novel host restriction factor MRPS6 mediates the inhibition of PDCoV infection in HIEC-6 cells.
Front. Immunol. 15:1381026.
doi: 10.3389/fimmu.2024.1381026

COPYRIGHT
© 2024 Jiang, Zhang, Li, Chen, Hao, Gao, Hao, Xu, Wang, Li and Jin. This is an open-access article distributed under the terms of the Creative Commons Attribution License (CC BY). The use, distribution or reproduction in other forums is permitted, provided the original author(s) and the copyright owner(s) are credited and that the original publication in this journal is cited, in accordance with accepted academic practice. No use, distribution or reproduction is permitted which does not comply with these terms.

A novel host restriction factor MRPS6 mediates the inhibition of PDCoV infection in HIEC-6 cells

Yuhang Jiang[1,2], Guoqing Zhang[2], Letian Li[2], Jing Chen[2], Pengfei Hao[2], Zihan Gao[2], Jiayi Hao[1,2], Zhiqiang Xu[2], Maopeng Wang[3]*, Chang Li[1,2]* and Ningyi Jin[1,2]*

[1]College of Veterinary Medicine, Northwest A&F University, Yangling, China, [2]Research Unit of Key Technologies for Prevention and Control of Virus Zoonoses, Chinese Academy of Medical Sciences, Changchun Institute of Veterinary Medicine, Chinese Academy of Agricultural Sciences, Changchun, China, [3]Wenzhou Key Laboratory for Virology and Immunology, Institute of Virology, Wenzhou University, Wenzhou, China

Introduction: Porcine deltacoronavirus (PDCoV) is a zoonotic pathogen with a global distribution, capable of infecting both pigs and humans. To mitigate the risk of cross-species transmission and potential outbreaks, it is crucial to characterize novel antiviral genes, particularly those from human hosts.

Methods: This research used HIEC-6 to investigate PDCoV infection. HIEC-6 cells were infected with PDCoV. Samples were collected 48 h postinfection for proteomic analysis.

Results: We discovered differential expression of MRPS6 gene at 48 h postinfection with PDCoV in HIEC-6 cells. The gene expression initially increased but then decreased. To further explore the role of MRPS6 in PDCoV infection, we conducted experiments involving the overexpression and knockdown of this gene in HIEC-6 and Caco2 cells, respectively. Our findings revealed that overexpression of MRPS6 significantly inhibited PDCoV infection in HIEC-6 cells, while knockdown of MRPS6 in Caco2 cells led to a significant increase of virus titer. Furthermore, we investigated the correlation between PDCoV infection and the expression of MRPS6. Subsequent investigations demonstrated that MRPS6 exerted an augmentative effect on the production of IFN-β through interferon pathway activation, consequently impeding the progression of PDCoV infection in cellular systems. In conclusion, this study utilized proteomic analysis to investigate the differential protein expression in PDCoV-infected HIEC-6 cells, providing evidence for the first time that the MRPS6 gene plays a restrictive role in PDCoV virus infection.

Discussion: Our findings initially provide the validation of MRPS6 as an upstream component of IFN-β pathway, in the promotion of IRF3, IRF7, STAT1, STAT2 and IFN-β production of HIEC-6 via dual-activation from interferon pathway.

KEYWORDS

PDCoV, proteomics, MRPS6, host restriction factor, IFN-β

1 Introduction

Coronaviruses (CoV) belong to a group of enveloped RNA viruses classified into four genera: alpha, beta, gamma, and delta. These viruses can induce respiratory and gastrointestinal diseases in both human and animal populations, with symptoms ranging in severity (1). Severe Acute Respiratory Syndrome Coronavirus (SARS-CoV), Middle East Respiratory Syndrome Coronavirus (MERS-CoV), and Severe Acute Respiratory Syndrome Coronavirus 2 (SARS-CoV-2) gave rise to significant epidemics with notable levels of morbidity and mortality in the years 2003, 2012, and 2019, respectively (2). Over 675 instances of animal outbreaks have been documented, leading to a total of over 2,000 animal infections, encompassing both domestic and wild species. (3). Civets as a direct source of SARS-CoV-2 (4). Non-primate model animals, including cats and dogs (5) ferrets (6) monkeys (7) baboons (8) etc. This suggests that SARS-CoV-2 can be transmitted between humans and animals. MERS is an exceedingly fatal respiratory ailment induced by a distinct *betacoronavirus* member known as MERS-CoV (9). The MERS-CoV similar to several other coronaviruses, originates in bats (10). Human transmission of MERS-CoV through the intermediary role of infected dromedary camels (11). The inaugural instance of human infection with the MERS-CoV was documented in the year 2012 (12). Coronaviruses possessing zoonotic potential entail consequential biosafety hazards, thereby presenting noteworthy disease burdens and economic ramifications for society.

PDCoV is a coronavirus that was initially discovered in Hong Kong, China in 2012 (13). Since then, outbreaks of PDCoV have been reported in the United States (14) and various countries in Asia (15–17). PDCoV can infect pigs of all ages, but piglets are more susceptible to the virus (18). The primary sites of infection are the distal jejunum and ileum, leading to symptoms such as watery diarrhea, vomiting, dehydration, and weight loss (19, 20). Their clinical manifestations are similar to those caused by porcine epidemic diarrhea virus (PEDV), transmissible gastroenteritis virus (TGEV), and co-infections (21). This virus poses a significant threat to the livestock industry, particularly due to its high piglet mortality rates. PDCoV exhibits a broad spectrum of infectivity across multiple species, including pigs, poultry, mice, leopard cats, pigeons, and even humans, indicating a potential risk to public health (21–26).

The entry of PDCoV into host cells is mediated by aminopeptidase N, which plays a crucial role in facilitating viral entry through the endocytosis pathway. Endocytic viral entry is a crucial determinant of the efficient replication of PDCoV (27). Its infection results in a decrease in peroxisome abundance, which serves as the site for MAVS activation, leading to the induction of IRF1 and subsequent production of type III interferon (IFN). Furthermore, PDCoV actively suppresses the type III IFN response as a strategy to evade host antiviral immunity (28). Ergosterol peroxide (EP) demonstrates inhibitory effects on PDCoV infection and regulates the immune responses of the host by suppressing the activation of NF-κB and p38/MAPK signaling pathways. HIEC cells, derived from the fetal immature small intestine, are susceptible to PDCoV infection (29), indicating its potential to spread disease among individuals (30). However, the precise mechanism underlying its cross-species infection remains unclear. To address this knowledge gap, the present study employed HIEC-6 as a cell model and conducted a comprehensive proteomic analysis. The aim was to elucidate the novel molecular mechanisms associated with PDCoV infection at the protein level and identify potential antiviral agents with efficacy against this pathogen.

Differential proteomics has emerged as a valuable tool for studying virus-host interactions and the modulation of cellular processes during infection (31). By investigating virus-host protein interactions, proteomics provides insights into the molecular mechanisms of viral replication and pathogenesis (32). While numerous inhibitory host proteins have been identified for PDCoV infection in pigs, there is a lack of specific studies investigating the relationship with human proteins or innate immune molecules. Thus, this experiment aims to provide a preliminary investigation into the association between the differential expression gene (DEG) MRPS6 and PDCoV infection in humans.

2 Materials and methods

2.1 Cells and viruses

HIEC-6, MA104, HEK293, HEK293T, DF1, MDCK, BHK21, ST, LLC-PK1, IPEC-J2, and Caco2 were kept in our laboratory (The cell lines present in this study were obtained from ATCC). All cells were cultured using Dulbecco's Modified Eagle's Medium (DMEM; Gibco) containing 10% fetal bovine serum (Gibco) and 1% penicillin-streptomycin solution (Hyclone). PDCoV (Genbank No. OK546242) was a kind gift from Prof. Bin Li (33).

2.2 Antibodies and reagents

HRP-conjugated goat anti-rabbit IgG (H+L) (CAT#A0208), Cy3-labeled goat anti-rabbit immunoglobulin (H+L) (Cat #A0516) and FITC-labeled goat anti-mouse immunoglobulin (H +L) (CAT#A0562) were purchased from Beyotime Biotech Inc. Lipo^{TM} RNAiMAX and LIpo^{TM} 3000 were purchased from Invitrogen. SYBR-Green (Promega) and Poly-IC (Merck, USA) were used in the experiments. Anti-PDCoV N rabbit polyclonal antibody was prepared in our laboratory. Specific antibodies for MRPS6 and GAPDH were separately purchased from ORIGENE and Genetex. Polyclonal antibody for IRF-3 was purchased from Sanying (Proteintech). Antibody for STAT1, STAT2, IRF7 and IFN-Beta was purchased from Cell Signaling Technology.

pCAGGS-MRPS6 was constructed in our laboratory. Briefly, MRPS6 was obtained by amplification using primers and pCAGGS-MRPS6 was obtained by subcloning *EcoR I* and Not *I* into pCAGGS (Inovogen Technologies). Recombinant plasmids were validated by PCR and sequencing.

2.3 Virus replication kinetics

LLC-PK1 cells were inoculated with PDCoV for virus replication. The virus was subsequently diluted with DMEM containing 10 µg/mL trypsin. After incubation at 37°C for 2 hours, the medium of host cell LLC-PK1 was changed to remove unattached virus until 50% cell were induced to produce cytopathic effect (CPE). The cells were then subjected to one cycle of freeze-thawing, and the supernatant containing the virus was collected by centrifugation at 12,000 rpm for 1 min.

2.4 One-step growth curve

HIEC-6 cells were seeded into 12-well plates at a concentration of 2×10^5 cells per well, incubated overnight to reach 70%–80% confluency, and infected with the PDCoV virus at a MOI of 1. The cell-virus admixture was harvested at time intervals of 6, 12, 24, 36, 48 and 60 hours postinfection. Each collected sample underwent a single freeze-thaw cycle, followed by centrifugation at 12,000 rpm for 1 min to precipitate cellular debris, thereby allowing for the isolation of the viral supernatant.

2.5 Virus titer assay

We have determined the virus titer as previous description (34). Briefly, HIEC-6 or Caco2 cells were seeded in 96-well plates at a density of 1×10^5 cells per well. The PDCoV samples were then diluted serially at a 10-fold dilution with 100 µL per well, and each sample was repeated three times. The $TCID_{50}$ (median tissue culture infectious dose) was subsequently calculated using the Reed-Muench method.

2.6 Plasmids, siRNA, poly-IC transfection

The coding sequence of human MRPS6 (NM_032476.4) was amplified from Caco2 cells and subsequently inserted into the pCAGGS vector. HIEC-6 cells were cultured until reaching 80% confluency and transfected with the pCAGGS-MRPS6 plasmid or poly-IC (60 mM per well) using LIpo^{TM} 3000 Transfection Reagent. MRPS6 siRNA(stB0013147A) purchased from RiboBio was transfected into Caco2 with 80–90% confluency with RNAiMAX transfection reagent for preparation.

2.7 Mass spectrometry analysis, data processing of proteomics

The protein samples were subjected to extraction and subsequently underwent quality control. Those samples that passed the quality control were then separated and subjected to liquid quality control in DDA mode. The obtained data from DDA scanning mode were searched against the Human Protein Data Bank using Spectronaut-Pulsar (version 14.0, Biognosys), a library search software. Once the search was completed, Spectronaut software (version 14.0, Biognosys) was utilized to directly generate spectral libraries. Additionally, interscan software was employed to annotate the GO functions, which included Pfam, PRINTS, ProDom, SMART, ProSite, and PANTHER databases. Functional protein family, and pathway analysis of identified proteins by KEGG (35). Volcano plot analysis, clustered heatmap analysis, and pathway enrichment analysis for DEGs (DEGs) were conducted. The Gene Ontology (GO) and Kyoto Encyclopedia of Genes and Genomes (KEGG) databases were utilized for pathway enrichment analysis. Additionally, potential protein-protein interactions (PPI) were predicted using the STRING DB software (http://STRING.embl.de/) (36).

2.8 Western blot

Cells were collected and lysed, and protein concentrations were determined by a bicinchoninic acid (BCA) protein assay kit (Beyotime, Cat#P0010). The proteins were mixed with loading buffer and denatured by boiling. Then, equal amounts (30 µg) were electrophoresed and transferred onto a nitrocellulose filter membrane, and then incubated overnight at 4°C with primary antibodies. After further incubation with HRP-conjugated secondary antibodies, the membranes were detected by the Amersham Imaging 600 system, with Pierce ECL Western blotting substrate (Thermo Fisher Scientific, Cat#32106) (37).

2.9 RT-qPCR

Total cellular RNA was extracted and quantified following the manufacturer's instructions (Sangon Biotech, Cat# B511311). Total RNA was employed as a template and subjected to reverse transcription using M-MLV reverse transcriptase (Promega) to generate complementary DNA (cDNA). The cDNA was subsequently subjected to a real-time quantitative polymerase chain reaction (RT-qPCR) using SYBR Green Master Mix mixed with primers from (Table 1) on a BIO-RAD CFX96 RT-qPCR system (BIO-RAD). The genes were then quantified using quantitative real-time PCR and analyzed using the $2^{-\Delta\Delta CT}$ method (38).

2.10 Immunofluorescence assay

HIEC-6 or Caco2 cell lines were seeded into 12-well plates at a density of 5×10^5 cells per well. The target plasmids were transfected and cultured for 36h. Subsequently, the cells were infected with the PDCoV virus at a MOI of 1 and cultured for an additional 24 hours. Following this, the cells were fixed with 4% paraformaldehyde for 30 minutes and washed thrice with PBS. The cells were then permeabilized with 0.1% Triton X-100 and blocked with 5% skimmed milk for 1 hour. Subsequently, the cells were incubated with FITC-coupled PDCoV N protein-specific primary antibody for 2 hours at 37°C. After washing with PBS, fluorescence photography was conducted.

TABLE 1 Primers for RT-qPCR in this study.

Name	Sequence
PDCoV-N-F	CTATGAGCCACCCACCAA
PDCoV-N-R	TCCCACTCCCAATCCTGT
MRPS6-F	ACGTACGATAGAGGCCCTGA
MRPS6-R	CCACCAAGAAATACCCGCCT
*IFN-β*F	TCTCCTGTTGTGCTTCTCCAC
*IFN-β*R	GCCTCCCATTCAATTGCCAC
*IRF-3*F	AGAGGCTCGTGATGGTCAAG
*IRF-3*R	AGGTCCACAGTATTCTCCAGG
GAPDH-F	CTACATGGTTTACATGTTCC
GAPDH-R	GGATCTCGCTCCTGGAAGAT

2.11 Flow cytometry

Samples were collected from different host cells at 24 hours postinfection with 1 MOI PDCoV. The cells were enzymatically digested using trypsin and subsequently resuspended. The cells were then permeabilized with 0.1% Triton X-100 and blocked with 5% skim milk for 1 hour. Subsequently, the cells were incubated with FITC-coupled PDCoV N protein-specific primary antibody for 2 hours at 37°C. After washing with PBS, fluorescence photography was conducted and analyzed by CytoFLEX flow cytometry.

2.12 Data analysis statistical analyses

Statistical significance between groups was determined using GraphPad Prism, version 9.3.1 Data were presented as means ± standard errors of the means (SEM) in all experiments and analyzed using a one-way ANOVA and T-test, and a P value of < 0.05 was considered to be statistically significant.

3 Result

3.1 Infection spectrum of PDCoV

We evaluated the infection range of PDCoV by inoculating them into ten different cell lines (HIEC-6, MA104, HEK293, HEK293T, DF1, MDCK, BHK21, ST, IPEC-J2, and Caco2). The PDCoV N was detected using a western blot to prove the existence and infection of the virus. The specific 42kDa bands were shown in all the cells. However, we discovered a higher expression from the result of avian-derived DF1, African green monkey embryonic kidney cells derived MA104, porcine-derived IPEC-J2, and human-derived Caco2 or HIEC-6 (Figure 1A). Subsequently, we opted for the utilization of HIEC-6 cells, which exhibited a greater level of infection, for subsequent experiments. We conducted an evaluation of the expression of PDCoV N protein at various time points (12h, 24h, 36h, and 48h). Immunoblot analysis revealed the presence of the target strip measuring 42kDa at all time intervals, with the maximum intensity observed at 24h. Subsequently, no significant changes in protein expression were observed (Figure 1B). The viral titer was assessed, with the highest level observed at 36h, reaching $10^{5.5}$

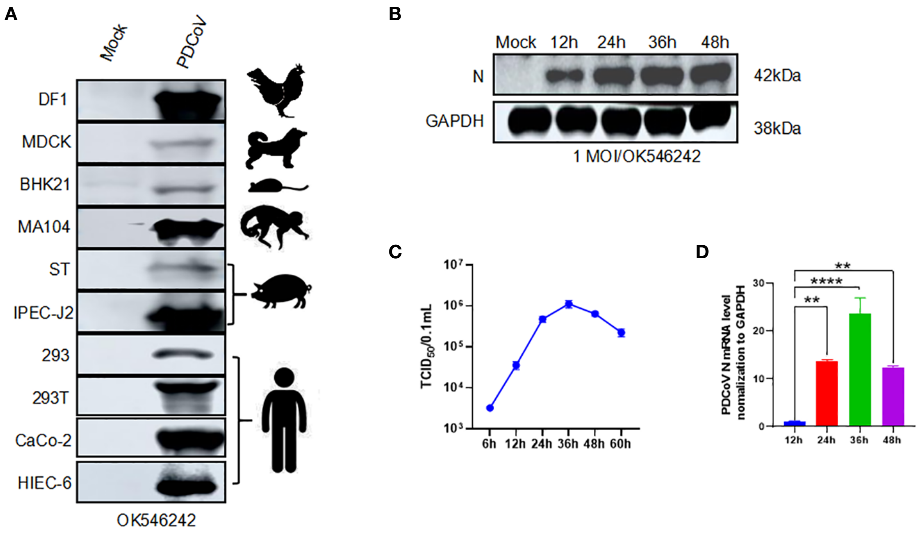

FIGURE 1
PDCoV infection modeling. We change it according to your suggestions: Figure 1 PDCoV infection modeling. **(A)** Western blot assay of PDCoV (OK546242) infected different kinds of cells with PDCoV N as the primary antibody. **(B)** Changes in PDCoV N protein at 12h, 24h, 36h, and 48h in PDCoV-infected HIEC-6 cells. **(C)** One-step growth curve of PDCoV in HIEC-6 cells, **(D)** Relative quantification analysis of PDCoV N in HIEC-6 cells infected with PDCoV, Statistical significance is determined by one-way ANOVA (**P<0.01; ****P<0.0001).

$TCID_{50}$/0.1ml (Figure 1C). To quantify the expression levels of PDCoV N, RT-qPCR was performed with GAPDH as the internal reference. The mRNA expression level PDCoV N expression level showed a significant difference at 48h (Figure 1D). In conclusion, PDCoV can infect HIEC-6 cells and replicate within HIEC-6.

3.2 PDCoV infection with HIEC-6 proteomics

The objective of this study was to examine the impact of PDCoV infection on HIEC-6 cells after 48 hours by evaluating alterations in gene expression induced by the virus. Uninfected cells were utilized as a control group (referred to as "Mock"). The 4D-DIA technique was employed to analyze the samples (Figure 2A). A total of 243 DEGs were identified at 48h, with 93 DEGs being upregulated and 150 DEGs being downregulated (Figures 2B, C and Supplementary Tables 1, 2). Gene ontology (GO) enrichment analysis demonstrated that the enriched biological processes were associated with mRNA polyadenylation, RNA processing, RNA methyltransferase activity, and other related processes (Figure 2D). Furthermore, KEGG pathway analysis revealed enrichment of pathways linked to the Rap1 signaling pathway, cytokine-cytokine receptor interaction, and cancer (Figure 2E).

3.3 MRPS6 changes in HIEC-6 cells infected with PDCoV

Significant differential expression of the MRPS6 gene was observed at 48 hours in PDCoV-infected HIEC-6 cells compared to uninfected cells, as determined by statistical analysis ($P < 0.05$) and a log2 fold change greater than 1.5. This finding was obtained through a comparative analysis of the volcanic plots, where the top 20 differentially expressed genes were identified and presented in Figure 3A. PDCoV-infected HIEC-6 cells were collected at different time points (12, 24, 36, and 48 hours) to investigate the expression levels of MRPS6 using RT-qPCR (Figure 3B). Western blot analysis (Figure 3C) confirmed the initial increase and subsequent decrease in MRPS6 expression from 24 to 48 hours. The highest expression of MRPS6 was observed at 24 hours of PDCoV infection. To compare MRPS6 expression between HIEC-6 and Caco2 cells, protein validation was performed, revealing significantly higher levels of MRPS6 in Caco2 cells compared to HIEC-6 cells (Figure 3D). Morphological analysis of PDCoV-infected HIEC-6 and Caco2 cells at 48h showed floating cells and vacuolated lesions, respectively (Figures 3E, F). At 48 hours post-infection, HIEC-6 cells infected with PDCoV exhibited a floating phenotype, while Caco2 cells displayed vacuolated lesions. These observations lay the groundwork for our subsequent investigations, which aim to elucidate the impact of PDCoV infection on the expression of MRPS6, evaluate the effects of MRPS6 overexpression in the HIEC-6 cell line, conduct knockdown experiments in the Caco2 cell line, and determine the $TCID_{50}$ based on the observed cellular lesions.

3.4 Overexpression of MRPS6 Inhibits PDCoV proliferation

HIEC-6 cells were utilized to investigate the overexpression of MRPS6 using the pCAGGS vector. After 36 hours of overexpression, the cells were infected with a virus at a MOI of 1. To assess the functional impact of MRPS6 overexpression, multiple experimental techniques were utilized, including Western blot analysis, RT-qPCR, $TCID_{50}$ assay, flow cytometry, and immunofluorescence. The primary antibody employed in this study was PDCoV N, which specifically detected a band at 42kDa. The results obtained from the Western blot analysis demonstrated a significant decrease in the expression of the target band, as well as the N protein, following the overexpression of MRPS6 (Figure 4A). Additionally, the $TCID_{50}$ assay revealed a reduction in viral titer in the supernatant at both 12h and 24h post-infection (Figure 4B). mRNA detection exhibited a notable disparity in N protein expression at both time points (Figure 4C). Flow cytometry analysis, utilizing FITC-coupled anti-PDCoV N antibody, exhibited a lower proportion of positive cells in HIEC-6 cells overexpressing MRPS6 in comparison to the plasmid-transfected group (Figure 4D). Finally, immunofluorescence results, utilizing PDCoV N as the primary antibody, indicated a significantly diminished specific fluorescence of N protein in cells overexpressing MRPS6 compared to non-transfected cells (Figure 4E). These findings suggest that the overexpression of MRPS6 can effectively reduce PDCoV virus infection.

3.5 Knockdown of MRPS6 promotes PDCoV proliferation

Subsequently To elucidate the functional role of MRPS6, a variety of experimental techniques were employed, including Western blot analysis, RT-qPCR, $TCID_{50}$, flow cytometry, and immunofluorescence. The primary antibody utilized in this investigation specifically targeted the PDCoV N protein, enabling the detection of a band at a molecular weight of 42 kDa. The results obtained from the Western blot analysis revealed an upregulation in the expression of the PDCoV N protein following MRPS6 inhibition (Figure 5A). Additionally, the $TCID_{50}$ assay demonstrated an increase in the viral titer in the supernatant at both 12h and 24h post-infection (Figure 5B). RT-qPCR analysis also exhibited a significant disparity in the expression of the N protein at both time points (Figure 5C). Flow cytometry analysis, utilizing a FITC-conjugated anti-PDCoV N antibody, displayed a higher percentage of positive cells in Caco2 cells with MRPS6 inhibition compared to the siRNA-NC group (Figure 5D). Finally, the immunofluorescence results, utilizing the PDCoV N protein as the primary antibody, revealed significantly higher specific fluorescence of N proteins in MRPS6-inhibited cells as opposed to untransfected cells (Figure 5E). These findings strongly indicate that MRPS6 inhibition effectively enhances PDCoV infection.

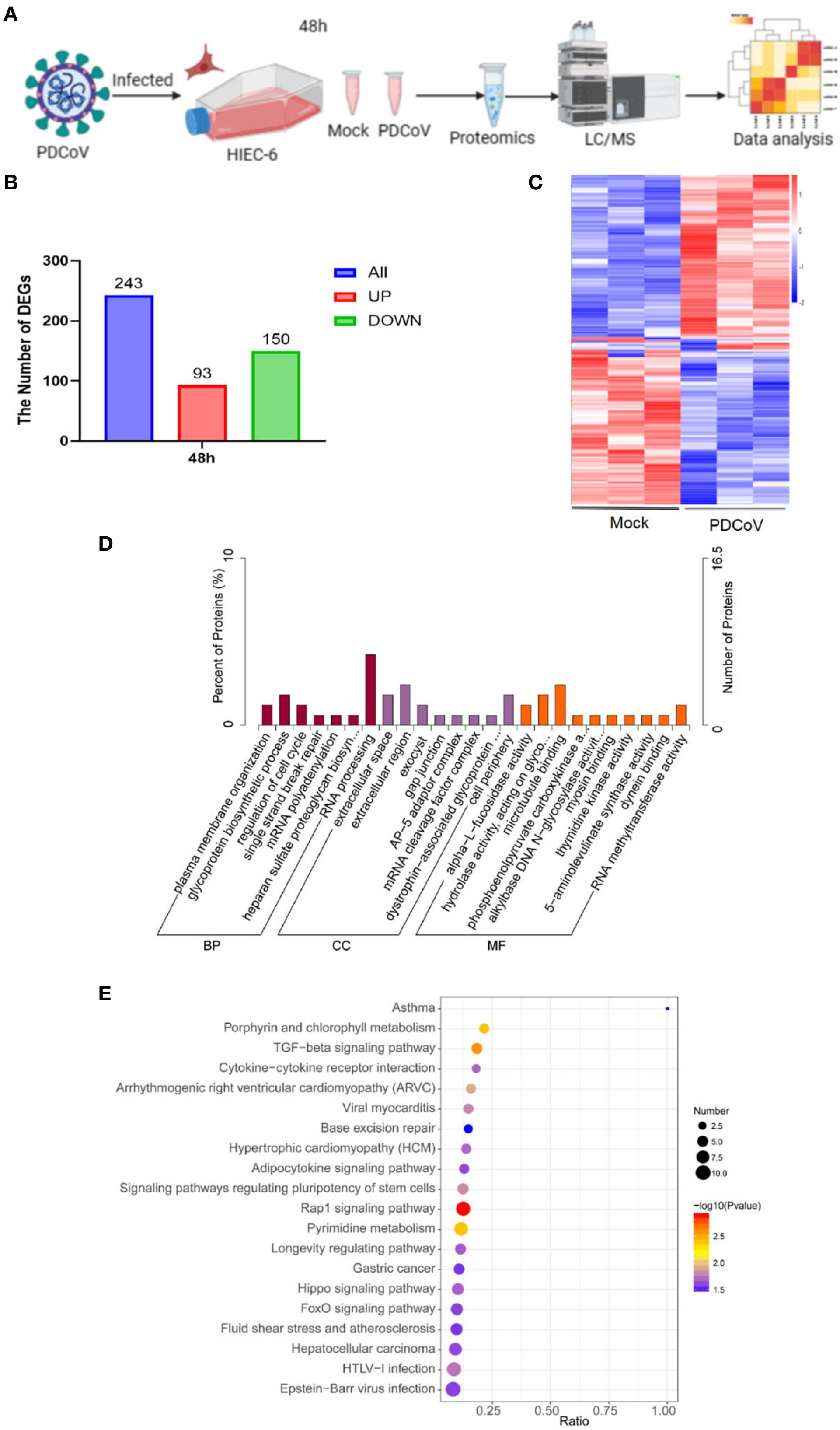

FIGURE 2
Proteomics analysis of all DEGs. **(A)** Flow of PDCoV-infected HIEC-6 cell proteomics experiments. **(B)** Number of DEGs at 48h. **(C)** Enrichment of DEGs heatmap at 48h. **(D)** GO annotation of differentially expressed genes or DEGs at 48h. **(E)** KEGG annotation of differentially expressed DEGs at 48h.

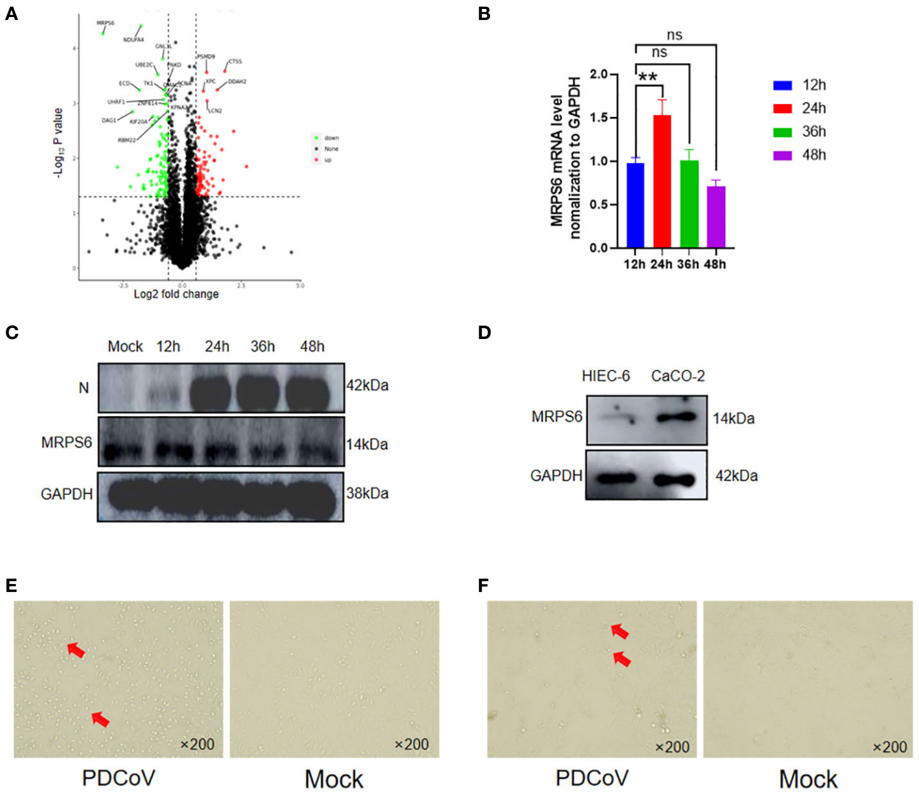

FIGURE 3
Differential Expression of MRPS6 in PDCoV-infected HIEC-6 cells. **(A)** Volcano map screening for DEGs of MRPS6. **(B)** mRNA changes of MRPS6 in HIEC-6 cells infected with PDCoV. **(C)** Changes of MRPS6 in HIEC-6 cells infected with PDCoV by western blot. **(D)** MRPS6 gene expression in HIEC-6 and Caco2 by western blot. **(E)** HIEC-6 cell lesion caused by PDCoV infection. **(F)** Caco2 cell lesions caused by PDCoV infection, Red arrow positions are cytopathic. Statistical significance is determined by one-way ANOVA (**P<0.01; n.s., not significant).

3.6 PDCoV replication and assembly correlates with MRPS6 expression

Investigations were conducted to assess the inhibitory effects of various concentrations of MRPS6 on PDCoV infection in HIEC-6 cells. The cells were transfected with either 1 μg, 2 μg, or 4 μg of MRPS6 and subsequently infected with PDCoV. The effects were determined using Western blot and RT-qPCR techniques. Our findings demonstrated that the overexpression of 4 μg of MRPS6 significantly inhibited PDCoV viruses to a greater extent compared to the overexpression of 1 μg and 2 μg of MRPS6 (Figures 6A, B). The inhibitory efficacy of MRPS6 on Porcine Deltacoronavirus (PDCoV) exhibited a dose-dependent relationship, with higher concentrations demonstrating a significantly greater inhibitory effect compared to lower concentrations. To investigate the potential impact of MRPS6 on the infection of PDCoV at different MOIs, HIEC-6 cells were transfected with 4 μg of MRPS6 and subsequently infected with PDCoV at MOIs of 0.1, 1, and 2. The infection was evaluated using Western blot and RT-qPCR techniques. The results demonstrated that the overexpression of 4 μg of MRPS6 had a significantly stronger inhibitory effect on PDCoV at an MOI of 0.1 compared to an MOI of 1 and 2 (Figures 6C, D). These findings suggest that MRPS6 exerts a more potent inhibitory effect on PDCoV at lower MOI values.

3.7 Predication and verification of proteins interaction with MRPS6

Identification of MRPS6-interacting proteins was conducted using proteomic data from HIEC-6 cells infected with PDCoV. A total of eight genes were found (Figure 7A), with SNF8, HIST1H1D, and MRPS18A showing up-regulation, while RPS16, POLR2J, TARBP1, and RPL4 showed down-regulation (Figure 7B). We examined whether MRPS6 exerts regulatory effects on IFN-β in HIEC-6 cells. Following MRPS6 overexpression and PDCoV inoculation, RT-qPCR analysis revealed that MRPS6 overexpression promoted IFN-β transcription (Figure 7C). Subsequently, we conducted knockdown experiments on MRPS6 in Caco2 cells, which were then infected with 1MOI PDCoV. The mRNA level of IFN-β was evaluated using RT-qPCR 6 hours later. The results demonstrated a significant reduction in the mRNA level of IFN-β upon MRPS6 knockdown (Figure 7D). Our findings also prove that MRPS6 in the HIEC-6 cell could be induced by poly-IC, and other main components of IFN-β pathway, such as STAT1, STAT2, IRF7 and even IFN-β itself, was upregulated due to the activation role (Figure 7E). Further data revealed maximal expression level of MRPS6 was at 24 hours post-transfection. The expression of IFN-β, STAT1, STAT2, and IRF7 was strongly correlated with MRPS6 overexpression (Figure 7F). It indicates

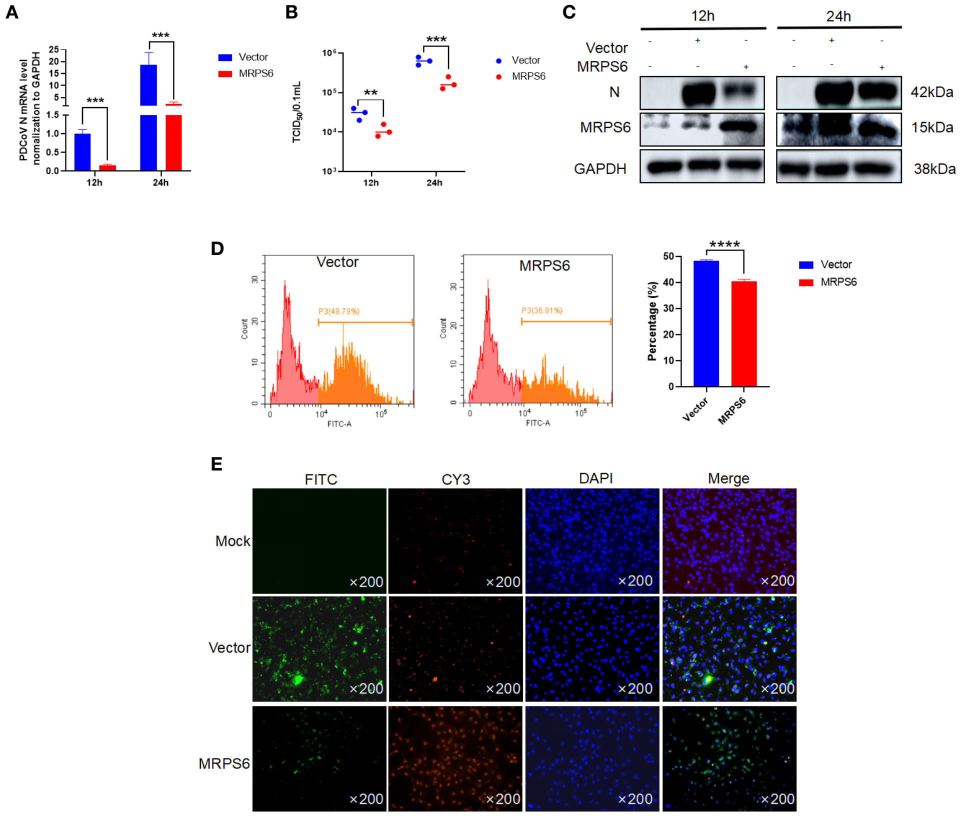

FIGURE 4
Overexpression of MRPS6 in HIEC-6 cells mediates the resistance of PDCoV infection. **(A)** Viral titers and copies are separately detected with RT-qPCR at 12 h and 24 h. **(B)** Viral titers and copies are separately detected with TCID$_{50}$. **(C)** Immunoblotting analysis of PDCoV N indicates the infection level with or without MRPS6 overexpression at 12h and 24h. **(D–E)** Flow cytometric and immunofluorescence assay were utilized to evaluate the infection at 24 h with PDCoV N antibody as the primary antibody and Cy3-labeled goat anti-rabbit immunoglobulin (Cy3). Statistical significance is determined by one-way ANOVA (**P<0.01; ***P<0.001; ****P<0.0001).

that MRPS6 can activate various downstream components from IFN-β pathway. Considering that IRF-3 is the primary transcription factor for IFN-β [38], we investigated the impact of MRPS6 on IRF-3 in HIEC-6 cell. Overexpression of MRPS6 in HIEC-6 cells resulted in increased protein and mRNA levels of IRF-3 (Figures 7G, H). Furthermore, we performed knockdown and overexpression experiments on MRPS6 in Caco2 cells and assessed the expression levels of IRF-3 using WB and RT-qPCR. The findings revealed a significant reduction in both the protein and mRNA levels of IRF-3 upon MRPS6 knockdown in Caco2 cells (Figures 7I, J).

Additionally, a previous study has demonstrated that RPS16, an MRPS6-interacting protein, plays a role in inhibiting viral replication and increasing the expression of type I interferon when its expression is knocked down (39). SNF8 has been demonstrated to interact with IRF3 and CBP to enhance the activation of the interferon antiviral response. This suggests that SNF8 is necessary for the optimal induction of the IRF3-dependent innate antiviral defense mechanism (40). Previous studies have postulated that HCV inhibits the translation of ISG proteins at the ribosome and confines viral replication to cellular compartments that are not susceptible to antiviral IFN-stimulated effector systems (41).

In this investigation, we believe that PDCoV infected HIEC-6 cells internalize the virus through receptor-mediated endocytosis. Viral RNA translocates to the Golgi apparatus in the presence of RPS16, a protein known to interact with MRPS6. From the Golgi, viral RNA is subsequently transported to the mitochondria, where MRPS6, a subunit of the mitochondrial ribosomal protein, facilitates the translation of viral proteins. Because poly-IC stimulation to HIEC-6 cell leads to increased MRPS6 expression and an associated upregulation of the interferon-β pathway, we confirmed that MRPS6 is involved in the interferon-β pathway. Overexpression of MRPS6 further amplifies IRF-3 and IRF-7 activation, which enhances IFN-β production. The increase in IFN-β levels consequently reactivates their receptors, culminating in the upregulation of STAT1 and STAT2. Thus, this is a dual activation of interferon pathway coupled with both IRFs and JAK-STAT pathway, which present an obvious anti-PDCoV mechanism shown as Figure 8.

4 Discussion

PDCoV is a novel enteric coronavirus that exhibits infectivity in multiple host species including pigs, cattle, chickens, and humans

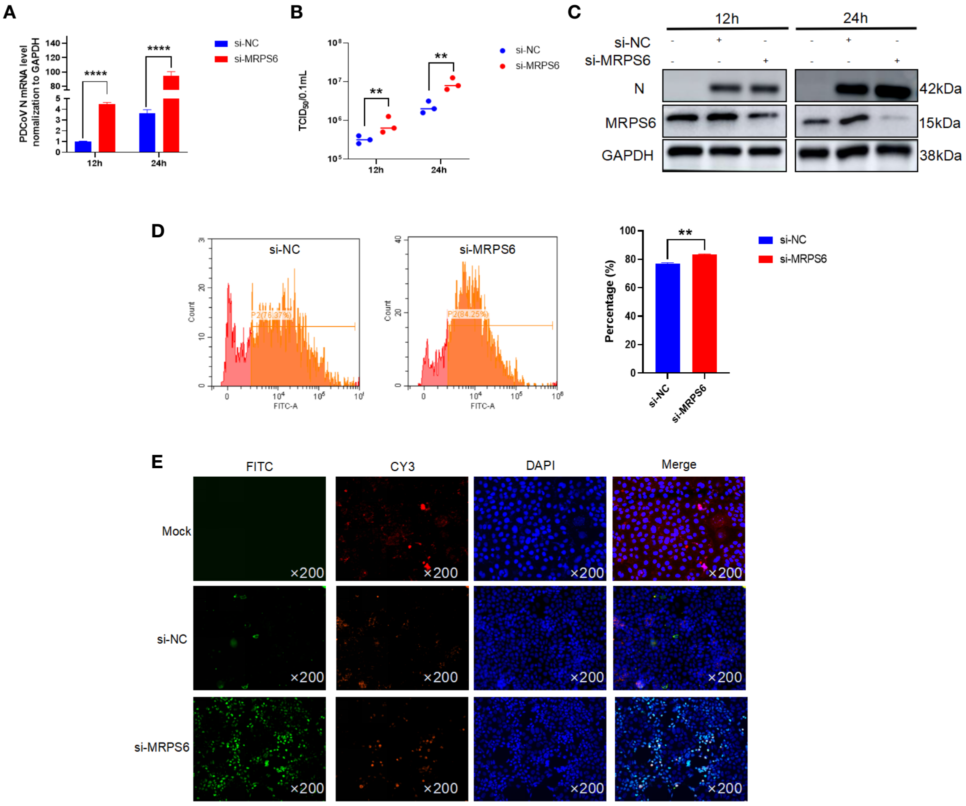

FIGURE 5

Knockdown of MRPS6 in Caco2 cells mediates the resistance of PDCoV infection. **(A)** Viral titers and copies are separately detected with RT-qPCR at 12 h and 24 h. **(B)** Viral titers and copies are separately detected with TCID$_{50}$. **(C)** Immunoblotting analysis of PDCoV N indicates the infection level with or without Knockdown of MRPS6 at 12h and 24h. **(D–E)** Flow cytometric and immunofluorescence assay were utilized to evaluate the infection at 24h with PDCoV N antibody as the primary antibody and Cy3-labeled goat anti-rabbit immunoglobulin (Cy3). Statistical significance is determined by one-way ANOVA (**P<0.01; ****P<0.0001).

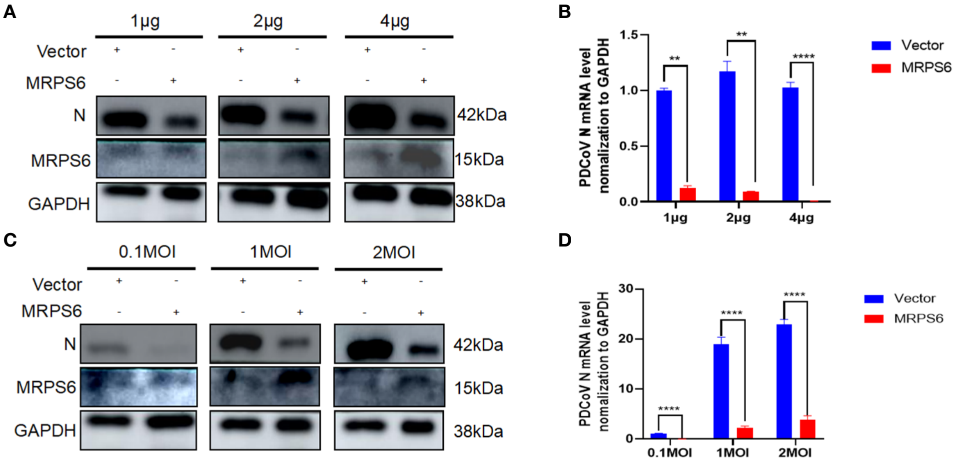

FIGURE 6

MRPS6 plasmid overexpression in HIEC-6 cells at 1 μg, 2 μg, and 4 μg following PDCoV infection using 1 MOI, MRPS6 plasmid overexpression in HIEC-6 cells at 2 μg following PDCoV viral infection using 0.1 MOI, 1 MOI, and 2MOI. **(A)** PDCoV infection using 1 MOI following MRPS6 plasmid overexpression at 1 μg, 2 μg and 4 μg, 24h immunoblotting assay of PDCoV N antibody as primary antibody **(B)** RT-qPCR assay of MRPS6 plasmid overexpression of 1 μg, 2 μg and 4 μg followed by PDCoV infection at 1 MOI, **(C)** PDCoV viral infection using MRPS6 plasmid overexpression of 2 μg in HIEC-6 cells with PDCoV N antibody at 0.1 MOI, 1 MOI and 2MOI, 24h immunoblotting assay of MRPS6 plasmid overexpression of 2 μg as primary antibody. PDCoV N antibody was used as a primary antibody in a 24-hour immunoblotting assay, **(D)** RT-qPCR assay of MRPS6 plasmid overexpressed in HIEC-6 cells for 2 μg and then infected with PDCoV virus using 0.1 MOI, 1 MOI, and 2MOI. Statistical significance is determined by one-way ANOVA (**P<0.01; ****P<0.0001).

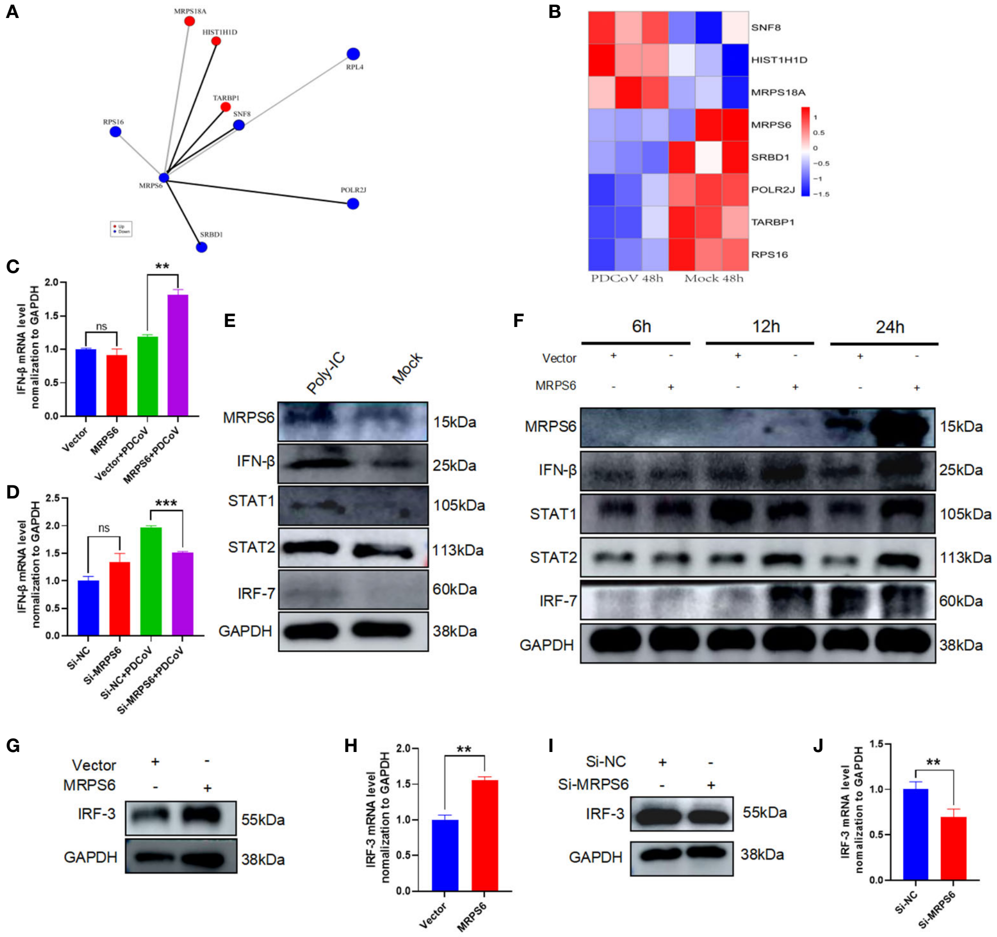

FIGURE 7
Analysis of MRPS6 interactions and speculation on MRPS6 antiviral pathway. **(A)** Proteins with significant Interaction with MRPS6. **(B)** Heatmap analysis of the expression of MRPS6-interacting proteins. **(C)** MRPS6 was overexpressed in HIEC-6 cells and infected with 1 MOI of PDCoV for 6h, and IFN-β mRNA levels were detected by RT-qPCR. **(D)** MRPS6 was knocked down in Caco2 cells and infected with 1 MOI of PDCoV for 6h, and IFN-β mRNA levels were detected by RT-qPCR. **(E)** Poly-IC stimulates activation of IFN pathway and STAT pathway in CaCo2 cells. **(F)** Overexpression of MRPS6 promotes activation of the IFN-β pathway with the JAK-STAT pathway at different times. **(G–H)** Western blot and RT-qPCR analysis showed the protein and mRNA levels of IRF-3 after 24h of transfection of the MRPS6 overexpression in HIEC-6 cells. **(I–J)** Western blot and qRT-PCR analysis revealed the protein and mRNA levels of IRF-3 after 24h of siRNA transfection in Caco2 cells. Statistical significance is determined by one-way ANOVA and T-test (**P<0.01; ***P<0.001; n.s., not significant).

(22, 42–44). However, the mechanisms underlying PDCoV's ability to infect humans and its potential for human-to-human transmission remain elusive, presenting a significant challenge for disease prevention agencies.

PDCoV-infected HIEC-6 cells were used in the experiment, and previous workers have demonstrated that PDCoV-infected HIEC-6 experimental (30). We conducted a comprehensive analysis of the proteomic variations induced by PDCoV infection in HIEC-6 cells at different time points. Since there have been no previous studies on the proteome of PDCoV infection in HIEC-6 cells, we deemed it essential to investigate these changes to facilitate future research in this area. Our analysis revealed that PDCoV has a broad host range, capable of infecting multiple species. Subsequently, we collected HIEC-6 cells infected with PDCoV at 48h, as well as corresponding control samples, and performed proteomic analysis. Consequently, we further investigated the differential protein MRPS6, which exhibited the highest level of differential expression at 48 hours post-infection, for subsequent studies.

MRPS6, also known as C21orf101, MRP-S6, RPMS6, S6mt, and bS6m, is a mitochondrial ribosomal protein. Existing studies primarily investigate the role of MRPS6 in tumorigenesis, particularly in breast cancer, where it has been shown to exert tumor-promoting effects (45). MRPS6 gene was detected to be highly expressed after breast cancer surgery (46). No documented evidence exists in the verifiable literature regarding the antiviral effects of MRPS6. However, in light of the devastating impact of pneumococcal pneumonia in 2020, researchers have put forth encouraging guidelines proposing the potential efficacy of ribosomal antiviral strategies as a more promising therapeutic approach (47). In this seminal investigation, we provide the inaugural evidence substantiating the inhibitory impact of MRPS6 overexpression in HIEC-6 cells on PDCoV viral infection. Drawing

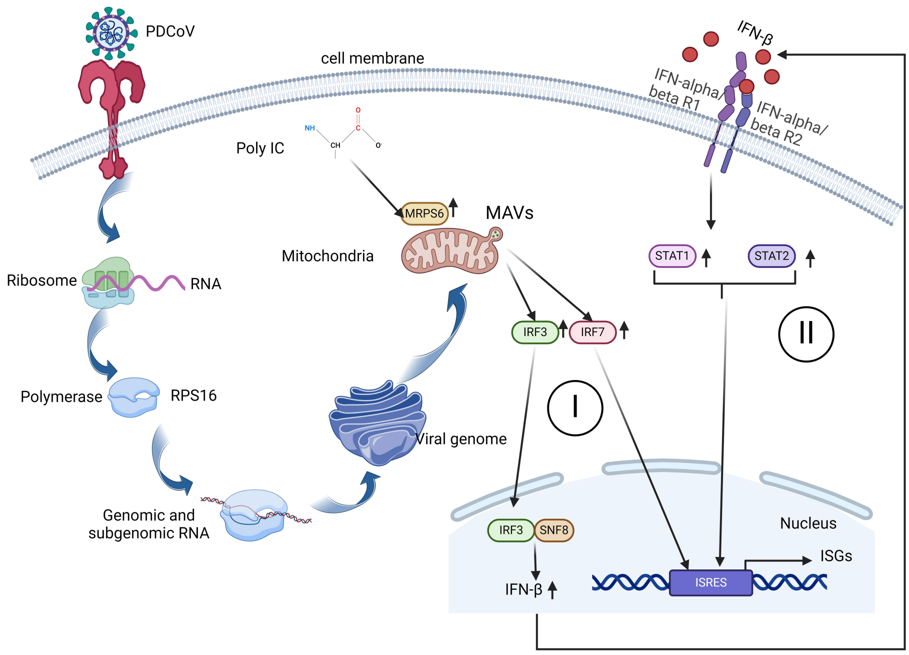

FIGURE 8
A schematic diagram of MRPS6 involvement in the PDCoV infection and interferon β pathways in the HIEC-6 cell line. Both PDCoV infection and poly-IC induce MRPS6 expression. Upregulated MRPS6 synergistically with the nucleic SNF8 induces IRF3, IRF7, STAT1/2, and IFN β protein production which are the main components of the IFN pathway. The next generation of IFN β would give a second wave of stimuli to strengthen interferon responses and produce more interferon stimulated genes.

upon the protein interactions of MRPS6, specifically RPS16, and SNF8, we postulate that the upregulation of MRPS6, concomitant with the downregulation of RPS16 or the upregulation of SNF8, engenders a hindrance in PDCoV viral replication.

In a prior study, it was elucidated that Toll-like receptors (TLRs) undergo activation after PDCoV infection in ST cells. Moreover, it was subsequently determined that the expression of TLR2 is augmented following PDCoV infection (43), as the activation of the TLR2 pathway during SARS-CoV-2 infection (48).In this study, HIEC-6 cells were infected with PDCoV. TLR2 on the surface of HIEC-6 cells facilitated the endocytosis of PDCoV and subsequently transported the virus to the Golgi apparatus using the ribosomal RPS16 transporter. Additionally, previous research has shown that RPS20 can inhibit the replication of CSFV in cells by regulating the activity of Toll-like receptor 3 (TLR3) (49). RRL10 acts as a direct downstream component of antiviral signaling in the antiviral defense pathway mediated by the bicistronic virus nuclear shuttle protein (NSP) interacting kinase (NIK) in plants (50, 51). Mitochondrial ribosomes serve as the site for protein translation within mitochondria, and MRPS6 facilitates the generation of mitochondrial antiviral proteins, MAVS, by influencing the translation of PDCoV proteins. Earlier studies have demonstrated that both MITA/STING and MRP exert substantial inhibitory effects on HBV replication *in vitro*. Additionally, MITA overexpression activates the IRF3-IFN pathway, implying that MITA/STING and MRP contribute to the regulation of HBV through the modulation of innate and adaptive immune responses (52). The ATP-binding transporter proteins MRP4 and MRP5 play a significant role in modulating the cellular export of drugs and signaling molecules (53). Overexpression of multidrug resistance-associated protein (MRP) hampers the induction of interferon-beta (IFN-β) mediated by the mediator of IRF3 activation (MITA) through the disruption of MITA-TBK1 interactions and the regulation of transcription factor 3 via TBK1-IFN (54). The generation of MAVS is instigated by PDCoV infection, resulting in a decrease in peroxisome abundance. PDCoV infection induces a diminution in peroxisome abundance, which serves as the cellular locus for MAVS-mediated IRF1 activation and type III interferons (IFN-III) production (28). Furthermore, Supraphysiological concentrations (16 μM) of selenomethionine (Se-Met), which led to increased expression of MAVS protein and phosphorylation of IRF3 (55), exhibited significant antiviral effects on PDCoV replication in LLC-PK1 cells. PDCoV infection induces the activation of MAVS, which subsequently activates the downstream molecule IRF3. Additionally, SNF8 acts in synergy with IRF3 and CBP to initiate the antiviral response mediated by interferon (IFN) (40). IRF3 localization in the nucleus is enhanced, facilitating IRF3 interaction with SNF8, thereby promoting the activation of the type I interferon (IFN) pathway, PGAM5 forms complexes with MyD88 and TRAF3, leading to the activation of the IFN I signaling pathway and subsequently inhibiting the replication of the PDCoV N protein (56). The researchers showcased that the NS7a protein of the PDCoV impedes the production of interferon-beta (IFN-β) by disrupting the interaction between IKKϵ and TRAF3, as well as interfering with the binding of IKKϵ to IRF3 (57). In this investigation, we hypothesized that MRPS6 possesses the ability to impede the infection caused by PDCoV by exerting regulatory effects on the interferon type I (IFN-I) signaling pathway. This modulation occurs through the targeting of IRF3, a downstream molecule of MAVS.

5 Conclusion

In this study, we performed a comparative proteomic analysis of HIEC-6 cells infected with PDCoV at 48h to simulate potential zoonotic infections in humans. To the best of our knowledge, this is the first proteomic analysis conducted using PDCoV-infected human intestinal cells. We also focused on the differential protein MRPS6 and investigated its expression and association with PDCoV infection. We observed that MRPS6 exhibited a certain antiviral effect against PDCoV infection, and the degree of PDCoV infection was correlated with the dosage of transfected MRPS6. We additionally performed initial experimental validation to support the potential inhibitory effect of MRPS6 on PDCoV infection via the IFN type I signaling pathway. Furthermore, this experiment generated substantial proteomic data, providing a solid foundation for future research on potential zoonotic diseases.

Data availability statement

The datasets presented in this study can be found in online repositories. The names of the repository/repositories and accession number(s) can be found below: PXD049713 (iProX).

Ethics statement

Ethical approval was not required for the studies on humans in accordance with the local legislation and institutional requirements because only commercially available established cell lines were used. Ethical approval was not required for the studies on animals in accordance with the local legislation and institutional requirements because only commercially available established cell lines were used.

Author contributions

YJ: Conceptualization, Data curation, Formal analysis, Software, Validation, Visualization, Writing – original draft. GZ: Conceptualization, Investigation, Methodology, Resources, Writing – original draft. LL: Methodology, Writing – original draft. JC: Formal analysis, Resources, Writing – original draft. PH: Investigation, Writing – original draft. ZG: Investigation, Writing – original draft. JH: Writing – original draft. ZX: Data curation, Writing – original draft. MW: Writing – review & editing. CL: Funding acquisition, Validation, Writing – review & editing. NJ: Conceptualization, Formal analysis, Funding acquisition, Methodology, Project administration, Resources, Writing – review & editing.

Funding

The author(s) declare financial support was received for the research, authorship, and/or publication of this article. This work was funded by identification, function and mechanism of interferon-induced proteins associated with PEDV and TGEV infections (2021YFD1801103–6), Project from National Center of Technology Innovation for Pigs (NCTIP-XD/B11) and Wenzhou Science and Technology Plan Project (X2023085, FSJH2022003).

Conflict of interest

The authors declare that the research was conducted in the absence of any commercial or financial relationships that could be construed as a potential conflict of interest.

Publisher's note

All claims expressed in this article are solely those of the authors and do not necessarily represent those of their affiliated organizations, or those of the publisher, the editors and the reviewers. Any product that may be evaluated in this article, or claim that may be made by its manufacturer, is not guaranteed or endorsed by the publisher.

Supplementary material

The Supplementary Material for this article can be found online at: https://www.frontiersin.org/articles/10.3389/fimmu.2024.1381026/full#supplementary-material

References

1. Ji W, Peng Q, Fang X, Li Z, Li Y, Xu C, et al. Structures of A deltacoronavirus spike protein bound to porcine and human receptors. *Nat Commun.* (2022) 13:1467. doi: 10.1038/s41467-022-29062-5

2. Hu B, Guo H, Zhou P, Shi ZL. Characteristics of sars-cov-2 and covid-19. *Nat Rev Microbiol.* (2021) 19:141–54. doi: 10.1038/s41579-020-00459-7

3. Miller MR, Braun E, Ip HS, Tyson GH. Domestic and wild animal samples and diagnostic testing for sars-cov-2. *Vet Q.* (2023) 43:1–11. doi: 10.1080/01652176.2023.2263864

4. Wang M, Yan M, Xu H, Liang W, Kan B, Zheng B, et al. Sars-cov infection in A restaurant from palm civet. *Emerg Infect Dis.* (2005) 11:1860–5. doi: 10.3201/eid1112.041293

5. Bosco-Lauth AM, Hartwig AE, Porter SM, Gordy PW, Nehring M, Byas AD, et al. Experimental infection of domestic dogs and cats with sars-cov-2: pathogenesis, transmission, and response to reexposure in cats. *Proc Natl Acad Sci U.S.A.* (2020) 117:26382–8. doi: 10.1073/pnas.2013102117

6. Richard M, Kok A, De Meulder D, Bestebroer TM, Lamers MM, Okba NMA, et al. Sars-cov-2 is transmitted via contact and via the air between ferrets. *Nat Commun.* (2020) 11:3496. doi: 10.1038/s41467-020-17367-2

7. Woolsey C, Borisevich V, Prasad AN, Agans KN, Deer DJ, Dobias NS, et al. Establishment of an african green monkey model for covid-19 and protection against re-infection. *Nat Immunol.* (2021) 22:86–98. doi: 10.1038/s41590-020-00835-8

8. Singh DK, Singh B, Ganatra SR, Gazi M, Cole J, Thippeshappa R, et al. Responses to acute infection with sars-cov-2 in the lungs of rhesus macaques, baboons and marmosets. *Nat Microbiol.* (2021) 6:73–86. doi: 10.1038/s41564-020-00841-4

9. Zumla A, Hui DS, Perlman S. Middle east respiratory syndrome. *Lancet.* (2015) 386:995–1007. doi: 10.1016/S0140-6736(15)60454-8

10. De Benedictis P, Marciano S, Scaravelli D, Priori P, Zecchin B, Capua I, et al. Alpha and lineage C betacov infections in italian bats. *Virus Genes.* (2014) 48:366–71. doi: 10.1007/s11262-013-1008-x

11. Mohd HA, Al-Tawfiq JA, Memish ZA. Middle east respiratory syndrome coronavirus (Mers-cov) origin and animal reservoir. *Virol J.* (2016) 13:87. doi: 10.1186/s12985-016-0544-0

12. Zaki AM, Van Boheemen S, Bestebroer TM, Osterhaus AD, Fouchier RA. Isolation of A novel coronavirus from A man with pneumonia in Saudi Arabia. *N Engl J Med.* (2012) 367:1814–20. doi: 10.1056/NEJMoa1211721

13. Woo PC, Lau SK, Lam CS, Lau CC, Tsang AK, Lau JH, et al. Discovery of seven novel mammalian and avian coronaviruses in the genus deltacoronavirus supports bat coronaviruses as the gene source of alphacoronavirus and betacoronavirus and avian coronaviruses as the gene source of gammacoronavirus and deltacoronavirus. *J Virol.* (2012) 86:3995–4008. doi: 10.1128/JVI.06540-11

14. Li G, Chen Q, Harmon KM, Yoon KJ, Schwartz KJ, Hoogland MJ, et al. Full-length genome sequence of porcine deltacoronavirus strain usa/ia/2014/8734. *Genome Announc.* (2014) 2(2):Me00278–14. doi: 10.1128/genomeA.00278-14

15. Lee S, Lee C. Complete genome characterization of korean porcine deltacoronavirus strain kor/knu14–04/2014. *Genome Announc.* (2014) 2(6):e01191–14. doi: 10.1128/genomeA.01191-14

16. Janetanakit T, Lumyai M, Bunpapong N, Boonyapisitsopa S, Chaiyawong S, Nonthabenjawan N, et al. Porcine deltacoronavirus, Thailan. *Emerg Infect Dis.* (2016) 22:757–9. doi: 10.3201/eid2204.151852

17. Le VP, Song S, An BH, Park GN, Pham NT, Le DQ, et al. A novel strain of porcine deltacoronavirus in Vietnam. *Arch Virol.* (2018) 163:203–7. doi: 10.1007/s00705-017-3594-8

18. Duan C. An updated review of porcine deltacoronavirus in terms of prevalence, pathogenicity, pathogenesis and antiviral strategy. *Front Vet Sci.* (2021) 8:811187. doi: 10.3389/fvets.2021.811187

19. Chen Q, Gauger P, Stafne M, Thomas J, Arruda P, Burrough E, et al. Pathogenicity and pathogenesis of A United States porcine deltacoronavirus cell culture isolate in 5-day-old neonatal piglets. *Virology.* (2015) 482:51–9. doi: 10.1016/j.virol.2015.03.024

20. Ma Y, Zhang Y, Liang X, Lou F, Oglesbee M, Krakowka S, et al. Origin, evolution, and virulence of porcine deltacoronaviruses in the United States. *Mbio.* (2015) 6: E00064. doi: 10.1128/mBio.00064-15

21. Li Y, Niu JW, Zhou X, Chu PP, Zhang KL, Gou HC, et al. Development of A multiplex qrt-pcr assay for the detection of porcine epidemic diarrhea virus, porcine transmissible gastroenteritis virus and porcine deltacoronavirus. *Front Vet Sci.* (2023) 10:1158585. doi: 10.3389/fvets.2023.1158585

22. Jung K, Hu H, Saif LJ. Calves are susceptible to infection with the newly emerged porcine deltacoronavirus, but not with the swine enteric alphacoronavirus, porcine epidemic diarrhea virus. *Arch Virol.* (2017) 162:2357–62. doi: 10.1007/s00705-017-3351-z

23. Li W, Hulswit RJG, Kenney SP, Widjaja I, Jung K, Alhamo MA, et al. Broad receptor engagement of an emerging global coronavirus may potentiate its diverse cross-species transmissibility. *Proc Natl Acad Sci U.S.A.* (2018) 115:E5135–43. doi: 10.1073/pnas.1802879115

24. Boley PA, Alhamo MA, Lossie G, Yadav KK, Vasquez-Lee M, Saif LJ, et al. Porcine deltacoronavirus infection and transmission in poultry, United States(1). *Emerg Infect Dis.* (2020) 26:255–65. doi: 10.3201/eid2602.190346

25. Zhuang Q, Liu S, Zhang X, Jiang W, Wang K, Wang S, et al. Surveillance and taxonomic analysis of the coronavirus dominant in pigeons in China. *Transbound Emerg Dis.* (2020) 67:1981–90. doi: 10.1111/tbed.13541

26. Zhang H, Ding Q, Yuan J, Han F, Wei Z, Hu H. Susceptibility to mice and potential evolutionary characteristics of porcine deltacoronavirus. *J Med Virol.* (2022) 94:5723–38. doi: 10.1002/jmv.28048

27. Yang YL, Liu J, Wang TY, Chen M, Wang G, Yang YB, et al. Aminopeptidase N is an entry co-factor triggering porcine deltacoronavirus entry via an endocytotic pathway. *J Virol.* (2021) 95:E0094421. doi: 10.1128/JVI.00944-21

28. Liu S, Fang P, Ke W, Wang J, Wang X, Xiao S, et al. Porcine deltacoronavirus (Pdcov) infection antagonizes interferon-Λ1 production. *Vet Microbiol.* (2020) 247:108785. doi: 10.1016/j.vetmic.2020.108785

29. Guezguez A, Paré F, Benoit YD, Basora N, Beaulieu JF. Modulation of stemness in A human normal intestinal epithelial crypt cell line by activation of the wnt signaling pathway. *Exp Cell Res.* (2014) 322:355–64. doi: 10.1016/j.yexcr.2014.02.009

30. Cruz-Pulido D, Boley PA, Ouma WZ, Alhamo MA, Saif LJ, Kenney SP. Comparative transcriptome profiling of human and pig intestinal epithelial cells after porcine deltacoronavirus infection. *Viruses.* (2021) 13(2):292. doi: 10.3390/v13020292

31. Li M, Ramage H, Cherry S. Deciphering flavivirus-host interactions using quantitative proteomics. *Curr Opin Immunol.* (2020) 66:90–7. doi: 10.1016/j.coi.2020.06.002

32. Shah PS, Beesabathuni NS, Fishburn AT, Kenaston MW, Minami SA, Pham OH, et al. Systems biology of virus-host protein interactions: from hypothesis generation to mechanisms of replication and pathogenesis. *Annu Rev Virol.* (2022) 9:397–415. doi: 10.1146/annurev-virology-100520-011851

33. Wang W, Li J, Fan B, Zhang X, Guo R, Zhao Y, et al. Development of A novel double antibody sandwich elisa for quantitative detection of porcine deltacoronavirus antigen. *Viruses.* (2021) 13(12):2403. doi: 10.3390/v13122403

34. Song L, Chen J, Hao P, Jiang Y, Xu W, Li L, et al. Differential transcriptomics analysis of ipec-J2 cells single or coinfected with porcine epidemic diarrhea virus and transmissible gastroenteritis virus. *Front Immunol.* (2022) 13:844657. doi: 10.3389/fimmu.2022.844657

35. Huang Da W, Sherman BT, Lempicki RA. Bioinformatics enrichment tools: paths toward the comprehensive functional analysis of large gene lists. *Nucleic Acids Res.* (2009) 37:1–13. doi: 10.1093/nar/gkn923

36. Szklarczyk D, Gable AL, Lyon D, Junge A, Wyder S, Huerta-Cepas J, et al. String V11: protein-protein association networks with increased coverage, supporting functional discovery in genome-wide experimental datasets. *Nucleic Acids Res.* (2019) 47:D607–13. doi: 10.1093/nar/gky1131

37. Pang Z, Hao P, Qu Q, Li L, Jiang Y, Xiao S, et al. Interferon-inducible transmembrane protein 3 (Ifitm3) restricts rotavirus infection. *Viruses.* (2022) 14 (11):2407. doi: 10.3390/v14112407

38. Chen J, Li P, Zou W, Jiang Y, Li L, Hao P, et al. Identification of A novel interferon lambda splice variant in chickens. *J Virol.* (2023) 97:E0174322. doi: 10.1128/jvi.01743-22

39. Wu W, Wang C, Xia C, Liu S, Mei Q. Microrna let-7 suppresses influenza A virus infection by targeting rps16 and enhancing type I interferon response. *Front Cell Infect Microbiol.* (2022) 12:904775. doi: 10.3389/fcimb.2022.904775

40. Kumthip K, Yang D, Li NL, Zhang Y, Fan M, Sethuraman A, et al. Pivotal role for the escrt-ii complex subunit eap30/snf8 in irf3-dependent innate antiviral defense. *PloS Pathog.* (2017) 13:E1006713. doi: 10.1371/journal.ppat.1006713

41. Heim MH, Thimme R. Innate and adaptive immune responses in hcv infections. *J Hepatol.* (2014) 61:S14–25. doi: 10.1016/j.jhep.2014.06.035

42. Liang Q, Zhang H, Li B, Ding Q, Wang Y, Gao W, et al. Susceptibility of chickens to porcine deltacoronavirus infection. *Viruses.* (2019) 11(6):573. doi: 10.3390/v11060573

43. Jin XH, Zhang YF, Yuan YX, Han L, Zhang GP, Hu H. Isolation, characterization and transcriptome analysis of porcine deltacoronavirus strain hnzk-02 from Henan Province, China. *Mol Immunol.* (2021) 134:86–99. doi: 10.1016/j.molimm.2021.03.006

44. Lednicky JA, Tagliamonte MS, White SK, Elbadry MA, Alam MM, Stephenson CJ, et al. Independent infections of porcine deltacoronavirus among Haitian children. *Nature.* (2021) 600:133–7. doi: 10.1038/s41586-021-04111-z

45. Oviya RP, Gopal G, Shirley SS, Sridevi V, Jayavelu S, Rajkumar T. Mitochondrial ribosomal small subunit proteins (Mrps) mrps6 and mrps23 show dysregulation in breast cancer affecting tumorigenic cellular processes. *Gene.* (2021) 790:145697. doi: 10.1016/j.gene.2021.145697

46. Lin X, Guo L, Lin X, Wang Y, Zhang G. Expression and prognosis analysis of mitochondrial ribosomal protein family in breast cancer. *Sci Rep.* (2022) 12:10658. doi: 10.1038/s41598-022-14724-7

47. Rofeal M, El-Malek FA. Ribosomal proteins as A possible tool for blocking sars-cov 2 virus replication for A potential prospective treatment. *Med Hypotheses.* (2020) 143:109904. doi: 10.1016/j.mehy.2020.109904

48. Planès R, Bert JB, Tairi S, Benmohamed L, Bahraoui E. Sars-cov-2 envelope (E) protein binds and activates tlr2 pathway: a novel molecular target for covid-19 interventions. *Viruses.* (2022) 14(5):999. doi: 10.3390/v14050999

49. Lv H, Dong W, Qian G, Wang J, Li X, Cao Z, et al. Us10, A novel npro-interacting protein, inhibits classical swine fever virus replication. *J Gen Virol.* (2017) 98:1679–92. doi: 10.1099/jgv.0.000867

50. Carvalho CM, Santos AA, Pires SR, Rocha CS, Saraiva DI, MaChado JP, et al. Regulated nuclear trafficking of rpl10a mediated by nik1 represents A defense strategy of plant cells against virus. *PloS Pathog.* (2008) 4:E1000247. doi: 10.1371/journal.ppat.1000247

51. Rocha CS, Santos AA, MaChado JP, Fontes EP. The ribosomal protein L10/qm-like protein is A component of the nik-mediated antiviral signaling. *Virology.* (2008) 380:165–9. doi: 10.1016/j.virol.2008.08.005

52. Liu S, Zhao K, Su X, Lu L, Zhao H, Zhang X, et al. Mita/sting and its alternative splicing isoform mrp restrict hepatitis B virus replication. *PloS One.* (2017) 12: E0169701. doi: 10.1371/journal.pone.0169701

53. Ritter CA, Jedlitschky G, Meyer Zu Schwabedissen H, Grube M, Köck K, Kroemer HK. Cellular export of drugs and signaling molecules by the atp-binding cassette transporters mrp4 (Abcc4) and mrp5 (Abcc5). *Drug Metab Rev.* (2005) 37:253–78. doi: 10.1081/DMR-200047984

54. Chen H, Pei R, Zhu W, Zeng R, Wang Y, Wang Y, et al. An alternative splicing isoform of mita antagonizes mita-mediated induction of type I ifns. *J Immunol.* (2014) 192:1162–70. doi: 10.4049/jimmunol.1300798

55. Ren Z, Jia G, He H, Ding T, Yu Y, Zuo Z, et al. Antiviral effect of selenomethionine on porcine deltacoronavirus in pig kidney epithelial cells. *Front Microbiol.* (2022) 13:846747. doi: 10.3389/fmicb.2022.846747

56. Yang X, Kong N, Qin W, Zhai X, Song Y, Tong W, et al. Pgam5 degrades pdcov N protein and activates type I interferon to antagonize viral replication. *J Virol.* (2023) 97:E0147023. doi: 10.1128/jvi.01470-23

57. Fang P, Fang L, Xia S, Ren J, Zhang J, Bai D, et al. Porcine deltacoronavirus accessory protein ns7a antagonizes ifn-Β Production by competing with traf3 and irf3 for binding to ikkϵ. *Front Cell Infect Microbiol.* (2020) 10:257. doi: 10.3389/fcimb.2020.00257

Frontiers in Immunology

TYPE Original Research
PUBLISHED 16 July 2024
DOI 10.3389/fimmu.2024.1438371

OPEN ACCESS

EDITED BY
Wei Wang,
Wenzhou University, China

REVIEWED BY
Xingxing Ren,
University of Science and Technology of China, China
Zixiang Zhu,
Chinese Academy of Agricultural Sciences, China

*CORRESPONDENCE
Jiyong Zhou
✉ jyzhou@zju.edu.cn

RECEIVED 25 May 2024
ACCEPTED 25 June 2024
PUBLISHED 16 July 2024

CITATION
Lu C, Li H, Chen W, Li H, Ma J, Peng P, Yan Y, Dong W, Jin Y, Pan S, Shang S, Gu J and Zhou J (2024) Immunological characteristics of a recombinant alphaherpesvirus with an envelope-embedded *Cap* protein of circovirus. *Front. Immunol.* 15:1438371. doi: 10.3389/fimmu.2024.1438371

COPYRIGHT
© 2024 Lu, Li, Chen, Li, Ma, Peng, Yan, Dong, Jin, Pan, Shang, Gu and Zhou. This is an open-access article distributed under the terms of the Creative Commons Attribution License (CC BY). The use, distribution or reproduction in other forums is permitted, provided the original author(s) and the copyright owner(s) are credited and that the original publication in this journal is cited, in accordance with accepted academic practice. No use, distribution or reproduction is permitted which does not comply with these terms.

Immunological characteristics of a recombinant alphaherpesvirus with an envelope-embedded *Cap* protein of circovirus

Chenhe Lu[1], Haimin Li[1], Wenjing Chen[1], Hui Li[2], Jiayu Ma[1], Peng Peng[1], Yan Yan[1], Weiren Dong[1], Yulan Jin[1], Shiyue Pan[1], Shaobin Shang[2], Jinyan Gu[1] and Jiyong Zhou[1,3*]

[1]MOA Key Laboratory of Animal Virology, Zhejiang University Center for Veterinary Sciences, Hangzhou, China, [2]College of Veterinary Medicine, Yangzhou University, Yangzhou, China, [3]State Key Laboratory for Diagnosis and Treatment of Infectious Diseases, First Affiliated Hospital, Zhejiang University, Hangzhou, China

Introduction: Variant pseudorabies virus (PRV) is a newly emerged zoonotic pathogen that can cause human blindness. PRV can take advantage of its large genome and multiple non-essential genes to construct recombinant attenuated vaccines carrying foreign genes. However, a major problem is that the foreign genes in recombinant PRV are only integrated into the genome for independent expression, rather than assembled on the surface of virion.

Methods: We reported a recombinant PRV with deleted gE/TK genes and an inserted porcine circovirus virus 2 (PCV2) *Cap* gene into the extracellular domain of the PRV gE gene using the Cre-loxP recombinant system combined with the CRISPR-Cas9 gene editing system. This recombinant PRV (PRV-Cap), with the envelope-embedded Cap protein, exhibits a similar replication ability to its parental virus.

Results: An immunogenicity assay revealed that PRV-Cap immunized mice have 100% resistance to lethal PRV and PCV2 attacks. Neutralization antibody and ELISPOT detections indicated that PRV-Cap can enhance neutralizing antibodies to PRV and produce IFN-γ secreting T cells specific for both PRV and PCV2. Immunological mechanistic investigation revealed that initial immunization with PRV-Cap stimulates significantly early activation and expansion of CD69$^+$ T cells, promoting the activation of CD4 Tfh cell dependent germinal B cells and producing effectively specific effector memory T and B cells. Booster immunization with PRV-Cap recalled the activation of PRV-specific IFN-γ$^+$IL-2$^+$CD4$^+$ T cells and IFN-γ$^+$TNF-α$^+$CD8$^+$ T cells, as well as PCV2-specific IFN-γ$^+$TNF-α$^+$CD8$^+$ T cells.

Conclusion: Collectively, our data suggested an immunological mechanism in that the recombinant PRV with envelope-assembled PCV2 Cap protein can serve as an excellent vaccine candidate for combined immunity against PRV and PCV2, and provided a cost-effective method for the production of PRV- PCV2 vaccine.

KEYWORDS

chimeric pseudorabies virus, circovirus, immunity, memory responses, IFN-γ

Introduction

Pseudorabies virus (PRV), as a representative member of *Alphaherpesviridae*, has a broad host spectrum, including domestic pigs, wild boars, cattle, sheep, goats, dogs, cats, mice, and rabbits (1–3). PRV infection results in great economic loss to the global pig industry (4, 5). Recently, a newly emerging variant of PRV (Type II) has been reported to be transmissible to humans, causing ocular, respiratory, or central nervous system diseases (6–8). Thus, PRV infection is a public health concern. Given that PRV deleting non-essential genes, i.e., TK, gE, gI, and gG genes, attenuate its virulence (9–14), thus, the classical PRV has been described to express foreign antigen proteins to explore the feasibility of PRV as a potential vaccine vector, such as GP5 protein of porcine reproductive and respiratory syndrome virus (PRRSV) (15), E2 protein of classical swine fever virus (CSFV) (16), foot-and-mouth disease virus VP1 protein (17), porcine parvovirus (PPV) VP2 protein (18), and Senecavirus A (SVA) VP2 protein (19). However, the immunoprotective mechanism of a combined vaccine against the newly emerging pseudorabies virus type 2 and porcine circovirus type 2 has not been reported.

Adaptive immunity, as an important immune mechanism, is composed of humoral immunity mediated by antigen-specific antibodies and cellular immunity, mainly composed of T cells (20). Effective humoral immune responses activated by exogenous pathogens or vaccine depend on the production of high-affinity antibodies (21). Germinal centers (GCs) are the microanatomical structures of clonal expansion and affinity maturation of B lymphocytes in secondary lymphoid organs after exposure to antigens (22). GCs perform positive selection on GC B lymphocytes to produce high-affinity antibodies by obtaining co-stimulatory signals from recruited T follicular helper cells (Tfh) (23, 24). Bcl6 is an important master regulator that drives the maturation of Tfh and GC B. Mature Tfh cells expressing CD40L bind to CD40 on the surface of GC B, and subsequently activate the NF-κB pathway to trigger the expansion of B cells (25–28). Tfh also secretes a variety of cytokines, mainly IL-21 (29), to promote the maintenance of GC B and the production of plasma cells. These signals together determine the fate of GC B and participate in humoral immune regulation (30).

In addition to humoral immunity, cell-mediated immunity also plays an important role in the defense against virus infections, including influenza virus (31, 32), Middle East respiratory syndrome coronavirus (33), severe acute respiratory syndrome coronavirus 2 (34–36), Hepatitis B virus (37), and human immunodeficiency virus (38). Cellular immunity not only reflects the antiviral effect during infection, but also can be used to evaluate the immune effect of vaccines (39). CD4 and CD8 T cells mediate adaptive cellular immune responses after maturation in the thymus and have important auxiliary effects in antigen-induced humoral immunity (40). Viruses can stimulate CD4 T cells to differentiate into a variety of subsets including Th1, Th2, Th17, and Tfh. Th1 CD4 T cells secrete cytokines, mainly including IFN-γ, TNF-α, and IL-2 (41–44). IFN-γ and TNF-α synergistically inhibit viral replication, while IL-2 promotes the expansion and activation of various T cells. Studies have shown that a single cytokine indicator is insufficient to accurately reflect immune protection and multifunctional T cells that simultaneously produce IFN-γ, IL-2, and TNF-α can provide a better evaluation of specific cellular immunity (45–48). At the same time, Th1 CD4 T cells activate cytotoxic T lymphocytes (CTLs) to release granzyme and perforin to clear infected cells by inducing programmed cell death (49, 50). Therefore, the comprehensive evaluation of cellular and humoral immunity is particularly important to understand antiviral immunity.

In this study, the Capsid protein (Cap) of PCV2 was selected to construct a recombinant virus using PRV type II as the vector. An efficient recombinant PRV with the Cap of PCV2 (PRV-Cap) was successfully rescued using a combination of the Cre-loxP recombinant system and the CRISPR-Cas9 gene editing system. The recombinant Cap-gE fusion protein was stably assembled in the viral envelope of PRV. PRV-Cap immunized mice showed 100% survival to lethal PRV and PCV2 attacks. The initial immunization of PRV-Cap activated the expansion of PRV and PCV2-specific T cells, promoting the activation of germinal B cells through CD4 Tfh cells to produce specific antibodies. The booster immunization of PRV-Cap recalled the activation of PRV-specific IFN-γ^+IL-2^+CD4^+ T cells, IFN-γ^+TNF-α^+CD8^+ T cells, and PCV2-specific IFN-γ^+TNF-α^+CD8^+ T cells. Our data suggested that PRV-Cap can effectively produce specific effector memory T cells (Tem) and memory B cells (MBCs) and exhibits weak secondary memory response after virulent PRV and PCV2 infection.

Materials and methods

Cells and viruses

Human embryonic kidney cells (HEK293T, ATCC CRL-11268), African green monkey kidney cells (Vero, CCL-81), and PCV-free PK-15 cells (ATCC-CCL-33) were cultured in Dulbecco's modified Eagle's medium (DMEM; Gibco, America) and supplemented with 10% heat-inactivated fetal bovine serum (FBS; Gibco, America). PCV2 strains HZ0201, PCV2 strains ZJ/c, PRV type II (PRV II) strains Dx (virulent, PRV Dx virus), and HD/c (gE/TK deletion, PRV HD/c virus) were stored in our laboratory (51, 52).

Antibodies and reagents

Mouse monoclonal antibodies (mAbs) against PCV2 Rep, PCV2 Cap, PRV gC, and PRV gD and rabbit pAbs to PRV VP5 were maintained in our laboratory (53, 54). Anti-β-actin (M1210-2) and rabbit anti-GFP (ET1602-7) polyclonal antibodies (pAbs) were obtained from Hangzhou HuaAn Biotechnology. Goat anti-mouse IgG H&L (10 nm Gold) was purchased from Abcam. Protein A/G PLUS-Agarose (sc-2003) was purchased from Santa Cruz Biotechnology. A UNIQ-10 Column Virus Genomic DNA Isolation Kit (CB94701427), Streptomycin sulfate (A610494-0050), and penicillin G sodium (A600135-0025) were purchased from Sangon Biotechnology. Phenol reagent for DNA Extraction (T0250) was purchased from Solarbio. ELISA kits for PRV gB antibody and PCV2 Cap antibody were purchased from Beijing Jinnuo Biotech Co., Ltd and Ringpu (Baoding) Biological Pharmaceutical Co. Ltd, respectively.

Construction for Cap protein of PCV2 transfer and US2 CRISPR-Cas9 gene editing vectors

The PRV envelope glycoprotein gE (US8) was selected as the insertion site for the PCV2 *Cap* fragment. Briefly, the signal peptide and transmembrane region of gE were predicted by the online software SignalP-5.0 Server and TMHMM Server v.2.0. The signal peptide sequence of gE contained the residues 1-430 in the extracellular region, the residues 431-453 in the transmembrane region, and the residues 454-579 in the intracellular region. The gE extracellular region residues 44-397 were replaced with PCV2 Cap to express a Cap-gE fusion protein. To enhance the expression of the Cap-gE fusion protein, the CMV promoter was inserted upstream of the gE signal peptide. Downstream of the fusion protein, an IRES sequence and the EGFP gene were added. On either side of the IRES-EGFP sequence, there were two loxP sites in the same direction for subsequent removal of the EGFP selection tag by the Cre enzyme. Figure 1A shows the skeleton of the Cap-gE homologous recombinant transfer vector that contains the sequence of CMV promoter, IRES, EGFP, and loxP sites. Primer pairs are listed in Table 1 for the construction of the Cap-gE transfer vector. The sequence scan for CRISPR online website was used to design sgRNA for the PRV *US9* gene sequence, and two primer pairs of sgRNA sequences with scores greater than 1.0 were synthesized as follows: PX459-US9-sgRNA1-sense and antisense primers: 5'-CACCGCGGCTCGCTGGCCCTGCTGC-3' and 5'-AAACGCAGCAGGGCCAGCGAGCCG-3'; PX459-US9-sgRNA2 sense and antisense primers: 5'-CACCGCCGTCCACCTGTGGATCCTG-3' and 5'-AAACCAGGATCCACAGGTGGACGG-3'. The synthesized primers were used to connect the px459 plasmid cut by the *BbsI* enzyme.

Rescue of recombinant virus

HEK293T cells were seeded on cell plates and were co-transfected with PRV HD/c virus genomic DNA, Cap transfer, and US9 CRISPR-Cas9 gene editing vectors by Jet prime transfection reagent (Polyplus-transfection, France) according to the manufacturer's instructions. After being cultured at 37°C for 6 h, the resultant cells were replaced with DMEM medium containing 2% FBS for another 48 h. The supernatant of the co-transfected cells with both green fluorescence and cytopathic effect (CPE) was used to inoculate into a 70-80% Vero cell monolayer at 37°C for 36 h. Subsequently, the plaque purification of the rescuing virus was performed under the condition of 2% low melting point agarose and was detected by PCR with gE-US7-9 primers (Supplementary Table 1). The resultant virus DNA was treated with Cre recombinase (New England Biolabs, USA) at 37°C for 30 min to remove the EGFP gene and the genome was then extracted and transfected into Vero cells as above described. After another five rounds of plaque purification, the pure recombinant PRV with the *Cap* fragment of the PCV2 genome was generated and its replication ability was determined by a 50% tissue culture infectious dose ($TCID_{50}$).

Immunoelectron microscopy

The cell debris in the viral supernatant was removed by a 0.22 μM filter and then a 20% Sorbitol Cushion (20% Sorbitol, 50 mM Tris HCl, 1 mM $MgCl_2$, PH7.2) was used for ultra-fast centrifugation at 100000 × *g*, at 4°C for 2 h to purify the virions. Each tube was covered with the sterilized PBS and deposited at 4°C overnight. The purified virus particles were incubated in a wet box and deposited on the surface of the copper mesh. Afterward, the mesh was incubated in closed buffer diluted Cap mAbs at 37°C for 1 h, and was then transferred to a wash buffer and washed five times. Subsequently, the mesh was incubated in colloidal gold conjugated secondary antibody for 1 h and was washed with buffer five times. Finally, each mesh was cleaned in distilled water three times. The dried mesh was used to observe virion morphology under transmission electron microscope (TEM) (HT7700, Hitachi, Japan) at 80 kV and photographed with a Gatan 830 CCD camera (55).

Immunofluorescence assay

For the immunofluorescence assays (IFA), cells were fixed with PBS (pH 7.4) containing 4% paraformaldehyde for 20 min at room temperature. After washing three times with PBST and blocking with 5% skim milk at 37°C for 1 h, the cells were incubated with the indicated primary antibodies at 37°C for 1.5 h, followed by incubation with FITC/AlexaFluor 546 labeled goat anti-rabbit or mouse IgG (KPL, America) at 37°C for another 1 h, and the nuclei were labeled with 1:5000 diluted DAPI (Solarbio, China) for 10 min. All IFA observations were performed under a fluorescence microscope (Olympas, Japan).

Western blotting

For Western blotting (WB), cells or viral concentrate were lysed in radioimmunoprecipitation assay strong lysis buffer containing 5% SDS (Beyotime, China), 1% Triton-100 (Sigma, America), and 50 mM Tris-HCl (Aladdin, China) at pH 7.5, and analyzed on SDS polyacrylamide gel electrophoresis. The separated protein bands were transferred to a nitrocellulose blotting membrane (GE Healthcare Life Science, America). After blocking with 5% skimmed milk containing 0.1% Tween 20 (Amresco, America) at 37°C for 30 min, the cells were incubated with indicated primary antibodies overnight at 4°C. The cells were then incubated with horseradish peroxidase-conjugated anti-mouse/rabbit IgG (Kirkegaard & Perry Laboratories, America) diluted 1:4000 in 5% skimmed milk for 2 h at room temperature, and visualized with a Super Signal West Femto substrate test kit (Thermo Fisher Scientific, America) using an AI680 Image 680 (GE Health Care, America).

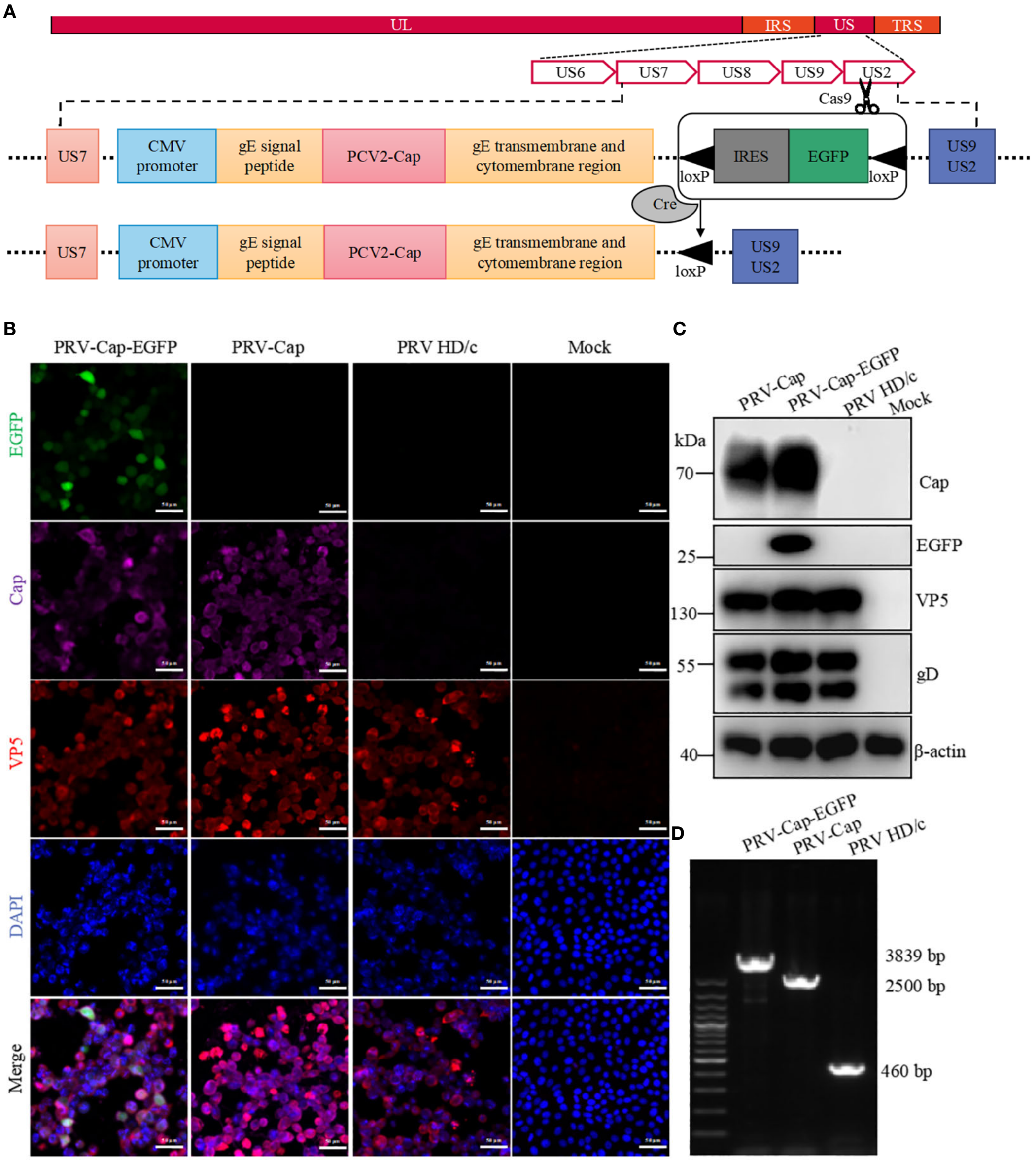

FIGURE 1
Generation of recombinant PRV with the Cap protein of PCV2. **(A)** The construction strategy of PRV-Cap. The PCV2 *Cap* gene was inserted into the *gE* extracellular region of parent PRV HD/c virus strain by homologous recombinant transfer vector, and then the fluorescent labeled *EGFP* gene was removed *in vitro* by the Cre-LoxP recombinant enzyme system to obtain the recombinant PRV with only the exogenous *Cap* gene. **(B)** IFA and **(C)** Western blotting assays of Cap-gE fusion protein expression in Vero cells inoculated with 1 MOI of PRV-Cap-EGFP, PRV-Cap, and PRV HD/c virus at 24 h post infection **(D)** Identification of inserting the *Cap* gene in Cap-EGFP and PRV-Cap by nucleic acid electrophoresis using gE-US7-9 primers.

Mice experiments

All animal care and experimental procedures were performed in accordance with the Animal Research Committee guidelines of Zhejiang University (No. ZJU20230315). One hundred and eighty 6-week-old specific-pathogen-free (SPF) C57BL/6 female mice were randomly divided into four groups that were intramuscularly immunized with PRV-Cap ($10^{7.5}$ $TCID_{50}$/ml, 0.1 ml; n=60), PRV HD/c virus ($10^{7.5}$ $TCID_{50}$/ml, 0.1 ml; n=25), PCV2 commercial vaccine (ZJ/C strain, 0.2 ml; n=25), or DMEM (Control, 0.1 ml; n=70), respectively. After that, the blood of five mice labeled in each group was collected from the suborbital venous plexus at 7 days post-vaccination (dpv) for Cap and gB antibody detection by ELISA and IFA assays. Four mice per group were anesthetized and euthanized at 21 dpv. Diluted serum samples were co-incubated with 100 $TCID_{50}$ PRV-DX or PCV2 ZJ/c at 37°C for 2 h and were then inoculated with PK-15 cells for 48 h to determine serum neutralization antibody titer by IFA. Immunized mice were intraperitoneally either inoculated with a lethal dose of PRV strain DX ($10^{6.5}$ $TCID_{50}$/ml, 0.1 ml) or PCV2 strain ZJ/c ($10^{7.0}$ $TCID_{50}$/ml, 0.45ml) at 21 dpv. The clinical signs of the inoculated mice were recorded every 12 h until 14 days post PRV infection or 21 days post PCV2 challenge. The dead or euthanized mice were immediately dissected, and the brain, lung, liver, spleen, and inguinal lymph nodes were collected for histopathology, immunohistology, virus isolation, and viral load

TABLE 1 Primers used for the construction of Cap-gE transfer vector.

Groups		Sequence(5′→3′)
Homologous left arm	LgE-F plus	GAATTCGAGCTCGGTACCCACGTCGCCGGCAGCGCCGTCCTC
	LgE-R-CMV plus	TTGATTACTATTAATAACTAGGTCTCAACCCCGGTGTGTG
CMV promoter	CMV-F-LgE plus	CACACACCGGGGTTGAGACCTAGTTATTAATAGTAATCAATTAC
	CMV-R-gESP plus	CGCAGCAGAAAGGGCCGCATGGTGGCGATCTGACGGTTCACTAAACCAG
gE signal peptide	gESP-F-CMV plus	GTGAACCGTCAGATCGCCACCATGCGGCCCTTTCTGCTGC
	gESP-R-Cap plus	CGGGTGTTGAAGATGCCATTGGCCGAGGGACTCGGGACCTCGGTGAC
PCV2 HZ0201 Cap	Cap-F-LgE plus	AGGTCCCGAGTCCCTCGGCCAATGGCATCTTCAACACCCGCCTCTC
	Cap-R-RgE plus	ATCGCGTCGTCGCCGCCGCCAGGGTTAAGTGGGGGGTCTTTAAG
Insertion domain of gE	gEKB-F-Cap plus	AAGACCCCCCACTTAACCCTGGCGGCGGCGACGACGCGATCTAC
	gEKB-R-loxP plus	ATAACTTCGTATAGCATACATTATACGAAGTTATTTAAGCGGGGCGGGACA
IRES sequence	IRES-F-loxP plus	TGTATGCTATACGAAGTTATGCCCCTCTCCCTCCCCCCCCCCTAA
	IRES-R-EGFP plus	CTTGCTCACCATTGTGGCCATATTATCATCGTGTTTT
EGFP sequence	EGFP-F-IRES plus	AATATGGCCACAATGGTGAGCAAGGGCGAGGAGCTGT
	EGFP-R-loxP plus	ATAACTTCGTATAGCATACATTATACGAAGTTATCTACTTGTACAGCTC
Homologous right arm	RgE-F-loxP plus	TGTATGCTATACGAAGTTATATACCGGGAGAACCGGTG
	RgE-R plus	GACGGCCAGTGCCAAGCTTGTTGTGGACCCGCGCGAACATGGCG

detection as described previously (56, 57). The other mice received a booster immunization at 28 days post initial immunization. The spleens collected from five mice per group at 7, 14, 21, and 28 days post initial immunization and 7 days post booster immunization were analyzed by enzyme linked immunospot (ELISpot) and flow cytometry (FCM) assays.

Histology and immunohistology staining

Tissue samples were fixed with 10% neutrally formalin and cut into 4 mm sections after paraffin-embedded. Immunohistochemical (IHC) staining were performed afterwards to determine the presence of PRV or PCV2 antigens in tissues. Tissue sections were incubated at 37°C with 500-fold diluted PRV gC or PCV2 Cap mAbs for 1 h and then at 37°C with HRP labeled goat anti-mouse antibodies for 1 h. The freshly prepared diaminobenzidine (DAB) was displayed at room temperature to produce brown-yellow positive particle precipitation. All slides were scanned and read using a panoramic microtome scanner (Pannoramic 1000, 3DHISTECH Ltd.) and evaluated by a single veterinary pathologist blinded to the immunization groups.

Real time quantitative PCR

The virus supernatant or tissue homogenate supernatant to be extracted was added with 20 μl protease K and 5 μl RNAase. F, bathed in water at 55°C for 2 h, and the DNA extraction phenol reagent (Solarbio, China) was added in the same volume. The reagent was vigorously mixed and allowed to stand, and centrifuged at 3000 × *g* for 10 min. The supernatant was added to equal volume premixed chloroform: isoamyl alcohol (24:1) and mixed gently. After centrifugation at 3000 × *g* for 10 min, the supernatant was added into 2-2.5 times the volume of pre-cooled anhydrous ethanol and treated at -20°C for 30 min. After centrifugation at 14000 × *g* for 10 min, the supernatant was discarded and the precipitation was washed with 1 ml 75% ethanol. The precipitation was completely dissolved with TE buffer after drying, and PRV gB, PCV2 Rep, and gapdh mRNA were then detected using ChamQ Universal SYBR qPCR Master Mix (Vazyme Biotechnology; Q711-02). Primers of gB and Rep are shown in Supplementary Table 1.

ELISpot assay

An ELISpot assay was conducted as stated (58). Briefly, single spleen cell samples from 2-week-immunized mice euthanized by CO_2 were prepared with RPMI 1640 (Gibco, America) containing 2% FBS through 200-mesh cell filtration screens. The cells were then treated with ammonium chloride potassium (ACK) lysis buffer (Solarbio, China) at 4°C for 5 min and then terminated with RPMI 1640 supplemented with 2% FBS in the same volume. After 500 × *g* centrifugation, the precipitate was suspended in RAPI 1640 containing 10% FBS. For the ELISpot assay, 5×10^5 cells/well were placed on ELISPOT PVDF 96-well plates (U-CyTech, Netherlands) pre-coated with mouse IFN-γ antibody and inactivated PCV2-ZJ/c or PRV-DX (MOI=1) as antigen or PMA/Ionomycin (MCE, America) mixture as positive control were added at 37°C for 24 h. Then, the ELISpot plates were treated according to the instructions from the manufacturer. The spots stained with 3-

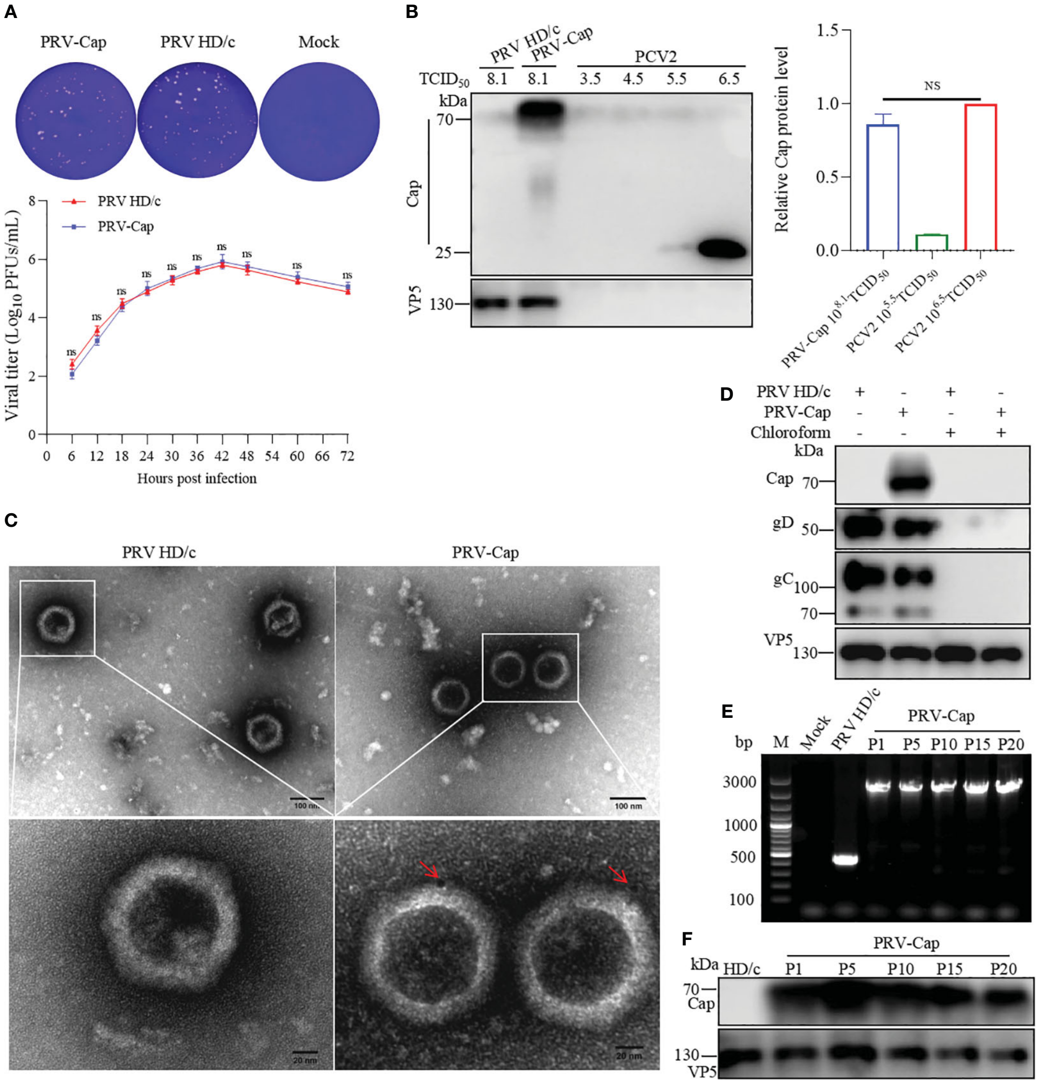

FIGURE 2
Detection of expression and genetic stability of Cap-gE chimeric protein in PRV-Cap. **(A)** One-step growth curves and plaque detection of PRV-Cap and parent PRV HD/c virus (MOI=1) infected PK-15 cells. The infected cells were incubated at 37°C for 2 h, washed with DMEM three times, and cells were finally cultured with DMEM containing 2% FBS. Viral titers were measured at indicated time points post infection. The plaque formation unit (PFU) was detected by the limited dilution plaque assay and $TCID_{50}$ was determined by Reed-Muench method. **(B)** The abundance of the Cap-gE fusion protein in the supernatant of PRV-Cap was detected by Western blotting compared with the original Cap protein of PCV2. **(C)** The virus particles purified by 20% Sorbitol Cushion ultra-centrifugation were examined by transmission electron microscopy with anti-Cap mAbs as described in Materials and methods. **(D)** The purified Cap virions were violently mixed with chloroform and ice bath for 20 min to remove the virus envelope for Western blotting detection. **(E)** The genome of PRV-Cap was extracted, and PCR detection and sequencing were performed with gE-US7-9 primers. **(F)** Western blotting detection of each generation of $10^{8.0}$ $TCID_{50}$/ml PRV-Cap supernatant. NS, p >0.05.

Amino-9-Ethylcarbazole (AEC) dye were quantified by the automatic immunospot analyzer (Cellular Technology Ltd., America) to determine the cytokine secretion amount of spleen cells in each group.

FCM assay

Splenocyte suspensions from immunized mice were prepared according to the ELISpot assay. For B cell surface staining, 1×10^6 cells plated in 96-well V-bottom plates were pretreated with Mouse Fc block (BD Biosciences, America) at a concentration of 25 μg/ml at 4°C for 10 min. Subsequently, the resultant cells were stained with the surface antibodies diluted with cell PBS containing 2% BSA and 25 μg/ml Fc block at 4°C for 30 min. For endonuclear staining, 1×10^6 cells were incubated with the surface antibodies at 4°C for 30 min. After centrifuge, the cells were treated with the Transcription Factor Buffer Set (BD Biosciences, America) for cell fixation and permeabilization. Cells were subsequently incubated with intranuclear antibodies diluted in permeabilization buffer at 4°C for 1 h. For intracellular cytokine staining (ICS), 2×10^6 splenocyte cells plated in 96-well U-bottom plates were incubated with corresponding viral antigen for stimulation at 37°C for 4 h. The resultant cells were incubated with Brefeldin A (MCE, America) with a concentration of 5 μg/ml overnight and were fixed with 4% PFA on an ice bath for 5 min and then permeabilizated with Cytofix/Cytoperm Kit (BD Biosciences, America) for 20 min (48, 59). Subsequently, the cells were incubated with mouse anti-IFN-γ, TNF-α, and IL-2 antibodies at 4°C for 30 min, washed twice, and resuspended in 200μl cell PBS containing 0.5% paraformaldehyde (PFA) for FACS analysis. At least 2×10^5 cells were collected using a BD FACSVerse Fortessa (BD Biosciences, America), and the data were analyzed using FlowJo software (Tree Star Inc., America). Details of antibodies used in the FCM are listed in Supplementary Table 2.

Statistical analysis

Statistical analysis was performed using GraphPad Prism 8.0 software, and all data are presented as the mean ± SD of three independent experiments. For all experiments, $p < 0.05$ was considered statistically significant. In the figures, not significant (ns): $p > 0.05$; *, $p < 0.05$; **, $p < 0.01$; ***, $p < 0.001$.

Results

Construction of the recombinant PRV type II with PCV2 Cap protein

To construct a recombinant virus expressing the Cap protein of PCV2 on the PRV II envelope, 293T cells were co-transfected with PRV II HD/c genome, pUC18-Cap-EGFP transfer vector, and US9 CRISPR-Cas9 gene editing vector to generate a recombinant PRV expressing both the Cap of PCV2 and EGFP (PRV-Cap-EGFP). At 48 h post transfection, the cells with an obvious green fluorescence were selected to inoculate into the Vero cell monolayer. To further generate PRV-Cap without the EGFP label, 293T cells were transfected with the Cre recombinase-treated PRV-Cap-EGFP genome. Subsequently, the cells with CPE and without fluorescence were used to infect Vero cells to obtain PRV-Cap. In immunofluorescence analysis, EGFP, PCV2 Cap, and VP5 of PRV were detected in PRV-Cap-EGFP infected cells, and only Cap and VP5 proteins were detectable in PRV-Cap infected cells (Figure 1B). Similar results are shown in the Western blot and PCR analyses (Figures 1C, D). These data indicate that the *Cap* gene of PCV2 was successfully inserted into the PRV genome and the PRV-Cap was rescued.

Characteristics of chimeric PRV with Cap protein of PCV2

To analyze the replication capacity of recombinant chimeric PRV-Cap, the virus titer was detected by a one-step growth curve using the plaque technique. The plaque formation test showed that the virus titer of the PRV-Cap had no significant difference compared to its parent PRV HD/c virus (Figure 2A), suggesting that the insertion of the *Cap* fragment in the gene *gE* does not affect the ability of PRV replication. To detect the expression level of Cap protein in PRV-Cap, we conducted a comparative analysis of PCV2 and PRV-Cap viruses. A Western blot assay revealed that the Cap concentration of the PRV-Cap with $10^{8.1}$ $TCID_{50}$/ml had no significant difference to PCV2 with $10^{6.5}$ $TCID_{50}$/ml (Figure 2B). To identify whether the Cap protein was orientated in the envelope of PRV II virion, the ultracentrifuged and purified PRV-Cap virions were stained with a colloidal gold conjugated anti-Cap antibody and observed by TEM. The result indicated that the Cap protein was displayed on the envelope of the PRV virion (Figure 2C). Consistently, the Cap protein was undetectable in the purified PRV-Cap with chloroform treatment in Western blot analysis (Figure 2D), revealing that the Cap protein of PCV2 was located on the PRV envelope. Moreover, to test the genetic stability of the *Cap* gene in recombinant PRV, the PRV-Cap was continuously passaged in PK-15 cells 20 times, and the genome of each generation was extracted for PCR detection. The results showed that the protein and nucleotide fragment of the *Cap* gene in the PRV-Cap could be detected from the 1st passage to 20th passage, revealing that the *Cap* gene in PRV-Cap was stable (Figures 2E, F). Collectively, these data confirmed that the PRV-Cap is a recombinant chimeric virus and that the Cap protein of PCV2 is embedded in the envelope of PRV.

Immunogenicity and safety of the PRV-Cap

To detect the immunoprotective ability of the PRV-Cap to host, the PRV-Cap was inoculated into 6-week-old C57BL/6 mice, while the parent PRV HD/c virus, PCV2 commercial ZJ/C inactivated vaccine, and DMEM were used as controls. The strategies and detailed time points of mice experiments are shown in Figure 3A. We detected antibody dynamics to evaluate the humoral immune response of the PRV-Cap inoculated mice. ELISA assays showed that the antibodies to both gB and Cap were detectable in the PRV-Cap inoculated mice at 7 dpv and reached a peak at 21 dpv. Interestingly, in PRV-Cap inoculated mice, the anti-gB antibodies were slightly higher than in parent PRV HD/c virus immunized mice (Figure 3B). Conversely, the antibodies against the Cap were significantly lower in PRV-Cap inoculated mice than in ZJ/C vaccine-immunized mice (Figure 3C). However, a similar trend was shown for neutralizing antibodies against PRV at 21 dpv (Figures 3D, E). These data suggest that the Cap protein in the PRV-Cap has a synergistic promoting effect on humoral immune responses of PRV. At 21 days post-inoculation, the PRV-Cap inoculated mice challenged with PCV2 and lethal PRV had a 100% survival, similar to those immunized with their parent PRV HD/c virus and ZJ/C vaccines (Figures 3F, G). The above-mentioned data verify that the PRV-Cap inoculated mice had complete immune resistance to PCV2 induced infection and death caused by lethal PRV infection.

To evaluate the environment safety of PRV-Cap, and replication of pathogenic PRV and PCV2, we conducted PCR detection, virus isolation, and histological and immunohistological observations of the PRV-Cap immunized mice. The virus excretion detection revealed that the fragments of the *gE* and *gB* genes were undetectable in PCR and the PRV-Cap could not be isolated from fecal samples of mice within 1 week after inoculation (data not

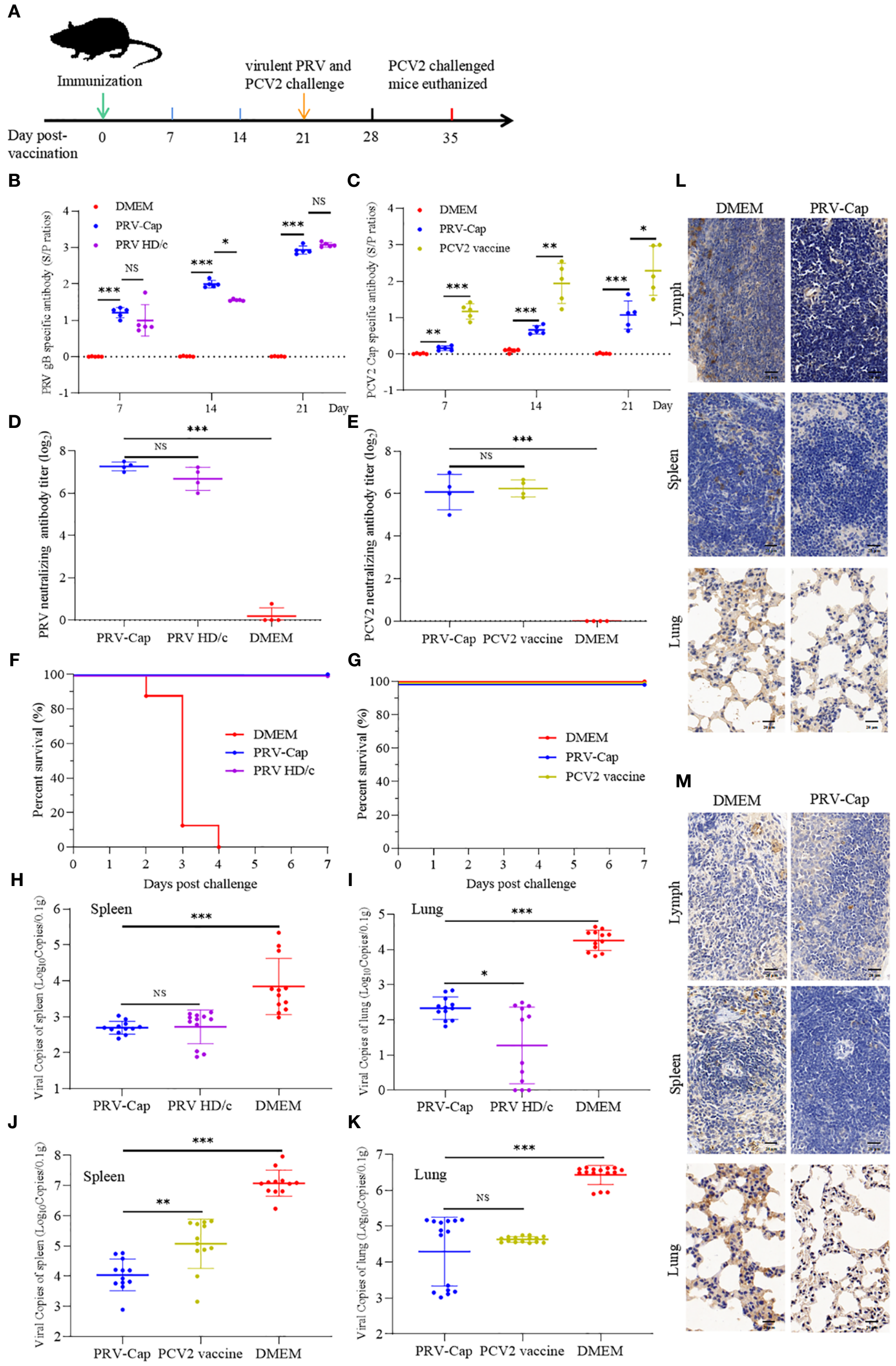

FIGURE 3
Immunogenicity of the PRV-Cap. **(A)** The mouse model of PRV-Cap vaccination. **(B, C)** The gB and Cap ELISA antibody titers at 7, 14, and 21 dpv. **(D, E)** Neutralization antibody titers against PRV or PCV2 at 21 dpv. **(F, G)** Survival rates of mice immunized post 3 weeks against PRV-DX ($10^{6.5}$ $TCID_{50}$/ml, 0.1 ml) or PCV2 ZJ/c ($10^{7.0}$ $TCID_{50}$/ml, 0.45ml) challenge. **(H, I)** The viral loads in the lungs and spleens of mice were measured by qPCR assay on 3rd day after PRV-DX challenge, and PRV genomic copies were calculated according to the CT value of the PRV-gB standard curve. **(J, K)** The viral loads in the lungs and spleens of mice were measured by qPCR assay on day 21 after PCV2 challenge, and PCV2 genomic copies were calculated according to the CT value of the PCV2-Rep standard curve. **(L, M)** Immunohistochemical analysis of the lungs, spleens and inguinal lymph nodes of PRV DX or PCV2 ZJ/c challenged mice. Magnification, 80x; Scale bars, 20 μm. Data are expressed as means ± standard errors of the means. NS, p >0.05; *, $p < 0.05$; **, $p < 0.01$; ***, $p < 0.001$.

shown). This suggests that mice immunized with the PRV-Cap do not excrete viruses into the environment through the digestive tract and are environmentally safe. After being challenged with PCV2 and lethal PRV, the spleens and lungs of the PRV-Cap immunized mice were observed to have no PRV and PCV2 antigens in immunohistological staining, in comparison with mock immunized mice (Figures 3L, M). Concurrently, in the qPCR assay, virus copies in spleens and lungs of the PRV-Cap immunized mice were significantly lower than that of mock immunized mice after PCV2 and PRV challenges (Figures 3H–K and Supplementary Figure 1). Moreover, in the virus isolation assay, PCV2 and PRV were undetectable in the spleens and lungs of the PRV-Cap immunized mice with PRV and PCV2 challenges for three consecutive rounds in PK-15 cells. These results demonstrate that the immunized mice of PRV with the chimeric Cap protein were environmentally safe.

PRV-Cap immunization induced early activation and expansion of lymphocytes

Type II C-type lectin receptor CD69 is a classical early marker of lymphocyte activation (60, 61), and nuclear antigen Ki67 is widely used to trace the proliferative activity of T cells after vaccine immunization or pathogen infection (62–64). To detect the activation and expansion of cellular and humoral immunity induced by PRV-Cap, we used multiparameter FCM to analyze the dynamics of CD69 and Ki67 in different T cell subsets and B cells. Based on the gating strategy for multicolor shown in Supplementary Figures 2A, B, in FCM analysis, it was observed that $CD69^+CD4^+$ T cells and $CD69^+B220^+$ B cells were significantly activated in Cap- and HD/c- virus vaccinated mice on the 7th day, and significant upregulation of $CD69^+CD8^+$ T cells and $CD69^+\gamma\delta$ T cells did not appear until the 14th day (Figures 4A, B). Moreover, $Ki67^+CD4^+$ T cells, $Ki67^+CD8^+$ T cells, and $Ki67^+B220^+$ B cells all showed a significant increase on the 7th day, and Ki67 levels of $CD4^+$ T cells and $CD8^+$ T cells declined on the 14th day while B cells remained unchanged (Figures 4C, D). Noticeably, the number of $CD69^+CD4^+$ T cells and $Ki67^+CD4^+$ T cells in PRV-Cap immunized mice was significantly higher than that in parent PRV HD/c virus immunized mice on the 7th day. Next, we analyzed the percentage of Tfh cells ($CD4^+PD\text{-}1^+BCl\text{-}6^+$), GC B cells ($B220^+GL7^+FAS^+$), and CD40-positive B cells ($CD19^+CD40^+$) in the spleens of immunized mice on the 7th and 14th day, according to the gating strategy shown in Supplementary Figures 2B, C. Figures 4E–G revealed that both PRV-Cap and PRV HD/c virus inoculated mice had a significant increase of Tfh, GC B, and CD40 positive B cells without a difference. In addition, the activation of NK cells and CTLs was analyzed using a lysosomal-associated membrane protein marker CD107a (65, 66) according to the gating strategy shown in Supplementary Figure 2D. Figure 4H shows that $CD107a^+$ NK cells and $CD107a^+CD8^+$ CTLs were significantly upregulated after PRV-Cap or PRV HD/c virus inoculation. Generally, the above-mentioned data demonstrate that the early activation and expansion of lymphocytes induced by PRV-Cap was superior to the parent PRV HD/c virus.

PRV-Cap immunization induced Th1 cytokine specific for PRV and PCV2

To detect the PRV-Cap-induced specific cellular immune response, splenocytes from the immunized mice at 14 days post-immunization were stimulated with either inactivated PRV-DX or PCV2. As shown in Figure 5A, the PRV-Cap vaccination induced dual (PRV and PCV2)-specific lymphocyte expansion, whereas the PRV HD/c virus or PCV2 vaccine immunization only induced a single specific expansion upon ex vivo re-stimulation. An ELISPOT assay showed that the vaccination of PRV-Cap induced more PCV2-specific IFN-γ spot-forming cells (SFC) than PCV2 immunization but induced comparable number of PRV-specific IFN-γ SFC to PRV HD/c virus immunization (Figure 5B). The gating strategy for cytokine detection is shown in Supplementary Figure 3A. In FCM assay (Figures 5C–H), PRV-specific single cytokine ($IFN\text{-}\gamma^+$, $TNF\text{-}\alpha^+$ or $IL\text{-}2^+$), double cytokine ($IFN\text{-}\gamma^+TNF\text{-}\alpha^+$, $IFN\text{-}\gamma^+IL\text{-}2^+$ or $TNF\text{-}\alpha^+IL\text{-}2^+$), and triple cytokine ($IFN\text{-}\gamma^+TNF\text{-}\alpha^+IL\text{-}2^+$) expressing CD4 T cells showed a significant increase in PRV-Cap and PRV HD/c virus immunized mice upon ex vivo restimulation with inactivated PRV compared to mock immunized mice. Interestingly, the PRV-Cap immunized mice produced more PCV2-specific IFN-γ secreting CD4 T cells than the PCV2 vaccine immunized mice upon ex vivo restimulation with inactivated PCV2. Similarly, Cap or PRV HD/c virus immunization induced PRV-specific $IFN\text{-}\gamma^+$, $TNF\text{-}\alpha^+$, or $IFN\text{-}\gamma^+TNF\text{-}\alpha^+$ $CD8^+$ T cells, but there was no significant difference between PRV-Cap and PRV HD/c virus. No CD8 T cells expressed with PCV2-specific cytokines were detected in the PRV-Cap and PCV2 vaccine immunized mice (Figures 5I–L). These data indicate that PRV-Cap immunization activates $CD4^+$ and $CD8^+$ T cell subsets, eliciting better T-cell immunity than PCV2 but not compromising anti-PRV immunity.

PRV-Cap immunization produced specific effector memory T and B cells

Memory T cells (Tm) and memory B cells (MBCs) are activated and differentiated during secondary infection, producing a fast and powerful immune response, which is particularly important for resistance to viral infection (24, 67–69). Therefore, we measured $CD4^+$ and $CD8^+$ memory T cells in primarily immunized mice at 14 days post-immunization according to the gating strategy shown in Supplementary Figure 3B. In this study, it was observed that memory Th1 cells ($CD4^+T\text{-}bet^+CD44^+$) showed a significant increase in mice inoculated with PRV-Cap and PRV HD/c virus compared to mice immunized with a mock treatment or PCV2 commercial vaccine. There was no significant difference between the PRV-Cap and PRV HD/c viruses (Figure 6A). In Tm, two cell subsets of central memory T cells (Tcm) and effector memory T cells (Tem), were defined based on differential expression of lymphocyte homing marker CD62L. Therefore, we measured the percentage of Tcm ($CD44^{hi}CD62L^{hi}$) and Tem ($CD44^{hi}CD62L^{lo}$) in $CD4^+$ Tm and $CD8^+$ Tm. The results showed that PRV-Cap and PRV HD/c virus immunization induced a significant increase in $CD4^+$ Tcm, $CD4^+$ Tem, and $CD8^+$ Tem in mice, while the

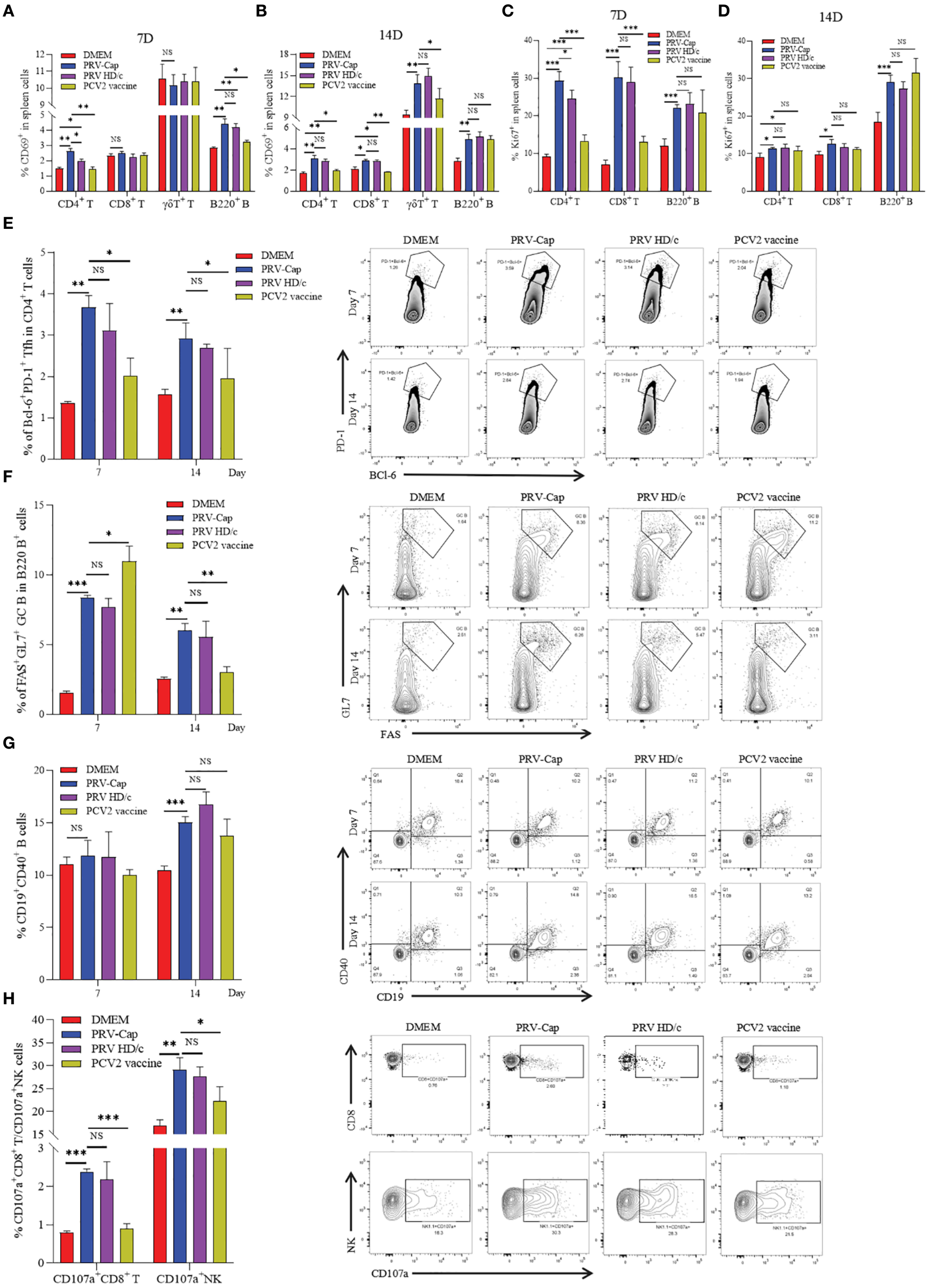

FIGURE 4

Dynamic changes of activation and expansion of different immune cell subsets after PRV-Cap immunization. **(A, B)** The expression of activation marker CD69 in CD4 T cells, CD8 T cells, γδ T cells, and B cells at 7 and 14 dpv. **(C, D)** The expression of expansion marker Ki67 in CD4 T cells, CD8 T cells, and B cells at 7 and 14 dpv. **(E, F)** The proportion and representative cytometric profiles of Tfh cells (CD4$^+$PD-1$^+$BCl-6$^+$) and GC B cells (B220$^+$GL7$^+$FAS$^+$) at 7 and 14 dpv. **(G)** The percentage and representative cytometric profiles of CD40-positive B cells (CD19$^+$CD40$^+$) at 7 and 14 dpv. **(H)** The expression and representative cytometric profiles of CD107a in NK cells and CTLs at 14 dpv. NS, $p > 0.05$; *, $p < 0.05$; **, $p < 0.01$; ***, $p < 0.001$.

commercial PCV2 vaccine only showed a significant increase in CD4$^+$ Tcm and CD8$^+$ Tcm (Figures 6B, C). In addition, we measured the percentage of MBCs (B220$^+$lgD$^-$CD138$^-$) based on the gating strategy shown in Supplementary Figure 2C. Figure 6D shows that PRV-Cap-induced MBCs are higher than PRV HD/c virus and PCV2 at 7 days post-immunization. These data demonstrate that PRV-Cap immunization induces the production of CD4$^+$ and CD8$^+$ effector memory T cells.

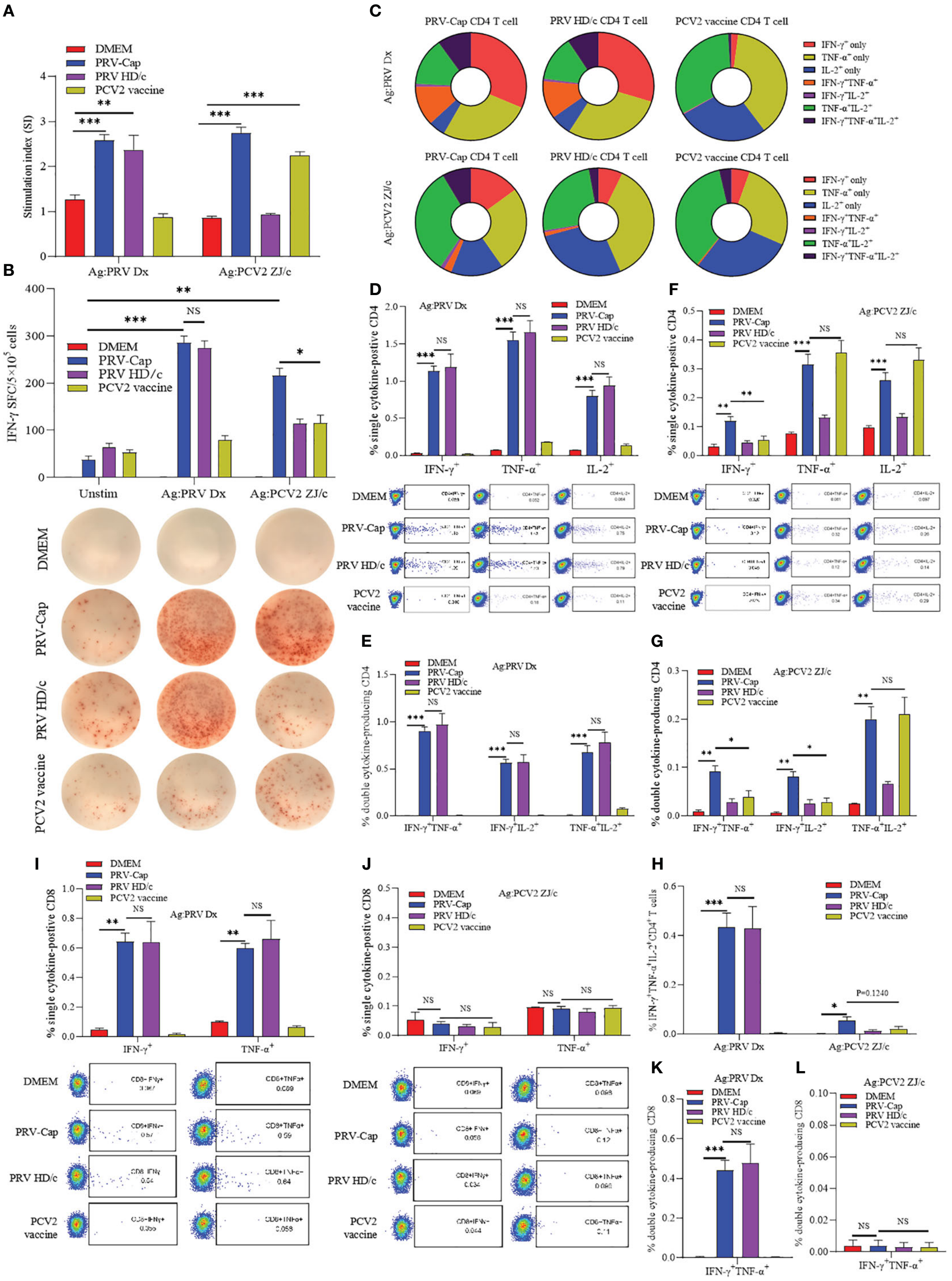

FIGURE 5
PRV and PCV2 specific cytokine production profile from splenocytes of PRV-Cap vaccinated mice at 14 dpv. **(A)** The specific proliferation response of splenocytes was detected using the CCK8 method. Splenic lymphocyte suspension was stimulated with PRV-DX or PCV2 inactivated antigen (MOI=1) for 48 h, then antigen-specific proliferative response was detected at OD450 using CCK8. The stimulation index (SI) = (test group OD450 - blank control OD450)/(negative control OD450 - blank control OD450). **(B)** Representative images of IFN-γ ELISpot wells and mean spot size from the various vaccine groups. The secreting spots forming cells (SFC) were counted using the ELISpot method after 24 h stimulation with PRV-DX or PCV2 inactivated antigen. **(C)** The proportion of PRV or PCV2 specific CD4$^+$ T cells that produced IFN-γ, TNF-α or IL-2 single cytokine, any two cytokines, and triple cytokines. **(D–H)** Percentage of CD4$^+$ T cells that produced single, double, and triple representative TH1 cytokines after PRV-DX or PCV2 stimulation (MOI=1, 24h). **(I–L)** Percentage of CD8$^+$ T cells that produced single or double cytokines after PRV-DX or PCV2 stimulation (MOI=1, 24h). Data expressed as mean ± sd from five mice per group. NS, p >0.05; *, p < 0.05; **, p < 0.01; ***, p < 0.001.

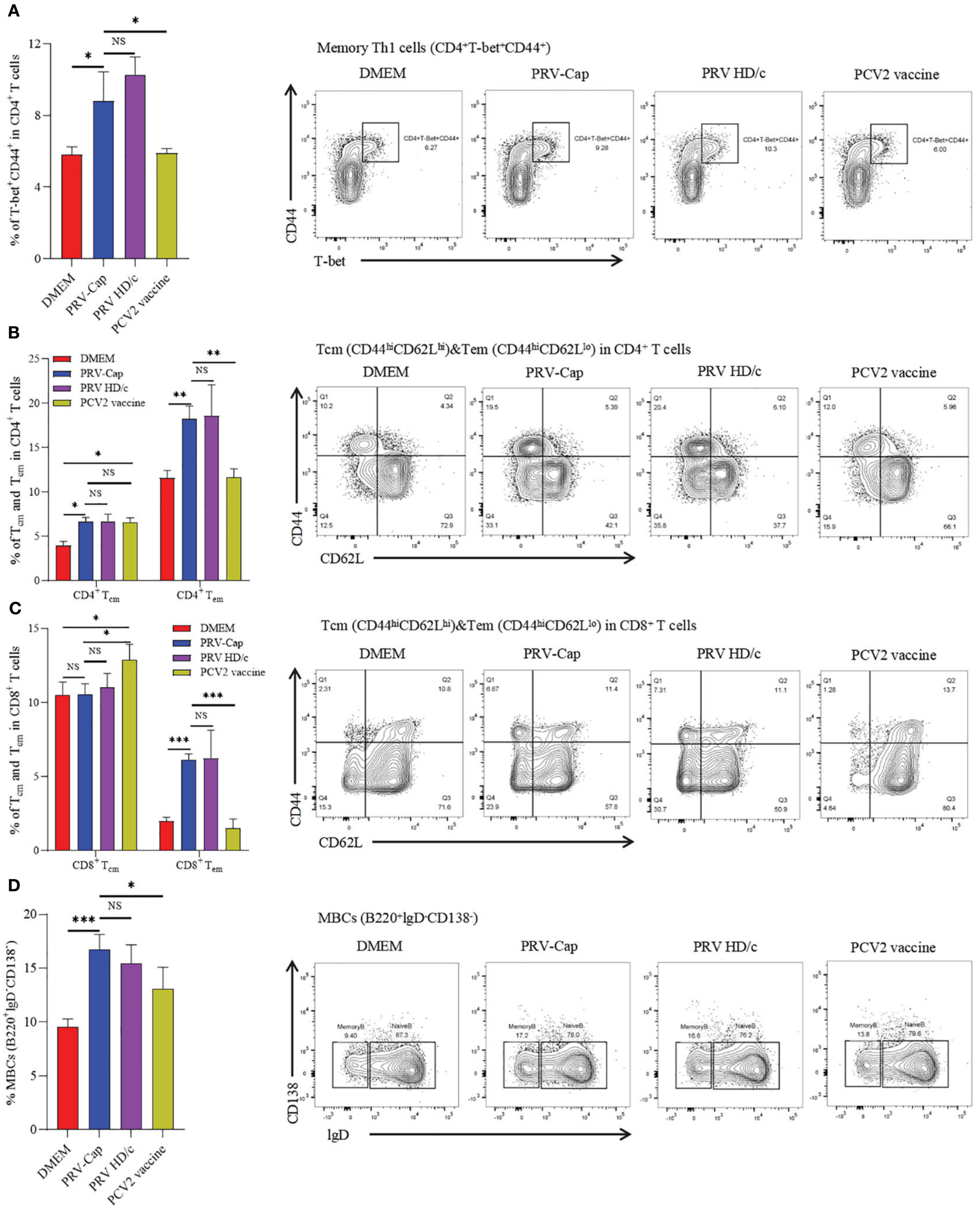

FIGURE 6
Percentage of memory T and memory B cells in splenocytes at 14 dpv. **(A)** The proportion and representative cytometric diagrams of $CD4^+$ memory Th1 cells. **(B, C)** Statistical analysis and representative cytometry diagrams of Tcm and Tem in $CD4^+$ or $CD8^+$ T cells. **(D)** The proportion and representative cytometric diagrams of MBCs in B220 positive B cells. Data expressed as mean ± sd from five mice per group. NS, $p > 0.05$; *, $p < 0.05$; **, $p < 0.01$; ***, $p < 0.001$.

The booster immunization with PRV and PCV2 recalls the reactivation of IFN-γ^+IL-2^+CD4^+ and IFN-γ^+TNF-α^+CD8^+ T cells

To further evaluate the memory response of the PRV-Cap induced T cells, the booster immunization with PRV-DX, PCV2-ZJ/c, and PRV-Cap was performed in mice at 28 days post initial immunization with the PRV-Cap. Subsequently, cytokine expression in T cells was examined by FCM at 7 days post-booster immunization. Figures 7A, C showed that the proportions of PRV-specific IFN-γ^+CD4^+ and IL-2^+CD4^+ T cells increased significantly after PRV booster immunization, while the percentage of TNF-α^+CD4^+, IFN-γ^+TNF-α^+CD4^+, TNF-α^+IL-2^+CD4^+, and IFN-γ^+TNF-α^+IL-2^+CD4^+ T cells continued to decrease, demonstrating that the PRV booster immunization only resulted in the upregulation of IFN-γ^+IL-2^+CD4^+ T cells. Conversely, the percentage of PCV2-specific single cytokine, double cytokine, and triple cytokine expressing CD4 T cells all showed a decrease in mice with PCV2 booster vaccination (Figures 7B, C),

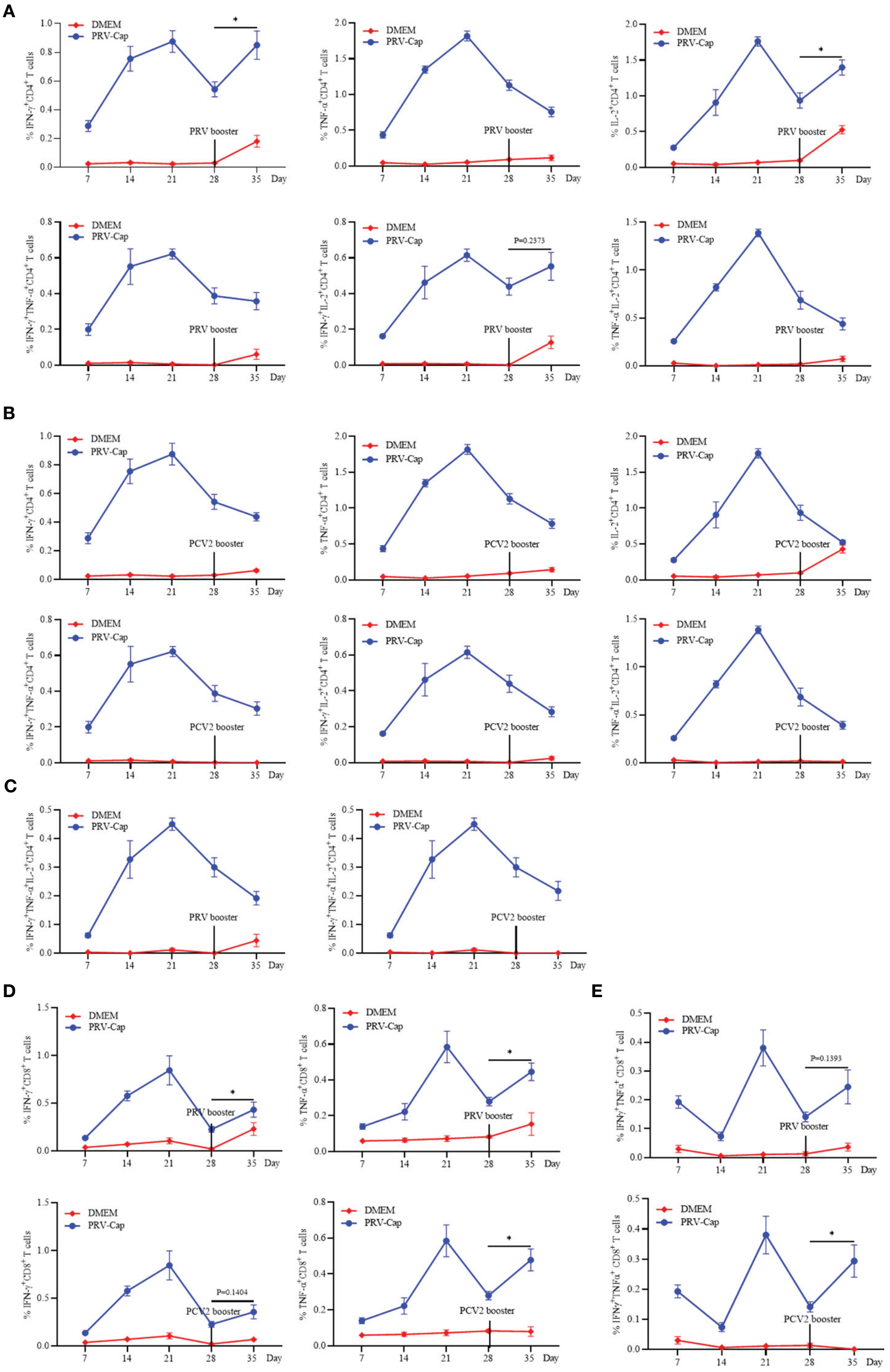

FIGURE 7
Analysis of the memory response of PRV-Cap induced T cells. The booster immunization with PRV-DX ($10^{6.5}$ $TCID_{50}$/ml, 0.1 ml) or PCV2 ($10^{7.0}$ $TCID_{50}$/ml, 0.45ml) was performed in mice at 28 days after initial immunization with the PRV-Cap. **(A–C)** Percentage of $CD4^+$ T cells stimulated by PRV-Cap (MOI=1, 24h) to produce single, double, and triple representative TH1 cytokines at 7, 14, 21, and 28 dpv and at 7 days post booster immunization with PRV-DX or PCV2. **(D, E)** Percentage of $CD8^+$ T cells stimulated by PRV-Cap (MOI=1, 24h) to produced single or double cytokines at 7, 14, 21, and 28 dpv and 7 days post booster immunization with PRV-DX or PCV2. Data expressed as mean ± sd from five mice per group. NS, p >0.05; *, p < 0.05; **, p < 0.01; ***, p < 0.001.

indicating that the PCV2 booster immunization could not stimulate an obvious reactivation of CD4 T cells. Similar trends appeared in mice with booster immunization with PRV-Cap at 28 days post initial immunization with the PRV-Cap (Supplementary Figure 4). Moreover, the percentage of IFN-γ^+CD8^+, TNF-α^+CD8^+, and IFN-γ^+TNF-α^+CD8^+ T cells showed a significant upregulation after both PRV and PCV2 booster immunization (Figures 7D, E). These results proved that PRV booster vaccination, rather than PCV2, could cause the memory response of IFN-γ$^+$IL-2$^+$CD4$^+$ T cells and the activation of IFN-γ$^+$TNF-α$^+$CD8$^+$ T cells could be reactivated after booster vaccinations.

Discussion

In recent years, the generation of recombinant vector vaccines has become an important research focus (70, 71). As an important zoonotic virus, PRV can take advantage of its large genome and multiple non-essential genes to construct recombinant attenuated vaccines carrying foreign genes. Research has shown that the PRV SA215 strain (TK$^-$/gE$^-$/gI$^-$ deleted) can be employed as a vector to insert PPV VP2 and EGFP expression box into the gI site using homologous recombination technology (18). Furthermore, gI and gE were replaced by the SVA VP2 and EGPF to obtain recombinant PRV (19). However, a major problem is that the foreign genes in recombinant PRV are only integrated into the genome for independent expression, rather than assembled on the surface of the virion. In this study, we selected a gE/TK virulence gene deficient PRV HD/c virus as the recombinant virus skeleton. We inserted the Cap gene of PCV2 into the extracellular domain of the PRV *gE* gene and added a cytomegalovirus promoter in front of the fusion gene to enhance the expression of the inserted gene. We also verified that the Cap protein expressed was embedded on the surface of the PRV envelope. In animal immunization tests, the recombinant PRV with the *Cap* gene induced higher levels of anti-PRV neutralizing antibodies compared to the parent PRV HD/c virus strain and exhibited excellent immune protection against both PRV and PCV2. These data demonstrate for the first time that there is no immune antagonism between the PCV2 Cap protein and PRV when the recombinant PRV carrying the Cap protein is inoculated, and that the Cap protein enhances the immune efficacy of PRV. Therefore, in view of the high replication ability of PRV-Cap, this study implies that using the recombinant PRV with the *Cap* gene of PCV2 to produce the Cap protein of PCV2 can not only significantly overcome the deficiency of PCV2 replication ability, but also achieves the effect of preventing two diseases with one dose of vaccine.

The effective host defense against viral infection depends on humoral and cellular immunity (20, 72). However, the mechanism of specific immune response induced by recombinant PRV has not been discussed in detail. Considering that the introduction of the Cap protein may affect the cellular and humoral immunity of PRV, we detected the activation and/or proliferation levels of CD4 T cells, CD8 T cells, γδT cells, NK cells, and B cells. Flow cytometry analysis revealed that PRV-Cap effectively mediated the specific activation and proliferation of all the aforementioned cell subsets. Previous studies have reported that Tfh can regulate the production of high-affinity antibodies by inducing GC B maturation (23–25). In this study, we demonstrated that PRV-Cap effectively stimulates the production of Tfh, GC B, and CD40-positive B cells, with no significant differences compared to PRV HD/c virus, indicating that the insertion of the Cap protein does not significantly affect the overall immunology of PRV. It is worth mentioning that the proportion of CD69 and Ki67 positive CD4 T cells of the recombinant PRV with the Cap protein was higher than that in the parent PRV HD/c virus on the 7th day, accompanied by a slight increase in the percentage of Tfh. Heterologous immunity mediated by the bystander effect in viral infection (73) may be the reason for the difference in antibody levels between PRV-Cap and PRV HD/c virus in the early immunization period.

Cytokines are small polypeptides or proteins that transmit information within cells and play a crucial role in immune regulation (74). IFN-γ, IL-2, and TNF-α are representative functional antiviral cytokines secreted by antigen-specific Th1 cell subpopulations and are essential for antiviral infection and immunological evaluation of vaccines (43, 44). IFN-γ, as the most vital antiviral cytokine, not only collaborates with TNF-α to inhibit viral replication, but also stimulates specific cytotoxic immunity and activates macrophages to phagocytic pathogens by recognizing virus-associated major histocompatibility complex (MHC) on the cell surface (45–48). Studies have shown that CD8$^+$ T cells can also secrete a variety of pro-inflammatory cytokines, mainly IFN-γ and TNF-α, to inhibit viral replication, and express various chemokines to recruit inflammatory cells to the site of infection (42, 75). In this study, both PRV-Cap and parent PRV HD/c virus induced strong PRV-specific cytokine production and similar cytokine expression profiles in CD4 T cells and CD8 T cells, and PRV-Cap synchronously mediates the production of PCV2-specific cytokines, suggesting that the insertion of PCV2 Cap protein did not affect the overall immunogenicity of PRV. Notably, the cytokines induced by PCV2 inactivated vaccine were mainly IL-2 and TNF-α secreted by CD4 T cell subsets, and only a small amount of IFN-γ was produced at the early stage, while the PRV-Cap induced stronger IFN-γ production and a higher proportion of IFN-γ SC expression profile compared to the inactivated commercial PCV2 vaccine. It has been reported that PCV2 inactivated and subunit vaccines exhibit weak IFN-γ secretion (76). The addition of IFN-γ enhances the proliferative response of PCV2-specific T lymphocytes and shows a better protective effect (77). Therefore, these data suggest that the recombinant PRV with the Cap protein may induce stronger PCV2-specific cellular immunity than PCV2 inactivated vaccine.

Memory T and B cells produced by vaccination are activated and differentiated during secondary infection or booster vaccination, exerting a rapid and robust immune response that is particularly important for antiviral infection (24, 67–69). In this study, we examined the phenotypes of Tm and MBCs after immunization. The results show that both the PRV-Cap and PRV HD/c viruses significantly increased memory Th1 cells, CD4$^+$ Tem, CD8$^+$ Tem, and MBCs, with a slight increase in CD4$^+$ Tcm, indicating that Cap insertion did not affect the overall memory cell phenotype. At the same time, our results show that inactivated commercial PCV2 exhibits weak T cell immune memory dominated by Tcm and weak B cell memory. To further evaluate the memory response of the PRV-Cap-induced T cells, we detected dynamic changes in cytokines in mice booster immunized with PRV-DX or PCV2-ZJ/c at 28 days post-immunization. PRV booster immunity only led to the upregulation of PRV-specific IFN-γ$^+$IL-2$^+$CD4$^+$ T cells and IFN-γ$^+$TNF-α$^+$CD8$^+$ T cells, while PCV2 booster immunization only enhanced IFN-γ$^+$TNF-α$^+$CD8$^+$ T cells but did not significantly stimulate CD4 T cell reactivation. This difference most likely corresponds to weak CD4 T memory cells mediated by PCV2 inactivated vaccine.

In summary, we constructed a recombinant PRV carrying the *Cap* gene of PCV2. The recombinant virus stably assembled the Cap-gE fused protein on the surface of its viral envelope and induced both humoral and cellular immunity against PRV and PCV2, which indicates that the PRV-Cap is a promising candidate vaccine against both PRV and PCV2.

Data availability statement

The raw data supporting the conclusions of this article will be made available by the authors, without undue reservation.

Ethics statement

The animal study was approved by Experimental animal welfare Ethics Review Committee, Zhejiang University. The study was conducted in accordance with the local legislation and institutional requirements.

Author contributions

CL: Conceptualization, Data curation, Formal analysis, Investigation, Methodology, Validation, Writing – original draft, Writing – review & editing. HML: Data curation, Investigation, Methodology, Validation, Writing – review & editing. WC: Project administration, Supervision, Validation, Resources, Writing – review & editing. HL: Investigation, Writing – review & editing. JM: Investigation, Writing – review & editing. PP: Investigation, Writing – review & editing. YY: Writing – review & editing. WD: Writing – review & editing. YJ: Writing – review & editing. SP: Writing – review & editing. SS: Methodology, Writing – review & editing. JG: Writing – review & editing. JZ: Funding acquisition, Methodology, Supervision, Writing – original draft, Writing – review & editing.

Funding

The author(s) declare financial support was received for the research, authorship, and/or publication of this article. This work was supported by National Key R&D program of China (2022YFD1800804), the Key Research and Development project of Zhejiang Province (2020C02011) and the Fundamental Research Funds for the Central Universities (2022-KYY-517101-0005).

Acknowledgments

We thank Weina Shang at the Core Facilities of Zhejiang University Life Sciences Institute for support with EM and confocal imaging. We thank Wei Yin and Chun Guo from the Core Facilities of Zhejiang University School of Medicine for their technical support.

Conflict of interest

The authors declare that the research was conducted in the absence of any commercial or financial relationships that could be construed as a potential conflict of interest.

Publisher's note

All claims expressed in this article are solely those of the authors and do not necessarily represent those of their affiliated organizations, or those of the publisher, the editors and the reviewers. Any product that may be evaluated in this article, or claim that may be made by its manufacturer, is not guaranteed or endorsed by the publisher.

Supplementary material

The Supplementary Material for this article can be found online at: https://www.frontiersin.org/articles/10.3389/fimmu.2024.1438371/full#supplementary-material

References

1. Liu A, Xue T, Zhao X, Zou J, Pu H, Hu X, et al. Pseudorabies virus associations in wild animals: review of potential reservoirs for cross-host transmission. *Viruses*. (2022) 14(10):2254. doi: 10.3390/v14102254

2. Tu L, Zhao J, Chen Q, Zhang S, Liang L, Tang X, et al. Assessing the risk of commercial vaccines against pseudorabies virus in cats. *Front Vet Sci*. (2022) 9:857834. doi: 10.3389/fvets.2022.857834

3. Zheng HH, Fu PF, Chen HY, Wang ZY. Pseudorabies virus: from pathogenesis to prevention strategies. *Viruses*. (2022) 14(8):1638. doi: 10.3390/v14081638

4. Liu X, Broberg E, Watanabe D, Dudek T, Deluca N, Knipe DM. Genetic engineering of a modified herpes simplex virus 1 vaccine vector. *Vaccine*. (2009) 27:2760–7. doi: 10.1016/j.vaccine.2009.03.003

5. Laval K, Enquist LW. The neuropathic itch caused by pseudorabies virus. *Pathogens*. (2020) 9(4):254. doi: 10.3390/pathogens9040254

6. Liu Q, Kuang Y, Li Y, Guo H, Zhou C, Guo S, et al. The epidemiology and variation in pseudorabies virus: A continuing challenge to pigs and humans. *Viruses*. (2022) 14(7):1463. doi: 10.3390/v14071463

7. Wong G, Lu J, Zhang W, Gao GF. Pseudorabies virus: a neglected zoonotic pathogen in humans? *Emerg Microbes Infect*. (2019) 8:150–4. doi: 10.1080/22221751.2018.1563459

8. Wang D, Tao X, Fei M, Chen J, Guo W, Li P, et al. Human encephalitis caused by pseudorabies virus infection: a case report. *J Neurovirol*. (2020) 26:442–8. doi: 10.1007/s13365-019-00822-2

9. Freuling CM, Muller TF, Mettenleiter TC. Vaccines against pseudorabies virus (PrV). *Vet Microbiol*. (2017) 206:3–9. doi: 10.1016/j.vetmic.2016.11.019

10. Cong X, Lei JL, Xia SL, Wang YM, Li Y, Li S, et al. Pathogenicity and immunogenicity of a gE/gI/TK gene-deleted pseudorabies virus variant in susceptible animals. *Vet Microbiol*. (2016) 182:170–7. doi: 10.1016/j.vetmic.2015.11.022

11. Mettenleiter TC, Klupp BG, Weiland F, Visser N. Characterization of a quadruple glycoprotein-deleted pseudorabies virus mutant for use as a biologically safe live virus vaccine. *J Gen Virol.* (1994) 75:1723–33. doi: 10.1099/0022-1317-75-7-1723

12. Zhang C, Guo L, Jia X, Wang T, Wang J, Sun Z, et al. Construction of a triple gene-deleted Chinese Pseudorabies virus variant and its efficacy study as a vaccine candidate on suckling piglets. *Vaccine.* (2015) 33:2432–7. doi: 10.1016/j.vaccine.2015.03.094

13. Hu RM, Zhou Q, Song WB, Sun EC, Zhang MM, He QG, et al. Novel pseudorabies virus variant with defects in TK, gE and gI protects growing pigs against lethal challenge. *Vaccine.* (2015) 33:5733–40. doi: 10.1016/j.vaccine.2015.09.066

14. Dong B, Zarlenga DS, Ren X. An overview of live attenuated recombinant pseudorabies viruses for use as novel vaccines. *J Immunol Res.* (2014) 2014:824630. doi: 10.1155/2014/824630

15. Jiang Y, Fang L, Xiao S, Zhang H, Pan Y, Luo R, et al. Immunogenicity and protective efficacy of recombinant pseudorabies virus expressing the two major membrane-associated proteins of porcine reproductive and respiratory syndrome virus. *Vaccine.* (2007) 25:547–60. doi: 10.1016/j.vaccine.2006.07.032

16. Tong W, Zheng H, Li GX, Gao F, Shan TL, Zhou YJ, et al. Recombinant pseudorabies virus expressing E2 of classical swine fever virus (CSFV) protects against both virulent pseudorabies virus and CSFV. *Antiviral Res.* (2020) 173:104652. doi: 10.1016/j.antiviral.2019.104652

17. Qian P, Li XM, Jin ML, Peng GQ, Chen HC. An approach to a FMD vaccine based on genetic engineered attenuated pseudorabies virus: one experiment using VP1 gene alone generates an antibody responds on FMD and pseudorabies in swine. *Vaccine.* (2004) 22:2129–36. doi: 10.1016/j.vaccine.2003.12.005

18. Chen Y, Guo W, Xu Z, Yan Q, Luo Y, Shi Q, et al. A novel recombinant pseudorabies virus expressing parvovirus VP2 gene: Immunogenicity and protective efficacy in swine. *Virol J.* (2011) 8:307. doi: 10.1186/1743-422X-8-307

19. Tao Q, Zhu L, Xu L, Yang Y, Zhang Y, Liu Z, et al. The construction and immunogenicity analyses of a recombinant pseudorabies virus with senecavirus A VP2 protein coexpression. *Microbiol Spectr.* (2023) 11:e0522922. doi: 10.1128/spectrum.05229-22

20. Primorac D, Vrdoljak K, Brlek P, Pavelic E, Molnar V, Matisic V, et al. Adaptive immune responses and immunity to SARS-CoV-2. *Front Immunol.* (2022) 13:848582. doi: 10.3389/fimmu.2022.848582

21. Eisen HN. Affinity enhancement of antibodies: how low-affinity antibodies produced early in immune responses are followed by high-affinity antibodies later and in memory B-cell responses. *Cancer Immunol Res.* (2014) 2:381–92. doi: 10.1158/2326-6066.CIR-14-0029

22. Victora GD, Nussenzweig MC. Germinal centers. *Annu Rev Immunol.* (2022) 40:413–42. doi: 10.1146/annurev-immunol-120419-022408

23. Cumpelik A, Heja D, Hu Y, Varano G, Ordikhani F, Roberto MP, et al. Dynamic regulation of B cell complement signaling is integral to germinal center responses. *Nat Immunol.* (2021) 22:757–68. doi: 10.1038/s41590-021-00926-0

24. Cyster JG, Allen CDC. B cell responses: cell interaction dynamics and decisions. *Cell.* (2019) 177:524–40. doi: 10.1016/j.cell.2019.03.016

25. Crotty S. Follicular helper CD4 T cells (TFH). *Annu Rev Immunol.* (2011) 29:621–63. doi: 10.1146/annurev-immunol-031210-101400

26. Liu X, Nurieva RI, Dong C. Transcriptional regulation of follicular T-helper (Tfh) cells. *Immunol Rev.* (2013) 252:139–45. doi: 10.1111/imr.12040

27. Nurieva RI, Chung Y, Martinez GJ, Yang XO, Tanaka S, Matskevitch TD, et al. Bcl6 mediates the development of T follicular helper cells. *Science.* (2009) 325:1001–5. doi: 10.1126/science.1176676

28. Elgueta R, Benson MJ, de Vries VC, Wasiuk A, Guo Y, Noelle RJ. Molecular mechanism and function of CD40/CD40L engagement in the immune system. *Immunol Rev.* (2009) 229:152–72. doi: 10.1111/j.1600-065X.2009.00782.x

29. Asao H. Interleukin-21 in viral infections. *Int J Mol Sci.* (2021) 22(17):9521. doi: 10.3390/ijms22179521

30. Shlomchik MJ, Luo W, Weisel F. Linking signaling and selection in the germinal center. *Immunol Rev.* (2019) 288:49–63. doi: 10.1111/imr.12744

31. Yang W, Liu X, Wang X. The immune system of chicken and its response to H9N2 avian influenza virus. *Vet Q.* (2023) 43:1–14. doi: 10.1080/01652176.2023.2228360

32. Vatzia E, Feest K, McNee A, Manjegowda T, Carr BV, Paudyal B, et al. Immunization with matrix-, nucleoprotein and neuraminidase protects against H3N2 influenza challenge in pH1N1 pre-exposed pigs. *NPJ Vaccines.* (2023) 8:19. doi: 10.1038/s41541-023-00620-2

33. Alhabbab RY, Algaissi A, Mahmoud AB, Alkayyal AA, Al-Amri S, Alfaleh MA, et al. Middle east respiratory syndrome coronavirus infection elicits long-lasting specific antibody, T and B cell immune responses in recovered individuals. *Clin Infect Dis.* (2023) 76:e308–18. doi: 10.1093/cid/ciac456

34. Seo YB, Ko A, Shin D, Kim J, Suh YS, Na J, et al. Potentiating the cross-reactive IFN-gamma T cell and polyfunctional T cell responses by heterologous GX-19N DNA booster in mice primed with either a COVID-19 mRNA vaccine or inactivated vaccine. *Int J Mol Sci.* (2023) 24(11):9753. doi: 10.3390/ijms24119753

35. Shen CF, Fu YC, Ho TS, Chen PL, Lee NY, Tsai BY, et al. Pre-existing humoral immunity and CD4(+) T cell response correlate with cross-reactivity against SARS-CoV-2 Omicron subvariants after heterologous prime-boost vaccination. *Clin Immunol.* (2023) 251:109342. doi: 10.1016/j.clim.2023.109342

36. Zhang Z, Mateus J, Coelho CH, Dan JM, Moderbacher CR, Galvez RI, et al. Humoral and cellular immune memory to four COVID-19 vaccines. *Cell.* (2022) 185:2434–2451 e17. doi: 10.1016/j.cell.2022.05.022

37. Wen C, Zhou Y, Zhou Y, Wang Y, Dong Z, Gu S, et al. HBV Core-specific CD4 (+) T cells correlate with sustained viral control upon off-treatment in HBeAg-positive chronic hepatitis B patients. *Antiviral Res.* (2023) 213:105585. doi: 10.1016/j.antiviral.2023.105585

38. Perdomo-Celis F, Taborda NA, Rugeles MT. CD8(+) T-cell response to HIV infection in the era of antiretroviral therapy. *Front Immunol.* (2019) 10:1896. doi: 10.3389/fimmu.2019.01896

39. Seder RA, Darrah PA, Roederer M. T-cell quality in memory and protection: implications for vaccine design. *Nat Rev Immunol.* (2008) 8:247–58. doi: 10.1038/nri2274

40. Ashby KM, Hogquist KA. A guide to thymic selection of T cells. *Nat Rev Immunol.* (2023) 24(2):103–17. doi: 10.1038/s41577-023-00911-8

41. Yamane H, Paul WE. Early signaling events that underlie fate decisions of naive CD4(+) T cells toward distinct T-helper cell subsets. *Immunol Rev.* (2013) 252:12–23. doi: 10.1111/imr.12032

42. Gupta M, Greer P, Mahanty S, Shieh WJ, Zaki SR, Ahmed R, et al. CD8-mediated protection against Ebola virus infection is perforin dependent. *J Immunol.* (2005) 174:4198–202. doi: 10.4049/jimmunol.174.7.4198

43. Cannons JL, Lu KT, Schwartzberg PL. T follicular helper cell diversity and plasticity. *Trends Immunol.* (2013) 34:200–7. doi: 10.1016/j.it.2013.01.001

44. Saravia J, Chapman NM, Chi H. Helper T cell differentiation. *Cell Mol Immunol.* (2019) 16:634–43. doi: 10.1038/s41423-019-0220-6

45. Darrah PA, Patel DT, De Luca PM, Lindsay RW, Davey DF, Flynn BJ, et al. Multifunctional TH1 cells define a correlate of vaccine-mediated protection against Leishmania major. *Nat Med.* (2007) 13:843–50. doi: 10.1038/nm1592

46. Wang H, Gan M, Wu B, Zeng R, Wang Z, Xu J, et al. Humoral and cellular immunity of two-dose inactivated COVID-19 vaccination in Chinese children: A prospective cohort study. *J Med Virol.* (2023) 95:e28380. doi: 10.1002/jmv.28380

47. Westerhof LM, McGuire K, MacLellan L, Flynn A, Gray JI, Thomas M, et al. Multifunctional cytokine production reveals functional superiority of memory CD4 T cells. *Eur J Immunol.* (2019) 49:2019–29. doi: 10.1002/eji.201848026

48. Kannanganat S, Ibegbu C, Chennareddi L, Robinson HL, Amara RR. Multiple-cytokine-producing antiviral CD4 T cells are functionally superior to single-cytokine-producing cells. *J Virol.* (2007) 81:8468–76. doi: 10.1128/JVI.00228-07

49. Harty JT, Tvinnereim AR, White DW. CD8+ T cell effector mechanisms in resistance to infection. *Annu Rev Immunol.* (2000) 18:275–308. doi: 10.1146/annurev.immunol.18.1.275

50. Voskoboinik I, Whisstock JC, Trapani JA. Perforin and granzymes: function, dysfunction and human pathology. *Nat Rev Immunol.* (2015) 15:388–400. doi: 10.1038/nri3839

51. Zhou JY, Chen QX, Ye JX, Shen HG, Chen TF, Shang SB. Serological investigation and genomic characterization of PCV2 isolates from different geographic regions of Zhejiang province in China. *Vet Res Commun.* (2006) 30:205–20. doi: 10.1007/s11259-006-3203-x

52. Jin YL, Yin D, Xing G, Huang YM, Fan CM, Fan CF, et al. The inactivated gE/TK gene-deleted vaccine against pseudorabies virus type II confers effective protection in mice and pigs. *Front Microbiol.* (2022) 13:943707. doi: 10.3389/fmicb.2022.943707

53. Zhou JY, Shang SB, Gong H, Chen QX, Wu JX, Shen HG, et al. *In vitro* expression, monoclonal antibody and bioactivity for capsid protein of porcine circovirus type II without nuclear localization signal. *J Biotechnol.* (2005) 118:201–11. doi: 10.1016/j.jbiotec.2005.02.017

54. Shang S-B, Jin Y-L, Jiang X-T, Zhou J-Y, Zhang X, Xing G, et al. Fine mapping of antigenic epitopes on capsid proteins of porcine circovirus, and antigenic phenotype of porcine circovirus Type 2. *Mol Immunol.* (2009) 46:327–34. doi: 10.1016/j.molimm.2008.10.028

55. Gulati NM, Torian U, Gallagher JR, Harris AK. Immunoelectron microscopy of viral antigens. *Curr Protoc Microbiol.* (2019) 53:e86. doi: 10.1002/cpmc.86

56. Wu K, Hu W, Zhou B, Li B, Li X, Yan Q, et al. Immunogenicity and immunoprotection of PCV2 virus-like particles incorporating dominant T and B cell antigenic epitopes paired with CD154 molecules in piglets and mice. *Int J Mol Sci.* (2022) 23(22):14126. doi: 10.3390/ijms232214126

57. Ren J, Tan S, Chen X, Yao J, Niu Z, Wang Y, et al. Genomic characterization and gE/gI-deleted strain construction of novel PRV variants isolated in central China. *Viruses.* (2023) 15(6):1237. doi: 10.3390/v15061237

58. Liang H, Xia J, Zhang R, Yang B, Wu J, Gui G, et al. ELISPOT assay of interferon-gamma secretion for evaluating human cytomegalovirus reactivation risk in allo-HSCT recipients. *J Med Virol.* (2021) 93:6301–8. doi: 10.1002/jmv.27120

59. Bianchi AT, Moonen-Leusen HW, van Milligen FJ, Savelkoul HF, Zwart RJ, Kimman TG. A mouse model to study immunity against pseudorabies virus infection: significance of CD4+ and CD8+ cells in protective immunity. *Vaccine.* (1998) 16:1550–8. doi: 10.1016/S0264-410X(98)00044-9

60. Cibrian D, Sanchez-Madrid F. CD69: from activation marker to metabolic gatekeeper. *Eur J Immunol*. (2017) 47:946–53. doi: 10.1002/eji.201646837

61. Lopez-Cabrera M, Santis AG, Fernandez-Ruiz E, Blacher R, Esch F, Sanchez-Mateos P, et al. Molecular cloning, expression, and chromosomal localization of the human earliest lymphocyte activation antigen AIM/CD69, a new member of the C-type animal lectin superfamily of signal-transmitting receptors. *J Exp Med*. (1993) 178:537–47. doi: 10.1084/jem.178.2.537

62. Sugata K, Yasunaga J, Kinosada H, Mitobe Y, Furuta R, Mahgoub M, et al. HTLV-1 viral factor HBZ induces CCR4 to promote T-cell migration and proliferation. *Cancer Res*. (2016) 76:5068–79. doi: 10.1158/0008-5472.CAN-16-0361

63. Talker SC, Stadler M, Koinig HC, Mair KH, Rodriguez-Gomez IM, Graage R, et al. Influenza A virus infection in pigs attracts multifunctional and cross-reactive T cells to the lung. *J Virol*. (2016) 90:9364–82. doi: 10.1128/JVI.01211-16

64. Wilkinson TM, Li CK, Chui CS, Huang AK, Perkins M, Liebner JC, et al. Preexisting influenza-specific CD4+ T cells correlate with disease protection against influenza challenge in humans. *Nat Med*. (2012) 18:274–80. doi: 10.1038/nm.2612

65. Gupta S, Agrawal S, Sandoval A, Su H, Tran M, Demirdag Y. SARS-CoV-2-specific and functional cytotoxic CD8 cells in primary antibody deficiency: natural infection and response to vaccine. *J Clin Immunol*. (2022) 42:914–22. doi: 10.1007/s10875-022-01256-y

66. Scorpio DG, Choi KS, Dumler JS. Anaplasma phagocytophilum-related defects in CD8, NKT, and NK lymphocyte cytotoxicity. *Front Immunol*. (2018) 9:710. doi: 10.3389/fimmu.2018.00710

67. Liu X, Li H, Li S, Yuan J, Pang Y. Maintenance and recall of memory T cell populations against tuberculosis: Implications for vaccine design. *Front Immunol*. (2023) 14:1100741. doi: 10.3389/fimmu.2023.1100741

68. Sallusto F, Geginat J, Lanzavecchia A. Central memory and effector memory T cell subsets: function, generation, and maintenance. *Annu Rev Immunol*. (2004) 22:745–63. doi: 10.1146/annurev.immunol.22.012703.104702

69. Tarke A, Coelho CH, Zhang Z, Dan JM, Yu ED, Methot N, et al. SARS-CoV-2 vaccination induces immunological T cell memory able to cross-recognize variants from Alpha to Omicron. *Cell*. (2022) 185:847–859.e11. doi: 10.1016/j.cell.2022.01.015

70. Kamel M, El-Sayed A. Utilization of herpesviridae as recombinant viral vectors in vaccine development against animal pathogens. *Virus Res*. (2019) 270:197648. doi: 10.1016/j.virusres.2019.197648

71. Wang S, Liang B, Wang W, Li L, Feng N, Zhao Y, et al. Viral vectored vaccines: design, development, preventive and therapeutic applications in human diseases. *Signal Transduct Target Ther*. (2023) 8:149. doi: 10.1038/s41392-023-01408-5

72. Chang CC, Algaissi A, Lai CC, Chang CK, Lin JS, Wang YS, et al. Subunit vaccines with a saponin-based adjuvant boost humoral and cellular immunity to MERS coronavirus. *Vaccine*. (2023) 41:3337–46. doi: 10.1016/j.vaccine.2023.04.006

73. Kim T-S, Shin E-C. The activation of bystander CD8+ T cells and their roles in viral infection. *Exp Mol Med*. (2019) 51:1–9. doi: 10.1038/s12276-019-0316-1

74. Ansel KM, Lee DU, Rao A. An epigenetic view of helper T cell differentiation. *Nat Immunol*. (2003) 4:616–23. doi: 10.1038/ni0703-616

75. Zhang X, Ali M, Pantuck MA, Yang X, Lin CR, Bahmed K, et al. CD8 T cell response and its released cytokine IFN-gamma are necessary for lung alveolar epithelial repair during bacterial pneumonia. *Front Immunol*. (2023) 14:1268078. doi: 10.3389/fimmu.2023.1268078

76. Koinig HC, Talker SC, Stadler M, Ladinig A, Graage R, Ritzmann M, et al. PCV2 vaccination induces IFN-gamma/TNF-alpha co-producing T cells with a potential role in protection. *Vet Res*. (2015) 46:20. doi: 10.1186/s13567-015-0157-4

77. Wang YP, Liu D, Guo LJ, Tang QH, Wei YW, Wu HL, et al. Enhanced protective immune response to PCV2 subunit vaccine by co-administration of recombinant porcine IFN-gamma in mice. *Vaccine*. (2013) 31:833–8. doi: 10.1016/j.vaccine.2012.11.062

Frontiers in Immunology

TYPE Original Research
PUBLISHED 02 August 2024
DOI 10.3389/fimmu.2024.1332444

Check for updates

OPEN ACCESS

EDITED BY
Xusheng Qiu,
Chinese Academy of Agricultural Sciences,
China

REVIEWED BY
Jianzhu Liu,
Shandong Agricultural University, China
Yao-Wei Huang,
Zhejiang University, China

*CORRESPONDENCE
Jue Liu
liujue@263.net

RECEIVED 02 November 2023
ACCEPTED 22 July 2024
PUBLISHED 02 August 2024

CITATION
Cui Y, Li S, Xu W, Xie J, Wang D, Hou L, Zhou J, Feng X and Liu J (2024) Intra- and inter-host origin, evolution dynamics and spatial-temporal transmission characteristics of circoviruses. *Front. Immunol.* 15:1332444. doi: 10.3389/fimmu.2024.1332444

COPYRIGHT
© 2024 Cui, Li, Xu, Xie, Wang, Hou, Zhou, Feng and Liu. This is an open-access article distributed under the terms of the Creative Commons Attribution License (CC BY). The use, distribution or reproduction in other forums is permitted, provided the original author(s) and the copyright owner(s) are credited and that the original publication in this journal is cited, in accordance with accepted academic practice. No use, distribution or reproduction is permitted which does not comply with these terms.

Intra- and inter-host origin, evolution dynamics and spatial-temporal transmission characteristics of circoviruses

Yongqiu Cui[1,2], Siting Li[1,2], Weiying Xu[1,2], Jiali Xie[1,2], Dedong Wang[1,2], Lei Hou[1,2], Jianwei Zhou[1,2], Xufei Feng[1,2] and Jue Liu[1,2]*

[1]College of Veterinary Medicine, Yangzhou University, Yangzhou, China, [2]Jiangsu Co-Innovation Center for Prevention and Control of Important Animal Infectious Diseases and Zoonoses, Yangzhou University, Yangzhou, China

Introduction: Since their identification in 1974, circoviruses have caused clinicopathological diseases in various animal species, including humans. However, their origin, transmission, and genetic evolution remain poorly understood.

Methods: In this study, the genome sequences of circovirus were obtained from GenBank, and the Bayesian stochastic search variable selection algorithm was employed to analyzed the evolution and origin of circovirus.

Results: Here, the evolutionary origin, mode of transmission, and genetic recombination of the circovirus were determined based on the available circovirus genome sequences. The origin of circoviruses can be traced back to fish circovirus, which might derive from fish genome, and human contributes to transmission of fish circovirus to other species. Furthermore, mosquitos, ticks, bats, and/or rodents might play a role as intermediate hosts in circovirus intra- and inter-species transmission. Two major lineages (A and B) of circoviruses are identified, and frequent recombination events accelerate their variation and spread. The time to the most recent common ancestor of circoviruses can be traced back to around A.D. 600 and has been evolving at a rate of 10^{-4} substitutions site^{-1} year^{-1} for a long time.

Discussion: These comprehensive findings shed light on the evolutionary origin, population dynamics, transmission model, and genetic recombination of the circovirus providing valuable insights for the development of prevention and control strategies against circovirus infections.

KEYWORDS

circovirus, evolutionary origin, phylodynamics, transmission, genetic recombination

1 Introduction

Circoviruses, belonging to the family Circoviridae (https://ictv.global/taxonomy), are non-enveloped, icosahedral symmetrical viruses with a circular single-stranded DNA genome of approximately 1.7–2.2 kb in length. They possess the smallest known viral genome and exhibit conserved genome organization. The replicase (Rep) protein, encoded by open reading frame 1 (ORF1), is involved in virus replication, while the major immunogenic capsid (Cap) protein encoded by ORF2 and is associated with host-protection (1).

Since the identification of the first circovirus, various pathological conditions in domestic animals have been linked to circoviral infections. Human circovirus (HCirV) can cause liver damage, evidenced by high HCirV genome copy numbers in the liver and blood with hepatic cytolysis (2). Canine circovirus is associated with diarrhea in dogs and facilitates parvovirus replication (3). Duck circovirus (DuCV) infects ducks of all ages and was initially reported in Mallard ducks, causing feathering disorders, growth retardation, and thinning, which are similar to the clinical symptoms of beak atrophy and dwarfism syndrome (4, 5). Goose circovirus (GCV) induces severe diarrhea, feather disorders, and short clubbed feathers (6, 7). Pigeon circovirus (PiCV) was first identified in a female racing pigeon that exhibited anorexia, lethargy, emaciation, and pectoral muscle atrophy (8, 9). Porcine circovirus type 1 (PCV1) was first described in 1974 and has been detected in both wild and farmed pigs, furthermore, antibodies against PCV1 were detected in human, mice, and cattle (10–12). Porcine circovirus type 2 (PCV2), identified in 1997, emerged as the predominant pathogen responsible for postweaning multisystemic wasting syndrome (PMWS), causing severe immunosuppression, and even death (13, 14). Furthermore, PCV2 has been detected in various other species such as rodents, insects, canines, ruminants, and shellfish, suggesting a wide host range (15–20). In 2015, a novel circovirus, named porcine circovirus type 3 (PCV3), was identified in aborted fetuses of sows. PCV3 is associated with porcine dermatitis and nephropathy syndrome (PDNS) and reproductive disorder symptoms, including lung collapse or failure, lobular pneumonia, multifocal hemorrhage, enlarged lymph nodes, hyperplasia, liver hyperemia and necrosis, kidney swelling or scattered hemorrhagic foci, and spleen enlargement, and it was detected in other species including cattle (21–24). In 2019, another newly identified circovirus, named porcine circovirus type 4 (PCV4) was found in pigs with clinical disease including PDNS in China (25). PCV4-positive pigs also show some other clinical signs, including fever, respiratory signs, and enteric signs; however, its pathogenicity has not been experimentally validated (26). Recent studies demonstrated that circoviruses isolated in birds can be traced back to fish circoviruses, and the ancestor of roundworm viruses is also a circovirus (27, 28).

Circoviruses have been discovered in multiple species and are responsible for substantial economic losses and poses a threat to public health. However, the origin, transmission, and evolutionary pathway (theory of evolution) of circovirus remains poorly understood. To address these gaps, this study aims to investigate the origin, population dynamics, and spreading patterns of circoviruses by analyzing a comprehensive dataset with an extended collection time window. By shedding light on circovirus origin, transmission models, and evolutionary patterns, this study will provide a valuable theoretical basis for the prevention and control of circovirus infections.

2 Materials and methods

2.1 Dataset preparation

The complete genome sequences of the circovirus genus were collected, including 4,195 strains of mammalian circovirus (bat, bear, chimpanzee, canine, human, civet, elk, mink, pig, rodent, and whale), 777 strains of avian circovirus (bird, duck, goose, swan, and penguin), 5 strains of mosquito circovirus, 8 strains of fish circovirus (babel, whale, and Silurus glanis), and 8 strains of tick circovirus genomes were downloaded from GenBank (Supplementary Table S1) (accessed on April 31, 2023) and annotated with collection year, location, and host when available. Multiple sequence alignments were performed using the fast Fourier transform algorithm, and manual checks and corrections were applied, and poorly aligned sequences and those sequences with premature stop codons or frame-shift mutation were excluded from the analysis (29). The substitution model was selected based on the BIC scores using ModelFinder (30). Molecular clock, population dynamics model, and discrete trait substitution model were determined using the Bayes factor (31). The relaxed lognormal molecular clock (32), skyline population model (33), and symmetric migration rate were selected (34).

2.2 Recombination detection

For recombination detection, we used SplitsTree software which conducts phi tests for recombination (35) and RDP 4.0 Beta software with eight methods for recombination detection (36). Phi detection was initially conducted, and if the *p*-value was less than 0.05, seven methods (RDP, CHIMAERA, 3SEQ, MAXCHI, GENECONV, BootScan, and SiScan) in the RDP software were used for further detection (37–43). After removing recombinant strains and recombination regions, the final datasets were obtained for further analysis.

2.3 Population parameter estimation/phylodynamic analysis

For the final datasets, a tip-dated serial coalescent analysis was performed using the Bayesian approach implemented in the BEAST V.1.10.4 package. This analysis estimated the time to the evolutionary rate, and population dynamics over time (34, 44). The preliminary analysis of the data is found that a uncorrected relaxed clock (lognormal) was the most appropriate molecular clock for next analysis. Distribution of rate heterogeneity model for most species of circovirus was set as GTR+F+I+G4, except PCV1 (HKY+F+G4), PCV2 (GTR+F+G4), and PCV4 (K2P+G4). In order to better evaluate the evolutionary relationship between different species of circovirus, we chose the Yule model to carry out the following calculation. And Bayesian Skyline (Coalescent) model was used to measure the dynamics of the circovirus population. Three independent runs were operated with a chain length of 1×10^{10} generations, and sampling them every 100,000 generations. Convergence was assessed using the Tracer software (v1.6; http://tree.bio.ed.ac.uk/software/tracer/) after a burn-in of 10%. Parameters with an effective sample size greater than 200 were accepted. Parameter estimation was summarized as median and 95% HPD. The Bayesian stochastic search variable selection (BSSVS) was employed to identify the most parsimonious description of the spreading process based on the BF test (34). The temporal signal of data set was assessed using the Bayesian evaluation of temporal signal (BETS). BETS compares the fit of the original heterochronous model (M_{het}) (with original sampling times) and the corresponding isochronous model (M_{iso}) (with a fixed rate). Marginal likelihood estimation (MLE) was performed using generalized stepping-stone sampling. Parameters were estimated using the MCMC approach implemented in BEAST (version 1.10.4). The BEAGLE library (version 3.1.0) was used to perform massive parallelization on computing architectures. A (log) Bayes factor $\log(P(Y|M_{het}))$ 2 $\log(P(Y|M_{iso}))$ of at least 5 indicates a strong temporal signal in the data set. To evaluate prediction results, a BF cut-off was applied: BF > 10 indicated very strong support, BF > 5 indicated strong support, and BF > 3 indicated positive support for circovirus spread. The final phylogenetic tree was constructed using FigTree (v.1.4.4) (http://tree.bio.ed.ac.uk/software/figtree/) and iTOL (https://itol.embl.de/) software.

2.4 Phylogenetic analysis

The complete data set without recombinant sequences was assessed for strength of phylogenetic signal by applying the likelihood mapping approach implemented in IQ-TREE (version 1.6.12) and MEGA 7.0 (81, 82). The nucleotide substitution saturation was estimated using Xia's test as implemented in the DAMBE (version 7.3.5). Xia's test compares an observed index of saturation substitution (I_{ss}) to a critical index of substitution saturation ($I_{ss.c}$). If Iss is significantly less than Iss.c, data will be considered as little saturation in transition and transversion, and data are good for phylogenetic analysis. The final phylogenetic tree was visualized using FigTree software (v.1.4.4) (https://github.com/rambaut/figtree/releases) and iTOL (https://itol.embl.de).

3 Results

3.1 Global distribution of animal circovirus

Circoviruses have been discovered in multiple species, with a total of 4,997 strains complete genome sequences from 19 species (mammals, aquatic animal, avians, and insects) analyzed in this study. Using the Bayesian algorithm and Maximum likelihood algorithm, it was observed that circoviruses are classified into two lineages, Lineage A and B (Figure 1, Supplementary Figure S1, Supporting Information). Lineage A includes avian circoviruses (duck-, goose-, swan-, bird-, penguin-, and pigeon-derived animal circoviruses) and circoviruses identified in aquatic animals. Lineage B consists of porcine, canine, fox, mink, mouse, and bat circoviruses, it also contains aquatic mammalian and beaked whale circoviruses. Notably, all currently known HCirV and PCV2 belong to either the Lineage A or B genera, and bat circovirus, as major intermediate hosts, are distributed in both lineages.

Meanwhile, it can be clearly observed that DuCV, GCV, PiCV, and PCVs were found to be the most widespread types of circoviruses (Figure 1). DuCV has a global distribution, first identified in Germany in 2003 and spreading to other regions in Europe (Poland), Americas (America and Brazil), and Asia (China, South Korea, and Vietnam) (Figure 2). GCV, identified in Germany in 1999, has regional distribution in Europe (Poland, Hungary, and the United Kingdom) and Asia (China) (Figure 2). PiCV, first recognized in Canada and Australia, has been found on all continents except Antarctica due to the long-distance flight capability of pigeons (Figure 2). PCV1, first identified in 1974, has spread in countries with developed pig farming, including the United States, Australia, Brazil, Canada, China, France, Hungary, and the United Kingdom (Figure 2). PCV2 was first identified in 1997 in western Canada and has been reported in dozens of countries worldwide (Argentina, Austria, Australia, the United States, Belgium, Brazil, Canada, China, Cuba, Croatia, Colombia, Denmark, France, Germany, Hungary, India, Italy, Japan, Poland, Portugal, Saint Kitts and Nevis, Singapore, Serbia, Spain, Sweden, Slovakia, South Korea, South Africa, Switzerland, Thailand, Malaysia, Netherlands, the United Kingdom, Vietnam, and Uruguay), indicating a global distribution (Figure 2). PCV3 was first identified in 2015 in the United States, though it has only been discovered for eight years, positive cases have been found and reported in the Americas (Brazil, Mexico, and, Colombia), Asia (China, South Korea, Japan, Thailand, Russia, Malaysia, and India), and Europe (Italy, Spain, Denmark, Germany, Hungary, Sweden, and Serbia), indicating a global distribution (Figure 2). PCV4, first identified in China in 2015, has a current low prevalence in China and South Korea (Figure 2).

3.2 Genetic recombination in animal circovirus

Recombination events have a negative impact on computer algorithms used in traceability research. In order to avoid adverse effects of the recombinant strain on the subsequent analysis, the recombinant strain needs to be excluded from the analysis. We employed RDP4 software to analyze recombination using full genomes. Several circovirus genome sequences exhibited recombination (Figure 3).

PiCV diverged into seven distinct clades (A–G) based on the *Cap* gene. Clade A emerged through recombination between

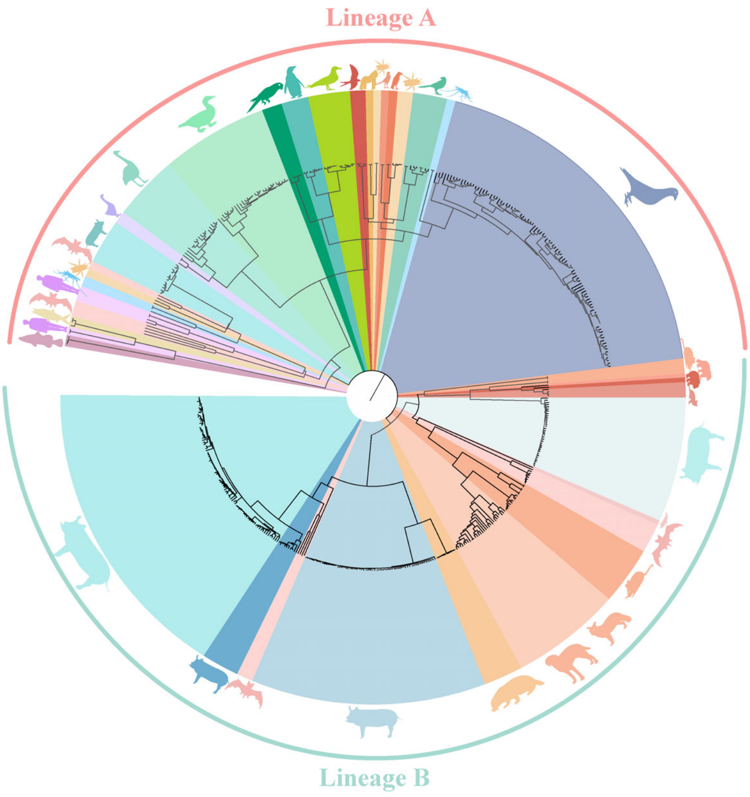

FIGURE 1
Phylogenetic tree of known circoviruses. The full-length genome sequences of circoviruses publicly available in GenBank was analyzed using BEAST 1.6, with 1,000,000,000 replicates. Different colors represent different circovirus lineages, Lineage A (Red) and B (Green). Different species are also marked with corresponding animal images.

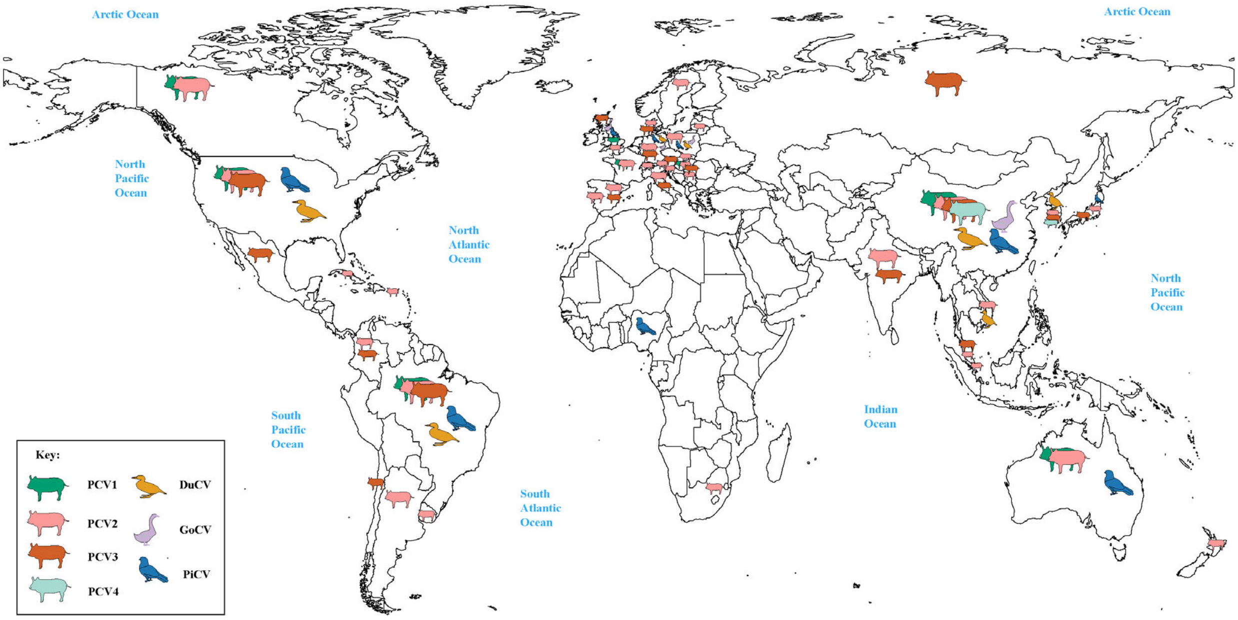

FIGURE 2
Global distribution of circoviruses. The colors green, pink, brown, light green, yellow, purple, and blue correspond to porcine circovirus 1 (PCV1), porcine circovirus 2 (PCV2), porcine circovirus 3 (PCV3), porcine circovirus 4 (PCV4), duck circovirus (DuCV), goose circovirus (GoCV), and pigeon circovirus (PiCV), respectively.

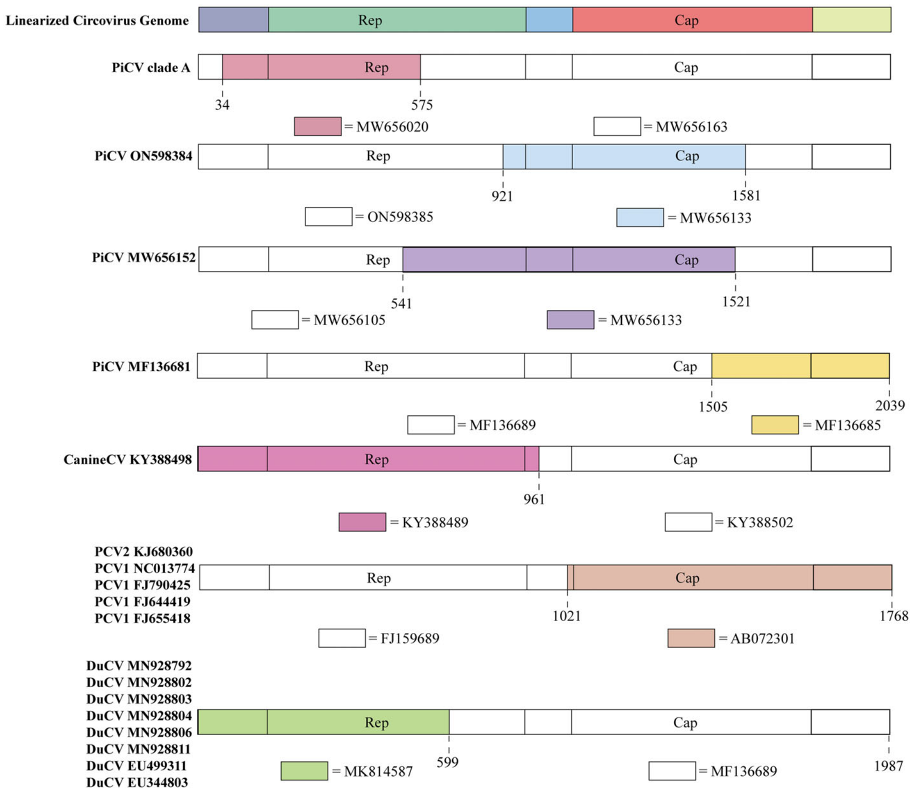

FIGURE 3
Recombination events in circoviruses. The colored regions in each animal circovirus represents genetic recombination at the genome sites with zoonotic circoviruses. Specific nucleotide locations where recombination occurred are shown as broken lines.

MW656163 (Pigeon, Poland, 2020) and MW656020 (Pigeon, Poland, 2020) at a breakpoint of 34–575 bp in the *Rep* gene (Figure 3). The recombination region of PiCV was present in both the *Rep* and *Cap* genes, and the PiCV strain MF136681 (Pigeon, Australia, 2023) emerged by recombination between MF136689 (Pigeon, Australia, 2023) and MF136685 (Pigeon, Australia, 2023) at the breakpoint of 1505–2039 (Figure 3). Furthermore, we detected recombination in both the *Cap* and *Rep* genes of two PiCV strains (ON598384 (Pigeon, China, 2021) and MW656152 (Pigeon, Poland, 2020)), with breakpoints at 921–1581 and 541–1521, respectively (Figure 3). PiCV exhibits the highest recombination frequency among circoviruses, suggesting constant mutations within pigeons, which accelerates the spread of the circovirus and poses a risk of cross-species transmission.

Recombination events were observed in different PCVs. PCV2 strains KJ680360 (Pig, China, 2012) and PCV1 (NC013774 (Pig, Canada, 2008), FJ790425 (Pig, Canada, 2009), FJ644419 (Pig, Canada, 2008), and FJ655418 (Pig, Canada, 2008)) originated through recombination between FJ159689 (Pig, China, 2007) and AB072301 (Pig, Japan, 2001), sharing the same breakpoints of 1021–1768 (Figure 3). The current design strategy for PCV2 chimeric vaccines involves replacing the *Cap* gene of PCV1 with the *Cap* gene of PCV2, which is consistent with the recombination region identified in the recombinant strains. Therefore, these recombinant PCV strains may be vaccine viruses, indicating that the recombination events between PCV1 and PCV2 might be caused by human intervention (45).

DuCV also exhibits potential for genetic recombination. An example is the recombination between the MF136689 (Duck, Australia, 2013) and MK814587 (Duck, China, 2019) strains at breakpoints 599–1987. DuCV recombinant strains include MN928792 (Duck, China, 2018), MN928802 (Duck, China, 2018), MN928803 (Duck, China, 2018), MN928804 (Duck, China, 2018), MN928806 (Duck, China, 2018), MN928811 (Duck, China, 2018), EU499311 (Duck, China, 2008), and EU344803 (Duck, China, 2007) (Figure 3).

Recombination was also detected in canine circoviruses, where recombination occurred between KY388489 (Dog, China, 2014) and KY388502 (Dog, China, 2015), both from China, with a breakpoint at the *Cap* gene (961–2063) (Figure 3).

In addition, some recombination events were also found (MK604479 (Pig, China, 2016), KY437725 (Pig, China, 2015), KP824722 (Pig, China, 2015), KJ679446 (Pig, Germany, 2012), MH465488 (Pig, China, 2018), KX929004 (Pig, China, 2015), and KC415249 (Pig, China, 2008)), but these recombination events were only detected in one parent, lacking the data of another parent. More in-depth analysis needs to be carried out after the increase of virus strain information in the future.

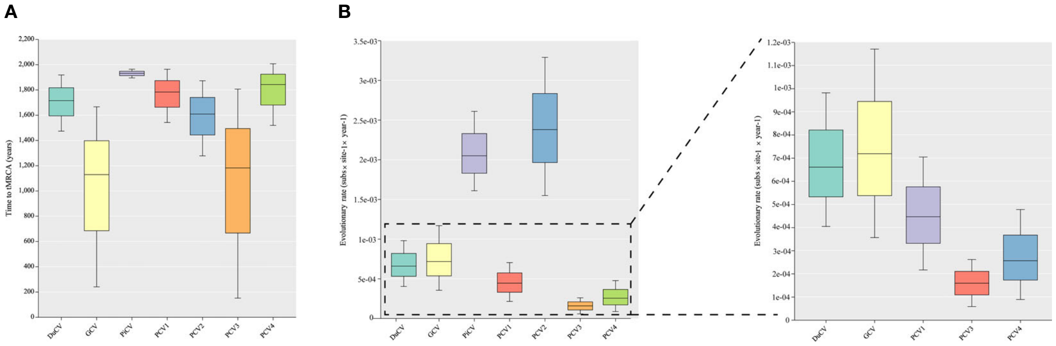

FIGURE 4
Estimation of the time to the most recent common ancestor (tMRCA) and substitution rates in duck circovirus (DuCV), goose circovirus (GCV), pigeon circovirus (PiCV), porcine circovirus 1 (PCV1), porcine circovirus 2 (PCV2), porcine circovirus 3 (PCV3), and porcine circovirus 4 (PCV4) complete genomes using BEAST (v.1.10.4). **(A)** Time to tMRCA for different species of circoviruses. **(B)** Substitution rates of different species of circoviruses.

3.3 Evolutionary and phylogenetic dynamic of animal circovirus

Bayesian analysis of complete circovirus genomes provided insights into the time of the most recent common ancestor (tMRCA), evolutionary rate, and trends in effective population size.

Although DuCV was first reported in 2003, its tMRCA can be traced back to 1715.42, with a nucleotide substitution rate of 6.6 × 10^{-4} substitutions site^{-1} year^{-1} (Figure 4). Based on the skyline plot, DuCV experienced population expansion until 2010. Afterward, the effective population size experienced a sharp change, including rapid decrease and increase. After several changes in population dynamics, DuCV's population size remained the same as it was before 2010 (Figure 5A).

The tMRCA and nucleotide substitution rates of the GCV complete genome were 1129.71 and 7.18 × 10^{-4} substitutions site^{-1} year^{-1}, respectively (Figure 4). Before 2010, it maintained a stable population range, but after 2010, it experienced a rapid decline. The population size began to increase in the past two years and has already exceeded the 2010 level (Figure 5B).

PiCV has a fast nucleotide substitution rate of 2.05 × 10^{-3} substitutions site^{-1} year^{-1} and based on the analysis of the tMRCA results (1931.16), it can be found that PiCV is a relatively new circovirus (Figure 4). Based on the skyline plot analysis results, it can be observed that PiCV displays similar population trends to the two other types of avian circoviruses (DuCV and GCV). The population size showed a decreased trend between 2010 and 2020; after 2020, the population began to increase (Figure 5C). Due to the rapid evolution and high recombination rates of PiCV, it is more susceptible to cross-species transmission, necessitating further in-depth studies.

Until now, PCV1 has spread in countries with developed pig farming, showing a nucleotide rate of 4.46 × 10^{-4} substitutions site^{-1} year^{-1}. The tMRCA of PCV1 can be traced back to 1783.291 (Figures 3, 4). Phylogenetic dynamic analysis indicates that the effective population size exhibited a stable growth trend before

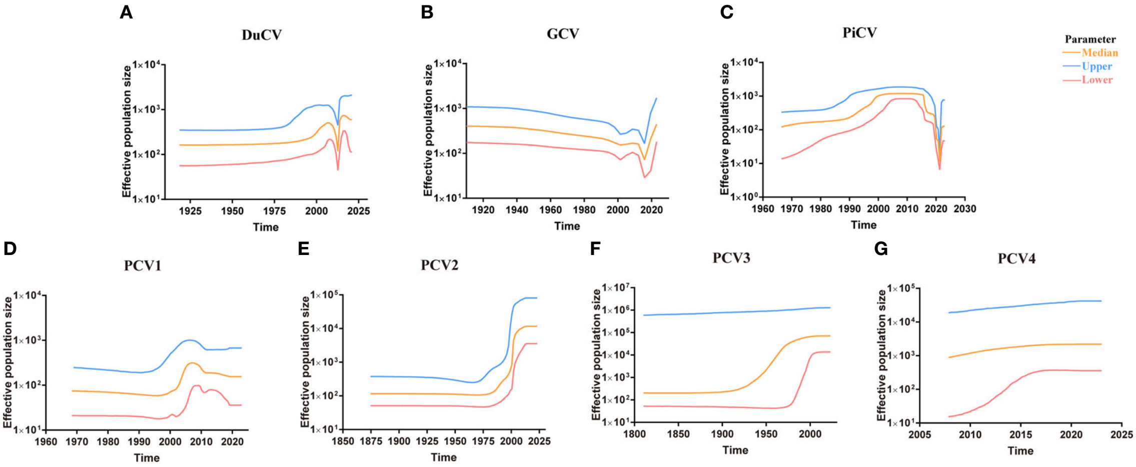

FIGURE 5
Circovirus population dynamics reconstructed based on complete genome datasets of **(A)** duck circovirus (DuCV), **(B)** goose circovirus (GCV), **(C)** pigeon circovirus (PiCV), **(D)** porcine circovirus 1 (PCV1), **(E)** porcine circovirus 2 (PCV2), **(F)** porcine circovirus 3 (PCV3), and **(G)** porcine circovirus 4 (PCV4). Different colors indicate upper, median, and lower boundaries, representing changes in the effective population size of different circovirus species.

2010, then a decreased trend between 2010 and 2020, after 2020 the population size remained relatively small (Figure 5D).

The tMRCA of PCV2's complete genome was 1608.99, with a high nucleotide substitution rate of 2.38×10^{-3} substitutions site^{-1} year^{-1} accelerating the emergence of new subgroups, which may cause greater harm (Figure 4). Based on the skyline plot results, it can be clearly observed that the population of PCV2 showed rapid expansion before 2018, but plateaued after 2018; the effective population size is maintained a relatively high level (Figure 5E).

The PCV3 can be traced back to 1182.203 with a nucleotide substitution rate of 1.59×10^{-4} substitutions site^{-1} year^{-1}, which proves that PCV3 is a very ancient virus, that predates PCV2 (Figure 4). Phylogenetic dynamic analysis indicated that the effective population size of PCV3 expanded rapidly from 1980 to 2018. After 2018, the population expansion plateaued, which is consistent with PCV2, and the effective population size level was similar to PCV2 (Figure 5F).

As a newly discovered circular virus, PCV4 is poorly understood. To better understand the phylogenetics of PCV4, ML and NJ methods were used to reconstruct the phylogenies of PCV4 complete genome. Two independent clades were observed in two different tress which displayed similar structures (Supplementary Figures S2A, B, Supporting Information). The PCV4a clade, included the earliest strain found in China in 2012 (MW600958), could be separated into two individual subclades with stable topological structure, termed PCV4a-1 and PCV4a-2 (Supplementary Figures S2A, B, Supporting Information). The tMRCA of PCV4 was 1842.916, and the mean substitution rate of the complete genome sequences of all PCV4 strains was 2.56×10^{-4} substitutions rate^{-1} year^{-1}, which was lower than PCV2 (2.38×10^{-3}), but close to PCV3 (1.59×10^{-4}) and PCV1 (4.46×10^{-4}) (Figure 4). The skyline plot result was consistent with the results of PCV2 and 3, it had an expansion trend before 2018 but plateaued after 2018 (Figure 5G).

3.4 The origin and transmission model of the emergent animal circovirus worldwide

To better understand the origin and transmission process of the circovirus, we analyzed complete circovirus genome sequence information using bioinformatic methods. The origin of circoviruses can be traced back to aquatic animals and humans (Figure 6, Supplementary Figure S3, Supporting Information). Mice and bats, as well as mosquitoes and ticks, serve as intermediate hosts for circovirus transmission in mammals and poultry, respectively (Figure 6, Supplementary Figure S3, Supporting Information). The origin of circoviruses in fish has provoked our interest, and previous research has found that fish plays an important role in endogenous retroviruses (ERV) evolution, promoting the transmission of ERV to amniotic animals (46). To discover potential target viral elements in fish genome, the tBLASTn algorithm was used to screen the potential target elements. (47). *Rep* gene of FCirV was found to possess a 98%-100% similarity to chromosome 1 in fish genome, and *Cap* gene of FCirV also showed high similarity (82%-98%) to chromosome 7 and X in fish genome. During the long-term evolution of aquatic animals, frequent recombination and fragment exchange between genomes led to the emergence of the first type of FCirV, which could be traced back to around A.D. 600 (Supplementary Figure S3, Supporting Information). Meanwhile, we also used tBLASTn algorithm to compare HCirV and FCirV, and found that they share a *Cap* and *Rep* gene similarity of 97% and 96%, respectively. This was confirmed by phylogenetic analysis as evidenced by fish and humans locating on the same clade (at the tree root) of the multispecies circovirus phylogenetic tree. These results indicate that the origin of circovirus is closely related to the aquatic animal genome, and that there is a close relationship between FCirV and HCirV.

Based on the analysis results, the ancestors of all PCVs are fish circovirus, but the species and numbers of intermediate host of the

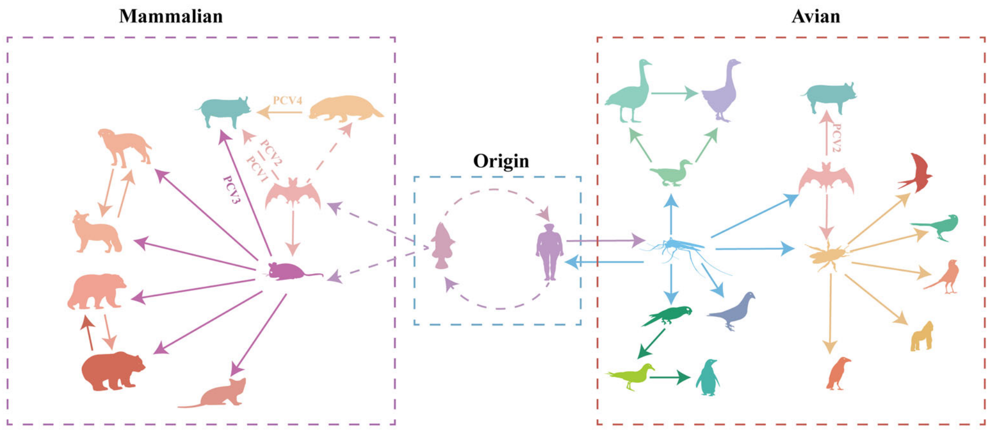

FIGURE 6
Transmission of circoviruses between different species. Each color represents different species of circovirus. Solid arrows represent direct transmission between the two species in question, while broken arrows represent suspected transmission.

different PCVs are different (Figure 6, Supplementary Figure S3, Supporting Information). PCV1 and PCV2 are directly transmitted by bats to pig herds (Figure 6, Supplementary Figure S3, Supporting Information). PCV3 was first transmitted by bats to rodents, and then transmitted to pigs (Figure 6, Supplementary Figure S3, Supporting Information). PCV4 was transmitted by bat circovirus to minks, and then to pig herds (Figure 6, Supplementary Figure S3, Supporting Information). PCV1 is currently considered to be non-pathogenic, while PCV2 and PCV3 pose a huge threat to the pig population, the virulence of PCV4 is still unclear; Whether the transmission of circoviruses through different intermediate hosts causes the differences in virulence needs to be verified.

4 Discussion

Since the first circovirus was identified in 1974 (10), most studies have focused on the genetic characterization of individual isolates and on clinical and epidemiological investigations. Here, we provide important insights into the origin, phylogenetic dynamic, and evolution process of animal circoviruses.

Previous studies suggest that the circovirus comes from the bat circovirus (5, 48). However, this study presents a more accurate determination of the origin of animal circovirus and proposes an evolutionary pathway (theory of evolution) that explains the emergence of animal circovirus worldwide. The findings indicate that the earliest origin of circovirus can be traced back to fish circovirus, there is a high homology between the FCirV and fish genome. The high similarity between the FCirV genome sequence and the fish genome can be explained by the mechanisms of circovirus replication. Animal genomes contain ssDNA virus-like sequences that resemble the circovirus rolling circle replication initiation protein gene, and eukaryotic genomes also have ssDNA *Rep* gene homologs (49, 50). The Rep protein can recognize DNA sequences in the host genome similar to the circovirus genome's origin of replication (hairpin loop) and can ligate RNA during the rolling circle replication of the ssDNA virus genome (50, 51). Another hypothesis suggests that the ssDNA virus can capture RNA virus sequence from host genome (52). An mRNA from a coinfecting virus is used as a primer for first or second-strand replication. The recombination of RNA-DNA would have to be followed by reverse transcription, presumably by a cellular reverse transcriptase (53). Recombination of the *Rep* and *Cap* gene is expected to occur. *Cap* gene can incorporate different nucleic acid genomes, and are critical for determining host range and evading host defenses (54, 55). Many ssDNA virus genomes contain unique *Cap* genes, which may originate from uncharacterized RNA viruses (56, 57). In general, positive-stranded ssDNA and ssRNA viruses were much more prone to having chimeric genes than negative-stranded ssRNA virus (51), the frequency of this deep recombination is unknown and is a critical area for future research.

Where there is water, there is life. All life activities originate from water. This shows that humans have a close relationship with water and aquatic animals. This close contact with aquatic animal provides an opportunity for the transmission of viruses across species. Consumption of meat and exposure to animal or human feces increase the chances of circovirus transmission (58). Wetlands are transitional zones between land and water, and as such have an ecosystem with special structures and functions (59). They serve as the cradle of abundant biodiversity in nature and play a vital role in the survival and development of human society. Wetlands are home to a diverse array of organisms, including aquatic animals such as fish, arthropods like mosquitoes, mammals including humans, bats, and mice, various plant species, amphibians, and a wide range of microorganisms. This intricate web of life facilitates significant interactions and contact between different animal species. The spread of circoviruses among poultry is facilitated by Lineage A circoviruses, which include avian and mosquito circoviruses. Mosquitos serve as an important intermediate host for various viruses, and have antiviral mechanisms to limit viral replication (60, 61). In addition, relevant studies have proved that complementing incomplete virus particles can co-infect mosquitos and result in the reconstitution of infectious virus that are able to disseminate into the mosquito salivary glands, suggesting that incomplete particles may play a significant role within hosts and between hosts transmission, reminiscent of the infection cycle of multipartite viruses (62). Mosquitoes play an essential role in the transmission of circoviruses. During the process of circovirus spread, mosquitoes serve as intermediate hosts. Once infection with a circovirus, mosquitoes undergo constant variations due to their antiviral characteristics, ultimately giving rise to a circovirus capable of infecting birds and waterfowl. Through bird and waterfowl migration, circoviruses can rapidly disseminate to different regions and adapt to infect ticks and bats during transmission. Ticks, being highly specialized hematophagous ectoparasites, primarily parasitize avian and mammalian species (63, 64). They also serve as important vectors for transmitting various pathogens, including viruses. Birds also have the potential to transport tick-borne pathogens by carrying infected ticks. This mode of transmission facilitates the circovirus's rapid spread, surpassing barriers such as fences, mountains, glaciers, deserts, and oceans, which are typically challenging for ticks to traverse (65). Overall, mosquitoes and ticks play important intermediate host roles in avian circovirus transmission.

To understand the factors that accelerate circoviral transmission in mammals, we examine mice and bats as intermediate hosts. In recent decades, several highly impactful zoonotic disease outbreaks, such as Hendra virus, Ebolavirus, Nipah virus, and coronaviruses, have been linked to bat-borne viruses (66–68). As the most abundant, diverse, and geographically dispersed vertebrates, bats have been found to carry 61 viruses (69). Being ancient mammals, bats are hypothesized to possess highly conserved cellular receptors that facilitate the transmission of viruses to other mammals (66). Bats spread viruses to other animals through their feeding habits. Due to the aerodynamics of flight, bats cannot consume large amounts of food. They rely on fruits for energy, but their feeding process involves chewing the fruits to extract sugars and high-energy components, followed by spitting out partially digested fruit remnants that drop to the ground. Subsequently, other animals, including rodents, can ingest these fruit remnants and become infected by viral particles present in the bat saliva, which constitutes the transmission rout of

SARS-CoV (70). Rodents carry more pathogens than bats and can act as a reservoir for emerging viruses (69, 71). As mentioned earlier, mice and mink could ingest fruits remnants dropped by bats, leading to their infection with bat circovirus. As a result, mice and minks bring the virus closer to human settlements, potentially leading to the infection of economic or companion animals like pigs and dogs. Thus, bats and rodents serve as reservoirs to expedite the transmission of circoviruses to mammals. These findings demonstrate that various circoviruses from mammals and avians are currently circulating in the wild, providing ample opportunities for circoviruses to undergo evolution and genetic recombination, potentially resulting in recombinant circoviruses that may be more virulent to animals, including humans. As a mammalian circovirus, PCV2 was expected to belong to Lineage B. Notably, our analysis revealed that PCV2 exists in both Lineages. Further investigation into the origin of PCV2 unveiled that both lineages derived from bat circoviruses. The difference lies in the fact that the bat circovirus in Lineage A may have directly originated from human or fish circoviruses, while the bat circovirus in Lineage B was derived from a circovirus carried by mosquitoes. This suggests a close relationship between the origin of PCV2 and bat circovirus, with a less intimate connection to earlier ancestors. While PCV1 shares similarities with PCV2, which directly descends from bat circovirus, PCV3 and PCV4 are not directly generated from pig herds infected by bat circovirus but involve other intermediate hosts. The transmission of PCV3 is closely associated with rodents, whereas PCV4 is linked to minks. These findings indicate that pigs serve as the final hosts, but different intermediate hosts give rise to distinct types of PCVs, which may also contribute to changes in their virulence.

Phylodynamic analysis revealed the earliest origin time, evolution rate, and population dynamics of various circovirus. Circoviruses have been found to be ancient viruses, dating back to approximately A.D. 600, and they undergo mutation rates approximately 10^{-4} substitutions site^{-1} year^{-1} over the long term. The population dynamics of avian circoviruses are influenced by their hosts prior to 2010, the population of avian circovirus remained stable. However, after 2010, there was a rapid decline, likely due to the outbreak of highly pathogenic avian influenza during that period (Figures 5A–C) (72–75). Most countries implemented culling measures as a means of prevention and control, which resulted in the loss of viable hosts for avian circoviruses and a subsequent decline in their population. Although highly pathogenic avian influenza remains a global threat, most countries have switched control measures from culling to vaccination, resulting in growing avian populations. This indicates that the host population size of avian circovirus infection is constantly expanding, however, there is currently no vaccine against avian circovirus, which has led to the expansion of the avian circovirus population in recent years (Figures 5A–C). This phenomenon also occurred in PCV species. Before 2018, the population of PCV showed an increasing trend, but after 2018, it plateaued (Figures 5D–G). This may be related to the outbreak of African swine fever virus (ASFV) in 2018 (76). To prevent the spread of ASFV, countries and regions around the world have implemented measures such as culling and improving biosafety prevention and control. These measures not only curtailed the spread of ASFV but also hindered the transmission of other pig-related viruses.

Recombination occurs during the long-term evolution of viruses. While the recombination frequency of DNA viruses is generally lower than that of RNA viruses, circoviruses have been found to undergo recombination, with avian circovirus displaying a higher recombination compared to mammalian circovirus (Figure 3). During viral replication, a set of sub-genomic RNAs is generated, increasing the homologous recombination rate among closely related genes from different lineages of circoviruses or other hosts/viruses through template switching (77). The circulation of viruses among multiple host species contributes to an increased rate of recombination. However, the precise mechanism of genetic recombination in circoviruses remains unclear, including the “breakpoints” in the viral genome where recombination occurs and the specific crossing points of recombinant genes between different viral strains or genotypes. These recombinant strains have different breakpoints (77). In addition, human factors may lead to the emergence of recombinant strains. PCV2 chimeric vaccines, which was based on the genomic backbone of the non-pathogenic PCV1 with the ORF2 *Cap* gene replaced by that of PCV2, have inadvertently led to the detection of chimeric PCV1–2 viruses in the field due to incomplete vaccine inactivation (45, 78). Recombination increases virus genetic diversity and may contribute to the adaptation of a new host (79, 80), and circoviruses have a high frequency of homologous DNA recombination possibly mediated by random template switching during genome replication thought to be mediated by a ‘copy choice’ mechanism of the virus itself.

Overall, this study provides an updated understanding of the origin, population dynamics, and evolution of circoviruses, highlighting the generation of novel viruses with high genetic diversity, and unpredictable changes in virulence and cross-species transmission during avian, aquatic anima, tardigrade, parasite, and mammalian infections. With multiple species of circoviruses circulating in the wild amongst different animal species that may constantly interact with one another, it is a matter of when not if, the next recombinant circovirus will emerge and cause another outbreak in mammals including the human population. These findings contribute to the assessment of circoviruses relevance for swine, avian, and fish industries and may aid in the planning of effective control strategies. It must be emphasized that this work just scratched the surface of circovirus history, biology, future, and constant re-evaluation of the present results will be mandatory to update and improve our understanding of this emergent viral behavior.

Data availability statement

The datasets presented in this study can be found in online repositories. The names of the repository/repositories and accession number(s) can be found in the article/Supplementary Material.

Author contributions

YC: Conceptualization, Formal Analysis, Investigation, Methodology, Software, Writing – original draft, Writing – review & editing. SL: Conceptualization, Investigation, Writing – original draft. WX: Formal Analysis, Methodology, Writing – original draft. JX: Data curation, Software, Writing – original draft. DW: Data curation, Writing – original draft. LH: Supervision, Writing – original draft. JZ: Formal Analysis, Writing – original draft. XF: Data curation, Writing – original draft. JL: Funding acquisition, Supervision, Writing – review & editing.

Funding

The author(s) declare financial support was received for the research, authorship, and/or publication of this article. This work was supported by the National Key Research and Development Program of China (2022YFD1800300), Introduction Program of High-Level Innovation and Entrepreneurship Talents in Jiangsu Province, 111 Project D18007, and Priority Academic Program Development of Jiangsu Higher Education Institutions (PAPD).

Acknowledgments

We thank Dr. Liang Wang at the Institute of Microbiology, Chinese Academy of Sciences for his valuable guidance and insightful opinions throughout this research. This study was conducted using the High-Performance Computing Cluster of the College of Veterinary Medicine, Yangzhou University.

Conflict of interest

The authors declare that the research was conducted in the absence of any commercial or financial relationships that could be construed as a potential conflict of interest.

The author(s) declared that they were an editorial board member of Frontiers, at the time of submission. This had no impact on the peer review process and the final decision.

Publisher's note

All claims expressed in this article are solely those of the authors and do not necessarily represent those of their affiliated organizations, or those of the publisher, the editors and the reviewers. Any product that may be evaluated in this article, or claim that may be made by its manufacturer, is not guaranteed or endorsed by the publisher.

Supplementary material

The Supplementary Material for this article can be found online at: https://www.frontiersin.org/articles/10.3389/fimmu.2024.1332444/full#supplementary-material

SUPPLEMENTARY FIGURE 1

ML Phylogenetic tree of known circoviruses. The full-length genome sequences of circoviruses publicly available in GenBank was analyzed using IQ-TREE software. Different species were marked by different colors.

SUPPLEMENTARY FIGURE 2

Phylogenetic analysis of the available complete genome of porcine circovirus 4 (PCV4). **(A)** Maximum likelihood tree reconstructed using IQ-Tree. **(B)** Neighbor-joining tree reconstructed using MEGA 6.0. Different clades are represented by different colors as indicated in the figures.

SUPPLEMENTARY FIGURE 3

Relationships among different species of circoviruses based on complete genome analysis. The MCC tree was reconstructed using BEAST (v.1.10.4), displaying ancestor hosts indicated by posterior probability. Different colored lines represent different species.

SUPPLEMENTARY TABLE 1

The strain information of the circovirus used in this study.

References

1. Hamel AL, Lin LL, Nayar GP. Nucleotide sequence of porcine circovirus associated with postweaning multisystemic wasting syndrome in pigs. *J Virol.* (1998) 72:5262–7. doi: 10.1128/JVI.72.6.5262-5267

2. Perot P, Fourgeaud J, Rouzaud C, Regnault B, Da Rocha N, Fontaine H, et al. Circovirus hepatitis infection in heart-lung transplant patient, France. *Emerg Infect Dis.* (2023) 29:286–93. doi: 10.3201/eid2902.221468

3. Hao X, Li Y, Chen H, Chen B, Liu R, Wu Y, et al. Canine circovirus suppresses the type I interferon response and protein expression but promotes CPV-2 replication. *Int J Mol Sci.* (2022) 23:6382. doi: 10.3390/ijms23126382

4. Hattermann K, Schmitt C, Soike D, Mankertz A. Cloning and sequencing of duck circovirus (DuCV). *Arch Virol.* (2003) 148:2471–80. doi: 10.1007/s00705-003-0181-y

5. Li P, Li J, Zhang R, Chen J, Wang W, Lan J, et al. Duck "beak atrophy and dwarfism syndrome" disease complex: Interplay of novel goose parvovirus-related virus and duck circovirus? *Transbound Emerg Dis.* (2018a) 65:345–51. doi: 10.1111/tbed.2018.65.issue-2

6. Soike D, Kohler B, Albrecht K. A circovirus-like infection in geese related to a runting syndrome. *Avian Pathol.* (1999) 28:199–202. doi: 10.1080/03079459994939

7. Niu X, Wang H, Wei L, Zhang M, Yang J, Chen H, et al. Epidemiological investigation of H9 avian influenza virus, Newcastle disease virus, Tembusu virus, goose parvovirus and goose circovirus infection of geese in China. *Transbound Emerg Dis.* (2018) 65:e304–16. doi: 10.1111/tbed.2018.65.issue-2

8. Woods LW, Latimer KS, Barr BC, Niagro FD, Campagnoli RP, Nordhausen RW, et al. Circovirus-like infection in a pigeon. *J Vet Diagn Invest.* (1993) 5:609–12. doi: 10.1177/104063879300500417

9. Phan TG, Vo NP, Boros A, Pankovics P, Reuter G, Li OT, et al. The viruses of wild pigeon droppings. *PLoS One.* (2013) 8:e72787. doi: 10.1371/journal.pone.0072787

10. Tischer I, Rasch R, Tochtermann G. Characterization of papovavirus-and picornavirus-like particles in permanent pig kidney cell lines. *Zentralbl Bakteriol Orig A.* (1974) 226:153–67.

11. Tischer I, Bode L, Apodaca J, Timm H, Peters D, Rasch R, et al. Presence of antibodies reacting with porcine circovirus in sera of humans, mice, and cattle. *Arch Virol.* (1995) 140:1427–39. doi: 10.1007/BF01322669

12. Opriessnig T, Karuppannan AK, Castro A, Xiao CT. Porcine circoviruses: current status, knowledge gaps and challenges. *Virus Res.* (2020) 286:198044. doi: 10.1016/j.virusres.2020.198044

13. Ellis J, Hassard L, Clark E, Harding J, Allan G, Willson P, et al. Isolation of circovirus from lesions of pigs with postweaning multisystemic wasting syndrome. *Can Vet J.* (1998) 39:44–51.

14. Morozov I, Sirinarumitr T, Sorden SD, Halbur PG, Morgan MK, Yoon KJ, et al. Detection of a novel strain of porcine circovirus in pigs with postweaning multisystemic wasting syndrome. *J Clin Microbiol*. (1998) 36:2535–41. doi: 10.1128/JCM.36.9.2535-2541

15. Blunt R, Mcorist S, Mckillen J, Mcnair I, Jiang T, Mellits K. House fly vector for porcine circovirus 2b on commercial pig farms. *Vet Microbiol*. (2011) 149:452–5. doi: 10.1016/j.vetmic.2010.11.019

16. Cadar D, Csagola A, Lorincz M, Tombacz K, Spinu M, Tuboly T. Detection of natural inter- and intra-genotype recombination events revealed by cap gene analysis and decreasing prevalence of PCV2 in wild boars. *Infect Genet Evol*. (2012) 12:420–7. doi: 10.1016/j.meegid.2012.01.014

17. Pinheiro AL, Bulos LH, Onofre TS, De Paula Gabardo M, De Carvalho OV, Fausto MC, et al. Verification of natural infection of peridomestic rodents by PCV2 on commercial swine farms. *Res Vet Sci*. (2013) 94:764–8. doi: 10.1016/j.rvsc.2012.10.006

18. Halami MY, Muller H, Bottcher J, Vahlenkamp TW. Whole-genome sequences of two strains of porcine circovirus 2 isolated from calves in Germany. *Genome Announc*. (2014) 2:e01150–13. doi: 10.1128/genomeA.01150-13

19. Krog JS, Larsen LE, Schultz AC. Enteric porcine viruses in farmed shellfish in Denmark. *Int J Food Microbiol*. (2014) 186:105–9. doi: 10.1016/j.ijfoodmicro

20. Song T, Hao J, Zhang R, Tang M, Li W, Hui W, et al. First detection and phylogenetic analysis of porcine circovirus type 2 in raccoon dogs. *BMC Vet Res*. (2019) 15:107. doi: 10.1186/s12917-019-1856-2

21. Faccini S, Barbieri I, Gilioli A, Sala G, Gibelli LR, Moreno A, et al. Detection and genetic characterization of porcine circovirus type 3 in Italy. *Transbound Emerg Dis*. (2017) 64:1661–4. doi: 10.1111/tbed.12714

22. Jiang H, Wang D, Wang J, Zhu S, She R, Ren X, et al. Induction of porcine dermatitis and nephropathy syndrome in piglets by infection with porcine circovirus type 3. *J Virol*. (2019) 93:e02045–18. doi: 10.1128/JVI.02045-18

23. Li G, He W, Zhu H, Bi Y, Wang R, Xing G, et al. Origin, genetic diversity, and evolutionary dynamics of novel porcine circovirus 3. *Adv Sci (Weinh)*. (2018b) 5:1800275. doi: 10.1002/advs.201800275

24. Li Y, Ma Zi, Liu M, Cao L, Zhang J, Jiao Q, et al. Porcine circovirus 3 in cattle in Shandong province of China: A retrospective study from 2011 to 2018. *Vet Microbiol*. (2020) 238:108824. doi: 10.1016/j.vetmic.2020.108824

25. Zhang HH, Hu WQ, Li JY, Liu TN, Zhou JY, Opriessnig T, et al. Novel circovirus species identified in farmed pigs designated as porcine circovirus 4, Hunan province, China. *Transbound Emerg Dis*. (2020) 67:1057–61. doi: 10.1111/tbed.13446

26. Wang D, Mai J, Yang Y, Xiao CT, Wang N. Current knowledge on epidemiology and evolution of novel porcine circovirus 4. *Vet Res*. (2022) 53:38. doi: 10.1186/s13567-022-01053-w

27. Rinder M, Baas N, Hagen E, Drasch K, Korbel R. Canary Bornavirus (Orthobornavirus serini) infections are associated with clinical symptoms in common canaries (Serinus canaria dom.). *Viruses*. (2022) 14:2187. doi: 10.3390/v14102187

28. Butkovic A, Kraberger S, Smeele Z, Martin DP, Schmidlin K, Fontenele RS, et al. Evolution of anelloviruses from a circovirus-like ancestor through gradual augmentation of the jelly-roll capsid protein. *Virus Evol*. (2023) 9:vead035. doi: 10.1093/ve/vead035

29. Katoh K, Standley DM. MAFFT multiple sequence alignment software version 7: improvements in performance and usability. *Mol Biol Evol*. (2013) 30:772–80. doi: 10.1093/molbev/mst010

30. Zhang D, Gao F, Jakovlic I, Zou H, Zhang J, Li WX, et al. PhyloSuite: An integrated and scalable desktop platform for streamlined molecular sequence data management and evolutionary phylogenetics studies. *Mol Ecol Resour*. (2020) 20:348–55. doi: 10.1111/1755-0998.13096

31. Baele G, Lemey P, Bedford T, Rambaut A, Suchard MA, Alekseyenko AV. Improving the accuracy of demographic and molecular clock model comparison while accommodating phylogenetic uncertainty. *Mol Biol Evol*. (2012) 29:2157–67. doi: 10.1093/molbev/mss084

32. Drummond AJ, Ho SYW, Phillips MJ, And Rambaut A. Relaxed phylogenetics and dating with confidence. *PLoS Biol*. (2006) 4:699–710. doi: 10.1371/journal.pbio.0040088

33. Drummond AJ, Rambaut A, Shapiro B, And Pybus OG. Bayesian coalescent inference of past population dynamics from molecular sequences. *Mol Biol Evol*. (2005) 22:1185–92. doi: 10.1093/molbev/msi103

34. Lemey P, Rambaut A, Drummond AJ, Suchard MA. Bayesian phylogeography finds its roots. *PLoS Comput Biol*. (2009) 5:e1000520. doi: 10.1371/journal.pcbi.1000520

35. Huson DH. SplitsTree: analyzing and visualizing evolutionary data. *Bioinformatics*. (1998) 14:68–73. doi: 10.1093/bioinformatics/14.1.68

36. Martin DP, Murrell B, Golden M, Khoosal A, Muhire B. RDP4: Detection and analysis of recombination patterns in virus genomes. *Virus Evol*. (2015) 1:vev003. doi: 10.1093/ve/vev003

37. Salminen MO, Carr JK, Burke DS, Mccutchan FE. Identification of breakpoints in intergenotypic recombinants of HIV type 1 by bootscanning. *AIDS Res Hum Retroviruses*. (1995) 11:1423–5. doi: 10.1089/aid.1995.11.1423

38. Padidam M, Sawyer S, Fauquet CM. Possible emergence of new geminiviruses by frequent recombination. *Virology*. (1999) 265:218–25. doi: 10.1006/viro.1999.0056

39. Gibbs MJ, Armstrong JS, Gibbs AJ. Sister-scanning: a Monte Carlo procedure for assessing signals in recombinant sequences. *Bioinformatics*. (2000) 16:573–82. doi: 10.1093/bioinformatics/16.7.573

40. Martin D, Rybicki E. RDP: detection of recombination amongst aligned sequences. *Bioinformatics*. (2000) 16:562–3. doi: 10.1093/bioinformatics/16.6.562

41. Wiuf C, Christensen T, Hein J. A simulation study of the reliability of recombination detection methods. *Mol Biol Evol*. (2001) 18:1929–39. doi: 10.1093/oxfordjournals.molbev.a003733

42. Boni MF, Posada D, Feldman MW. An exact nonparametric method for inferring mosaic structure in sequence triplets. *Genetics*. (2007) 176:1035–47. doi: 10.1534/genetics.106.068874

43. Arenas M, Posada D. The effect of recombination on the reconstruction of ancestral sequences. *Genetics*. (2010) 184:1133–U429. doi: 10.1534/genetics.109.113423

44. Suchard MA, Lemey P, Baele G, Ayres DL, Drummond AJ, Rambaut A. Bayesian phylogenetic and phylodynamic data integration using BEAST 1.10. *Virus Evol*. (2018) 4:vey016. doi: 10.1093/ve/vey016

45. Gagnon CA, Music N, Fontaine G, Tremblay D, Harel J. Emergence of a new type of porcine circovirus in swine (PCV): a type 1 and type 2 PCV recombinant. *Vet Microbiol*. (2010) 144:18–23. doi: 10.1016/j.vetmic.2009.09.072

46. Chen Y, Wang X, Liao ME, Song Y, Zhang YY, CUI J. Evolution and genetic diversity of the retroviral envelope in anamniotes. *J Virol*. (2022) 96:e0207221. doi: 10.1128/jvi.02072-21

47. Johnson M, Zaretskaya I, Raytselis Y, Merezhuk Y, Mcginnis S, Madden TL. NCBI BLAST: a better web interface. *Nucleic Acids Res*. (2008) 36:W5–9. doi: 10.1093/nar/gkn201

48. Cui YQ, Hou L, Pan Y, Feng XF, Zhou JW, Wang DD, et al. Reconstruction of the evolutionary origin, phylodynamics, and phylogeography of the porcine circovirus type 3. *Front Microbiol*. (2022) 13:898212. doi: 10.3389/fmicb.2022.898212

49. Katzourakis A, Gifford RJ. Endogenous viral elements in animal genomes. *PLoS Genet*. (2010) 6:e1001191. doi: 10.1371/journal.pgen.1001191

50. Liu H, Fu Y, Li B, Yu X, Xie J, Cheng J, et al. Widespread horizontal gene transfer from circular single-stranded DNA viruses to eukaryotic genomes. *BMC Evol Biol*. (2011) 11:276. doi: 10.1186/1471-2148-11-276

51. Stedman KM. Deep recombination: RNA and ssDNA virus genes in DNA virus and host genomes. *Annu Rev Virol*. (2015) 2:203–17. doi: 10.1146/annurev-virology-100114-055127

52. Stedman K. Mechanisms for RNA capture by ssDNA viruses: Grand theft RNA. *J Mol Evol*. (2013) 76:359–64. doi: 10.1007/s00239-013-9569-9

53. Prak ET, Kazazian H. H., JR. Mobile elements and the human genome. *Nat Rev Genet*. (2000) 1:134–44. doi: 10.1038/35038572

54. Diemer GS, Stedman KM. A novel virus genome discovered in an extreme environment suggests recombination between unrelated groups of RNA and DNA viruses. *Biol Direct*. (2012) 7:13. doi: 10.1186/1745-6150-7-13

55. Roux S, Enault F, Bronner G, Vaulot D, Forterre P, Krupovic M. Chimeric viruses blur the borders between the major groups of eukaryotic single-stranded DNA viruses. *Nat Commun*. (2013) 4:2700. doi: 10.1038/ncomms3700

56. Rosario K, Duffy S, Breitbart M. A field guide to eukaryotic circular single-stranded DNA viruses: insights gained from metagenomics. *Arch Virol*. (2012) 157:1851–71. doi: 10.1007/s00705-012-1391-y

57. Monjane AL, Martin DP, Lakay F, Muhire BM, Pande D, Varsani A, et al. Extensive recombination-induced disruption of genetic interactions is highly deleterious but can be partially reversed by small numbers of secondary recombination events. *J Virol*. (2014) 88:7843–51. doi: 10.1128/JVI.00709-14

58. Li L, Kapoor A, Slikas B, Bamidele OS, Wang C, Shaukat S, et al. Multiple diverse circoviruses infect farm animals and are commonly found in human and chimpanzee feces. *J Virol*. (2010) 84:1674–82. doi: 10.1128/JVI.02109-09

59. Hu S, Niu Z, Chen Y, Li L, Zhang H. Global wetlands: Potential distribution, wetland loss, and status. *Sci Total Environ*. (2017) 586:319–27. doi: 10.1016/j.scitotenv.2017.02.001

60. Cheng G, Liu Y, Wang PH, Xiao XP. Mosquito defense strategies against viral infection. *Trends Parasitol*. (2016) 32:177–86. doi: 10.1016/j.pt.2015.09.009

61. Novelo M, Hall MD, Pak D, Young PR, Holmes EC, Mcgraw EA. Intra-host growth kinetics of dengue virus in the mosquito Aedes aEgypti. *PLoS Pathog*. (2019) 15:e1008218. doi: 10.1371/journal.ppat.1008218

62. Bermudez-mendez E, Bronsvoort KF, Zwart MP, Van de water S, Cardenas-rey I, Vloet RPM, et al. Incomplete bunyavirus particles can cooperatively support virus infection and spread. *PLoS Biol*. (2022) 20:e3001870. doi: 10.1371/journal.pbio.3001870

63. Shi J, Hu Z, Deng F, Shen S. Tick-borne viruses. *Virol Sin*. (2018) 33:21–43. doi: 10.1007/s12250-018-0019-0

64. Casel MA, Park SJ, Choi YK. Severe fever with thrombocytopenia syndrome virus: emerging novel phlebovirus and their control strategy. *Exp Mol Med*. (2021) 53:713–22. doi: 10.1038/s12276-021-00610-1

65. Hasle G. Transport of ixodid ticks and tick-borne pathogens by migratory birds. *Front Cell Infect Microbiol*. (2013) 3:48. doi: 10.3389/fcimb.2013.00048

66. Calisher CH, Childs JE, Field HE, Holmes KV, Schountz T. Bats: important reservoir hosts of emerging viruses. *Clin Microbiol Rev*. (2006) 19:531–45. doi: 10.1128/CMR.00017-06

67. Wong S, Lau S, Woo P, Yuen KY. Bats as a continuing source of emerging infections in humans. *Rev Med Virol*. (2007) 17:67–91. doi: 10.1002/rmv.520

68. Zhou P, Yang XL, Wang XG, Hu B, Zhang L, Zhang W, et al. Addendum: A pneumonia outbreak associated with a new coronavirus of probable bat origin. *Nature*. (2020) 588:E6. doi: 10.1038/s41586-020-2951-z

69. Luis AD, Hayman DT, O'shea TJ, Cryan PM, Gilbert AT, Pulliam JR, et al. A comparison of bats and rodents as reservoirs of zoonotic viruses: are bats special? *Proc Biol Sci*. (2013) 280:20122753. doi: 10.1098/rspb.2012.2753

70. Dobson AP. Virology. What links bats to emerging infectious diseases? *Science*. (2005) 310:628–9. doi: 10.1126/science.1120872

71. Larsen BB, Gryseels S, Otto HW, Worobey M. Evolution and diversity of bat and rodent paramyxoviruses from North America. *J Virol*. (2022) 96:e0109821. doi: 10.1128/jvi.01098-21

72. Zhou J, Sun W, Wang J, Guo J, Yin W, Wu N, et al. Characterization of the H5N1 highly pathogenic avian influenza virus derived from wild pikas in China. *J Virol*. (2009) 83:8957–64. doi: 10.1128/JVI.00793-09

73. Neumann G, Chen H, Gao GF, Shu Y, Kawaoka Y. H5N1 influenza viruses: outbreaks and biological properties. *Cell Res*. (2010) 20:51–61. doi: 10.1038/cr.2009.124

74. Shi J, Deng G, Kong H, Gu C, Ma S, Yin X, et al. H7N9 virulent mutants detected in chickens in China pose an increased threat to humans. *Cell Res*. (2017) 27:1409–21. doi: 10.1038/cr.2017.129

75. Shi J, Zeng X, Cui P, Yan C, Chen H. Alarming situation of emerging H5 and H7 avian influenza and effective control strategies. *Emerg Microbes Infect*. (2023) 12:2155072. doi: 10.1080/22221751.2022.2155072

76. Zhao D, Liu R, Zhang X, Li F, Wang J, Zhang J, et al. Replication and virulence in pigs of the first African swine fever virus isolated in China. *Emerg Microbes Infect*. (2019) 8:438–47. doi: 10.1080/22221751.2019.1590128

77. Su S, Wong G, Shi WF, Liu J, Lai ACK, Zhou JY, et al. Epidemiology, genetic recombination, and pathogenesis of coronaviruses. *Trends Microbiol*. (2016) 24:490–502. doi: 10.1016/j.tim.2016.03.003

78. Fenaux M, Opriessnig T, Halbur PG, Elvinger F, Meng XJ. A chimeric porcine circovirus (PCV) with the immunogenic capsid gene of the pathogenic PCV type 2 (PCV2) cloned into the genomic backbone of the nonpathogenic PCV1 induces protective immunity against PCV2 infection in pigs. *J Virol*. (2004) 78:6297–303. doi: 10.1128/JVI.78.12.6297-6303

79. Forni D, Cagliani R, Clerici M, Sironi M. Molecular evolution of human coronavirus genomes. *Trends Microbiol*. (2017) 25:35–48. doi: 10.1016/j.tim.2016.09.001

80. Singh D, Yi SV. On the origin and evolution of SARS-CoV-2. *Exp Mol Med*. (2021) 53:537–47. doi: 10.1038/s12276-021-00604-z

81. Kumar S, Stecher G, Tamura K. MEGA7: Molecular evolutionary genetics analysis version 7.0 for bigger datasets. *Mol Biol Evol*. (2016) 33:1870–4. doi: 10.1093/molbev/msw054

82. Nguyen LT, Schmidt HA, Von Haeseler A, Minh BQ. IQ-TREE: a fast and effective stochastic algorithm for estimating maximum-likelihood phylogenies. *Mol Biol Evol*. (2015) 32:268–74. doi: 10.1093/molbev/msu300

frontiers | Frontiers in Immunology

TYPE Original Research
PUBLISHED 13 September 2024
DOI 10.3389/fimmu.2024.1382675

Check for updates

OPEN ACCESS

EDITED BY
Wei Wang,
Wenzhou University, China

REVIEWED BY
Wanglong Zheng,
Yangzhou University, China
Yuqiang Cheng,
Shanghai Jiao Tong University, China

*CORRESPONDENCE
Hong Jia
jiahong@caas.cn
Peng Zhao
zhaopeng@sdau.edu.cn

RECEIVED 06 February 2024
ACCEPTED 26 August 2024
PUBLISHED 13 September 2024

CITATION
Wang Z, He Y, Huang Y, Zhai W, Tao C, Chu Y, Pang Z, Zhu H, Zhao P and Jia H (2024) African swine fever virus MGF360-4L protein attenuates type I interferon response by suppressing the phosphorylation of IRF3. *Front. Immunol.* 15:1382675. doi: 10.3389/fimmu.2024.1382675

COPYRIGHT
© 2024 Wang, He, Huang, Zhai, Tao, Chu, Pang, Zhu, Zhao and Jia. This is an open-access article distributed under the terms of the Creative Commons Attribution License (CC BY). The use, distribution or reproduction in other forums is permitted, provided the original author(s) and the copyright owner(s) are credited and that the original publication in this journal is cited, in accordance with accepted academic practice. No use, distribution or reproduction is permitted which does not comply with these terms.

African swine fever virus MGF360-4L protein attenuates type I interferon response by suppressing the phosphorylation of IRF3

Zhen Wang[1,2], Yuheng He[2], Ying Huang[2], Wenzhu Zhai[2], Chunhao Tao[2], Yuanyuan Chu[2], Zhongbao Pang[2], Hongfei Zhu[2], Peng Zhao[1*] and Hong Jia[2*]

[1]College of Veterinary Medicine, Shandong Agricultural University, Tai'an, Shandong, China, [2]Institute of Animal Sciences, Chinese Academy of Agricultural Sciences, Beijing, China

African swine fever (ASF) is a highly contagious and lethal disease of swine caused by African swine fever virus (ASFV), and the mortality rate caused by virulent stains can approach 100%. Many ASFV viral proteins suppress the interferon production to evade the host's innate immune responses. However, whether ASFV MGF360-4L could inhibit type I interferon (IFN-I) signaling pathway and the underlying molecular mechanisms remain unknown. Our study, indicated that ASFV MGF360-4L could negatively regulates the cGAS-STING mediated IFN-I signaling pathway. Overexpressing ASFV MGF360-4L could inhibit the cGAS/STING signaling pathway by inhibiting the interferon-β promoter activity, which was induced by cGAS/STING, TBK1, and IRF3-5D, and further reduced the transcriptional levels of ISG15, ISG54, ISG56, STAT1, STAT2, and TYK2. Confocal microscopy and immunoprecipitation revealed that MGF360-4L co-localized and interacted with IRF3, and WB revealed that ASFV MGF360-4L suppressed the phosphorylation of IRF3. 4L-F2 (75-162 aa) and 4L-F3 (146-387 aa) were the crucial immunosuppressive domains and sites. Altogether, our study reveals ASFV MGF360-4L inhibited cGAS-STING mediated IFN-I signaling pathways, which provides insights into an evasion strategy of ASFV involving in host's innate immune responses.

KEYWORDS

African swine fever virus, MGF360-4L, type I interferon, suppress, phosphorylation

1 Introduction

African swine fever virus (ASFV) is a DNA arbovirus of swine which is the only member of the genus Asfivirus in the family Asfarviridae (1). The genome consists of a linear double-stranded DNA molecule ranging from 170 to 190 kb, encoding 150 to 200 proteins, including 68 structural proteins and more than 100 nonstructural proteins (2, 3). Numerous studies have shown that Many proteins of ASFV play important roles in viral assembly, replication, virus–host interaction, and immune evasion (4–9). African swine fever (ASF) is a an acute hemorrhagic and highly contagious disease of domestic and wild pigs caused by ASFV, with mortality of rates up to 100%. In the early 1920s, ASF was first reported in Kenya (10), then spread to most sub-Saharan African countries, the Russian Federation, Transcaucasus, some Eastern and Central European countries, Sardinia, and Southeast and East Asia (11, 12). In 2018, ASF was introduced into China, caused substantial economic losses and threatening the global pig industry (13, 14). So it has been listed as a notifiable disease by the World Organization for Animal Health (9, 15, 16), formerly known as the Office International des Epizooties. To date, no safe and effective commercial vaccines are available for ASF. Thus, the prevention and control of ASF mainly depend on strict biosecurity measures, which have economic burden. So, it is urgently and necessarily to develop a safe and effective ASF vaccine.

As the first line of defense against invading pathogens, innate immune responses rapidly detect pathogens and initiate a series of measures to kill them. Type I interferon (IFN) is produced upon recognition of pathogen-associated molecular patterns through host pattern recognition receptors (17). Cells have various strategies to combat pathogenic invasion. When DNA viruses infect the host cell, cyclic GMP-AMP synthase (cGAS) recognizes and binds to viral genomic DNA, subsequently catalyzing the synthesis of the second messenger molecule cGAMP. The dimerized stimulator of the interferon gene (STING) binds to cGAMP, causing a conformational change (18, 19). STING recruits TANK-binding kinase (TBK1) and traffics from the endoplasmic reticulum to a perinuclear endosomal compartment, leading to the activation of IFN regulatory factor 3 (IRF3) and resulting in IFN-β production (20). As ASFV is a double-stranded DNA virus, it can be sensed by cGAS (21). However, ASFV has evolved multiple strategies to inhibit the production of IFN-I by negatively regulating the antiviral cGAS-STING signaling pathway; numerous studies have demonstrated this. For example, the ASFV MGF360-14L protein was found to promote the degradation of IRF3 through TRIM21, thus negatively regulating IFN-I signaling (22). Cui et al. proved that the ASFV M1249L protein antagonizes IFN-I production by suppressing the phosphorylation of TBK1 and degrading IRF3 (23). Proteins such as E120R (24, 25), DP96R (26), and MGF505-11R (27) also inhibit IFN-β production by negatively regulating the cGAS/STING signaling pathway. Multigene family 360 (MGF360) and MGF530/505 of ASFV are involved in regulating IFN-I. The members of MGF360 are associated with virus virulence and, consequently, have been targeted for the development of live attenuated vaccine (28, 29). ASFV MGF360-4L, which contains 387 amino acids, is a member of the MGF360 family. Previous research has shown that MGF360-4L inhibits the cGAS/STING-mediated activation of the IFN-β promoter through a double luciferase assay. After adapting to the vero cells, BA71V became a non-virulent ASFV, the genomic changes include the deletion of the MGF360-4L. However, the molecular mechanism of host antiviral innate immune responses has not been clarified.

In this study, we found that overexpression of MGF360-4L could significantly inhibit the activation of IFN-β promoter activity and suppress the mRNA levels of IFN-β and interferon-stimulated genes (ISGs). Further research showed that MGF360-4L could interact with IRF3 and suppress the phosphorylation of IRF3, thereby inhibiting the cGAS-STING mediated IFN-I signaling pathways. Our findings reveal a novel function of ASFV MGF360-4L and provide a new candidate gene for ASFV live-attenuated vaccines.

2 Materials and methods

2.1 Viruses and cells

Human embryonic kidney 293T (HEK293T) and porcine kidney 15 (PK-15) cells were obtained from Type Culture Collection of Chinese Academy of Science and cultured in Dulbecco's modified Eagle's medium supplemented with 10% fetal bovine serum, 100 U/ml penicillin, and 100 μg/ml streptomycin at 37 °C with 5% CO_2. Vesicular Stomatitis Virus (VSV-GFP) was a gift from Dr Liqi Zhu of Yangzhou University, VSV-GFP is tagged with GFP and stably express green fluorescence.

2.2 Antibodies and reagents

Monoclonal rabbit anti-hemagglutinin, anti-TBK1/NAK, anti-phospho-TBK1/NAK (Ser172), anti-IRF-3, anti-phospho-IRF-3 (Ser396), anti-glyceraldehyde 3-phosphate dehydrogenase (GAPDH), and horseradish peroxidase-conjugated goat anti-rabbit IgG were purchased from Cell Signaling Technology (USA). Rabbit monoclonal anti-flag and anti-GFP were obtained from Proteintech (USA). Rabbit IgG and mouse IgG were supplied by Beyotime (China). Alexa Fluor 594-conjugated goat anti-rabbit IgG antibody and Alexa Fluor 488-conjugated goat anti-mouse IgG antibody were purchased from ZSGB-BIO (China). 2′3′-cGAMP was acquired from MedChemExpress (USA). poly (dA:dT) was bought from InvivoGen (Hong Kong, China). jetPRIME transfection reagent and double-luciferase reporter assay kit were obtained from Polyplus Transfection (France) and TransGen (China), respectively.

2.3 Plasmids

The full length sequence of ASFV MGF360-4L was synthesized, referencing the genome of ASFV CADC-HN09 (GenBank submission No. MZ614662.1), and cloned into the p3×Flag-CMV-7.1 vector by GenScript (China). The hemagglutinin (HA)-tagged cGAS, STING, and IRF3 were generated using the methods previously described by Wang et al. (26). The IFN-β and NF-κB promoter luciferase reporter plasmids, as well as the pRL-TK plasmids, were purchased from Genomeditech (China). The Flag-tagged TBK1 expression plasmid was stored in our laboratory.

2.4 Dual-luciferase reporter assay

HEK293T cells were seeded into 48-well plates and cultured overnight to 80% confluence. They were then co-transfected with MGF360-4L or control vector plasmids, along with IFN-β or NF-κB (20 ng/well) promoter and pRL-TK (2 ng/well) plasmids as an internal control. After 24 h of transfection, the cells were collected and lysed. The whole-cell lysates were measured using a double-luciferase reporter assay kit (TransGen Biotech, China), following the manufacturer's protocols. The relative luciferase activity was determined by calculating the ratio of firefly luciferase to Renilla luciferase activity.

2.5 RNA extraction and quantitative reverse transcription polymerase chain reaction

Total RNA was extracted from HEK293T cells and PK-15 cells using the TRIzol reagent (Thermo Fisher Scientific), following the manufacturer's instructions, and was reverse transcribed using the RT master mix (TaKaRa). The reverse transcription products were then detected using the ABI 7900HT real-time PCR system with the SYBR Green Master Mix (TOYOBO). The relative mRNA levels of the target genes were normalized to the pig GAPDH or human GAPDH mRNA levels. The abundance of individual mRNA transcripts was calculated using the $2^{-\Delta\Delta CT}$ method. The primers listed in Table 1 are used for the quantitative reverse transcription polymerase chain reaction (RT-qPCR).

2.6 Co-immunoprecipitation assays

HEK293T cells were seeded into six-well plates and cultured overnight to 80% confluence. They were then co-transfected with MGF360-4L-Flag and IRF3-HA. After 24 h of transfection, the cells were lysed on ice using Pierce$^{\text{TM}}$ IP Lysis Buffer (Thermo Fisher Scientific), supplemented with a phosphatase and protease inhibitor cocktail. Protein A/G magnetic beads (MedChemExpress) were incubated with either the indicated antibody or control IgG for 2 h at 4°C. Subsequently, the samples were incubated with the protein A/G magnetic beads-Ab-Ag complex for 2 h at 4°C. After incubation, the samples were washed thrice with elution buffer and then boiled in sodium dodecyl sulfate (SDS) loading buffer.

2.7 Confocal microscopy and co-localization analysis

MGF360-4L-Flag and IRF3-HA expression plasmids were transfected into HEK293T cells and PK-15 cells. After 24 h of transfection, the cells were fixed with 4% paraformaldehyde for 30 min at room temperature, then permeabilized with 0.1% Triton X-100 for 15 min. Subsequently, the cells were blocked with 5% BSA for 1 h. Next, they were incubated with corresponding primary antibodies at 4°C overnight. Following this, the cells were incubated with Alexa Fluor 594 or 488-conjugated secondary antibodies for 2 h and then stained with 4-methyl-6-phenylindole for 10 min. The samples were examined using the Leica TCS SP8 confocal system (Leica Microsystems).

TABLE 1 Primers used for qPCR in this study.

Prime	Sequence (5′-3′)	Target gene
pIFN-β-F	GTGGAACTTGATGGGCAGAT	Porcine IFN-β gene
pIFN-β-R	TTCCTCCTCCATGATTTCCTC	
pGAPDH-F	CGTCCCTGAGACACGATGGT	Porcine GAPDH gene
pGAPDH-R	GGAACATGTAGACCATGTAG	
hISG56-F	GCTTTCAAATCCCTTCCGCTAT	Human ISG56 gene
hISG56-R	GCCTTGGCCCGTTCATAAT	
hISG54-F	CACCTCTGGACTGGCAATAGC	Human ISG54 gene
hISG54-R	GTCAGGATTCAGCCGAATGG	
hISG15-F	GGGACCTGACGGTGAAGATG	Human ISG15 gene
hISG15-R	CGCCGATCTTCTGGGTGAT	
hIFN-β-F	ATGACCAACAAGTGTCTCCTCC	Human IFN-*β* gene
hIFN-*β*-R	GCTCATGGAAAGAGCTGTAGTG	
hGAPDH-F	TCATGACCACAGTCCATGCC	Human GAPDH gene
hGAPDH-R	GGATGACCTTGCCCACAGCC	
hJAK1-F	CTCTCTGTCACAACCTCTTCGC	Human JAK1 gene
hJAK1-R	TTGGTAAAGTAGAACCTCATGCG	
hSTAT1-F	AATGTGAAGGACAAGGTTATG	Human STAT1 gene
hSTAT1-R	TTGGTCTCGTGTTCTCTG	
hSTAT2-F	AATCATCCGCCATTACCA	HumanSTAT2 gene
hSTAT2-R	AGTTCATCCACCTGTCTATT	
hSTAT3-F	GGAGAAACAGGATGGCCCAA	Human STAT3 gene
hSTAT3-R	ATCCAAGGGGCCAGAAACTG	
hTYK2-F	CAGCCCCGTGTTCTGGTATG	Human TYK2 gene
hTYK2-R VSV-F VSV-R	GAAAGGACGCCTCTGTCTCC TGCAAGGAAAGCATTGAACAA GAGGAGTCACCTGGACAATCAC	VSV G gene

2.8 Western blot analysis

The cells were harvested and washed with cold phosphate-buffered saline, then lysed on ice with the radio immunoprecipitation assay buffer (CWBIO), supplemented with a protease and phosphatase inhibitor cocktail (CWBIO). After centrifuging the cell lysis buffer at 4°C for 10 min, we collected the lysed supernatant. Total protein content was quantified using the Pierce^{TM} bicinchoninic acid protein assay kit (Thermo Fisher Scientific). The cell supernatants were denatured with 5× SDS-polyacrylamide gel electrophoresis loading buffer (CWBIO) for 10 min. Each sample was separated by SDS-polyacrylamide gel electrophoresis, then transferred to Immobilon-NC membranes (Millipore). The membranes were blocked with 5% (w/v) skim milk dissolved in Tris-buffered saline containing 0.1% Tween 20 at room temperature for 2 h. Incubation with the appropriate primary antibody was performed at 4°C overnight. After incubation with secondary antibodies, the membranes were visualized using the ECL western blotting substrate (Tanon).

2.9 Statistical analysis

All experiments were independently performed at least three times. Statistical analyses were conducted using Student's test and one-way analysis of variance with GraphPad Prism 5.0 software. Statistical significance was defined as *, $p<0.05$; **, $p<0.01$; and ***, $p<0.001$.

3 Results

3.1 ASFV MGF360-4L inhibits the cGAS-STING signaling pathway

Previous studies in our laboratory have identified MGF360-4L as an inhibitor in the cGAS/STING-induced signaling pathways. To further confirm these results, PK-15 cells were transfected with MGF360-4L-Flag and subsequently treated with 1 μg/mL poly(dA:dT). The mRNA level of IFN-β was then detected using quantitative PCR (qPCR). As shown in Figure 1A, MGF360-4L significantly inhibited poly (dA:dT)-induced IFN-β mRNA expression. HEK293T cells were transfected with the MGF360-4L-Flag expression plasmid, along with either an IFN-β-luciferase or an NF-κB-luciferase reporter, pRL-TK, and cGAS-HA and STING-HA expression plasmids. At 24 h post-transfection, the cells were collected for double luciferase assay. The results showed that MGF360-4L significantly inhibited cGAS/STING-induced IFN-β promoter activation (Figure 1B); however, it did not inhibit NF-κB promoter activation (Figure 1C).

3.2 ASFV MGF360-4L inhibits IFN-β promoter activation and decreases IFN-β mRNA expression level in a dose-dependent manner

HEK293T cells were transfected with IFN-β-luc and pRL-TK plasmids, along with cGAS-HA, STING-HA, and various doses of MGF360-4L-Flag. Through the DLR assay, the overexpression of MGF360-4L significantly inhibited cGAS/STING-induced IFN-β promoter activities in a dose-dependent manner (Figure 2A). The results of qPCR were consistent with those of the dual luciferase assay (Figure 2B).

3.3 ASFV MGF360-4L impairs the transcription of IFN-stimulated genes in response to 2′3′-cGAMP treatment

To investigate whether the MGF360-4L protein affects the expression of ISGs, we explored how IFN-β induces a series of

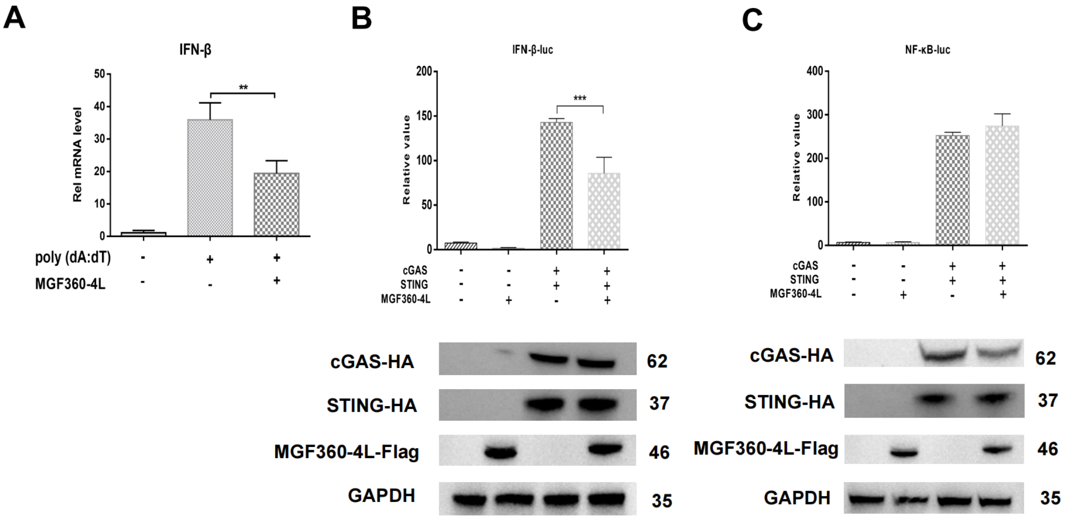

FIGURE 1
ASFV MGF360-4L suppressed IFN-β transcription mediated by the cGAS/STING pathway. **(A)** HEK293T cells were transfected with ASFV MGF360-4L-Flag, treated with 1 μg/ml poly (dA:dT), and then harvested. The IFN-β mRNA levels were then detected. **(B, C)** HEK293T cells were co-transfected with IFN-β-luc (20 ng) or NF-κB-luc (20 ng), pRL-TK (2 ng), cGAS-HA (10 ng), STING-HA (40 ng), and MGF360-4L-Flag (100 ng). After 24 h of transfection, promoter activation was detected using DLR assay kits, and the expression of cGAS-HA, STING-HA, and MGF360-4L-Flag was examined using western blot assay. **, $p<0.01$; and ***, $p<0.001$.

ISGs to produce a strong antiviral response. We detected the mRNA levels of ISG15, ISG54, and ISG56 in HEK293T cells and PK-15 cells were treated with 2′3′-cGAMP (Figures 3A–F). The results indicated that ASFV MGF360-4L considerably inhibited the transcriptional activity of ISG54 (Figure 3B) and ISG56 (Figure 3C) in HEK 293T cells, and reduced the mRNA levels of ISG15 (Figure 3D), ISG54 (Figure 3E) and ISG56 (Figure 3F) in PK-15 cells. These data suggest that ASFV MGF360-4L downregulates IFN-I downstream antiviral genes.

3.4 ASFV MGF360-4L is involved in inhibiting the mRNA levels of STAT1, STAT2, and TYK2

We investigated various ISGs that are induced via the Janus kinase (JAK)-signal transducer and activator of transcription (STAT) pathway (30). We found that ASFV MGF360-4L inhibited the mRNA levels of ISG15, ISG54 and ISG56. To explore the impact of MGF360-4L on JAK/STAT signaling pathways, HEK293T cells and PK-15 cells were transfected with MGF360-4L and subsequently treated with 2′3′-cGAMP. Total RNA was extracted and reverse-transcribed into cDNA. The expression of JAK1, TYK2, STAT1, STAT2, and STAT3 was evaluated by qPCR (Figures 4A–J). The results indicated that ASFV MGF360-4L significantly reduced the transcription levels of STAT1 (Figure 4B), STAT2 (Figure 4C), and TYK2 (Figure 4E) in HEK 293T cells, and inhibited the transcriptional activity of STAT2 (Figure 4H) and TYK2 (Figure 4J) in PK-15 cells. We speculated that ASFV MGF360-4L may negatively regulate the JAK/STAT signaling pathway.

3.5 ASFV MGF360-4L can disturb the cGAS/STING signaling mediated antiviral responses

The cGAS/STING signaling pathway has broad antiviral functions (31); thus, we wanted to determine whether ASFV MGF360-4L inhibits cGAS/STING mediated antiviral responses. Therefore, the HEK293T cells were infected with VSV-GFP, which stably expresses green fluorescent protein. In the presence of ASFV MGF360-4L, the transcription and expression levels of VSV-GFP were significantly increased (Figures 5A, D), which was evidenced by fluorescence microscopy (Figure 5E). In the presence of cGAS-HA, STING-HA, and MGF360-4L-Flag, the mRNA levels of IFN-β and ISG56 were significantly reduced (Figures 5B, C), suggesting that ASFV MGF360-4L may inhibit the cGAS/STING signaling pathway. Taken together, these data indicate that ASFV MGF360-4L potentially inhibits the cGAS/STING signaling mediated anti-VSV responses.

3.6 ASFV MGF360-4L inhibits the cGAS/STING pathway by suppressing IRF3 phosphorylation

To explore the molecular mechanism underlying the ASFV MGF360-4L inhibition of the cGAS/STING pathway, HEK293T cells were transfected. The transfection involved a plasmid TBK1-Flag or an HA-tagged, active mutant of IRF3 (IRF3-5D-HA), along with an IFN-β-luc, pRL-TK, and MGF360-4L-Flag. The results showed that ASFV MGF360-4L inhibited the IFN-β promoter activity, which was induced by TBK1 (Figure 6A) and IRF3-5D

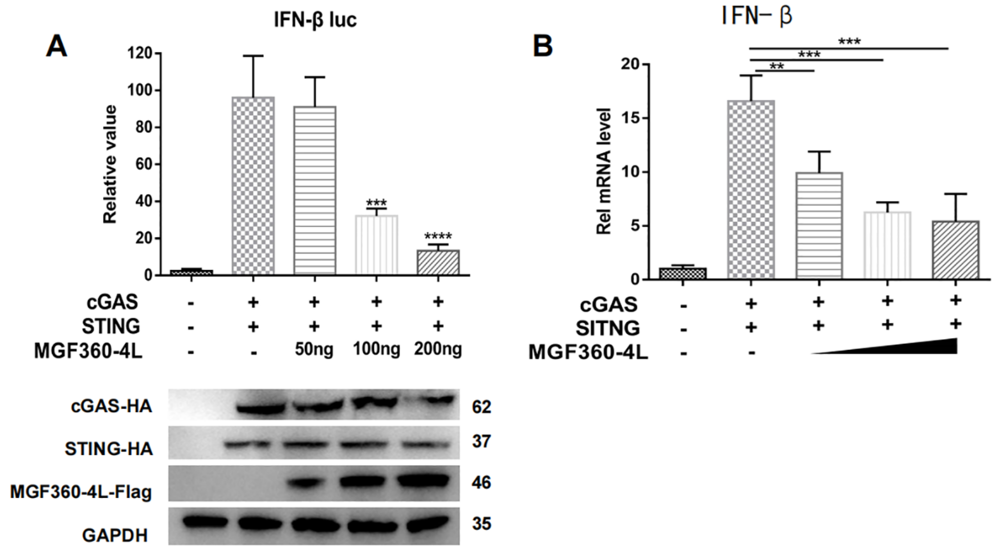

FIGURE 2
ASFV MGF360-4L inhibited IFN-β promoter activity and the mRNA levels of IFN-β in a dose-dependent manner. HEK293T cells were co-transfected with cGAS-HA, STING-HA and p3×Flag-CMV-7.1 empty vector were the control comparison group. **(A)** HEK293T cells were co-transfected with IFN-β-luc (20 ng), pRL-TK (2 ng), cGAS-HA (40 ng), and STING-HA (160 ng), along with increased amounts of ASFV MGF360-4L-flag (0 ng, 50 ng, 100 ng, 200 ng). At 24 h post-transfection, the expression of cGAS-HA, STING-HA, and MGF360-4L-Flag was detected using western blotting. Promoter activity was measured using a DLR kit. **(B)** HEK293T cells were co-transfected with cGAS-HA (40 ng) and STING-HA (160 ng), along with increased amounts of ASFV MGF360-4L-flag (0 ng, 50 ng, 100 ng, 200 ng) or the p3×Flag-CMV-7.1 empty vector, and the mRNA levels of IFN-β were then detected using qPCR. **, p<0.01; ***, p<0.001; and ****, p<0.0001.

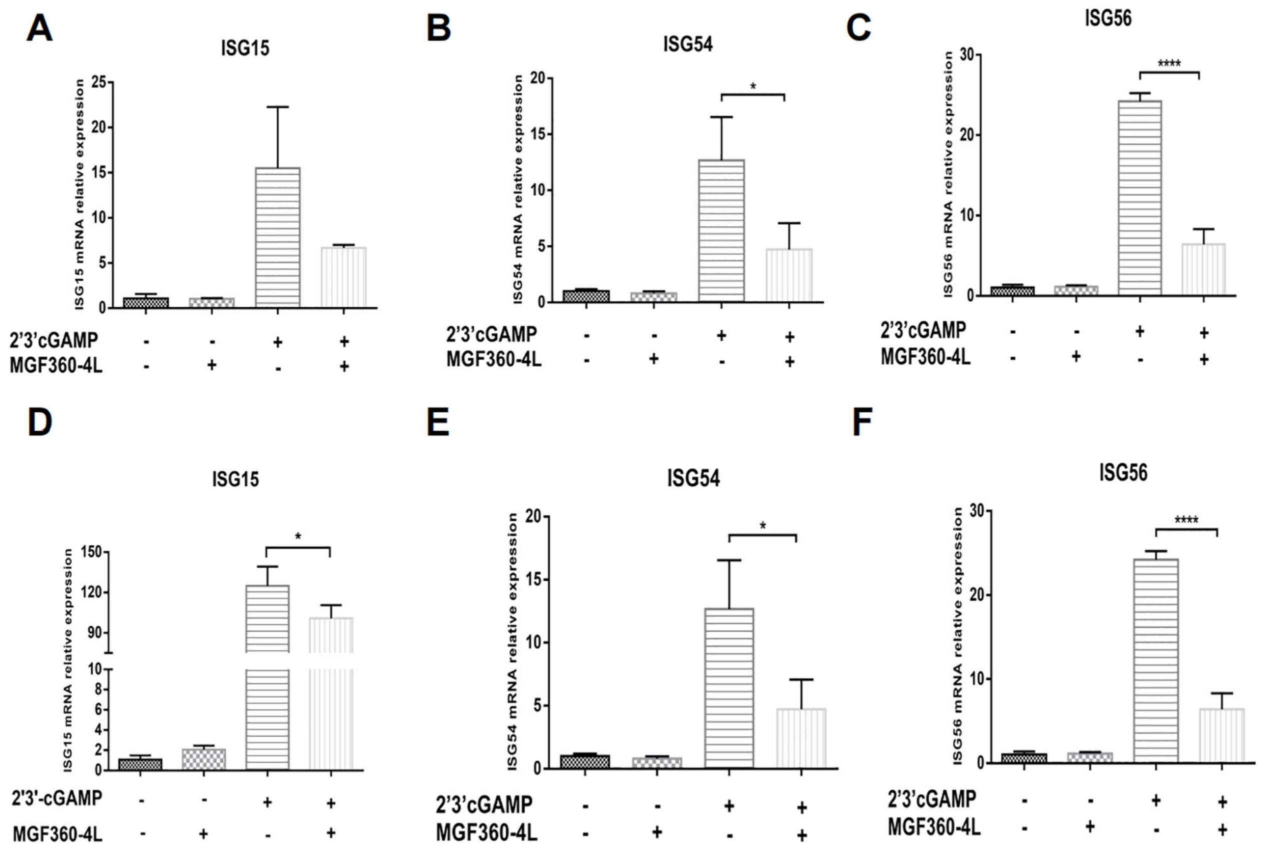

FIGURE 3
ASFV MGF360-4L reduced the mRNA levels of ISG15, ISG54 and ISG56. **(A–C)** HEK293T cells were transfected with MGF360-4L-Flag (200 ng) expression plasmid or the p3×Flag-CMV-7.1 empty vector (200 ng). At 16 h post-transfection, cells were treated with 2′3′-cGAMP (2 μg/ml) for another 12 h, then harvested and lysed, followed by RT-qPCR detection of ISG15 **(A)**, ISG54 **(B)**, and ISG56 **(C)** mRNA. **(D–F)** PK-15 cells were transfected with MGF360-4L-Flag (200 ng) expression plasmid or the p3×Flag-CMV-7.1 empty vector (200 ng). At 16 h post-transfection, cells were treated with 2′3′-cGAMP (2 μg/ml) for another 12 h, then harvested and lysed, followed by RT-qPCR detection of ISG15 **(D)**, ISG54 **(E)**, and ISG56 **(F)** mRNA. *, p<0.05; and ****, p<0.0001.

(Figure 6B). Furthermore, it inhibited the expression of the IRF3-5D protein (Figure 6B), while the exogenous expression of TBK1 remained unchanged (Figure 6A). Further research showed that ASFV MGF360-4L inhibited the phosphorylation of IRF3 induced by cGAS/STING (Figure 7A), without altering the endogenous protein levels of IRF3, we transfected different dose of ASFV MGF360-4L, the results showed that the overexpression of MGF360-4L suppressed the phosphorylation of IRF3 induced by cGAS/STING in a dose-dependent manner (Figure 7B). At the same time, we also proved that MGF360-4L could suppress the phosphorylation of IRF3 in PK-15 cells (Figure 7C). These results suggest that ASFV MGF360-4L inhibits the cGAS/STING signaling pathway by suppressing IRF3 phosphorylation.

3.7 ASFV MGF360-4L interacts with IRF3

Previous studies have proven that several viral proteins antagonize IFN-I production by interacting with IRF3 (32). To determine whether MGF360-4L interacts with IRF3, HEK293T cells were co-transfected with MGF360-4L-Flag and IRF3-HA expression plasmids. Co-immunoprecipitation results confirmed the interaction between MGF360-4L and IRF3 (Figure 8A). We also found that MGF360-4L co-localized with IRF3 in the cytoplasm when the two proteins were co-expressed in HEK293T cells and PK-15 cells (Figures 8B, C), These results show that MGF360-4L could interact and co-localize with IRF3.

3.8 ASFV MGF360-4L regions are responsible for inhibitory activity

To identify the crucial domains in ASFV MGF360-4L that are related to its immunosuppressive function, three truncated mutants of MGF360-4L, namely 4L-F1 (1-88 aa), 4L-F2 (75-162 aa), and 4L-F3 (146-387 aa), were constructed. We found that 4L-F2 inhibited the IFN-β promoter activity induced by cGAS/STING and IRF3-5D (Figures 9A, C), 4L-F3 significantly inhibited the IFN-β promoter activity induced by cGAS/STING, TBK1, and IRF3-5D (Figures 9A–C), and 4L-F3 reduced the mRNA level of IFN-β

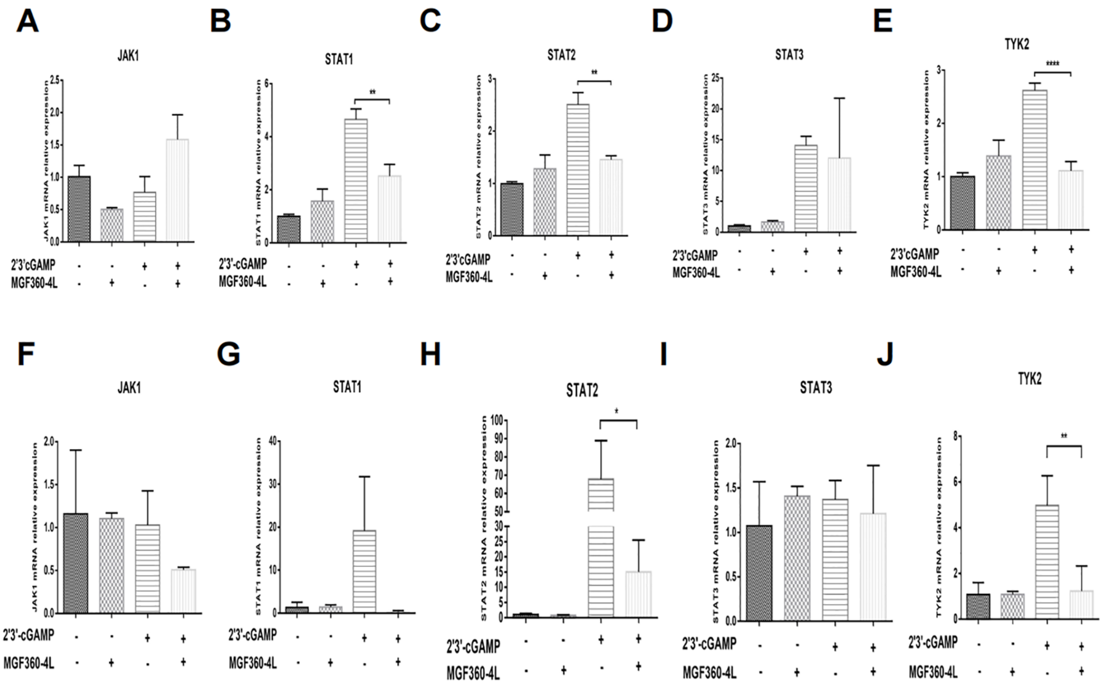

FIGURE 4
ASFV MGF360-4L suppressed the transcription levels of STAT1, STAT2, and TYK2. **(A–E)** HEK293T cells were transfected with MGF360-4L-Flag (200 ng) expression plasmid or the p3×Flag-CMV-7.1 empty vector (200 ng). At 16 h post-transfection, cells were treated with 2′3′-cGAMP (2 μg/ml) for another 12 h. Total RNA was then extracted from cell lysates, followed by RT-qPCR detection of JAK1 **(A)**, STAT1 **(B)**, STAT2 **(C)**, STAT3 **(D)**, and TYK2 **(E)** mRNA. **(F–J)** PK-15 cells were transfected with MGF360-4L-Flag (200 ng) expression plasmid or the p3×Flag-CMV-7.1 empty vector (200 ng). At 16 h post-transfection, cells were treated with 2′3′-cGAMP (2 μg/ml) for another 12 h. Total RNA was then extracted from cell lysates, followed by RT-qPCR detection of JAK1 **(F)**, STAT1 **(G)**, STAT2 **(H)**, STAT3 **(I)**, and TYK2 **(J)** mRNA. *, p<0.05; **, p<0.01; and ****, p<0.0001.

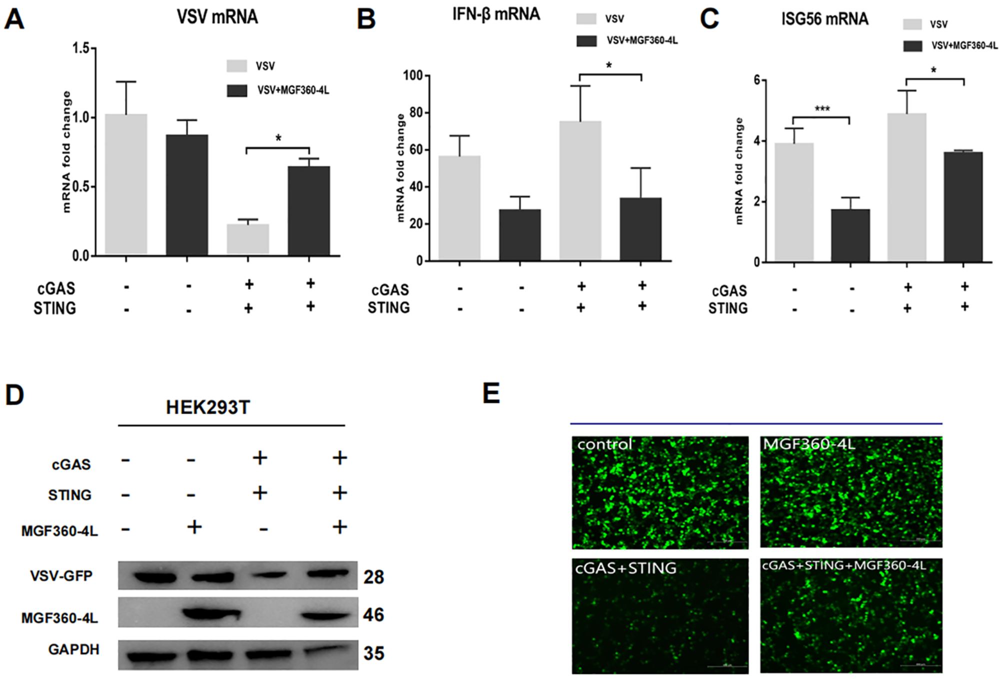

FIGURE 5
Effects of MGF360-4L on the cGAS/STING signaling mediated anti-VSV activity. **(A–E)** HEK293T cells were cultured overnight to 80% confluence. They were then co-transfected with cGAS-HA (40 ng), STING-HA (160 ng), and MGF360-4L-Flag (200 ng) for 16 h. The cells were infected with VSV-GFP for 8 h. **(A–C)** The mRNA levels of VSV, INF-β, and ISG56 were detected using RT-qPCR. The GFP signals from the VSV replicates were observed using fluorescence microscopy **(E)** and analyzed using western blotting **(D)**. *, p<0.05; and ***, p<0.001.

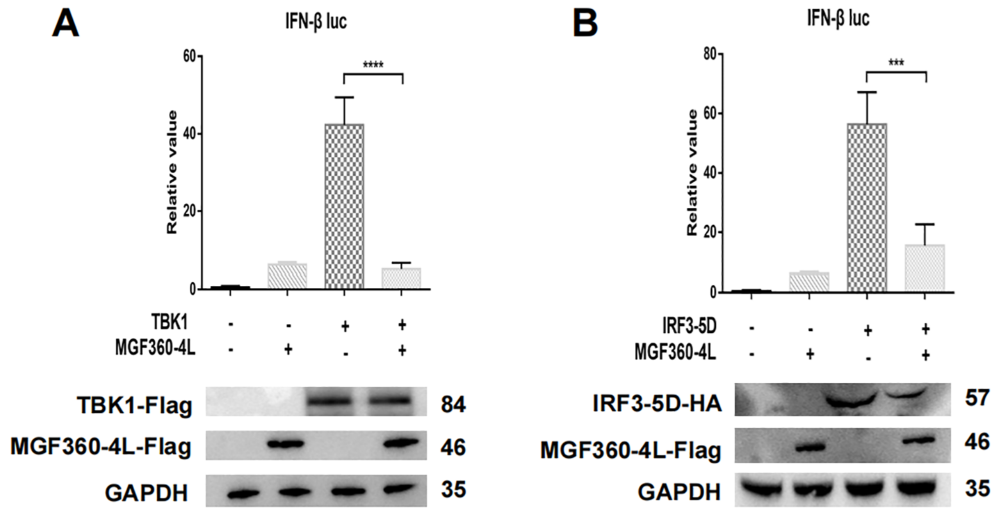

FIGURE 6
ASFV MGF360-4L inhibited the IFN- β promoter activity induced by TBK1 and IRF3-5D. **(A, B)** HEK 293T cells were co-transfected with IFN-β-luc (20 ng), pRL-TK (2 ng), MGF360-4L-Flag (200 ng) and TBK1-Flag (200 ng) or IRF3-5D-HA (200 ng), then harvested and lysed. Promoter activation was detected using DLR assay kits, and the expression of cGAS-HA, STING-HA, and MGF360-4L was examined using western blot assay. ***, p<0.001, and ****, p<0.0001.

(Figure 9D). Thus, we speculate that the domains and sites within 4L-F2 and 4L-F3 are responsible for immunosuppressive effects.

4 Discussion

IFN-I represents the most effective mechanism through which the host exerts innate immunity against viral infections (33). Upon infection with DNA viruses, the viral DNA can be sensed by the host cytosolic DNA sensor cGAS, initiating a series of antiviral signaling pathways that result in the induction of IFN-β and ISG expression to combat viral infections. Many viruses have taken multiple strategies to evade host immune defenses by inhibiting the cGAS/STING signal pathway. Foot-and-Mouth Disease Virus (FMDV) and Senecavalley virus (SVV) attenuate IFN-I production by inhibiting the expression of the IRF3 protein (34, 35). Human cytomegalovirus facilitates the proteasome-dependent degradation of STING and blocks the cGAS/STING pathway (36).

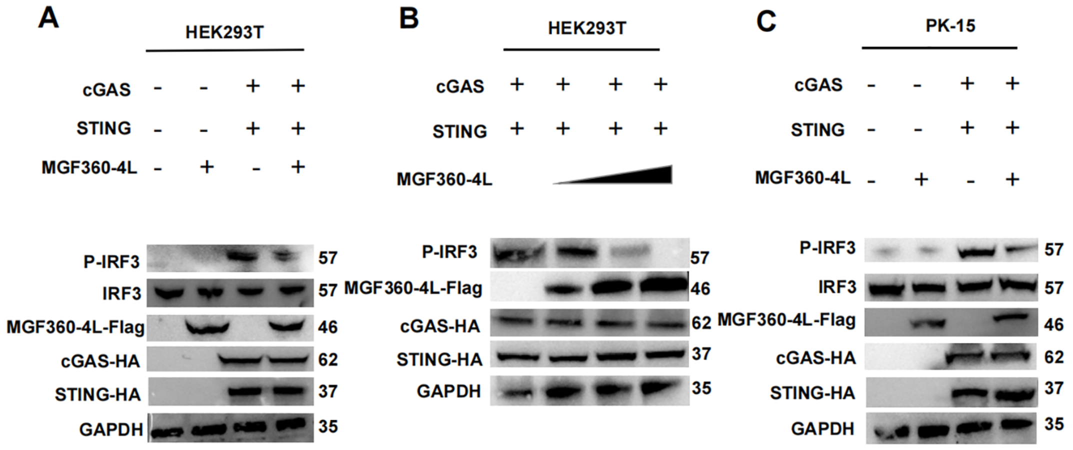

FIGURE 7
ASFV MGF360-4L inhibited the cGAS/STING pathway by suppressing the phosphorylation of IRF3. **(A)** HEK293T cells were co-transfected with cGAS-HA (40 ng), STING-HA (160 ng) and ASFV MGF360-4L-Flag (200 ng). After 24 h of transfection, the expression of cGAS-HA, STING-HA, and MGF360-4L-Flag was examined using western blot assay. **(B)** HEK293T cells were co-transfected with cGAS-HA (40 ng), and STING-HA (160 ng), along with increased amounts of ASFV MGF360-4L-flag (0 ng, 50 ng, 100 ng, 200 ng). At 24 h post-transfection, the expression of cGAS-HA, STING-HA, and MGF360-4L-Flag was detected using western blotting. **(C)** PK-15 cells were co-transfected with cGAS-HA (40 ng), STING-HA (160 ng) and ASFV MGF360-4L-Flag (200 ng). After 24 h of transfection, the expression of cGAS-HA, STING-HA, and MGF360-4L-Flag was examined using western blot assay.

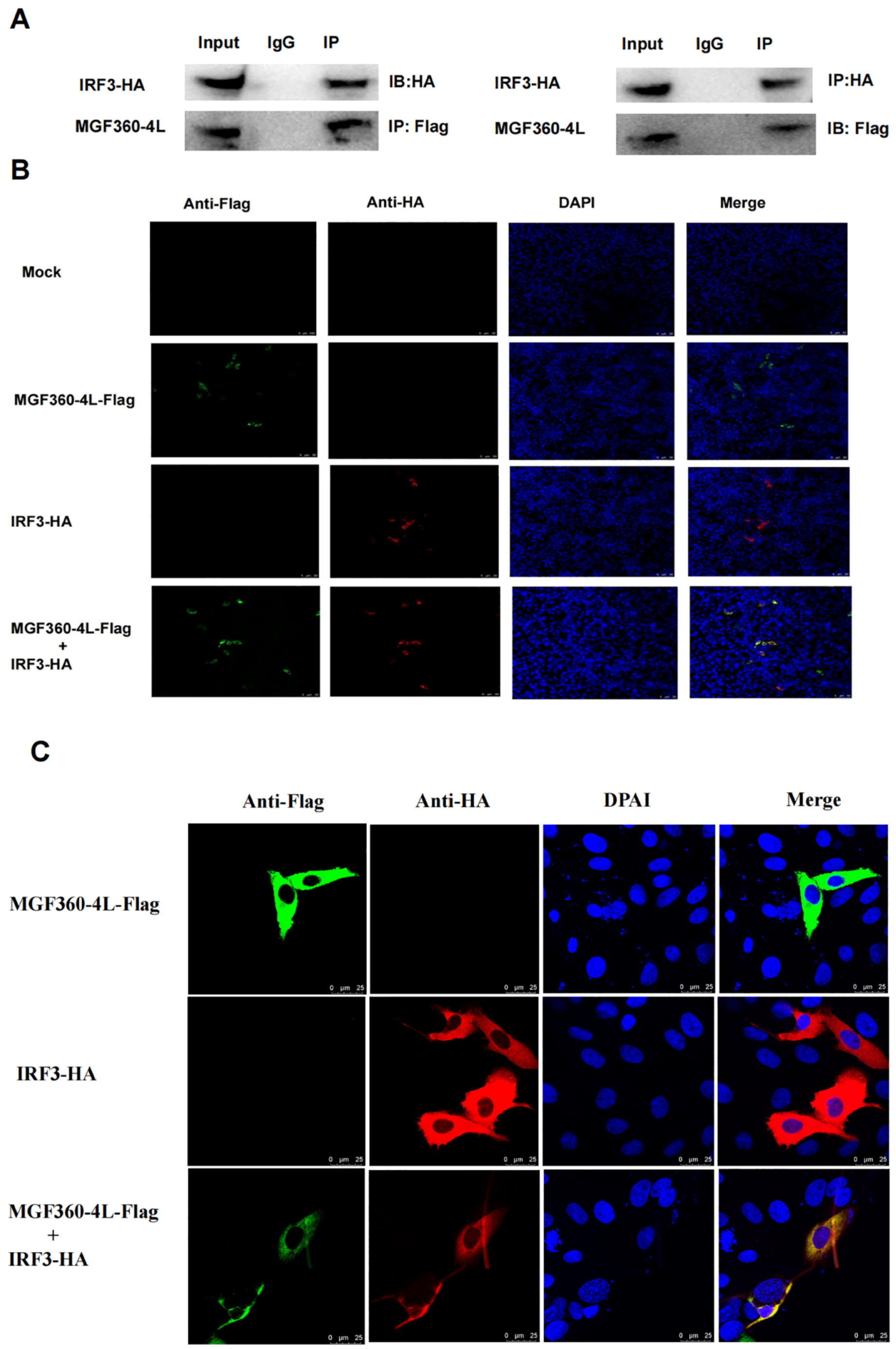

FIGURE 8
MGF360-4L interacted and co-localized with IRF3. **(A)** MGF360-4L interacted with IRF3 in the overexpression system. HEK 293T cells were transfected with the indicated plasmids (5 μg each). IgG was used for control immunoprecipitation. Co-immunoprecipitation and immunoblotting analyses were performed with the indicated Abs. **(B, C)** Co-localization of MGF360-4L with IRF3. HEK 293T **(B)** cells and PK-15 cells **(C)** were transfected with MGF360-4L-Flag and IRF3-HA expression plasmids. After 24 h of transfection, MGF360-4L-Flag and IRF3-HA were stained with mouse-anti-Flag (green) and rabbit-anti-HA (red), and the nuclei were stained with DAPI (blue). Confocal assays were performed using Leica TCS SP8.

Increasing evidence has shown that ASFV has developed a series of strategies to reduce IFN production and inhibit IFN-I signaling pathways. For instance, ASFV pE120R interferes with the interaction between IRF3 and TBK1, thereby inhibiting the activation of IRF3 and suppressing the production of IFN-I (24). ASFV pI215L inhibits the production of IFN-I by recruiting the E3 ubiquitin ligase RNF138 to facilitate the degradation of RNF128, thereby inhibiting RNF128-mediated k63-linked polyubiquitination of TBK1 (37). Preventing the antiviral immune response is crucial for the proliferation of ASFV. Probably for this reason, the ASFV genome encodes several proteins dedicated to the control of IFN-I, mainly within the MGF360 and MGF505/530 multigene families, aiming to evade host defenses (29, 38–40). For example, ASFV pMGF505-7R reduces IFN-I production by promoting ULK1-mediated STING degradation and inhibiting IRF3 phosphorylation and nuclear translocation (41). ASFV MGF360-14L negatively regulates IFN-I signaling by targeting IRF3 (22). ASFV MGF360-4L is a member of MGF360 multigene families, while whether ASFV MGF360-4L could inhibit IFN-I signaling pathway and the underlying molecular mechanisms IFN-I remain unknown. In our study, ASFV MGF360-4L was firstly identified as a new inhibitor of IFN-I induced by cGAS/STING pathway (Figure 10). Firstly, ASFV MGF360-4L inhibited IFN-β promoter activity induced by cGAS/STING, TBK1, and IRF3-5D, reduced the mRNA levels of IFN-β, ISG15, ISG54, and ISG56, and might antagonize the JAK/STAT signaling pathway. Second, ASFV MGF360-4L disrupted the cGAS/STING signaling mediated antiviral responses, leading to increased yields of VSV-GFP in cells transfected with cGAS, STING, and MGF360-4L compared with cells transfected with cGAS and STING. Third, ASFV MGF360-4L could interact with IRF3, and suppressed the phosphorylation of IRF3, thereby blocking the cGAS/STING signaling pathway. IRF3 is a key transcription factor capable of inducing IFN-I and facilitating the expression of numerous genes involved in the innate immune response (42). Fourth, we identified crucial domains related to immunosuppressive function through DLR and qPCR. We speculated that 4L-F2 (75-162 aa) and 4L-F3 (146-387 aa) contain immunosuppressive domains and sites.

ASFV has caused severe economic losses to the global pig industry; thus, investigating the functions of ASFV proteins and

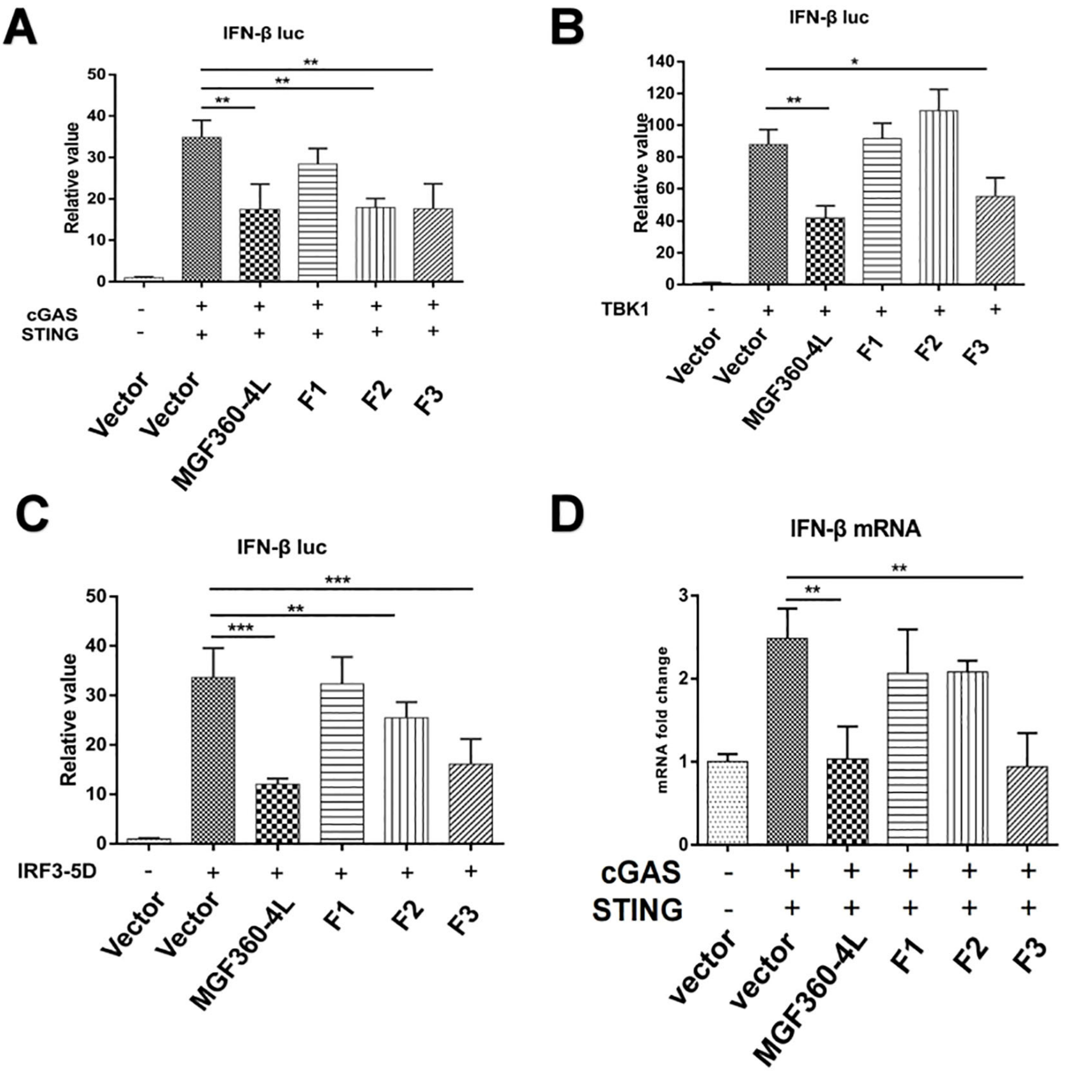

FIGURE 9
Regions of ASFV MGF360-4L responsible for inhibitory activity. **(A–C)** Luciferase assays in HEK293T cells were performed to detect the activation of the IFN-β promoter following the expression of empty vector, cGAS-HA and STING-HA, TBK1-Flag, or IRF3-5D-HA in the presence of empty vector, and full-length MGF360-4L-Flag, 4L-F1-Flag (1-88 aa), 4L-F2-Flag (75-162 aa), or 4L-F3-Flag (146-387 aa) plasmids. **(D)** HEK293T cells were co-transfected with cGAS-HA, STING-HA, and full-length MGF360-4L-Flag, 4L-F1-Flag (1-88 aa), 4L-F2-Flag (75-162 aa), or 4L-F3-Flag (146-387 aa) plasmids. At 24 h post-transfection, the mRNA levels of IFN-β were detected using RT-qPCR. *, $p<0.05$; **, $p<0.01$; and ***, $p<0.001$.

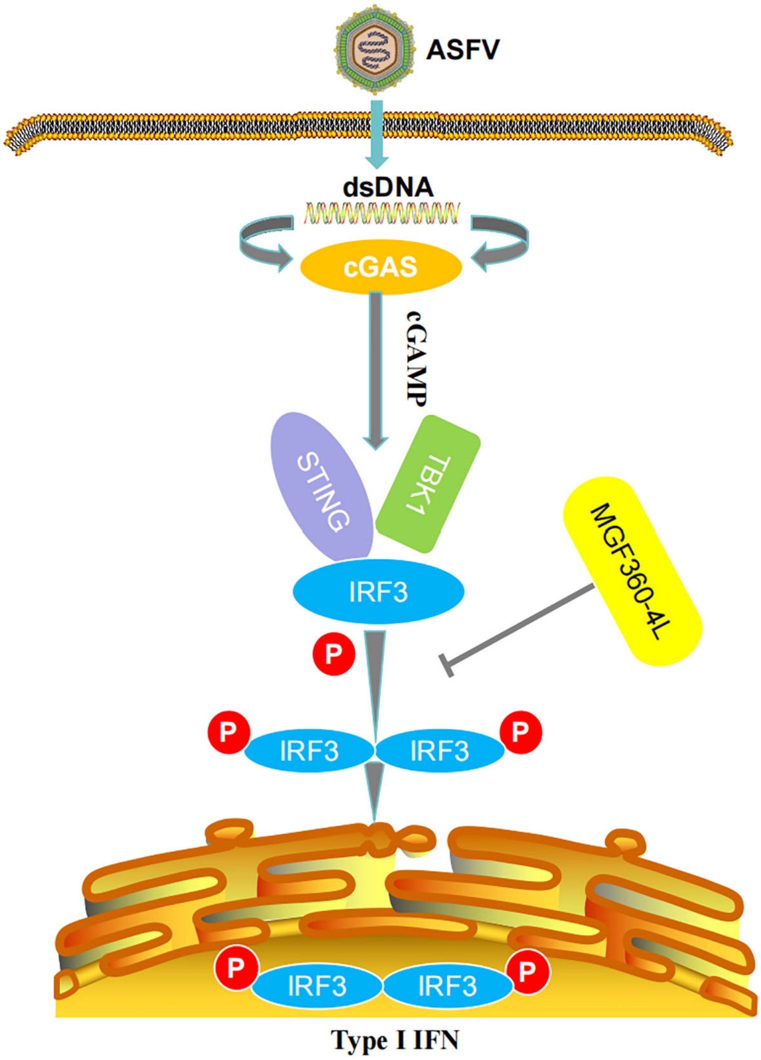

FIGURE 10
Schematic diagram of the mechanism of MGF360-4L-mediated IFN-β signaling inhibition. ASFV MGF360-4L interacted with IRF3 and suppressed the phosphorylation of IRF3 to help the virus escape the host immune response.

elucidating the immune evasion mechanism are needed. In this study, we found that ASFV MGF360-4L suppressed the phosphorylation of IRF3, thereby inhibiting the type I IFN response induced by cGAS/STING. This study provides a novel strategy for understanding ASFV-mediated immune evasion mechanisms.

Data availability statement

The original contributions presented in the study are included in the article/supplementary material. Further inquiries can be directed to the corresponding authors.

Author contributions

ZW: Data curation, Formal analysis, Writing – original draft, Investigation, Software. YHH: Formal analysis, Methodology, Writing – original draft. YH: Data curation, Formal analysis, Software, Writing – original draft. WZ: Data curation, Formal analysis, Methodology, Writing – original draft. CT: Data curation, Formal analysis, Writing – original draft. YC: Data curation, Writing – original draft. ZP: Formal analysis, Writing – original draft. HZ: Project administration, Funding acquisition, Writing – review & editing. PZ: Project administration, Supervision, Writing – review & editing. HJ: Funding acquisition, Project administration, Supervision, Writing – review & editing.

Funding

The author(s) declare financial support was received for the research, authorship, and/or publication of this article. This work was supported by the National Key Research and Development Program of China (2021YFD1801200) and the Yunnan Key Research and Development Project (202103AC100001), the

Earmarked Fund for CARS (CARS36), and the Agricultural Science and Technology Innovation Program (no. ASTIP-IAS-11).

Conflict of interest

The authors declare that the research was conducted in the absence of any commercial or financial relationships that could be construed as a potential conflict of interest.

Publisher's note

All claims expressed in this article are solely those of the authors and do not necessarily represent those of their affiliated organizations, or those of the publisher, the editors and the reviewers. Any product that may be evaluated in this article, or claim that may be made by its manufacturer, is not guaranteed or endorsed by the publisher.

References

1. Alonso C, Borca M, Dixon L, Revilla Y, Rodriguez F, Escribano JM, et al. ICTV virus taxonomy profile: asfarviridae. *J Gen Virol.* (2018) 99:613–4. doi: 10.1099/jgv.0.001049

2. Karger A, Pérez-Núñez D, Urquiza J, Hinojar P, Alonso C, Freitas FB, et al. An update on African swine fever virology. *Viruses.* (2019) 11(9):864. doi: 10.3390/v11090864

3. Alejo A, Matamoros T, Guerra M, Andrés G. A proteomic atlas of the African swine fever virus particle. *J Virol.* (2018) 92(23):e01293–18. doi: 10.1128/jvi.01293-18

4. Dixon LK, Chapman DA, Netherton CL, Upton C. African swine fever virus replication and genomics. *Virus Res.* (2013) 173:3–14. doi: 10.1016/j.virusres.2012.10.020

5. Revilla Y, Pérez-Núñez D, Richt JA. African swine fever virus biology and vaccine approaches. *Adv Virus Res.* (2018) 100:41–74. doi: 10.1016/bs.aivir.2017.10.002

6. Galindo I, Alonso C. African swine fever virus: A review. *Viruses.* (2017) 9(5):103. doi: 10.3390/v9050103

7. Li G, Liu X, Yang M, Zhang G, Wang Z, Guo K, et al. Crystal structure of African swine fever virus pS273R protease and implications for inhibitor design. *J Virol.* (2020) 94(10):e02125–19. doi: 10.1128/jvi.02125-19

8. Li G, Wang C, Yang M, Cao L, Fu D, Liu X, et al. Structural Insight into African Swine Fever Virus dUTPase Reveals a Novel Folding Pattern in the dUTPase Family. *J Virol.* (2020) 94(4):e01698–19. doi: 10.1128/jvi.01698-19

9. Dixon LK, Sun H, Roberts H. African swine fever. *Antiviral Res.* (2019) 165:34–41. doi: 10.1016/j.antiviral.2019.02.018

10. Eustace Montgomery R. On A form of swine fever occurring in British East Africa (Kenya colony). *J Comp Pathol Ther.* (1921) 34:159–91. doi: 10.1016/S0368-1742(21)80031-4

11. Dixon LK, Stahl K, Jori F, Vial L, Pfeiffer DU. African swine fever epidemiology and control. *Annu Rev Anim Biosci.* (2020) 8:221–46. doi: 10.1146/annurev-animal-021419-083741

12. Shen X, Pu Z, Li Y, Yu S, Guo F, Luo T, et al. Phylogeographic patterns of the African swine fever virus. *J Infect.* (2019) 79:174–87. doi: 10.1016/j.jinf.2019.05.004

13. Sánchez-Cordón PJ, Montoya M, Reis AL, Dixon LK. African swine fever: A re-emerging viral disease threatening the global pig industry. *Vet J.* (2018) 233:41–8. doi: 10.1016/j.tvjl.2017.12.025

14. Zhou X, Li N, Luo Y, Liu Y, Miao F, Chen T, et al. Emergence of African swine fever in China, 2018. *Transbound Emerg Dis.* (2018) 65:1482–4. doi: 10.1111/tbed.12989

15. Wu K, Liu J, Wang L, Fan S, Li Z, Li Y, et al. Current state of global African swine fever vaccine development under the prevalence and transmission of ASF in China. *Vaccines (Basel).* (2020) 8(3):531. doi: 10.3390/vaccines8030531

16. Zhao D, Liu R, Zhang X, Li F, Wang J, Zhang J, et al. Replication and virulence in pigs of the first African swine fever virus isolated in China. *Emerg Microbes Infect.* (2019) 8:438–47. doi: 10.1080/22221751.2019.1590128

17. Kawai T, Akira S. Innate immune recognition of viral infection. *Nat Immunol.* (2006) 7:131–7. doi: 10.1038/ni1303

18. Barrado-Gil L, Del Puerto A, Galindo I, Cuesta-Geijo M, García-Dorival I, de Motes CM, et al. African swine fever virus ubiquitin-conjugating enzyme is an immunomodulator targeting NF-κB activation. *Viruses.* (2021) 13(6):1160. doi: 10.3390/v13061160

19. Yang J, Li S, Feng T, Zhang X, Yang F, Cao W, et al. African swine fever virus F317L protein inhibits NF-κB activation to evade host immune response and promote viral replication. *mSphere.* (2021) 6:e0065821. doi: 10.1128/mSphere.00658-21

20. Ishikawa H, Barber GN. The STING pathway and regulation of innate immune signaling in response to DNA pathogens. *Cell Mol Life Sci.* (2011) 68:1157–65. doi: 10.1007/s00018-010-0605-2

21. García-Belmonte R, Pérez-Núñez D, Pittau M, Richt JA, Revilla Y. African Swine Fever Virus Armenia/07 Virulent Strain Controls Interferon Beta Production through the cGAS-STING Pathway. *J Virol.* (2019) 93(12):e02298–18. doi: 10.1128/jvi.02298-18

22. Wang Y, Cui S, Xin T, Wang X, Yu H, Chen S, et al. African swine fever virus MGF360-14L negatively regulates type I interferon signaling by targeting IRF3. *Front Cell Infect Microbiol.* (2021) 11:818969. doi: 10.3389/fcimb.2021.818969

23. Cui S, Wang Y, Gao X, Xin T, Wang X, Yu H, et al. African swine fever virus M1249L protein antagonizes type I interferon production via suppressing phosphorylation of TBK1 and degrading IRF3. *Virus Res.* (2022) 319:198872. doi: 10.1016/j.virusres.2022.198872

24. Liu H, Zhu Z, Feng T, Ma Z, Xue Q, Wu P, et al. African swine fever virus E120R protein inhibits interferon beta production by interacting with IRF3 to block its activation. *J Virol.* (2021) 95:e0082421. doi: 10.1128/jvi.00824-21

25. Cui S, Wang Y, Chen S, Fang L, Jiang Y, Guo X, et al. African swine fever virus E120R inhibited Cgas-STING-mediated IFN-βand NF-κB pathways. *Anim Res One Health.* (2023) 2:1–11. doi: 10.1002/aro2.38

26. Wang X, Wu J, Wu Y, Chen H, Zhang S, Li J, et al. Inhibition of cGAS-STING-TBK1 signaling pathway by DP96R of ASFV China 2018/1. *Biochem Biophys Res Commun.* (2018) 506:437–43. doi: 10.1016/j.bbrc.2018.10.103

27. Yang K, Huang Q, Wang R, Zeng Y, Cheng M, Xue Y, et al. Corrigendum to "African swine fever virus MGF505-11R inhibits type I interferon production by negatively regulating the cGAS-STING-mediated signaling pathway. *Vet Microbiol.* (2023) 285:109723. doi: 10.1016/j.vetmic.2023.109723

28. O'Donnell V, Holinka LG, Sanford B, Krug PW, Carlson J, Pacheco JM, et al. African swine fever virus Georgia isolate harboring deletions of 9GL and MGF360/505 genes is highly attenuated in swine but does not confer protection against parental virus challenge. *Virus Res.* (2016) 221:8–14. doi: 10.1016/j.virusres.2016.05.014

29. O'Donnell V, Holinka LG, Gladue DP, Sanford B, Krug PW, Lu X, et al. African swine fever virus Georgia isolate harboring deletions of MGF360 and MGF505 genes is attenuated in swine and confers protection against challenge with virulent parental virus. *J Virol.* (2015) 89:6048–56. doi: 10.1128/jvi.00554-15

30. Li YH, Peng JL, Xu ZS, Xiong MG, Wu HN, Wang SY, et al. African swine fever virus cysteine protease pS273R inhibits type I interferon signaling by mediating STAT2 degradation. *J Virol.* (2023) 97:e0194222. doi: 10.1128/jvi.01942-22

31. Li S, Yang J, Zhu Y, Ji X, Wang K, Jiang S, et al. Chicken DNA sensing cGAS-STING signal pathway mediates broad spectrum antiviral functions. *Vaccines (Basel).* (2020) 8(3):369. doi: 10.3390/vaccines8030369

32. Ye G, Liu H, Liu X, Chen W, Li J, Zhao D, et al. African swine fever virus H240R protein inhibits the production of type I interferon through disrupting the oligomerization of STING. *J Virol.* (2023) 97:e0057723. doi: 10.1128/jvi.00577-23

33. Piret J, Boivin G. Innate immune response during herpes simplex virus encephalitis and development of immunomodulatory strategies. *Rev Med Virol.* (2015) 25:300–19. doi: 10.1002/rmv.1848

34. Wang D, Fang L, Luo R, Ye R, Fang Y, Xie L, et al. Foot-and-mouth disease virus leader proteinase inhibits dsRNA-induced type I interferon transcription by decreasing interferon regulatory factor 3/7 in protein levels. *Biochem Biophys Res Commun.* (2010) 399:72–8. doi: 10.1016/j.bbrc.2010.07.044

35. Xue Q, Liu H, Zhu Z, Yang F, Ma L, Cai X, et al. Seneca Valley Virus 3C(pro) abrogates the IRF3- and IRF7-mediated innate immune response by degrading IRF3 and IRF7. *Virology.* (2018) 518:1–7. doi: 10.1016/j.virol.2018.01.028

36. Kim JE, Kim YE, Stinski MF, Ahn JH, Song YJ. Human Cytomegalovirus IE2 86 kDa Protein Induces STING Degradation and Inhibits cGAMP-Mediated IFN-β Induction. *Front Microbiol.* (2017) 8:1854. doi: 10.3389/fmicb.2017.01854

37. Huang L, Xu W, Liu H, Xue M, Liu X, Zhang K, et al. Correction: African Swine Fever Virus pI215L Negatively Regulates cGAS-STING Signaling Pathway through Recruiting RNF138 to Inhibit K63-Linked Ubiquitination of TBK1. *J Immunol.* (2022) 208:1510–1. doi: 10.4049/jimmunol.2101201

38. Afonso CL, Piccone ME, Zaffuto KM, Neilan J, Kutish GF, Lu Z, et al. African swine fever virus multigene family 360 and 530 genes affect host interferon response. *J Virol.* (2004) 78:1858–64. doi: 10.1128/jvi.78.4.1858-1864.2004

39. Correia S, Ventura S, Parkhouse RM. Identification and utility of innate immune system evasion mechanisms of ASFV. *Virus Res*. (2013) 173:87–100. doi: 10.1016/j.virusres.2012.10.013

40. Reis AL, Abrams CC, Goatley LC, Netherton C, Chapman DG, Sanchez-Cordon P, et al. Deletion of African swine fever virus interferon inhibitors from the genome of a virulent isolate reduces virulence in domestic pigs and induces a protective response. *Vaccine*. (2016) 34:4698–705. doi: 10.1016/j.vaccine.2016.08.011

41. Li D, Yang W, Li L, Li P, Ma Z, Zhang J, et al. African swine fever virus MGF-505-7R negatively regulates cGAS-STING-mediated signaling pathway. *J Immunol*. (2021) 206:1844–57. doi: 10.4049/jimmunol.2001110

42. Canivet C, Rhéaume C, Lebel M, Piret J, Gosselin J, Boivin G. Both IRF3 and especially IRF7 play a key role to orchestrate an effective cerebral inflammatory response in a mouse model of herpes simplex virus encephalitis. *J Neurovirol*. (2018) 24:761–8. doi: 10.1007/s13365-018-0666-9

Frontiers in
Immunology

Explores novel approaches and diagnoses to treat immune disorders.

The official journal of the International Union of Immunological Societies (IUIS) and the most cited in its field, leading the way for research across basic, translational and clinical immunology.

Discover the latest Research Topics

See more →

Frontiers

Avenue du Tribunal-Fédéral 34
1005 Lausanne, Switzerland
frontiersin.org

Contact us

+41 (0)21 510 17 00
frontiersin.org/about/contact